JOTCS A
Journal of the Turkish Chemical Society Section: A Chemistry
Turkish Chemical Society

Cefoperazone metal complexes and their antimicrobial investigations

Mehmet Emin ÇINAR[1], Taner ERDOĞAN[2] and Ayşegül GÖLCÜ[1]*

[1]Istanbul Technical University, Faculty of Science and Letters, Department of Chemistry, Istanbul, Turkey
[2]Kocaeli Univ, Kocaeli Vocational School, Dept Chem & Chem Proc Technol, Kocaeli, Turkey.

Abstract: Transition metal (Cd(II), Co(II), Cu(II), Fe(III), Ni(II), Pd(II), Pt(II), Ru(III), Zn(II)) complexes of cefoperazone (CFP) were synthesized and their spectroscopic (IR, UV-Vis), magnetic, thermal (DTA-TG), and mass spectral investigations were conducted to characterize the metal-based complexes. Detailed insights into the electronic structures were provided by performing density functional theory (DFT) computations. Their antimicrobial studies were realized rendering their activities compared to that of the commercial cefoperazone.

Keywords: Cefoperazone, metal complexes, antimicrobial studies, computation.

Submitted: April 16, 2020. **Accepted:** January 14, 2021.

Cite this: Çınar M, Erdoğan T, Gölcü A. Cefoperazone metal complexes and their antimicrobial investigations. JOTCSA. 2021;8(1):375–90.

DOI: https://10.18596/jotcsa.721414.

***Corresponding author. E-mail:** aysgolcu@itu.edu.tr.

INTRODUCTION

Cephalosporins are in the group of ß-lactams and have been utilized since 1948 widely (1,2). All the cephalosporins were derived from 7-amino cephalosporinic acid. Incorporation of side chains altered both the anti-bacterial activity and the pharmacokinetic properties. They are categorized into five classes based on their antimicrobial activities. The new classes demonstrate greater activity against Gram-negative bacteria with respect to the earlier classes. Cephalosporins impede the synthesis of bacterial cell-wall. However, the presence of ß-lactamases can destruct the ß-lactam ring and hence deactivate cephalosporins (3). Cefoperazone is placed in a third class of cephalosporin antibiotics, including cefixime (CFX) and cefpodoxime (CPD) and more resistant to hydrolysis by the β-lactamases, with higher efficiency against gram negative and lower efficacy against gram positive. They also play important roles in treatment of infections, such as Pseudomonas bacterial, respiratory and urinary contagions. Cephalosporins form metal-based complexes via coordination of metal ions to electron donor units of Cephalosporins, which significantly affects chemical properties of antibiotics and hence their antimicrobial activities, toxicities, pharmacokinetics and resistance to hydrolysis (4). Some important works have been devoted to the synthesis and characterization of metal complexes (Fe(III), Co(II), Ni(II), Cu(II), Cd (II), Cr(III), Mn(II), Zn(II) and Hg(II)) of cefoperazone (3,5). Complexation behavior of cefoperazone was described in the literature to be both bidentate and tetradentate proposed in metal coordinated dimer complexes and in polymeric structure with the cefoperazone ligand bridging between metal centers (Figure 1). We report here the synthesis, characterization and antimicrobial investigations of cefoperazone metal complexes. To the best of our knowledge, there is no DFT level studies employed to elaborate experimental findings. In this work, computation was utilized to shed light on the intriguing properties of cefoperazone metal complexes.

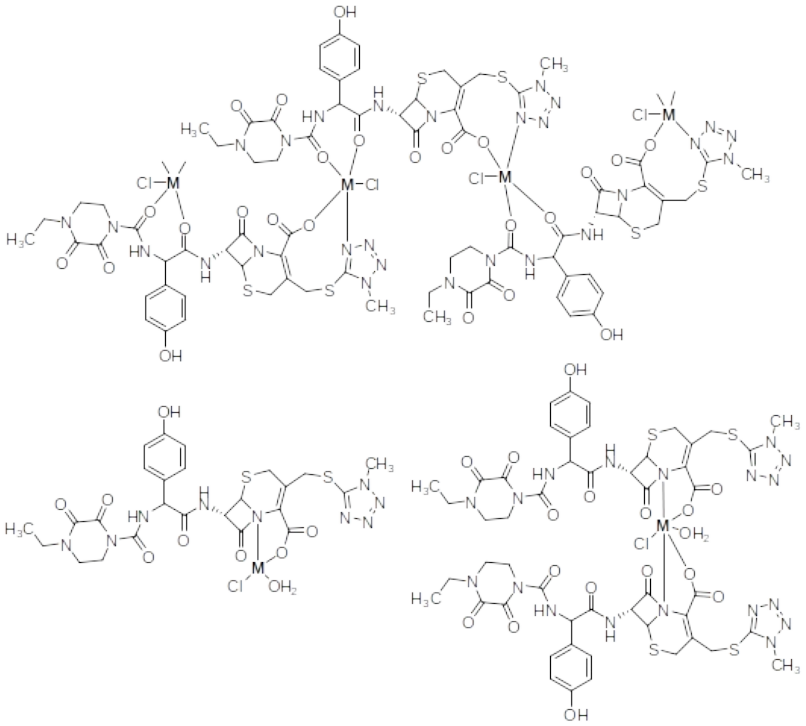

Figure 1. Reported cefoperazone metal complexes (3–5).

EXPERIMENTAL SECTION

Chemicals and apparatus

Cefoperazone sodium (CFP) and was supplied from Pfizer Pharm. Inc. (Istanbul, Turkey). EtOH, n-hexane, ACN, DEE, MeOH, acetone, $CuCl_2{\cdot}2H_2O$, $CoCl_2{\cdot}6H_2O$, $NiCl_2{\cdot}6H_2O$, $ZnCl_2{\cdot}2H_2O$, $CdCl_2$, $FeCl_3{\cdot}6H_2O$, $PtCl_2$ and $RuCl_3{\cdot}3H_2O$, NaOH, anhydrous Na_2SO_4, H_2SO_4 and HCl were purchased from Fluka (Darmstadt, Germany) and Merck (Darmstadt, Germany). All the chemicals and solvents were reagent grade and were used as purchased. All samples were prepared in spectrophotometric grade solvents.

Aluminum Thin layer chromatography (TLC) plates, silica gel coated with fluorescent indicator F254, were obtained from Merck (Darmstadt, Germany). Elemental analyses were performed using a LECO CHNS 932 elemental analyzer (TUBITAK instrumental analysis laboratory, Ankara, Turkey). Infrared spectra of the compounds were obtained using KBr pellets (4000-400 cm^{-1}) with a Shimadzu FTIR 8300 spectrometer. The UV-Vis spectra were obtained in the 200-1000 nm range by a PerkinElmer Lambda 45 spectrophotometer (Kahramanmaras Sutcu Imam University, Chemistry Department, Kahramanmaras¸ Turkey). Mass analyses of the metal-based compounds were performed under atmospheric pressure using chemical ionization method on an LC/MS-APCI Agilent 1100 MSD spectrometer (TUBITAK instrumental analysis laboratory, Ankara, Turkey and Central Research Laboratory of the Inonu University, Malatya, Turkey). ^{1}H NMR and ^{13}C NMR spectra were recorded on a Bruker Avence DPX-400 instrument. TMS was used as an internal standard and DMSO-d_6 as a solvent (TUBITAK instrumental analysis laboratory, Ankara, Turkey). The quantity of metal in the metal complexes was measured using Ati Unicam 929 Model AA Spectrometer, operating the parameters; Nebulizer flow: 0.8 L/min, auxiliary flow: 0.2 L/min, plasma flow: 1.7 L/min, Sample flow rate: 1.5 mL/min, equilibration time: 15 s, RF power: 1452 W (Kahramanmaras Sutcu Imam University, USKIM, Kahramanmaras¸ Turkey). Thermal analysis and stability of the metal complexes were realized under a nitrogen atmosphere at a heating rate 10 °C/min on a Pyris Diamond DTA/TG DSC Thermal System (Çanakkale 18 Mart University, University, Faculty of Arts and Sciences, Department of Chemistry, Çanakkale, Turkey). Magnetic susceptibility measurements were performed by applying the Gouy method involving $Hg[Co(SCN)_4]$ as a standard. Conductivity measurements were conducted on Toa Conductivity Meter 405 (DSİ, Kahramanmaras¸ Turkey). Melting points of the compounds were measured on Electrothermal 9200 and uncorrected. Molecular structures were drawn using ChemDraw software.

Synthesis

General procedure

For Cu(II), Co(II), Ni(II), Zn(II), Cd(II), Fe(III) and Ru(III) complexes: To a solution of 5.00 mL of deionized water and 20.0 mL of methanol in 100

mL two-necked round-bottomed flask was added CEFOBID (668 mg, 1 mmol). The solute was dissolved by heating the mixture up to reflux temperature on a magnetic stirrer. To the prepared solution was introduced 1 mmol of metal salt ($CuCl_2{\cdot}2H_2O$, $CoCl_2{\cdot}6H_2O$, $NiCl_2{\cdot}6H_2O$, $ZnCl_2{\cdot}2H_2O$, $CdCl_2$, $FeCl_3{\cdot}6H_2O$ and $RuCl_3{\cdot}3H_2O$) in 10 mL of methanol. Resulting mixture was refluxed for 24 h and the completion of reaction was checked by TLC. After that the mixture was filtered off and the solid residue was successively washed with deionized water, MeOH, and diethyl ether. The solid products were dried under vacuum. Newly synthesized cefoperazone metal-based complexes were characterized by spectroscopic methods.

[Cd(H_2O)(CFP)Cl]: Beige solid; m.p.: 193 °C. FTIR (KBr): ν_{max} 3450 (OH), 3252 (br. m.), 2980 (NH_2), 1667 (Amide C=O), 1607 (Acid M-OOC), 801 (M-N), 761 cm^{-1} (M-O). Anal. Calcd. (810.54): C, 37.05; H, 3.48; N, 15.55; Cd, 13.87. Found: C, 37.09; H, 3.53; N, 15.50; Cd, 13.90.

[Co(H_2O)(CFP)Cl]: Dark brown solid; m.p.: 213 °C. FTIR (KBr): ν_{max} 3486 (OH), 3386, 2984 (NH_2), 1661 (Amide C=O), 1610 (Acid M-OOC), 755 cm^{-1} (M-O). Anal. Calcd. (757.06): C, 39.66; H, 3.73; N, 16.65; Co, 7.78. Found: C, 39.70; H, 3.75; N, 16.63; Co, 7.85.

[Cu(H_2O)(CFP)Cl]: Brown solid; m.p.: 220 °C. FTIR (KBr): ν_{max} 3440 (OH), 3249, 3134 (NH_2), 1774 (Amide C=O), 1618 (Acid M-OOC), 751 cm^{-1} (M-O). Anal. Calcd. (761.67): C, 39.42; H, 3.71; N, 16.55; Cu, 8.34. Found: C, 39.40; H, 3.78; N, 16.65; Cu, 8.33.

[Fe(H_2O)$_2$(CFP)Cl_2]: Black solid; m.p.: 201 °C. FTIR (KBr): ν_{max} 3208 (br. s, OH), 2980 (NH_2), 1661 (Amide C=O), 1612 (Acid M-OOC), 805 (M-N), 761 cm^{-1} (M-O). Anal. Calcd. (807.44): C, 37.19; H, 3.74; N, 15.61; Fe, 6.92. Found: C, 37.20; H, 3.75; N, 15.60; Fe, 6.90.

[Ni(H_2O)(CFP)Cl]: Light brown solid; m.p.: 220 °C. FTIR (KBr): ν_{max} 3281 (br. s, OH), 2984 (NH_2), 1667 (Amide C=O), 1609 (Acid M-OOC), 761 cm^{-1} (M-O). Anal. Calcd. (756.82): C, 39.67; H, 3.73; N, 16.66; Ni, 7.76. Found: C, 39.70; H, 3.70; N, 16.70; Ni, 7.71.

[Ru(H_2O)$_2$(CFP)Cl_2]: Black solid; m.p.: 305 °C. FTIR (KBr): ν_{max} 3205 (br. s, OH), 2980 (NH2), 1657 (Amide C=O), 1617 (Acid M-OOC), 822 (M-N), 763 cm^{-1} (M-O). Anal. Calcd. (852.67): C, 35.22; H, 3.55; N, 14.78; Ru, 11.85. Found: C, 35.25; H, 3.55; N, 14.80; Ru, 11.80.

[Zn(H_2O)(CFP)Cl]: Beige solid; m.p.: 181 °C. FTIR (KBr): ν_{max} 3440 (br. m, OH), 3281, 2944 (NH2), 1667 (Amide C=O), 1597 (Acid M-OOC), 779 (M-N), 760 cm^{-1} (M-O). Anal. Calcd. (763.54): C, 39.33; H, 3.70; N, 16.51; Zn, 8.57. Found: C, 39.30; H, 3.71; N, 16.54; Zn, 8.53.

Pt(II) complex of cefoperazone

CEFOBID (668 mg, 1 mmol) was dissolved in 1.00 mL of deionized water and 20.0 mL of ethanol in 100 mL two-necked round-bottomed flask by heating the reaction mixture up to reflux temperature on a magnetic stirrer. To the prepared solution was introduced $PtCl_2$ (266 mg, 1 mmol) in 2.00 mL of DMSO. Resulting mixture was refluxed for 8 h and the completion of reaction was checked by TLC. After that the mixture was filtered off and the solid residue was successively washed with deionized water, MeOH, and diethyl ether. The product was dried under vacuum.

[Pt(H_2O)(CFP)Cl]: Brown solid; m.p.: 119 °C. FTIR (KBr): ν_{max} 3446 (br. s, OH), 3243, 3010 (NH_2), 1676 (Amide C=O), 1626 (Acid M-OOC), 778 (M-N), 718 cm^{-1} (M-O). Anal. Calcd. (893.21): C, 33.62; H, 3.16; N, 14.11; Pt, 21.84. Found: C, 33.60; H, 3.15; N, 14.10; Pt, 21.89.

Pd(II) complex of cefoperazone

To a solution of $Pd(CH_3COOH)_2$ (325 mg, 1 mmol) in 20.0 mL of acetic acid was added of CEFOBID (668 mg, 1 mmol). Resulting mixture was stirred at 40 °C for 8 h. After that the mixture was filtered off and the solid residue was successively washed with deionized water, MeOH, and diethyl ether. The product was dried under vacuum.

[Pd(H_2O)(CFP)(OAc)]: Brown solid; m.p.: > 300 °C. FTIR (KBr): ν_{max} 3201 (br. s., OH), 3059 (NH_2), 1763 (Amide C=O), 1587 (Acid M-OOC), 825 (M-N), 755 cm^{-1} (M-O). Anal. Calcd. (828.14): C, 39.16; H, 3.77; N, 15.22; Pd, 12.85. Found: C, 39.15; H, 3.80; N, 15.18; Pd, 12.81.

Computational details

Geometry optimizations, frequency analyses, molecular electrostatic potential map (MEP), and frontier molecular orbital (FMO) calculations were performed at DFT B3LYP (Becke, 3-parameter, Lee–Yang–Parr) level of theory using 6-31+G(d,p) basis set as implemented in Gaussian 09 Rev.D.01 package (6) owing to the good performance of the functional in the prediction of geometries (7,8). A scaling factor of 0.9632 suggested by Irikura et al. was applied to calculate the spectra of both cefoperazone and its sodium salt (9). The visualization and analysis of electronic wavefunctions were realized with GaussView5 (10), Avogadro 1.1.1 (11), Multiwfn (12) and GaussSum 3.0 (13) softwares. The minima of the investigated compounds were verified by analyzing the harmonic vibrational frequencies using analytical second derivatives, which have NIMAG=0. Incorporation of the solvent effects was realized by using self-consistent reaction field with the integral equation formalism of the Polarizable Continuum

Model (IEFPCM) (14,15,16) as implemented in Gaussian 09 package. DMSO (ε = 46.826) was selected as a solvent to mimic the UV-Vis measurement conditions. TD–DFT B3LYP/6-31+G(d,p) calculations including solvent effects (DMSO) were applied to obtain vertical excitations.

Antimicrobial studies

The in-vitro investigation of antimicrobial activity of the metal-based complexes of was performed using *Candida albicans* (fungus), *Staphylococcus aureus 65383*, *Escherichia coli ATCC 298925*, *Klebsiella pneumoniae FMC 5*, *Bacillus megaterium DSM 32*, *Kluvyeromyces fragilis A 230*, *Mycobacterium smegmatis CCM 2067*, *Bacillus cereus EÜ 2630*, *Pseudomonas aeruginosa 9027*, *Enterococcus cloacea ATCC 13047*, *Micrococcus luteus LA 2971*, and *Saccharomyces cerevisiae WET 136* (fungus), using agar well diffusion method. Bacterial strains and fungi were incubated at 37± 0.1 °C in nutrient agar medium and at 25± 0.1 °C in dextrose, respectively, for 24 h. 100 µL of these solutions were taken into Petri dishes (9 cm). Later, Müller Hinton and dextrose agars, sterilized in one balloon and cooled down to 45–50 °C, were portioned to 15 mL of sterilized Petri dishes homogenously. In addition to these Petri dishes, 500 µg of synthesized compounds was added to 6 mL of sterilized test plates. These prepared test plates were introduced to agars. Diameters of inhibition zones, indicating the activity of compounds, were recorded (17).

RESULTS AND DISCUSSION

Synthesis and Characterization

Cefoperazone-metal-based complexes were achieved by refluxing the reaction mixture containing 1 mmol of CFP, dissolved in 25 mL of H_2O/MeOH (1:4, v/v), and 1 mmol of corresponding metal chloride salts ($CuCl_2{\cdot}2H_2O$, $CoCl_2{\cdot}6H_2O$, $NiCl_2{\cdot}6H_2O$, $ZnCl_2{\cdot}2H_2O$, $CdCl_2$, $FeCl_3{\cdot}6H_2O$ and $RuCl_3{\cdot}3H_2O$) in 10 mL of MeOH for 24 h in moderate to good yields (50 - 70%). In case of Pt(II) complex, $PtCl_2$ was dissolved in 2 mL of dimethyl sulfoxide (DMSO) and the resulting solution was refluxed for 8 h rendering the target Pt(II)-based complex in 59% yield. Moreover, synthesis of Pd(II) complex was realized by considering $Pd(OAc)_2$ salt dissolved in 20 mL of AcOH. The mixture was heated up to 40 °C for 8 h to provide the required Pd(II) complex in 57% yield.

IR spectroscopic characterization of all the synthesized metal based complexes involves analysis of the vibrational modes attributed to the coordination of functional units to metal centers owing to the similarity of the IR spectrum of cefoperazone to those of its complexes. Vibrational frequency of the ring carbonyl unit shifts to higher wave numbers as a result of increase in strain of the ring. Therefore, the lactam and the 2,3-piperazinedione carbonyl vibrations show up around 1710 and 1650 cm^{-1}, respectively, in the spectra of cefoperazone and its metal-based complexes (18). The amide carbonyl band of cefoperazone is at 1756 cm^{-1} while metal complexation shifted the corresponding vibrational bands to lower wavenumbers at around 1670 cm^{-1} indicative of coordination of metal to oxygen (19). On the other side, second amide carbonyl band appears in higher frequencies indicating lack of contribution of the nitrogen atom to the coordination (20). As a result, IR spectroscopic analyses depict the coordination of metals to cefoperazone ligand via oxygens of the amide carbonyl groups. The lactam and piperazinedione carbonyl groups demonstrated the absence of any significant shift of vibrational bands in metal coordination illustrating the lack of coordination with lactam and piperazinedione carbonyl units. The stretching vibrations of metal nitrogen bond in the range of 778-825 cm^{-1} supports the coordination of tetrazole unit to the metal ion via the nitrogen atom except than the Co(II), Cu(II) and Ni(II) complexes. Moreover, the N–H stretching vibrations of amide groups in cefoperazone appear at 3286 cm^{-1}, which slightly shifted in the metal based complexes pointing out the non-coordinated free units (5,21). According to analyses of vibrational frequencies, metal coordination involves one tetrazole nitrogen, two amide oxygens and one carboxylate oxygen of cefoperazone, that is, cefoperazone is a tetradentate chelating agent in metal complexes excluding Co(II), Cu(II) and Ni(II) complexes (Figure 3 and Figure 5). Unlike the other metals, Cu and Ni do not coordinate to nitrogen of tetrazole ring in a tetrahedral structure (3), in which cefoperazone behaves as tridentate chelating agent.

Thermal analyses of metal-based complexes demonstrated endothermic decompositions at around 100 °C indicating the loss of water from complexes in the case of Ru(III) (4%) and Pt(II) (4%) complexes, and the loss of water and Cl- anions together with one of the tetrazole units (13%) from Ni(II) complex owing to the free conformation of tetrazole units. The loss of the second tetrazole was observed at around 175 °C. They moreover depicted the stability of the complexes up to 160 and 200 °C for Ru(III) and Pt(II) complexes, respectively (Figure 2).

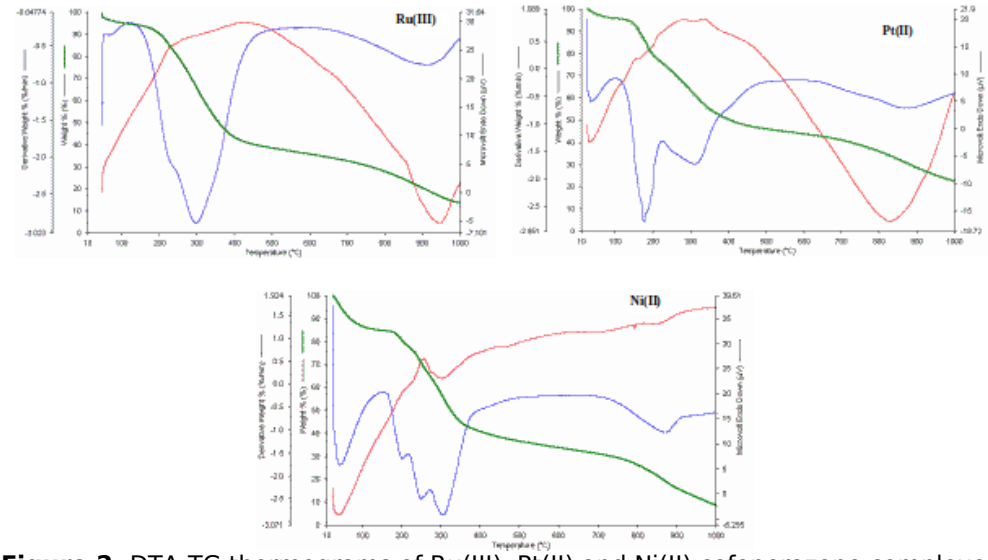

Figure 2. DTA-TG thermograms of Ru(III), Pt(II) and Ni(II) cefoperazone complexes.

Conductivity measurements realized in $1x10^{-3}$ M of DMSO at room temperature resulted in that the solutions of all the complexes are non-electrolytes, involving the coordination of chloride ion to the metal center, except than Co(II), Cu(II) and Ni(II) complexes which have conductivities (Λ) of 211, 161 and 167 Ω^{-1} cm^2 mol^{-1}. The obtained magnetic moments (μ_{eff}) indicate high spin ions in octahedral fields Fe(III) complex has a magnetic moment of 5.30 B.M. which is well in alignment with high spin d^5 system possessing five unpaired electrons. μ_{eff} value of Co(II) complex was measured to be 4.26 B.M. suggesting Co(II) in five or six coordinate geometry with a high spin configuration. μ_{eff} value of Cu(II) complex was recorded as 1.83 B.M., matching well with the calculated magnetic moment of 1.73 B.M. for a d^9 configuration (5). Ru(III) shows a low-spin octahedral geometry and its magnetic moment was measured to be 1.85 B.M.

The Job-Plot constructed performing three independent titrations of Fe(III) cation with cefoperazone anion indicated that the molar ratio of Fe(III) and CFP is 1, indicative of 1:1 complex formation (Figure 4).

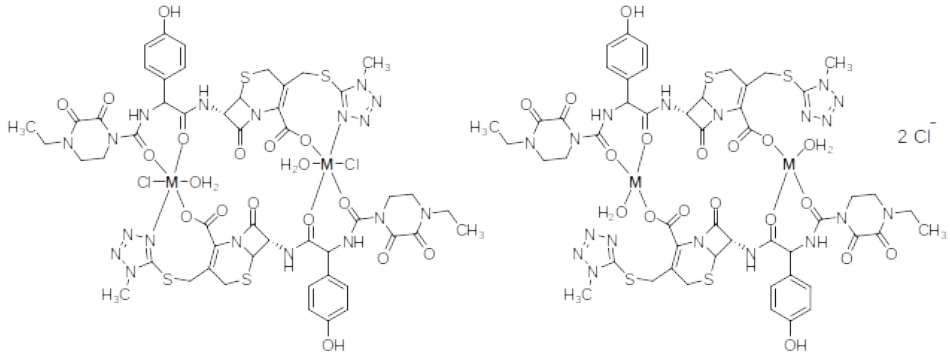

Figure 3. Octahedral metal(II) complexes of cefoperazone apart from Co(II), Cu(II) and Ni(II) having lack of coordination to tetrazole nitrogen in tetrahedral structure accompanied by chloride anion.

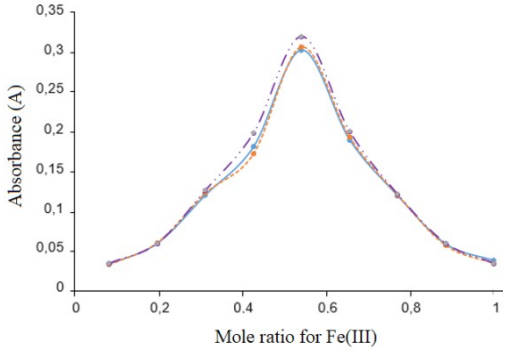

Figure 4. Job plot constructed using results from three independent titrations of Fe(III) cation with cefoperazone anion.

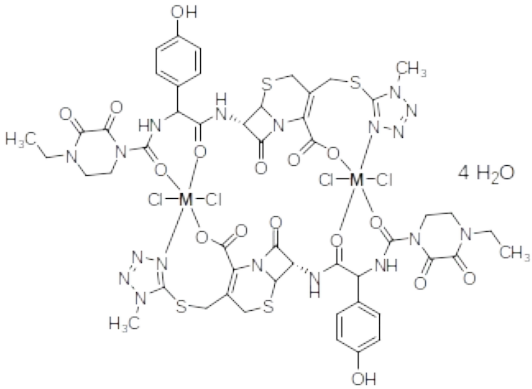

Figure 5. Fe(III) and Ru(III) complexes of cefoperazone.

Optical investigations

Optical properties of the cefoperazone and its metal-based complexes were investigated in $1x10^{-4}$ M solution of DMSO, rendering absorption maxima between 250-270 nm attributed to a π→π* transition emerging from the NC–S moiety (22). While the absorption bands of tetrazole units were detected at 290-320 nm and assigned to the π→π* electronic transitions, the recorded UV-Vis bands at around 370 nm originated from sulfur atoms and characterized as the n→π* type electronic transitions (23). The almost unsaturated structure of cefoperazone results in the intense UV absorption accompanied by a tail in the visible region, which impedes detection of the relatively week d-d electronic transitions of the cobalt(II) and iron(II) ions. The Co(II) complex demonstrated a broad absorption band at 625 nm assigned to a d-d electronic transition. Pt(II), Pd(II) and Cd(II) cefoperazone complexes had the smallest λ_{max} values of 315, 345 and 374 nm, respectively, whereas the absorption maxima of Zn(II), Ru(III), Co(II) and Fe(III) CFP complexes were detected between 528 and 671 nm. The highest λ_{max} values were recorded for complexes of Cu(II) as 730 nm and Ni(II) as 853 nm.

Computation

The optimized geometries and vibrational spectra of cefoperazone and cefoperazone sodium at B3LYP level are given in Figure 6. The predicted vibrational spectrum of the sodium salt is well in alignment with the experimentally recorded spectrum (24). The estimated vibrations are listed as; 3685 (phenolic -OH stretching), 3491 (-NH stretching adjacent to lactam), 3371 cm^{-1} (-NH stretching proximate to piperazinedione), 1723 (C=O stretching in lactam), 1706 and 1697 (C=O stretching in piperazinedione), 1583 (C=O stretching of COO-) and 1494 and 1487 cm^{-1} (bending of -NH groups).

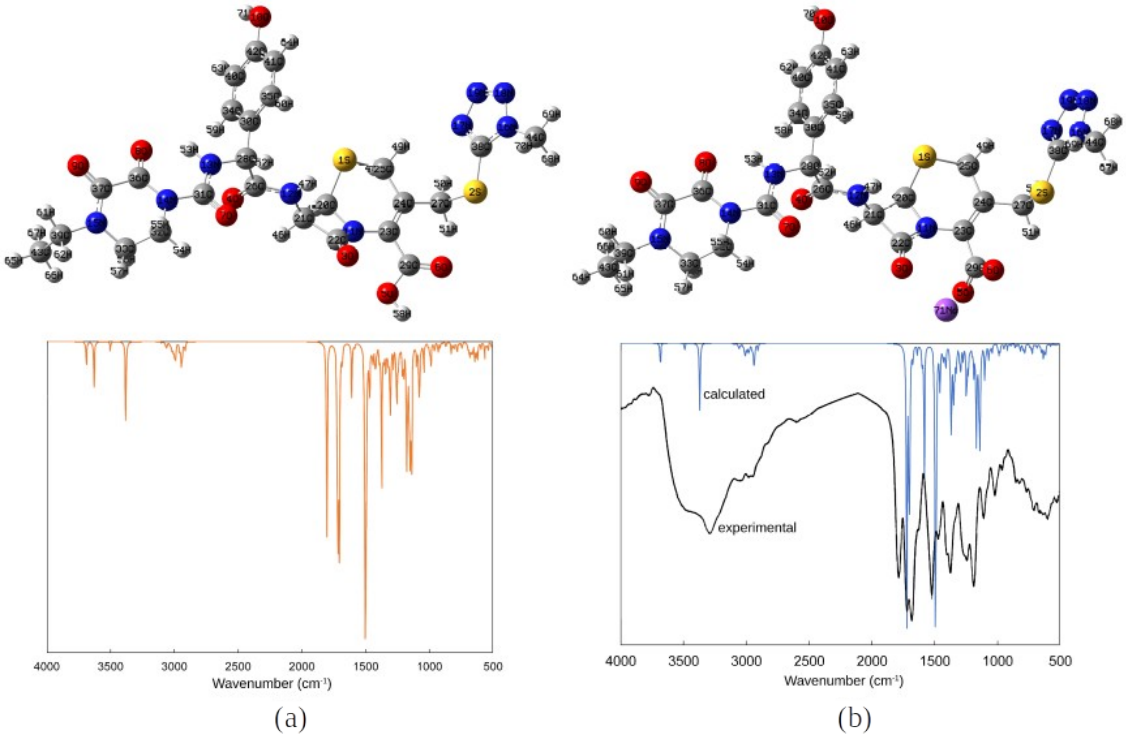

Figure 6. Optimized structures and vibrational spectra of (a) cefoperazone and (b) cefoperazone sodium at B3LYP/6-31+G(d,p) level.

Molecular Electrostatic Potential (MEP) maps illustrate the charge distributions of molecules and give information about the electron rich and electron deficient parts of the investigated molecules. MEP maps of cefoperazone and cefoperazone sodium obtained at the same level of theory are depicted in Figure 7. For both cefoperazone and cefoperazone sodium, it was observed that negative charges were mainly located on the carbonyl oxygens in both calculated molecules, whereas the positive charge was exclusively found on the sodium atom.

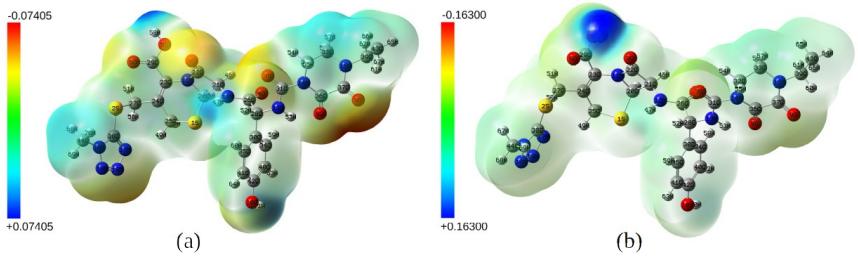

Figure 7. MEP maps of cefoperazone (a) and cefoperazone sodium (b).

Frontier molecular orbitals (FMO) of cefoperazone and cefoperazone sodium, and the predicted HOMO-LUMO gaps are demonstrated in Figure 8. The estimated HOMO-LUMO gap of cefoperazone sodium is slightly larger than that of cefoperazone by 0.12 eV emerging from the destabilization of the FMO by sodium cation. Destabilization significantly reflected to the LUMO of salt results in higher laying HOMO and LUMO with energies of -6.48 and -2.06 eV compared to those of cefoperazone with -6.56 and -2.27 eV, respectively. Hence, HOMO-LUMO gap increases in sodium salt. While HOMO is mainly located on phenol unit in cefoperazone, LUMO is observed on lactam and COO^- substituted six-membered ring. However, HOMO is lying on the sodium coordinated fragment spreading over the tetrazole unit of cefoperazone salt and LUMO is mainly on piperazinedione group with a small contribution of the adjacent amide unit.

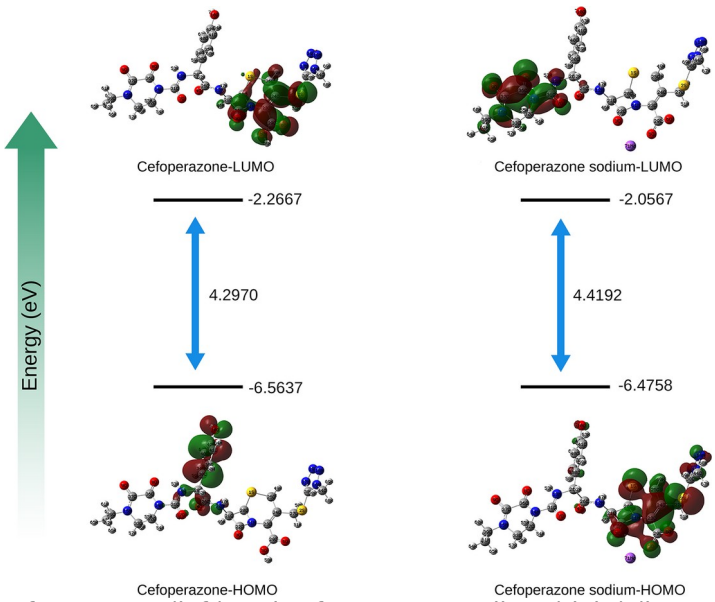

Figure 8. FMOs of cefoperazone (left) and cefoperazone sodium (right) (isosurface values= 0.02).

The vertical excitation energies and UV-Vis spectra, predicted from the time-dependent DFT calculations by incorporation of solvent effect (DMSO), are given in Table 1 and Figure 9, respectively. The calculated spectral properties of cefoperazone and cefoperazone sodium are in good agreement with the recorded absorption values. Coordination of Na^+ led to the bathochromic shift from 285 to 294 nm. The λ_{max} values of cefoperazone and cefoperazone sodium arise from the HOMO-3→LUMO (83%) and HOMO→LUMO+1 (99%) transitions, respectively.

Table 1. Excited state electronic transitions obtained from (IEFPCM:DMSO)−TD-B3LYP/6-31+G(d,p) level computations (H: HOMO, L: LUMO, F: Oscillatory strength).

Compound	λ_{abs} (nm)	Energy (eV)	*F*	Major contribution (%)
Cefoperazone	285	4.35	0.213	H-3→L (83)
	309	4.01	0.036	H-2→L (85); H-2→L (85)
	331	3.74	0.049	H-1→L (90)
Cefoperazone Sodium	294	4.22	0.129	H→L+1 (99); H-4→L+1 (19); H-2→L+1 (12)
	298	4.16	0.014	H-2→L+1 (47); H→L (37); H→L+1 (10)
	299	4.15	0.024	H→L (56); H-2→L+1 (27); H→L+1 (11)

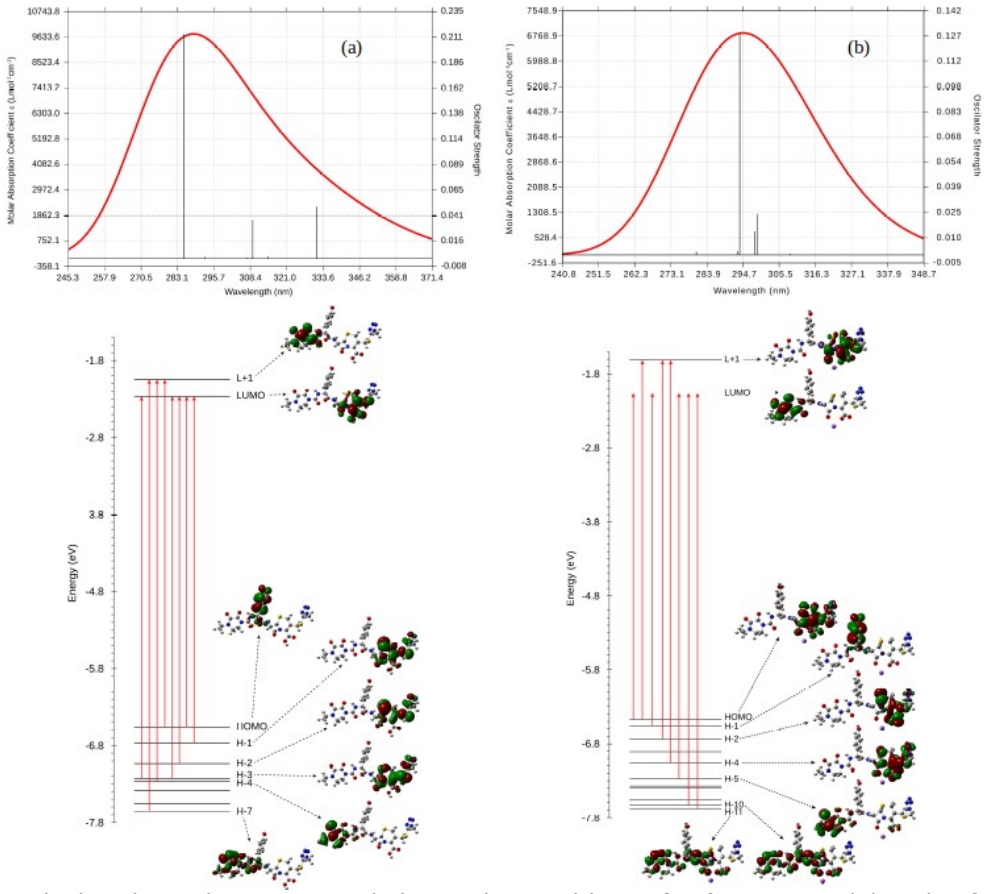

Figure 9. Calculated UV-Vis Spectra and electronic transitions of cefoperazone (a) and cefoperazone sodium (b).

Antimicrobial studies

The susceptibility of some bacteria and fungi against cefoperazone and its metal-based complexes was corroborated by measuring the diameter of inhibition. Cefoperazone and its complexes gave rise to the bactericide diameters of larger than 20 mm indicative of a good activity (25,26). The results are listed in Table 2, depicting different behavior of the metal-based complexes with respect to cefoperazone.

Table 2. Antibacterial activity of cefoperazone and its metal-based complexes against some bacteria and fungi.

Compound	**1**	**2**	**3**	**4**	**5**	**6**	**7**	**8**	**9**	**10**	**11**	**12**
CFP	9	5	8	10	7	9	4	-	-	-	-	7
$[Cd(H_2O)(CFP)Cl]$	38	35	34	12	7	35	8	8	7	7	14	9
$[Co(H_2O)(CFP)Cl]$	30	34	30	8	8	29	15	9	-	10	-	28
$[Cu(H_2O)(CFP)Cl]$	23	20	22	8	12	25	14	11	-	11	7	19
$[Fe(H_2O)_2(CFP)Cl_2]$	20	15	20	-	7	33	16	11	16	9	-	36
$[Ni(H_2O)(CFP)Cl]$	15	16	20	8	10	30	10	12	7	10	-	24
$[Pt(H_2O)(CFP)Cl]$	14	10	17	13	19	16	12	20	7	12	-	17
$[Pt(H_2O)(CFP)Cl]$	21	18	21	26	20	30	25	20	24	8	12	20
$[Ru(H_2O)_2(CFP)Cl_2]$	25	14	20	23	14	23	16	15	20	15	14	24
$[Zn(H_2O)(CFP)Cl]$	23	35	34	7	8	24	22	13	19	12	-	37

Bacteria and fungi: 1) *Candida albicans* (fungus), 2) *Staphylococcus aureus* 65383, 3) *Escherichia coli ATCC 298925*, 4) *Klebsiella pneumoniae FMC 5*, 5) *Bacillus megaterium DSM 32*, 6) *Kluvyeromyces fragilis A 230*, 7) *Mycobacterium smegmatis CCM 2067*, 8) *Bacillus cereus EÜ 2630*, 9) *Pseudomonas aeruginosa 9027*, 10) *Enterococcus cloacea ATCC 13047*, 11) *Micrococcus luteus LA 2971*, 12) *Saccharomyces cerevisiae WET 136* (fungus).

While all metal complexes excluding Pd(II) demonstrated good activity against *Escherichia coli ATCC 298925* and *Kluvyeromyces fragilis A 230*, none of the compounds rendered good bactericidal

activity against *Bacillus megaterium DSM 32*, *Enterococcus cloacea ATCC 13047,* and *Micrococcus luteus LA 2971*. Co(II), Cu(II), Fe(III), Ni(II), Zn(II) demonstrated to be less active than free cefoperazone against *Klebsiella pneumoniae FMC 5*. The highest antibacterial activity was recorded by Cd(II) against *Candida albicans*, and Fe(III) and Zn(II) against *Saccharomyces cerevisiae WET 136*.

CONCLUSION

Metal-based cefoperazones characterized to have 1:1 metal to antibiotic stoichiometry were synthesized and their spectroscopic analyses were performed. Their antimicrobial investigations illustrated good activities of all the metal complexes excluding Pd(II) against *Escherichia coli ATCC 298925* and *Kluvyeromyces fragilis A 230*. The highest antibacterial activities were observed by Cd(II) against *Candida albicans*, and Fe(III) and Zn(II) against *Saccharomyces cerevisiae WET 136*. DFT computations were conducted to shed light on the electronic structure of cefoperazone and its sodium salt. Detailed analyses of the predicted results helped us get a glimpse of metal based cefoperazone complexes. Based on the results, it is stated that character of metal ion and of microorganism play important roles in efficiency of antibacterial activities.

ACKNOWLEDGEMENTS

The authors wish to thank TUBITAK (Project No: 105T371) for the financial support; Kahramanmaras Sutcu Imam University, Chemistry Department for laboratory environments; and Kahramanmaras Sutcu Imam University, Biology Department for cell culture studies. We thank the Istanbul Technical University for the laboratory (L105) facilities to redo the experiments. We are indebted to the Kocaeli University for the computer time provided.

SUPPLEMENTARY INFORMATION

IR spectra of cefoperazone and its metal-based complexes.

REFERENCES

1. Badr IHA, Saleh GA, Sayed SM, Nour El-Deen DAM. A Novel Membrane Sensor for Batch and Flow Injection Potentiometric Determination of Cefazolin Sodium in Pharmaceutical Preparations. Int. J. Electrochem. Sci. 2014;9:1621-36.

2. Percin-Ozkorucuklu S, Uka B, Yildirim-Bastemur G. Voltammetric analysis of cephalexin and cefazolin in pharmaceutical formulations and biological samples. Journal of the Turkish Chemical Society, Section A: Chemistry. 2019;6:217-24.

3. Masoud MS, Ali AE, Elasala GS, Kolkaila SA. Spectroscopic Studies and Thermal Analysis on Cefoperazone Metal Complexes. J. Chem. Pharm. Res. 2017;9:171-9.

4. Alekseev VG. Metal complexes of penicillins and cephalosporins. Pharm. Chem. J. 2012;45:679-97.

5. Anacona JR, Bravo A, Lopez ME. Cefoperazone metal complexes: synthesis and characterization. J. Chil. Chem. Soc. 2013;58:1520-3.

6. Frisch MJ, Trucks GW, Schlegel HB, Scuseria GE, Robb MA, Cheeseman JR, Scalmani G, Barone V, Petersson GA, Nakatsuji H, Li X, Caricato M, Marenich AV, Bloino J, Janesko BG, Gomperts R, Mennucci B, Hratchian HP, Ortiz JV, Izmaylov AF, Sonnenberg JL, Williams-Young D, Ding F, Lipparini F, Egidi F, Goings J, Peng B, Petrone A, Henderson T, Ranasinghe D, Zakrzewski VG, Gao J, Rega N, Zheng G, Liang W, Hada M, Ehara M, Toyota K, Fukuda R, Hasegawa J, Ishida M, Nakajima T, Honda Y, Kitao O, Nakai H, Vreven T, Throssell K, Montgomery JA Jr, Peralta JE, Ogliaro F, Bearpark MJ, Heyd JJ, Brothers EN, Kudin KN, Staroverov VN, Keith TA, Kobayashi R, Normand J, Raghavachari K, Rendell AP, Burant JC, Iyengar SS, Tomasi J, Cossi M, Millam JM, Klene M, Adamo C, Cammi R, Ochterski JW, Martin RL, Morokuma K, Farkas O, Foresman JB, Fox DJ. Gaussian 09, Rev.D.01, Gaussian, Inc., Wallingford CT, 2013.

7. Ceylan BI.Oxovanadium(IV)-containing N2O2 chelate complex; crystal structure determination and DFT. Journal of the Turkish Chemical Society, Section A: Chemistry. 2016;3:393-402.

8. Akdemir N. Synthesis, characterization, and investigation of the spectroscopic properties of novel peripherally 2,3,5-trimethylphenoxy substituted Cu and Co phthalocyanines, computational and experimental studies of 4-(2,3,5-trimethylphenoxy)phthalonitrile. Journal of the Turkish Chemical Society, Section A: Chemistry. 2016;3:683-706.

9. Irikura KK, Johnson RD, Kacker RN. Uncertainties in scaling factors for ab initio vibrational frequencies. J. Phys. Chem. A. 2005;109:8430-37.

10. Dennington R, Keith T, Millam J. GaussView, Version 5. 2009, Semichem Inc.: Shawnee Mission, KS.

11. Hanwell MD, Curtis DE, Lonie DC, Vandermeersch T, Zurek E, Hutchison GRJ. Avogadro: an advanced semantic chemical editor, visualization, and analysis platform. Cheminformatics. 2012;4:1-17.

12. Lu T, Chen F. Multiwfn: A multifunctional wavefunction analyzer. J. Comput. Chem. 2012;33:580-92.

13. O'Boyle NM, Tenderholt AL, Langner KM. cclib: A library for package–independent computational chemistry algorithms. J. Comp. Chem. 2008;29:839-45.

14. Cancès E, Mennucci B, Tomasi J. A new integral equation formalism for the polarizable continuum model: Theoretical background and applications to isotropic and anisotropic dielectrics. J. Chem. Phys. 1997;107:3032-41.

15. Cancès E, Mennucci B. New applications of integral equations methods for solvation continuum models: ionic solutions and liquid crystals. J. Math. Chem. 1998;23:309-26.

16. Mennucci B, Cancès E, Tomasi J. Evaluation of Solvent Effects in Isotropic and Anisotropic Dielectrics and in Ionic Solutions with a Unified Integral Equation Method: Theoretical Bases, Computational Implementation, and Numerical Applications. J. Phys. Chem. B. 1997;101:10506-17.

17. Anacona J, Silva GD. Synthesis and antibacterial activity of cefotaxime metal complexes. J. Chil. Chem. Soc. 2005;50:447-50.

18. Fuliaş A, Bobric A, Vlase G, Vlase T, Doca N. Thermal stability and biological interactions. of some cephalosporins. Rev. Roum. Chim. 2011;56:959-66.

19. Barnes DJ, Chapman RL, Stephens FS, Vagg RS. Studies on the metal-amide bond. VII. Metal complexes of the flexible N4 ligand N,N′-bis(2′-pyridinecarboxamide)1,2-ethane. Inorg. Chim. Acta. 1981;51:155-62.

20. Garg BS, Bhojak N, Dwivedi P, Kumar V. Copper(II) complexes of acid amide derivatives of 2-aminopyridineand an exogenous ligand. Transit. Metal. Chem. 1999;24: 463-6.

21. Anacona JR, Bravo A, Lopez ME, Antibacterial Activity of Cefoperazone Metal Complexes. Lat. Am. J. Pharm. 2012;31:27-31.

22. Franchini GC, Giusti A, Preti C, Tosi L, Zannini P. Coordinating ability of methylpiperidine dithiocarbamates towards platinum group metals. Polyhedron, 1985, 9, 1553-1558.

23. Castillo M, Criado JJ, Macias B, Vaquero MV. Chemistry of dithiocarbamate derivatives of amino acids. I. Study of some dithiocarbamate derivatives of linear α-amino acids and their nickel(II) complexes. Inorg. Chim. Acta. 1986;124:127-32.

24. El-Aziz AOA, El-Dars FM, Radowan AA. Novel all-solid contact Copper (II) - selective sensor based on Cefoperazone and poly(3,4-ethylenedioxythiophene) (PEDOT) as conducting polymer. Journal of Inventions in Biomedical and Pharmaceutical Sciences (JIBPS). 2016;1:24-31.

25. Shungu, DL, Tutlane V, Gadebusch HH. Multicenter evaluation of the proposed quality control limits and interpretive zone standards for in vitro susceptibility testing with norfloxacin. J. Clin. Microbiol. 1983;18:988-91.

26. Shungu DL, Weinberg E, Gadebusch, HH. Tentative interpretive standards for disk diffusion susceptibility testing with norfloxacin (MK-0366, AM-715). Antimicrob. Agents Chemother. 1983;23:256-60.

Supplementary Information

Investigation of cefoperazone metal complexes: an experimental and computational study

Mehmet Emin Çınar[1], Taner Erdoğan[2] and Ayşegül Gölcü[1,*]
[1]Department of Chemistry, Faculty of Science and Letters, Istanbul Technical University, Istanbul, Turkey
[2]Kocaeli Univ, Kocaeli Vocat Sch, Dept Chem & Chem Proc Technol, Kocaeli, Turkey.
*Correspondence: aysgolcu@itu.edu.tr

IR spectra of cefoperazone and its metal complexes

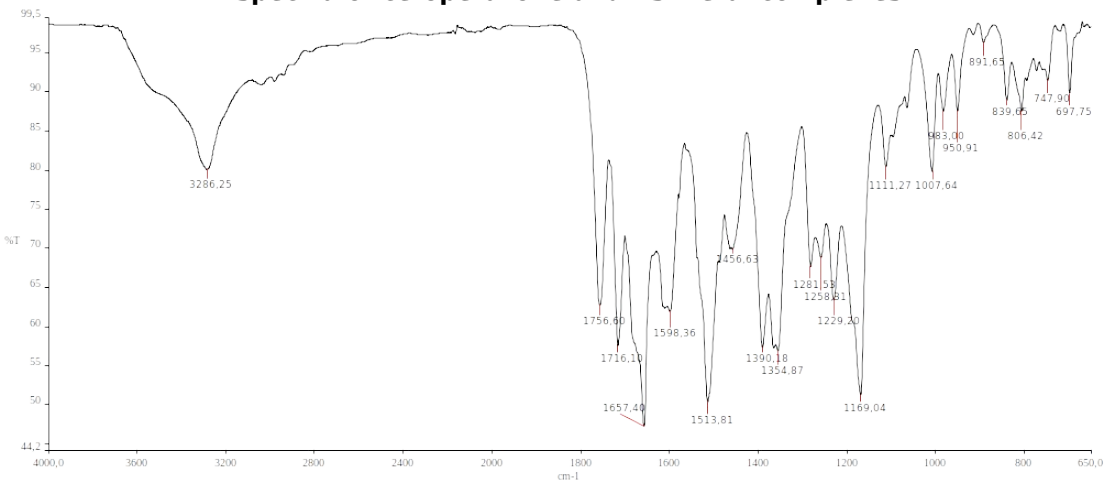

Figure S1. IR spectrum of **cefoperazone**.

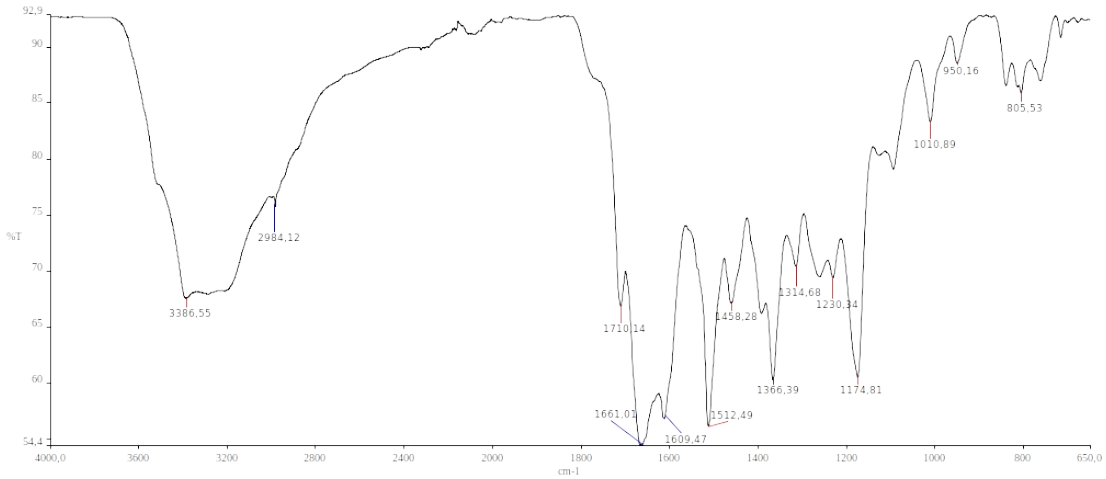

Figure S2. IR spectrum of **Cu(II)-cefoperazone complex**.

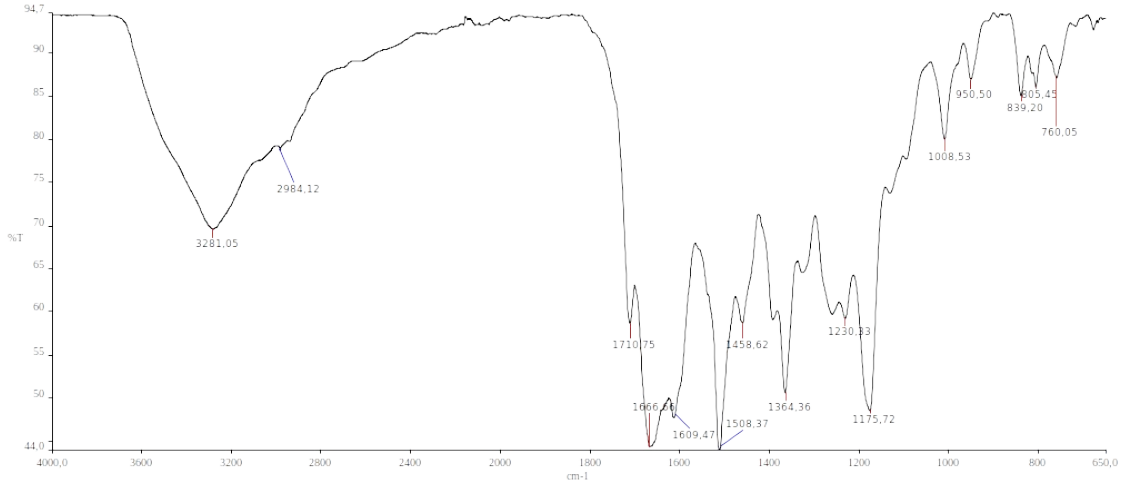

Figure S3. IR spectrum of **Co(II)-cefoperazone** complex.

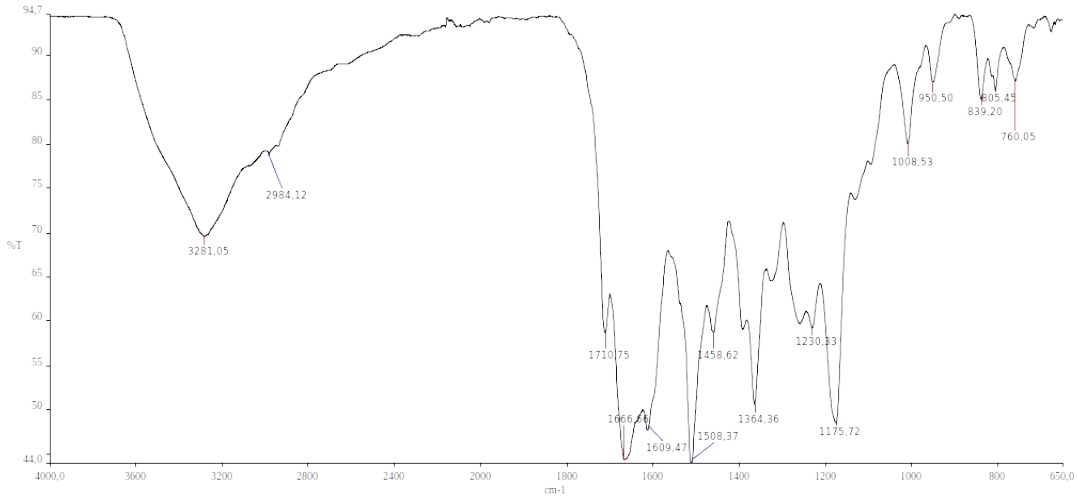

Figure S4. IR spectrum of **Ni(II)-cefoperazone** complex.

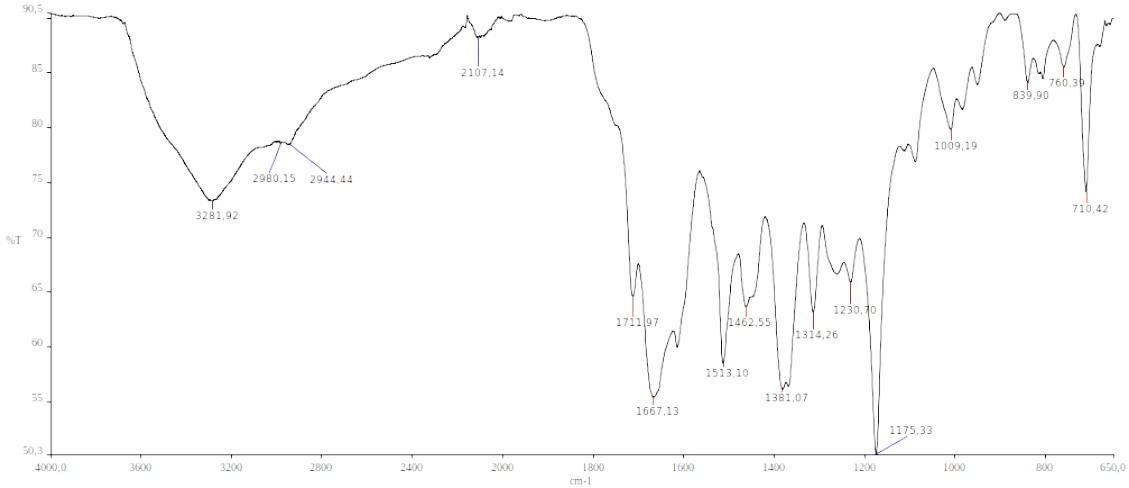

Figure S5. IR spectrum of **Zn(II)-cefoperazone** complex.

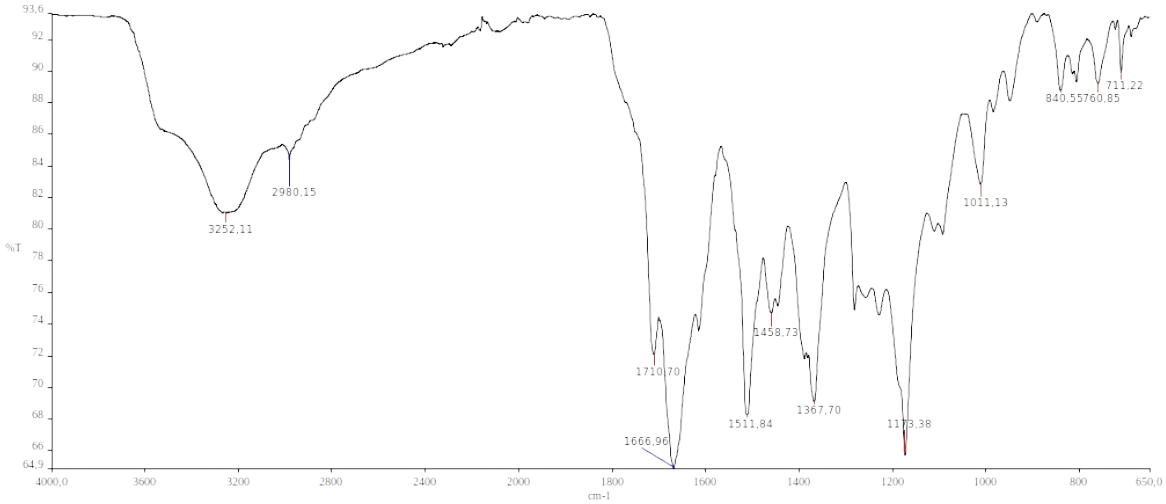

Figure S6. IR spectrum of **Cd(II)-cefoperazone** complex.

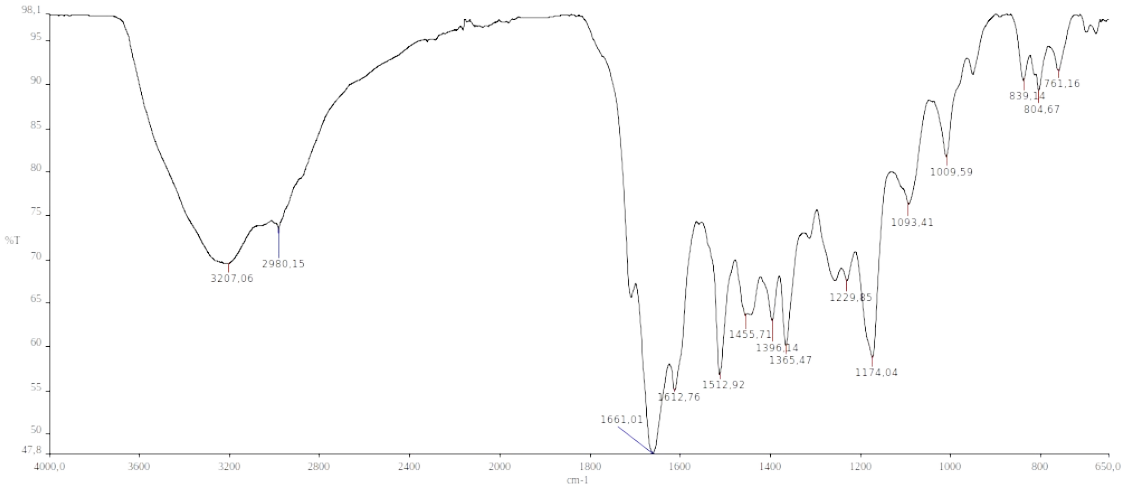

Figure S7. IR spectrum of **Fe(III)-cefoperazone** complex.

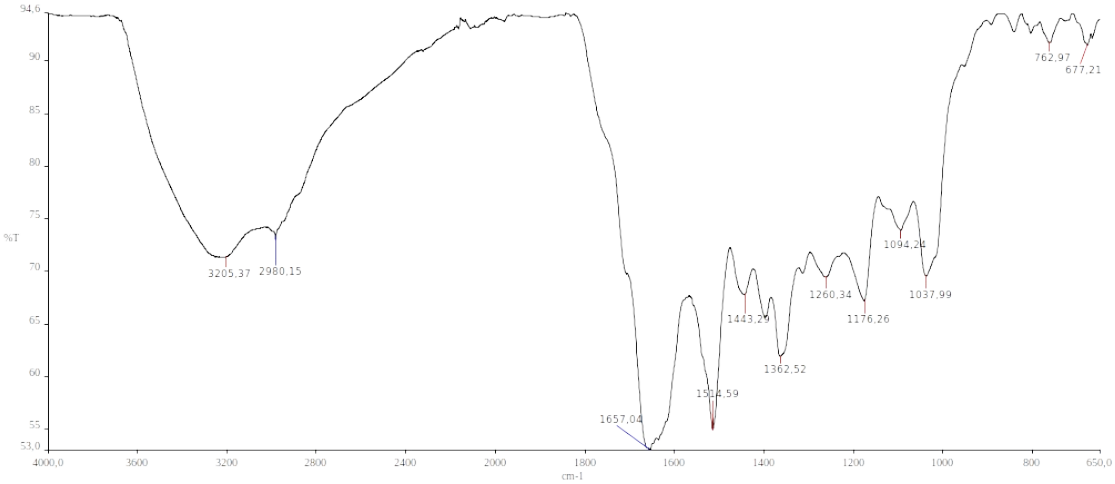

Figure S8. IR spectrum of **Ru(III)-cefoperazone** complex.

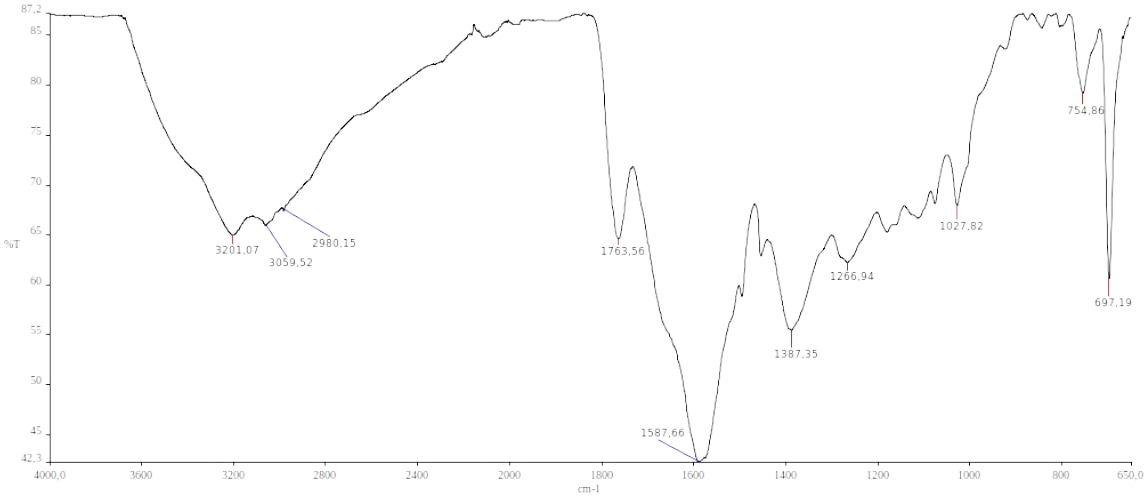

Figure S9. IR spectrum of Pd(II)-cefoperazone complex.

JOTCS A
Journal of the Turkish Chemical Society
Section: A
Chemistry
TURKISH CHEMICAL SOCIETY

Bioassay-Guided Separation Approach for Characterization of New Antibacterial Fractions from the Stem Roots Extracts of *Archidendron jiringa*

Noviany[1,*], Dicky Sialdian[1], Andi Setiawan[1], Bambang Irawan[2], Mohamad Nurul Azmi[3], Sutopo Hadi[1]

[1]Department of Chemistry, Faculty of Mathematics and Natural Sciences, University of Lampung, Bandar Lampung 35145, Lampung, Indonesia
[2]Department of Biology, Faculty of Mathematics and Natural Sciences, University of Lampung, Bandar Lampung 35145, Lampung, Indonesia
[3]School of Chemical Sciences, Universiti Sains Malaysia, Minden 11800, Penang, Malaysia

Abstract: Infectious diseases caused by bacteria has become a global health issue, especially antibacterial drug resistance. The most serious concern with antibacterial resistance is that some bacteria became resistant to almost all antibacterial drugs, which makes them less effective. *Archidendron jiringa* is one of the most potent medicinal plants to be developed as a new source of antibacterial components. In current study, based on the antibacterial assay-guided approach, the separation of bioactive fractions of *A. jiringa* stem roots was carried out through several stages including isolation, fractionation, and characterization. The stages of isolation of secondary metabolites were conducted by gradually extraction followed by fractionation using chromatographic methods. The antibacterial potential of extracts was evaluated by the disc diffusion and microdilution methods employing the resazurin assay against one Gram-negative resistant bacteria, *Escherichia coli*, and one Gram-positive bacteria, *Bacillus subtilis*. Among three extracts obtained, ethyl acetate and methanol extracts demonstrated to be the most significant antibacterial effects, while no antibacterial activity was shown on the n-hexane extract. The fractionation of ethyl acetate extract led to the isolation of the most bioactive fractions (E_28_15 and E_28_16) with the MIC's values ranging of 12.5–25 µg/mL for both resistant bacteria. Due to the low amount, only the fraction E_28_16 was subjected to analysis by ^{1}H-NMR spectroscopy. The results exhibited that the bioactive fraction was obtained as a mixture of at least three major constituents. However, the purification of the bioactive fraction is required, to further clarify the antibacterial compound that can be utilized as a new promising antibacterial agent. The bioassay-guided separation approach and the dye resazurin as an indicator of the growth of bacteria are applied for the first time for the phytopharmacological investigation from this plant. The present study represented the most effective method for subsequent finding and isolation of potential novel antibacterial constituents from *A. jiringa* stem roots, in particular against the multi-drug resistant strains.

Keywords: *A. jiringa*, antibacterial assay, bioassay-guided separation, medicinal plant

Submitted: November 25, 2020. **Accepted:** January 27, 2021.

Cite this: Noviany N, Sialdian D, Setiawan A, Irawan B, Azmi MN, Hadi S. Bioassay-Guided Separation Approach for Characterization of New Antibacterial Fractions from the Stem Roots Extracts of Archidendron jiringa. JOTCSA. 2021;8(2):391–402.

DOI: https://doi.org/10.18596/jotcsa.831054.

***Corresponding author. E-mail:** NOVIANY@FMIPA.UNILA.AC.ID.

INTRODUCTION

Infectious disease is a serious global health problem, and every year, it causes deaths of 13 million people worldwide, especially in developing countries like Indonesia (1, 2). WHO (World Health Organization) data show that viral, bacterial, fungal and parasitic infections are the biggest cause of death for the world's population. The use of antibiotics in the prevention of infectious diseases is the only solution (3). However, continuous use of antibiotics raises new problems for health, especially the resistance of microorganisms that causes infection (1, 2). Bacteria are the most abundant organisms and widespread in living things. In terms of distribution and number, most bacteria may cause disease in humans and other living things (3). *B. subtilis* and *E. coli* are the most common pathogenic bacteria in humans; *E. coli* is a Gram negative bacterium found in the large intestine of humans, and is a major cause of diarrheal diseases, especially in infants and children (1-3). The mortality rate from diarrhea in Indonesia is still around 7.4%, while the mortality rate due to persistent diarrhea is higher at 45%. In 1,000 inhabitants, 200–374 subjects experience diarrhea, with 60%–70% of whom are children under the age of 5 (4).

Bacterial resistance to antibiotics is a problem that has not been resolved until now (3, 5, 6). The *E. coli* resistants to chloramphenicol group of antibiotics and amoxicillin have long been reported (2, 3, 7, 8). The greater the percentage of bacterial resistance to an antibiotic state that bacteria are no longer susceptible to these antibiotics. Various studies to overcome the bacterial resistance were carried out, but no effective reports exist. Thus, investigating new antibacterial substances that are still active and selective is necessary. The search for antibiotic sources from natural ingredients is still the main trend for researchers. The ability of bioactive compounds of natural materials as a healing medium is estimated because of the content of secondary metabolites, including terpenoids, steroids, coumarin, flavonoids, and alkaloids (10-18).

One of the plants that has not been studied intensively in Indonesia is the family of Fabaceae (18, 19). The Fabaceae family demonstrates quite interesting bioactivity such as antibacterial (18, 19), antituberculosis (20), antioxidants (21), anticancer (22), and antimalarial (18, 23). The jengkol plant (*A. jiringa* (Jack) I. C. Nielsen), which belongs to the Fabaceae family, is commonly used by the Indonesian people as traditional medicine (18). Jengkol leaves are efficacious as medicine for eczema, scabies, sores, and ulcers, and the skin of the fruit is used as ulcerative medicine. Several studies were carried out on jengkol plants, including the leaves, fruit peel, and seeds (18, 19, 21, 24). The phytochemical screening has been done on jengkol fruit peel, seeds, bark, and leaves extracts (24). Based on this screening, from the parts of jengkol contain alkaloids, steroids, triterpenoids, glycosides, saponins, flavonoids, and tannins. However, research on the stem roots of the jengkol plant was never performed.

In our ongoing investigation for new lead constituents from medicinal plants, we elaborated the bioactive secondary metabolites of *A. jiringa* stem roots and assayed their antibacterial activity. The aims of the study were to obtain antibacterial active fractions from the stem roots of *A. jiringa*, based on the bioassay-guided separation approach through their antibacterial property.

EXPERIMENTAL SECTION

Plant Materials

Samples of the stem roots of *A. jiringa* were assembled on January 25, 2018 from Unila's Housing area at Gedongmeneng District, Bandar Lampung, Lampung Province, Indonesia. The plant specimens (NV6/NRGD/2018) were identified at the Herbarium Bogoriense, LIPI Bogor, Indonesia.

General Experimental Procedures

TLC was performed on silica gel 60 GF_{254} plates (Merck; 0.25 mm) and sprayed with staining reagen $Ce(SO_4)_2$. Column chromatography (CC) was made on silica gel (Kieselgel 60, 70–230 mesh ASTM; Merck) and Sephadex LH-20. ^{1}H NMR spectrum was measured in acetone-d_6 (TMS as an internal standard), on an NMR Agilent 500 MHz spectrophotometer (Agilent Technologies, JNM-ECZ500R/S1) or Bruker 500 MHz spectrometer. Finally, *Microplate Reader* Hospitex-Italy was used to measure the absorbance resulted on the resazurin assay, while UV spectra were performed using an Eppendorf BioSpectrometer kinetic instrument.

Bacterial Strains and Biochemicals

Ampicillin and chloramphenicol were purchased from Sigma Aldrich, and resazurin sodium salt was purchased from Sigma Aldrich. Gram-positive bacteria, *B. subtilis* ITBCCB148, was obtained from the Microbiology and Fermentation Technology Laboratory, Bandung Institute of Technology, Gram-negative bacteria, *E. coli* UNIATCC25922, nutrient agar broth, disposable sterile petri dishes (Idealcare), disposable syringe, micropipette tips, sterile tissue culture 96-well plates.

Preparation of Extracts

Fresh chopped stem roots of *A. jiringa* (2.5 kg) were cleaned by rinsing under running tap water to remove soil and dirt. The samples were dried in an open space for three weeks, and the air-dried roots are finally ground into a powder form. The powdered air-dried stem roots (1.5 kg) were extracted with a polar gradient polarity of solvent using the maceration technique. The solvent used at this stage starts from the solvent which exhibits the lowest polarity, *n*-hexane, followed by ethyl acetate (EtOAc), and finally with a high polarity organic solvent, methanol. Each extraction was conducted three times in each type of solvent. Before changing the type of solvent, the extract residue is first air

dried for at least three days or until the residue is dry/free of solvent. The filtrates obtained from maceration obtained from polar gradient solvents are then separated from the residue by ordinary filtration. The filtrates are then concentrated under reduced pressure using a vacuum rotary evaporator to yield *n*-hexane (3.6 kg), EtOAc (55.8 kg), and methanol (67.2 kg) extracts, respectively. Using agar disc diffusion and microdilution methods, each extract obtained was subjected to an assay of its antibacterial activity. The most active extract was further isolated and fractionated through the bioassay-guided separation approach. The general research flowchart can be seen in Figure 1.

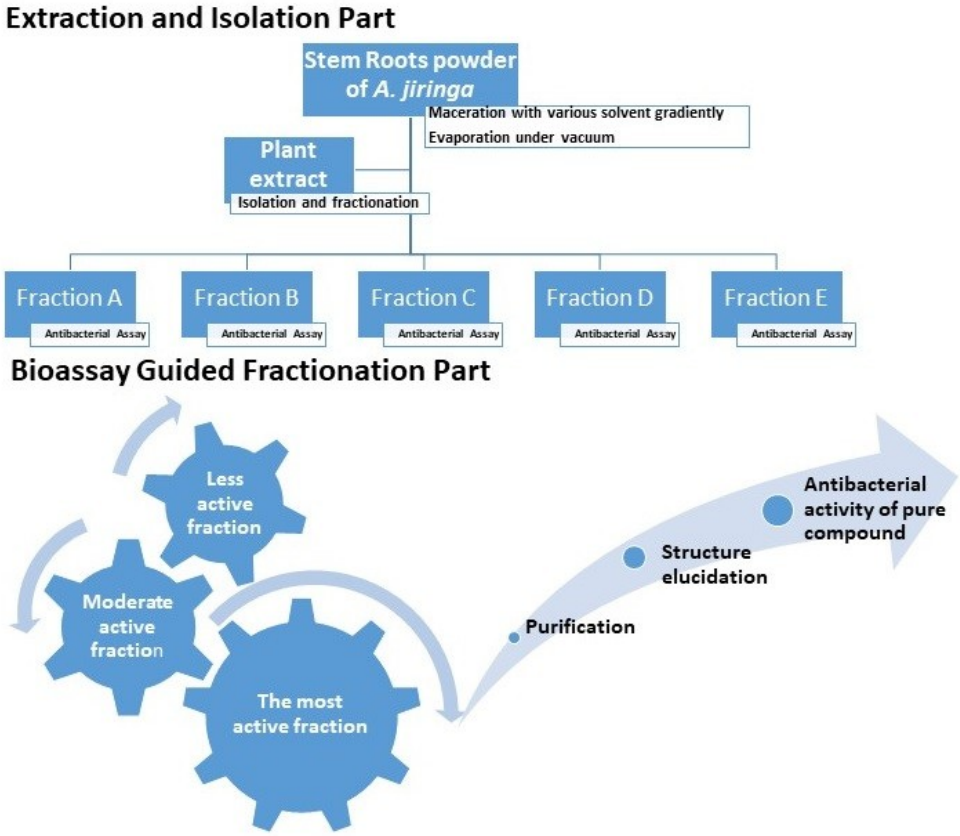

Figure 1. Research flow chart of bioassay guided separation.

Bioassay-guided Separation of Ethyl Acetate Extract

Based on the antibacterial activity results of extracts, the EtOAc extract (55.8 g) was selected to be isolated and fractionated further using the VLC method on silica gel (35–70 Mesh). The column was eluted with a stepwise gradient polarity of the solvent systems, including *n*-hexane–EtOAc (100%-0% of *n*-hexane), EtOAc-acetone (100%–0% of EtOAc), and acetone-MeOH (100%-0% of acetone), affording 23 fractions (200 mL each). According to their chemicals profile analyzed by TLC and their proton NMR spectrum, these fractions were grouped and combined into seven primary fractions, E_21 (fr.1–10), E_22 (fr.11), E_23 (fr.12), E_24 (fr.13), E_25 (fr.14–15), E_26 (fr.16–19), E_27 (fr.20–23) (Figure 2). All fractions E_21–E_27 were tested for their antibacterial property separately using disc diffusion and microdilution methods. Among all fractions tested, three fractions exhibited antibacterial activity against both bacterial strains with quite similar MIC's values, therefore fraction E_22 (439.5 mg) was subjected to further fraction due to the simplest chemical profile on its TLC. Fraction E_22 was redissolved in acetone and then purified with CC on silica gel G-60 (35–70 Mesh) using *n*-hexane/isopropyl alcohol with the ratio volumes of 70/30, 60/40, 50/50, and 40/60, generating six major subfractions, E_22a (132.0 mg), E_22b (8.4 mg), E_22c (9.0 mg), E_22d (47.0 mg), E_22e (2.0 mg), and E_22f (50.3 mg). Using microdilution methods, all subfractions were screened against both bacterial strains tested. The MIC's values and optical density (OD) means of bioactive subfractions were described on Table 2. Among them, two subfractions (E_22e and E_22f) performed the most antibacterial activity against *B. subtilis* and *E. coli*, with the MIC's values ranging of 12.5–25 µg/mL. Only subfraction E_22f was selected to be analyzed further by ^{1}H-NMR spectroscopy as exhibiting sufficient quantity.

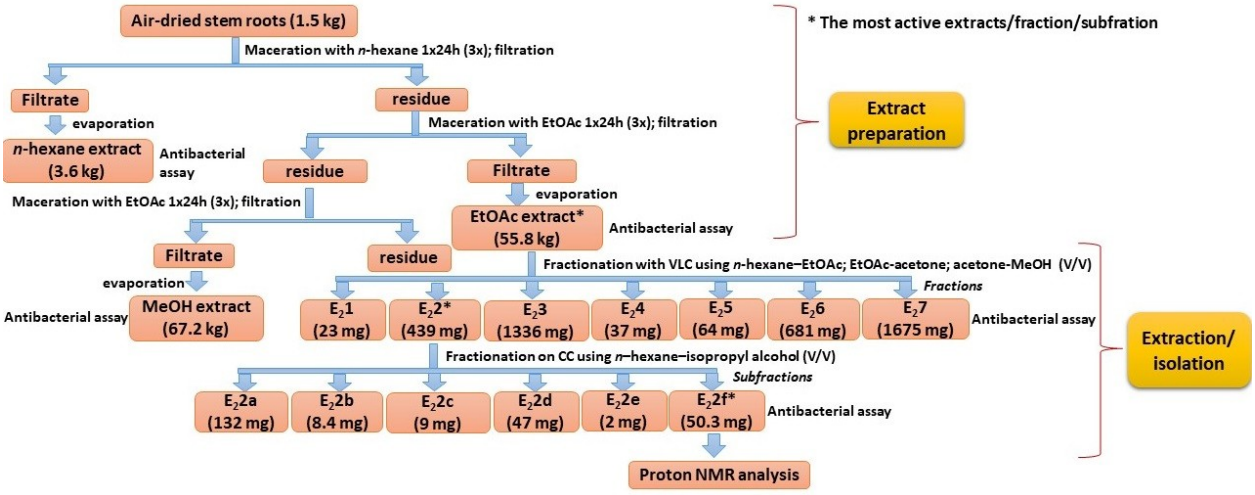

Figure 2. Scheme of bioassay guided separation of EtOAc extract subfractions.

Phytochemical Screening

The phytochemical screening was performed for triterpenes/steroids, alkaloids, flavonoids, and saponins, by using the standard procedures (25). The formation of precipitate or the color intensity was applied for analytical response of screening results.

Evaluation of Antibacterial Activity

For the testing antibacterial activity, the microbial strains employed in the biological assay are gram positive bacteria, *Bacillus subtilis*. Gram negative bacteria, *Escherichia coli*, have been obtained from a stock culture from Hospital Abdul Muluk, Bandar Lampung, Indonesia. To maintain stock culture, original cultures are further stored at a low temperature in the refrigerator. Fresh cultures are used for testing antibacterial activity using disc diffusion assay and dilution methods.

Disc diffusion assay

The antibacterial activity of the stem roots extract (*n*-hexane, ethyl acetate, and methanol) were tested by the disc diffusion method (26) against pathogenic bacteria gram negative (*E. coli*) and gram positive (*B. subtilis*). In this method, freshly prepared agar media is dispensed into the sterilized petri-dish. The agar is allowed to solidify, and 100 µL of the bacterial suspension was poured over the agar media and spread by a spreader or a rod. Ampicillin and chloramphenicol (30 µg/dish) is used as a positive control, while methanol is used as a negative control. In each culture medium petri-dish, four disks were used, one disk of antibiotics, two discs separately for (*n*-hexane, ethyl acetate, and methanol) extracts, and one disk used as a control (methanol). The plates are sealed and incubated overnight at 37 °C in the incubator. Next, antibacterial activity is assigned by measuring the inhibition zone formed around the discs, and the diameter of zone of inhibition (mean of three replicates SD) as indicated by clear area was measured to determine the antibacterial activity. The experiment is replicated three times to confirm the reproducibility.

Determination of MIC via Resazurin Assay

Resazurin assay was carried out in 96-well plates titration with some minor modification (27). In the complete nutrient broth, two-fold dilutions of plant extracts and antibiotics were prepared in the test wells. The final concentration (20 µL of each bacterial suspension) was added to 180 µl of antibiotics and plant extracts (30–0.02 mg/mL in sequence) contained in the culture medium, as well as the antibiotics concentrations of 0.06 mg/mL and 0.12 mg/mL for amphicilin and chloramphenicol, respectively. For the comparative study, control plates were prepared only with the culture medium and bacterial suspension. The plates were sealed and incubated for 12 hours at 37 °C for an additional 5 hours. At 1-hour intervals, plates were observed for a blue to pink and pink to colorless color change in living bacterial strains containing wells. Preliminary micro titer plate assay reveals that the fast decolonization of resazurin extract does not exhibit antibacterial potential. The bioactivity of extracts was screened, which shows that the extracts inhibit the dye reduction.

RESULTS AND DISCUSSION

The plant material was macerated using gradient polarity of solvent and afforded *n*-hexane (3.6 kg), EtOAc (55.8 kg), and methanol (67.2 kg) extracts. EtOAc extract performed the most bioactive extract against two bacterial strains, *E. coli* and *B. subtilis*, using agar disc diffusion and microdilution methods. Using the diffusion method, extracts of *n*-hexane, EtOAc, and methanol obtained from the extraction stage were each screened for antibacterial activity tests against *E. coli* and *B. subtilis* bacteria. Bioactivity test results in bacteria *E. coli* and *B. subtilis* were observed based on the diameter of inhibition zones, as tabulated in Table 1.

Table 1. The results of inhibitory zone of the extracts (in mm) against *E. coli* and *B. subtilis.*

	E. coli			*B. subtilis*		
Concentration	***n*-hexane**	**EtOAc**	**MeOH**	***n*-hexane**	**EtOAc**	**MeOH**
0.3 mg/disc	-	10	8	-	8	7
0.5 mg/disc	-	11	9	-	9	8

The results of the antibacterial screening test on the three extracts by diffusion method showed that EtOAc extract exhibited better bioactivity, compared to n-hexane and methanol extracts. Furthermore, the repetition of the antibacterial activity test carried out using a dilution method in order to determine the minimum inhibitory concentration (MIC) of each fraction. The results of the MIC test of the three extracts using the dilution method against *E. coli* and *B. subtilis* bacteria can be seen in Figure 3, while the optical density (OD) values can be seen in Table 2.

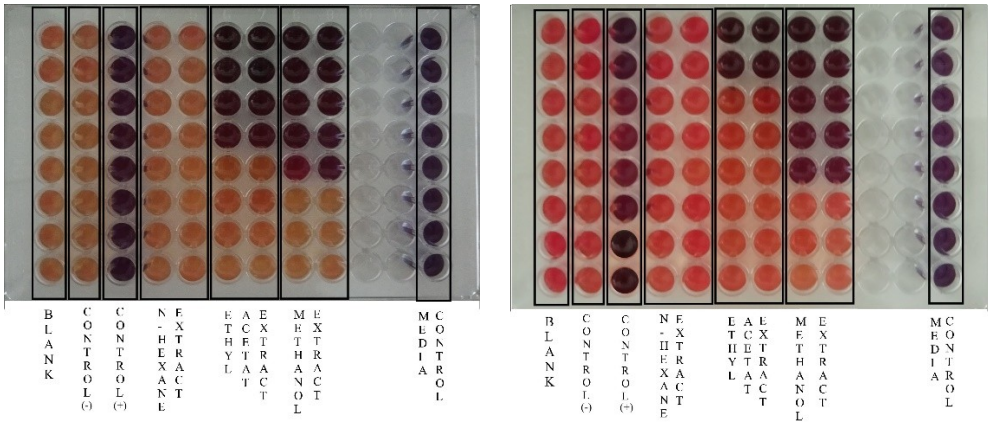

(a) (b)

Figure 3. MIC testing of n-hexane, EtOAc, and methanol extracts using 96-well plates (a) on *E. coli* (b) bacteria on *B. subtilis* bacteria.

Table 2. The results of MIC test of *n*-hexane, EtOAc, and methanol extract using dilution method against *E. coli* and *B. Subtilis.*

No	**Type of extract**	**Average of OD on *E. coli****	**Average of OD on *B. subtilis****	**MIC (µg/mL) on *E. coli***	**MIC (µg/mL) on *B. subtilis***
1	*n*–hexane	0.76838	0.54231	-	-
2	EtOAc	1.88706	1.48556	12.5	50
3	Methanol	1.68644	1.66288	6.25	6.25
4	Positive control	1.773	1.48025	0.78	0.78
5	Negative control	0.74013	0.57575	-	-

The test results based on Table 2 show that semi-polar EtOAc extract and polar methanol demonstrate a minimum inhibitory concentration better than *n*-hexane extract. In this dilution antibacterial test, using visual observation is not sufficient to observe the presence or absence of bacterial growth; however, this tends to be subjective from each person's eyesight so the risk of error is relatively greater. This occurs because the color test makes it difficult to observe, so absorbance values before and after incubation are used to help determine the presence or absence of bacteria. The wavelength used to measure the number of microbes is 600 nm, because cells in the mitochondria and cytoplasm absorb at that wavelength (28). After incubation for 18 hours and

measuring the OD, the addition of the reaction color was resazurin and was reincubated for 4 hours until the color changed. This color change occurred because resazurin exhibits a blue color that is not fluorescent, and it can be reduced to a fluorescent pink color. The change in color from blue to pink is an indicator of cell reduction. The color change of resazurin is carried out by enzymes in cells in the mitochondria and cytoplasm (27).

Based on the results of the antibacterial tests that were carried out, EtOAc extract was chosen for the fractionation and purification process because it exhibits the best antibacterial activity in inhibiting bacterial growth to a minimum inhibitory concentration of 12.5 and 50 µg/mL, compared to extract *n*-hexane, which demonstrates no inhibition at all. The results of fractionation with the VLC process showed that a separation was present between semi-polar components and non-polar components, resulting in seven combined fractions, namely $E_2$1 (fr.1–10; 23 mg), $E_2$2 (fr.11; 439.5 mg), $E_2$3 (fr.12; 1,336 mg), $E_2$4 (fr.13), $E_2$5 (fr.14–15), $E_2$6 (fr.16–19), $E_2$7 (fr.20–23; 1,675 mg). All these fractions were screened for antibacterial activity using the agar diffusion method, and the results obtained were tabulated in Table 3.

Table 3. The diameter of inhibition zone (mm) of VLC-1 and VLC-2 fractions against *E.coli* and *B. subtilis*

	E. coli				*B. subtilis*			
Concentration	**$E_2$1**	**$E_2$2**	**$E_2$3**	**$E_2$7**	**$E_2$1**	**$E_2$2**	**$E_2$3**	**$E_2$7**
0.3 mg / disk	7	10	8	7	7	10	8	7
0.5 mg / disk	7	11	8	8	7	12	9	8

Using a dilution method to determine the MIC value, each antibacterial active fraction obtained above was then re-tested for bioactivity. The results of the MIC test can be seen in Figure 4, and the average OD of each fraction can be seen in Table 4.

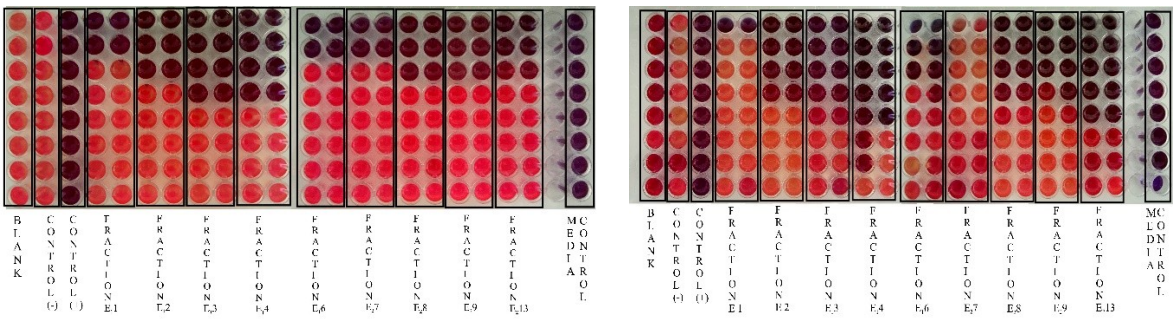

(a) (b)

Figure 4. The MIC test on VLC fractions against: (a) *E. coli;* (b) *B. subtilis.*

Table 4. The result of *MIC* test of VLC fraction against *E. coli* and *B. subtilis* using dilution method.

No	**Fraction code**	**OD average on *E. coli***	**OD average on *B. subtilis***	**MIC (µg/mL) on *E. coli***	**MIC (µg/mL) on *B. subtilis***
1	$E_2$1	1.16363	1.02819	50	-
2	$E_2$2	1.49338	1.54488	25	25
3	$E_2$3	1.25269	1.74956	25	25
4	$E_2$7	1.39525	2.34931	25	6,25
5	Positive control	2.16563	2.28425	0,78	0,78
6	Negative control	0.86413	0.60838	-	-

From the test results shown in Table 4, it was found that the fractions of $E_2$2, $E_2$3, and $E_2$7 gave a smaller value of the minimum inhibitory concentration compared to other fractions both against *E. coli* and B. subtilis bacteria. The $E_2$2 fraction (439.5 mg) was then selected for further purification by mass consideration. Phytochemical screening, especially flavonoid and phenolic tests, was carried out on the $E_2$8 fraction, which showed positive tests for the presence of flavonoids and phenolics. Purification of the $E_2$2 fraction (439.5 mg) produced six main subfractions, namely $E_2$2a (132.0 mg), $E_2$2b (8.4 mg), $E_2$2c (9.0 mg), $E_2$2d (47.0 mg), $E_2$2e (2.0 mg), and $E_2$2f (50.3 mg). Then, the subfractions were carried out using MIC test 96-well plates, to determine the minimum inhibitory concentration of the subfraction. The results of MIC on *E. coli* bacteria are that the $E_2$2c, $E_2$2d, $E_2$2e, and $E_2$2f fractions exhibit a better minimum inhibitory concentration compared to other fractions. However, the MIC results in B. subtilis bacteria all fractions showed lower inhibitory ability than in *E. coli* bacteria. The results of the $E_2$2 subfraction MIC can be seen in Figure 5 and for the average OD of each fraction can be seen in Table 5.

Table 5. The result of MIC test on $E_2$8$_1$ subfraction using 96-well plates against *E. coli* and *B. subtilis*

No	Subfraction code	Average of OD on *E. coli*	Average of OD on *B. subtilis*	MIC (µg/mL) in *E. coli*	MIC (µg/mL) in *B. subtilis*
1	$E_2$2a	1.49731	1.27825	50	100
2	$E_2$2b	1.44425	1.22788	50	50
3	$E_2$2c	1.29094	0.99919	25	50
4	$E_2$2d	1.25900	0.84613	25	50
5	$E_2$2e	1.39463	1.18294	12,5	25
6	$E_2$2f	1.34638	1.14100	25	25
7	Positive control	1.54525	1.45938	0,78	0,78
8	Negative control	0.85238	0.56950	0	0

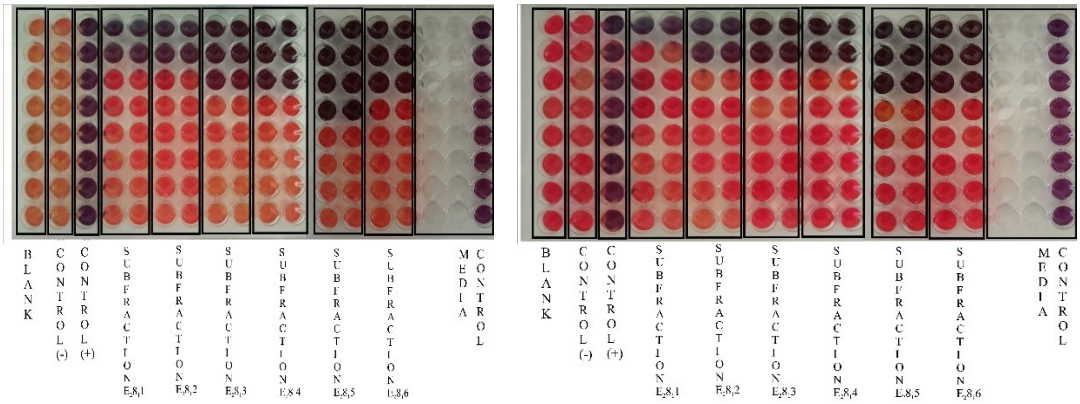

(a) (b)

Figure 5. MIC test on $E_2$2 subfractions using 96-well plates against*:* (a) *E. coli;* (b) *B. subtilis.*

Based on the results obtained, a decrease in the minimum inhibitory concentration can be seen compared to the antibacterial activity test on the VLC results as observed on the purification results of the $E_2$2 fraction. This fact occurs due to the possible composition of active compounds contained in the sample. According to Priya *et al.* (29), when an increase or decrease in a component of an active compound occurs, a possibility of influencing the activeness of the compound itself exists. From the test results shown in Table 5, researchers found that the $E_2$2e and $E_2$2f subfractions gave a smaller minimum inhibitory concentration value compared to other subfractions, both against *E. coli* and B. subtilis bacteria. Among them, two subfractions ($E_2$2e and $E_2$2f) performed the most antibacterial activity against *B. subtilis* and *E. coli*, with the MIC's values ranging from 12.5–25 µg/mL.

However, $E_2$2f was chosen to be further characterized because in terms of quantity more than $E_2$2e. As can be seen in Figure 6, subsequent

characterization of the $E_2$2f subfraction was carried out using proton nuclear magnetic spectroscopy (^{1}H-NMR).

The spectrum shown in Figure 6 indicates that the $E_2$2f subfraction is not pure. However, interpretation of the ^{1}H-NMR data can still be done, by referring to the results of the phytochemical test of the fraction which shows the content of phenolic compounds or flavonoids in the subfraction. Therefore, a comparison reporting the presence of phenolic or flavonoid compounds in the same plant type is sought in journals to estimate the types of bioactive compounds which are obtained. From the NMR spectrum of proton $E_2$2f subfraction, the results show indications of aromatic protons in the chemical shift region δ_H 6–7. The signal for the methoxy group (–OCH_3) at δ_H 3.7, the proton signal at δ_H 8.01 with the peak of the chemical shift of the hydroxyl group (-OH) attached to an aromatic ring. As well as the typical peaks for alkanes at δ_H 0.89-2.2.

The isolation of phenolic compounds from the fruit skin of jengkol plants, and the researchers identified them as 1-(2,6-dihydroxy-4-methoxyphenyl) decan-1-one (Figure 7) has previously been reported (30). Based on the comparison of the proton chemical shift values between the isolated subfraction and 1-(2,6-dihydroxy-4-methoxyphenyl) decan-1-one, researchers estimated that the main active compound contained in the $E_2$2f subfraction is a phenolic compound, namely 1-(2, 6-dihydroxy-4-methoxyphenyl) decan-1-one. However, further purification in the $E_2$2f subfraction still needs to be performed, to ensure the active compounds which are responsible for inhibition of the test bacteria. The results obtained in the spectrum exhibit similarities with the spectrum that was reported by others (30), as can be seen in Table 6. However, antibacterial studies have not yet been found against compound 1-(2,6-dihydroxy-4-methoxyphenyl) decan-1-one, so it is thought to be synergistic: between compounds 1-(2,6-dihydroxy-4-methoxyphenyl) decan-1-one with other compounds that cause antibacterial activity, as seen in the antibacterial test results in fractions of VLC results.

Table 6. Comparison of chemical shifts in ^{1}H-NMR subfraction $E_2$2f with compounds 1-(2,6-dihydroxy-4-methoxyphenyl)decan-1-one.

No	Proton type	δ_H proton in Subfraction $E_2$8$_1$6 (ppm)	δ_H Proton in reference compound (30)
1	Aromatic	6 - 7	7.04
2	Methoxy	3.7	3.79
3	Hydroxy Aromatic	8.01	8.01
4	Alkane	0.89 -2.2	0.89-2.21

Based on the results of interpretation of ^{1}H-NMR, data seen in Table 7 indicate that the $E_2$2f subfraction is not pure, but it is seen in the integration that indicates the possibility of the presence of three mixed compounds distributed in the chemical shift region δ_H 0.89–8.01 ppm. The first group exhibits chemical shifts that are distributed in the area of δ_H 8.01, 6.8, 6.79, 6.76, 6.74, 6.20, 5.87, 4.58, 3.99, 2.53, and 1.67 ppm. The second group is distributed in the area of chemical shift δ_H 7.05, 6.82, 5.91, and 4.20 ppm. Whereas, the third group was distributed in the area of chemical shift δ_H 6.36, 6.29, and 0.89 ppm. The complete shift of proton chemistry and its integration can be seen in Table 7.

Table 7. Coupling constant and ^{1}H-NMR Integration of $E_2$2f subfraction.

No	δ_H (ppm)	Multiplicity	Integration	J (Hz)*
1	8.01	*d*	0.90 ^{1}	16.5
2	7.05	*d*	0.26 ^{2}	2.5
3	6.8	*d*	0.91 ^{1}	2.5
4	6.82	*d*	0.69 ^{2}	1.5
5	6.79	*m*	1.23 ^{1}	4
6	6.76	*d*	2.23 ^{1}	1.5
7	6.74	*d*	2.23 ^{1}	1.5
8	6.36	*d*	0.33 ^{3}	2.5
9	6.29	*d*	0.31 ^{3}	2.5
10	6.20	*m*	2.50 ^{1}	2.5
9	5.91	*m*	0.42 ^{2}	2.5
10	5.87	*m*	2.00 ^{1}	2
13	4.58	*m*	2.40 ^{1}	7.5
14	4.20	*t*	0.45 ^{2}	4
15	3.70	*m*	3.21 ^{1}	3
16	2.53	*m*	2.10 ^{1}	3.5
17	1.67	*m*	1.24 ^{1}	5.5
18	0.89	*m*	0.58 ^{3}	8.5

Superscripted 1, 2, and 3 are codes for different types of groups of compounds.

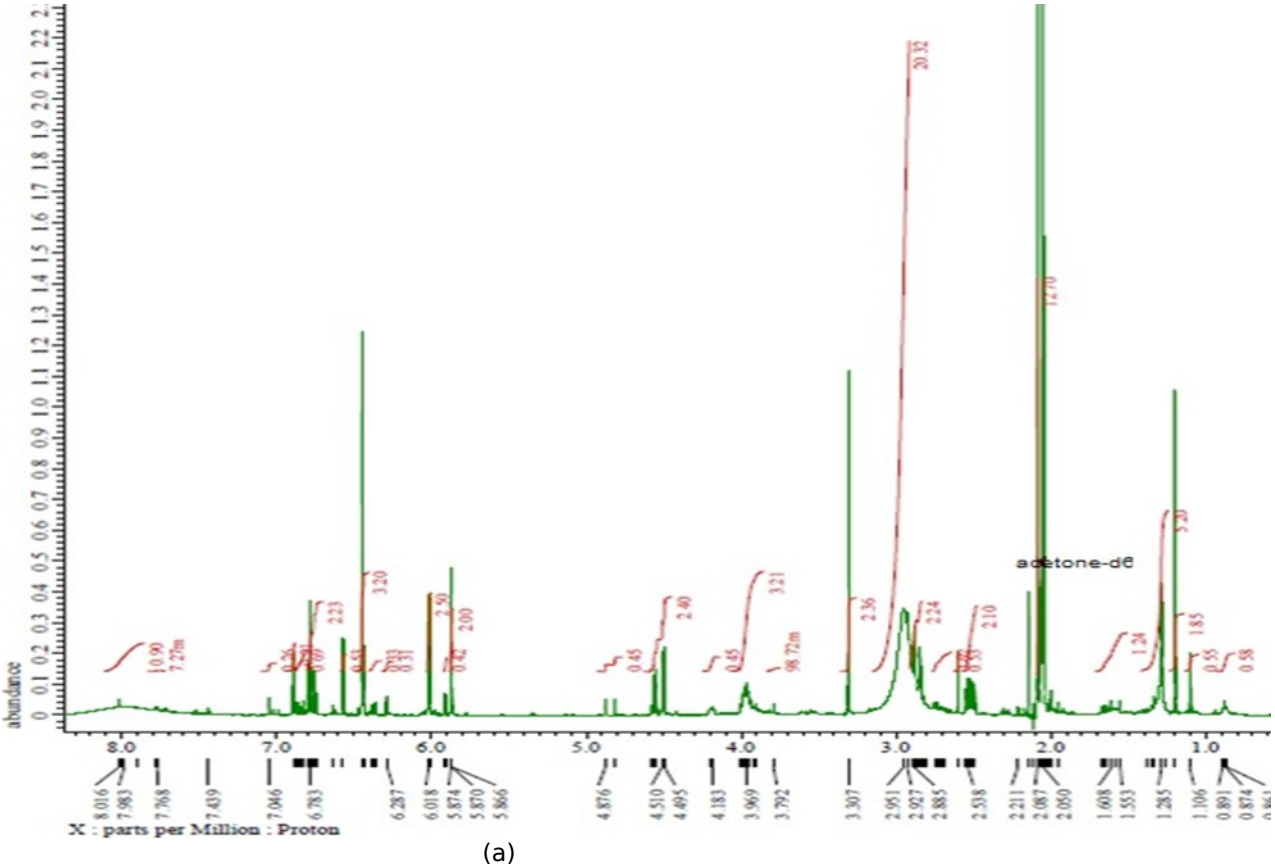

(a)

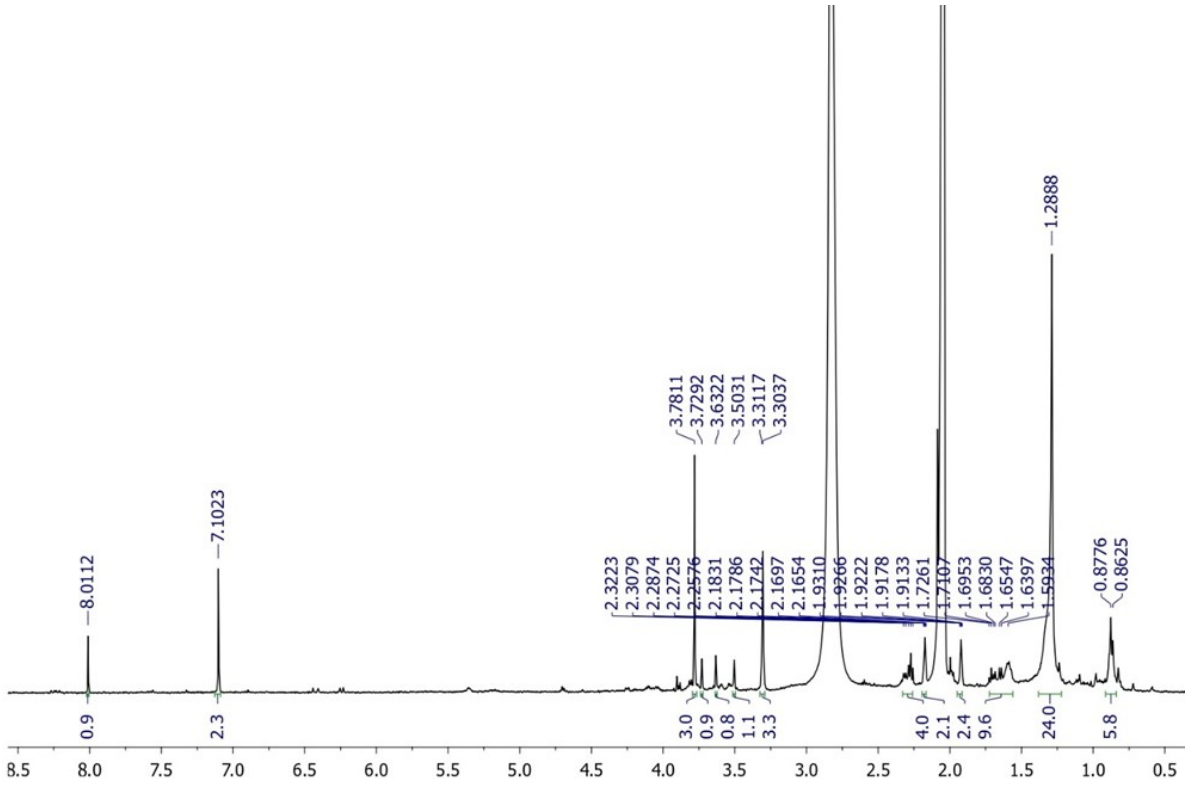

(b)

Figure 6. ^{1}H-NMR spectra of (a) $E_2$2f subfraction; (b) Reference compound (30).

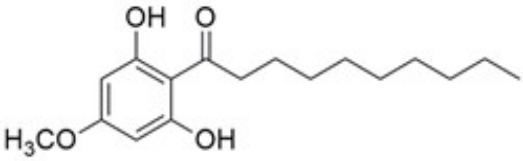

Figure 7. Structure of compound 1- (2,6-dihydroxy-4-methoxyphenyl) decan-1-one.

CONCLUSIONS

The EtOAc extract of jengkol (*A. jiringa* (Jack) I. C. Nielsen) root bark exhibits antibacterial activity against *E. coli* and *B. subtilis* bacteria, which is better than the *n*-hexane extract. Compared to other fractions from the same column, the E13 fraction and E28 fraction exhibit better antibacterial activity against *E. coli* and *B. subtilis* bacteria. The E13 fraction and E28 fraction exhibit better antibacterial activity against *E. coli* and *B. subtilis*, compared to the E13 subfraction and E28 fraction as a result of its purification. Based on the ^{1}H-NMR result data, the compounds detected in the E_28_16 subfraction are a phenolic compound type. Lastly, this study is the first reported from this plant and the potential exists to further investigate the invention of new promising antibacterial agent from plants.

ACKNOWLEDGMENTS

The authors would like to thank to the Institute of Research and Community Services, Universitas Lampung that provided fund for this project to be undertaken through Penelitian Kerjasama Internasional/International Research Collaboration 2019 (No.3093/UN26.21/PN/2019). The authors would like to thank Enago (www.enago.com) for the English language proofread and review. We also gratefully acknowledge UPT LTSIT of the University of Lampung for technical assistance.

CONFLICTS OF INTEREST

The authors declare no conflicts of interest**.**

REFERENCES

1. Van TTH, Nguyen HNK, Smooker PJ, Coloe PJ. The antibiotic resistance characteristics of non-typhoidal *Salmonella enterica* isolated from food-producing animals, retail meat and humans in South East Asia**.** *Int. J. Food Microbiol.* 2012**;** 154: 98-106.

2. Sulaiman M, Hassan Y, Taskin-Tok T, Noundou XS. Synthesis, Antibacterial Activity and Docking Studies Of Benzyl Alcohol Derivatives. *J. Turk. Chem. Soc. Sect. A: Chem.* 2020; 7(2): 481-8.

3. World Health Organization. WHO Global Strategy for Containment of Antimicrobial Resistance. *World Health Organization.* 2001**;** 53–5.

4. Oyofo BA, Lesmana M, Subekti D, Tjaniadi P, Larasati W, Putri M, Simanjuntak CH, Punjabi NH, Santoso W, Muzahar, Sukarma, Sriwati, Sarumpaet S, Abdi M, Tjindi R, Ma'ani H, Sumardiati A, Handayani H, Campbell JR, Alexander WA, Beecham III HJ, Corwin AL. Surveillance of bacterial pathogens of diarrhea disease in Indonesia. *Diagn. Mic. Infec. Dis,* 2002; 44: 227-34.

5. Annissa, Suhartati T, Yandri, Hadi S. Antibacterial Activity of Diphenyltin(IV) and Triphenyltin(IV) 3-Chlorobenzoate againts *Pseudomonas aeruginosa and Bacillus subtilis. Orient. J. Chem.* 2017; 33: 1133-9.

6. Hadi S, Hermawati E, Noviany, Suhartati T, Yandri. Antibacterial Activity Test of DiphenyltinIV) Dibenzoate and Triphenyltin(IV) Benzoate Compounds against *Bacillus substilis and Pseudomonas aeruginosa. Asian J. Microbiol. Biotech. Env. Sci.* 2018; 20; 113-9.

7. Bischoff KM, White DG, Mcdermott PF, Zhao S, Gaines S, Maurer JJ. Characterization of Chloramphenicol Resistance in Beta-Hemolytic *Escherichia coli* Associated with Diarrhea in Neonatal Swine. *J. Clin. Microbiol.* 2002; 40: 389–94.

8. Bischoff KM, White DG, Hume ME, Poole TL, Nisbet DJ. The chloramphenicol resistance gene *cmlA* is disseminated on transferable plasmids that confer multiple-drug resistance in swine *Escherichia coli*. *FEMS Microbiol. Lett.* 2005; 243: 285–91.

9. Stapleton P, Wu PJ, King A, Shannon K, French G, Phillips I. Incidence and mechanisms of resistance to the combination of amoxicillin and clavulanic acid in *Escherichia coli*. *Antimicrob. Agents Chemother.* 1995; 39: 2478–83.

10. Küçük S, Soyer P, Tunali Y. Determination of Antimicrobial and Biological Activities of *Salvia sclarea L.* (Lamiaceae) Extracts. *J. Turk. Chem. Soc. Sect. A: Chem.* 2019; 6 (1): 15–20.

11. Noviany N, Samadi A, Carpenter EL, Abugrain ME, Hadi S, Purwitasari N, Indra G, Indra A, Mahmud T. Structural revision of sesbagrandiflorains A and B, and synthesis and biological evaluation of 6-methoxy-2-arylbenzofuran derivatives. *J. Nat. Med.* 2020; August (online first).

12. Noviany N, Osman H, Mohamad S, Hadi S. Antibacterial activity of extracts and compounds from the roots of *Sesbania grandiflora* (Leguminosae). *Res. J. Chem. Environ.* 2020; 24(8): 108-13.

13. Hadi S, Noviany. The Isolation of Hopeaphenol, a Tetramer Stilbene, from *Shorea ovalis* Blume. *Adv. Nat. Appl. Sci.* 2009; 3(1): 107-12.

14. Suhartati T, Yandri, Suwandi JF, Hadi S. In vitro and in vivo antiplasmodial activity of oxyresveratrol and artonine isolated from two Artocarpus plants in Indonesia. *Orient. J. Chem.* 2010; 26(3): 825-30.

15. Noviany N, Nurhidayat A, Hadi S, Suhartati T, Aziz M, Purwitasari N, Subasman I. Sesbagrandiflorain A and B: isolation of two new 2-arylbenzofurans from the stem bark of *Sesbania grandiflora. Nat. Prod. Res.* 2018; 32(21): 2558-64.

16. Suhartati T, Epriyanti E, Borisha I, Yandri, Suwandi JF, Yuwono SD, Qudus HI, Hadi S. In Vivo Antimalarial Test of Artocarpin and in vitro Antimalarial Test of Artonin M Isolated from Artocarpus. *Rev. Chim.* 2020; 71(5): 400-8.

17. Noviany N, Samadi A, Yuliyan N, Hadi S, Aziz M, Purwitasari N, Mohamad S, Ismail NN, Gable KP, Mahmud T. Structure characterization and biological activity of 2-arylbenzofurans from an Indonesian plant, *Sesbania grandiflora* (L.) Pers. *Phytochem. Lett.* 2020; 35: 211-5.

18. Lim TK. *Archidendron jiringa*. In: Edible Medicinal and Non-Medicinal Plants. Springer, Dordrecht. 2012; 835 p.

19. Charungchitrak S, Petsom A, Sangvanich P, Karnchanatat A. Antifungal and antibacterial activities of lectin from the seeds of *Archidendron jiringa* Nielsen. *Food Chem.* 2011; 126: 1025-32.

20. Hasan N, Osman H, Mohamad S, Chong WK, Awang K, Zahariluddin ASM. The Chemical Components of *Sesbania grandiflora* Root and Their Antituberculosis Activity. *Pharmaceuticals.* 2012; 5: 882-9.

21. Lubis MY, Siburian R, Marpaung L, Simanjuntak P, Nasution MP. Methyl Gallate from Jiringa (*Archidendron Jiringa*) and Antioxidant Activity. *Asian J. Pharm. Clin. Res,* 2018; 11: 346-50.

22. Laladhas KP, Cheriyan VT, Puliappadamba VT, Bava SV, Unnithan RG, Vijayammal PL, Anto RJ. A novel protein fraction from *Sesbania grandiflora* shows potential anticancer and chemopreventive efficacy, in vitro and in vivo. *J. Cell Mol. Med.* 2010;14: 636-46.

23. Gbeassor. M, Kedjagni AY, Koumaglo K, De Souza C, Agbo K, Aklikokou K, Amegbo KA. In vitro antimalarial activity of six medicinal plants. *Phytother. Res.* 1990; 4: 115–7.

24. Bunawan H, Dusik L, Bunawan SN, Amin NM. Botany, Traditional Uses, Phytochemistry and Pharmacology of *Archidendron jiringa*: A Review. *Global J. Pharmacol.* 2013; 7: 474-8.

25. Gul R, Jan SU, _Faridullah S, Sherani S, Jahan N. Preliminary Phytochemical Screening, Quantitative Analysis of Alkaloids, and Antioxidant Activity of Crude Plant Extracts from *Ephedra intermedia* Indigenous to Balochistan. *Sci. World. J.* 2017; Article ID 5873648.

26. Bauer AW, Kirby WMM, Sheriss JC, Turck M. Antibiotic susceptibility testing by a standardized single disk method. *Am. J. Clin. Pathol*. 1966; 45(4): 493-6.

27. Sarker SD, Nahar L, Kumarasamy Y. Microtitre plate-based antibacterial assay incorporating resazurin as an indicator of cell growth, and its application in the in vitro antibacterial screening of phytochemicals. *Methods,* 2007; 42: 321-4.

28. Begot C, Desnier I, Daudin JD, Labadie JC, Lebert A. Recommendations for calculating growth parameters by optical density measurements. *J. Microbiol. Meth.* 1996; 25: 225-32.

29. Priya V, Mallika J, Surapaneni KM, Saraswathi P, Chandra SG. Antimicrobacterial Activity of Pericarp Exstract of *Garcinia mangostana* Linn. *Int. J. Pharm. Sci. Res.* 2010; 8: 278-81.

30. Sopian A, Darmawan A, Simanjuntak P. Identification of phenolic compounds in Ethylacetate extract of Jengkol skin fruit. *Ej. Poltektegal.* 2019; 8: 51-5. (in Indonesian).

JOTCSA Journal of the Turkish Chemical Society Section: A Chemistry

TURKISH CHEMICAL SOCIETY

Phytochemical Screening and Antibacterial Activity of *Pistacia atlantica* and *Pinus canariensis* Leaf Extracts

Obaida ALHAJALI* and **Adnan ALI-NIZAM**
Damascus University, Faculty of Science, Damascus, Syria

Abstract: The qualitative detection of phytochemical compounds of extracts was carried out using color reagents, total content of phenols and flavonoids was specified using Folin-Ciocalteu and aluminum chloride method, respectively, and antioxidant activity was determined through its ability to free radicals scavenging using DPPH radical. The efficacy of the plant extracts against pathogenic bacteria was studied by agar well diffusion method with different concentrations, and microdilution method was used to measure minimum inhibitory concentration (MIC) of all plant extracts. The results showed presence of tannins, phenols, and flavonoids in all extracts of both plants, while saponins were found in aqueous extracts only, cardiac glycosides and coumarins were absent in all plant extracts. Ethanolic extract of *Pistacia atlantica* recorded the highest content of phenols and flavonoids as 263.76 ± 0.53 (mg GAE/g Dw) and 46.83 ± 0.55 (mg RE/g Dw), respectively. While aqueous extract of *Pinus canariensis* recorded the lowest content of of phenols and flavonoids 30.11 ± 0.37 (mg GAE/g Dw) and 5.43 ± 0.38 (mg RE/g Dw), respectively. Both plants have been shown to have good antioxidant activity, as ethanolic extract of P. atlantica recorded the best ability to free radicals scavenging 90.27% ±1.51, ethanolic extracts of both plants were the most effective in inhibiting bacteria especially at high concentrations (500 mg/mL); the inhibition zone diameter of *P. atlantica* extract reached 33.56 mm against *Shigella boydii*, while aqueous extract of *P. canariensis* was the most effective against *Pseudomonas aeruginosa*; the inhibition zone diameter was 21 mm. MIC ranged between 5.468 and 43.75 mg/mL depending on plant extract and bacterial species. This confirms the importance of plant extracts as a natural source of antibacterial to confront problems of increasing bacterial resistance to antibiotics that threaten public health.

Keywords: Total phenolic, flavonoid, DPPH, antibacterial activity, MIC value, Pistacia atlantica, Pinus canariensis.

Submitted: December 04, 2020. Accepted: February 06, 2021.

Cite this: ALHAJALI O, ALI-NIZAM A. Phytochemical Screening and Antibacterial Activity of Pistacia atlantica and Pinus canariensis Leaf Extracts. JOTCSA. 2021;8(2):403–18.

DOI: https://doi.org/10.18596/jotcsa.836074.

***Corresponding author. E-mail:** obaida.alhajali20@gmail.com.

INTRODUCTION

Plants have shown an important role in treating and preventing many diseases in pharmacology since past time, and plant extracts were used to treat various diseases such as diarrhea, sleep disorders and cough, infections, cancer, cardiovascular, and diabetes, due to their wide spread and diversity, and they contain many compounds with therapeutic characteristics. In addition, medicinal plants have been shown to possess the advantage of having low side effects compared to antibiotics (1, 2). About 80% of the world's population depends on traditional medicine according to WHO estimates. As a result, the demands of plant extracts for medicinal purposes in many countries had been increased (3). It was focused on that secondary metabolites in medicinal plants are characterized with different medicinal properties. On the other hand, detection of genes of Staphylococci maintained increasing antibiotic resistance as well as: amoxicillin/ clavulanic acid 65%, ampicillin 70%. Percentage of presence of MRSA strains was 15% and MRCNS was 6.66% (4). Occurrence of bacterial multidrug resistance feature side effects of medicine use induced WHO to maintaining importance of plants therapy (5). The random use of antibiotics used to treat diseases sometimes led to negative side effects on the host as immune response, allergic reactions,

and hypersensitivity, which necessitated to develop alternative drugs from different sources such as plants (6). A positive effect of *Myrtus communis* extracts occurred against pathogenic bacteria (7), and the effect of Lamiaceae plants extracts as Mentha and Ocimum; which induce to isolate and study phytochemicals for explaining its effects against microorganisms (8).

Pistacia atlantica (Anacardiaceae) is a tree with a length of 2-5 m, its branches are grayish-white and have leaves composed of 9 to 11 leaflets (pinnate compound leaves). Oleoresin is secreted by the trunk featuring a yellowish-green color and a mild smell (9), and it contains many chemical compounds in various parts of the plant: α-pinene, limonene, β-pinene, terpinolene, camphene, bornyl acetate, sabinene, p-mentha-1 (7),8 diene, Δ^3-carene, spathulenol, masticadienonic acid, morolic acid, gallic acid, oleanolic acid, tetragalloylquinic acid, quinic acid, quercetin-3-glucoside, 3-O-acetyl-3-epiisomasticadienolic acid, 3-methoxycarpachromene, β-myrcene, (9, 10, 11). P. atlantica has antibacterial activity, as a research has indicated that it has widespread inhibitory effects against number of Gram (-) bacteria (*E. coli, Proteus mirabilis, Pseudomonas aeruginosa, Enterobacter cloacea, Salmonella typhi, Acinetobacter baumannii*) and Gram (+) (*Staphylococcus aureus, Listeria monocytogenes*) (12, 13), and antifungal properties against some microorganisms (*Aspergillus fumigates, Aspergillus flavus, Aspergillus niger, Candida sp*) (14), and anti-adenovirus agent (15), and anti-inflammatory activity (16).

Pinus canariensis (Pinaceae) is an evergreen tree reaches more than 30 m high, resin canals in wood, bark, leaves and often cones, Dwarf shoots (fascicles) hold three long (20– 30 cm) needles (17). Analysis of the essential oil showed 116 compounds; more than 100 substances belonging to terpenoids: (sesquiterpenes, monoterpenes, and diterpenes) by 52.1%, 42.7%, and 4.8% respectively, the most important substances of monoterpenes are (α-pinene 23.1%, β- pinene 1.6%, myrcene 5.8%, limonene 10.1%) (18). Another study showed the presence of monoterpenes 30.7%, the most important of which were (α- pinene 14.6%, β- pinene 1.2%, myrcene 6.4%, and limonene 7.9%), and sesquiterpenes 66.6%, (as germacrene D formed the main compound 44%, then β-caryophyllene 8.7%), and diterpenes 2.4% (19). Pinus in traditional medicine are used for respiratory system as antiseptic and expectorant, also for gastrointestinal disorders, urinary system diseases and for the treatment of skin diseases. Pine needles extracts showed effect against a range of bacteria as (*Staphylococcus aureus, Escherichia coli, Pseudomonas aeruginosa,* and *Bacillus cereus*) (20) pine needles showed exhibit strong antioxidant, antimutagenic and also antitumor effects in vivo and point to their potential usefulness in cancer prevention (21).

The increase in the infectious diseases and the development of bacterial resistance to antibiotics, and their side effects necessitate search for new compounds that are effective against pathogenic bacteria. This research aims qualitative (alkaloids, cardiac glycosides, resins, tannins, flavonoids, saponins, phenols, and coumarins) and quantitative screening (total phenolic and flavonoid contents), and study of antioxidant activity of *Pistacia atlantica* and *Pinus canariensis* leaf extracts, and testing their bioactivity against pathogenic bacteria.

MATERIALS AND METHODS

Collection of Samples

Samples of *Pistacia atlantica* and *Pinus canariensis* leaves were collected in Sweida area (Syria) in September of 2019, and washed with distilled water to remove impurities, and dried in shadow for 14 days, and ground into a dry soft powder, and powders were stored in refrigerator at 4 °C until use (13).

Preparation of Extracts

Aqueous and ethanolic extracts were prepared using Soxhlet method; 50 grams of powdered leaves were separately extracted in 500 mL of water and ethanol at a ratio 1:10 (w/v) for 7 h, and filtered using Whatman filter paper №1. Filtrates were evaporated using a rotary evaporator under vacuum at 40 °C and kept in refrigerator at 4 °C until they were used (22). All extracts were sterilized before use by filtration through membrane filters 0.45 µm. Determination of percentage yield (%) was calculated using the formula (23):

yield % = (weight of final dried extract / weight of initial dried plant sample) x 100

Phytochemical Qualitative Screening Test

Test for Alkaloids

a-Dragendorff's reagent test: A few drops of Dragendorff's reagent were added to (1 mL) of each extracts and mixed, then diluted hydrochloric acid (2 mL) (HCl) were added. formation of precipitate of reddish-yellow color indicates appearance of alkaloids.

b- Mayer's test: To each 1 mL of studied extracts a few drops of Meyer's reagent were added. Formation of a creamy white precipitate indicates appearance of alkaloids (24).

Test of Cardiac glycosides

Keller Killiani Test: 1 mL of anhydrous acetic acid added to each extract of plant and shaken, then a few drops of ferric chloride were added, and 2-3 drops of sulfuric acid (concentrated) were added carefully to the test tube, appearance of a reddish-brown-colored ring at the junction of two layers, which confirms the positive test (24, 25).

Test for Resins
Turbidity test: 10 mL of distilled water was added to each plant extract, to which a few drops of 4% HCl were added. Appearance of turbidity in solution indicates presence of resins (25).

Test of Tannins
Lead acetate Test: A few drops of lead acetate were added to 1 mL of plant extract. Formation of a large white-brown precipitate indicates presence of tannins (24).

Tests for Flavonoids
a- Shinoda Test: 0.5 g of magnesium powder was added to each plant extract, then a few drops of concentrated hydrochloric acid were added. Appearance of a red color indicates presence of flavonoids.
b- Alkaline Test: Sodium hydroxide solution was added to 1-2 mL of each plant extract. A yellow to red color formed in test tube confirms presence of flavonoids (24, 25, 26).

Test for Saponins
One mL of plant extract was added to 20 mL of distilled water, and shaken vigorously for 5-10 minutes. Formation of a froth column that does not disappear by adding HCl indicates presence of saponins (25, 26, 27).

Test for Phenols
To each plant extract was added 1 mL of $FeCl_3$ (5%). Formation of bluish-black color indicates presence of phenols (25).

Test for Coumarins
One mL of each extract were taken in separate tubes, and covered with a filter paper moistened with 1N NaOH solution, and heated for a few minutes. When these tubes yield a yellow fluorescence under UV light, this indicates the presence of coumarins (24).

Phytochemical Quantitative Screening Test

Total phenolic content (TPC)
TPC in all plant extracts were measured by the Folin–Ciocalteu method, 1000 µL of each sample of concentration of 0.011 g/mL was added to 4.8 mL distilled water, 4 mL sodium carbonate 2% (Na_2CO_3) and 200 µL of Folin- Ciocalteu reagent and mixed fully, the absorbance was recorded at 760 nm by a spectrophotometer after 60 min of incubation, distilled water was used as a blank. A calibration curve of gallic acid solutions were prepared in ethanol at different concentrations 0 to 300 ppm (Figure 1), and the results were estimated as gallic acid equivalent for each gram of dry plant extract (mg GAE/g Dw). Total phenolic contents of samples were determined in triplicate (28, 29).

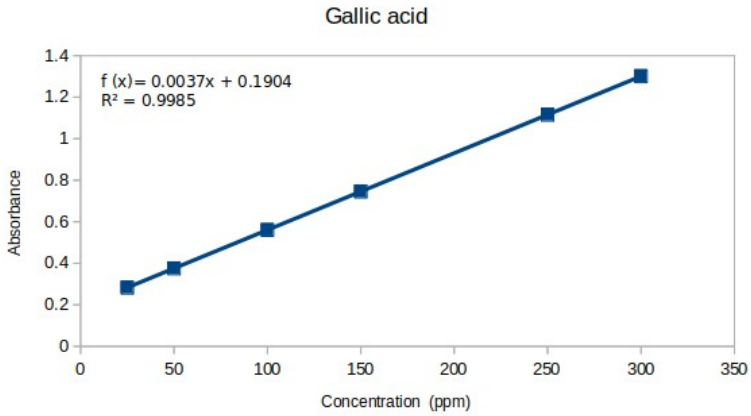

Figure 1. Calibration curve of gallic acid.

Total Flavonoid content (TFC)
TFC was measured using aluminum chloride method $AlCl_3,6H_2O$ in the plant extracts, each plant extract (0.5 mL) was added to distilled water (2 mL) and 150 µL of sodium nitrite $NaNO_2$ (5% w/v). After 5 minutes, 10% of aluminum chloride solution (150 µL) was added to mixture, then incubated in the dark for 6 min. Finally, 4% of NaOH (2 mL) was added and mixed well, after 15 minutes of incubation in the dark the solutions turned to pink. Distilled water was used as a blank, the absorbance was recorded at 510 nm by a spectrophotometer, a calibration curve of rutin solutions were prepared at different concentrations 0 to 150 ppm (Figure 2), and the results were estimated as rutin equivalent per gram of dry plant extract (mg RE/g Dw). Total flavonoid of samples were measured in triplicate (30).

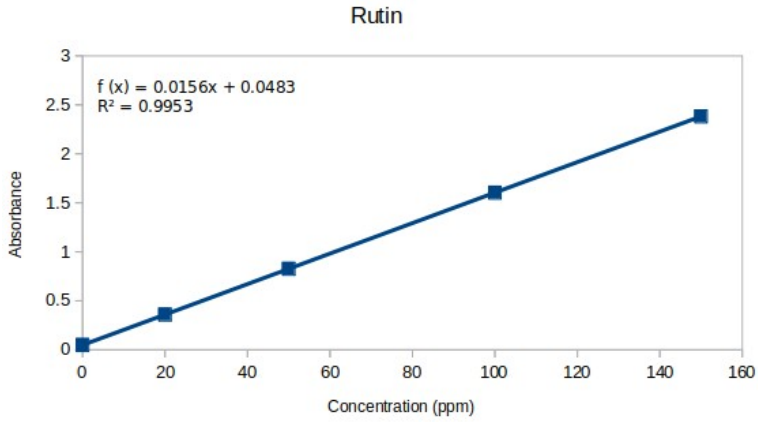

Figure 2. Calibration curve of rutin.

Antioxidant Activity

DPPH Radical Scavenging Activity Assay

Each plant extract (300 µL) of concentration of 0.001 g/mL was added in test tubes separately, and 3 mL of DPPH in ethanol (45 µg/mL) was added to each tube and mixed vigorously, after 30 min of incubation without light the absorbance was recorded at 515 nm by a spectrophotometer. The results were presented compared to ascorbic acid which was prepared as standard with different concentrations from 0 to 0.5 mM/L (Figure 3). The results were calculated as a percentage (%) using the following formula (31):

$$\text{Scavenging DPPH (\%)} = A_{control} - A_{sample} / A_{control} \times 100$$

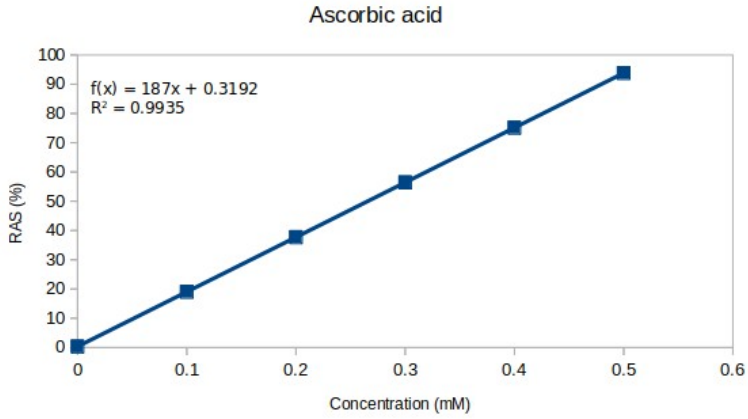

Figure 3. Calibration curve of ascorbic acid.

Antibacterial Susceptibility Test

Bacterial Isolates

The antibacterial test was carried out using: *Staphylococcus aureus, Klebsiella pneumoniae, E. coli, Proteus mirabilis, Pseudomonas aeruginosa, Shigella boydii,* and *Enterobacter cloacae*, were obtained from the microbiology Laboratory - Department of Plant Biology, Faculty of Science at the university of Damascus (Syria).

Antibacterial Activity

The bacterial susceptibility tests for plant extracts were performed by agar well diffusion method on Mueller-Hinton agar. The bacterial isolates were activated for 24 h at 37 °C on nutrient agar, then a bacterial suspension was prepared in a saline solution [sterile NaCl 0.85% (w/v)]. Turbidity of prepared bacterial suspension was 0.5 McFarland (10^8 CFU/mL). The suspension was used to inoculate 9-cm-diameter Petri dishes with a sterile cotton swab, after that 5-6 wells (4 mm diameter) were punched in the agar plate, and 50 µL of plant extracts were added in each well. All plates were placed in the refrigerator (4 °C) for 2 h in order to allow diffusion of plant extracts into the medium. Then the plates were incubated for 24 h at 37 °C. After incubation, inhibition zone diameters were measured to determine the effectiveness of extracts against tested bacteria. Tests were performed in triplicates per experiment and the average of the results was taken, the plant extracts were dissolved in dimethyl sulfoxide solution (DMSO) to obtain the concentrations 500, 350, 250, 150, 50 mg/mL. DMSO solution was used as negative control, and the antibiotics Moxifloxacin 5 mcg and Gentamicin 10 mcg as positive control (30, 32).

Determination of MIC

MIC was measured by nutrient broth microdilution in microtitration plates containing 96 well (33, 34)

with some modifications. The turbidity of prepared bacterial suspension was 0.5 McFarland (10^8 CFU/mL). First, the dry extracts were dissolved in DMSO to obtain a concentration of (350 mg/mL) to be tested, then serial two-fold dilution was performed in a concentration range of 0.683 to 350 mg/mL. For each test batch, two control wells were prepared; negative control: nutrient broth medium (50 µL) and bacterial suspension (50 µL) in first well, positive control: plant extract (50 µL) and bacterial suspension (50 µL) in second well, all wells except the second were filled with the nutrient broth (50 µL). Then, 50 µL of plant extract at the highest concentration (350 mg/mL) were added to the third well and mixed, 50 µL of mixture was taken for fourth well and so until serial decreasing concentrations were obtained in the rest of the wells. Then the wells were inoculated with bacterial suspension 50 µL, and the plates were incubated for 24 h at 37 °C. Each well contained 100 µL (final volume). After incubation, a solution (20 µL) of 2,3,5-triphenyltetrazolium chloride (TTC) dissolved in water (0.01%, w/v) was added to each well and plates were incubated for an additional 2 h. Results were estimated visually by observing the color change from yellow to red, which is an indication of bacterial growth and determined MIC as lowest concentration in which it appeared medium in yellow (no red color) (33).

Statistical Analysis

SPSS software (version 22) was used by one-way ANOVA to analyze the data statistically. Pearson's correlation was used to determine the correlation between TPC, TFC and antioxidant activity. Data was considered statistically significant at minimum level of $P < 0.05$.

RESULTS AND DISCUSSION

Phytochemical qualitative screening of active chemical compounds

Pistacia atlantica extracts were distinguished by their high (very rich) of phenolic, tannin, and flavonoid contents and they were higher than and Pinus canariensis extracts (Table 1).

Saponins were found with a high content in P. canariensis aqueous extract, as a column of foam was formed more than 3 cm high and foam did not disappear after adding HCl.

A high content of resin were found in ethanolic extract of P. canariensis, while it was absent in the aqueous extract of Pistacia atlantica, while alkaloids were absent in aqueous and ethanolic extracts of P. atlantica, and found only in a small amount in aqueous extract of Pinus canariensis. Coumarins and cardiac glycosides were not found in all extracts of both plants. For detection of active chemical compounds in P. atlantica leaves extracts; two studies in Libya and Armenia indicated that extracts contained phenols, flavonoids, and tannins. However, the study in Armenia showed the presence of coumarins, and this difference with our research may be due to the difference in the genetic combination of the plant, climatic conditions, and geographical location, in addition to the extraction methods and the quality of the solvents used (35, 36). No references were found concerned with phytochemical screening of Pinus canariensis extracts. Our results were however similar to many studies that indicated presence of phenols, saponins, and tannins in other species of the pine genus (37).

Table 1. Phytochemical screening of *Pistacia atlantica* and *Pinus canariensis* leaves extracts.

Chemical components	*P. atlantica*		*P. canariensis*	
	Aqueous extract	Ethanolic extract	Aqueous extract	Ethanolic extract
Alkaloids	-	-	+	-
Cardiac glycosides	-	-	-	-
Resins	-	+	+	++
Tannins	+++	+++	+++	++
Phenols	+++	+++	++	++
Flavonoids	++	++	+	+
Saponins	+	-	+++	-
Coumarins	-	-	-	-

−: absence , +: presence in small quantities, ++: presence in high quantities, +++: presence in very high quantities.

Determination of yields, TPC, and TFC of P. atlantica and P. canariensis leaves extracts

Yields of plant extracts differed according to extraction solvent used and plant species. The yields of ethanolic and aqueous extracts of Pistacia atlantica were 30.12% ± 0.14 and 24.20% ± 0.08, respectively, significantly higher than the yields of ethanolic and aqueous extracts of Pinus canariensis which amounted to 20.53% ± 0.09 and 15.77% ± 0.04, respectively (Table 2).

Results showed that TPC and TFC varies between both plants; P. atlantica extracts contained higher concentrations of phenols and flavonoids compared to P. canariensis extracts, phenolic contents of ethanolic extracts of P. atlantica and P. canariensis were 263.76 ± 0.53, and 40.52 ± 0.58 mg GAE/g

Dw, respectively, while aqueous extracts reached 241.64 ± 0.16 and 30.11 ± 0.37 mg GAE/g Dw for the studied species, respectively. While the flavonoid contents of ethanolic extract of P. atlantica and P. canariensis reached 46.83 ± 0.55 and 9.80 ± 0.12 mg RE/g Dw, respectively, and the aqueous extract of P. atlantica and P. canariensis reached 31.81 ± 0.26 and 5.43 ± 0.38, respectively (Table 2).

Results of our study are consistent with many studies that prove that P. atlantica leaves extracts contain a good content of phenols and flavonoids at varying proportions, as one of the studies conducted in Tunisia showed TPC and TFC in ethanolic extract is higher than in aqueous, as TPC of ethanolic and aqueous extracts reached 68.23 ± 0.8 and 20.07 ± 0.2 mg GAE/g Dw, respectively, while TFC reached 44 ± 0.8, and 15 ± 0.2 mg RE/g Dw for ethanolic and aqueous extracts, respectively (38).

TPC in aqueous, ethyl acetate, and n-butanol extracts of P. atlantica leaves in Algeria were 421.01 ± 8.92, 514.81 ± 2.10, and 376.34 ± 3.43 mg GAE/g Dw, respectively, while TFC were 44.51 ± 0.29, 126.43 ± 1.31, and 103.77 ± 1.07 mg CE/g DW for previous extracts, respectively (39). One study was concerned in studying the effect of growing area, harvest time, and gender on phenolic and flavonoids compounds of P. atlantica leaves extracts. Results showed that phenols ranged between 79.00 ± 13 and 259 ± 8 mg GAE/g Dw, while flavonoids ranged between 0.65 ± 0.10 and 2.81 ± 0.88 mg QE/g DW depending on the study period, phenolic contents of leaves is shown to decrease from spring to autumn; the content was affected by harvest time and growing region more than plant gender (male or female) (40).

No references were found concerning with TPC and TFC of P. canariensis extracts. Therefore, these results were compared with the results of research conducted on other species of pine genus, one of these studies determined TPC and TFC in aqueous, ethanol, and n-butanol extracts of Pinus roxburghii and Pinus wallichiana; phenolic contents of different solvents ranged 3.94 ± 0.03, 10.08 ± 0.06, and 8.55 ± 0.28 mg GAE/g Dw respectively for Pinus roxburghii, while ranged 4.09 ± 0.43 and 4.06 ± 1.12 mg GAE/g Dw for ethanolic and butanol extracts respectively for Pinus wallichiana, while the phenolic contents were absent in aqueous extract for Pinus wallichiana (41). Results of the study conducted in Tunisia to determine content of phenols and flavonoids in ethanol extracts of leaves of 19 subspecies of Pinus nigra showed that total phenols ranged from 15.67 ± 1.95 and 47.53 ± 1.32 mg GAE/g Dw, and amount of flavonoids varies from 1.69 ± 0.32 and 3.97 0.17 mg RE/g Dw (42), while the study conducted in Romania showed a good content of phenols 78.22 ± 0.44 mg GAE/g Dw and flavonoids 19.84 ± 0.57 mg CE/g DW for Pinus cembra needle extract (aqueous methanol extract 80%) (20).

It should be noted that content of phenols and flavonoids in plant species in general is affected by different environmental factors characteristic of each geographical region, in addition to the difference in time of samples collection which in turn depended on growth rate, genetic diversity, different methods of storing and drying samples, and difference in extraction methods and solvent used in preparation of plant samples (39).

Table 2. Yields, TPC, and TFC in *Pistacia atlantica* and *Pinus canariensis* leaves extracts.

Plant species	Plant extract	Yields (%)	Contents	
			Total phenolic (TP) (mg GAE/g Dw)	Total Flavonoid (TF) (mg RE/g Dw)
P. atlantica	Aqueous	24.20 ± 0.08	241.64 ± 0.16	31.81 ± 0.26
	Ethanolic	30.12 ± 0.14	263.76 ± 0.53	46.83 ± 0.55
P. canariensis	Aqueous	15.77 ± 0.04	30.11 ± 0.37	5.43 ± 0.38
	Ethanolic	20.53 ± 0.09	40.52 ± 0.58	9.80 ± 0.12

Antioxidant activity

Antioxidant activity was determined by calculating percentage of ability to DPPH radical scavenging as shown in Table 3. Results showed a good efficacy of plant extracts in scavenged DPPH radical, as antioxidant efficacy was arranged as follows: ethanolic extract of *P. atlantica* 90.27%, aqueous extract of *P. atlantica* 81.77%, ethanolic extract of *P. canariensis* 52.40%, aqueous extract of *P. canariensis* 38.44 %, this arrangement corresponds to the order of total content of phenols and flavonoids in the studied plant extracts and confirms the role of these compounds as antioxidants. It was found that the concentration of ascorbic acid corresponding to the concentration of plant extracts and is able to record the same percentage of DPPH scavenging less than the concentration of the plant extracts by 11.42 - 19.04 double, as shown in Table 3. Therefore, both plants have good capacity in scavenging DPPH radical, and thus have antioxidant efficacy.

Phenolic compounds power as antioxidant is due to their ability to chelate metals, and their capacity as

donors of hydrogen and electron from hydroxyl group allowing scavenging free radicals (43, 44), and corresponds to many studies that have shown that there was a strong correlation between content of phenols and antioxidant activity, confirming their responsibility as antioxidants (30, 45).

Results of the statistical study using Pearson's correlation showed a strong positive correlation 0.976 between efficiency of extracts in DPPH radical scavenging and their total phenolic contents, and their total flavonoid contents 0.974, this confirms responsibility of these compounds for plant extracts efficiency as antioxidant.

Table 3. Antioxidant activity of *P. atlantica* and *Pinus canariensis* leaves extract.

Species	Plant extracts	Concentration of extract (g/mL)	DPPH (%)	Corresponding concentration of ascorbic acid (g/mL)	Comparison of extracts efficiency with ascorbic acid
Pistacia atlantica	Aqueous	0.001	81.77 ±1.32	7×10^{-5}	14.28
	Ethanolic	0.001	90.27 ±1.51	8.75×10^{-5}	11.42
Pinus canariensis	Aqueous	0.001	38.44 ± 0.33	3.5×10^{-5}	28.57
	Ethanolic	0.001	52.40 ± 0.47	5.25×10^{-5}	19.04

Antibacterial activity

Antibacterial activity of Pistacia atlantica

Table 4 and Figure 4 shows results of antibacterial activity of P. atlantica leaves extracts, ethanolic extract was found to be more effective and broad-spectrum inhibition of bacterial growth compared to aqueous extract.

The highest inhibition zone diameter average of ethanolic extract was 14.83, 19.33, 20.96, 23, 26, and 33.56 mm for *E. coli, Klebsiella pneumoniae, Enterobacter cloacae, Proteus mirabilis, Staphylococcus aureus,* and *Shigella boydii*, respectively, at 500 mg/mL.

The lowest inhibition zone diameter average of ethanolic extract was 10.7, 10.9, 12.16, 18.5 and 26.0 mm for *Pseudomonas aeruginosa, Proteus mirabilis, Enterobacter cloacae, Staphylococcus aureus,* and *Shigella boydii*, respectively, at 50 mg/mL.

Ethanolic extract showed inhibitory activity of bacteria at all studied concentrations except for *E. coli* and *Klebsiella pneumoniae* at 50 mg/mL.

The highest inhibition zone diameter average of aqueous extract was 11.0, 12.0, 13.25, 18.25, 24.65 and 29.25 mm for *E. coli, Enterobacter cloacae, Proteus mirabilis, Staphylococcus aureus* and *Shigella boydii,* respectively at 500 mg/mL.

Aqueous extract didn't show any antibacterial activity at 50 mg/mL except of *E. coli, Pseudomonas aeruginosa,* and *Shigella boydii*, as inhibition zone diameter average was 5.5, 7.5 and 18.2 mm, respectively.

While *Klebsiella pneumoniae* and *Enterobacter cloacae* didn't show sensitivity against aqueous extract except at concentrations 350 and 500 mg/mL, and equal efficacy of ethanolic and aqueous extracts against *Pseudomonas aeruginosa* were observed at a concentration of 500 mg/mL, the inhibition zone diameter average were 16.83 and 16.74 mm, respectively. The higher of extracts concentration increases their efficiency in bacteria.

Table 4. Antibacterial activity (inhibition zone diameters average, mm) of *Pistacia atlantica* leaves extracts.

Bacterial Strains	Concentrations mg/mL	Aqueous Extract	Ethanolic Extract	Moxifloxacin 5 mcg	Gentamicin 10 mcg	DMSO
E.coli	50	5.5 ± 0.5	0.0	0.0	16.5 ± 0.5	0
	150	6.75 ± 0.25	8.9 ± 0.1			
	250	8 ± 0.0	10.43 ± 0.40			
	350	8.5 ± 0.5	13.5 ± 0.5			
	500	12 ± 1	14.83 ± 0.28			
Klebsiella pneumoniae	50	0.0	0.0	31.5 ± 0.5	18.16 ± 0.28	0
	150	0.0	10.03 ± 0.55			
	250	0.0	13.33 ± 0.76			
	350	6.5 ± 0.5	15.96 ± 0.45			
	500	11 ± 1	19.33 ± 0.57			
Enterobacter cloacae	50	0.0	12.16 ± 0.76	29 ± 0.0	17.75 ± 0.25	0
	150	0.0	15.03 ± 0.25			
	250	0.0	16.7 ± 0.3			
	350	10.5 ± 0.5	18.5 ± 0.5			
	500	13.25 ± 0.75	20.96 ± 0.45			
Shigella boydii	50	18.2 ± 0.8	26 ± 1	30.25 ± 0.25	25.75 ± 0.75	0
	150	20.5 ± 0.5	28.5 ± 0.5			
	250	21.5 ± 0.5	30.4 ± 0.4			
	350	24.5 ± 0.5	31.25 ± 0.25			
	500	29.25 ± 0.75	33.56 ± 0.51			
Pseudomonas aeruginosa	50	7.5 ± 0.5	10.7 ± 0.46	22.75 ± 0.75	21.5 ± 0.5	0
	150	11.1 ± 0.1	12.5 ± 0.5			
	250	12 ± 0.0	13.8 ± 0.28			
	350	14.5 ± 0.9	14.9 ± 0.17			
	500	16.74 ± 0.8	16.83 ± 0.65			
Proteus mirabilis	50	0.0	10.9 ± 0.55	0.0	0.0	0
	150	8.85 ± 0.15	14.5 ± 0.5			
	250	12 ± 1	18.05 ± 0.25			
	350	14.9 ± 0.1	20.13 ± 0.40			
	500	18.25 ± 0.25	23 ± 0.2			
Staphylococcus aureus	50	0.0	18.5 ± 0.5	32 ± 1	10.25 ± 0.25	0
	150	14.25 ± 0.75	20.33 ± 1.15			
	250	17.4 ± 0.2	22 ± 1			
	350	21.5 ± 0.5	24 ± 0.0			
	500	24.65 ± 0.35	26 ± 0.2			

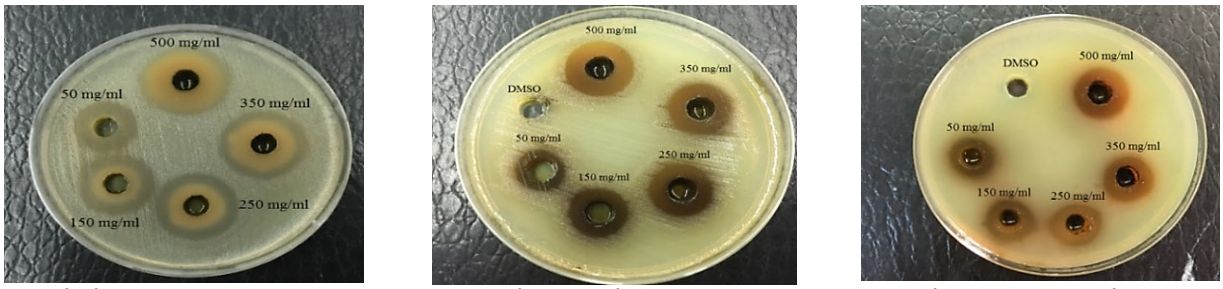

Staphylococcus aureus *Enterobacter cloacae* *Pseudomonas aeruginosa*

Effect of ethanolic extracts of *Pistacia atlantica* against the microorganisms above

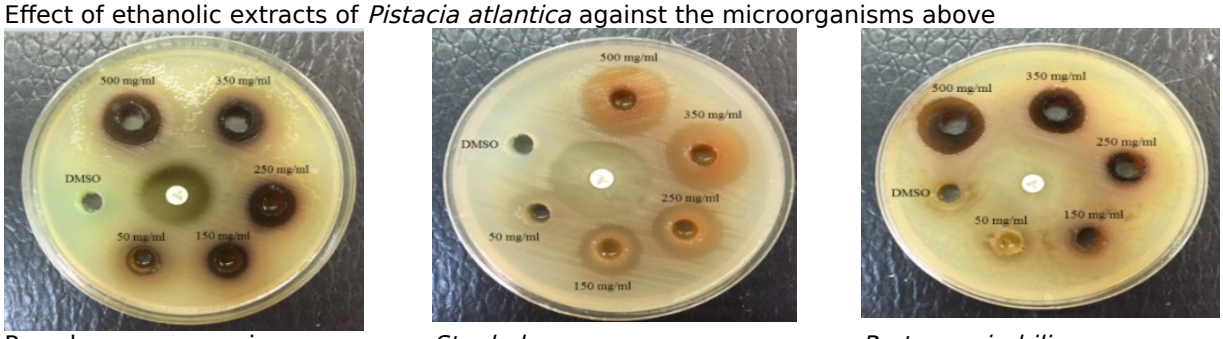

Pseudomonas aeruginosa *Staphylococcus aureus* *Proteus mirabilis*

Effect of aqueous extracts of *Pistacia atlantica* against the microorganisms above

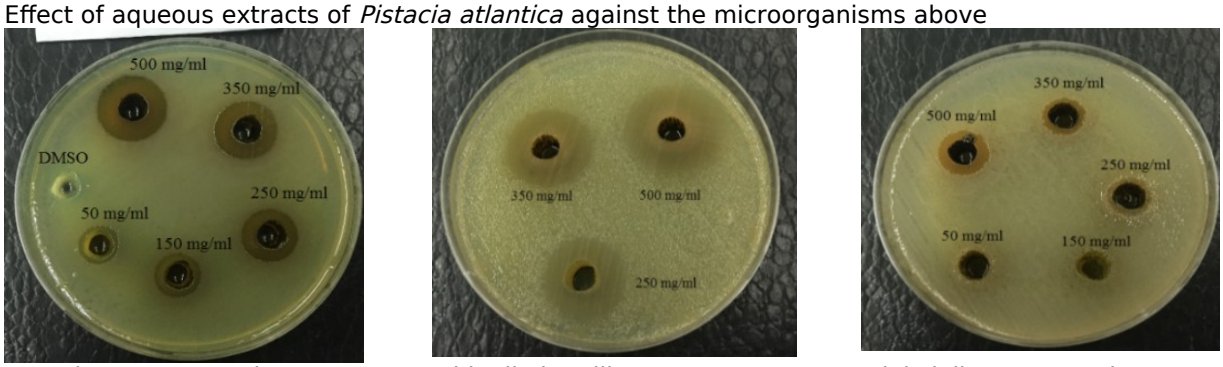

Pseudomonas aeruginosa *Shigella boydii* *Klebsiella pneumoniae*

Effect of ethanolic extracts of *Pinus canariensis* against the microorganisms above

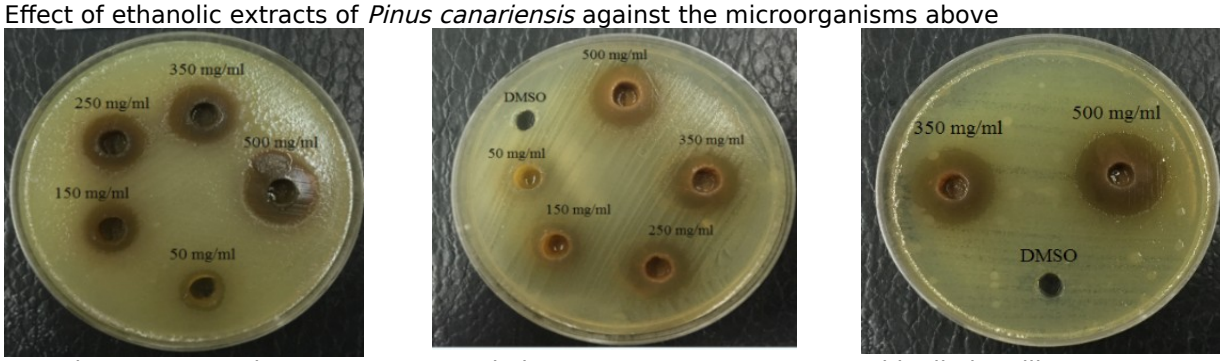

Pseudomonas aeruginosa *Staphylococcus aureus* *Shigella boydii*

Effect of aqueous extracts of *Pinus canariensis* against the microorganisms above

Figure 4. Effect of different extracts of plants against bacteria.

Results are in agreement with one of studies that indicated efficacy of ethanolic extract against *E. coli* and *Pseudomonas aeruginosa* reached 14 ± 0.9 and 16 ± 0.3 mm, respectively, while its results were less effective against *Staphylococcus aureus* which reached 14±1 mm (38). Also, efficacy of Pistacia atlantica extracts against *Klebsiella pneumoniae* was reported, which was recorded 13 ± 0.3 mm (46), and the results of this research did not agree with results (35); which did not show of *P. atlantica* leaves extract efficacy against Gram(-) bacteria *Proteus vulgaris*, and *E. coli*, but its efficacy against *Staphylococcus saprophyticus* was 8 mm, and boiled distilled water extract of *P. atlantica* leaves showed an inhibitory effect for *Streptococcus mutans* and *Streptococcus mitis* 19 and 25 mm, respectively, it was less effective against *Streptococcus salivarius* 5 mm (47).

Antibacterial activity of Pinus canariensis

Results of Table 5 and Figure 4 showed that aqueous leaves extract was more effective than ethanolic extract in inhibition of Pseudomonas aeruginosa growth at all concentrations; the highest inhibition zone diameter average was 21 mm at a concentration of 500 mg/mL. Ethanolic extract was the most effective in inhibition of *E. coli, Klebsiella pneumoniae, Enterobacter cloacae, Proteus mirabilis, Staphylococcus aureus,* and *Shigella boydii*; the highest inhibition zone diameter average was 14.16, 14.25, 15.5, 15.75, 22.75 and 29.56 mm, respectively at concentration 500 mg/mL.

Effect of aqueous and ethanolic extract on bacteria at concentration 50 mg/mL was not observed with exception of *Pseudomonas aeruginosa* and *Shigella boydii*.

The highest inhibition zone diameter average of aqueous extract for *Staphylococcus aureus* and *Shigella boydii* 18.5 and 23.4 mm respectively, and the lowest inhibition zone diameter average for *Proteus mirabilis* and *E. coli* 11.5 and 11.16 mm respectively, at 500 mg/mL. Aqueous extract showed no effect in of *Proteus mirabilis, Enterobacter cloacae, Klebsiella pneumoniae,* and E. coli at concentrations of 50, 150 and 250 mg/mL, inhibition zone diameter average didn't exceed 13 mm in *Klebsiella pneumoniae* and *Enterobacter cloacae* at concentration of 500 mg/mL, the effect of concentrations of extracts in bacteria growth was observed, as with increasing concentration, inhibition zone diameter increased. Compared with another studies, Pinus leaves extracts (water, ethanol, chloroform, and petroleum ether) showed efficacy against E. coli, Klebsiella pneumoniae, Salmonella typhi and Enterobacter aerogene, and better efficacy was of petroleum ether, chloroform, water, and ethanol extracts, inhibition zone diameter average didn't exceed 10 mm in water and ethanol extracts (22). Results of the research are in agreement with the study conducted in Iran, where efficacy of ethanolic leaves extract reached 70% against clinical isolates Pseudomonas aeruginosa and E. coli and Proteus vulgaris 17, 15.66 and 15.50 mm, respectively, while it was less effective against Staphylococcus aureus, which was 16 mm (48).

Aqueous and ethanolic extract of Pinus leaves showed a lower effect against Pseudomonas aeruginosa with inhibition zone diameter average of 9.5 and 11 mm, respectively, while our results show a better effect against this Pseudomonas aeruginosa, effect of ethanolic extract was absent on Salmonella typhi, and inhibition zone diameter average of aqueous extract against E. coli was 11 mm, and this is in agreement with the results of our study (49) .

The difference in efficiency of these extracts compared to previous studies is due to various reasons, the most important of which are: difference of tested bacterial isolates, as a current study used multi-resistant bacteria, the difference in solvent and thus difference in quality of active compounds extracted, and the difference of extraction methods and concentration of used plant extract. Results showed that some plant extracts have better antibacterial activity than antibiotics Moxifloxacin 5 mcg and Gentamicin 10 mcg, and DMSO solution didn't show any effect in tested bacteria, this confirms that DMSO doesn't have any antimicrobial activity, where plant extracts recorded significant ($P<0.05$) antibacterial activity between all bacterial inhibition zone diameters averages.

The efficiency of plant extracts is due to they contain many chemical compounds (secondary metabolites) that have antibacterial activity with different mechanisms; phenolic compounds interaction with bacterial cell wall (either they bind to outer membrane or peptidoglycan), and interaction with membrane proteins (increasing membrane permeability). In addition to their ability to inhibition of biofilm formation, and to inhibition of bacterial enzymes, thus preventing bacterial growth. Found that Gram(-) bacteria are more resistant than Gram(+) bacteria to phenolic compounds actions; due to differences in cell wall structure, as outer membrane of Gram(-) bacteria is mainly composed of lipopolysaccharides (LPS) (50, 51, 52). It should be noted that this antimicrobial activity is not only related to quantities of phenolic compounds but also related to structure of these compounds (site(s) and number of hydroxyl groups on phenol group) (53). Nonspecific interactions of flavonoids can induce structural changes in properties of membrane and its can cause metabolic dysfunction and finally lead to bacterial death. Moreover, they are inhibit of synthesis of cell envelope, nucleic acid, and ATP, in addition to their ability to inhibition of bacterial toxins (54). Tannins may be related to their ability to inactivate microbial adhesins, have a role on inhibition of enzymes essential to metabolism process; such as proteolytic macerating enzymes, and their ability to inactivate cell envelope transport proteins, and their ability to complex with cell wall, while, saponins cause cell walls permeability disruption, and thus cause toxicity in cell (53).

Determination of MIC for P. atlantica and P. canariensis extracts

MIC of aqueous extract of *P. atlantica* ranged from 10.937 mg/mL for *Proteus mirabilis* to 43.75 mg/mL for *Pseudomonas aeruginosa*, while ethanolic extract of *P. atlantica* ranged from 5.468 mg/mL for *E. coli, Enterobacter cloacae, Shigella boydii, Proteus mirabilis,* and *Staphylococcus aureus* to 10.937 mg/mL for *Klebsiella pneumoniae* and *Pseudomonas aeruginosa*, the aqueous extract *of*

P. canariensis ranged from 21.875 mg/mL for *E. coli, Shigella boydii,* and *Staphylococcus aureus* to 43.75 mg/mL for *Klebsiella pneumoniae, Enterobacter cloacae, Pseudomonas aeruginosa, and Proteus mirabilis,* while ethanolic extract of *P. canariensis* ranged from 5.468 mg/mL for *Staphylococcus aureus* to 21.875 mg/mL for *Klebsiella pneumoniae, Enterobacter cloacae,* and *Pseudomonas aeruginosa* as shown in Table 6. Compared with the Tunisian study, MIC of ethanolic extract of *P. atlantica* leaves reached 25 mg/mL for *E. coli*, 6.25 mg/mL for *Pseudomonas aeruginosa* and 12.5 for Staphylococcus aureus and Salmonella typhimurium, the values obtained in the current study are better for E. coli and Staphylococcus aureus (38). MIC of ethanolic extract of pinus leaves reached 7.29 mg/mL for Pseudomonas aeruginosa, 9.37 mg/mL for Staphylococcus aureus, 16.66 mg/mL for E.coli and Proteus vulgaris, results of MIC in the current study are better for E. coli and Staphylococcus aureus (48). Difference in these values can be explained by different sensitivity and resistance of tested bacterial isolates, and difference in environment and genetic combination of plant.

CONCLUSION

The current study showed of *P. atlantica* extracts gave a higher yield than of *P. canariensis* extracts. Phytochemical compounds (tannins, phenols, and flavonoids) were found in the extracts of both plants, while saponins were present in the aqueous extracts only. *P. atlantica* extracts contained a higher content of phenols and flavonoids compared to *P. canariensis* extracts, while all extracts had antioxidant activity which could be a suitable alternative to synthetic antioxidants, and all extracts showed antibacterial activity, but not all concentrations showed bioactivity against some of tested bacterial species, it was found that antibacterial activity increases with increasing concentration of plant extracts, and *Shigella boydii* was the most sensitive against of extracts of both plants, therefore, more studies are needed to isolate bioactive compounds from both plants extracts, which will help in development of medicinal and pharmaceutical products.

Table 5. Antibacterial activity (inhibition zone diameters average, mm) of *Pinus canariensis* leaves extracts.

Bacterial Strains	Concentrations mg/ mL	Aqueous Extract	Ethanolic Extract	Moxifloxacin (5 mcg)	Gentamicin (10 mcg)	DMSO
E. coli	50	0.0	0.0	0.0	0.5 ± 16.5	0
	150	0.0	0.0			
	250	0.0	9.75 ± 0.25			
	350	0.0	12.7 ± 0.3			
	500	11.16 ± 0.76	14.16 ± 0.76			
Klebsiella pneumoniae	50	0.0	0.0	31.5 ± 0.5	18.16 ± 0.28	0
	150	0.0	0.0			
	250	0.0	10.5 ± 0.5			
	350	11.75 ± 0.25	12.13 ± 0.23			
	500	12.75 ± 0.25	14.25 ± 0.25			
Enterobacter cloacae	50	0.0	0.0	29 ± 0.0	17.75 ± 0.25	0
	150	0.0	9.5 ± 0.5			
	250	0.0	12.03 ± 0.55			
	350	8.66 ± 0.76	13.25 ± 0.25			
	500	13 ± 1	15.5 ± 0.5			
Shigella boydii	50	14.1 ± 0.36	19.25 ± 0.25	30.25 ± 0.25	25.75 ± 0.75	0
	150	17.66 ± 0.57	21.3 ± 0.3			
	250	19.5 ± 0.5	23 ± 0.0			
	350	20.6 ± 0.4	24.66 ± 0.57			

	500	23.4 ± 0.36	29.56 ± 0.51			
Pseudomonas aeruginosa	50	10.5 ± 0.5	10.25 ± 0.25	22.75 ± 0.75	21.5 ± 0.5	0
	150	13.3 ± 0.2	12.25 ± 0.25			
	250	16.25 ± 0.25	14.5 ± 0.5			
	350	17.7 ± 0.3	17 ± 0.0			
	500	21 ± 1	18.5 ± 0.5			
Proteus mirabilis	50	0.0	0.0	0.0	0.0	0
	150	0.0	0.0			
	250	0.0	9.5 ± 0.5			
	350	9.25 ± 0.25	11.75 ± 0.75			
	500	11.5 ± 0.5	15.75 ± 0.25			
Staphylococcus aureus	50	0.0	13 ± 0.5	32 ± 1	10.25 ± 0.25	0
	150	8.4 ± 0.36	15.25 ± 0.25			
	250	13.53 ± 0.50	18.06 ± 0.11			
	350	15.75 ± 0.25	20 ± 0.0			
	500	18.5 ± 0.5	22.75 ± 0.75			

Table 6. MIC of *Pistacia atlantica* and *Pinus canariensis* leaves extracts.

Bacterial strains	***P. atlantica***		***P. canariensis***	
	Aqueous extract mg/mL	**Ethanolic extract mg/mL**	**Aqueous extract mg/mL**	**Ethanolic extract mg/mL**
E. coli	21.875	5.468	21.875	10.937
Klebsiella pneumoniae	21.875	10.937	43.75	21.875
Enterobacter cloacae	21.875	5.468	43.75	21.875
Shigella boydii	21.875	5.468	21.875	10.937
Pseudomonas aeruginosa	43.75	10.937	43.75	21.875
Proteus mirabilis	10.937	5.468	43.75	10.937
Staphylococcus aureus	21.875	5.468	21.875	5.468

REFERENCES

1. Sarker SD. Pharmacognosy in modern pharmacy curricula. Pharmacognosy magazine. 2012 Apr;8(30):91. DOI: 10.4103/0973-1296.96545.

2. Bahmani M, Saki K, Asadbeygi M, Adineh A, Saberianpour S, Rafieian-Kopaei M, Bahmani F, Bahmani E. The effects of nutritional and medicinal mastic herb (Pistacia atlantica). Journal of Chemical and Pharmaceutical Research. 2015(1):646-53.

3. World Health Organization. WHO guidelines on safety monitoring of herbal medicines in pharmacovigilance systems. World Health Organization; 2004.

4. Ali - Nizam A, Hussain M. Prevalence, Antibiotic resistance of Staphylococcus aureus, CNS and determination of MRSA, MRCNS strains in clinical samples. Tishreen University Journal for Research and Scientific Studies-Biological Sciences Series. 2016; 38(1):167-80.

5. Lopez-Romero JC, González-Ríos H, Borges A, Simões M. Antibacterial effects and mode of action of selected essential oils components against Escherichia coli and Staphylococcus aureus. Evidence-Based Complementary and Alternative Medicine. 2015 Jan 1;2015. doi: 10.1155/2015/795435.

6. Krishnamurthy V, Chandrashekar S, Kumar M, Sagar D. Efficiency of Crude Extract of Ocimum sanctum, Ocimum gratissimum and Ocimum basilicum leaves against bacterial pathogens. Int. J. Curr. Microbiol. App. Sci. 2018; 7(4): 2609-15.

7. Layqa M, Ali–Nizam A, Alqadi I. Antibacterial Activity of White and Blue Wild Myrtle Parts Extracts Against Staphylococcus aureus and Staphylococcus epidermidis. Egypt. J. Microbiol. 2015; 50, 17- 29.

8. ASSIS FV, Siqueira FL, Goncalves IE, Lacerda RP, Nascimento RA, Araujo SG, Andrade JT, Herrera K, Lima LA, Ferreira J. Antibacterial activity of Lamiaceae plant extracts in clinical isolates of multidrug-resistant bacteria. Anais da Academia Brasileira de Ciências. 2018 Apr;90(2):1665-70. Doi: 10.1590/0001-3765201820160870.

9. Mahjoub F, Rezayat KA, Yousefi M, Mohebbi M, Salari R. Pistacia atlantica Desf. A review of its traditional uses, phytochemicals and pharmacology. Journal of medicine and life. 2018 Jul;11(3):180. Doi: 10.25122/jml-2017-0055.

10. Mecherara-Idjeri S, Hassani A, Castola V, Casanova J. Composition of leaf, fruit and gall essential oils of Algerian Pistacia atlantica Desf. Journal of Essential Oil Research. 2008 May 1;20(3):215-9. Doi: 10.1080/10412905.2008.9699995.

11. Bozorgi M, Memariani Z, Mobli M, Salehi Surmaghi MH, Shams-Ardekani MR, Rahimi R. Five Pistacia species (P. vera, P. atlantica, P. terebinthus, P. khinjuk, and P. lentiscus): a review of their traditional uses, phytochemistry, and pharmacology. The Scientific World Journal. 2013 Jan 1;2013. Doi: 10.1155/2013/219815.

12. Benhammou N, Bekkara FA, Panovska TK. Antioxidant and antimicrobial activities of the Pistacia lentiscus and Pistacia atlantica extracts. African Journal of Pharmacy and Pharmacology. 2008 Apr 30;2(2):022-8. Doi: 10.5897/AJPP.9000056.

13. Asma A, Boumediene T, Mohammed B, Nourelhouda T, Mebrouka B. Antibacterial activity and physicochemical characteristics of Pistacia atlantica extracts. Der Pharma Chemica. 2016; 8(12): 162-68.

14. Shialy Z, Zarrin M, Nejad BS, Naanaie SY. In vitro antifungal properties of Pistacia atlantica and olive extracts on different fungal species. Current medical mycology. 2015 Dec;1(4):40. Doi 10.18869/acadpub.cmm.1.4.40.

15. Karimi A, Moradi MT, Gafourian A. In vitro anti-adenovirus activity and antioxidant potential of

Pistacia atlantica Desf. leaves. Research Journal of Pharmacognosy (RJP). 2020;7(2).

16. Hajjaj G, Chakour R, Bahlouli A, Tajani M, Cherrah Y, Zellou A. Evaluation of CNS activity and anti-inflammatory effect of Pistacia atlantica desf. essential oil from Morocco. Pharm Chem J. 2018;5:86-94.

17. Navascués, M. Genetic diversity of the endemic Canary Island pine tree, Pinus canariensis (Doctoral dissertation), University of East Anglia, Norwich. 2005.

18. Pfeifhofer HW. Composition of the essential oil of Pinus canariensis Sweet ex Sprengel. Flavour and fragrance journal. 2000 Jul;15(4):266-70. Doi: 10.1002/1099-1026(200007/08)15:4<266::AID-FFJ908>3.0.CO;2-E.

19. Ioannou E, Koutsaviti A, Tzakou O, Roussis V. The genus Pinus: a comparative study on the needle essential oil composition of 46 pine species. Phytochemistry Reviews. 2014 Dec 1;13(4):741-68. Doi: 10.1007/s11101-014-9338-4.

20. Apetrei CL, Tuchilus C, Aprotosoaie AC, Oprea A, Malterud KE, Miron A. Chemical, antioxidant and antimicrobial investigations of Pinus cembra L. bark and needles. Molecules. 2011 Sep;16(9):7773-88. DOI:10.3390/molecules16097773.

21. Kwak CS, Moon SC, Lee MS. Antioxidant, antimutagenic, and antitumor effects of pine needles (Pinus densiflora). Nutrition and cancer. 2006 Nov 1;56(2):162-71. Doi: 10.1207/s15327914nc5602_7.

22. Bissa, S, Bohra, A. Antibacterial Potental of Three Naked-Seeded (Gymnosperm) Plants, Microbiology Laboratory, J. N. V. University, India, Natural Product Radiance. 2008; 7(5): 420-25.

23. Teresa M, Bandiola B. Extraction and qualitative phytochemical screening of medicinal plants: A brief summary. International Journal of Pharmacy. 2018;8(1):137-43.

24. Archana P, Samatha T, Mahitha B, Chamundeswari NR. Preliminary phytochemical screening from leaf and seed extracts of Senna alata L. Roxb-an ethno medicinal plant. Int J Pharm Biol Res. 2012;3:82-9.

25. Sati SC, Kumar P. Assessment of Himalayan juniper, Juniperus squamata buch–ham ex d. don for phytochemical screening and antimicrobial potential against some infection causing pathogens. World J Pharmaceut Res. 2015 Jul 23;4:998-1011.

26. Olabiyi TI, Oyedunmade EE, Ibikunle GJ, Ojo OA, Adesina GO, Adelasoye KA, Ogunniran TA. Chemical composition and bio-nematicidal potential of some weed extracts on Meloidogyne incognita under laboratory conditions. Plant Sciences Research. 2008;1(2):30-5. Doi:pares.2008.30.35.

27. Savithramma N, Rao ML, Suhrulatha D. Screening of medicinal plants for secondary metabolites. Middle-East Journal of Scientific Research. 2011;8(3):579-84.

28. Shaghaghi M, Manzoori JL, Jouyban A. Determination of total phenols in tea infusions, tomato and apple juice by terbium sensitized fluorescence method as an alternative approach to the Folin–Ciocalteu spectrophotometric method. Food chemistry. 2008 May 15;108(2):695-701. Doi: 10.1016/j.foodchem.2007.11.008.

29. AlHafez M, Kheder F, AlJoubbeh M. Polyphenols, flavonoids and (-)-epigallocatechin gallate in tea leaves and in their infusions under various conditions. Nutrition & Food Science. 2014 Sep 2; 44(5): 455-63. Doi: 10.1108/NFS-10-2013-0119.

30. Sharma A, Goyal R, Sharma L. Potential biological efficacy of Pinus plant species against oxidative, inflammatory and microbial disorders. BMC complementary and alternative medicine. 2015 Dec 1;16(1):35. Doi: 10.1186/s12906-016-1011-6.

31. Sarikurkcu C, Arisoy K, Tepe B, Cakir A, Abali G, Mete E. Studies on the antioxidant activity of essential oil and different solvent extracts of Vitex agnus castus L. fruits from Turkey. Food and Chemical Toxicology. 2009 Oct 1;47(10):2479-83. Doi: 10.1016/j.fct.2009.07.005.

32. Perez C. Antibiotic assay by agar-well diffusion method. Acta Biol Med Exp. 1990;15:113-5.

33. Langfield RD, Scarano FJ, Heitzman ME, Kondo M, Hammond GB, Neto CC. Use of a modified microplate bioassay method to investigate antibacterial activity in the Peruvian medicinal plant Peperomia galioides. Journal of ethnopharmacology. 2004 Oct 1;94(2-3):279-81. Doi: 10.1016/j.jep.2004.06.013.

34. Balouiri M, Sadiki M, Ibnsouda SK. Methods for in vitro evaluating antimicrobial activity: A review. Journal of pharmaceutical analysis. 2016 Apr 1;6(2):71-9. Doi: 10.1016/j.jpha.2015.11.005.

35. Edrah S, Alafid F, Kumar A. Preliminary phytochemical screening and antibacterial activity of Pistacia atlantica and Prunus persica plants of Libyan origin. International Journal of Science and Research. 2013;6:14.

36. Khudoyan SH, Karapetyan LG, Zakaryan NH, Antonyan AA, Nanagulyan SG. Chemical composition and bioactivity of extracts from leaves

and branches of Armenian Pistacia Atlantica Desf. Chemistry and Biology, 2018 Apr 15; 52(1): 37-44.

37. Akhtar N, Mirza B. Phytochemical analysis and comprehensive evaluation of antimicrobial and antioxidant properties of 61 medicinal plant species. Arabian Journal of Chemistry. 2018 Dec 1;11(8):1223-35. Doi: 10.1016/j.arabjc.2015.01.013.

38. Rigane G, Ghazghazi H, Aouadhi C, Ben Salem R, Nasr Z. Phenolic content, antioxidant capacity and antimicrobial activity of leaf extracts from Pistacia atlantica. Natural product research. 2017 Mar 19;31(6):696-9. Doi: 10.1080/14786419.2016.1212035.

39. Benamar H, Marouf A, Bennaceur M. Phytochemical composition, antioxidant and acetylcholinesterase inhibitory activities of aqueous extract and fractions of Pistacia atlantica subsp. atlantica from Algeria. Journal of Herbs, Spices & Medicinal Plants. 2018 Jul 3;24(3):229-44. Doi: 10.1080/10496475.2018.1446204.

40. Ben Ahmed Z, Yousfi M, Viaene J, Dejaegher B, Demeyer K, Mangelings D, Vander Heyden Y. Seasonal, gender and regional variations in total phenolic, flavonoid, and condensed tannins contents and in antioxidant properties from Pistacia atlantica ssp. leaves. Pharmaceutical biology. 2017 Jan 1;55(1):1185-94. Doi: 10.1080/13880209.2017.1291690.

41. Maimoona A, Naeem I, Saddiqe Z, Ali N. Analysis of total flavonoids and phenolics in different fractions of bark and needle extracts of Pinus roxburghii and Pinus wallichiana. Journal of Medicinal Plants Research. 2011 Oct 9;5(21):5216-20. Doi: 10.5897/JMPR.9000082.

42. Fkiri S, Mezni F, Ouarghi A, Ghazghazi H, KHOUJA ML, Khaldi A, Nasr Z. Variability of phenolic compounds and antioxidant efficacy in needles extracts of Pinus nigra Arn. Journal of new sciences, Agriculture and Biotechnology 2018; 53 (1): 3528-35.

43. Amri O, Elguiche R, Tahrouch S, Zekhnini A, Hatimi A. Antifungal and antioxidant activities of some aromatic and medicinal plants from the southwest of Morocco. Journal of chemical and pharmaceutical Research. 2015;7(7):672-8.

44. Hatamnia AA, Rostamzad A, Hosseini M, Abbaspour N, Darvishzadeh R, Malekzadeh P, Aminzadeh BM. Antioxidant capacity and phenolic composition of leaves from 10 Bene (Pistacia atlantica subsp. kurdica) genotypes. Natural product research. 2016 Mar 3;30(5):600-4.

45. Malekzadeh P, Hatamnia AA, Nourollahi K. Total phenolic content and antioxidant activity of fruit and leaf of Bene (Pistacia atlantica subsp. Kurdica) Ilam province. in Plant Physiology. 2015 Oct 1;6(1):1543-9. Doi: 10.1080/14786419.2015.1028060.

46. Mahdavi Meymand Z, Moshafi MH, Forotanfar H. Antibacterial activity of metanolic extract of 12 herbal species on 6 bacterial strains using cylinder-plate method. Journal of Rafsanjan University of Medical Sciences. 2009 Dec 10;8(3):227-38.

47. Roozegar MA, Jalilian FA, Havasian MR, Panahi J, Pakzad I. Antimicrobial effect of Pistacia atlantica leaf extract. Bioinformation. 2016;12(1):19. Doi: 10.6026/97320630012019.

48. Nozohour Y, Golmohammadi R, Mirnejad R, Moghaddam MM, Fartashvand M.Comparison of Antibacterial Activities of Walnut (Juglans regia L.) and Pine (Pinus halepensis Mill.) Leaves Alcoholic Extracts against Bacteria Isolated from Burn Wound Infections, Acta Microbiologica Hellenica. 2019; 64(2): 47-56.

49. AL-Shekhany YN, Al-Juboori MK. Antibacterial activity of ethanol and aqueous extracts of some Perennial plants against three gram negative pathogenic bacteria from Koya city–Kurdistan Region-Northern Iraq. Diyala Journal For Pure Science. 2017;13(3-part 1):135-49.

50. Cowan MM. Plant products as antimicrobial agents. Clinical microbiology reviews. 1999 Oct 1;12(4):564-82. Doi : 10.24237/djps.1303.224B.

51. Sabbineni, J. Phenol-An effective antibacterial Agent, Research & Reviews. Journal of Medicinal & Organic Chemistry. 2016 ; 3(2): 182-91.

52. Papuc C, Goran GV, Predescu CN, Nicorescu V, Stefan G. Plant polyphenols as antioxidant and antibacterial agents for shelf-life extension of meat and meat products: Classification, structures, sources, and action mechanisms. Comprehensive Reviews in Food Science and Food Safety. 2017 Nov;16(6):1243-68. Doi: 10.1111/1541-4337.12298.

53. Omojate Godstime C, Enwa Felix O, Jewo Augustina O, Eze Christopher O. Mechanisms of antimicrobial actions of phytochemicals against enteric pathogens–a review. J Pharm Chem Biol Sci. 2014 Aug;2(2):77-85.

54. Górniak I, Bartoszewski R, Króliczewski J. Comprehensive review of antimicrobial activities of plant flavonoids. Phytochemistry Reviews. 2019 Feb 15;18(1):241-72. Doi: 10.1007/s11101-018-9591-z.

JOTCSA Journal of the Turkish Chemical Society Section: A Chemistry

TURKISH CHEMICAL SOCIETY

Effect of Al_2O_3 Doping on Antibacterial Activity of 45S5 Bioactive Glass

Yeliz Başaran Elalmış[1]*

[1]Yildiz Technical University, Faculty of Chemical and Metallurgical Engineering, Department of Bioengineering, 34220, İstanbul, Turkey.

Abstract: 45S5 bioactive glasses (BGs) are special class of glasses that form chemical bonds with surrounding bone tissue, which is due to the dissolution behavior of these glass materials. Furthermore, BG shows an antibacterial effect since the dissolution of BG results with high aqueous pH that affect bacterial viability. In this study, the antibacterial activity of Al_2O_3 doped bioactive glasses (AGs) was evaluated. AGs were produced via the melt quenching method. Functional groups of glasses were evaluated with Fourier Transform Infrared (FTIR) analysis, and glassy structure was evaluated by X-ray diffraction (XRD). Specific surface area, particle size information, and density of milled BG and AGs were obtained using surface area and porosity instrument, laser scattering particle size distribution analyzer and He pycnometer, respectively. Antibacterial activity of bioactive glasses was investigated on *Staphylococcus aureus* and *Escherichia coli* via Standard Colony Count Method at 50 mg/mL concentration and different time points, pH change of the media in the presence of BG and AGs at 50 mg/mL concentration was also measured at identical time points. XRD analysis revealed amorphous structure of BG and AGs. Similar specific surface area, particle size and density values were obtained for BG and produced AGs. Antibacterial test results showed that Al_2O_3 doped 45S5 bioactive glasses had decreased antibacterial activity compared to 45S5 bioactive glass for both bacteria studied.

Keywords: Bioactive glass, Al_2O_3 doped bioactive glass, antibacterial activity.

Submitted: December 04, 2020. **Accepted:** February 08, 2021.

Cite this: Başaran Elalmış Y. Effect of Al2O3 Doping on Antibacterial Activity of 45S5 Bioactive Glass. JOTCSA. 2021; 8(2):421–30.

DOI: https://doi.org/10.18596/jotcsa.835912.

***Corresponding author. E-mail:** elalmis@yildiz.edu.tr.

INTRODUCTION

Materials that have been designed to yield particular biological activity are generally described as bioactive materials. By definition a bioactive material is a material that undergoes significant surface reactions after implantation and lead to hydroxyapatite (HA)-like layer formation, responsible for firm tissue bonding (1). Bioactive glass (BG) which is commonly constituted of SiO_2, CaO, P_2O_5, and Na_2O is a special type of glass system (2). This silicate glass is based on SiO_2 network which forms the 3D glass. Low SiO_2 content in comparison with more durable silicate glasses, high glass network modifier (Na_2O and CaO) content, and high CaO:P_2O_5 ratio are the key properties of 45S5 glass which lead to the bioactivity (1).

Fibrous tissue surrounds the artificial materials after implantation into bone defects. However, Hench and coworkers discovered in 1971 that Bioglass® (in Na_2O-CaO-SiO_2-P_2O_5 system) does not lead to fibrous tissue formation, instead contact and form firm chemical bonds with surrounding bone tissue (3). Frequently used silicate BGs form a bone like HA layer which is fundamental for strong bone-material interfacial bonding. Bioactivity and bone bonding mechanism mostly for 45S5 Bioglass® has been broadly studied (*in vitro* and *in vivo*), degradation of biomaterials and subsequent HA layer formation on their surface provides the bonding ability of glass and glass-ceramics. Formed surface HA layer mimics the mineral composition of bone (4). Osteoblasts produce collagen fibrils at the interface and hydroxycarbonated apatite (HCA) crystals bond to this collagen fibrils, which creates a firm chemical interface. HA layer formation is a result of chemical

reaction series on the implant surface when contact with the bodily fluids (5). Following successive steps are involved in this series of reactions. Ion dissolution from BG structure into the medium takes place during the 1st step. 2nd step involves the reaction between dissolved Ca^{2+} and $(PO_4)^{3-}$ ions, and subsequent amorphous calcium phosphate (ACP) precipitation. ACP growth is induced during the 3rd step due to the pH instability and increased ion dissolution, and finally incorporation of media $(OH)^-$ and $(CO_3)^{2-}$ ions to the ACP layer, and crystallization as HA layer takes place during the 4th step (4). Briefly, reactions taking place on the surface of the bioactive silicate glass (for instance 45S5 Bioglass®) material and following cellular reactions lead to the bonding to the living bone tissue. Furthermore, release and substitution of crucial concentrations of soluble Si, Ca, P and Na ions lead to the favorable extracellular and intracellular reactions that rapidly promote bone formation (6).

Bone regeneration ability of 45S5 BG has led to its wide clinical use as bone filling material. Furthermore, it was stated that BG could enhance healing of wounded soft tissue. Prevention of infection during the healing of wounded skin is a crucial matter. Usually, in clinic antibiotics are used against infection. Thus, wound dressing materials that enhance the healing of the wound and show antibacterial activity as well would be useful (7). BG antibacterial activity was attributed to be mainly due to the high pH and osmotic effects which are caused by alkali ion release from the BG and non-physiological silica, sodium and calcium concentrations (7, 8).

Glass materials that are planned to be used as implants in the human body must have solubility to a certain degree to be able to attach to the tissue. These glasses are bioactive and they contain SiO_2 less than around 60%, higher SiO_2 contents lead to decreased solubility so that the surface reactions required for the bioactivity cannot take place (9). In the case of long term implants decreased solubility without bioactivity loss may be practical (10). Glass solubility reduction can be provided via increasing silica content, or decreasing modifier content, or adding multivalent cations. Generally, alumina is considered as glass structure stabilizer due to its non-bridging oxygen elimination behavior. In addition to this, dissolution is also retarded by surface alumina silicate film formation (9).

Al_2O_3 addition to glass is the conventional way of glass solubility control. However, the addition of alumina may have an inhibitory effect on bone bonding. It was found in a previously reported study that Al_2O_3 at 1.5 wt% could be added with no interference to mineralization of osteoid (11). Bioactive glasses with high Al_2O_3 content (1.5-2.5 mol%) were reported to show cytotoxic effect on human osteosarcoma U2-OS cells (12).

In this study, 45S5 bioactive glasses with 1 and 2 wt % Al_2O_3 content were prepared. The antibacterial effect of prepared Al_2O_3 doped bioactive glasses and 45S5 bioactive glass (Bone-G Active®, Meta Bioengineering and R&D Services Inc., Turkey) was evaluated on *Escherichia coli* and *Staphylococcus aureus* in relation with the changes in pH.

EXPERIMENTAL SECTION

Materials

Aluminum oxide and silicon dioxide (quartz) were from Riedel de Haën (Sigma-Aldrich Laborchemikalien GmbH, Seelze, Germany). $CaCO_3$, $Na_2HPO_4.2H_2O$, and $NaHCO_3$ were obtained from Merck Chemicals (Darmstadt, Germany). 45S5 bioactive glass (Bone-G Active®) was obtained as a gift sample from Meta Bioengineering and R&D Services Inc., Turkey. *Escherichia coli* (ATCC 25922) and *Staphylococcus aureus* (ATCC 25923) used in this study were from the American Type Culture Collection. Media and chemicals used in the microbial testing were obtained from Sigma-Aldrich.

Production of bioactive glass and alumina doped bioactive glass materials

To produce melt-derived alumina doped 45S5 bioactive glasses a mixture of SiO_2, $NaHCO_3$ as source of Na_2O, $CaCO_3$ as source of CaO, $Na_2HPO_4.2H_2O$ as sources of Na_2O and P_2O_5, and Al_2O_3 were melted in predetermined amounts. Bone-G Active® and produced Al_2O_3 doped glasses and their compositions are given in Table 1. Al_2O_3 doped bioactive glasses were produced according to a previously reported method (13, 14). Briefly, raw materials were first weighed, homogeneously mixed, and melted in a platinum crucible at 1400 °C, and then quenched into the water at room temperature. Glassy particles were dried and crushed for homogeneity, melted again (1450 °C, 2 hours) and poured into the casting plate. Production process was completed by the annealing of the bioactive glasses in an oven at 550 °C. Bone-G Active® and prepared bioactive glasses were crashed and subsequently ground to powder using a planetary ball mill (PM 400, Retsch GmbH, Haan, Germany). Bone-G Active® was abbreviated as BG, and produced 1 wt% Al_2O_3 doped 45S5 as AG1, and 2 wt % Al_2O_3 doped 45S5 as AG2.

Table 1: Bioactive glasses and their compositions.

Glass	Composition	Description
BG	SiO_2 45 wt%, Na_2O 24.5 wt%, CaO 24.5 wt% and P_2O_5 6 wt%	Bone-G Active®
AG1	SiO_2 45 wt%, Na_2O 24.5 wt%, CaO 23.5 wt%, P_2O_5 6 wt% and Al_2O_3 1 wt%	1 wt% Al_2O_3 doped 45S5 glass
AG2	SiO_2 45 wt%, Na_2O 24.5 wt%, CaO 22.5 wt%, P_2O_5 6 wt% and Al_2O_3 2 wt%	2 wt% Al_2O_3 doped 45S5 glass

Characterization of produced bioactive glass and Al_2O_3 doped bioactive glasses

Functional groups of glass structures were evaluated using a Fourier tansform infrared spectrometer (FTIR, Shimadzu, IR Prestige 21) in the wavenumber range of 2000–650 cm^{-1} and 4 cm^{-1} resolution. X-Ray diffractions of BG, AG1 and AG2 obtained with Rigaku D/Max-2200 Ultima diffractometer (40kV, 30mA) using CuKα radiation source in the 2θ range of 10–90° with 0.08° step size. Specific surface area of BG, and produced AG1 and AG2 samples was determined at 77 K by N_2 adsorption with the use of a surface area and porosity instrument (Micromeritics, TriStar II). Samples were outgassed prior to analysis at 90°C for 1 h and 250°C for 2 hours under N_2 flow. Specific surface area was calculated using Brunauer-Emmett-Teller (BET) method (0.05 < p/po < 0.30). Particle size distribution of BG, AG1 and AG2 powders was evaluated using laser scattering particle size distribution analyzer (Horiba, LA-350), and density of glass powders was measured using helium pycnometer (Thermo Scientific, Pycnomatic ATC).

Antibacterial activity of 45S5 bioactive glass and alumina doped bioactive glasses

In this study two classic bacteria, Gram-positive *Staphylococcus aureus* (*S.aureus*, ATCC25923), and Gram-negative *Escherichia coli* (*E.coli*, ATCC25922) were used to investigate bactericidal activity. The antimicrobial tests were performed using the modified American Standard ASTM E2149-01 method (15), in which samples are stirred constantly in bacterial suspension and thus, ensure good contact between the sample and the bacteria (16). *S.aureus* and *E.coli* were incubated at 37°C overnight, and preserved on nutrient plates. Concentrations of bacterial solution were standardized using the relationship between absorbance at 590 nm (OD590) and colony forming units (CFU) per milliliter determined by the plate count method. 100 mL of *E.coli* or *S.aureus* suspension prepared in 0.1 M aqueous phosphate buffered saline (pH 7.0, 10^{11} cells/mL) was added into the sterile Erlenmeyer flasks containing 50 mL of nutrient broth. Bacteria were suspended with the addition of 10 mL saline solution (0.9% NaCl) to obtain approximately 10^6 CFU/mL, prior to the antibacterial testing. Variation in antibacterial activity depending on the bioactive glass type was determined using 50 mg/mL BG, AG1 or AG2. Bioactive glass powders were added in to 1 mL of bacterial suspension and antibacterial activity was determined after 0 min, 10 min, 1 h, 6h, and 24 h of incubation for both bacteria. 10 µL of bacterial suspension was taken after above-mentioned incubation times and plated on nutrient agar plates overnight. The colonies formed were counted via Standard Colony Count Method and antibacterial activity was calculated using Eq. 1 (17). Bacterial solution without bioactive glass powders was used as control.

Where, $C_{control}$ is cell count of control and $C_{survivor}$ is the survivor count of test.

$$AA(\%) = \frac{(C_{Control} - C_{survivor})}{C_{control}} \times 100 \quad \text{(Eq. 1)}$$

pH measurements

BG, AG1 and AG2 particles were added into flasks containing 5 mL nutrient broth medium at concentration of 50 mg/mL. After stirring for 1 min, the solutions were placed at 37 °C for 24 hours. The pH values of the media were measured at certain time points (i.e., 0 min, 10 min, 1 h, 6 h, and 24 h).

RESULTS AND DISCUSSION

Characterization of bioactive glasses

FTIR spectra of milled BG, AG1 and AG2 powders are presented in Figure 1. Main absorption bands identified in the FTIR spectra were around 738 cm^{-1}, 866 cm^{-1}, 910 cm^{-1}, 1005 cm^{-1}, and 1454 cm^{-1} for the prepared glass powders. The bands present around 738 cm^{-1} in the FTIR spectra of BG, AG1 and AG2 were attributed to the bending mode of Si–O–Si, characteristic for silicate materials containing non-bridging oxygen atoms. Stretching vibrations of SiO_4 and PO_4 are generally assigned to the broad and strong intensity band observed between 800 and 1300 cm^{-1} (18). Strong absorption peak around 1005 cm^{-1} can be attributed to the asymmetric stretching vibrations of Si–O–Si bridging oxygen atoms, the absorption peak at 910 cm^{-1} and shoulder at 866 cm^{-1} (missing in the AG2 FTIR spectra) were attributed to Si – O stretching which were due to the presence of non-bridging oxygen atoms (18-20). Small peak around 1454 cm^{-1} was due to the ionic carbonate groups adsorbed on the bioactive glass surfaces (19, 21).

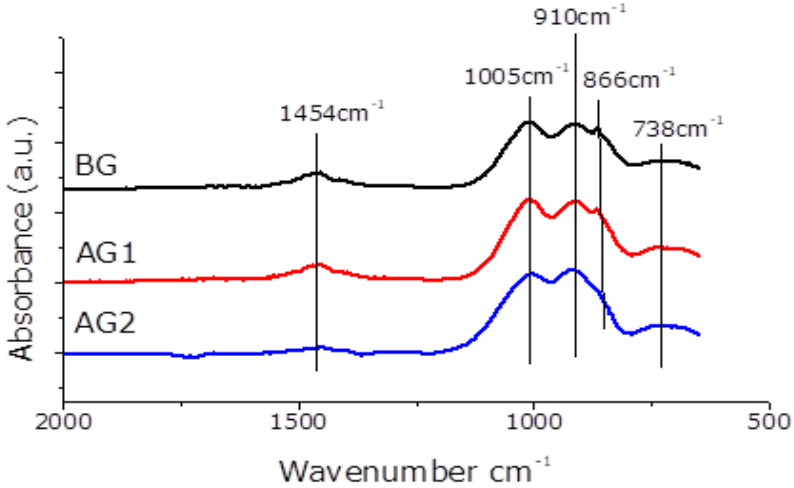

Figure 1: FTIR spectra of BG, AG1, and AG2.

XRD patterns of BG, AG1, and AG2 are presented in Figure 2. As seen, the crystalline peaks were absent in XRD patterns of the bioactive glass samples. However, a broad peak around 2θ=30° which indicates the amorphous structure typical for glassy phases (22) was observed in XRD patterns of the BG, AG1, and AG2.

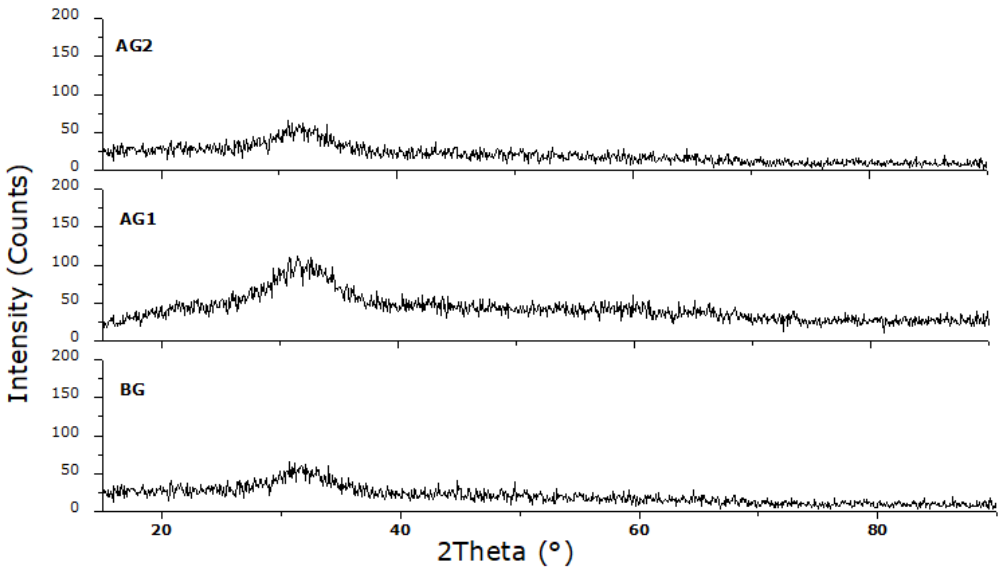

Figure 2: XRD patterns of BG, AG1 and AG2.

BG and produced melt-derived AG1 and AG2 were ground into powder using planetary ball mill prior to antibacterial tests. Specific surface area (S_{BET}), particle size information and density values of milled BG, AG1, and AG2 are presented in Table 2 and particle size distributions of BG, AG1 and AG2 are given in Figure 3. As can be seen from the results presented surface area, particle size and density values of BG, AG1, and AG2 powders were similar, which is attributed to be highly dependent on the glass production method and subsequently applied milling process.

Table 2: Specific surface area (S_{BET}), particle size information and density values of BG, AG1, and AG2

Sample	S_{BET} (m^2/g)	Particle size information		Density (g/cc)
		$D_{0.5}$ (µm)	Span	
BG	0.76	13.98	3.73	2.70
AG1	0.82	13.99	4.49	2.65
AG2	1.07	14.33	5.75	2.63

Antibacterial activity of the glass is essentially dependent on its composition. Since, it effects the ion release rate and consequently the pH and osmolarity of the media which have central effect on the antibacterial activity. Particle size, surface area, porosity, and morphology properties of the glass

materials can also influence their antibacterial activity (4). Additionally, this activity is dependent on the glass concentration and tested microorganism (23). Silicate network dissolution rate is effected by the particle size of the powder so that the rate of dissolution increases with the decrease in particle size (22). In this study, BG and produced AG1 and AG2 glasses were milled at certain conditions to obtain glass powders with similar particle size to eliminate the potential effect of particle size on the ion release. Since the aim of the study was to evaluate the antibacterial activity on the bacteria studied depending on the Al_2O_3 content of the glasses, surface area was also determined, which is also stated to play an important role in glass dissolution and accordingly antibacterial activity of milled glass powders.

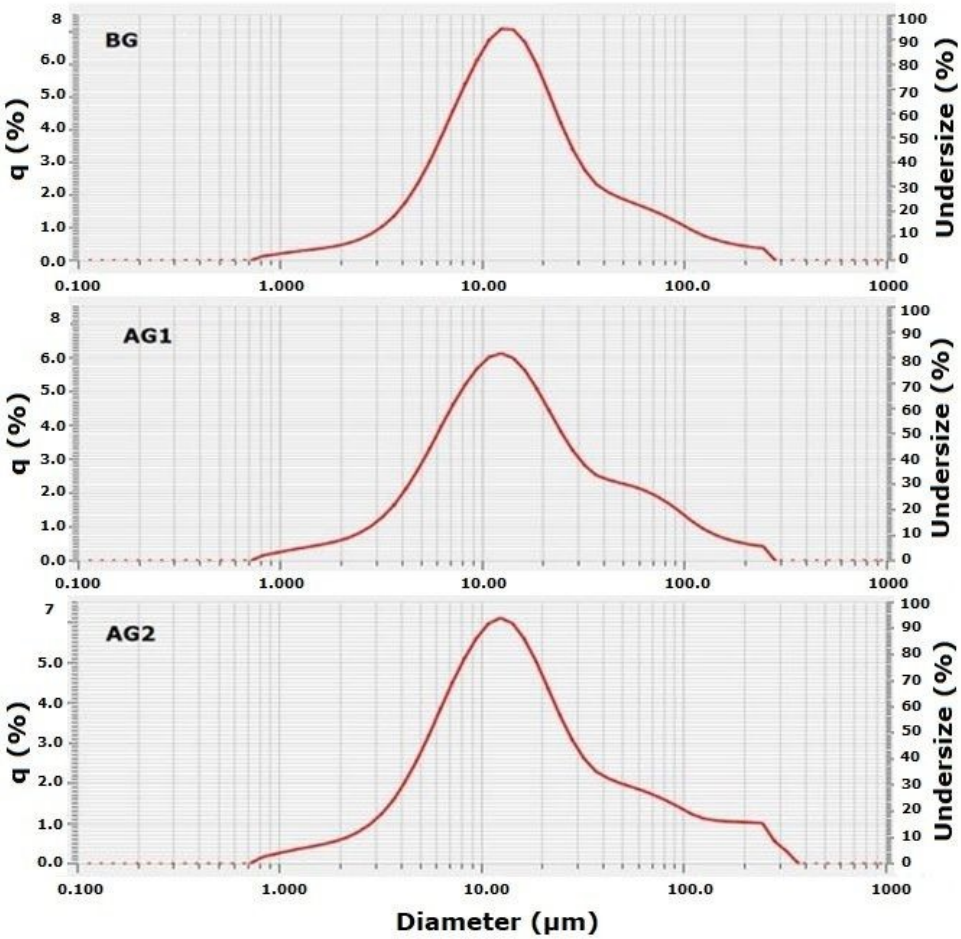

Figure 3: Particle size distributions of BG, AG1, and AG2.

Antibacterial Activity of Bioactive Glasses, and pH Changes

Antibacterial activity of BG, AG1, and AG2 at 50 mg/mL concentration was determined at different time points (i.e. 0 min, 10 min, 1h, 6 h, and 24 h) as may be seen in Fig. 4. BG exhibited antibacterial effect against two pathogenic bacteria at 6th hour with bactericidal percentages of 42% and 46% for *E.coli* and *S.aureus*, respectively. On the other hand, at 6th hour AG1 exhibited antibacterial effect with bactericidal percentage of 20% on *S.aureus* only. AG2 did not exhibit antibacterial effect at 6th hour on both bacteria.

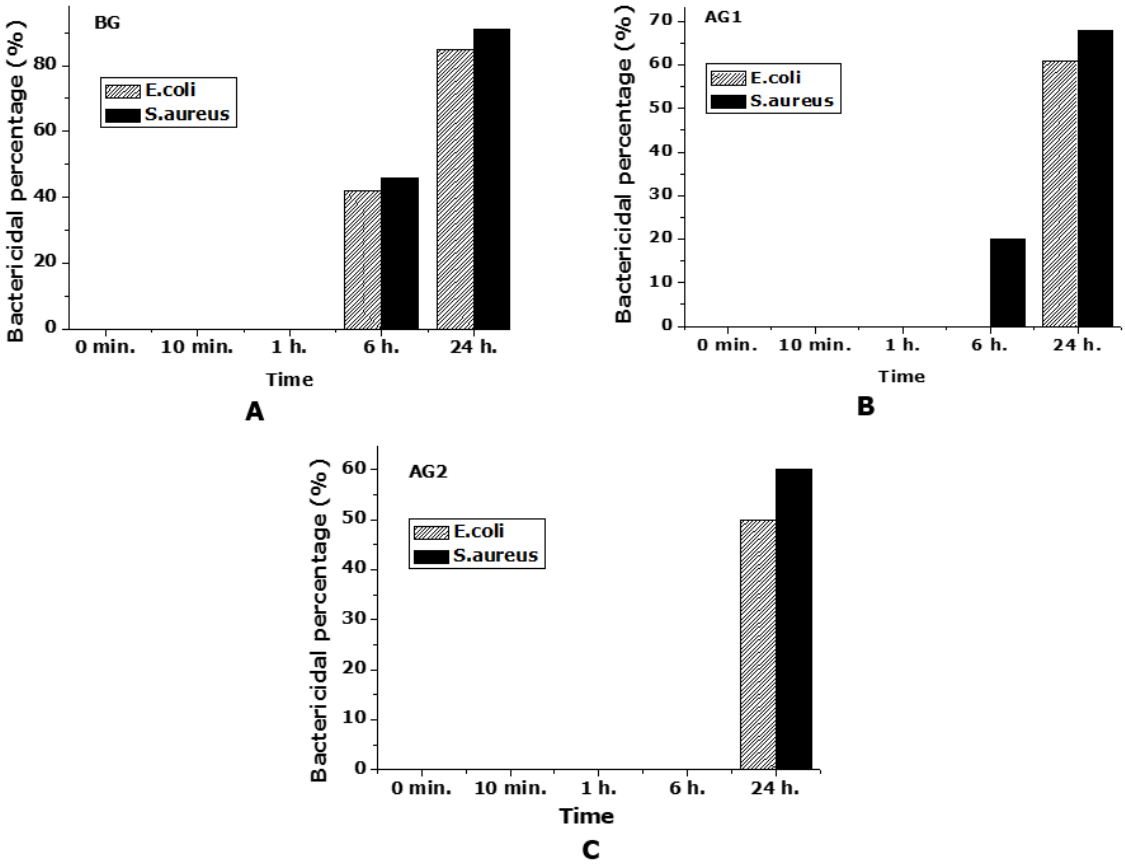

Figure 4: Bactericidal percentages of A) BG, B) AG1, and C) AG2 at concentrations of 50 mg/mL depending on time.

It was observed that antibacterial effect of BG and produced Al_2O_3 doped bioactive glasses (AG1 and AG2) was in the BG>AG1>AG2 order after 24 hours of incubation for both bacteria (Fig. 5). BG showed 91% antibacterial effect against *S.aureus* and 85% antibacterial effect against *E.coli* after 24 hours of incubation.

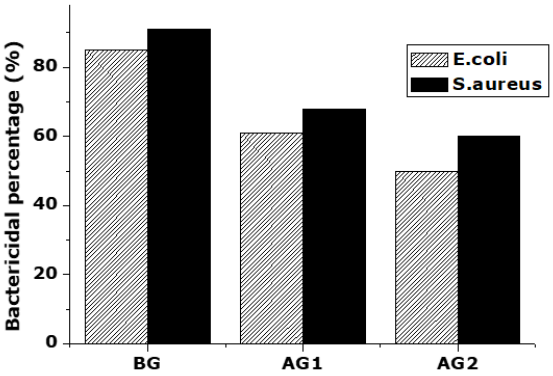

Figure 5: Bactericidal percentages of BG, AG1, and AG2 after 24 h of incubation at bioactive glass concentrations of 50 mg/mL.

The aqueous pH values of 50 mg/mL BG, AG1 or AG2 containing suspensions increased with incubation time as seen in Figure 6. 0 time point represented the pH of the nutrient broth media before the addition of bioactive glass samples. pH value of the BG containing media increased from 7.1 to 8.4 in the first hour, in contrast there was no significant difference in pH values of AG1 and AG2 containing suspensions in the first hour. pH values of BG, AG1, and AG2 containing suspensions were 9.1, 8.2, and 7.9 at the 6th hour, respectively. pH increase of BG and produced Al_2O_3 doped bioactive glass containing broth displayed the order of BG>AG1>AG2 after 24 hours of incubation. 45S5 bioactive glass (BG) showed pH values clearly higher than the alumina doped glasses (Fig. 6). The change

observed in aqueous pH values of the BG, AG1, and AG2 containing suspensions was in accordance with the bactericidal behavior of these bioactive glass samples.

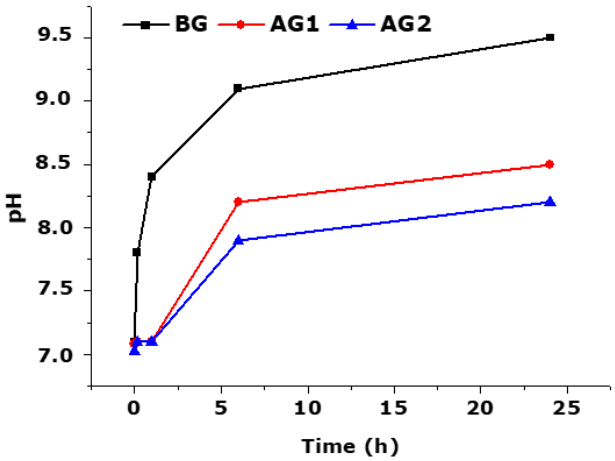

Figure 6: pH change depending on incubation time.

Antibacterial effect of bioactive glasses was mainly attributed to the high pH values resulting from the alkali ion release from the bioactive particles, in previous reports (7, 24-25). Reaction series taking place on the bioactive glass surface in aqueous media such as, soluble silica, calcium, and sodium release, led to an increased pH value (7). Zhang et al. (24) reported that higher glass dissolution tendency lead to higher increases in solution pH and alkali ions concentrations, which results with better antibacterial activity of the glass. Thus, mechanism of dissolution of bioactive glasses is crucial in the evaluation of glass antibacterial activity, and high antibacterial activity glasses are probably glasses with high dissolution rate (24).

Increase in nutrient broth pH in the presence of Al_2O_3 doped bioactive glasses, AG1 and AG2, was significantly low compared to nutrient broth pH increase containing traditional 45S5 bioactive glass BG. This is probably due to the elimination of some non-bridging oxygen by Al_2O_3, which decreases the solubility of the glass (5).

Alkaline ion release, specially Ca^{2+} ions, and increase in medium pH cause the antibacterial activity of glass-ceramic and glass materials. Ion release increase the osmolarity and the pH, leading to unbalanced bacterial intracellular Ca^{2+}, depolarizes the bacterial cell membrane and subsequently kills the bacterial cells. Thus antibacterial activity of these materials is dependent on the rate of ion release in aqueous media (4). Consequently, bioactive glass antibacterial activity mechanism probably depends on the combination of parameters, which include glass network dissolution caused osmotic effect and high pH, and also network-modifying ions (26).

CONCLUSION

The following conclusion was reached within the limitations of this study, which is on the effect of alumina doping on antibacterial activity of 45S5 bioactive glass. Alumina addition to 45S5 bioactive glass structure resulted in decreased antibacterial activity and decreased the pH increment which was regarded to be associated with decreased ion dissolution from glass structure. Alumina is considered as glass structure stabilizer due to its non-bridging oxygen elimination behavior, which results in decreased glass dissolution and thus antibacterial effect.

ACKNOWLEDGMENTS

The author would like to thank Meta Bioengineering and R&D Services Inc. (Turkey) for their kind supply of Bone-G Active®. The author also would like to thank Prof. Dr. Melda Altıkatoğlu Yapaöz (Faculty of Arts & Science, Department of Chemistry, Yildiz Technical University) for her help in the antibacterial tests of the bioactive glass samples.

REFERENCES

1. Rahaman MN, Day DE, Bal BS, Fu Q, Jung SB, Bonewald LF, Tomsia AP. Bioactive glass in tissue engineering. Acta Biomaterialia. 2011 Jun;7(6):2355–73. Doi: 10.1016/j.actbio.2011.03.016.

2. Bellantone M, Williams HD, Hench LL. Broad-spectrum bactericidal activity of Ag_2O-doped bioactive glass. Antimicrobial Agents and Chemotherapy. 2020 Jun;46(6):1940–45. Doi: 10.1128/AAC.46.6.1940–1945.2002.

3. Kokubo T. Surface chemistry of bioactive glass-ceramics. Journal of Non-Crystalline Solids. 1990 Apr;120(1-3):138–51. Doi: 10.1016/0022-3093(90)90199-V.

4. Fernandes JS, Gentile P, Pires RA, Reis RL, Hatton PV. Multifunctional bioactive glass and glass-ceramic biomaterials with antibacterial properties for repair

and regeneration of bone tissue. Acta Biomaterialia. 2017 Sep;59:2–11. Doi: 10.1016/j.actbio.2017.06.046.

5. Rabiee SM, Nazparvar N, Azizian M, Vashaee D, Tayebi L. Effect of ion substitution on properties of bioactive glasses: A review. Ceramics International. 2015 Jul;41(6):7241–51. Doi: 10.1016/j.ceramint.2015.02.140.

6. Gerhardt LC, Boccaccini AR. Bioactive glass and glass-ceramic scaffolds for bone tissue engineering. Materials. 2010 Jul; 3(7):3867–910. Doi: 10.3390/ma3073867.

7. Hu S, Chang J, Liu M, Ning C. Study on antibacterial effect of 45S5 Bioglass®. Journal of Materials Science: Materials in Medicine. 2009 Jan; 20(1):281–86. Doi: 10.1007/s10856-008-3564-5.

8. Abushahba F, Söderling E, Aalto-Setälä L, Sangder J, Hupa L, O Närhi T. Antibacterial properties of bioactive glass particle abraded titanium against *Streptococcus mutans*. Biomedical Physics and Engineering Express. 2018 Apr; 4:045002. Doi: 10.1088/2057-1976/aabeee.

9. Andersson ÖH, Södergård A. Solubility and film formation of phosphate and alumina containing silicate glasses. Journal of Non-Crystalline Solids. 1999 Apr; 246(1-2):9–15. Doi: 10.1016/S0022-3093(99)00072-1.

10. El-Kheshen AA, Khaliafa FA, Saad EA, Elwan RL. Effect of Al_2O_3 addition on bioactivity, thermal and mechanical properties of some bioactive glasses. Ceramics International. 2008 Sep; 34(7):1667–73. Doi: 10.1016/j.ceramint.2007.05.016.

11. Andersson ÖH, Liu G, Karlsson KH, Niemi L, Miettinen J, Juhanoja J. *In vivo* behaviour of glasses in the SiO_2-Na_2O-CaO-P_2O_5-Al_2O_3-B_2O_3 system. Journal of Materials Science: Materials in Medicine. 1990 Nov; 1(4):219–27. Doi: 10.1007/BF00701080.

12. Tripathi H, Hira SK, Kumar AS, Gupta U, Manna PP, Singh SP. Structural characterization and in vitro bioactivity assessment of SiO_2–CaO–P_2O_5–K_2O–Al_2O_3 glass as bioactive ceramic material. Ceramics International. 2015 Nov; 41(9):11756–69. Doi: 10.1016/j.ceramint.2015.05.143.

13. Karakuzu-Ikizler B, Terzioglu P, Basaran-Elalmis Y, Tekerek BS, Yucel S. Role of magnesium and aluminum substitution on the structural properties and bioactivity of bioglasses synthesized from biogenic silica. Bioactive Materials. 2020 Mar; 5(1):66–73. Doi: 10.1016/j.bioactmat.2019.12.007.

14. Karakuzu-Ikizler B, Terzioglu P, Oduncu-Tekerek BS, Yücel S. Effect of selenium incorporation on the structure and in vitro bioactivity of 45S5 bioglass. Journal of The Australian Ceramic Society. 2020 Jun; 56(2):697–709. Doi: 10.1007/s41779-019-00388-6.

15. Kesmez O. Preparation of anti-bacterial biocomposite nanofibers fabricated by electrospinning method. Journal of the Turkish Chemical Society Section A: Chemistry. 2020 Feb; 7(1):125–42. Doi: 10.18596/jotcsa. 590621.

16. Demir C, Süer NC, Yapaöz MA, Kebir N, Okullu SO, Kocagoz T, Eren T. Biocidal activity of ROMP-polymer coatings containing quaternary phosphonium groups. Progress in Organic Coatings. 2019 Oct; 135:299–305. Doi: 10.1016/j.porgcoat.2019.06.008.

17. Palantoken A, Yilmaz MS, Yapaoz MA, Tulunay EY, Eren T, Piskin S. Dual antimicrobial effects induced by hydrogel incorporated with UV-curable quaternary ammonium polyethyleneimine and $AgNO_3$. Materials Science and Engineering C-Materials For Biological Applications. 2016 Nov; 68:494–504. Doi: 10.1016/j.msec.2016.06.005.

18. Dziadek M, Zagrajczuk B, Jelen P, Olejniczak Z, Cholewa-Kowalska K. Structural variations of bioactive glasses obtained by different synthesis routes. Ceramics International. 2016 Oct; 42(13):14700–14709. Doi: 10.1016/j.ceramint.2016.06.095.

19. Hoppe A, Meszaros R, Stähli C, Romeis S, Schmidt J, Peukert W, Marelli B, Nazhat SN, Wondraczek L, Lao J, Jallot E, Boccaccini AR. *In vitro* reactivity of Cu doped 45S5 Bioglass® derived scaffolds for bone tissue engineering. Journal of Materials Chemistry B. 2013 Nov;41:5659–5674. Doi: 10.1039/c3tb21007c.

20. Lefebvre L, Chevalier J, Gremillard L, Zenati R, Thollet G, Bernache-Assolant D, Govin A. Structural transformations of bioactive glass 45S5 with thermal treatments. Acta Materialia. 2007 Jun;55(10):3305–3313. Doi: 10.1016/j.actamat.2007.01.029.

21. Romeis S, Hoppe A, Eisermann C, Schneider N, Boccaccini AR, Schmidt J, Peukert W. Enhancing i*n vitro* bioactivity of melt-derived 45S5 Bioglass® by comminution in a stirred media mill. Journal of the American Ceramic Society. 2014 Jan;97(1):150–156. Doi: 10.1111/jace.12615.

22. Sepulveda P, Jones JR, Hench LL. *In vitro* dissolution of melt-derived 45S5 and sol-gel derived 58S bioactive glasses. Journal of Biomedical Materials Research. 2002 Aug;61(2):301–311. Doi: 10.1002/jbm.10207.

23. Gorriti MF, López JMP, Boccaccini AR, Audisio C, Gorustovich AA. *In vitro* study of the antibacterial activity of bioactive glass-ceramic scaffolds. Advanced Engineering Materials. 2009 Jul;11(7):B67–B70. Doi: 10.1002/adem.200900081.

24. Zhang D, Leppäranta O, Munukka E, Ylänen H, Viljanen MK, Eerola E, Hupa M, Hupa L. Antibacterial effects and dissolution behavior of six bioactive glasses. Journal of Biomedical Materials Research

Part A. 2010 May;93A(2):475–483. Doi: 10.1002/jbm.a.32564.

25. Allan I, Newman H, Wilson M. Antibacterial activity of particulate Bioglass® against supra-and subgingival bacteria. Biomaterials. 2001 Jun;22(12):1683–1687. Doi: 10.1016/S0142-9612(00)00330-6.

26. Leppäranta O, Vaahtio M, Peltola T, Zhang D, Hupa L, Hupa M, Ylänen H, Salonen JI, Viljanen MK, Eerola E. Antibacterial effect of bioactive glasses on clinically important anaerobic bacteria *in vitro*. Journal of Materials Science: Materials in Medicine. 2008 Feb;19(2):547–551. Doi: 10.1007/s10856-007-3018-5.

JOTCSA Journal of the Turkish Chemical Society Section: A Chemistry

TURKISH CHEMICAL SOCIETY

Inhibitory effects of novel benzamide derivatives towards acetylcholinesterase enzyme

Cem YAMALI[1,2]*, Halise Inci GUL[2]*, Serkan LEVENT[3], Yeliz DEMIR[4]

[1]Department of Basic Pharmaceutical Sciences, Faculty of Pharmacy, Cukurova University, Adana, Turkey
[2]Department of Pharmaceutical Chemistry, Faculty of Pharmacy, Ataturk University, Erzurum, Turkey
[3]Department of Pharmaceutical Chemistry, Faculty of Pharmacy, Anadolu University, Eskişehir, Turkey
[4]Department of Pharmacy Services, Nihat Delibalta Gole Vocational High School, Ardahan University, Ardahan, Turkey

Abstract: Alzheimer's disease is one of the diseases which is identified by progressive memory loss and cognitive deficits leading to a decline in the lifespan of the patients. The drugs used in the clinic show palliative properties and they are unable to modify disease progression. In this study, *N*-(4-(*N*-(diaminomethylene)sulfamoyl)phenyl)-2-(substituted-benzamido)benzamide derivatives were synthesized and evaluated towards acetylcholinesterase (AChE, E.C.3.1.1.7) enzyme which is the most studied enzyme regarding Alzheimer's disease. The inhibition constants (Ki) of the compounds synthesized towards the AChE enzyme were in the range of 15.51 ± 1.88 - 41.24 ± 10.13 nM. The most effective compound with the lowest Ki = 15.51 ± 1.88 nM, 2-benzamido-*N*-(4-(*N*-(diaminomethylene)sulfamoyl)phenyl)benzamide **6**, can be reported as a lead compound of this study. Bioactivity results obtained by this study may provide useful information on the development of novel and potent inhibitors targeting Alzheimer's disease.

Keywords: Acetylcholinesterase, benzamide, sulfaguanidine, Alzheimer's disease.

Submitted: December 17, 2020. **Accepted:** February 08, 2021.

Cite this: Yamali C, Gul HI, Levent S, Demir Y. Inhibitory effects of novel benzamide derivatives towards acetylcholinesterase enzyme. JOTCSA. 2021;8(2):429–34.

DOI: https://doi.org/10.18596/jotcsa.842465.

***Corresponding authors. E-mail:** (c.yamali@yahoo.com) (incigul@atauni.edu.tr)

INTRODUCTION

Alzheimer's disease (AD) is identified by progressive memory loss and cognitive deficits leading to declining in the lifespan of the patients. Despite its complicated molecular pathogenesis, several treatments have been used at the clinic (1).

Manipulation of cholinergic activity by decreased production of acetylcholine (ACh) or abnormal acetylcholinesterase (AChE) activity is the most-studied clinical approach. Two types of cholinesterases (ChEs) were identified as acetylcholinesterase (AChE) and butyrylcholinesterase (BChE, pseudo-cholinesterase). Both ChEs have a role in the breakdown of ACh into choline and acetate (2). Cholinesterase inhibitors (ChEIs) as drug or drug candidates enhance the synaptic level of ACh by inhibiting ChEs in a dose-dependent manner (3).

According to the cholinergic hypothesis, to design inhibitors as antagonists of AChE and to discover molecules to bind with ACh receptors as agonists are the major strategies to control the amount of ACh in the synaptic cleft (4). Even drugs used in the clinic could improve the cognitive symptoms, they are unable to modify disease progression and they also show a different mode of actions, pharmacokinetics, and side effects. To date, several ChEIs are approved for the treatment of AD such as donepezil, rivastigmine, and galantamine. Even tacrine was the first drug used in AD, it is no longer used due to severe side effects. Notwithstanding scientific efforts, there is still no effective therapeutics for the prevention and treatment of AD (5-7).

A variety of chemical scaffolds has been reported with anti-AD effects. Benzamide derivative incorporating isoquinoline moiety was reported as the most potent candidate against human AChE with

Ki of 6.47 nM (4). As another attractive pharmacophoric group for AD, guanidine skeleton shows promising biological activities (8). Hydrazones having guanidine core as butyrylcholinesterase inhibitors (8), and cyclic acyl guanidine carbamate type compounds as ChEIs were reported with promising inhibitory potencies (6).

Our research group focused on primary sulfonamide derivatives and their bioactivities on CA I, CA II, CA IX, CA XII, and/or cholinesterase enzymes and their anticancer effects as potent drug candidates (9-12). This is the first study regarding some novel secondary sulfonamides to extend our earlier investigations. Novel sulfaguanidine bearing benzamide derivatives having the chemical structure of *N*-(4-(*N*-(diaminomethylene)sulfamoyl)phenyl)-2-(substituted-benzamido)benzamides **6-9** were designed, synthesized, and evaluated towards AChE enzyme to find out novel and potent AChE enzyme inhibitors for further experiments.

EXPERIMENTAL SECTION

Chemistry

NMR spectra of the compounds were recorded by Bruker AVANCE III 400 MHz (Bruker, Karlsruhe, Germany) in DMSO - *d6* (Merck KGaA, Darmstadt, Germany). LCMS-IT-TOF system (Shimadzu, Tokyo, Japan) was used for HRMS spectra. Electrothermal 9100 (IA9100, Bibby Scientific Limited, Staffordshire, UK) device was used to measure melting points (Mp). TLC-Silicagel HF254 (Merck Art 5715) plate was used to check the reaction process using UV lamp (Spectroline, ENF-240C/ FE, New York, U.S.A). DCM:MeOH mixture was used as a TLC solvent system.

Synthesis of 2-(4-substituted phenyl)-4*H*-benzo(d)(1,3)oxazin-4-ones, 2-5 (13, 14)

Methyl anthranilate (33 g) was stirred in NaOH solution (2N, 150 mL) at room temperature for 30 hours. The mixture was poured into 100 mL of ice water and neutralized by HCl (37%). The white solid 2-aminobenzoic acid (1) was filtered, washed with water, and dried. To a solution of 2-aminobenzoic acid (1, anthranilic acid) (14.6 mmol) in pyridine (30) at 0-5 ° C, a suitable benzoyl chloride (21.9 mmol) was added while stirring. After 30 min, the mixture was stirred at room temperature for 3-7 hours. The mixture was then treated with $NaHCO_3$ solution (10%, 50 mL) to remove the unreacted acid. Then the white solid obtained was filtered and washed with water several times to remove excess pyridine. The white color intermediates were used for the next step without further purification since the compounds are single spots on TLC plates. Experimental data for the raw intermediates were given below. Yield 60%, mp = 120-122 °C. HRMS (ESI-MS) $C_{14}H_9NO_2$ *m/z* Calc. $(M+H)^+$ 224.0706; Found: 224.0695. Compound **3**: Yield 65%, mp = 150-151 °C. Compound **4**: Yield 71%, mp = 169-171 °C. HRMS (ESI-MS) $C_{14}H_8NO_2F$ *m/z* Calc. $(M+H)^+$ 242.0612; Found: 242.0623. Compound **5**: Yield 64%, mp = 90-92 °C. HRMS (ESI-MS) $C_{15}H_8NO_2F_3$ *m/z* Calc. $(M+H)^+$ 292.0580; Found. 292.0574.

Synthesis of benzamide derivatives 6-9, Figure 1

Sulfaguanidine (1 mmol) was added into a suitable 2-(4-substituted phenyl)-4*H*-benzo(d)(1,3)oxazin-4-ones (**2-5**) (1 mmol) solution in hot acetic acid (20 mL). The mixture was refluxed for 24 hours. After completion of the reaction, it was poured into cold water (100 mL). The solid product was precipitated out and filtered. The crude was washed with water and dried. The compounds were purified by crystallization using suitable solvents mentioned below. The chemical structures were confirmed by ^{1}H NMR, ^{13}C NMR, and HRMS.

2-Benzamido-*N*-(4-(*N*-(diaminomethylene)sulfamoyl)phenyl)benzamide, 6

White solid (methanol:DMF:water), 42% yield, mp = 294-295 °C. ^{1}H NMR (DMSO-*d6*, 400 MHz, ppm) δ 11.50 (s, 1H, -CONH-), 10.78 (s, 1H, -CONH-), 8.42 (d, J = 8.3 Hz, 1H, ArH), 7.94-7.90 (m, 3H, ArH), 7.86 (d, J = 8.7 Hz, 2H, ArH), 7.76 (d, J = 8.7 Hz, 2H, ArH), 7.64-7.53 (m, 4H, ArH), 7.29 (t, J = 7.5 Hz, 1H, ArH), 6.74 (bs, 4H, $-NH_2$ x 2). ^{13}C NMR (DMSO-*d6*, 100 MHz, ppm) δ 168.1, 165.2, 158.6, 141.6, 140.2, 138.9, 134.9, 132.9, 132.5, 129.6, 129.3, 127.6, 126.9, 123.9, 123.8, 122.1, 120.8. HRMS (ESI-MS) $C_{21}H_{19}N_5O_4S$ *m/z* Calc. $(M+H)^+$ 438.1231; Found 438.1232.

N-(4-(*N*-(diaminomethylene)sulfamoyl)phenyl)-2-(4-methoxybenzamido) benzamide, 7

White solid (methanol:acetone:water), 33% yield, mp = 235-236 °C. ^{1}H NMR (DMSO-*d6*, 400 MHz, ppm) δ 11.43 (s, 1H, -CONH-), 10.76 (s, 1H, -CONH-), 8.43 (d, J = 8.3 Hz, 1H, ArH), 7.91-7.87 (m, 3H, ArH), 7.83 (d, J = 8.7 Hz, 2H, ArH), 7.75 (d, J = 8.6 Hz, 2H, ArH), 7.61 (t, J = 7.7 Hz, 1H, ArH), 7.28 (t, J = 7.7 Hz, 1H, ArH), 7.09 (d, J = 8.3 Hz, 2H, ArH), 6.71 (bs, 4H, $-NH_2$ x 2), 3.82 (s, 3H, $-OCH_3$). ^{13}C NMR (DMSO-*d6*, 100 MHz, ppm) δ 168.2, 164.6, 162.7, 158.6, 141.5, 140.2, 139.3, 129.6, 129.5, 129.4, 126.9, 126.8, 123.6, 123.2, 121.9, 120.9, 114.6, 55.9. HRMS (ESI-MS) $C_{22}H_{21}N_5O_5S$ *m/z* Calc. $(M+H)^+$ 468.1336; Found 468.1340.

N-(4-(*N*-(diaminomethylene)sulfamoyl)phenyl)-2-(4-fluorobenzamido)benzamide, 8

White solid (methanol:DMF:water), 34% yield, mp = 285-287 °C. ^{1}H NMR (DMSO-*d6*, 400 MHz, ppm) δ 11.39 (s, 1H, -CONH-), 10.76 (s, 1H, -CONH-), 8.32 (d, J = 8.2 Hz, 1H, ArH), 7.97 (t, J = 6.4 Hz, 2H, ArH), 7.88 (d, J = 7.8 Hz, 1H, ArH), 7.81 (d, J = 8.5 Hz, 2H, ArH), 7.74 (d, J = 8.5 Hz, 2H, ArH), 7.62 (t, J = 7.6 Hz, 1H, ArH), 7.39 (d, J = 8.5 Hz, 2H, ArH), 7.30 (t, J = 7.3 Hz, 1H, ArH), 6.69 (bs, 4H, $-NH_2$ x 2). ^{13}C NMR (DMSO-*d6*, 100 MHz, ppm) δ 167.9, 164.7 (d, J_{CF} = 248 Hz), 163.4, 158.6, 141.6, 140.1, 138.7, 132.8, 131.4, 130.3 (d, J_{CF} = 9 Hz), 129.6, 126.9, 124.3,

124.1, 122.4, 120.8, 116.3 (d, J_{CF} = 22 Hz). HRMS (ESI-MS) $C_{21}H_{18}N_5O_4FS$ *m/z* Calc. $(M+H)^+$ 456.1136; Found 456.1136.

***N*-(4-(*N*-(diaminomethylene)sulfamoyl)phenyl)-2-(4(trifluoromethyl) benzamido)benzamide, 9**
White solid (methanol:DMF:water), 30% yield, mp = 297-299 °C. ^{1}H NMR (DMSO-*d6*, 400 MHz, ppm) *δ* 11.49 (s, 1H, -CONH-), 10.77 (s, 1H, -CONH-), 8.28 (d, *J* = 8.2 Hz, 1H, ArH), 8.09 (d, *J* = 8.2 Hz, 2H, ArH), 7.94 (d, *J* = 8.3 Hz, 2H, ArH), 7.89 (d, *J* = 7.8 Hz, 1H, ArH), 7.82 (d, *J* = 8.7 Hz, 2H, ArH), 7.73 (d, *J* = 8.7 Hz, 2H, ArH), 7.63 (t, *J* = 7.5 Hz, 1H, ArH), 7.33 (t, *J* = 7.5 Hz, 1H, ArH), 6.69 (bs, 4H, -NH_2 x 2). ^{13}C NMR (DMSO-*d6*, 100 MHz, ppm) *δ* 167.8, 164.2, 158.6, 141.6, 140.1, 138.8, 138.2, 132.7, 132.2 (d, J_{CF} = 32 Hz), 129.6, 128.6, 126.9, 126.3 (d, J_{CF} = 3 Hz), 124.9, 124.5, 124.3 (d, J_{CF} = 271 Hz), 122.7, 120.7. HRMS (ESI-MS) $C_{22}H_{18}N_5O_4F_3S$ *m/z* Calc. $(M+H)^+$ 506.1111; Found 506.1104.

AChE inhibition assay

5,5'-Dithiobis(2-nitrobenzoic acid) (DTNB, D8130), acetylthiocholine iodide (AChI, 01480) and AChE from Electrophorus electricus (C2888, Type V-S), were acquired from Sigma-Aldrich Chemie GmbH (Taufkirchen, Germany). *In vitro* effects on AChE activity of the compounds were evaluated according to the Ellman's assay (15) as previously reported (16, 17). AChI was used as the substrate at 412 nm. Tacrine (TAC) was used as a control drug. One enzyme unit (EU) was defined as the hydrolysis of 1.0 µmol acetylcholine to choline and acetate per minute at pH = 8 at 37 °C. All the measurements were repeated three times. The analysis results were expressed as means of triplicate assays ± SEM.

RESULTS and DISCUSSION

The novel compounds **6-9** were synthesized in three steps by the method outlined in Figure 1. Firstly, a starting compound methyl anthranilate was hydrolyzed under basic conditions to afford 2-aminobenzoic acid, **1**. The chemical structure was confirmed with NMRs. Methyl peak belonging ester moiety of methyl anthranilate did not appear in ^{1}H NMR spectra. This data showed that methyl anthranilate turned into its acid derivative. In the second step, compound **1** was reacted with several benzoyl chlorides in pyridine and the cyclic intermediate compounds, 2-(4-substituted phenyl)-4*H*-benzo(d)(1,3)oxazin-4-ones (**2-5**), were isolated from the reaction media. Finally, compounds **2-5** reacted with sulfaguanidine in acetic acid solution by heating to obtain final compounds **6-9**.

Different benzoxazine derivatives of intermediates were transformed into the respective quinazolinone derivatives by a condensation reaction with several amine derivatives in pyridine (14) and acetic acid *via* microwave heating (18). Herein, we isolated and confirmed open-chain forms of the compounds under the conditions applied. Chemical structures of the compounds were elucidated successfully by the spectral methods. According to NMRs and HRMS results of the representative compound **7**, signals of two amide protons were seen at 11.43 ppm (s, 1H, -CONH-) and 10.76 ppm (s, 1H, -CONH-). These two protons testified that the isolated compound was not a quinazolinone derivative. Besides, -NH_2 protons belong to guanidine moiety was seen as a broad singlet at 6.71 ppm. Furthermore, ^{13}C NMR spectra confirmed the chemical structure of compound **7** as it showed a total of 18 carbon peaks as expected. Calculated and measured m/z values are also compatible in HRMS spectra as reported in the experimental section.

According to our preliminary experiments based on the different projects (unpublished data), we obtained a series of quinazolinone-type benzenesulfonamides in considerable high yields under reflux conditions in acetic acid. In this study, we used sulfaguanidine as another kind of starting compound having primary amine. In the previous study, we easily isolated the ring-closed product after cooled the reaction medium. However, in this study, we isolated open-chain compounds in the same conditions. Reaction time was extended to increase products' yield, however, starting material did not consume totally. Moreover, the reaction medium had also more than three spots which have very similar Rf values. After isolation of the open-chain target products 6-9, side products left in the acetic acid. We tried some extraction processes to isolate them, but it was not successful. Therefore, we are planning to use the microwave irradiation technique and using different mole ratios to improve the reaction's yield and time for future study.

Benzamide derivative compounds **6-9** were evaluated towards the AChE enzyme that is one of the targets for the treatment of AD. Inhibition results were shown in Table 1. All of the compounds were more effective inhibitors than reference drug Tacrine according to Ki values. Ki values were in the range of 15.51 ± 1.88 - 41.24 ± 10.13 nM in Table 1. The compounds **6-9** were 1.2-3.2 times more potent than Tacrine (Ki = 49.23 ± 2.67 nM) in terms of Ki values.

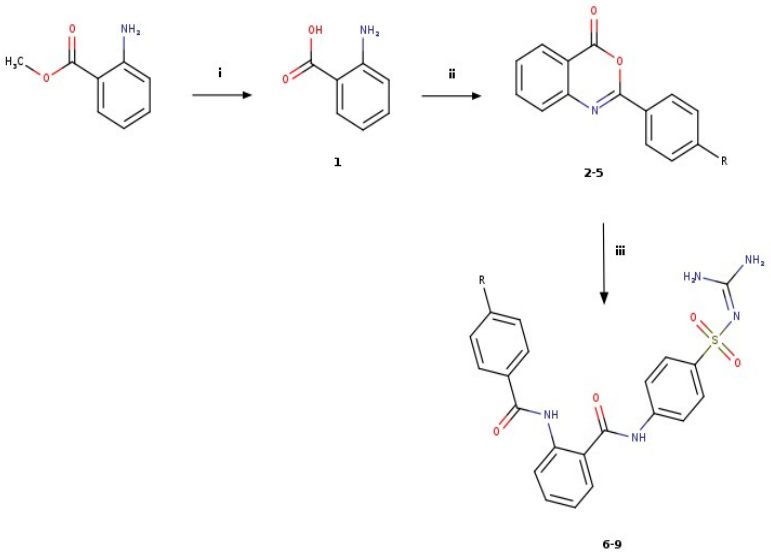

Figure 1. Synthetic method of the target compounds **6-9.**

Reagents and conditions. i : NaOH solution (2 N), HCl (37%), rt. ii: Benzoyl chloride derivative (R = H- (6), -OCH3 (7), -F (8), -CF3 (9)), pyridine, 0 - 5 °C, NaHCO3 (10%). iii: Sulfaguanidine, acetic acid, reflux.

The nonsubstituted compound **6** was the most promising AChE inhibitor among others. Substitution of methoxy (for **7**), fluoro (for **8**), and trifluoromethylene (for **9**) groups on phenyl ring decreased the enzyme inhibitory potency in 2.4, 2.6, and 2.7 times compared to parent compound **6**, respectively. Substitution of the *para* position of phenyl ring with different groups led to decrease inhibition potency. Fluorine substitution is one of the useful modifications in medicinal chemistry to increase bioactivity, bioavailability, stability, and lipophilicity of the compounds (19-21). However, in our study, using halogen substituents did not improve bioactivity significantly when compared to compound **6**. Even three of the compounds moderately inhibited, they are effective at the nanomolar level towards AChE enzyme when compared to the reference drug.

Table 1. AChE enzyme inhibitory results of the compounds.

Code	Chemical Formula	AChE, Ki (nM)
6	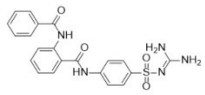	15.51 ± 1.88
7	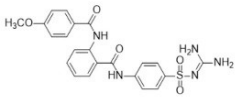	37.39 ± 6.38
8	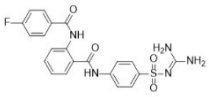	39.55 ± 10.23
9	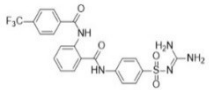	41.24 ± 10.13
Tacrine		49.23 ± 2.67

CONCLUSION

Here we reported synthesis, structure elucidation, and AChE enzyme inhibitory studies of a small series of novel benzamide derivatives having sulfaguanidine moiety. According to spectroscopic results, we obtained an open-chain structure of the compounds instead of quinazolinone derivatives. The compounds showed nanomolar inhibition level towards the AChE enzyme. The results indicated that compound **6** had remarkable inhibitory potency with the lowest Ki value compared to reference drug Tacrine. Therefore, the lead compound **6** can be evaluated on different targets of AD in future studies.

ACKNOWLEDGEMENTS

We would like thank to Prof. Dr. Ilhami Gulcin for his valuable scientific supports.

CONFLICT OF INTEREST

The authors declare that they have no conflict of interest.

REFERENCES

1. Wajid S, Khatoon A, Khan MA, Zafar H, Kanwal S et al. Microwave-assisted organic synthesis, structure-activity relationship, kinetics and molecular docking studies of non-cytotoxic benzamide derivatives as selective butyrylcholinesterase inhibitors. Bioorganic and Medicinal Chemistry. 2019;27(18): 4030-40. doi: 10.1016/j.bmc.2019.07.015.

2. Kratky M, Stepankova S, Vorcakova K, Svarcova M, Vinsova J. Novel cholinesterase inhibitors based on O-aromatic N,N-disubstituted carbamates and thiocarbamates. Molecules. 2016;21(2): 191-201. doi: 10.3390/molecules21020191.

3. Oliveira C, Bagetta D, Cagide F, Teixeira J, Amorim R, Silva T, et al. Benzoic acid-derived nitrones: A new class of potential acetylcholinesterase inhibitors and neuroprotective agents. European Journal of Medicinal Chemistry. 2019;174:116-29. doi: 10.1016/j.ejmech.2019.04.026.

4. Peng DY, Sun Q, Zhu XL, Lin HY, Chen Q, Yu NX, et al. Design, synthesis, and bioevaluation of benzamides: novel acetylcholinesterase inhibitors with multi-functions on butylcholinesterase, Aβ aggregation, and β-secretase. Bioorganic and Medicinal Chemistry. 2012;20(22):6739-50. doi: 10.1016/j.bmc.2012.09.016.

5. https://www.nia.nih.gov/health/how-alzheimers-disease-treated, December 2020.

6. Darras FH, Kling B, Sawatzky E, Heilmann J, Decker M. Cyclic acyl guanidines bearing carbamate moieties allow potent and dirigible cholinesterase inhibition of either acetyl- or butyrylcholinesterase. Bioorganic and Medicinal Chemistry. 2014;22(17):5020-34. doi: 10.1016/j.bmc.2014.06.010.

7. Yiannopoulou KG, Papageorgiou SG. Current and future treatments for Alzheimer's disease. Therapeutic Advances in Neurological Disorders. 2013;6(1):19–33. doi: 10.1177/1756285612461679.

8. Sekutor M, Mlinaric-Majerski K, Hrenar T, Tomic S, Primozic I. Adamantane-substituted guanylhydrazones: novel inhibitors of butyrylcholinesterase. Bioorganic Chemistry. 2012;41-42:28-34. doi: 10.1016/j.bioorg.2012.01.004.

9. Gul HI, Yamali C, Bulbuller M, Kirmizibayrak PB, Gul M, Angeli A, et al. Anticancer effects of new dibenzenesulfonamides by inducing apoptosis and autophagy pathways and their carbonic anhydrase inhibitory effects on hCA I, hCA II, hCA IX, hCA XII isoenzymes. Bioorganic Chemistry. 2018;78:290-97. doi: 10.1016/j.bioorg.2018.03.027.

10. Gul HI, Yamali C, Sakagami H, Angeli A, Leitans J, Kazaks A, et al. New anticancer drug candidates sulfonamides as selective hCA IX or hCA XII inhibitors. Bioorganic Chemistry. 2018;77:411-19. doi: 10.1016/j.bioorg.2018.01.021.

11. Yamali C, Gul HI, Ece A, Taslimi P, Gulcin I. Synthesis, molecular modeling, and biological evaluation of 4-(5-aryl-3-(thiophen-2-yl)-4,5-dihydro-1*H*-pyrazol-1-yl) benzenesulfonamides toward acetylcholinesterase, carbonic anhydrase I and II enzymes. Chemical Biology and Drug Design. 2018;91(4):854-66. doi: 10.1111/cbdd.13149.

12. Yamali C, Gul HI, Kazaz C, Levent S, Gulcin I. Synthesis, structure elucidation, and in vitro pharmacological evaluation of novel polyfluoro substituted pyrazoline type sulfonamides as multi-target agents for inhibition of acetylcholinesterase and carbonic anhydrase I and II enzymes. Bioorganic Chemistry. 2020;96:103627. doi: 10.1016/j.bioorg.2020.103627.

13. Zhu J, Yang HY, Chen Y, Lin HZ, Li Q, Mo J, et al. Synthesis, pharmacology and molecular docking on multifunctional tacrine-ferulic acid hybrids as cholinesterase inhibitors against Alzheimer's disease. Journal of Enzym Inhibition and Medicinal Chemistry. 2018;33(1):496-06. doi: 10.1080/14756366.2018.1430691.

14. Asundaria ST, Patel NS, Patel KC. Synthesis, characterization, and antimicrobial studies of novel 1,3,4-thiadiazolium-5-thiolates. Medicinal Chemistry Research. 2012;21:1199-06. doi: 10.1007/s00044-011-9632-2.

15. Ellman GL, Courtney KD, Andres V, Jr., Feather-Stone RM. A new and rapid colorimetric determination of acetylcholinesterase activity.

Biochemical Pharmacology. 1961;7:88-95. doi: 10.1016/0006-2952(61)90145-9.

16. Yamali C, Gul HI, Demir Y, Kazaz C, Gulcin I. Synthesis and bioactivities of 1-(4-hydroxyphenyl)-2-((heteroaryl) thio) ethanones as carbonic anhydrase I, II and acetylcholinesterase inhibitors. Turkish Journal of Chemistry. 2020; 44(4), 1058-67. doi:10.3906/kim-2004-36.

17. Yamali C, Gul HI, Cakir T, Demir Y, Gulcin I. Aminoalkylated Phenolic Chalcones: Investigation of Biological Effects on Acetylcholinesterase and carbonic anhydrase I and II as potential lead enzyme inhibitors. Letters in Drug Design and Discovery. 2002;17(10): 1283-92. doi: 10.2174/1570180817999200520123510.

18. Selvam P, Vijayalakshimi P, Smee DF, Gowen BB, Julander JG, Day CW, et al. Novel 3-sulphonamido-quinazolin-4(3H)-one derivatives: microwave-assisted synthesis and evaluation of antiviral activities against respiratory and biodefense viruses. Antiviral Chemistry and Chemotherapy. 2007;18(5):301-5. doi: 10.1177/095632020701800506.

19. Gillis EP, Eastman KJ, Hill MD, Donnelly DJ, Meanwell NA. Applications of fluorine in medicinal chemistry. Journal of Medicinal Chemistry. 2015;58(21):8315-59. doi: 10.1021/acs.jmedchem.5b00258.

20. Yamali C, Gul HI, Ozgun DO, Sakagami H, Umemura N, Kazaz C, et al. Synthesis and cytotoxic activities of difluoro-dimethoxy chalcones. Anticancer Agents in Medicinal Chemistry. 2017;17(10):1426-33. doi: 10.2174/1871520617666170327123909.

21. Yamali C, Ozgun DO, Gul HI et al. Synthesis and structure elucidation of 1-(2,5/3,5-difluorophenyl)-3-(2,3/2,4/2,5/3,4-dimethoxyphenyl)-2-propen-1-ones as anticancer agents. Medicinal Chemistry Research 2017;26:2015-23. doi: 10.1007/s00044-017-1911-0.

JOTCSA Journal of the Turkish Chemical Society Section: A Chemistry

TURKISH CHEMICAL SOCIETY

Kinetics of human butyrylcholinesterase inhibition by 1,9-dimethyl-methylene blue

Kevser BIBEROGLU*

Department of Biochemistry, School of Pharmacy, Hacettepe University, 06230, Ankara, Turkey.

Abstract: Alzheimer's disease (AD) is an irreversible and progressive neurodegenerative disorder, characterized by β-amyloid plaques, neurofibrillary tangles, and loss of cholinergic neurons. Butyrylcholinesterase (BChE) inhibition is a critical strategy for the treatment of AD since BChE causes inactivation of neurotransmitter acetylcholine and has positive effects on promoting the formation of β-amyloid fibrils. Our previous studies showed that various phenothiazine-derived compounds such as thionine and toluidine blue O (TBO) cause a potent inhibition of human cholinesterases. TBO was also found to affect amyloid precursor protein processing in-vitro and in-vivo models of AD. In this study, it was aimed to determine the inhibitory effect of 1,9-dimethyl-methylene blue (DMMB), a phenothiazine-derived compound, on human plasma BChE and explore its inhibitory mechanism. The inhibition of human BChE was assessed by the colorimetric method of Ellman using butyrylthiocholine as substrate and 0-0.375 μM of DMMB. The kinetic findings showed that DMMB acts as a linear mixed-type inhibitor of human BChE with K_i value of 23 ± 0.004 nM and α= 3.6 ± 1.6. In conclusion, DMMB, which is a potent inhibitor effective at nM level, may be helpful in designing new cholinesterase inhibitors for the treatment of AD.

Keywords: Alzheimer's disease, butyrylcholinesterase, 1,9-dimethyl-methylene blue, cholinesterase inhibition, phenothiazine.

Submitted: January 04, 2021. **Accepted:** February 16, 2021.

Cite this: Biberoğlu K. Kinetics of human butyrylcholinesterase inhibition by 1,9-dimethyl-methylene blue. JOTCSA. 2021;8(2):435–42.

DOI: https://doi.org/10.18596/jotcsa.853598.

***Corresponding author.** E-mail: kevserb@hacettepe.edu.tr.

INTRODUCTION

There are two types of cholinesterases in all mammalian tissues: Acetylcholinesterase (AChE, EC 3.1.1.7) and butyrylcholinesterase (BChE, EC 3.1.1.8) (1). These are known as sister enzymes, but they differ from each other genetically, structurally and for enzyme kinetics. BChE (also called as pseudocholinesterase or plasma cholinesterase) is a serine hydrolase that has a toxicological and clinical importance in scavenging and detoxifying ester containing compounds like succinylcholine, aspirin, cocaine, organophosphates, carbamate pesticides, and chemical warfare agents (1-3). It can accommodate larger substrates and displays wider substrate specificity than AChE (3). AChE is mainly localized in neurons whereas BChE is primarily expressed in white matter and glia (4). Alzheimer's disease (AD) is a cerebral disorder characterized clinically by problems with memory function, cognitive decline and behavioral impairments (5). Histopathological hallmarks of the disease include extracellular aggregates of the amyloid β-peptide (Aβ), so-called amyloid plaques in the parenchyma of the brain and intraneuronal neurofibrillary tangles containing abnormally phosphorylated tau (6). Moreover, the cholinergic dysfunction is accompanied by a progressive decline in the level of neurotransmitter acetylcholine (7-9). Unfortunately, currently approved pharmacotherapies including cholinesterase inhibitors (ChEIs) and *N*-methyl D-aspartate antagonists provide only transient symptomatic benefit and there is no effective treatment to prevent or halt the disease yet (10).

Besides of the cholinergic functions, both AChE and BChE are involved in the Aβ fibril formation that increases the neurotoxicity of Aβ peptides (11). In addition to these results, several ChEIs such as tacrine, donepezil, or huperzine A have been shown

to have neuroprotective effects against amyloid-induced toxicity (12). Due to the reciprocal connections between amyloid pathology and cholinergic function, the development of new ChEIs which reduce the hallmarks of AD has attracted great attention (13). Nowadays, cationic phenothiazine-derived compounds have shown to be prominent drug candidates for the treatment of AD due to their inhibitory effects on cholinesterase activity (14, 15), Aβ pathology, and tau aggregation (16-18). Phenothiazines which are six-membered heterocyclic compounds containing nitrogen and sulfur were discovered during second half of the 19th century. The first clinical use of phenothiazines was for the treatment of malarial infections (19). These compounds can exhibit inhibitory effects on several proteins due to their chemical structure (20, 21). For instance, they can inhibit calcium-dependent proteins such as calmodulin and protein kinase C which have important roles in cellular physiology (22). Phenothiazine-structured compounds are the most commonly prescribed psychotropic drugs in the world (23). Apart from their main neuroleptic actions, these compounds also show a wide spectrum of pharmacological/biological activities such as antifungal, antiprotozoal, antiviral, antihistaminic, antibacterial, or antiemetic activities (19). They have been also suggested to destroy cancer cells by targeting various signaling pathways in vitro and in vivo, but the most outstanding mechanism is their directly damaging effect on DNA (19, 24). Among phenothiazine-structured compounds, methylene blue (MethB) is a previously known cholinesterase inhibitor (25) which has shown promising results in phase II clinical trials for the treatment of AD (26).

In a recent research performed in our laboratory, we have tested the inhibitory effects of numerous phenothiazine-structured compounds on different types of cholinesterases (15). The findings showed that toluidine blue O (TBO) and thionine (TH) are highly potent inhibitors of both human BChE and human erythrocyte AChE with K_i in the nM-μM range (15). In addition, TBO was also found to affect amyloid precursor protein processing in-vitro and in-vivo models of AD (16, 17). These results encouraged us to test whether a structurally closely related cationic phenothiazine compound, 1,9-dimethyl-methylene blue (DMMB) (Figure 1) shows an inhibitory effect on human plasma BChE.

In the present study, the inhibitory effect of DMMB and its inhibitory mechanism were determined on human plasma BChE for the first time. The kinetic results indicate that DMMB has a high inhibitory potential on human plasma BChE with a K_i value in nM range.

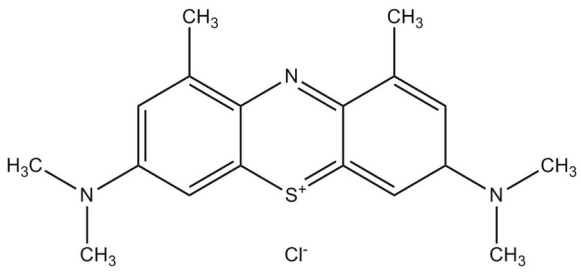

Figure 1. The chemical structure of 1,9-dimethyl-methylene blue.

EXPERIMENTAL SECTION

Chemicals

All reagent grade chemicals including butyrylthiocholine iodide (BTC), 5,5′-dithiobis (2-nitrobenzoic acid) (DTNB, Ellman's reagent), and DMMB were purchased from Sigma-Aldrich (Germany). All other chemicals were purchased from Merck or Sigma-Aldrich (Germany), if not indicated otherwise. Stock solution of DMMB (4.8 mM) was freshly prepared in methanol on the day of use.

Purification of Butyrylcholinesterase

Purification of human BChE from outdated human plasma was performed in two steps:

1. DEAE-Trisacryl anion exchange chromatography (Sigma-Aldrich)
2. Affinity chromatography on procainamide Sepharose 4B as described previously (27). (Specific activity, 44 U/mg; purification, 250 fold).

Inhibitory Potency of DMMB

The inhibitory potential of DMMB on BChE was tested at different inhibitor concentrations (0.03125 μM, 0.0625 μM, 0.125 μM, 0.25 μM and 0.375 μM) in the presence of 0.4 mM BTC. The half-maximal inhibitory concentration (IC_{50}) value was calculated by plotting a graph of percent remaining activity versus log [inhibitor] by using GraphPad Prism 5.0.

Butyrylcholinesterase Activity Assay and Inhibition Studies

BChE hydrolysis of BTC (0.05-0.4 mM) was measured spectrophotometrically in MOPS buffer (50 mM, pH 8) at 25°C in the presence of DTNB (0.125 mM) according to the Ellman method (28). The reactions were started by adding 0.01 U/mL BChE. The rate of increase of absorbance was monitored at 412 nm on a Shimadzu UV-1601 UV-Visible spectrophotometer (Kyoto, Japan). Enzyme activity was determined according to the linear segments of the progress curves in the initial 60 sec period using the extinction coeffient of 14.2 mM^{-1} cm^{-1}. The inhibition of BChE was studied by adding 0-0.375 μM DMMB to the reaction mixture (final volume was 1.2 mL). The presence of methanol (≤1.25% (v/v)) in the reaction mixture did not affect enzyme activity (14).

Kinetic Analysis

The kinetic parameters of inhibitory activity of DMMB on human BChE was evaluated at 5 different concentrations of BTC and 6 different concentrations of DMMB. The initial rate data were analyzed according to a simplified rapid equilibrium model for linear mixed-type inhibition (Scheme I; β = 0). The corresponding rate equation, Dixon equation and the [S]-dependence of the observed slope in Dixon plots of 1/V versus [I] at constant [BTC] are shown in Equations I, II, and III, respectively (29). The kinetic parameters inactivation rate constant (K_i) and (α) were calculated from Dixon slope replots using Equation (III) (29).

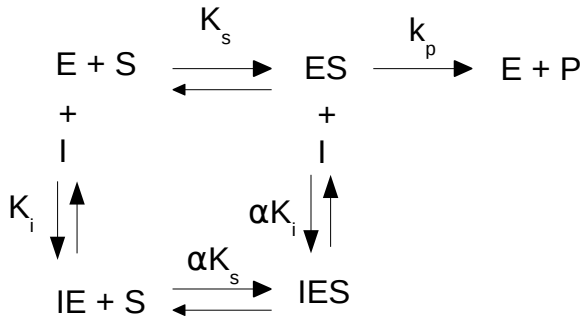

Scheme I. Rapid equilibrium model for linear mixed-inhibition.

E: enzyme; S: substrate; I: inhibitor; ES: enzyme-substrate complex; IE: inhibitor-enzyme complex; IES: inhibitor-enzyme-substrate complex; P: product; K_s: the dissociation constant for ES complex; K_i: the dissociation constant for the breakdown of IE complex to E+I; k_p: the rate constant for the breakdown of ES complex to E+P; αK_i: the dissociation constant for the breakdown of IES complex to ES+I and αK_s: the dissociation constant for the breakdown of IES complex to IE+S.

Equations I and III were derivated from simplified rapid equilibrium model for linear mixed-type inhibition (Scheme I; β=0). If $[E]_{Total}$ is written in terms of [ES], equation I can be obtained: (v: initial velocity; k_p: the rate constant for the breakdown of ES to E+P; V_{max}: maximum velocity; $[E]_{Total}$: total concentration of enzyme; [E]: concentration of free enzyme, [ES]: concentration of enzyme-substrate complex; [EI]: concentration of enzyme-inhibitor complex; [EIS]: concentration of enzyme-inhibitor-substrate complex; K_s: the dissociation constant for ES complex; K_i: the dissociation constant for the breakdown of IE complex to E+I; αK_i: the dissociation constant for the breakdown of IES complex to ES+I; αK_s: the dissociation constant for the breakdown of IES complex to IE+S).

$$V = k_p[ES]$$

$$[E]_{Total} = [E] + [ES] + [EI] + [EIS]$$

$$K_s = \frac{[E][S]}{[ES]}; [E] = \frac{[ES]K_s}{[S]}$$

$$K_i = \frac{[E][I]}{[EI]}; [EI] = \frac{[E][I]}{K_i} = \frac{[ES]K_s[I]}{[S]K_i}$$

$$\alpha K_i = \frac{[ES][I]}{[EIS]}; [EIS] = \frac{[ES][I]}{\alpha K_i}$$

$$[E]_{Total} = \frac{[ES][K_s]}{[S]} + [ES] + \frac{[ES]K_s[I]}{[S]K_i} + \frac{[ES][I]}{\alpha K_i}$$

$$[E]_{Total} = [ES]\left[\frac{K_s}{[S]} + 1 + \frac{K_s[I]}{[S]K_i} + \frac{[I]}{\alpha K_i}\right]; [ES] = \frac{[E]_{Total}}{\frac{K_s}{[S]} + 1 + \frac{K_s[I]}{[S]K_i} + \frac{[I]}{\alpha K_i}}$$

▪

$$V = k_p[ES]$$

$$V = \frac{k_p[E]_{Total}[S]}{K_s\left[1+\frac{[I]}{K_i}\right]+[S]\left[\frac{[I]}{\alpha K_i}\right]}$$

$$V_{max} = k_p[E]_{Total}$$

$$V = \frac{V_{max}[S]}{K_s\left(1+\frac{[I]}{K_i}\right)+[S]\left(1+\frac{[I]}{\alpha K_i}\right)} \quad \text{(I)}$$

The rate equation (Eq.1) for linear mixed type may be converted a linear form in which the varied ligand is [I] (Eq.2).

$$V^{-1} = \frac{[S]+\alpha K_s}{\alpha K_i V_{max}[S]}[I]+\frac{[S]+K_s}{V_{max}[S]} \quad \text{(II)}$$

(Dixon Equation)

$$Dixon\ \ slope = \frac{K_s}{K_i V_{max}[S]}+\frac{1}{\alpha K_i V_{max}} \quad \text{(III)}$$

RESULTS

Inhibitory Potency of DMMB

The human BChE activity was found to be inhibited in a dose-dependent manner, with an estimated IC_{50} value of 116 nM (Figure 2). The percent remaining activity showed a residual activity of 18% at the highest dose of DMMB.

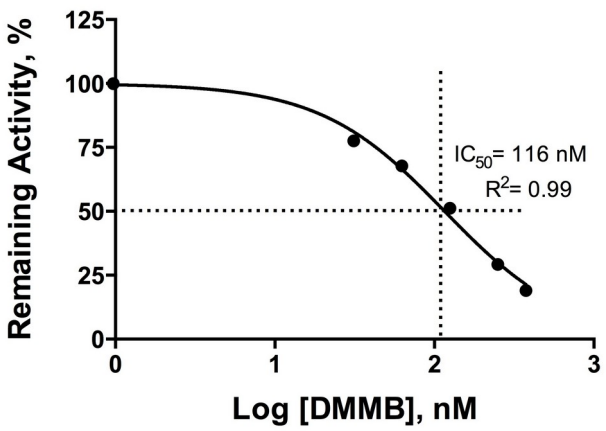

Figure 2. Inhibitory activity of DMMB against human plasma BChE. Dose response curve for the quantification of the correlation between DMMB concentration and the inhibitory effect. 100% equals the BChE activity in the absence of DMMB. IC_{50}: Half-maximal inhibitory concentration.

Inhibition of Human Butyrylcholinesterase by DMMB

Kinetic analysis results showed that DMMB acts as a linear, reversible inhibitor of human plasma BChE. The Dixon plots were found to be linear (β=0) at different substrate concentrations. Dixon plots and the secondary slope replot of the inhibition of human BChE by DMMB are shown in Figure 3A and Figure 3B. The slope replot of DMMB pointed to a linear mixed-type inhibition (1<α<∞) of human plasma BChE. K_i value was found to be 23 (±0.004) nM and α value was 3.6 (±1.6) derived from Dixon slope replot (based on K_s=32.2 (±2.03) μM and V_{max}=10 (±0.58) μM/min using Lineweaver-Burk plot

without DMMB) (Table I). Since the value of α is greater than 1 and smaller than ∞, this situation also supports that DMMB acts as a linear mixed-type inhibitior of BChE.

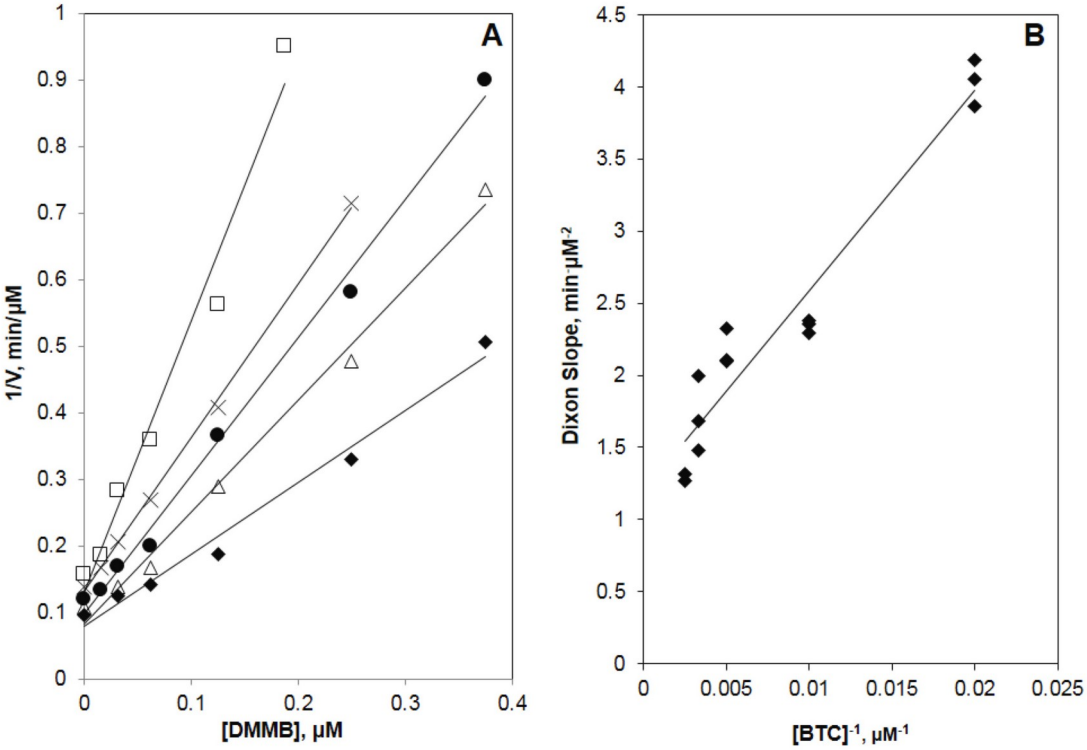

Figure 3. The inhibition of human BChE by 1,9-dimethyl-methylene blue. (A) Dixon plots of the inhibition at 400 (◆), 300 (△), 200 (●), 100 (×) and 50 (□) μM butyrylthiocholine. Each point is the average of three independent experiments (B) Slope replot of pooled data from three independent experiments.

Table 1: Kinetic parameters for the inhibition of human BChE by DMMB.

Enzyme	Inhibitor	Inhibition type	K_i, nM	α[b]	β[c]
Human Butyrylcholinesterase	1,9-dimethyl-methylene blue	Linear mixed	23±0.004[a]	3.6±1.6	0

[a] All data are shown as mean ± SD. [b] α is the factor by which Ks changes when inhibitor occupies the enzyme. [c] reduction in the catalytic kinetic constant is captured by a factor, β.

DISCUSSION

BChE can hydrolyze the neurotransmitter acetylcholine like AChE and it is one of the important targets in the treatment of AD (30). Recent evidences have suggested that BChE shows an important effect on modulation of motor control, cognition and behavior due to possible regulatory function of BChE on acetylcholine levels. Besides, BChE inhibitors have been shown to improve learning performance in rats and mitigate neurotoxic β-amyloid peptide levels (31). It was reported that there is a positive correlation between increased levels of BChE and development of amyloid-rich neuritic plaques in AD patient brain tissues (32). Darvesh et al. has suggested that knock-out of BChE gene in a mouse model, including five human familial AD genes (5XFAD) showed reduced fibrillar Aβ plaque deposition due to lack of BChE (33). Also, according to an AChE knockout mouse study, BChE was found to be more abundant than AChE activity in most tissues of mice (34). In AD, AChE activity decreases progressively in specific brain regions while BChE activity dramatically increases (35, 36). Therefore, it is noteworthy to explore new BChE inhibitors due to their possible inhibitory effects on cholinesterases or amyloid precursor protein (APP) metabolism for the treatment of AD. Cationic phenothiazine-derived compounds have been used since long time ago because of their pharmacological or biological activities (37) and most of them are in clinical use (38). Among these compounds, MethB has recently gained prominence as a potential therapeutic for the treatment of neurodegenerative disorders like AD. MethB can significantly inhibit both AChE and BChE (25, 39). This inhibition may show, at least in part, beneficial contribution to treatment of AD (40). Despite having a cationic structure, MethB can cross through the blood-brain barrier (BBB) after

conversion to its reduced form (uncharged leuco-form) (40). The fact that nerve tissues have a high affinity for the leuco form of MethB was confirmed by exposing tissue sections to air (or by treating them with iron chloride). This resulted in the conversion of the reduced form of MethB to its oxidized colored form (41).

DMMB, also known as Taylor's blue, is a structurally related derivative of MethB and contains two additional methyl groups (42). DMMB is widely used in the tissue staining applications due to its metachromatic property (43). In terms of its photodynamic action, DMMB has been shown to be more efficacious on tumor cells, viruses, and parasites (43, 44) than MethB. DMMB has lipophilic nature. Although there is no evidence, DMMB is expected to cross BBB similar to MethB. The results of Taylor et al. indicate that DMMB not only stains erythrocyte membranes but also stains the entire erytrocyte blue-green (42). It has shown that pharmacological actions of DMMB are superior to those of MethB. For instance, DMMB exhibits higher potency in inhibiting monoamine oxidase A, compared to MethB (45). The photodynamic action of DMMB has been found to be more efficacious in treatment of microbial infections due to its high lipophilic character, compared to other photosensitizers, including MethB (46). An earlier study has demonstrated that MethB yielded a complex pattern of human BChE inhibition (Intrinsic K'=420±0.04 nM) and indicates cooperative binding at more than one site (47) whereas our results show that DMMB is a linear mixed-type inhibitior of human BChE (23±0.004 nM) and it is ~18-fold more potent than MethB. Although DMMB shows the same kinetic pattern as ethopropazine (K_i=37±0.07; α=8.4±2), a phenothiazine-derived compound (47), DMMB inhibits human plasma BChE more strongly. A recent study also demonstrated that DMMB has a 55-fold higher potency than MethB for inhibition of tau-tau binding in vitro (48). Therefore, DMMB deserves more detailed studies as a potential candidate for the treatment of AD.

In our previous studies, various phenothiazine-structured compounds have been searched for possible inhibition of human cholinesterases (15). The findings showed that methylene violet (MV) caused a linear mixed type-inhibition and K_i value was 0.66±0.06 μM. Toluidine blue O (TBO; K_i=0.008±0.003 μM) and thionine (TH; K_i=2.1±0.42 μM) acted as nonlinear inhibitor of human BChE. Besides, TBO also caused linear mixed-type inhibition of human erythrocyte AChE with K_i=0.041±0.05 μM (15). In addition to its strong inhibitory effects on both AChE and BChE, it was shown that both TBO and TH mitigate the levels of secreted Aβ peptides in cell model of AD (PS70 cells) while only TBO affects hippocampal amyloid pathology by decreasing the levels of insoluble Aβ species in a transgenic mouse model of AD (16, 17). In our recent study, azure B, the major metabolite of MethB, has been shown to decrease the levels of secreted APPα and Aβ peptides significantly. A significant decrease has also been observed in the levels of intracellular total APP (49). Considering our previous results, a phenothiazine-structured compound, DMMB which is a highly effective BChE inhibitor (23±0.004 nM) can be also a potent inhibitor of AChE. Further testing would be also useful for designing and development of new cholinesterase inhibitors. This study represents the first report of inhibition of human BChE by DMMB. AD is a multifactorial disease and due to direct relationship between cholinergic system and APP metabolism, it is also worth determining the effects of DMMB on APP metabolism in future investigations.

CONCLUSION

These kinetic findings indicate that DMMB is a potent inhibitor of human plasma BChE with K_i value in nM range. In conclusion, DMMB may be useful in designing new cholinesterase inhibitors for the treatment of AD.

CONFLICT OF INTEREST

The author declares that there are no conflicts of interest.

REFERENCES

1. Taylor P, Radić Z. The cholinesterases: from genes to proteins. Annu Rev Pharmacol Toxicol. 1994;34:281-320.

2. Masson P, Rochu D. Catalytic bioscavengers against toxic esters, an alternative approach for prophylaxis and treatments of poisonings. Acta Naturae. 2009;1(1):68-79.

3. Nicolet Y, Lockridge O, Masson P, Fontecilla-Camps JC, Nachon F. Crystal structure of human butyrylcholinesterase and of its complexes with substrate and products. J Biol Chem. 2003;278(42):41141-7.

4. Darvesh S, Hopkins DA, Geula C. Neurobiology of butyrylcholinesterase. Nat Rev Neurosci. 2003;4(2):131-8.

5. Zvěřová M. Clinical aspects of Alzheimer's disease. Clin Biochem. 2019;72:3-6.

6. LaFerla FM, Oddo S. Alzheimer's disease: Abeta, tau and synaptic dysfunction. Trends Mol Med. 2005;11(4):170-6.

7. Perry EK, Perry RH, Blessed G, Tomlinson BE. Changes in brain cholinesterases in senile dementia of Alzheimer type. Neuropathol Appl Neurobiol. 1978;4(4):273-7.

8. Ferreira-Vieira TH, Guimaraes IM, Silva FR, Ribeiro FM. Alzheimer's disease: Targeting the Cholinergic System. Curr Neuropharmacol. 2016;14(1):101-15.

9. Mesulam MM. Cholinergic circuitry of the human nucleus basalis and its fate in Alzheimer's disease. J Comp Neurol. 2013;521(18):4124-44.

10. Yiannopoulou KG, Papageorgiou SG. Current and future treatments for Alzheimer's disease. Ther Adv Neurol Disord. 2013;6(1):19-33.

11. Geula C, Mesulam MM. Cholinesterases and the pathology of Alzheimer disease. Alzheimer disease and associated disorders. 1995;9 Suppl 2:23-8.

12. Nordberg A. Mechanisms behind the neuroprotective actions of cholinesterase inhibitors in Alzheimer disease. Alzheimer Dis Assoc Disord. 2006;20(2 Suppl 1):S12-8.

13. Longo FM, Massa SM. Neuroprotective strategies in Alzheimer's disease. NeuroRx. 2004;1(1):117-27.

14. Sezgin Z, Biberoglu K, Chupakhin V, Makhaeva GF, Tacal O. Determination of binding points of methylene blue and cationic phenoxazine dyes on human butyrylcholinesterase. Arch Biochem Biophys. 2013;532(1):32-8.

15. Biberoglu K, Tek MY, Ghasemi ST, Tacal O. Toluidine blue O is a potent inhibitor of human cholinesterases. Arch Biochem Biophys. 2016;604:57-62.

16. Yuksel M, Biberoglu K, Onder S, Akbulut KG, Tacal O. Effects of phenothiazine-structured compounds on APP processing in Alzheimer's disease cellular model. Biochimie. 2017;138:82-9.

17. Yuksel M, Biberoglu K, Onder S, Akbulut KG, Tacal O. Toluidine blue O modifies hippocampal amyloid pathology in a transgenic mouse model of Alzheimer's disease. Biochimie. 2018;146:105-12.

18. Taniguchi S, Suzuki N, Masuda M, Hisanaga S, Iwatsubo T, Goedert M, et al. Inhibition of heparin-induced tau filament formation by phenothiazines, polyphenols, and porphyrins. J Biol Chem. 2005;280(9):7614-23.

19. Varga B, Csonka Á, Csonka A, Molnár J, Amaral L, Spengler G. Possible Biological and Clinical Applications of Phenothiazines. Anticancer Res. 2017;37(11):5983-93.

20. Ford JM, Prozialeck WC, Hait WN. Structural features determining activity of phenothiazines and related drugs for inhibition of cell growth and reversal of multidrug resistance. Mol Pharmacol. 1989;35(1):105-15.

21. Jaszczyszyn A, Gąsiorowski K, Świątek P, Malinka W, Cieślik-Boczula K, Petrus J, et al. Chemical structure of phenothiazines and their biological activity. Pharmacol Rep. 2012;64(1):16-23.

22. Weiss B, Prozialeck WC, Wallace TL. Interaction of drugs with calmodulin. Biochemical, pharmacological and clinical implications. Biochem Pharmacol. 1982;31(13):2217-26.

23. Fourrier A, Gasquet I, Allicar MP, Bouhassira M, Lépine JP, Bégaud B. Patterns of neuroleptic drug prescription: a national cross-sectional survey of a random sample of French psychiatrists. Br J Clin Pharmacol. 2000;49(1):80-6.

24. Choi JH, Yang YR, Lee SK, Kim SH, Kim YH, Cha JY, et al. Potential inhibition of PDK1/Akt signaling by phenothiazines suppresses cancer cell proliferation and survival. Ann N Y Acad Sci. 2008;1138:393-403.

25. Augustinsson K-B. Methylene blue as an inhibitor of acetylcholine-esterase. Acta Chem Scand. 1950;4:536-42.

26. Wischik C, Staff R. Challenges in the conduct of disease-modifying trials in AD: practical experience from a phase 2 trial of Tau-aggregation inhibitor therapy. J Nutr Health Aging. 2009;13(4):367-9.

27. Biberoglu K, Tacal Ö, Akbulut H. The role of Phe329 in binding of cationic triarylmethane dyes to human butyrylcholinesterase. Arch Biochem Biophys. 2011;511(1-2):64-8.

28. Ellman GL, Courtney KD, Andres V, Jr., Feather-Stone RM. A new and rapid colorimetric determination of acetylcholinesterase activity. Biochem Pharmacol. 1961;7:88-95.

29. Segel IH. Enzyme kinetics: behavior and analysis of rapid equilibrium and steady state enzyme systems: Wiley New York:; 1975.

30. Lane RM, Potkin SG, Enz A. Targeting acetylcholinesterase and butyrylcholinesterase in dementia. Int J Neuropsychopharmacol. 2006;9(1):101-24.

31. Greig NH, Utsuki T, Ingram DK, Wang Y, Pepeu G, Scali C, et al. Selective butyrylcholinesterase inhibition elevates brain acetylcholine, augments learning and lowers Alzheimer beta-amyloid peptide in rodent. Proc Natl Acad Sci U S A. 2005;102(47):17213-8.

32. Guillozet AL, Smiley JF, Mash DC, Mesulam MM. Butyrylcholinesterase in the life cycle of amyloid plaques. Ann Neurol. 1997;42(6):909-18.

33. Reid GA, Darvesh S. Butyrylcholinesterase-knockout reduces brain deposition of fibrillar β-amyloid in an Alzheimer mouse model. Neuroscience. 2015;298:424-35.

34. Li B, Stribley JA, Ticu A, Xie W, Schopfer LM, Hammond P, et al. Abundant tissue butyrylcholinesterase and its possible function in the acetylcholinesterase knockout mouse. J Neurochem. 2000;75(3):1320-31.

35. Perry EK, Tomlinson BE, Blessed G, Bergmann K, Gibson PH, Perry RH. Correlation of cholinergic abnormalities with senile plaques and mental test scores in senile dementia. Br Med J. 1978;2(6150):1457-9.

36. Arendt T, Brückner MK, Lange M, Bigl V. Changes in acetylcholinesterase and butyrylcholinesterase in Alzheimer's disease resemble embryonic development--a study of molecular forms. Neurochem Int. 1992;21(3):381-96.

37. Gupta RK, editor Phenothiazines and 1,4-benzothiazines : chemical and biomedical aspects1988.

38. Keyzer H. Thiazines and structurally related compounds. 1992.

39. Pfaffendorf M, Bruning TA, Batnik HD, van Zwieten PA. The interaction between methylene blue and the cholinergic system. Br J Pharmacol. 1997;122(1):95-8.

40. Oz M, Lorke DE, Hasan M, Petroianu GA. Cellular and molecular actions of Methylene Blue in the nervous system. Med Res Rev. 2011;31(1):93-117.

41. Ehrlich P. Ueber die Methylenblaureaction der lebenden Nervensubstanz. DMW-Deutsche Medizinische Wochenschrift. 1886;12(04):49-52.

42. Taylor KB, Jeffree GM. A new basic metachromatic dye, 1:9-Dimethyl Methylene Blue. The Histochemical Journal. 1969;1(3):199-204.

43. Mohammad T, Morrison H. Photonuclease activity of Taylor's blue. Bioorg Med Chem Lett. 1999;9(15):2249-54.

44. Pereira LM, Mota CM, Baroni L, Bronzon da Costa CM, Brochi JCV, Wainwright M, et al. Inhibitory action of phenothiazinium dyes against Neospora caninum. Scientific Reports. 2020;10(1):7483.

45. Delport A, Harvey BH, Petzer A, Petzer JP. The monoamine oxidase inhibition properties of selected structural analogues of methylene blue. Toxicol Appl Pharmacol. 2017;325:1-8.

46. Santos DA, Crugeira PJL, Nunes IPF, de Almeida PF, Pinheiro ALB. A novel technique of antimicrobial photodynamic therapy - aPDT using 1,9-dimethyl-methylene blue zinc chloride double salt-DMMB and polarized light on Staphylococcus aureus. J Photochem Photobiol B. 2019;200:111646.

47. Küçükkilinç T, Ozer I. Multi-site inhibition of human plasma cholinesterase by cationic phenoxazine and phenothiazine dyes. Archives of biochemistry and biophysics. 2007;461(2):294-8.

48. Harrington CR, Storey JM, Clunas S, Harrington KA, Horsley D, Ishaq A, et al. Cellular Models of Aggregation-dependent Template-directed Proteolysis to Characterize Tau Aggregation Inhibitors for Treatment of Alzheimer Disease. J Biol Chem. 2015;290(17):10862-75.

49. Biberoglu K, Yuksel M, Tacal O. Azure B affects amyloid precursor protein metabolism in PS70 cells. Chem Biol Interact. 2019;299:88-93.

JOTCS A
Journal of the Turkish Chemical Society
Section: A Chemistry
TURKISH CHEMICAL SOCIETY

Quercetin particles with lower inhibitory activity for α-glucosidase and negligible effects on blood clotting

Mehtap SAHINER[1]* and Selin Sagbas SUNER[2]
[1]Department of Fashion Design, Canakkale Applied Science, Canakkale Onsekiz Mart University, Terzioglu Campus, 17100, Canakkale, Turkey.
[2]Department of Chemistry, Faculty of Science and Arts, Canakkale Onsekiz Mart University, Terzioglu Campus, 17100, Canakkale, Turkey

Abstract: Poly(quercetin) (p(QR)) particles were synthesized by using poly (ethylene glycol) diglycidyl ether (PEGGE) crosslinker in a single step via a microemulsion system. The morphological, size, and functional analysis of the prepared particles were examined by optical microscope, scanning electron microscope (SEM), dynamic light scattering (DLS) measurements, and FT-IR spectroscopy. P(QR) particles were found to have spherical shape with 372±9 nm size range based on SEM images and DLS measurements. The zeta potential measurements, performed at different pH conditions, and potentiometric titration of p(QR) particles revealed that the isoelectric point and pKa values were around pH 2.5 and 2.3, respectively. Ferric reducing antioxidant power (FRAP) was determined for QR and p(QR) particles at pH 3.6 and found to be 9.4 and 0.43 µg of reduced Fe(II). The effects of QR and p(QR) particles on α-glucosidase enzyme activity were investigated at pH 6.9 and QR molecules and p(QR) particles can inhibit the α-glucosidase enzyme by 89.3% and 24.7%, respectively. The fluorescence spectroscopy of QR and p(QR) with fibrinogen showed that p(QR) particles do not induce clotting of blood.

Keywords: Quercetin particles; α-glucosidase inhibitor; fibrinogen binding; antioxidant.

Submitted: November 14, 2020. **Accepted:** February 22, 2021.

Cite this: Sahiner M, Suner SS. Quercetin particles with lower inhibitory activity for α-glucosidase and negligible effects on blood clotting. JOTCSA. 2021;8(2):443–52.

DOI: https://doi.org/10.18596/jotcsa.825868.

***Corresponding author. E-mail:** sahinerm78@gmail.com.

INTRODUCTION

Polyphenolics obtained from natural sources are known as flavonoids and have natural antioxidant and antibacterial properties due to the hydroxyl groups in their chemical structure. They are usually found in fruits, roots, leaves or stems of plants (1–3). As they possess antioxidant, antimicrobial and hemostatic properties, polyphenolics are potentially considered as drugs for healing cancers and wounds and attract great interest in many areas including medicine, food, and cosmetics (4–7). Quercetin (QR) is a flavonoid commonly found in many plants such as onion, tea, apple peel, parsley, citrus, sage, white grapes, red grapes and so on. It was shown *in vivo* and *in vitro* that quercetin can prevent oxidative stress by capturing free radicals in the body due to antioxidant properties, can be used in the treatment of hypertension by lowering blood pressure, and can prevent inflammation with anti-cancer effects (3). Some flavonoids such as quercetin are used in the body and they can interact with enzymes causing their activation and/or inactivation (inhibition) (8).

It is recognized that enzymes break down sugar and when long chain sugars are broken down into a single molecule sugar unit in the body, they can pass into the blood causing an increase in glucose level of the blood. There are many treatments for high glucose levels, e.g., the use of insulin hormone for the treatment of hyperglycemia. Also, one of these treatments is inhibition of the α-glucosidase enzyme, and some flavonoids are known to inhibit the α-amylase enzyme (8–10).

In the biomedical applications of any materials, there are always interactions with blood and cells that need to be considered seriously. Fibrinogen is one of the human plasma proteins that has significant and effective role in the coagulation of blood

and cell adhesion. The concentration of fibrinogen in the human body can change in the 2-4 g/L range (11). During the blood coagulation process, fibrinogen interacts with thrombin resulting in conversion to fibrin and subsequent clot formation. Preserving the proper protein structure and conformation are also significant factors to maintain the activity of fibrinogen. Alteration of fibrinogen is therefore an essential method to study the interaction between materials and blood (12).

Earlier, our group reported the preparation of p(QR) nanoparticles by cross-linking QR molecules with polyethylene glycol glycidyl ether (PEGGE) in lecithin-gasoline reverse micellar microemulsion (13). The hydrolytic degradation, hemolysis, blood clotting index for human blood, cytotoxicity, and cancer cell viability were reported (13). Here, we report the effects of QR and p(QR) on α-glucosidase enzyme activity. The solutions of QR molecule and p(QR) particles at different concentrations were incubated with α-glucosidase enzyme at pH 6.9 to determine the inhibition capability. Furthermore, the interaction of QR and p(QR) with fibrinogen was investigated to estimate the coagulation effects in blood.

MATERIAL AND METHOD

Materials

Quercetin dehydrate (QR, Sigma, >95%), L-α-lecithin (granular, Acros Organic, 98%), poly (ethylene glycol) diglycidyl ether (PEGGE, Mn: 500, Aldrich), triethylamine (TEA, 99.5%, Sigma Aldrich) sodium hydroxide (Sigma-Aldrich), gasoline (95 octane, Total), cyclohexane (99.5%, Sigma-Aldrich), and ethyl alcohol (Birkim, 9%) were used as received. Ultra-pure distilled water was obtained from GFL, 2108 and Millipore Direct-Q3 UV (18,2 MΩ.cm). Sodium nitrite from Acros, aluminum chloride (Alfa Aesar), 5,6-Diphenyl-3-(2-pyridyl)-1,2,4-triazine-4,4-disulfonic acid disodium salt hydrate (Alfa Aesar), sodium acetate anhydrous (Fisher, 99%), and hydrochloric acid (Sigma, 37%) were used for antioxidant tests. Bovine fibrinogen (Alfa Aesar) was used for fibrinogen interaction. α-Glucosidase from *Saccharomyces cerevisiae* (Sigma Aldrich) and *p*-nitrophenyl- α-D-glucopyranose (Sigma Aldrich) were used for α-glucosidase activity.

Synthesis of p(QR) particles

P(QR) particles were synthesized by using PEGGE as crosslinker in lecithin-gasoline microemulsion medium according to a previous procedure with some modifications (13,14). In short, 3 mL of 0.1 g/mL concentration of QR in 1 M NaOH aqueous solution was placed in 150 mL 0.1 M lecithin-gasoline solution at 50 °C at 750 rpm mixing rate. After 10 min, PEGGE at 300% mole ratio of QR and 20 µL triethylamine as accelerator were added into the emulsion medium under constant mixing and the reaction continued for 12 h at 50 °C. The prepared p(QR) particles were precipitated via centrifuge at 10,000 rpm for 10 min. Then, the precipitated p(QR) particles were washed with gasoline and cyclohexane, ethanol:water mixture three times and then with acetone by using centrifugation to precipitate/resuspend at 10,000 rpm for 10 min. The prepared p(QR) particles were dried in an oven at 50 °C for further use.

Characterization of p(QR) particles

The morphological structure of p(QR) particles was assessed by optical microscope (Olympus BX-53) and scanning electron microscope (SEM, Jeol JSM-5600 LV). For SEM analysis, p(QR) particles were coated with gold/palladium and analyzed at 20 kV operating voltage. Hydrodynamic size distribution of p(QR) particles was determined by dynamic light scattering (DLS, Brookhaven Ins. Corp., 90Plus/BIMAS). Zeta potential (ZP) measurements of the particles were completed by using Brookhaven Inst. Corp., BIC ZetaPlus analyzer at different solution pHs. Briefly, 10 mg of p(QR) particles were dispersed in 0.001 M 50 mL KCl aqueous solution and the ZP of the particles was measured in the pH 2-12 range to calculate the isoelectric point (IEP) of p(QR) particles. DLS and ZP analyses were measured ten times and the obtained results are given as averages with corresponding standard deviations. Potentiometric titration of p(QR) particles was carried to determine the equivalent point and pKa values of p(QR) particles. Briefly, 50 mg p(QR) particles were suspended in 0.01 M 50 mL KCl aqueous solution, and the pH of this suspension was adjusted to 2 by using 0.01 M HCl aqueous solution and titrated by using 0.01 M NaOH aqueous solution up to pH 12. Thermogravimetric analysis (TGA) of p(QR) particles was done by using a TG analyzer (SII TG/DTA 6300, Japan) in the temperature range 50-1000 °C. P(QR) particles weighing about 5 mg were heated at 10 °C/mL heating rate under N_2 atmosphere with 100 mL/min flow rate.

Determination of antioxidant properties of p(QR) via iron reduction potential FRAP TEST

The iron reduction potential (FRAP) of QR and p(QR) particles was investigated with a UV-Vis spectrophotometer at 595 nm according to the literature (15,16). Briefly, 0.3 M acetate buffer was prepared at pH 3.6. Tripyridyl triazine (TPTZ) solution at 10 mM concentration was prepared using 2.5 mL 40 mM HCl. Acetate buffer with 25 mL volume was mixed with 2.5 mL of TPTZ solution and 2.5 mL of 20 mM $FeCl_3H_2O$ (in acetate buffer) was mixed to obtain Fe(III)- TPTZ complex. P(QR) were suspended in acetate buffer at 0.5 mg/mL and QR molecules were dissolved in ethanol at 0.5 mg/mL. The FRAP test was done using 3 mL of the prepared Fe-TPTZ complex solution.

QR solution and p(QR) suspended particles were prepared as 0.5 mg/mL solution. First, the UV-visible spectra of the Fe-TPTZ complex was measured at 595 nm, and 5-80 µL volumes of QR and/or p(QR) particle suspensions were placed into Fe-TPTZ complex solution and stirred for 4 minutes with plastic pipette tips. Then, the UV-Vis spectra was

recorded and the difference between the absorbance values was calculated as µmol Fe(II) reduced. $FeSO_4 \cdot 7H_2O$ was used as the Fe(II) source to complex with TPTZ as standard to generate a calibration curve to be used in determination of Fe(II) reduced by QR and/or p(QR) particles. Gallic acid (GA) was taken as a reference material.

Total flavonoid content (TFC) of QR and p(QR) particles

The TFC tests for QR and p(QR) were done using a UV-Vis spectrophotometer at 405 nm in accordance with the literature with some modifications (17). QR solution and p(QR) particle suspension in distilled water at 170 ppm and 0.5 mL volume was placed in 10-mL tubes. Distilled water, 2 mL, was added to these 10-mL tubes. 5 minutes later, 0.15 mL of 5% $NaNO_2$ was added and after another 5 minutes, 0.15 mL of 10% $AlCl_3 \cdot 6H_2O$ was added to this medium. After another 5 minutes, 1 M 1 mL of NaOH was added to this mixture. After keeping this solution still for another 15 minutes, the UV-Vis spectrum of this solution was read at 405 nm. $NaNO_2$ and $AlCl_3.6H_2O$ mixture solution in DI water was used as blank. Gallic acid was used as standard.

Inhibitory capacity of QR and p(QR) for α-glucosidase

The inhibition capacity of QR and p(QR) particles for the enzyme, α-glucosidase, was examined according to the reported literature (18–20). The QR solution was prepared at 0.075, 0.15, 0.3 and 0.375 mg/mL concentrations. From these solutions, 70 µL was taken, placed in 96 well-plates and incubated for 10 minutes. To these solutions, 70 µL of enzyme solution at 0.06 unit/mL was added. Then, 70 µL substrate (1.66 mM *p*-nitrophenyl-α-D-glucoside solution in 67 mM phosphate buffer) was added and left for 30 minutes and the absorbance value was measured at 405 nm using a micro plate reader (Thermo Multiskan Go). Inhibition% values were calculated using equation (1) and compared to a control with 70 µL buffer solution in place of the QR or p(QR) eluate (18, 20). For p(QR) particles, 0.375, 0.75, 1.5 and 3 mg/mL suspensions were prepared and added to the well-plates and the same procedures were carried out.

$$\text{Inhibition of } \alpha-\text{glucosidase enzyme } \% = \left(\left[1 - \frac{\Delta A_{405}^{Sample}}{\Delta A_{405}^{Control}}\right]\right) \times 100$$

$$\text{Inhibition of } \alpha-\text{glucosidase enzyme } \% = \left(\left[1 - \frac{\Delta A_{405}^{Sample}}{\Delta A_{405}^{Control}}\right]\right) \times 100$$

Equation (1)

Fibrinogen interaction

The interactions of QR and p(QR) particles with fibrinogen were investigated according to the literature (13). The effect of QR and p(QR) on the fluorescence properties of fibrinogen was monitored by fluorescence spectroscopy (Thermo Scientific Lumina Spectrophotometer). A fibrinogen solution at 0.2 mg/mL concentration was prepared in distilled water. Different concentrations of QR or p(QR), 15-250 µg/mL in PBS, were mixed with fibrinogen solution in 1:1 ratio by volume. The width of the excitation and emission slit was set as 5 nm and the excitation wavelength of 280 nm was used. The scanning range was set between 280-420 nm. The interaction of QR and p(QR) particles with fibrinogen was determined in terms of the reduction in the fluorescence intensity.

RESULTS AND DISCUSSION

Quercetin (QR) is a well-known flavonoid-based phenolic that has promising use in a wide range of biological applications including as antimicrobial, antioxidant, anticancer, and anti-inflammatory material (21-24). The phenolic structure of QR was considered to be monomeric and was crosslinked with an epoxy group containing crosslinkers, e.g., PEGGE, to prepare degradable p(QR) particles. In p(QR) particle synthesis, QR was dissolved in basic aqueous solution and transferred to a lecithin-gasoline microemulsion solution to create water-in-oil emulsion medium. PEGGE as crosslinker was added into the reaction medium containing epoxy groups can readily react with phenolic hydroxyl groups on quercetin in basic conditions. Sahiner et al. reported the synthesis, characterization, and degradability of p(QR) particles crosslinked with PEGGE (14). Also, the antioxidant, blood compatibility, cytotoxicity, and anticancer properties of these particles were reported (14). In this study, the degradable p(QR) particles were prepared with the same process to investigate their binding and/or inhibitory effect on alpha glycosidase enzyme activity for blood clotting mechanisms. The sizes of p(QR) particles were illustrated by optic microscope and SEM images as shown in Figure 1a and 1b.

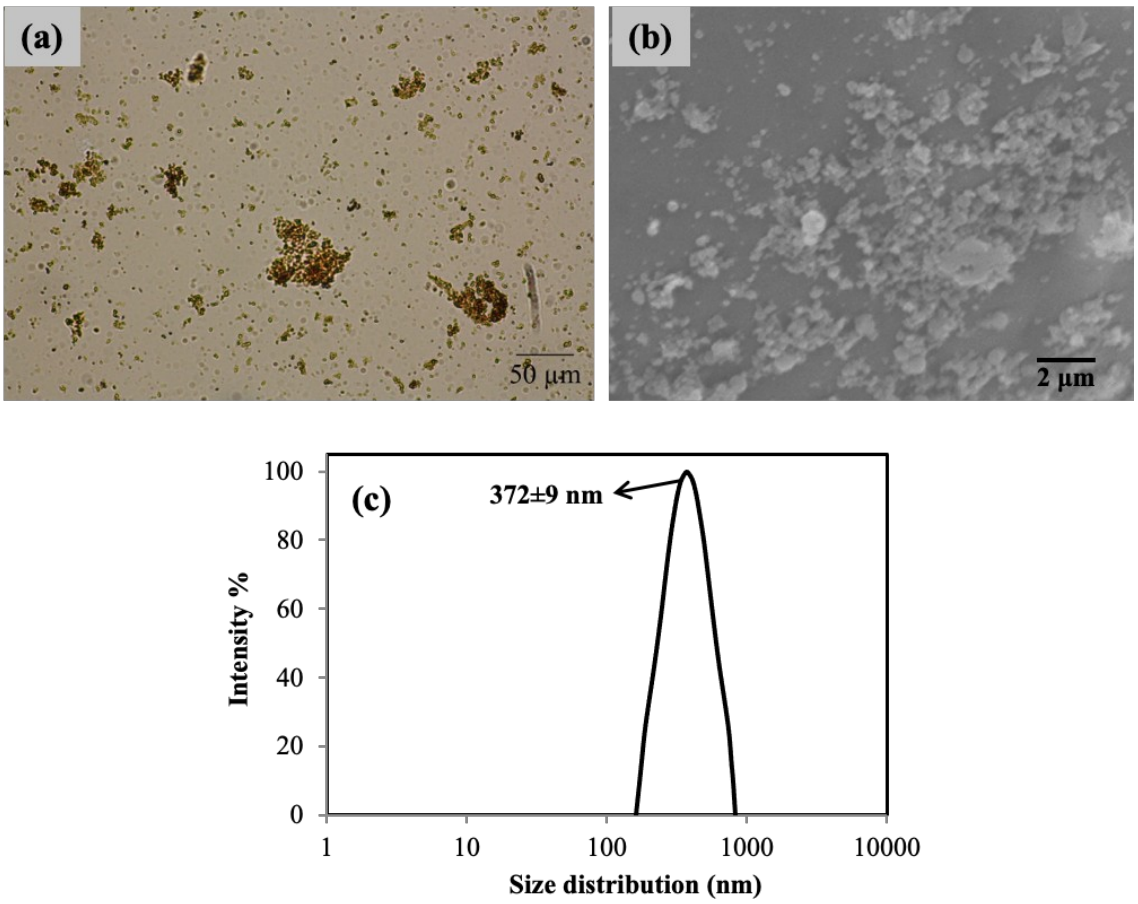

Figure 1. (a) Optical microscope and (b) SEM images of p(QR) particles and (c) hydrodynamic size distribution.

It is obvious from the images that p(QR) particles are spherical with sub-micron size range. The hydrodynamic size distribution of the p(QR) particles was measured between 160 nm and 820 nm size range with 372±9 nm average particle size. These results signified that the prepared p(QR) particles have nanometer size range and can be used as an injectable material for *in vitro* and *in vivo* applications.

Thermal degradation of PEGGE-crosslinked p(QR) particles was determined by thermogravimetric analysis (TGA) by heating about 5 mg p(QR) particles from 50 °C to 1000 °C under N_2 atmosphere. The corresponding TGA thermogram is shown in Figure 2.

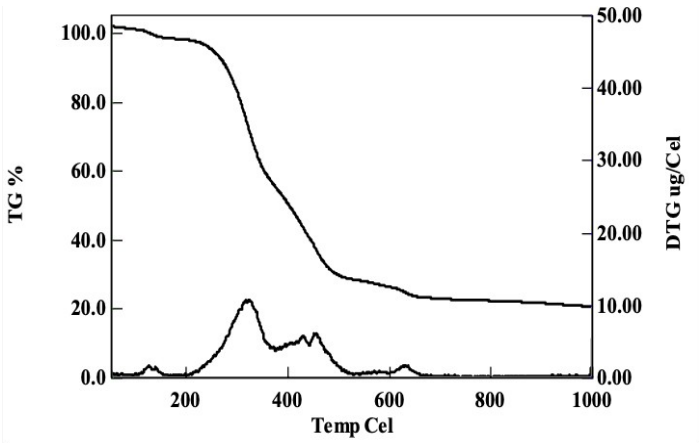

Figure 2. Thermogram of PEGGE-crosslinked p(QR) particles.

The first degradation was obtained in the 118-154 °C range with slight weight loss about 1.4% because of bound water in the polymeric structure. Then, two main degradations were observed in 205-350 and 370-490 °C ranges with 39.2 and 69.6% cumulative weight loss, respectively. After 500 °C, degradation was slightly increased with 79.4% cumulative weight loss. As reported in an earlier study, QR monomer was reported to be thermally more stable than PEGGE-crosslinked p(QR) particles up to nearly 900 °C because of more oxyethylene structure coming from the PEGGE crosslinker into the particle network (3).

Zeta potential values of p(QR) particles were measured in pH 2-12 solution to determine the isoelectric point, as shown in Figure 3a. According to the results, p(QR) particles had slightly positive character with +5.5±3.2 mV at pH 2 in acidic pHs, whereas zeta potential values gradually decreased to -27.2 from -3.7 mV up to pH 7 and were almost stable at pH 7-12 with more negative charges. The isoelectric point of p(QR) particles was found to be pH 2.5 where the zero zeta potential value was measured and there is a balance between positive and negative charges on the particle surface.

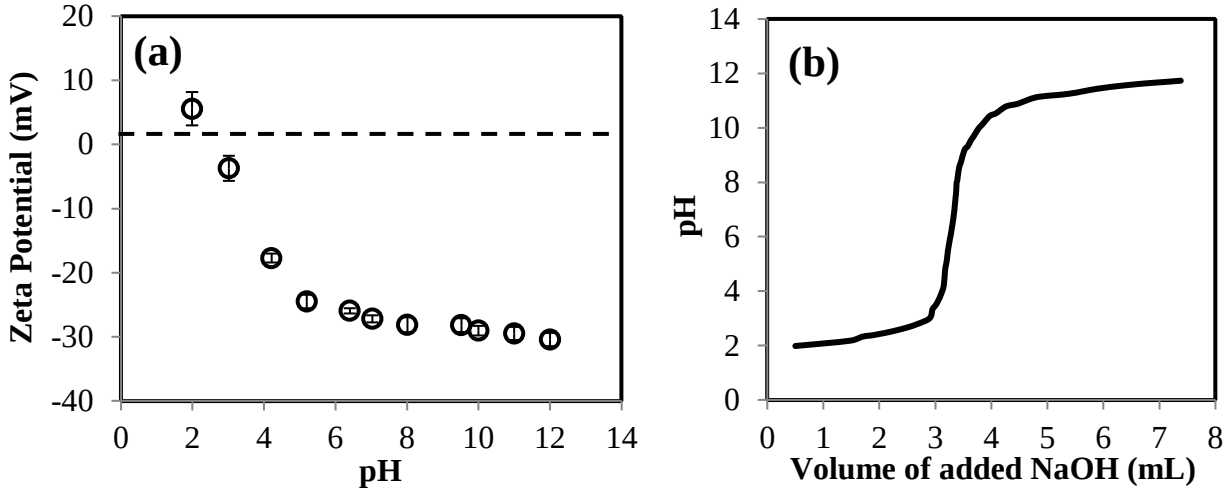

Figure 3. (a) Zeta potential values of p(QR) particles in different solution pHs, and (b) potentiometric titration of p(QR) particles by using 0.1 M NaOH aqueous solution.

Furthermore, potentiometric titration of p(QR) particles was carried out in pH 2-12 range to calculate equivalent point and pKa values of the p(QR) particles, as demonstrated in Figure 3(b). It was found that the equivalent point of p(QR) particles was about pH 7.6 with 2.3 pKa value. It is clear that p(QR) particles have only one pKa value coming from the phenolic hydroxyl groups in the particle structure and the pKa value of p(QR) particles was very close to the isoelectric point of the particles as expected since some of the hydroxyl available on QR molecules are used up during crosslinking with PEGGE. These results support the view that p(QR) particles are negatively charged at physiological conditions, e.g., at pH 7.4, and these negative p(QR) particles can readily interact with positively-charged biomacromolecules including some enzymes and proteins.

Ferric reducing antioxidant power (FRAP Test) of p(QR) particles

The FRAP test is an antioxidant test that is generally carried out at pH 3.6. It was reported that reduction of Fe(III) to Fe(II) ion by phenolic compounds can be used for the determination of their antioxidant power (25). Since, QR is not soluble in acetate buffer, the ethanolic solution of QR was used as comparison for p(QR) particles. As presented in Figure 4, the QR molecule reduces Fe(III) ions well compared with gallic acid (GA) which is generally used as reference. Gallic acid of 5 µg and QR were found to reduce Fe(III) to 15.75±1.5 µg and 9.4±1.74 µg Fe(II), respectively. The same amount of p(QR) particles (5 µg) in acetate buffer resulted in 0.43±0.07 µg Fe(II).

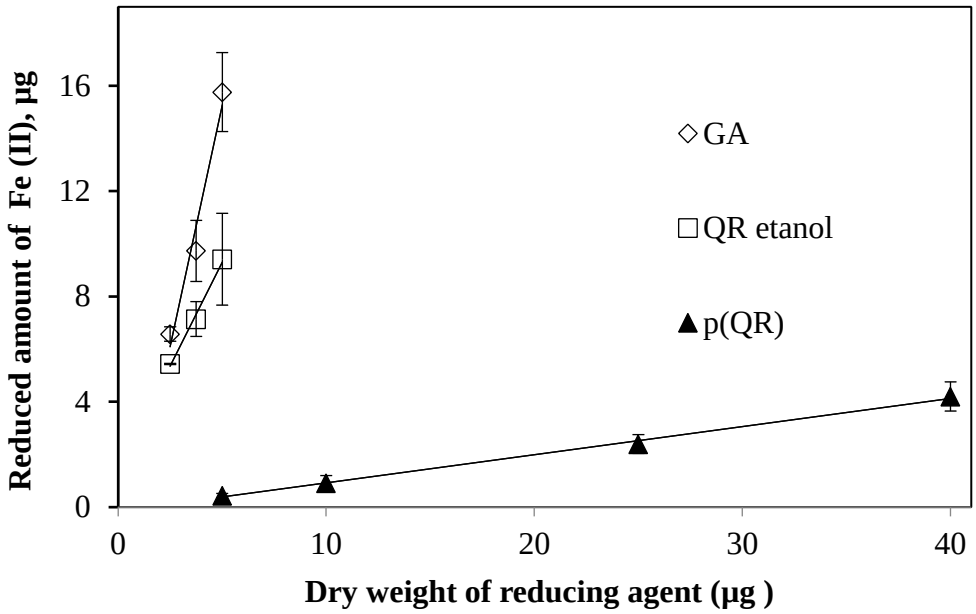

Figure 4. FRAP test for QR in ethanolic solution and p(QR) solution in acetate buffer at pH 3.6 (Gallic acid is used for comparison).

Although the Fe(III) reduction capacity of p(QR) seems to be lower than the QR molecule, p(QR) particles still have reducing capability as 10 µg p(QR) can result in about 1 µg of Fe(II) ions. The reducing capacity of p(QR) particles revealed a linear relationship with amount of p(QR) particles used and reduced forms of Fe(III) ions (Fe(II)).

Total flavonoid content (TFC TEST) of p(QR) particles

Total flavonoid content is another assay to determine the antioxidant properties of materials. The TFC of QR and p(QR) particles were examined, and the results are given in Table 1. GA equivalent value (µg/mL) was taken as standard. It is apparent that QR molecules and p(QR) values are higher than GA. As GA is not a flavonoid, this outcome is reasonable. As 170 ppm QR cannot be prepared in DI water, 170 ppm QR solution was prepared in ethanol and used in TFC tests. The results for TFC and FRAP that were only tested for 5 µg of material are summarized in Table 1.

Table 1. TFC (170 ppm) and FRAP (5 µg) values for GA, QR and p(QR) particles.

Materials	*TFC (ppm)	*FRAP (5 µg)
GA	170	15.8±1.8
QR	275.3±22.6	9.4±0.8
p(QR)	439.9±93.3	0.4±0.1

* The results shown are expressed as means ±SD of three independent experiments.

It is obvious from the table that the TFC values are much higher for QR and p(QR) in comparison to GA, and the FRAP values at low concentration of 5 µg is much higher for GA than for QR and p(QR). This is reasonable as GA has much higher Fe(III) reducing capacity than QR molecule and p(QR) particles. The antioxidant capacity of a phenolic compound strongly depends on the chemical nature of the flavonoid and the nature of the employed tests.

The inhibitory effect of p(QR) particle on α-glucosidase

The effect of QR and p(QR) particles on the enzyme activity of α-glucosidase was determined by interacting them at pH 6.9 in PBS. The inhibition values of α-glucosidase enzyme are given in Figure 5 (a) and (b), respectively.

As clearly seen in Figure 5 (a), as the clf112 concentration increased from 0.025 to 0.12 mg/mL, the α-glucosidase enzyme inhibition increased from 27.4 to 89.3% with an almost linear relationship between the amount of QR and the inhibition% of α-glucosidase enzyme. The p(QR) particles, on the other hand, as demonstrated in Figure 5 (b) revealed lower enzyme inhibition capability. From the figure, p(QR) particles can only inhibit 24.7% of α-glucosidase enzyme at 0.06 unit/mL mg/mL concentration against a maximum concentration of 1.0 mg/mL.

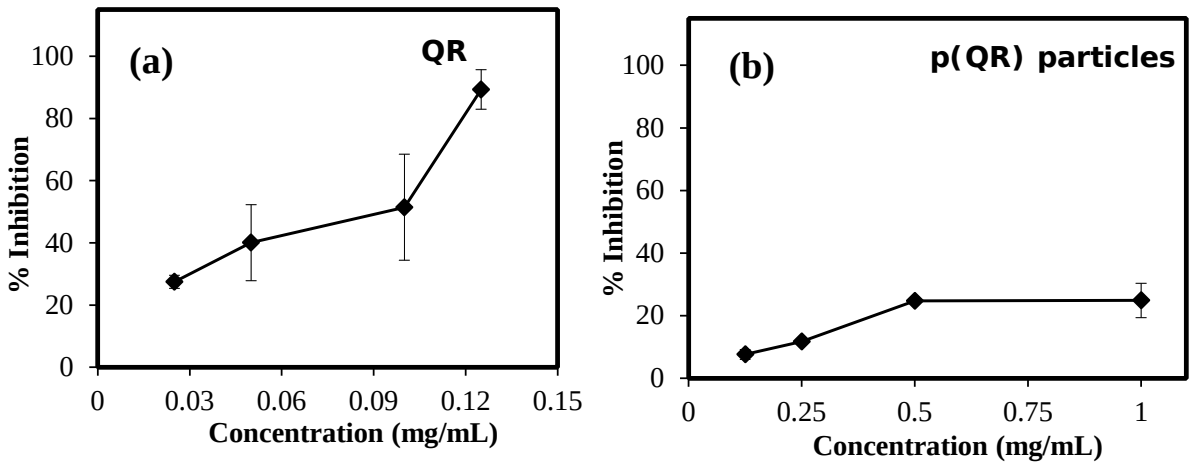

Figure 5 α-glucosidase enzyme inhibition % of (a) QR molecules, and (b) p(QR) particles.

The interaction of QR and p(QR) particles with fibrinogen

In the coagulation process, fibrinogen, a plasma protein, interacts with thrombin to form fibrin. The protein structure and conformation are significant factors in retaining the activity of fibrinogen. Biomaterials can interact with plasma protein and may influence or trigger the clotting mechanism. Therefore, analysis of and changes in protein molecules upon interaction with biomaterials in the blood has paramount significance. Generally, fluorescence spectroscopy is employed as an effective and comparable tool to determine these interactions. Fluorescence intensity is related and associated with the number of tryptophan residues in fibrinogen and tryptophan residues are generally located in the hydrophobic core of fibrinogen (12). The change in the tryptophan residue conformation results in a change in the intensity of the fluorescent emission. So, fluorescence spectroscopy can be readily employed to probe the microenvironment of fibrinogen (12,26).

QR and p(QR) were interacted with fibrinogen at varying concentrations and the corresponding fluorescence emission spectroscopy is presented in Figure 6 (a) and (b), respectively. The emission of fibrinogen at 0.1 mg/mL in DI water has a florescent intensity of about 64,700 at 341 nm. As seen in Figure 6 (a), the peaks for fibrinogen started to decrease with the increase in the concentration QR, e.g., 15, 31,62.5, 125, and 250 µg/mL. A similar test was also done for p(QR) particles as shown in Figure 6 (b). It is apparent from the figure that p(QR) particles are not as effective as QR molecules in reducing the fluorescence emission of fibrinogen. Only 250 µg/mL p(QR) particles decreased the fibrinogen peak to 51762 intensity as seen in Figure 6 (b).

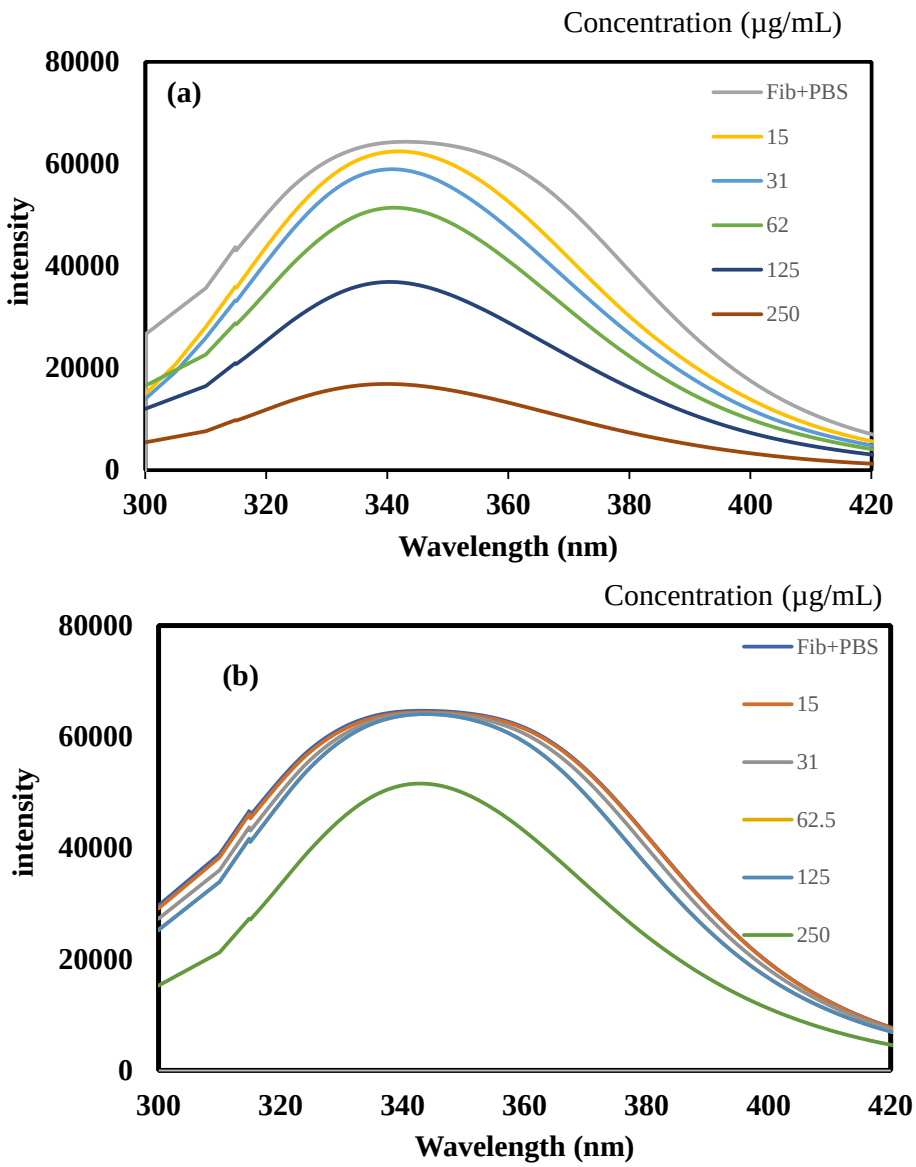

Figure 6. Fluorescent emission of (a) QR molecule (b) p(QR) particles at different concentrations [Excitation wavelength: 280 nm].

Earlier, p(QR) particles were reported to degrade to about 2.4% in PBS over 100 hours at pH 7.4 (14), suggesting that lower amounts of QR molecules (e.g., <15 µg/mL) cannot trigger a clotting effect by interacting with fibrinogen residues in blood proteins. Therefore, p(QR) particles with controllable degradation profile can be used without triggering blood clotting.

CONCLUSION

The isoelectric point of p(QR) particles was found to be pH 2.5 and the particles are negatively charged above this value. As α-glucosidase inhibition is important in connection with diabetes, defined as abnormal elevation of blood glucose levels, and is associated with cardiovascular diseases such as hypertension, the use p(QR) to inhibit this enzyme may be very useful in biomedical applications. The hydrolytic enzymes such as α-glucosidase play significant roles in controlling blood sugar for carbohydrate nutrition in the treatment of type 2 diabetes. The α-glucosidase enzyme interaction with QR and p(QR) particles resulted in inhibition of the enzyme, suggesting higher inhibition values for QR molecules even at extremely low concentrations. As the degradation of p(QR) particles can be controlled with the amount of crosslinker (PEGGE) used, the amount of QR molecules released can also be controlled resulting in inhibition% of the enzyme. These results show that QR is a good α-glucosidase enzyme inhibitor and can be used for lowering blood sugar after digestion in patients with high blood sugar. The p(QR) particle, on the other hand, does not exceed 24.7% inhibition even at a concentration of 1 mg/mL. It was also shown that fibrinogen residues in blood proteins can interact with QR molecule in concentration depending on manner as

QR and p(QR) could affect the structure and conformation of fibrinogen. Also, p(QR) particles have negligible effect on fibrinogen residue suggesting that these particles can be readily used in blood contacting biomedical applications by specifically controlling the amount of QR molecules coming from the corresponding particles. Therefore, QR molecules and p(QR) particles may be used for biomedical applications. For example, QR molecules may be suitable for bleeding wounds or to control + bleeding after tooth extraction, while p(QR) particles maybe used up to 125 µg/mL concentration for intravenous applications without any thrombus.

ACKNOWLEDGEMENT

This work is supported by the Scientific Research Commission of Canakkale Onsekiz Mart University (COMU BAP, FBA-2018-2725).

REFERENCES

1. Buchweitz M, Kroon PA, Rich GT, Wilde PJ. Quercetin solubilisation in bile salts: A comparison with sodium dodecyl sulphate. Food Chem 2016 Nov;211:356–64.

2. Leopoldini M, Russo N, Toscano M. The molecular basis of working mechanism of natural polyphenolic antioxidants. Food Chem 2011 Mar;125(2):288–306.

3. Sahiner N. One step poly(quercetin) particle preparation as biocolloid and its characterization. Colloids Surfaces A Physicochem Eng Asp 2014 Jun;452:173–80.

4. Tan L, Zhou X, Wu K, Yang D, Jiao Y, Zhou C. Tannic acid/CaII anchored on the surface of chitin nanofiber sponge by layer-by-layer deposition: Integrating effective antibacterial and hemostatic performance. Int J Biol Macromol 2020 Sep;159:304–15.

5. Terao J. Factors modulating bioavailability of quercetin-related flavonoids and the consequences of their vascular function. Biochem Pharmacol 2017 Sep;139:15–23.

6. Cherubim DJ, Martins CV, Fariña L, Lucca RA. Polyphenols as natural antioxidants in cosmetics applications. J Cosmet Dermatol 2020 Jan 7;19(1):33–7.

7. Wang W, Sun C, Mao L, Ma P, Liu F, Yang J, et al. The biological activities, chemical stability, metabolism and delivery systems of quercetin: A review. Trends Food Sci Technol 2016 Oct;56:21–38.

8. Baldissarelli J, Santi A, Schmatz R, Zanini D, Cardoso AM, Abadalla FH, et al. Quercetin changes purinergic enzyme activities and oxidative profile in platelets of rats with hypothyroidism. Biomed Pharmacother 2016 Dec;84:1849–57.

9. Balasubramaniam V, Mustar S, Mustafa Khalid N, Abd Rashed A, Mohd Noh MF, Wilcox MD, et al. Inhibitory activities of three Malaysian edible seaweeds on lipase and α-amylase. J Appl Phycol 2013 Oct 25;25(5):1405–12.

10. Zaharudin N, Salmeán AA, Dragsted LO. Inhibitory effects of edible seaweeds, polyphenolics and alginates on the activities of porcine pancreatic α-amylase. Food Chem 2018 Apr;245:1196–203.

11. Zhu Y, Liu R, Wu D, Yu Q, Shea KJ, Zhu Q. Engineered polymer nanoparticles incorporating L-amino acid groups as affinity reagents for fibrinogen. J Pharm Anal 2020 Oct; doi:10.1016/j.jpha.2020.10.004

12. Deng L, Qi Y, Liu Z, Xi Y, Xue W. Effect of tannic acid on blood components and functions. Colloid Surface B 2019;184(September):110505.

13. Sahiner N, Sagbas S, Sahiner M, Silan C, Aktas N, Turk M. Biocompatible and biodegradable poly(Tannic Acid) hydrogel with antimicrobial and antioxidant properties. Int J Biol Macromol 2016; 82. 150–9.

14. Sahiner N, Sagbas S, Sahiner M, Aktas N. Degradable natural phenolic based particles with micro-and nano-size range. Recent Patents Mater Sci 2018;11(1). 33-40.

15. Tadapaneni RK, Banaszewski K, Patazca E, Edirisinghe I, Cappozzo J, Jackson L, et al. Effect of high-pressure processing and milk on the anthocyanin composition and antioxidant capacity of strawberry-based beverages. J Agric Food Chem 2012;60(23):5795–802.

16. Firuzi O, Lacanna A, Petrucci R, Marrosu G, Saso L. Evaluation of the antioxidant activity of flavonoids by “ferric reducing antioxidant power” assay and cyclic voltammetry. Biochim Biophys Acta - Gen Subj 2005 Jan;1721(1–3):174–84.

17. Li Y, Ma D, Sun D, Wang C, Zhang J, Xie Y, et al. Total phenolic, flavonoid content, and antioxidant activity of flour, noodles, and steamed bread made from different colored wheat grains by three milling methods. Crop J 2015;3(4):328–34.

18. Sahiner M, Blake DA, Fullerton ML, Suner SS, Sunol AK, Sahiner N. Enhancement of biocompatibility and carbohydrate absorption control potential of rosmarinic acid through crosslinking into microparticles. Int J Biol Macromol 2019;137.

19. Sahiner N, Sagbas S, Sahiner M, Blake DA, Reed WF. Polydopamine particles as nontoxic, blood compatible, antioxidant and drug delivery materials. Colloid Surface B 2018 Dec;172:618–26.

20. Sahiner M, Sahiner N, Sagbas S, Fullerton ML,

Blake DA. Fabrication of Biodegradable Poly(naringin) Particles with Antioxidant Activity and Low Toxicity. ACS Omega 2018;3(12).

21. Júnior SD da C, Santos JV de O, Campos LA de A, Pereira MA, Magalhães NSS, Cavalcanti IMF. Antibacterial and antibiofilm activities of quercetin against clinical isolates of Staphyloccocus aureus and Staphylococcus saprophyticus with resistance profile. Int J Environ Agric Biotechnol 2018;3(5):1948–58.

22. Chen C, Zhou J, Ji C. Quercetin: A potential drug to reverse multidrug resistance. Life Sci 2010 Sep;87(11–12):333–8.

23. Wojdyło A, Samoticha J, Chmielewska J. Effect of different pre-treatment maceration techniques on the content of phenolic compounds and color of Dornfelder wines elaborated in cold climate. Food Chem. 2021 Mar;339:127888. doi:10.1016/j.foodchem.2020.127888

24. Dhanaraj T, Mohan M, Arunakaran J. Quercetin attenuates metastatic ability of human metastatic ovarian cancer cells via modulating multiple signaling molecules involved in cell survival, proliferation, migration and adhesion. Arch Biochem Biophys 2021 Feb;108795.

25. Zhao F-Q, Wang G-F, Xu D, Zhang H-Y, Cui Y-L, Wang Q-S. Glycyrrhizin mediated liver-targeted alginate nanogels delivers quercetin to relieve acute liver failure. Int J Biol Macromol 2021 Jan;168:93–104.

26. Hu Q, Zhang Y, Wang C, Xu J, Wu J, Liu Z, et al. Hemocompatibility evaluation in vitro of methoxy polyethyleneglycol-polycaprolactone copolymer solutions. J Biomed Mater Res Part A 2016 Mar;104(3):802–12.

JOTCS A
Journal of the Turkish Chemical Society
Section: A
Chemistry
TURKISH CHEMICAL SOCIETY

Investigation of the dyeing properties of the colorant extracted from *Juglans regia* L. leaves on cellulosic and protein fabrics

Adem Önal[1]*, Oguz Özbek[2], Filiz Vanlioglu[3], Ahmet Turan Teker[3], and Duygu Boyraz[3]

[1]Tokat Gaziosmanpasa University, Natural Dyes Application and Research Center, 60250, Tokat, Turkey.
[2]Zonguldak Bülent Ecevit University, Science and Technology, Application and Research Center, 67600, Zonguldak, Turkey.
[3]Tokat Maturation Institute, 60100, Tokat, Turkey.

Abstract: Dyeing properties of different fabric species were investigated using leaf extract of *Juglans regia* L. For this purpose, wool and cotton fabrics were dyed using brown napthaquinone colorant extracted from walnut leaves by pre-mordanting, meta-mordanting and post-mordanting methods in the presence of ferrous sulfate ($FeSO_4.7H_2O$), copper(II) sulfate ($CuSO_4.5H_2O$) and alum sulfate ($AlK(SO_4)_2.12H_2O$) at medium pH. Color codes were determined with Pantone Color Guide, and K/S and *L* a* b** values were determined using color measurement spectrophotometer, and also washing-, crocking-fastness levels were evaluated using gray scale. High fastness colors were obtained in general in the present study.

Keywords: *Juglans regia* L., mordant, wool, cotton, fastness.

Submitted: January 09, 2021. **Accepted:** February 24, 2021.

Cite this: Önal A, Özbek O, Vanlioglu F, Teker AT, Boyraz D. Investigation of the dyeing properties of the colorant extracted from *Juglans regia* L. leaves on cellulosic and protein fabrics. JOTCSA. 2021;8(2):453–60.

DOI: https://doi.org/10.18596/jotcsa.856975.

***Corresponding author:** E-mail: adem.onal@gop.edu.tr, Tel: +903562521616-3074.

INTRODUCTION

The use of natural dyes generally obtained from different parts of plants such as flowers, leaves, bark, roots, and stems has began in China and Central Asia, and these dyes were used to dye various materials such as clothes, rugs, and carpets (1). Synthesis, processing, and use of synthetic dyes are considered highly harmful to the environment and human health. They may cause carcinogenic, toxic, and allergic effects, especially on humans. Therefore, natural dyes and pigments can be considered as very important alternatives to synthetic dyes (2–4). In addition, there is a growing interest in recent years for the use of natural dyes by researchers due to their biodegradable, non-allergenic, non-toxic, and environmentally friendly properties (5, 6). Natural dyes, as reported by multiple studies, have several biological properties such as antibacterial and insecticidal functions, possibly due to their natural origin (7). Due to their low cost, wastes obtained from plants can be considered as important raw materials for the textile industry (8). Considering all these advantages, different national and international institutes conduct researches to improve the extraction of colors from natural resources (9). There are many studies in the literature on natural dyeing for different fiber types (10–12).

Natural products are used in many areas of the industry due to their biological activities and versatile applications (13–15). *Juglans regia* L. is commonly known as walnut tree and belongs to *Juglandaceae* family. *Juglans regia* L. is mostly grown in uncultivated, temperate regions and poor soil and, is cultivated commercially in geographical regions including Western South America, United States, Asia and Southern Europe (16). In addition, Turkey, in terms of manufacture and import of walnut, has a very important place in the world.

Chemical interactions that occur between plant species are called allelopathy, and organic compounds that play a role in allelopathy are called allelochemicals. One of these allelochemicals is Juglone (Figure 1), which is responsible for walnut allelopathy (17). It was reported that juglone is the main coloring component which is found in walnut husks, root, leaves, and stem bark (18, 19). Apart from natural dyeing, walnuts have been found to be beneficial in alternative medicine and are used to treat various ailments such as infectious diseases, diuretic, asthma, skin diseases, stomach-ache and eczema, traditionally (20).

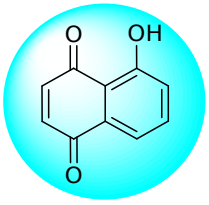

Figure 1: Chemical structure of Juglone (5-Hydroxy-1,4-naphthoquinone)

In the present study, the dyeing properties of different fabric species were investigated using leaves extract of *Juglans regia* L. For this purpose, pre-mordanting, meta-mordanting and post-mordanting methods were performed using ferrous sulfate ($FeSO_4.7H_2O$), copper sulfate ($CuSO_4.5H_2O$), and alum ($AlK(SO_4)_2.12H_2O$) at a medium pH. Color codes and K/S values were determined and high fastness of dyed samples were obtained in general.

EXPERIMENTAL SECTION

Reagents and Equipments

All chemicals and mordants ($CuSO_4.5H_2O$, $FeSO_4.7H_2O$, $AlK(SO_4)_2.12H_2O$) were obtained from Sigma Aldrich. Distilled water was used in all steps of the study. Extraction was performed using soxhlet apparatus. The color properties of the dyed samples were evaluated by Premier Colorscan SS 6200A Spectrophotometer in terms of CIELab values (*L**, *a**, *b**, *C**) and color strength (*K/S*) values. While washing fastness values were determined according to ISO 105-C06 standards, dry and wet crock fastness of dyed fabrics were determined according to ISO 105-X12 method (21).

Methods

Natural Dye Extraction and Mordanting

In the present study, fresh (green) *Juglans regia* L. leaves used as a natural dye source was collected from Tokat (Turkey). 50 g of green walnut leaves was refluxed on soxhlet apparatus in distilled water until it becomes colorless. This procedure was repeated until 5 liters of color extract is obtained, and finally all extracts were combined (22). Ferrous sulfate, copper sulfate, and alum sulfate were used as mordants, and the dyeing procedures were performed as pre-mordanting, meta-mordanting, and post-mordanting. Pre-mordanting, meta-mordanting, and post-mordanting methods were applied as performed in our previous studies (23, 24).

RESULTS AND DISCUSSION

Determination of color performance

After dyeing, the samples were exposed to sunlight for 200 h and, light fastness of dyed samples were rated on 1–8 grey scale. After dyeing, the dyed fabric samples were taken out and soaping was done (30 min at 45 °C). The dyed samples were washed several times to remove unfixed surface dye. The pre-, meta- and post- mordanting dyed samples were investigated for different properties such as color strength, washing fastness, and light fastness. The wash fastness was determined by keeping the liquor to material ratio at 50:1. Color strength was expressed as K/S values of the dyed samples using the Kubelka-Munk equation (25):

$$K/S=\frac{(1-R)^2}{2R} \quad (1)$$

where K is the absorption coefficient, R is the reflectance of the dyed sample and S is the scattering coefficient.

K/S and *L*, a*, b** values of wool and cotton fabrics are given in Table 1. *L** is the lightness or luminance value, which ranges from 0 to 100, and the higher lightness value represent lower color yield. The lower *L** values indicate that the sample become darker than that of the control sample. *a** values run from negative (green) to positive (red) and *b** values run from negative (blue) to positive (yellow) (26).

Table 1: K/S and *L*a*b** values of cotton and woolen fabrics.

Fabric	Mordant	*L**	*a**	*b**	K/S
Cotton	$FeSO_4$	50.09220	3.2035	11.6849	8.84863
Cotton	$FeSO_4$	38.2095	-0.6540	5.8743	13.6510
Cotton	$FeSO_4$	57.8050	5.4138	22.5157	8.16812
Cotton	$CuSO_4$	61.0601	1.8038	10.6227	3.37569
Cotton	$CuSO_4$	50.4130	4.3318	11.3770	6.78419
Cotton	$CuSO_4$	67.9525	0.3574	9.5092	2.17486
Cotton	$AlK(SO_4)_2$	63.2240	1.9043	12.8670	4.61283
Cotton	$AlK(SO_4)_2$	70.2700	2.5259	10.1383	3.08468
Cotton	$AlK(SO_4)_2$	70.2642	0.8801	7.5420	1.79238
Wool	$FeSO_4$	62.2755	-0.0560	5.2680	2.52778
Wool	$FeSO_4$	65.9266	0.1176	5.3012	2.12176
Wool	$FeSO_4$	57.9216	0.2145	11.7485	5.41675
Wool	$CuSO_4$	65.6697	1.4781	10.1613	2.16557
Wool	$CuSO_4$	53.0520	4.0574	12.9911	5.9045
Wool	$CuSO_4$	68.3023	-0.0140	9.1994	1.76316
Wool	$AlK(SO_4)_2$	70.7843	1.1885	10.0900	2.12717
Wool	$AlK(SO_4)_2$	69.6861	0.5437	11.1085	3.62508
Wool	$AlK(SO_4)_2$	70.8454	0.7576	7.9840	1.56455
Unmordant cotton	-	69.7925	1.3569	9.0152	2.15633
Unmordant wool	-	1.6091	0.9240	6.0562	2.18797

As seen in Table 1, different intensity and brightness or color tones were obtained in the dyed cotton fabrics. Predominantly greenish yellow and brown tones were obtained. The value of *a** is negative and the color has shifted to brown with ferrous sulfate. The highest K/S (13.65) value is obtained for ferrous sulfate using meta mordanting method.

For dyeing of woolen fabrics, yellow, khaki and brown color tones are obtained and the highest K/S (5.90) value is obtained for copper sulfate using meta mordanting method.

Fastness values and color codes of dyed cotton samples are given in Table 2.

Table 2: Fastness values and color codes of dyed cotton samples.

Method	Mordant	pH	Light fastness	Washing fastness	Rubbing (wet/dry)	Color code (Pantone)
T1	$FeSO_4$	4.50	5/6	4	4 – 5	1265CS C:0 M:7 Y:100 K:55
T2	$FeSO_4$	4.50	6	5	4 – 4/5	112CS C:0 M:14 Y:100 K:53
T3	$FeSO_4$	4.50	5/6	4	4 – 4/5	105CS C:65 M:55 Y:98 K:0
T1	$CuSO_4$	3.55	5/6	5	4 – 5	103CS C:0 M:7 Y:100 K:30
T2	$CuSO_4$	3.55	5	3	4 – 4/5	117CS C:0 M:25 Y:100 K:23
T3	$CuSO_4$	3.55	6	3/4	4 – 4	104CS C:0 M:6 Y:100 K:42
T1	$AlK(SO_4)_2$	5.20	5	3/4	4/5 – 5	110CS C:0 M:19 Y:100 K:15
T2	$AlK(SO_4)_2$	5.20	5	4	4 – 5	109CS C:0 M:8 Y:100 K:3
T3	$AlK(SO_4)_2$	5.20	5	4	4 – 5	4535CS C:0 M:4 Y:25 K:22
	Unmordant	7.25	5/6	4	4 – 4/5	605CS C:0 M:0 Y:90 K:18

T1: Pre- mord., T2: Meta- mord., T3: Post- mord., Wash and rubbing 5 (maximum) to 1 (very poor) and Light 8 (maximum) to 1 (very poor)

For dyeing experiments, using $FeSO_4$ wet, dry rubbing and washing fastness values are 4.5, approximately. Light fastness values are between 5–7. These results are generally considered acceptable. For $CuSO_4$, all fastness values are found to be very good except washing and light fastness. When the dyeing was made with $AlK(SO_4)_2$, all results are 4.0 and over. Fastness values are 4.0 and higher for unmordanting dyeings.

Fastness values and color codes for dyed woolen fabrics are given in Table 3.

Table 3: Fastness values and color codes of dyed woolen fabrics.

Method	Mordant	pH	Light	Wash	Rubbing (wet/dry)	Color code
T1	$FeSO_4$	4.50	6	3/4	4/5	111CS C:0 M:16 Y:100 K:45
T2	$FeSO_4$	4.50	6/7	4	5/5	365CS C:13 M:0 Y:94 K:74
T3	$FeSO_4$	4.50	6	3/4	4/5	382CS C:23 M:0 Y:95 K:0
T1	$CuSO_4$	3.55	5/6	3	4/5	4515CS C:0 M:8 Y:46 K:40
T2	$CuSO_4$	3.55	4/5	4	4/5	451CS C:2 M:0 Y:38 K:45
T3	$CuSO_4$	3.55	4	2/3	4/5	103CS C:0 M:7 Y:100 K:30
T1	$AlK(SO_4)_2$	5.20	4/5	3	5/5	105CS C:65 M:55 Y:98 K:45
T2	$AlK(SO_4)_2$	5.20	4/5	3	4/5	1265CS C:0 M:31 Y:98 K:64
T3	$AlK(SO_4)_2$	5.20	4/5	2/3	4/5	398CS C:4 M:0 Y:100 K:40
	Unmordant	7.25	5/6	4/5	5-4/5	618CS C:0 M:3 Y:77 K:44

T1:Pre- mord., T2: Meta mord., T3: Post mord., Wash and rubbing 5 (maximum) to 1 (very poor) and Light 8 (maximum) to 1 (very poor)

In Table 3, it can be seen that the wash fastness values of ferrous sulfate is higher than those of copper sulfate and alum. However, the wash fastnesses are low and other fastnessess are high for last mordanting for copper sulfate. In addition, the wash fastnesses are low and other fastnesses are at a good level for alum. Fastness values for unmordanted dyes are 4.0 and above.

Predicted dyeing mechanism

Treatment with mordant salts of the natural fabrics, facilitates the bonding of dye, changes the color tone and increases the fastness. As a result permanent colors are obtained. If we discuss the dyeing mechanism, Al^{3+} and Fe^{2+} ions have six coordination numbers, and they are able to make complexes in the octahedral configuration. The proposed mechanism for dyeing of wool and juglone are given in Figure 2 (27). The unoccupied regions of the metal ions can be filled with H_2O molecules, oxochrome groups of the dyestuff or free amino and carboxyl groups of wool fabric.

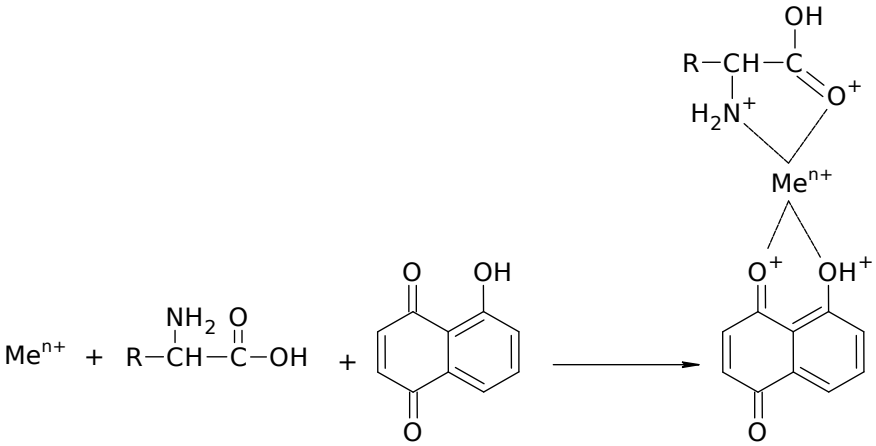

Figure 2: Proposed mechanism of dyeing of wool fabric with 5-hydroxy-1,4-naphthalene dione.

Cotton has a cellulosic structure, here, coordinated covalent bonding occurs between $-CH_2O-$ groups of cellulose and metal cation (Me^{n+}: Fe^{2+}, Cu^{2+}, Al^{3+}). The suggested mechanism for dyeing of cotton is given in Figure 3.

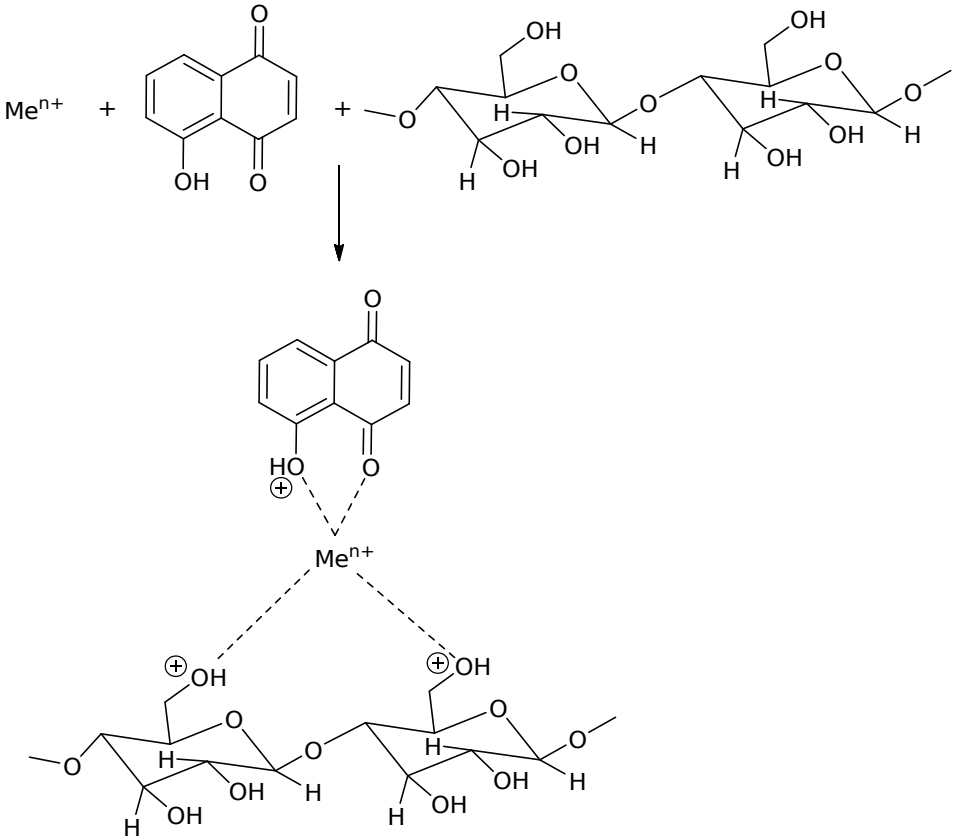

Figure 3: Proposed mechanism of dyeing of cotton fabric with 5-hydroxy-1,4-naphthalene dione.

CONCLUSIONS

In this study, the *Juglans regia* L. leaves were used for dyeing of cotton and wool fabrics. Natural dye solution was extracted and applied to the selected fabrics by pre- mordanting, meta-mordanting, and post- mordanting techniques using the following metal salts, copper sulfate, ferrous sulfate, and alum. We obtained brown, yellow, green, khaki color tones, and they have high fastness colors.

The color tones were observed to change when the dyeing techniques and mordant were changed. Darker colors were obtained for all three mordants in the meta-mordanting method. However, lighter color tones were obtained for all three mordants in the post- mordanting. Yellow and khaki tones were obtained in the dyeing of cotton fabric; while green and brown tones were obtained in dyeing of woolen fabric. The dyeing efficiency in terms of mordant can be ordered as Ferrous sulfate > Copper sulfate > Alum > unmordant.

Consequently, data obtained in the present study showed that *Juglans regia* L. leaves can be used as a natural dyestuff source in dyeing of cotton and woolen fabrics with suitable mordants.

ACKNOWLEDGEMENTS

The authors would like to thank research assistant Caglar Berkel (Tokat Gaziosmanpasa University, Department of Molecular Biology and Genetics) for his contributions.

REFERENCES

1. Eser F, Aktas E, Onal A. Dyeing quality of walnut shells on polyester and polyester viscose blended fabrics. Indian Journal of Fibre & Textile Research. 2016;41:188–94.

2. Ali S, Nisar N, Hussain T. Dyeing properties of natural dyes extracted from eucalyptus. Journal of the Textile Institute. 2007;98:559-62. DOI: 10.1080/00405000701556079

3. Khan MA, Ul-Islamb S, Mohammad F. Extraction of natural dye from walnut bark and its dyeing properties on wool yarn. Journal of Natural Fibers. 2016;4:458–69. DOI: 10.1080/15440478. 2015.1055033

4. Geelani SM, Ara S, Mir NA, Bhat SJA, Mishra PK, Hameed OM, Qazi G. Natural dyeing of fabrics using *Quercus robur* L. (fruit cups) dye and *Punica*

granatum L. (peel) mordant The Journal of Phytopharmacology, 2013;2(6):52-8.

5. Mongkholrattanasit R, Krystufek J, Wiener J, Vikova M. UV protection properties of silk fabric dyed with eucalyptus leaf extract. The Journal of The Textile Institute. 2011;102:272–9. DOI: 10.1080/00405001003722369

6. Mirjalili M, Karimi L. Extraction and Characterization of natural dye from green walnut shells and its use in dyeing polyamide: focus on antibacterial properties. Journal of Chemistry. 2013;1–9. DOI: 10.1155/2013/375352

7. Ali A, Nishkam A. Extraction of dye from walnut shell and dyeing of natural fibre. IOSR Journal of Polymer and Textile Engineering. 2016;3:7–9. DOI: 10.9790/019X-03010709

8. Bechtold T, Mussak R, Mahmud-Ali A, Ganglberger E, Geissler S. Extraction of natural dyes for textile dyeing from coloured plant wastes released from the food and beverage industry. Journal of the Science of Food and Agriculture. 2006;86:233–42. DOI: 10.1002/jsfa.2360

9. Verma N, Gupta NP, Parthsarthy S. Eco-friendly dyeing of wool. Indian Textile Journal, 1998;108:82-83.

10. Gupta DP, Gulrajani ML. Studies on dyeing with natural dye Juglone (5-hydroxy-1,4-naphtalenedione). Indian Journal of Fibre & Textile Research. 1993;18:202-6.

11. Gungor M, Cesme M, Golcu A. Isolation of colour component from italic *juglans regia* L.: chromatographic determination, spectrophotometric investigation and dyeing properties. Research Journal of Textile and Apparel. 2012;16:1-9.

12. Mirjalili M, Nazarpoor K, Karimi L. EcoFriendly dyeing of wool using natural dye from weld as co-partner with synthetic dye. Journal of Cleaner Production. 2011;19:1045–51. DOI: 10.1016/j.jclepro.2011.02.001

13. Gürdere MB, Aydın A, Yencilek B, Ertürk F, Özbek O, Erkan S, Budak Y, Ceylan M. Synthesis, antiproliferative and cytotoxic activities, DNA binding features and molecular docking study of novel enamine derivatives. Chemistry & Biodiversity. 2020;17:e2000139. DOI: 10.1002/cbdv.202000139

14. Ozbek O, Budak Y, Berkel C, Ozyigit C, Yanar Y. The use of *Marrubium vulgare* L. plant extracts in the control of fungal plant pathogens. International Journal of Agriculture, Environment and Food Sciences. 2020;4(4):476-82. DOI: 10.31015/jaefs.2020.4.11

15. Özbek O, Budak Y, Özyiğit C., Yanar Y. Evaluation of antifungal activities of *Grindelia robusta* Nutt., *Tanacetum praeteritum* subsp. *praeteritum* and *Alchemilla vulgaris* L. extracts against plant pathogenic fungi. Turkish Journal of Science and Health. 2021;2(1):57-63.

16. Bukhari MN, Shahid-ul-Islam, Shabbir M, Rather LJ, Shahid M, Singh U, Khan MA, Mohammad F. Dyeing studies and fastness properties of brown naphtoquinone colorant extracted from Juglans regia L on natural protein fiber using different metal salt mordants. Textiles and Clothing Sustainability. 2017;3:1–9. DOI: 10.1186/s40689-016-0025-2

17. Terzi I, Kocaçalışkan I. Alleviation of juglone stress by plant growth regulators in germination of cress seeds. Scientific Research and Essay. 2009;4(5):436-439.

18. Park JH, Gatewood BM, Ramaswamy GT. Naturally occurring quinones and flavonoid dyes for wool: Insect feeding deterrent. Journal of Applied Polymer Science. 2005;98:322-8. DOI: 10.1002/app.22039

19. Mouhajir F, Pedersen JA, Rejdali M, Towers GHN. Phenolics in Moroccan medicinal plant species as studied by electron spin resonance spectroscopy. Pharmaceutical Biology. 2008;39:391–8. DOI: 10.1076/phbi.39.5.391.5893

20. Jaiswal BS, Tailang M. Juglans regia: a review of its traditional uses phytochemistry and pharmacology. Indo American Journal of Pharmaceutical Research. 2017;9:390-8. DOI: 10.5281/zenodo.1036380

21. Test methods for the colour fastness of leather & dyes (TFL Leather Technology Ltd. Germany), 2004, 2.

22. Önal A, Özbek O, Nached S. The production of antiviral–breathing mask against SARS-CoV-2 using some herbal essential oils. Journal of the Turkish Chemical Society Section A: Chemistry. 2020;7(3):821–6. DOI: 10.18596/jotcsa.788410

23. Önal A, Eser F, Akıncı I. Extraction of dyestuff from basil (*ocimum basilium*) and investigation of dyeing properties of cotton and wool fabrics using (urea+ammonia+calcium oxalate) mixture. Journal of New Result in Science. 2013;2:19–25.

24. Önal A. Extraction of dyestuff from onion (*Allium cepa* L.) and its application in the dyeing of wool, feathered-leather and cotton. Turkish Journal of Chemistry. 1996;20:194–203.

25. Džimbeg-Malčić V, Barbarić-Mikočević Z, Itrić K. Kubelka-munk theory in describing optical properties of paper (I). Technical Gazette. 2011;18:117–24.

26. Leon K, Mery D, Pedreschi F, Leon J. Color measurement in *L** *a** *b** units from RGB digital images. Food Research International. 2006;39(10):1084–91. DOI: 10.1016/j.foodres. 2006.03.006

27. Önal A. Extraction of dyestuff from madder plant (*Rubia Tinctorum* L.) and dyeing of wool, feathered-leather and cotton. Turkish Journal of Chemistry. 1996;20:204–13.

JOURNAL OF THE TURKISH CHEMICAL SOCIETY SECTION: A CHEMISTRY

TURKISH CHEMICAL SOCIETY

Sodium-Neutralized Sulfated Polymers as Polymeric Salt Hydrates for Thermal Energy Storage

Elif Adıgüzel and Cemil Alkan*

Department of Chemistry, Tokat Gaziosmanpaşa University, Tokat 60240, Turkey

Abstract: Salt hydrates are latent storage materials with exterior properties like energy storage density, availability, and cost efficiency. However, many of them have handicaps, not overcome yet, like irreversibility, corrosion, and overcooling. In this work, it is aimed to produce polymer-based salt hydrates for the first time. For this reason, some selected polymers (polyvinyl alcohol (PVA), poly(ethylene-co-acrylic acid) (PEAA) and polystyrene (PS) have been functionalized through chemical processes to impart salt clusters in the matrix consisting of some water together. For sulfonation and sodium neutralization, known procedures at molecular basis have been used, as for the characterization, FTIR was exploited. Thermal energy storage properties like phase change temperature, enthalpies, specific heat values, phase change reversibility, and total enthalpy have been determined using differential scanning calorimetry (DSC) technique. Furthermore, surface characteristics through contact angle measurements are considered as remarkable to monitor the change in the nature (hydrophobicity) of the polymeric system.

Keywords: Energy storage; phase change material; salt hydrate; sodium sulfate.

Submitted: May 14, 2020. **Accepted:** February 28, 2021.

Cite this: Adiguzel E, Alkan C. Sodium-Neutralized Sulfated Polymers as Polymeric Salt Hydrates for Thermal Energy Storage. JOTCSA. 2021;8(2):461–70.

DOI: https://doi.org/10.18596/jotcsa.737622.

***Corresponding author. E-mail:** cemil.alkan@gop.edu.tr. Tel.: +90-3562521616; fax: +90-3562521285.

INTRODUCTION

Thermal energy storage (TES) materials are widely interested due to enormous potential declared in the literature. TES is performed by holding thermal energy for later utilization. It is well known as the most yielding way of energy storage. Also it has become an advanced storage technology for sophisticated applications in thermal comfort and sensory property of textiles, protecting electronics, cooling power systems, residual heat recovery in factories, etc. It is very effective on reducing the mismatch of the sources and needs (1-4).

Thermal energy is stored and retrieved both as sensible and latent heats in physically changing systems. Specific heat capacity of materials is the case point for sensible storage. The temperature change determines charging or discharging in other words uptake or release of energy. Latent heat storage system is based on heat uptake or release during phase changing. The system stores energy isothermally because temperature is constant during phase change. Thermo-chemical energy storage reveals by breaking and reforming of molecular bonds in reversible chemical reaction. Heat of reaction determines the storage and release capacity (5-8).

Phase change materials (PCMs) are distributed mainly into two groups: organics e.g. paraffin or inorganic e.g. ice or salt hydrates like sodium sulfate decahydrate (Glauber salt, $Na_2SO_4.10H_2O$) and calcium chloride hexahydrate ($CaCl_2.6H_2O$). Some of hydrated salts as PCMs have enormously large latent heat storage density (~300 kJ/m^3), low cost, and easy availability. But they are generally problematic due to their well known drawbacks like phase separation (9), sub-cooling (10,11), and corrosion (12,13).

For instance, $Na_2SO_4.10H_2O$, may turn to a mixture of $Na_2SO_4.3H_2O$ particles and Na_2SO_4 aqueous solution during heating/cooling cycles by the time. Melting point of $CaCl_2.6H_2O$, is at around 28 °C, but

it may not crystallize even at ~0 °C if there is no nucleating agent in the system (14).

Energy storage capacities of hydrated salts are generally large. $Na_2SO_4.10H_2O$ is used as a PCM because it has huge storage potential due to its high hydration number leading to considerable crystallization energy (254 J/g) (15), high thermal conductivity and low cost compared to most PCMs like paraffins. Biswas (1977) and Marks (1980) investigated the content of water during crystallization of Glauber's salt (16,17). Their works showed that Glauber's salt could store 1.79 times latent energy of water.

Polymeric salt hydrates declared here is a new definition for TES materials. It means hydrated salts in a polymer backbone to form ionic crystals. The level of functionalization and neutralization in polymeric salt hydrates differs from ionomers in which the level of functionalization is about 10% at most. On the other hand, polymeric salt hydrates differ from ionized polymers. Ionization is another process just bearing ionic points in the backbone and its level is generally around 30% of the total repeating units. Ionic clusters in the ionized polymers do not accommodate hydration water. In this work, it is aimed to reach as high weight percentages of hydration in salt clusters as possible. The weight percentage of the clusters determinate the amount of energy stored and released during heating and cooling respectively. In this study, sulfonation and sodium hydroxide (NaOH) neutralization were chosen to form polymeric salt hydrates for the aim of producing polymers with sodium neutralized sulfated group with hydrated water. When hydrated salt property is imparted to a polymeric backbone the new material will be a shape stabilized polymeric salt hydrate resulting in solution shaping property. In addition, they may have some potential for other possible applications. For example, they could be used as matrix for salt hydrates to produce compatible blends and composites for TES applications.

As polymeric salt hydrates, poly(vinyl alcohol) (PVA), poly(ethylene-co-acrylic acid) (PEAA) and polystyrene (PS) which can be processed in solution or in melt were chosen as polymeric precursor materials. They are sulfated according to the procedures similar to literature (18-21) and neutralized using NaOH solution. Sulfur trioxide complexes with amines such as pyridinium and triethylamine have been used extensively for the synthesis of sulfate esters of alcohols as well as other organic transformations (19). Polymeric sulfated PVA (SPVA) and sodium-neutralized SPVA (Na-SPVA), sulfated PEAA (SPEAA) and sodium-neutralized SPEAA (Na-SPEAA), and sulfated PS (SPS) and sodium-neutralized SPS (Na-SPS) were characterized by Fourier Transform Infrared (FT-IR) spectroscopy by comparison to precursor polymers. The TES property and physical properties of them were tested to reveal applicability. The changes in physical properties can be accepted as the evidence of the synthesis and therefore surface contact angles were determined.

MATERIALS AND METHODS

Materials

Polyvinyl alcohol (Sigma Aldrich, Mw=124,000 g/mol), Poly(ethylene-co-acrylic acid) (Sigma Aldrich, acrylic acid 5 wt%), polystyrene (Sigma Aldrich, Mw=192,000 g/mol), Sulfur trioxide (Aldrich), triethylamine (Merck), PVA (Fluka), PEAA (Aldrich), PS (Aldrich), toluene (Carlo Erba), isopropyl alcohol (Carlo Erba), dimethylformamide (DMF, Merck), NaOH (Sigma Aldrich), sulfuric acid (Sigma Aldrich), acetic anhydride (Sigma Aldrich), 1,2-dichloroethane (Merck) were all used as received.

Methods

Synthesis of SPVA and Na-SPVA Polymers

For the sulfonation and neutralization, common procedures as depicted in Figure 1 were used. For sulfonation, 10 g of sulfur trioxide-triethylamine complex was added to a solution of 10 g PVA in 150 mL of anhydrous DMF in a round bottomed flask equipped with a condenser. The mixtures were stirred at 50 °C for 48 h. The SPVA was obtained after evaporation of the solvent under vacuum, washing the polymer with triethylamine (15 mL) and drying under vacuum to constant weight. Neutralization was done by using saturated solution of NaOH. 87.6% of OH groups of the PVA were sulfonated and sodium neutralized according to the calculations.

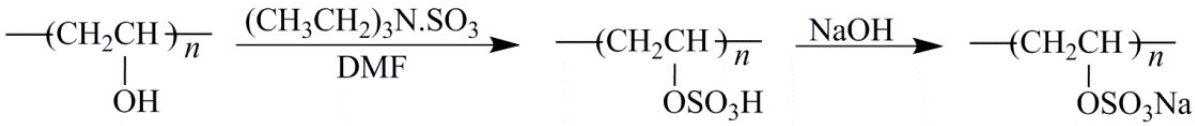

Figure 1. Synthetic scheme of SPVA and Na-SPVA polymer.

Synthesis of the SPEAA and Na-SPEAA Polymers

PEAA was also sulfated using the same procedure with PVA. The only difference is that 10 g of sulfur trioxide-triethylamine complex was added to a solution of 10 g PEAA in 150 mL of solvent (85% toluene-15% isopropyl alcohol) in a round-bottomed flask with a condenser. Rigorous stirring was performed at 50 °C for 48 h. The SPEAA was washed with triethylamine (15 mL) and vacuum-dried. Then, neutralization was conducted in 85% toluene-15% isopropyl alcohol mixture using NaOH solution. The outline of the synthesis was depicted in Figure 2. 84.3% of $-CO_2H$ groups of the PEAA was sulfonated

and sodium- neutralized according to the calculations.

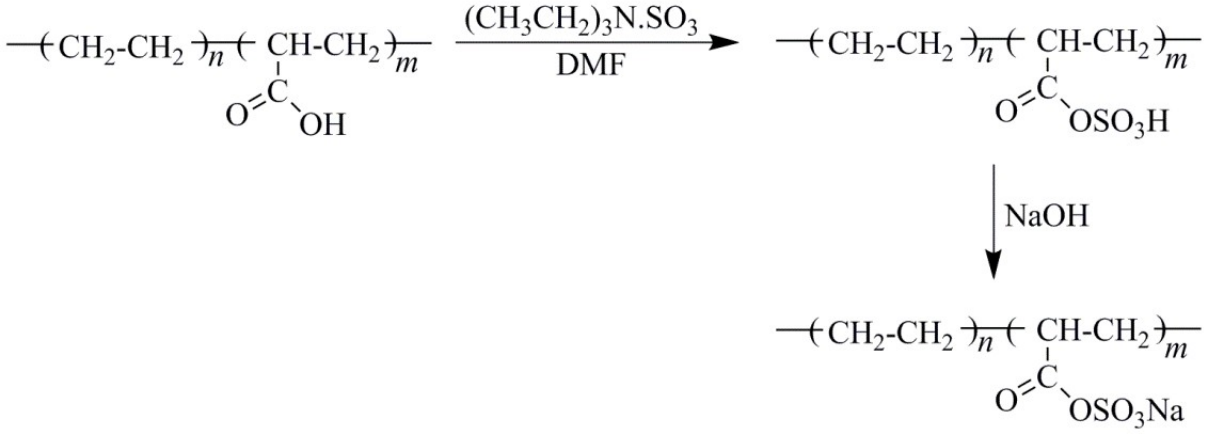

Figure 2. Synthetic scheme of SPEAA and Na-SPEAA polymers.

Synthesis of the SPS and Na-SPS polymers
1.33 mL of H_2SO_4 and 2.358 mL of acetic anhydride were added to solution of 10 g of PS in 125 mL of dichloroethane and this mixture was rigorously stirred for 1 h. And then the mixture was dropwise added to 2 L boiling water. The SPS was obtained after evaporation of the solvent under vacuum. Then the SPS was neutralized with a saturated solution of NaOH. Figure 3 shows the synthetic scheme of SPS and Na-SPS (21). 14.7% of phenyl groups of the PS was sulfonated and sodium-neutralized according to the calculations.

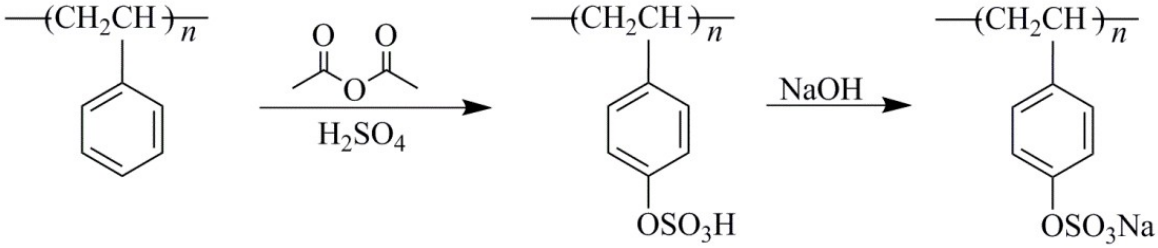

Figure 3. Synthetic scheme of SPS and Na-SPS polymers.

Determination of degree of sulfonation and metal neutralization
The resultant solution from the sulfonation process is stirred for 2 h at 50 °C. Then it is transferred to deionized water. The sulfonated polymers are precipitated, filtered, and dried at room temperature as the solution obtained from filtration is used to determine the degree of sulfonation. Sulfonated polymer samples in a mixture of toluene/methanol (1/9 v/v) solution, with phenolphthalein indicator, are titrated with 0.02 M NaOH solution. NaOH solution is standardized with primary standard potassium hydrogen phthalate according to ASTM E 200–91 (22,23). Due to weak acid and strong base reaction, sulfonated polymers are accepted as fully neutralized.

Characterization
TES systems should have phase-separated salt hydrate crystal domains in the matrix of the polymer since the enthalpy is born as a result of the water uptake or release from the packed crystalline structure. In polymeric salt hydrates ionic crystalline clusters were intentionally distributed in the polymer matrix with water in the cage of the crystalline parts, so that the water would be released from the packed system to the same volume. PVA, PEAA, and PS with hydrophilic, amphiphilic and hydrophobic characters were chosen as precursor molecules, respectively. Hydrophobicity would be effective in the structure of clusters distributed in the matrix. Water was expected to come from the hydrophilic parts to the clusters when needed. To maintain homogeneity, the polymers are formed in solution by mechanical mixing. Thermophysical characteristics of prepared polymeric salt hydrates have been investigated by a differential scanning calorimeter (DSC) instrument (Netzsch-DSC 214 Polyma). Total enthalpy of the materials was calculated according to our previous studies (24,25). Besides DSC is also used for Cp measurement of Na-SPVA, Na-SPEAA and Na-SPS.

RESULTS AND DISCUSSION

FTIR Spectroscopy Analysis of Sulfonation Processes
Figure 4 shows FTIR spectra of PVA and its sulfated derivative (the left picture in the first row), PEAA and its sulfated derivative (the right picture in the first row), and PS and its sulfated derivative (the picture in the second row). Pristine polymers are used for comparison to sulfated derivatives.

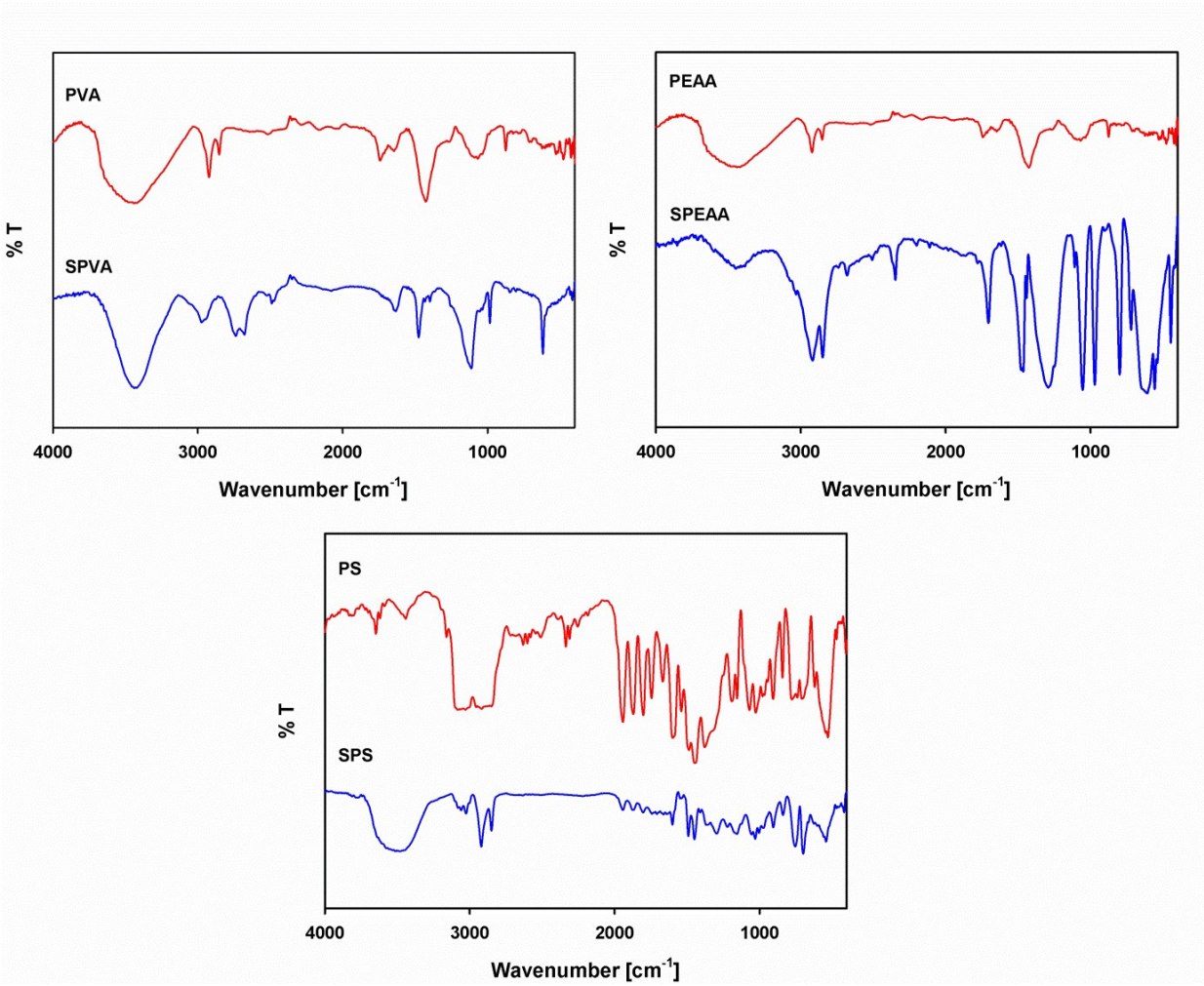

Figure 4. FTIR spectra of the pristine polymers and their sulfated derivatives.

C-H bending peaks of PVA were observed at 1646 and 1742 cm^{-1} as stretching peaks were observed at around 2853 and 2922 cm^{-1} in the spectrum. Besides, hydrogen bonding peaks due to hydroxyl groups interactions were broad and observed between 3048 and 3720 cm^{-1}. Also, C-H bending peaks of SPVA were observed at 1610 and 1697 cm^{-1} as stretching peaks were observed at around 2675 and 2732 cm^{-1}. Moreover, hydrogen bonding peaks placed between 3166 and 3635 cm^{-1}. These shifts were accepted as evidence of the change in the structure. In addition, the peak at around 2976 cm^{-1} was due to C-H stretching peaks as $-OSO_3$ stretching peak at 986 cm^{-1} were only observed in the SPVA.

C-H stretching peaks of PEAA were observed at 2851 and 2917 cm^{-1} as hydrogen bonding peaks were observed at 3087 and 3697 cm^{-1}. In addition, carboxyl stretching peaks were present at 1750 cm^{-1}. Additionally, SPEAA FTIR spectrum showed C-H stretching peaks at 2851 cm^{-1} and 2920 cm^{-1}. On the other hand, hydrogen bonding peaks were observed at 3254 and 3693 cm^{-1} after sulfonation. SPEAA polymer resulted in 954, 1054 and 3036 cm^{-1} stretching peaks for $-OSO_3$ groups.

C-H stretching peaks of aromatic PS arose at 2993-3112 cm^{-1} as aliphatic C-H stretching peaks were observed at 2833 and 2972 cm^{-1} in PS spectrum. SPS spectrum showed some differences in aromatic C-H stretching that were at 3028 cm^{-1} and 3063 cm^{-1} and aliphatic C-H stretching that were 2851 and 2920 cm^{-1}. Besides, SPS showed a broad peak for hydrogen bonding at between 3227 and 3728 cm^{-1}. Furthermore, SPS spectrum showed some extra peaks at 1152, 1186, and 3157 cm^{-1} in shoulder form for $-SO_3H$ groups.

Thermophysical and TES characteristics of sodium neutralized sulfated polymers

Figure 5 represents DSC thermograms of Na-SPVA, Na-SPEAA, and Na-SPS. According to the graphs, reversible phase changes of Na-SPVA and Na-SPS were clear as Na-SPEAA did not show any phase transition. If the phase change temperatures and enthalpies were compared to the best-known sodium sulfonate material, Glauber salt, the temperatures were found as much lower. It can be explained by the extended morphology of sodium-neutralized sulfated clusters. Also, it is interesting that the enthalpy of phase changes for both Na-SPVA and NaSPS were considerable during heating

and cooling (Table 1). Because that the DSC was operated twice for each sample and almost completely same results were found in both run, i.e. reversibility was proven for the sodium neutralized sulfated species. The data from the graphs were tabulated in Table 1. It was another important remark for the results that the overcooling in the polymers was reasonable.

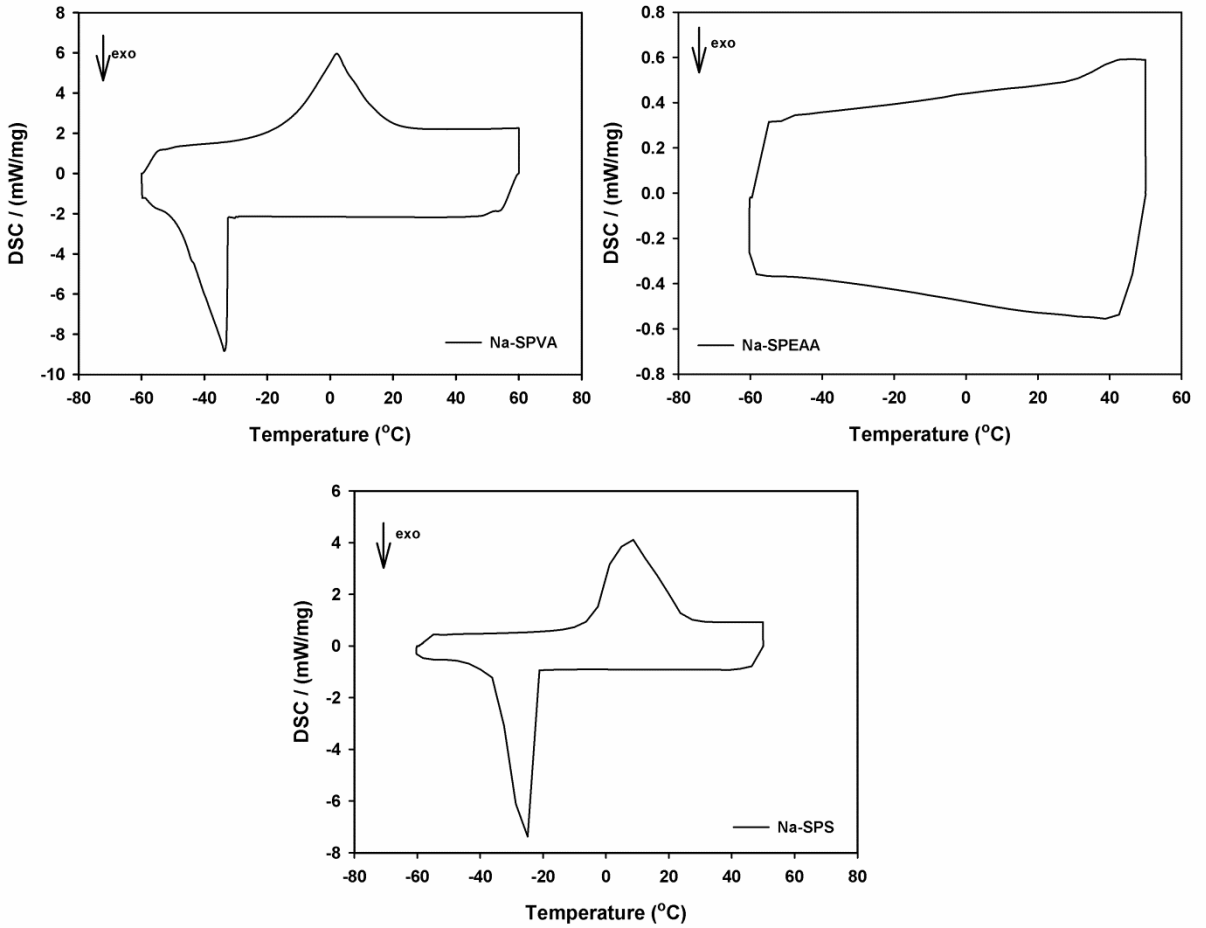

Figure 5. DSC Thermograms of sodium neutralized sulfated polymers.

Table 1. Summary of DSC data for Na-SPVA, Na-SPEAA, and Na-SPS samples phase transitions.

Materials	Periods	Onset Temperature (˚C)	Peak Temperature (˚C)	Enthalpy (J/g)
Na-SPVA	**Heating**	-14.0	2.2	293.7
	Cooling	-33.0	-34.0	241.5
Na-SPS	**Heating**	-1.2	1.7	239.9
	Cooling	-16.0	-17.0	211.6
Na-SPEAA	**Heating**	-	-	-
	Cooling	-	-	-

The reason why sulfonated and sodium-neutralized sulfonated poly(ethylene-co-acrylic acid) copolymer does not show phase transition behavior is that acrylic acid component is present in polymer structure at 5%. This low rate could not form ionic clusters when sulfonated and neutralized with sodium. For this reason, it could not contain water and could not release it at a certain temperature.

Cp versus temperature relationships for Na-SPVA, Na-SPEAA, and Na-SPS were shown in Figure 6. As expected the Cp around the phase change abruptly increased (theoretically infinite).

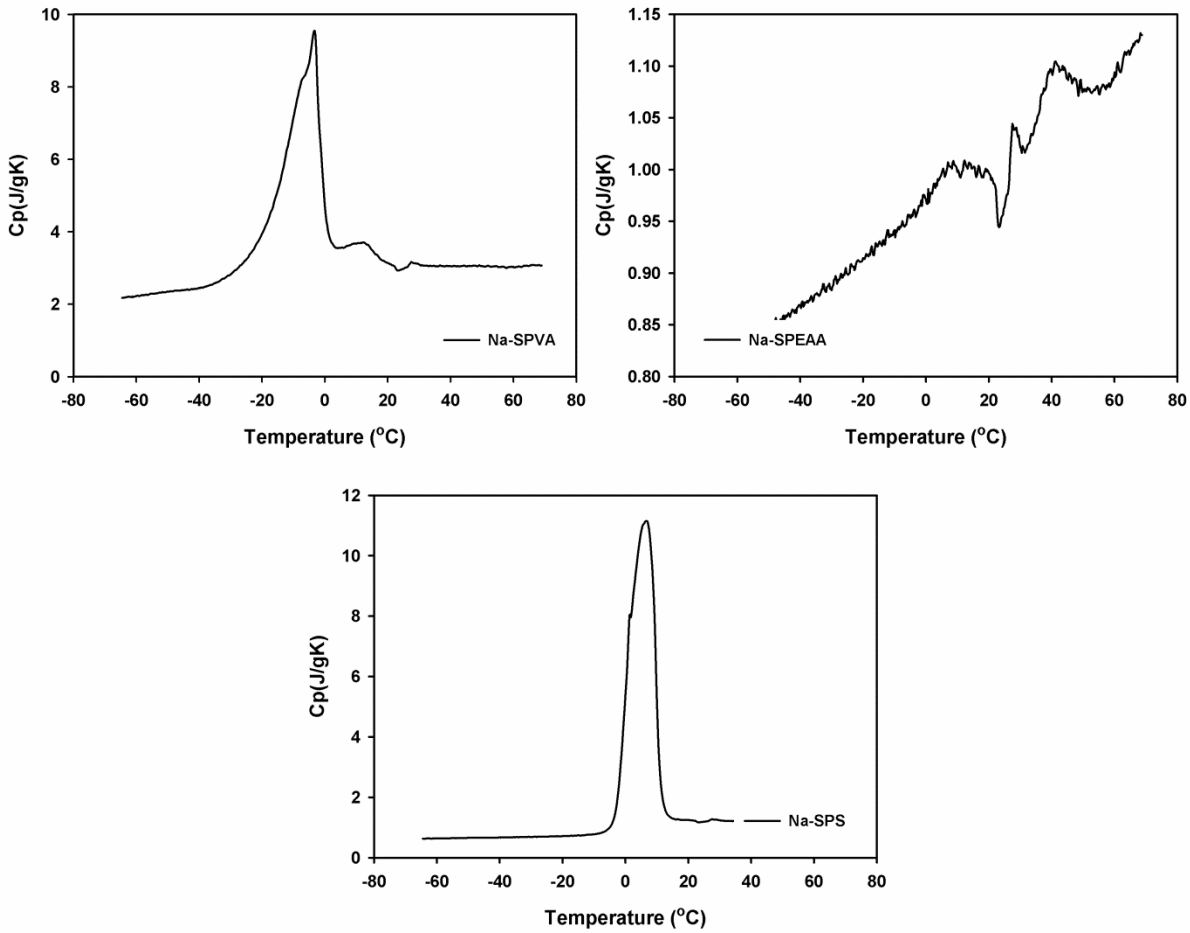

Figure 6. Cp versus temperature relationships for Na-SPVA, Na-SPEAA, and Na-SPS samples

Figure 7 shows total enthalpy curves upon temperature increase for Na-SPS. According to the curves 1278 J/g energy was stored between -60 °C and 60 °C as a total of latent and sensible heat. Most of this energy is latent-based.

Total enthalpy curves have been studied in two runs in order to prove reversibility. Reversibility is one of the main problems of salt hydrate systems. It is well known that active thermal storage systems using salt hydrates showed irreversible working. The curve for both runs resulted in the same formation proving reversibility. Fortunately, the phase transition temperature was very low for Na-SPVA and therefore it probably resulted in the continuous presence of the water in the clusters when released.

The curves for Na-SPEAA showed no phase transitions and total enthalpy stored was due to sensible heat storage capability. According to the graph, Na-SPEAA polymer stored 14 J/g of thermal energy between -60 °C and 40 °C reversibly.

At last, Na-SPS polymer stored and released 537 J/g of energy as sensible and latent heat between -60 °C and 40 °C reversibly. Majority of this heat is due to phase changing. The two runs repeated the curves and proved reversibility.

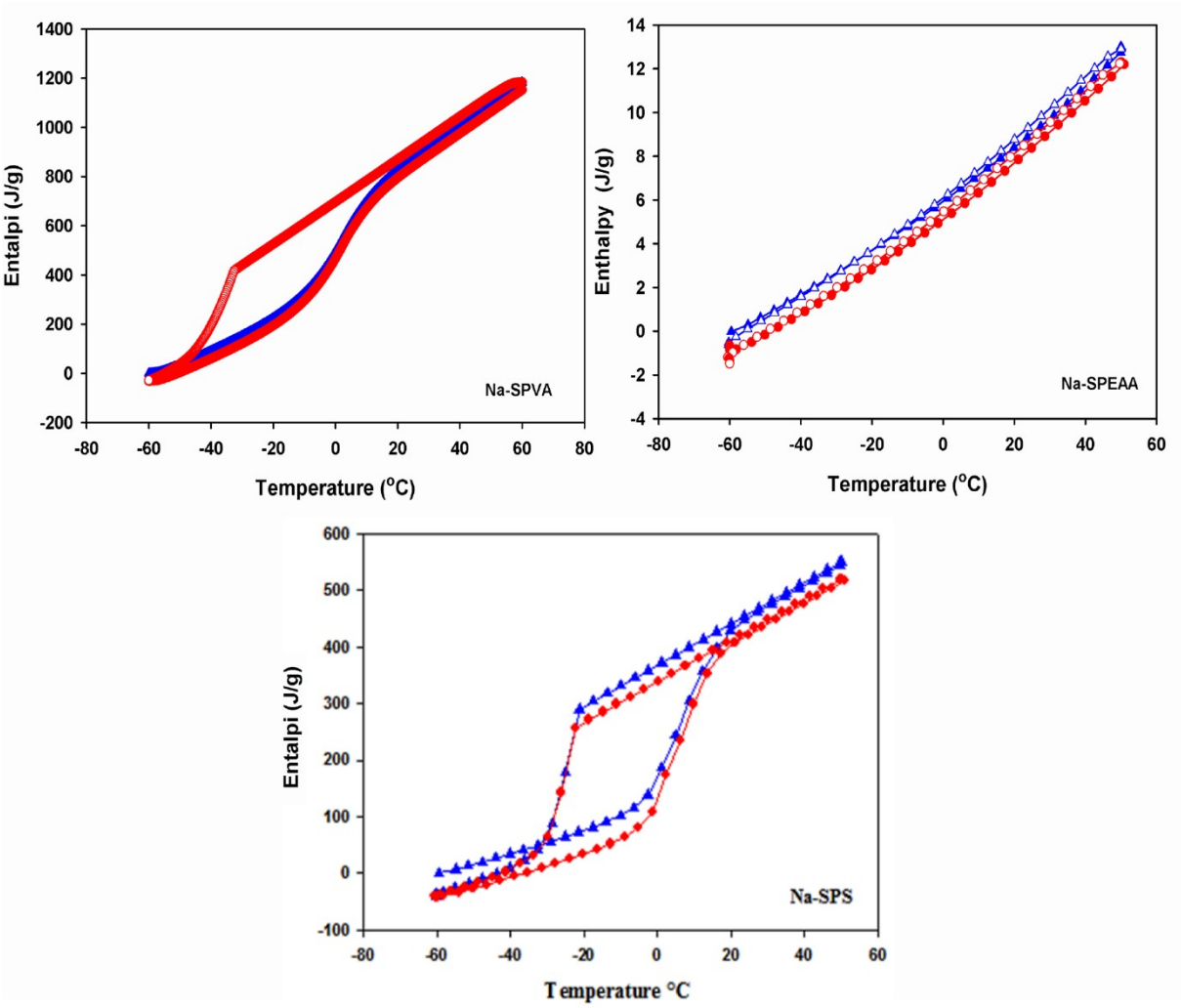

Figure 7. Total enthalpy curves for Na-SPVA, Na-SPEAA, and Na-SPS for 2 runs.

Surface character of the SPVA, SPEAA, and SPS polymers

Chemical changes performed on pure polymers were expected to result in a change in hydrophobicity compared to the pristine polymers used, as sulfated materials are highly hygroscopic. Sulfuric acid itself was one of the best moisture absorbent materials and sulfonation induces modified polymers hydrophilicity. Contact angle measurement is the best way to determine the change in hydrophilic property. Figure 8 shows the photographs of the water droplets on the polymer samples, while Table 2 shows the contact angle values (right side, left side and mean).

According to contact angle measurements it was found that sulfonation had always increased surface wettability. The least effected one was the most hydrophobic one, PS.

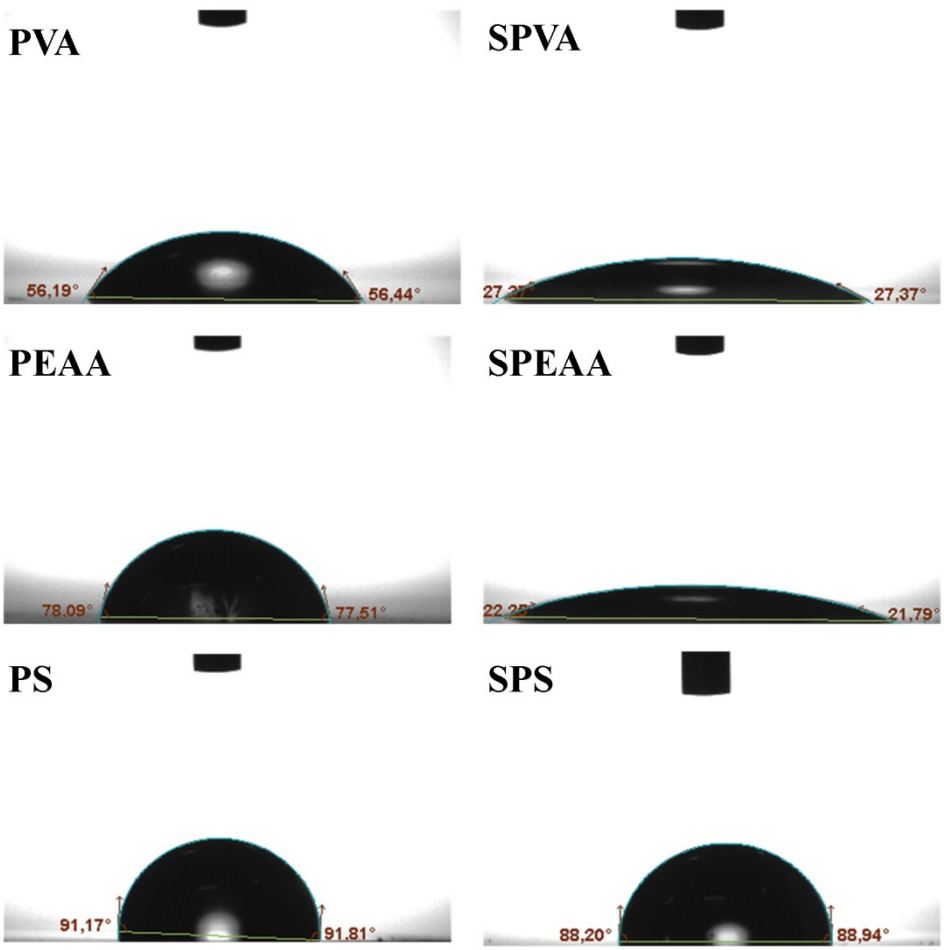

Figure 8. Contact angles of pristine polymers and SPVA, SPEAA, and SPS.

Table 2. Contact angles of the pristine polymers and Na-SPVA, Na-SPEAA, and Na-SPS with water (from both left and right sides)

Material	Contact angle (left)	contact angle (right)	contact angle (mean)
PVA	56.19	56.44	54.32
SPVA	27.27	27.37	27.32
PEAA	78.09	77.51	77.80
SPEAA	22.25	21.79	22.02
PS	91.17	91.81	91.49
SPS	88.20	88.94	88.57

CONCLUSIONS

Some newly defined polymeric salt hydrates have been produced and tested for their thermal energy storage characteristics for the first time. The work was inspired from the polymeric electrolytic batteries. The ionic clusters were operated for water packing and serving as hydrated salt for TES instead of electronic conduction. To start with the sulfonated polymeric salt hydrates at least the phase change ability was achieved. Although they were not as effective as the inspiration sources, they could be developed to reach better performance characteristics in the following studies.

PVA, PEAA, and PS were chosen as polymeric compounds with decreasing hydrophobicity character. However, PVA and PS were converted to sulfated species trapping water in the ionic clusters as PEAA was somehow different and not trapping water in the structure. Therefore, it was to say that PEAA was not a suitable material for TES operations as the other polymeric salt hydrates. The resultant of sulfonation in Na-SPEAA was somehow different compound than a sulfated species and neutralized version was also something else than a sulfonate with water to be used as an energy storage source.

Enthalpies of the Na-SPVA and Na-SPS were very satisfactory although the phase transition temperatures decreased drastically. Actually, the materials with phase change ability were potential candidates for their working temperature in some applications. On the other hand, probably the decrease could be prevented by some further studies and better polymeric salt hydrates can be prepared.

ACKNOWLEDGEMENTS

The author would like to acknowledge the support to INOTES project in the scope of EU ERA NET New Indigo Program funded by Scientific and Technological Research Council of Turkey (TÜBİTAK, Project No: 114M121).

REFERENCES

1. Nazir H, Batool M, Osorioc FJB, Isaza-Ruiz M, Xu X, Vignarooban K, Phelan P, Inamuddin, Kannan AM. Recent developments in phase change materials for energy storage applications: A review. Int J Heat and Mass Trans 2019;129:491-523. https://doi.org/10.1016/j.ijheatmasstransfer.2018.09.126

2. Zhang N, Yuan Y, Cao X, Du Y, Zhang Z, Gui Y. Latent Heat Thermal Energy Storage Systems with Solid–Liquid Phase Change Materials: A Review. Adv Eng Mater 2018;20(6):1-30. https://doi.org/10.1002/adem.201700753

3. Du K, Calautit J, Wang Z, Wu Y, Liu H. A review of the applications of phase change materials in cooling, heating and power generation in different temperature ranges. Appl Energ 2018;220:242-273. https://doi.org/10.1016/j.apenergy.2018.03.005

4. Efimova A, Pinnau S, Mischke M, Breitkopf C, Ruck M, Schmid P. Development of salt hydrate eutectics as latent heat storage for air conditioning and cooling. Thermochim Acta 2014;575:276-278. https://doi.org/10.1016/j.tca.2013.11.011

5. Cunha JP, Eame P. Thermal energy storage for low and medium temperature applications using phase change materials-A review. Appl Energ 2016;177:227-38. https://doi.org/10.1016/j.apenergy.2016.05.097

6. Su W, Darkwa J, Kokogiannakis G. Review of solid–liquid phase change materials and their encapsulation Technologies. Renew Sust Energ Rev 2015;48:373-91. https://doi.org/10.1016/j.rser.2015.04.044

7. Xu B, Li P, Chan C. Application of phase change materials for thermal energy storage in concentrated solar thermal power plants: A review to recent developments. Appl Energ 2015;160:286-307. https://doi.org/10.1016/j.apenergy.2015.09.016

8. Huang J, Wang T, Zhu P, Xiao J. Preparation, characterization, and thermal properties of the microencapsulation of a hydrated salt as phase change energy storage materials. Thermochim Acta 2013;557:1-6. https://doi.org/10.1016/j.tca.2013.01.019

9. Cabeza LF, Svensson G, Hiebler S, Mehling H. Thermal Performance of Sodium Acetate Trihydrate Thickened with Different Materials as Phase Change Energy Storage Material. Appl Therm Eng 2003;23:1697-704. https://doi.org/10.1016/S1359-4311(03)00107-8

10. Zhang Y, Zhou G, Lin K, Zhang Q, Di H. Application of Latent Heat Thermal Energy Storage in Buildings: State-of-the-Art and Outlook. Build Environ 2007;42(6):2197–209. https://doi.org/10.1016/j.buildenv.2006.07.023

11. Gök Ö, Yilmaz MÖ, Paksoy HÖ. Stabilization of Glauber's salt for latent heat storage online.. Proceedings of the 10th International Conference on Thermal Energy Storage, ECOSTOCK. June31 May – 22006. Available from: http://intraweb.stockton.edu/eyos/energy_studies/content/docs/FINAL_PAPERS/4B-4.pdf

12. Cabeza LF, Illa J, Roca J, Badia F, Mehling H, Hiebler S. Immersion corrosion tests on metal-salt hydrate pairs used for latent heat storage in the 32 to 36°C temperature range. Mater Corrosion 2001;52(2):140-6. https://doi.org/10.1002/1521-4176(200102)52:2<140::AID-MACO140>3.0.CO;2-R

13. Cabeza LF, Roca J, Nogués M, Mehling H, Hiebler S. Immersion corrosion tests on metal-salt hydrate pairs used for latent heat storage in the 48 to 58 °C temperature range. Mater Corrosion 2002;53(12):902-7. https://doi.org/10.1002/maco.200290004

14. Riffat S, Mempouo BM, Fang W. Phase change material developments: a review. Int J Ambient Energ 2013;36(3):102-15. https://doi.org/10.1080/01430750.2013.823106

15. Saito A, Okawa S, Shintani T, Iwamoto R. On the heat removal characteristics and the analytical model of a thermal energy storage capsule using gelled Glauber’s salt as the PCM. Int J Heat and Mass Trans 2001;44:4693–701. https://doi.org/10.1016/S0017-9310(01)00113-2

16. Biswas DR. Thermal energy storage using sodium sulfate decahydrate and water. Sol Energ 1977;19:99–100. https://escholarship.org/uc/item/59x1d2xv

17. Marks S. An investigation of the thermal energy storage capacity of Glauber's salt with respect to thermal cycling. Sol Energ 1980;25:255–8. https://doi.org/10.1016/0038-092X(80)90332-1

18. Manikowski A, Koziol A, Czajkowska-Wojciechowska E. An alternative route for fondaparinux sodium synthesis via selective hydrogenations and sulfation of appropriate pentasaccharides Carbohydr Res 2012;361,155-61

19. Nair V, Bernstein S. A convenient procedure for the preparation of triethylamine-sulfurtrioxide Organic Prep Proced Int, 1987;19:6,466-7. DOI: 10.1080/00304948709356213

20. Gilbert EE. The Reactions of Sulfur Trioxide, and Its Adducts, with Organic Compounds. *Chem Rev* 1962;62(6):549-89. DOI: 10.1021/cr60220a003

21. Alkan C, Aras L. Miscibility of polystyrene-based ionomers with poly(2,6-dibromo-1,4phenylene oxide) J Appl Polym Sci 2001;82:3558-67. https://doi.org/10.1002/app.2218

22. Piccioni F, Giorgi I, Passaglia E, Ruggeri G, Aglietto M. Blending of styrene-block-butadiene-block-styrene copolymer with sulfonated vinyl aromatic polymers Polm Int 2001;50:714-21. https://doi.org/10.1002/pi.692

23. ASTM-E200–91, Standard Practice for Preparation, Standardization, and Storage of Standard and Reagent Solutions for Chemical Analysis, 1991.

24. Özkayalar S, Adıgüzel E, Alay Aksoy S, Alkan C. Reversible color-changing and thermal-energy storing nanocapsules of three-component thermochromic dyes, Mater Chem and Phys 2020;252,123162. https://doi.org/10.1016/j.matchemphys.2020.123162

25. Alkan C, Günther E, Hiebler S, Himpel M. Complexing blends of polyacrylic acid-polyethylene glycol and poly(ethylene-co-acrylic acid)-polyethylene glycol as shape stabilized phase change materials. Energ Conver Manage. 2012;64:364-70. https://doi.org/10.1016/j.enconman.2012.06.003

JOTCS A
Journal of the Turkish Chemical Society
Section: A
Chemistry
TURKISH CHEMICAL SOCIETY

Functionalized Sepiolitic Clay Nanofibers as a Natural Ingredient in Medical Cosmetics

Birgül BENLİ[1*] and Ecehan Aygül GÖNÜL[2]

[1]Istanbul Technical University, Nanoscience and Nanoengineering Graduation School& Mining Faculty, Mineral Processing Engineering Department, 34469, Maslak, Turkey

[2]Istanbul Bilgi University, School of Applied Sciences, Department of Fashion Design, 34440, Turkey

Abstract: Medical clay, also known as medicinal clay, was first used in Mesopotamia around 2500 BC and is still a relevant topic today. Among typical medical clays, sepiolite, a fibrous clay in the family of palygorskite is often ignored by cosmetic brands as it is not found abundantly in nature as much as other clays like bentonite. However, much of the world reserves of this clay are in Turkey. In this study, antibacterial sepiolite clay was prepared from nanosilver added dispersed sepiolite samples. These Ag-nanoparticles (Ag-NPs) were formed according to green synthesis under microwave heating using the additives like alginate polymer and ascorbic acid later these fibers were put through serial dilution antibacterial tests using gram +/- bacteria (ATCC 25922 and ATCC 25923) for general quality control and determining minimum inhibitory concentrations. Although the best antibacterial clay samples (Ag-NPs have theoretically 30 mg/L of silver content) were washed at least five times with distilled water, it was observed that their antibacterial stability was still maintained. Finally, the morphology of sepiolite fibers smaller than 40 nm was characterized by AFM images show that highly dispersed single fibers can be used as a natural raw material and have a great opportunity in the development of new products in the cosmetic and medical sector.

Keywords: Antibacterial Clay, Sepiolite, Clay masks, Cosmetics, Medical Clay.

Submitted: December 25, 2020. **Accepted:** February 28, 2021.

Cite this: Benli B, Gönül EA. Functionalized Sepiolitic Clay Nanofibers as a Natural Ingredient in Medical Cosmetics. JOTCSA. 2021;8(2):471–6.

DOI: https://doi.org/10.18596/jotcsa.847163.

***Corresponding author. E-mail:** benli@itu.edu.tr.

INTRODUCTION

Natural clay is a great alternative biodegradable fiber to be used in several innovative applications, its usage almost as old as mankind itself (1). Examples of different cultures in different periods using clays include; Native Americans who have used clays as a natural treatment to purify, protect the skin from the sun taking advantage of their excellent sun protection factor (SPF) properties, and heal the skin against bruises and wounds. Even animals, especially elephants, naturally use mud to keep insects away, protect themselves from excessive sun, to heal and protect their skin. Therefore, it can be said that clay and clay minerals have various usages as seen in Figure 1.

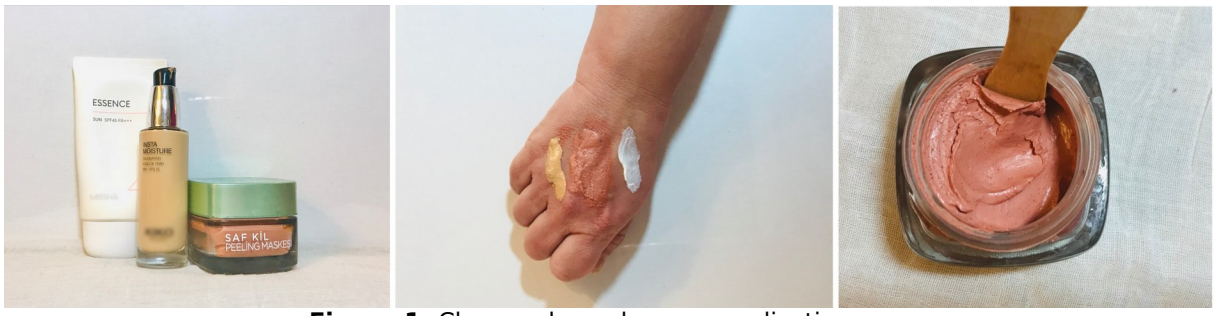

Figure 1. Clay masks and cream applications.

When mentioning medicinal clay often kaolin, bentonite, palygorskite (attapulgite) are considered, these group of clays has various uses as antibacterial agents, drug release matrixes, and high effective adsorbents in skin care and beauty products (2,3). These fibrous clays are also desirable for being cheap as well as being sustainable for the environment. Sepiolite, a medical clay, has a unique natural mineral structure. Sepiolite is especially important since Turkey has the second-largest reservoir in the world as it is abundantly found in Eskişehir. Sepiolite is a hydrated magnesium silicate in a group of structural family of 2:1 phyllosilicates and a theoretical chemical formula of $Mg_8Si_{12}O_{30}(OH)_4(OH_2)_4{\cdot}8H_2O$. Its non-lamellar structural arrangement is similar to those of tubular halloysite (2,3). This tubular structure creates open channels filled with both zeolitic and crystallized water (4,5). Talc-like ribbons being linked to the next by inversion of SiO_4 tetrahedra along a set of Si-O-Si bonds parallel to the fiber axis can be regarded as structural blocks alternating with structural cavities also called tunnels, associated with the internal surface of the silicates that grow up in the fiber direction. These tunnels and open channels occur in the unique structure of sepiolite fibers. The shape of sepiolite clay is either fibrous or can be seen as a fiber bundle under the atomic force microscopy (5), although the length of sepiolite fibers changes from different regions (6,7). Figure 2 presents the inner tunnels and channels on the external surfaces of fibrous clays. The presence of zeolitic channels and the fibrous crystalline structure are the main reasons for fascinating fibrous structure, surface morphology, porosity, high surface area, and surface activity, production of stable dispersions at low concentrations (8,9). These properties help produce unique catalytical, sorptive, and rheological characteristics for nanotechnological applications such as nanocomposites, anti-bacterial nanocoatings, and biosensors.

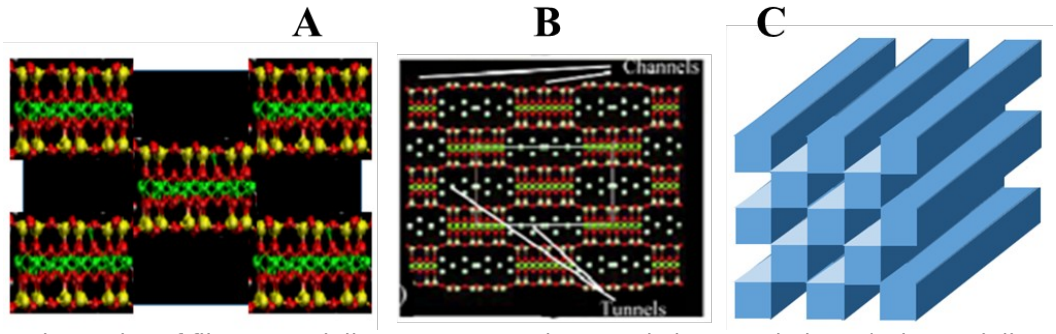

Figure 2. Schematics of fibrous sepiolite structure and textural characteristics: A) The sepiolite crystalline structure; red- oxygen atoms, yellow- silicon atoms, and green- magnesium atoms. B) the simulation result of molecular dynamics for the basal surface of sepiolite containing channels and tunnels; C) ideal the cross-section of sepiolite fiber.

On the other hand, silver has been used for its antibacterial properties from ancient times such as silver vessels that preserve water and keep liquid fresh as well as silver coins. As the grain size decreases to the nanometric scale, silver nanoparticles have different antibacterial properties such as strong toxicity to microorganisms, especially since silver has a larger surface area and higher surface reaction activities than the form of the metal structure (11). Therefore, this study aims to investigate the antibacterial potential of high-quality sepiolite nanofibers from the natural raw clay mineral via in-situ green synthesis of Ag-NPs. Therefore, this study aims to investigate the antibacterial potential of high-quality sepiolite nanofibers from natural raw clay mineral, through the in-situ green synthesis of Ag-NPs on fibers.

MATERIALS AND METHODS

The raw sepiolite samples were kindly obtained from the Tolsa Co., Turktaciri in Turkey. The main constituents were analyzed by ICP (inductively coupled plasma) spectrophotometry (ACME

Analytical Lab., Canada), and quantitatively common metal oxides were determined as 49.85 wt. of SiO_2, 2.38 wt. of Al_2O_3, 0.87 wt. of Fe_2O_3, 2.65 wt. of CaO and 20.15 wt. of MgO. X-ray diffraction analyses were performed for mineralogical characterization of the sample (Shimadzu XRD-6000, Shimadzu Corp., Tokyo, Japan). It was mineralogically found that the sample consists of 85±3 % sepiolite, and together with dolomite along with minor minerals such as illite, palygorskite, calcite, smectite, dolomite, quartz, cristobalite, and feldspar. The sample was washed in water and dried at room temperature. Then, several multi-step processes were applied such as high-speed mixing, overnight-sedimentation, and drying steps that were applied several times to be able to prepare nano dispersed clay colloids from fibrous sepiolite clays. The antibacterial properties of the sample were assessed by measuring its effectiveness against gram-negative (*Escherichia coli*, ATCC 25922) and gram-positive (*Staphylococcus aureus*). The microorganisms were obtained from the Culture Collections and Microorganisms Center in the Istanbul-Cerrahpaşa University (Turkey). A growth medium was prepared with a 50:50 mixture of LB broth (Luria-Bertani broth, Merck) and Agar-agar (Merck). Serial dilution tests for antibacterial susceptibility tests were performed according to the method shown in Figure 3 and the lowest antibacterial fiber concentration was determined by observing the fiber amount that inhibits the apparent growth of a microorganism known as the minimum inhibitory concentration (MIC).

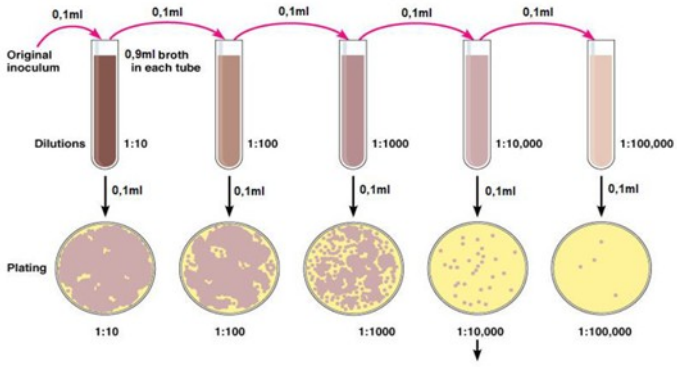

Figure 3. Main steps of the Serial Dilution method to determine minimum inhibitory concentration.

Green synthesis of silver nanoparticles and Ag-Sep antibacterial material

1% (w/v) sodium alginate solution was prepared in long-term mixing at room temperature. 1% (w/v) ascorbic acid solution and 50 mM $AgNO_3$ solution were dissolved in 25 mL. The solutions later were mixed and heated using a microwave for a total of 15 minutes. Lastly, 1% NaOH and 1 N HCl were used to adjust the pH of the solutions when needed. Afterward, the prepared solutions were centrifuged at 15000 rpm for 15 minutes. And then silver nanoparticles containing the suspension was added into 3% of dispersed sepiolite solution and treated in a microwave oven at 200 °C for 5 min. This sample was called as Ag-Sep.

Atomic Force Microscopy (AFM) Studies

AFM images of the particles were conducted using Park Systems, XE-70E in contact mode with 0.5 Hz scanning speed. During contact mode measurements, NSC36/Cr–Au type of cantilevers was selected. Before measurements, all samples were specifically prepared similarly to our previous study (12). Briefly, one drop of 1% of sepiolite dispersion contains Ag-NPs (theoretically 50 mg/L silver content) were dropped on the cleavage of fresh mica substrate. In the moisture-controlled medium ambient conditions (22±2 °C) AFM measurements were taken. Using UV Cleaner (Bioforce Nanosciences) each cantilever was exposed to UV/O_3 for 15 min and high purity nitrogen gases before each experiment to decontamination for any possible organic reactive on each cantilever. All AFM images were processed by Park Systems, XEI Image Processor.

RESULTS AND DISCUSSION

Silver nanoparticles were successfully enabled with sepiolite fibers to gain antibacterial properties. Bacterial strength notably increased up to 20 mg/L in silver content for both gram-negative *E.coli* and gram-positive *S.aureus.* And then, their efficiency to gram +/- bacteria was seen after the content reached 25 mg/L Ag^+ to the theoretical silver concentration. The results are shown in Figure 3. On the other hand, it was clear that the pure raw sepiolite fibers have not any inhibitory effect on the antibacterial properties against neither *S. Aureus* nor *E. coli.*

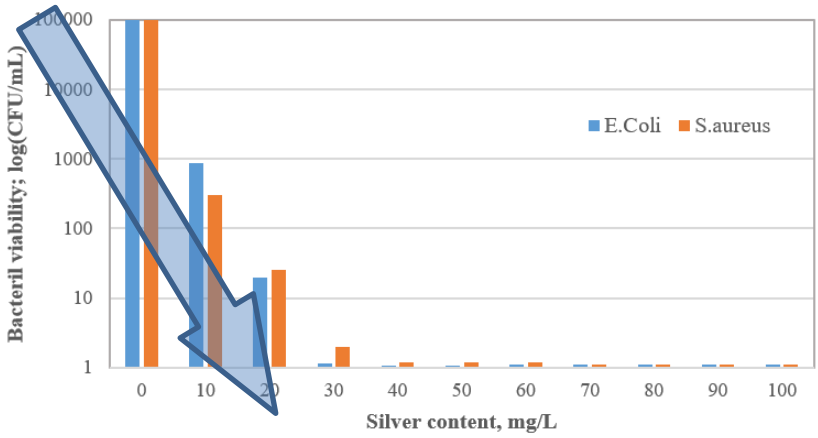

Figure 3. Bacterial viability of gram +/- bacteria against silver nanoparticle added sepiolite fibers.

Figure 4 shows the sepiolite was homogeneously dispersed in Ag-NPs contained aqueous solution. We can say that even after two months, it is still suspended in the water. However, it is seen that the dispersion of the other untreated sepiolite has already settled.

The success of the procedure was examined with AFM images. Also, the size and shape of the fibrous type of sepiolite were determined by Atomic Force Microscopy (AFM) in Contact Mode. This image proves the size and shape of the fibers as a morphological approach using at least 30-line profile analysis. The fibers were dispersed together into two categories: mostly separated fibers and little bundles. These dispersed ones are the size of 200±11 nm in diameter and 1±0.4 µ of length. In this image, excess clay particles and silver nanoparticles were also seen on the cleavage mica substrate. On the other hand, small bundles below 200 nm diameters in sizes were measured such as 143±6 nm in diameter (Figure 5).

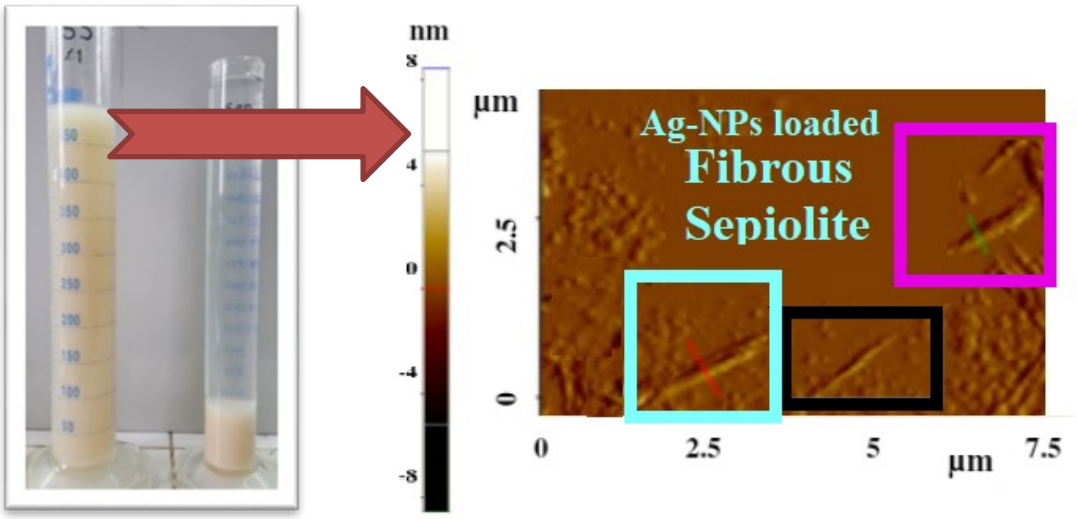

Figure 4. Sepiolite dispersion and AFM image of silver nanoparticles loaded sepiolite fibers on fresh mica cleavage.

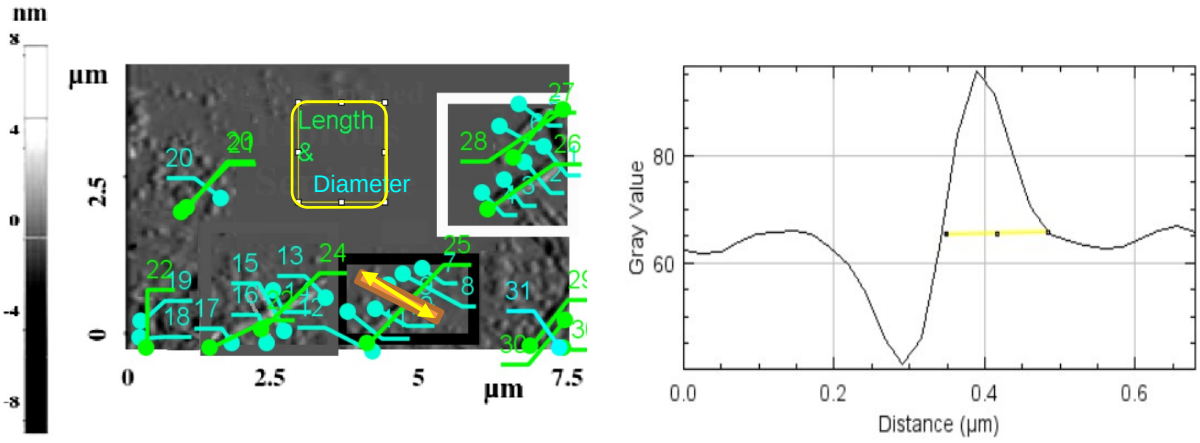

Figure 5. AFM topographic image (left) as sepiolite fibers, line profile (right) indicating a fiber diameter of 143 nm.

Mechanism of interaction between bacteria and sepiolite

Bacterial cell walls are negatively charged under physiologic conditions. This is due to the functional groups on the surface of the bacteria. These functional groups like carboxylates in lipoproteins cause a net negative charge. In the case of the outer membrane of *E. coli*, a gram-negative bacterium covering a thin layer of peptidoglycan, that provides a hydrophilic surface. Similarly, Gram + bacteria have a peptidoglycan layer that is much thicker and attracts more positive ions. Gram + bacteria are more vulnerable to the attack of antibacterial silver agents and damage more like Figure 6.

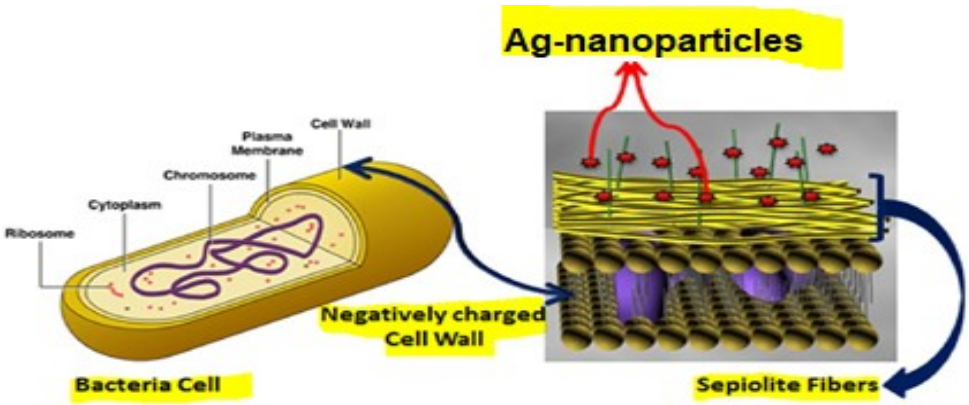

Figure 6. The mechanism of the interaction between bacteria and antibacterial clay-based structure.

One of the mechanisms is the silver adsorption from AgNPs added sepiolite fibers on the cell membrane. Here, the main ionic interaction is the mobility of silver ions (Ag^+) from the solution to the cell membrane. The released silver ions might have damaged the cell membrane after the biosorption of silver causes mostly by protein coagulation. Also, other biological processes are possible like cell wall pits, respiratory chain inactivation, reduction of membrane permeability, and biosorption process. On the other hand, penetration to the bacteria could be taken into account for small-sized AgNPs. Therefore, the induced permeability of the cell membrane is mainly dominant.

CONCLUSION

Antibacterial sepiolite fibers separated from their impurities and loaded with silver nanoparticles show excellent antibacterial activity. In this study, high-quality sepiolite nanofibers are deliberated from natural raw Turkish clay by easy and effective mixing and sedimentation process. After green synthesis of silver nanoparticles, 30 mg/L theoretical silver content was enough to obtain antibacterial fibers. The anisotropic surface structure of sepiolite fibers was also investigated by the morphological analysis from AFM images. In conclusion, sepiolite an often overlooked clay has proven to be an adequate ingredient for cosmetics namely skincare to be used as an active ingredient for its

antibacterial and good adsorbent properties which could pair up well in medical cosmetics as effective drug carriers.

ACKNOWLEDGEMENTS

The authors would like to thank the Engineering Research Group of the Scientific and Technological Research Council of Turkey (TUBITAK) for supporting our project: MAG-217M275 entitled *Improvement of Surface Properties of Body-soluble Magnesium Implants by Coating with Biodegradable Alginate Based Sepiolite Composite Thin Films*. This paper was presented at the 4th International Cosmetic Congress as an oral presentation.

REFERENCES

1 Benli, B. Nanotechnology with clay-based nanostructures since ancient ages. Kibited, 2008; 1(3): 143-62.

2 Galan, EP. The identification and nomenclature of sepiolite and palygorskite (a historical perspective). In book: Natural Mineral Nanotubes: Properties and Applications, Pooria Pasbakhsh, G. Jock Churchman (Editors), Apple Academic Press. 2015, Chapter 3: 69-84.

3 Galindo-Lopez, A, Viseras, C. Pharmaceutical and Cosmetic Applications of Clays. Interface Science and Technology, 2004; 1: 267-89.

4 Cavallaro, G, Fakhrullin, R, Pasbakhh, P. Clay nanoparticles: Properties and Applications. 2020, 1st Edition, Elsevier.

5 Benli, B, Du, H, Celik, MS. The anisotropic characteristics of natural fibrous sepiolite as revealed by contact angle, surface free energy, AFM, and molecular dynamics simulation. Colloid. Surface. 2012; A 408: 22–31.

6 García-Romero, E. & Suárez, M. Sepiolite–palygorskite: Textural study and genetic considerations. Appl. Clay Sci. 2013; 86: 129–44.

7 Tian, L., Wang, L., Wang, K. et al. The preparation and properties of porous sepiolite Ceramics. Sci. Rep. 2019; 9: 7337.

8 Benli, B, Yalın, C. The influence of silver and copper ions on the antibacterial activity and local electrical properties of single sepiolite fiber: A conductive atomic force microscopy (C-AFM) study. Applied Clay Science. 2017; 146: 449-56.

9 Ruiz-Hitzky, E. Molecular access to intracrystalline tunnels of sepiolite. J. Mater. Chem., 2001; 11: 86-91.

10 Aranda, P, Darder, M, Wicklein, B, Rytwo, G, Ruiz-Hitzky, E. Clay–Organic Interfaces for Design of Functional Hybrid Materials. (Eds. Delvile, M, Taubert, A) Hybrid Organic-Inorganic Interfaces: Towards Advanced Functional Materials. Wiley-VCH Verlag GmbH & Co., 2017.

11 Ipe, DS, Kumar PT, Sudheesh, LRM, Hamlet, SM. Silver Nanoparticles at Biocompatible Dosage Synergistically Increases Bacterial Susceptibility to Antibiotics. Frontiers in Microbiology. 2020; 11, 1074: 1-11.

12 Benli, B. Effects of humic acid release from sepiolite on the interfacial and rheological properties of alkaline dispersions. Applied Clay Science. 2014; 102: 1-7.

JOTCS A
Journal of the Turkish Chemical Society Section: A Chemistry
TURKISH CHEMICAL SOCIETY

The Effect of the Hydrothermal and Thermal Deactivations on the Adsorptive Properties and Liquid Permeability of a Silica Gel

Hasan Ceylan[1], Abdullah Devrim Pekdemir[2], Müşerref Önal[3*], and Yüksel Sarıkaya[3]

[1]Maltepe University, Faculty of Education, 34857 Maltepe, İstanbul, Turkey
[2]Graduate School of Natural and Applied Sciences, Ankara University, Ankara, Turkey
[3]Department of Chemistry, Faculty of Science, Ankara University, Ankara, Turkey

Abstract: Three samples taken from a silica gel Hypersil were hydrothermally treated, washed, and dried under different conditions. The portions from the obtained samples were heated over a temperature range of 300 and 850 °C for 16 h. Surface area and pore volume of all the treated samples were determined respectively by nitrogen adsorption data at 77 K and mercury porosimetry. The volumetric flow rate and permeability of the isopropyl alcohol on the columns filled with the prepared samples were determined depending both the inlet pressure and packing pressure. The optimum conditions to prepare a column filling material with the heights permeability were discussed.

Keywords: Permeability,pore volume, silica gel, surface area, volumetric flow rate.

Submitted: June 15, 2020. **Accepted:** March 01, 2021.

Cite this: Ceylan H, Pekdemir AD, Önal M, Sarıkaya Y. The Effect of the Hydrothermal and Thermal Deactivations on the Adsorptive Properties and Liquid Permeability of a Silica Gel. JOTCSA. 2021;8(2):477–82.

DOI: https://doi.org/10.18596/jotcsa.753130.

***Corresponding author. E-mail:** onal@science.ankara.edu.tr Tel.: +90 312 21267 20 / 1173, Fax: +90 312 2232395.

INTRODUCTION

Chromatography is a physicochemical analysis method to determine the composition of gaseous and liquid mixtures depending on the difference adsorption/desorption and diffusion rates for their constituents on the compacted porous solids (1-4). The void spaces inside and among the solid particles of internal width less than 2 nm, between 2 and 50 nm, and larger than 50 nm are called micropores, mesopores, and macropores, respectively. Recently, voids of internal width less than 100 nm are named as nanopores (5).

Artificial hydrogels as well as biogenic and volcanic opals are the porous silica polymorphs (6-8). Silica gels have been generally prepared through the selective acid leaching of the silicates such as clay and zeolite minerals (9-11). Also, similar hydrogels have been synthesized by the condensation polymerization of silicic acid (H_4SiO_4). The rate of this reaction changes depending on pH, concentration and temperature (5). Furthermore, they are derived through base-catalyzed hydrolysis of silanes such as tetramethoxysilane $Si(OCH_3)_4$, tetraethoxysilane, $Si(OC_2H_5)_4$, and silicon tetrachloride, $SiCl_4$ (12-16).

Silica hydrogels have been modified hydrothermal, thermal, aging, and washing at different conditions according to the usage areas such as chromatographic material, adsorbent, catalyst support, and desiccant (17-19). So, the aim of the present study is to evaluate the optimum conditions to obtain a material from a silica gel with the maximum permeability.

MATERIAL AND METHODS

The silica gel used was Hypersil (*H*) 5 µm (580x8) supplied by Shandon Company, UK. Each of three modified samples and coded as *H1*, *H2*, and *H3* were prepared from 200 g Hypersil through the different treatments as follows. Isopropyl alcohol employed as eluent was supplied from Merck Chemical Company.

H1: Hypersil suspension in an aqueous solution contains 2.5% NH_3 by mass was heated in an autoclave at 175 °C for 22 h, under 10 bar. The hydrothermally aged wet samples were washed with distilled water, dried with a hot airflow, and then stored in a tightly closed plastic bottle.

H2: The same hydrothermal treatment was conducted with the exception that the time was 18 h. Furthermore, the sample was washed with water and acetone, respectively. Then similarly dried and stored.

H3: The hydrothermal treatment was similar but the time was 18.5h. In addition, the aged samples were washed respectively with water, acetone, and dichloroethane and also dried in a rotary evaporator.

The batches from the *H1*, *H2*, and *H3* were heated in a muffle furnace at 300, 500, 640, 700, 770, and 850 °C for 16 h and then stored to use for further experiments.

The specific surface area of the Hypersil and its hydrothermally treated samples *H1*, *H2*, and *H3* as well as their heat treated samples was determined from the nitrogen adsorption data at -196°C, using Brunauer, Emmett, and Teller (BET) method (5, 20). The specific pore volume for the same samples was estimated using Hg-porosimetry under an applied pressure of 40 bar.

The *H1*, *H2*, *H3* and their heated samples at 640°C for 16h were packed into columns 10 cm long and 0.2 cm radius using the slurry-packing method (21-23). Volumetric flow rate ($\dot{v}$ = dv / dt) of the isopropylalcohol on the packed columns at 14 bar was measured depending on the inlet pressure which is consecutively increased up to 550 bar.

Similar measurements were carried out using the columns packed 69 bar (p_2) with the unheated *H1*, *H2*, and *H3* samples. The inlet pressure (p_1) was increased step by step up to 550 bar. The $\dot{v}_1$ value was measured for each p_1. Each p_1 was affected as packing pressure (p_2=p_1) for the latter measurement. However, the applied inlet pressure was removed after each step, then increased up to a constant value of 69 bar (p_1) and $\dot{v}_2$ value was measured. The corresponding k_1 and k_2 permeabilities were evaluated using the $\dot{v}_1$ and $\dot{v}_2$ values.

RESULTS AND DISCUSSION

Adsorptive properties

The specific surface area of Hypersil was found as *S* (BET-N_2)=251 m^2g^{-1}. The *S* value for the *H1*, *H2*, and *H3* silica gels as well as their heat treated samples was determined using the same method. Their changes depending on the hydrothermal treatments and their heating temperatures are given in Figure 1. The curves indicate that the specific surface area is greatly decreased by the hydrothermal treatments. The *S* value reaches to zero at 850 °C. The *H3* curve is seen more regular than the others.

The specific pore volume of Hypersil was found as *V*=0.93 cm^3g^{-1} using a Hg-porosimeter under the applied pressure of 40 bar. The *V* values for the other samples mentioned above were determined by similar a method. Their changes depending on the hydrothermal treatments and their heating temperatures are given in Figure 2. The *V* values strictly increase by the modification to obtain *H1*, and *H2* samples whereas for *H3* it is not much. The *V* values reached to zero at 850°C. The most regular curve is for *H3* silica gel. Changes in the *S* and *V* values are due to the removing of hydrogen bonded water molecules as well as chemical bonded hydroxyls and silanol groups from the surface of the silica gel particles during the hydrothermal and thermal deactivations.

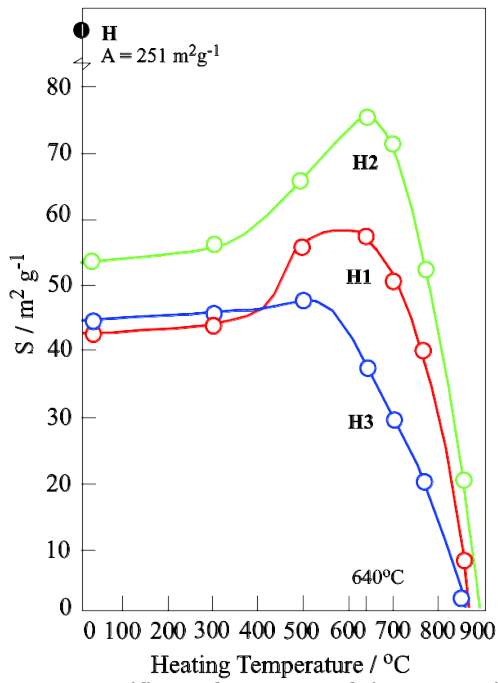

Figure 1. Specific surface area of the Hypersil (*H*), its hydrothermally deactivated samples (*H*1, *H*2, *H*3) and their heated portions.

Volumetric flow rate

Variation of the volumetric flow rate $\dot{v}$ = (dv / dt) of isopropyl alcohol on the columns packed under 14 bar with the *H1*, *H2*, and *H3* samples and their heated portions at 640 °C for 16 h are shown in Figure 3. The irregular curves reveal that the v values decrease after the heating of the hydrothermally deactivated samples. The $\dot{v}$ value for *H3* sample is greater than the others at least 20 fold.

The inlet pressure is also affected as a packing pressure on the columns and causes the shrinkage of the samples. Decrease of the length for the *H1*, *H2*, and *H3* columns was found as 4.5, 4.5 and 1.2 cm during the inlet pressure is increased to the 550 bar. On the contrary, shrinkage of the columns

partly decreases the v̇ depending on the packed materials. This shrinkage is affected at least the v̇ for the *H3* column. So, this sample is more convenient to use as a chromatographic material.

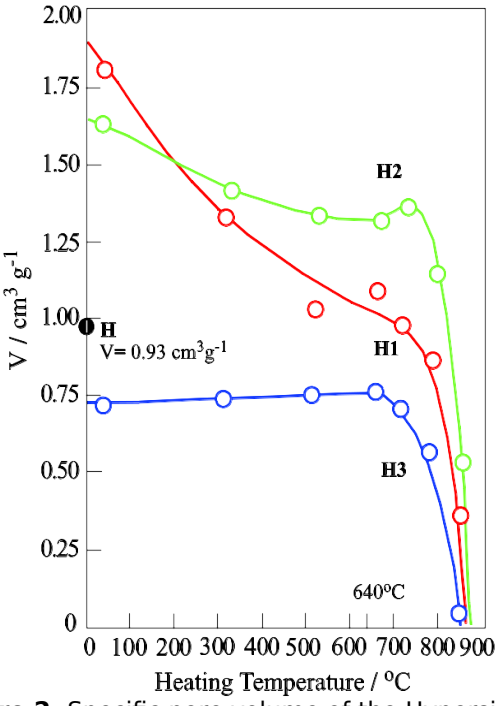

Figure 2. Specific pore volume of the Hypersil (*H*), its hydrothermally deactivated samples (*H*1, *H*2, *H*3) and their heated portions.

The v̇ value is defined with the Darcy equation:

$$\dot{v} = k\frac{A\,p_1}{L\,\mu} \qquad (1)$$

where A and L are the cross section and length of the filling material inside the column, p_1 is the inlet pressure to the liquid, μ is the viscosity of this liquid and k is a proportion coefficient known as permeability. The conditions of

$$\dot{v}/p_1 = kA/\mu = constant \qquad (2)$$

indicates the laminar (viscous) flow according to the fluid mechanics (24). However, the straight lines plotted at the lower values of the inlet pressures show the laminar flows (LF). When the p_1 value is increased the laminar flows disappeared.

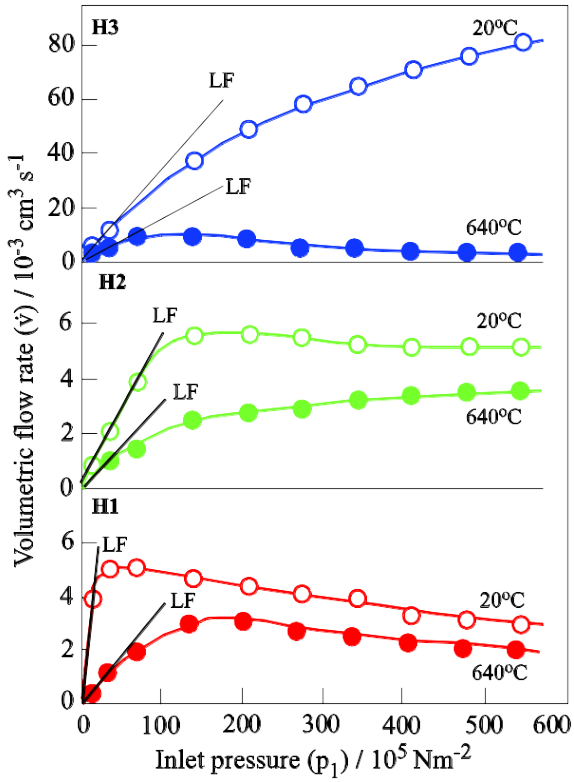

Figure 3. The effect of the inlet pressure on the volumetric flow rate of the isopropyl alcohol on the columns packed at 14 bar using *H*1, *H*2, *H*3 and their heated samples.

Permeability

Isopropyl alcohol permeability of the columns can be evaluated from Darcy equation depending on the p_1 and v̇ using given column parameters and viscosity (μ) of the eluent. Accordingly, a relationship for the permeability was evaluated in the following form:

$$k\left(cm^2\right) = \left(6.847\,x\,10^{-2}\,N\,m^{-2}\,s\right)\frac{\dot{v}\left(cm^3\,s^{-1}\right)}{p_1\,Nm^{-2}} \qquad (3)$$

by taking μ= 2.86 x 10^{-3} $Nm^{-2}s$, r = 0.2 cm (A= πr^2), and L= 10 cm in the Darcy equation. Permeability-pressure curves are derived from the flow rate-pressure curves.

The change in the permeability of the *H1*, *H2*, and *H3* columns packed at 69 bar with the inlet pressure is given in Figure 4. Accordingly, the *H3* column has the heights permeability among the three columns. Also, its change rate with the inlet pressure is lower than the others.

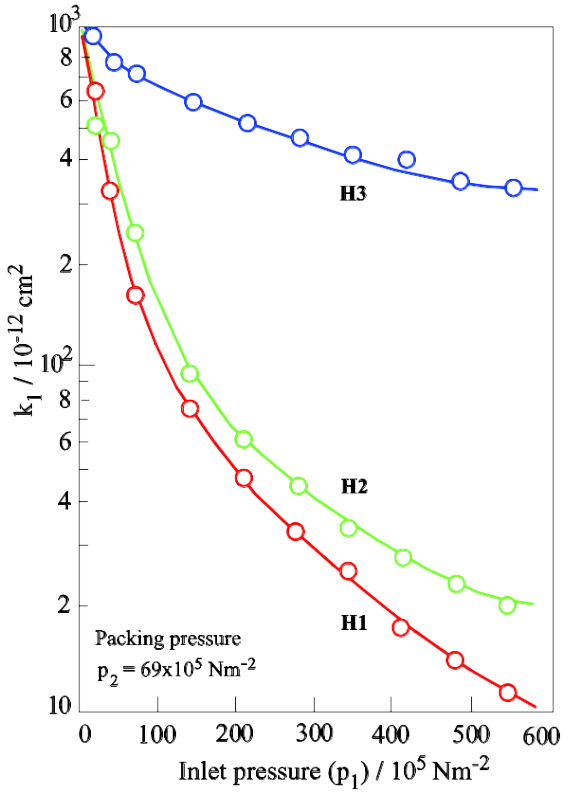

Figure 4. The effect of the inlet pressure on the permeability for the isopropyl alcohol on the *H*1, *H*2, and *H*3 columns packed at 69 bar.

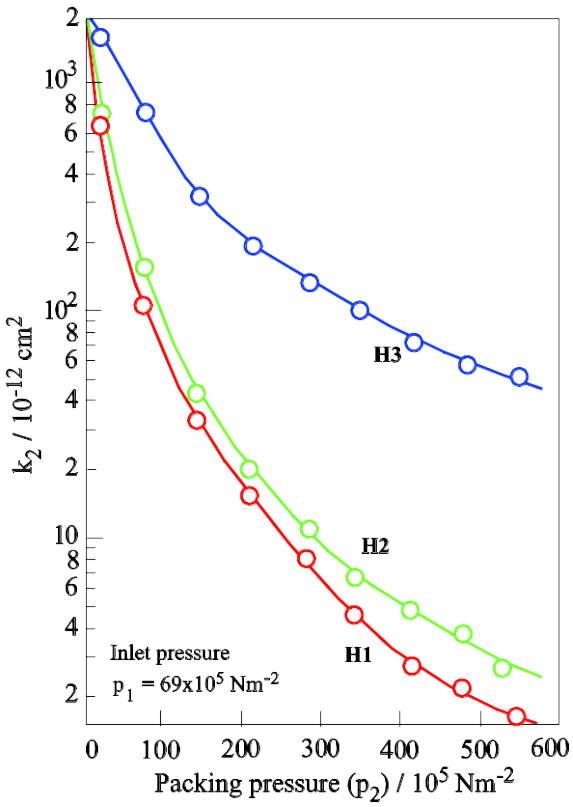

Figure 5. The effect of the packing pressure on the permeability of isopropyl alcohol on the *H*1, *H*2, *H*3 columns at the constant inlet pressure of 69 bar.

The change in the permeability of the same columns with the packing pressure at a constant inlet pressure of 69 bar is shown in Figure 5. A decrease in the permeability with the increasing of the packing pressure at a constant inlet pressure of 69 bar is much more than that inlet pressure. This difference is due to the effect of the inlet pressure during the first measurement as a packing pressure for the second measurement. Accordingly, the change rate of the permeability with the packing pressure increases in the order of *H1*, *H2*, and *H3* samples. This result also shows that the *H3* sample is more convenient packed material for the chromatography columns.

CONCLUSION

Change in the chromatographic properties of the hydrothermally and thermally deactivated porous solid may be generally examined through surface area, pore volume, and particle size determination. These physicochemical properties can be arranged to the desired aspect by change in the deactivation parameters such as temperature, time, washing, material and drying process. The fluid permeability of the treated samples was determined. Fluid permeability on the columns packed with the treated solids was examined with respect to the column packing pressure and inlet pressure for the flow. The sample with the heights permeability is selected as a chromatographic material.

ACKNOWLEDGMENTS

The authors are thankful to the Edinburgh University for experimental support and the Ankara University Research Fund (Project No:16L043013) for financial support to this work.

REFERENCES

1. Scott RPW, Kucera P. Some aspect of the chromatographic properties of thermally modified silica gel. Journal of Chromatographic Science 1975;13:337-43.

2. Du Fresne von Hohenesche C, Ehwald V, Unger KK. Development of standardoperation procedures for the manufacture of n-octadecyl bonded silicas as packing material in certified reference columns for reserved-phase liquid chromatography. Journal of Chromatography A 2004;1025:177-87.

3. Skudas R, Grimes BA, Thommes M, Unger KK. Flow-through pore characteristics of monolithic silicas and their impact on column performance in high-performance liquid chromatography. Journal of Chromatography A 2009;1216:2625-36.

4. Shirasaka H, Shimonosono T, Hirata Y, Sameshima S. Analysis of gas permeability of porous alumina powder compacts. Journal of Asian Ceramic Societies 2013;1:368-73.

5. Rouquerol F, Rouquerol J, Sing KSW, Llewellyn P, Maurin G. Adsorption by powders and porous solids. Elsevier; 2014.

6. Choi J, Fujita H, Ogura M, Sakoda A. Confinement effect on enthalpy of fusion and melting point of organic phase change materials in cylindrical nanoscape of mesoporous silica and carbon. Adsorption 2018;24:345-55.

7. Ding H, Li J, Gao Y, Zhao D, Shi D, Mao G, Liu S, Tan X. Preparation of silica nanoparticles from waste silicon sludge. Powder Technology 2015;284;231-6.

8. Li J, Xu L, Zheng N, Wang H, Lu F, Li S. Biomimetic synthesized bimodal nanoporous silica: Bimodal mesostructure formation and application for ibuprofen delivery. Materials Science and Engineering C 2016;58:1105-11.

9. Temuujin J, Okada K, MacKenzie KJD. Preparation of porous silica from vermiculite by selective leaching. Applied Clay Science 2003;22:187-95.

10. Hu X, Yan X, Zhou M, Komarneni S. One-step synthesis of nanostructured mesoporous ZIF-8/silica composites. Microporous and Mesoporous Materials 2016;219:311-6.

11. Krasucka P, Stefaniak W, Kierys A, Goworek J. One-pot synthesis of two different highly porous silica materials. Microporous and Mesoporous Materials 2016;221:14-22.

12. Lee BI, Quesnel E. Low density silica gels and solvent permeability. Journal of the European Ceramic Society 1998;18:123-9.

13. Klotz M, Ayral A, Guizard C, Cot L. Synthesis and characterization of silica membranes exhibiting an ordered mesoporosity. Control of the porous texture and effect on the membrane permeability. Separation and Purification Technology 2001;25:71-8.

14. Azzouz I, Essoussi A, Fleury J, Haudebourg R., Thiebaut D, Vial J. Feasibility of the preparation of silica monoliths for gas chromatography: Fast separation of light hydrocarbons. Journal of Chromatography A 2015;1383:127-33.

15. Beygi H, Karimi EZ, Farazi R, Ebrahimi F. A statistical approach to synthesis of functionally modified silica nanoparticles. Journal of Alloys and Compounds 2016;654:308-14.

16. Kato N, Kato N. High-yield hydrothermal synthesis of mesoporous silica hollow capsules. Microporous and Mesoporous Materials 2016;219:230-9.

17. Scherer GW. Effect of drying on properties of silica gel. Journal of Non-Crystalline Solids 1997;215:155-68.

18. Gunawan S, Ismadji S, Ju Y-H. Design and operation of a modified silica gel column chromatography. Journal of the Chinese Institute of Chemical Engineers 2008;39;625-33.

19. Mignot M, Sebban M, Tchapla A, Mercier O, Cardinael P, PeulonAgasse V. Thermal pretreatments of superficially porous silica particles for high-performance liquid chromatography: Surface control, structural characterization and chromatographic evaluation. Journal of Chromatography A 2015;1419:45-57.

20. Sarıkaya Y, Ceylan H, Önal M, Pekdemir AD. Thermal deactivation kinetics and thermodynamics of a silica gel using surface area data. Journal of Thermal Analysis and Calorimetry 2021;doi.org/10.1007/s10973-020-10132-z.

21. Cherrak DE, Al-Bokari M, Drumm EC, Guiochon G. Behavior of packing materials in axially compressed chromatographic columns. Journal of Chromatography A 2001;943:15-31.

22. Núñez O, Nakanishi K, Tanaka N, Preparation of monolithic silica columns for high-performance liquid chromatography. Journal of Chromatography A 2008;1191:231-52.

23. Hara T, Makino S, Watanabe Y, Ikegami T, Cabrera K, Smarsly B, Tanaka N. The performance of hybrid monolithic capillary columns prepared by changing feed ratios of tetramethoxysilane and methyltrimethoxysilane. Journal of Chromatography A2010;1217:89-98.

24. Anisah S, KanezashiM, Nagasawa H, Tsuru T. Hydrothermal stability and properties of TiO_2-ZrO_2 (5/5) nanofiltration membranes at high temperatures. Separation and Purification Technology 2019; 212:1001-12.

JOTCS A
Journal of the Turkish Chemical Society
Section: A
Chemistry
TURKISH CHEMICAL SOCIETY

In Vitro Antioxidant Activities of Methanol Extracts of Three *Achillea* Species from Turkey

Zehra Tekin[1], F.Zehra Küçükbay[2], Ahmet Dikme[2]

[1]Adıyaman University, Faculty of Pharmacy, Department of Basic Pharmaceutical Sciences, Adıyaman, Turkey

[2]İnönü University, Faculty of Pharmacy, Department of Basic Pharmaceutical Sciences, Malatya, Turkey

Abstract: In this study, total phenolics and flavonoid compounds of methanolic extract concentrations of three medicinal plant, Asteraceae (Compositae) L. genus that are grown in Turkey and belong to the genus Achillea, were determined with the goal of measuring their antioxidant activities. Antioxidant capacity was measured by widely used iron reducing power, DPPH radical scavenging activity and metal chelating capacity. The antioxidant activities of the achillea extracts used in the study were compared with the standard antioxidants (BHA, BHT and *α*-tocopherol), which were frequently used as antioxidant food additives. According to the free radical scavenging activity antioxidant results, all the extracts exhibited higher DPPH radical scavenging activity than the standards used. The extract from *A.boissieri* showed remarkable 2,2-diphenyl-1-picrylhydrazyl free radical scavenging activity (68.51% at 37.5 µg/mL) comparable with synthetic antioxidants. The ferric reducing antioxidant power was found to be moderate in methanolic extract of Achillea species, whereas the chelating capacity of the extracts were found to be lower as compared to the standards. In addition, total phenolic, flavonoid and flavonol content of all extracts were measured spectrophotometrically and the results were expressed as "gallic acid equivalent" or "quercetin equivalent". The total phenolic content was expressed as equivalents of gallic acid and the results were observed to range from 11.86 to 23.63 mg/g dry extract weight. The total flavonoid concentrations of Achillea extracts were expressed as quercetin equivalent. Flavonoid content ranged from 15.05 to 29.70 mg/g. Total flavonol concentrations of the extracts were determined to be between 5.92 and 7.20 mg/g in terms of quercetin equivalent. This study showed that Achillea L. species, which has been used for treatment in Anatolia for years, can be used as a potential natural antioxidant source.

Keywords: Phenolic content, flavonoid content, antioxidant activity, *Achillea L.* species

Submitted: January 28, 2021. **Accepted:** March 20, 2021.

Cite this: Tekin Z, Küçükbay FZ, Dikme A. In Vitro Antioxidant Activities of Methanol Extracts of Three Achillea Species from Turkey. JOTCSA. 2021;8(2):483–90.

DOI: https://doi.org/10.18596/jotcsa.867455.

***Corresponding author. E-mail:** zehra.kucukbay@inonu.edu.tr.

INTRODUCTION

A free radical can be defined as any chemical species that are capable of existing with one or more unpaired outer shell electrons (1). Their high chemical reactivity due to the presence of an unpaired electron makes them highly unstable (2) and in an attempt to reach stability. The unpaired electron in a free radical can either donate an electron to or receive an electron from other molecules such as proteins, lipids, carbohydrates, and nucleic acids. This process causes damage to cell and tissue or various diseases from cardiovascular diseases to the promotion of cancer (3,4). Antioxidant compounds act by controlling oxidative stress through different reaction mechanisms and may prevent the occurrence of these diseases (5).

A variety of plant materials are potential sources of natural antioxidants. A plant-based antioxidants may support the antioxidative defense (6-8). The

genus *Achillea* L., comprising about 120 species, is mainly spread over the northern hemisphere. The species occur throughout Europe, Asia, China and North Africa, however its center of diversity is located in SE Europe and SW Asia. (9,10) Many *Achillea* L. species are used for the various ailment in Turkish folk medicine due to their high nutritional value and valuable biological activities (11,12).

The fact that Achillea species have a mythological history, the number of endemic species is quite high, their use among the people is widespread, and their pharmacological effects have prompted us to study these species. In our study, it was aimed to elucidate the chemical structures of the aerial parts of *Achillea cretica, Achillea boissieri* and *Achillea nobilis* subsp. *spiylea* collected from different locations of Turkey, which are widely used among the public, and to investigate the antioxidant effects of the species. Radical scavenging of 2,2-diphenyl-1-picryl-hydrazyl (DPPH), metal chelating power and ferric reducing power assays were used to measure the antioxidant capacities of the extracts.

EXPERIMENTAL SECTION

Chemicals

All reagents were purchased from Merck (Darmstadt, Germany), Sigma–Aldrich (Steinheim, Germany), Acros Organics (Thermo Fisher Scientific, Reel, Belgium) and Fisher Scientific (Hampton, NH), while all solvents used were of analytical grade.

Plant materials and extracts preparation

A. boissieri was collected in August 2007 at the flowering period from Elbistan, between Kabaktepe-Sariguzel, 1600 m altitude from Kahramanmaras Province (Turkey). The voucher specimen have been deposited in the Herbarium of Inonu University (INU) in Malatya, Turkey (INU-Collector No: TA 2594).

A. cretica L. (Asteraceae) was collected in June 2004 at the flowering period from Datça-Knidos, Muğla province, Turkey (2100 m above sea level). The voucher specimen has been deposited in the Herbarium of Inönü University (INU) in Malatya, Turkey (INU-Collector No: BY 15634).

A. nobilis subsp. *spiylea* was collected in June 2004 at the flowering period from Spil Mountain, 1100 m altitude from Manisa Province (Turkey). The voucher specimen has been deposited in the Herbarium of Inonu University (INU) in Malatya, Turkey (INU-Collector No: BY 15750).

The aerial parts of the three *Achillea* L. species were dried in shade for 7 days with occasional mixing and cut into small pieces. The dried stock samples were kept in airtight containers at 4 °C for future extraction. After taking 20.000 ± 0.001 g of dried plant samples prepared as described above, it was extracted with methanol using the Soxhlet extraction method until it was completely exhausted. The methanol extracts were concentrated using a rotary evaporator (Heidolph Laborota 4000, Heidolph Instruments, GmbH and Co, Germany) at 40 °C to obtain a viscous liquid. The concentrated extract was transferred to a 25 mL beaker and the remaining solvent was evaporated in the laboratory. The extracts dried after evaporation were weighed to calculate the yield and were stored at +4 ºC in a refrigerator until further analyses. The percentage yield for the extracts was as given in Table 1.

Total phenolic content (TPC)

The content of total phenolics of *Achillea* L. extracts was determined using Folin-Ciocalteu's reagent according to the method of Singleton et al. (13). The absorbance of reaction mixtures was measured at 765 nm (Shimadzu model UV-1601, Japan). The total amount of phenolic substance was calculated from the standard calibration curve prepared using the gallic acid standard, which is a phenolic compound. The results are expressed as mg GAE/g extracts on the gallic acid equivalent by using the regression equation of the curve obtained. Spectrophotometric measurements were repeated three times for each sample, and the total phenolic content was indicated by taking the average of triplicate measurements.

Total flavonoid and flavonols content

The content of total flavonoids of extracts was determined according to the procedure described by Zhishen et al. (1999) (14). Total flavonoid content of the extracts was determined spectrophotometrically according to the aluminum chloride/sodium nitrite method. Total flavonol content was determined by the method described by Yermakov et al. (1987) with minor modifications (15). Briefly, 1 mL of extract was mixed with 1 mL of $AlCl_3$ (%2) and 3 mL of sodium acetate (50 g/L). After 150 min the absorbance of the test solution was measured at 440 nm against blank solution. Total flavonoid/flavonol content of the extracts in certain concentration ranges was calculated according to the quercetin standard curve prepared by working in triplicate, results were expressed as mg of quercetin equivalent per gram dry extract.

Antioxidant Activities of *Achillea* Extracts

Antioxidant assay by DPPH radical scavenging activity

The 1,1-diphenyl-2-picrylhydrazyl (DPPH) scavenging activity of *Achillea* L. extracts was performed according to methodology described by Blois (1958)(16). This method involves the reduction of the DPPH (2,2-diphenyl-1-picrylhydrazyl) radical with compounds that tend to give hydrogen atoms, resulting in the loss of purple color of the solution at the first moment and this ratio is based on spectrophotometric measurement of the absorbance of the solution. BHA, BHT and alpha-tocopherol were used as standards. As a control, ethanol was used. The absorbance was measured at 517 nm and the

absorbance values of the samples were evaluated against the control. Free radical scavenging activity was calculated using the following equation:

$$\% \text{ Inhibition} = (A_B - A_{S/S}) / A_B \times 100$$

A_B is the absorbance of control and $A_{S/S}$ is the absorbance of the analyzed standard/sample.

Ferric-reducing antioxidant power assay

The reducing power, which is one of the antioxidant activity determination methods, was determined based on the method applied by Oyaizu (1986) (17). In this experiment, the yellow color turns pale green and blue, depending on the antioxidant concentration in the samples. The color produced by the reduction of $Fe^{3+} \rightarrow Fe^{2+}$ the change is determined by monitoring at 700 nm. Increased absorbance of the mixture indicates stronger reducing influence of the extract.

Metal chelating activity

Metal chelating activity was determined by measuring the formation of the Fe^{2+}-ferrozine complex according to Carter (1971)(18). The Fe(III)-ferrozine method is based on the principle that Fe(III) forms the complex of ferrozine and Fe(III)-ferrozine, and this complex reacts with antioxidants and is reduced to the magenta-colored Fe(II)-ferrozine complex (absorption maximum at 562 nm) (19). Therefore, the change in color was measured using a spectrophotometer against blank at 562 nm. The percentage inhibition of ferrozine–Fe^{2+} complex formation was calculated as $(A_{control} - A_{sample/standard})/A_{control} \times 100$, where $A_{control}$ is the absorbance of control reaction (without analyzed sample extract), and A_{sample}/ $A_{standard}$ is the absorbance of the analyzed sample/standard. The values are presented as the mean of three measurements.

RESULTS AND DISCUSSION

The medicinal plants are huge natural sources of secondary compounds with health-promoting properties. The polyphenols derived from plants have significant antioxidant effects, which allow them to provide health benefits. Epidemiological evidence and clinical trial data obtained from in vivo and in vitro studies have shown that diets based on herbal products rich in polyphenols can reduce the risk of chronic diseases, especially cancer. Polyphenolic substances, which are named according to the number of rings and structural elements they contain, generally have a phenol ring as in phenolic acid and alcohols. More than 8000 types of polyphenols have so far been identified in nature. The four most important groups of dietary phenolics are flavonoids, phenolic acids, polyphenolic amides and other polyphenols such as curcumin in turmeric, resveratrol in red wine and 5-caffeoylquinic acid in black carrot roots. Flavonoids are the largest group of plant phenols, with more than 6000 types. There are several significant groups of flavonoids, including flavonol, flavanol, isoflavon, flavon, flavanon and anthocyanin (20-22).

Phenolic acid constituents in plant kingdom are mainly divided into hydroxybenzoic acid and hydroxycinnamic acid. These compounds possess much higher in vitro antioxidant activity than well-known antioxidant vitamins, although some of them are also regarded as anticarcinogenic (23,24). Polyphenolic amides include capsaicinoids in chili peppers and avenanthramides in oats (25,26). Both animal studies and laboratory studies have confirmed that phenolic amides have antioxidant activities (27-29). The species included in the genus *Achillea* L., which contain important bioactive components, have been used for therapeutic purposes in many parts of the world for centuries.

This study focused primarily on the determination of antioxidant activity of methanolic extract of Turkish *Achillea cretica, Achillea boissieri* and *Achillea nobilis* subsp. *spiylea* by *in vitro* methods. We measured the phenolic, flavonoid and flavonol contents in the *A.cretica*, *A. boissieri* and *A. nobilis* subsp. *spiyle*a extracts we obtained.

Table 1. Analysis of main antioxidant fractions contained in *A. cretica, A. boissieri* and *A. nobilis subsp. spiylea* extracts.

Samples	Yield (%)	Phenolics (mg GAE/g plant extract)	Flavonoids (mg QUE/g plant extract)	Flavonols (mg QUE/g plant extract)
A. cretica	0.807 ± 0.170	11.86 ± 0.09	15.05 ± 0.17	15.92 ± 0.11
A. boissieri	5.375 ± 0.810	23,63 ± 0.17	29.70 ± 0.03	17.20 ± 0.19
A.nobilis* subsp. *spiylea	7.114 ± 1.200	17.33 ± 0.09	18.20 ± 0.03	16.95 ± 0.04

Each value is the mean ± SD of three independent measurements. Phenolics, gallic acid equivalents; flavonoids and flavonols, quercetin equivalents.

The results (Table 1) showed that the *A. boissieri* extract exhibited higher total phenolics content as compared to the *A. cretica* and *A. nobilis subsp*. *spiylea* extracts which were approximately about 23.63 mg GAE/g for *A. boissieri* extract, 11.86 mg GAE/g for *A. cretica* extract, and 17.33 mg GAE/g for *A. nobilis subsp*. *spiylea* extract. The contents of flavonoids and flavonols were also higher in A. boissieri extract than in *A. cretica* and *A. nobilis* subsp. *spiylea*. This result clearly indicates that *A.*

boissieri extract contains more antioxidants than the *A. cretica* and *A. nobilis subsp*. *spiylea* extract.

Anti-oxidant effects of plant extracts

The DPPH radical scavenging activity results are shown in Figure 1 as comparable with known antioxidants BHT and BHA. From the analysis of Figure 1, we can conclude that the scavenging effects of *A. cretica, A. boissieri* and *A. nobilis subsp*. *spiylea* extracts on DPPH radicals were excellent, especially in the case of A. boissieri. The antioxidative effect of extracts studied is due to the phenolic components. Similar results were obtained earlier for the species of Achillea L. from Turkey (30,31).

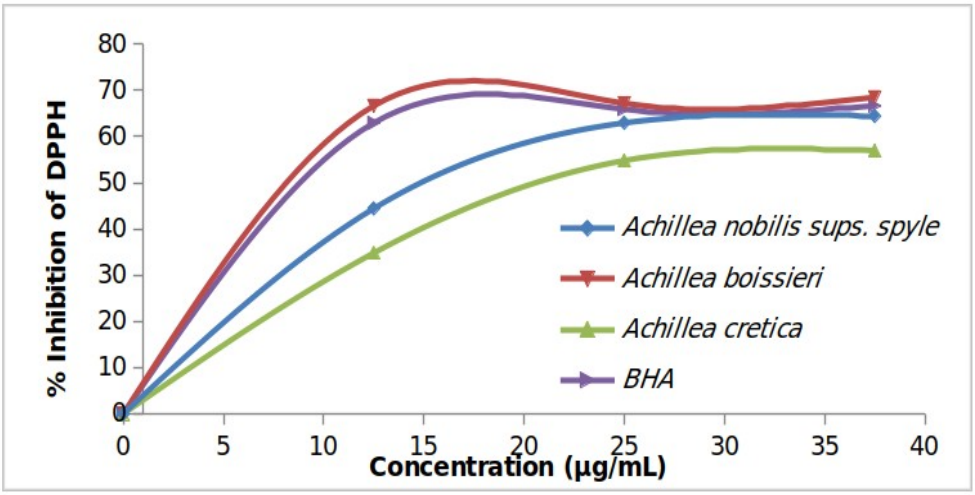

Figure 1 . Dose-dependent scavenging activity of the extracts and the standard BHA, BHT, and alpha-tocopherol on 1,1-diphenyl-2-picrylhydrazyl inhibition.

As described above, the antioxidants such as phenolic acids and flavonoids were present in considerable amount in the extracts of *A. cretica, A. boissieri* and *A. nobilis* subsp. *spiylea*. The prepared methanol extracts of *A. cretica, A. boissieri* and *A. nobilis* subsp. *spiylea* were compared with the standard BHA, BHT and alpha-tocopherol antioxidants. Like the radical scavenging activity, the reducing power of the extracts and standard increase with the increase in amount of the extracts from the selected plants and standard concentrations (Figure 2). At the minimum concentration of extract/standards used in this study (i.e. 5.88 µg/mL), *A. boissieri, A. nobilis* subsp. *spiylea, A. cretica* and butylated hydroxyanisole (BHA) had activity values 0.111 ± 0.001, 0.102 ± 0.001, 0.098 ± 0.001 and 0.630 ± 0.001, respectively whereas at the highest concentration (i.e. 44.11 µg/mL), the activity values of *A. boissieri, A. nobilis* subsp. *spiylea, A. cretica* and butylated hydroxyanisole (BHA) were 0.343 ± 0.001, 0.229 ± 0.001, 0.167 ± 0.002 and 2.108 ± 0.003, respectively.

Metal chelating activities of standard antioxidants and extracts were tested at various concentrations (12.5-125 µg/mL). Calculated % inhibition values are given in Figure 3. The higher the calculated % inhibition value, the higher the metal chelate activity was accepted and the results were evaluated. EDTA-Na_2 was excellent chelator for ferrous ions and its chelating capacity was 94.311% at a concentration of 125 µg/mL. BHA, alpha-tocopherol, *A. cretica* and *A. nobilis* subsp. *spiylea* did not show chelating capacity at all concentrations as well. This proves that these extracts and reference compounds have a lower capacity to chelate them with ferrous ions compared to the standard chelator EDTA. In a previous study with Achillea species, *Achillea aleppica* D.C. subsp. *aleppica*, *Achillea aleppica* D.C. subsp. *zederbaueri* (Hayek) Hub.-Mor and *Achillea biebersteinii* Afan. species that have compared antioxidant activity, antimicrobial activity and total phenolic amounts, it has been reported that *Achillea biebersteinii* Afan. species were richer than other species in terms of total phenolic. Also, Barış et al. (2011) used EDTA solution as the standard chelator in their study with Achillea species. They found that extracts in this system were not a better chelator than EDTA solution, which was a good chelator (32).

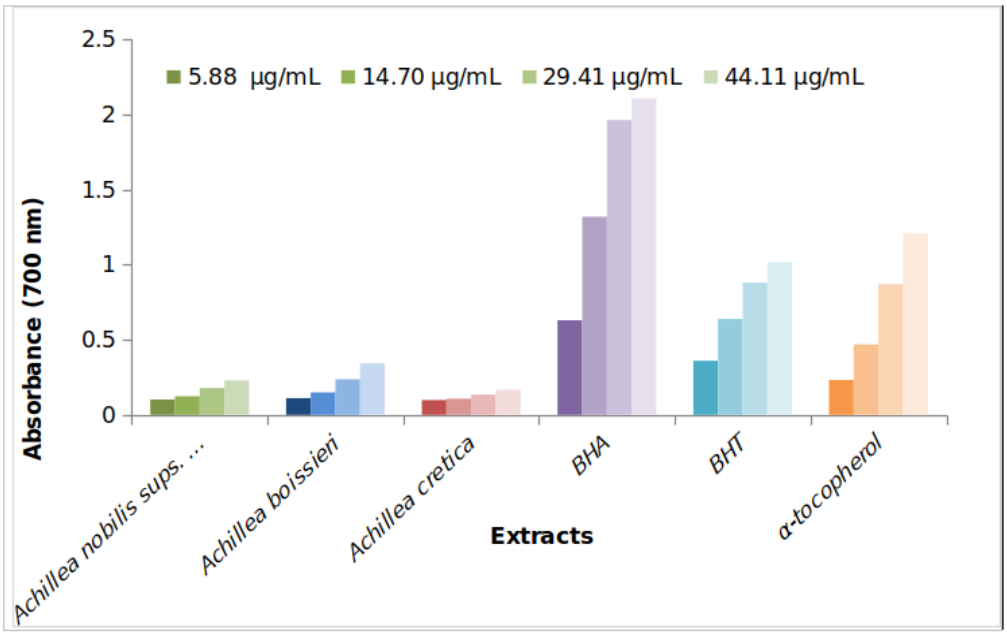

Figure 2. The reducing power of extracts and reference compounds. Values were reported as means ± SD in triplicate.

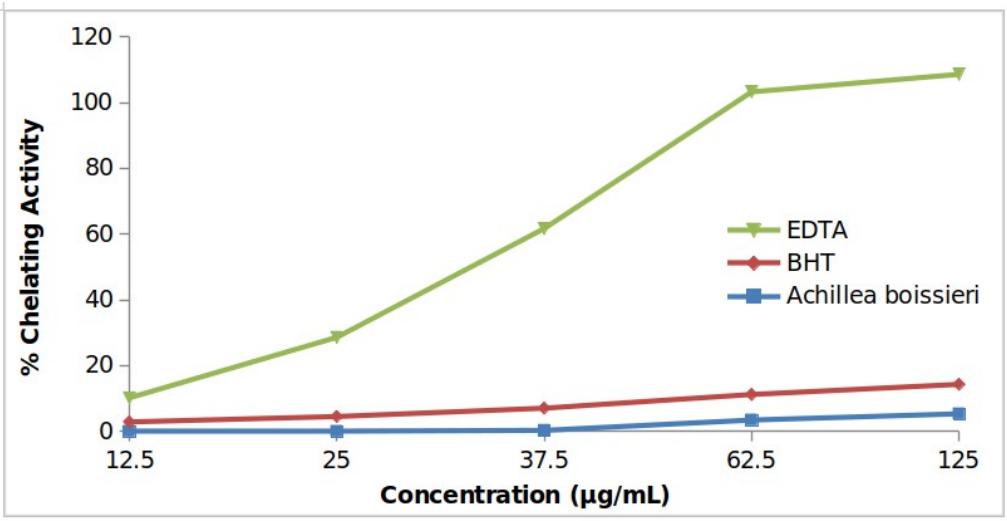

Figure 3. Metal chelating activities of *Achillea* extracts at different concentrations. Data are expressed as means ± SD values (n=3).

CONCLUSIONS

Achillea species have been preferred as folk remedies for various purposes for a long time. Therefore, the species named *A. boissieri, A. nobilis* subsp. *spiylea* and *A. cretica*, which spread in Turkey, were investigated in terms of antioxidant activity and amounts of phenolic/flavonoid/flavonol compound. As a result of the literature studies, no antioxidant properties were evaluated for these 3 species used in our research. Especially, the DPPH radical scavenging activities of *A. boissieri* methanol extract was determined to be higher compared to the standard used BHA and can be used as a herbal antioxidant. It is believed that the results of this study will contribute to increasing studies on the use of natural compounds in many fields, especially in food, pharmacy, medicine and natural therapy. The fact that the biological properties of the studied plant were investigated for the first time with this study increases the original value of the study. As a result, the studies conducted are very original studies in terms of this species, which has not been found before. In the following studies, isolation, purification and clarification of the structure of

active compounds with bioactivity can be carried out.

ACKNOWLEDGEMENTS

We would like to thank Inönü University Scientific Research Projects Commission Chair for their support for the thesis with the project numbered TLO-2020-2029 as undergraduate thesis. Special thanks to Prof.Dr. Turan Arabacı for identification of the Achillea species.

Conflicts of interest
There is no potential or existing conflict of interest between our scientific work and our personal situation.

REFERENCES

1. Cheeseman KH., Slater TF., An introduction to free radicals chemistry, British Medical Bulletin, 1993; 49; 481–93.

2. Martínez-Cayuela M., Oxygen free radicals and human disease, Biochimie, 1995; 77; 147-61.

3. Phaniendra A., Jestadi DB., Periyasamy L., Free Radicals: Properties, Sources, Targets, and Their Implication in Various Diseases, Indian Journal of Clinical Biochemistry, 2015; 30(1); 11–26. http://doi.org/10.1007/s12291-014-0446-0)

4. Rahman K., Studies on free radicals, antioxidants and cofactors, Clinical Interventions in Aging, 2007; 2(2); 219-236.

5. Devasagayam TP., Tilak JC., Boloor KK., Sane KS., Ghaskadbi SS., Lele RD., Free radicals and antioxidants in human health: Current status and future prospects, The Journal of the Association of Physicians of India, 2004; 52; 794-804.

6. Möller P., Loft S., Dietary antioxidants and beneficial effect on oxidatively damaged DNA, Free Radical Biology and Medicine, 2006; 41; 388–415.

7. Krishnaiah D., Sarbatly R., Nithyanandam R., A review of the antioxidant potential of medicinal plant species, Food and Bioproducts Processing, 2011; 89; 217–33.

8. Katarzyna S., Anna B-K., Natalia V., Anna G-C., Sebastian G., Phenolic Composition of the Leaves of Pyrola rotundifolia L. and Their Antioxidant and Cytotoxic Activity, Molecules. 2020; 25(7); 1-16.

9. Si XT., Zhang ML., Shi QW,. Kiyota H., Chemical constituents of the plants in the genus Achillea, Chemistry & Biodiversity, 2006; 3: 1163–1180.

10. Baser KHC., Buchbauer G., Handbook of Essential Oils: Science, Technology and Applications, Second Edition New York: CRC Press, 2015 9781466590465, p 52-53.

11. Yeşilada E., Honda G., Sezik E., Tabata M., Goto K., Ikeshiro Y., Traditional medicine in Turkey IV. Folk medicine in the Mediterranean subdivision, Journal of Ethnopharmacology, 1993; 39; 31-38.

12. Baytop T. Türkiye'de Bitkiler ile Tedavi. Phytoterapy in Turkey (2 nd Edition.), Nobel Tıp Printing Press (1999) Istanbul.

13. Singleton VL., Orthofer R., Lamuela-Raventos, RM., Analysis of total phenols and other oxidation substrates and antioxidants by means of Folin-Ciocalteu reagent, Methods in Enzymology, 1999; 299; 152-78.

14. Zhishen J., Mengcheng T., Jianming W., The determination of flavonoid contents in mulberry and their scavenging effects on superoxide radicals, Food Chemistry, 1999; 64; 555-59.

15. Yermakov AI., Arasimov VV., Yarosh, NP., Methods of biochemical analysis of plants. Leningrad, Russia: Agropromizdat, 1987.

16. Blois MS., Antioxidant determinations by the use of a stable free radical, Nature, 1958; 181; 1199-200.

17. Oyaizu M., Studies on Product of Browning Reaction Prepared from Glucose Amine, Japanese Journal of Nutrition 1986; 44; 307-315.

18. Carter P., Spectrophotometric determination of serum iron at the submicrogram level with a new reagent (ferrozine). Analytical Biochemistry 1971; 40; 450-458.

19. Stookey LL., Ferrozine-A new spectrophotometric reagent for iron, Analytical Chemistry, 1970; 42(7); 779–781.

20. Priyadarsini KI., The Chemistry of Curcumin: From Extraction to Therapeutic Agent, Molecules, 2014; 19(12); 20091–20112.

21. Sun Y., Qiao L., Shen Y., Jiang P., Chen J., Ye X.; Phytochemical Profile and Antioxidant Activity of Physiological Drop of Citrus Fruits, Journal of Food Science, 2013; 78(1); C37-C42.

22. Alasalvar C., Grigor JM., Zhang D., Quantick PC., Shahidi F., Comparison of volatiles, phenolics, sugars, antioxidant vitamins, and sensory quality of different colored carrot varieties, Journal of Agricultural and Food Chemistry, 2001; 49(3);1410-1416.

23. Rocha LD., Monteiro MC., Anderson JT., Anticancer properties of hydroxycinnamic acids-A Review. Cancer and Clinical Oncology, 2012; 1; 109-121.

24. Tanaka T., Tanaka T., Tanaka M., Potential Cancer Chemopreventive Activity of Protocatechuic Acid, Journal of Experimental & Clinical Medicine, 2011; 3; 27–33.

25. Davis CB., Markey CE., Busch MA., Busch KW., Determination of capsaicinoids in habanero peppers by chemometric analysis of UV spectral data, Journal of Agricultural and Food Chemistry, 2007; 55(15); 5925-5933.

26. Boz H., Phenolic Amides (Avenanthramides) in Oats – A review, Czech Journal of Food Sciences, 2015; 33(5); 399–404.

27. Peterson DM., Hahn MJ., Emmons CL., Oat avenanthramides exhibit antioxidant activities in vitro, Food Chemistry, 2002; 79; 473–478.

28. Chen CY., Milbury PE., Kwak HK., Collins FW.,Samuel P., Blumberg JB., Avenanthramides and phenolic acids from oats are bioavailable and act synergistically with vitamin C to enhance hamster and human LDL resistance to oxidation, The Journal of Nutrition, 2004; 134; 1459-1466.

29. Hassan MH.,, Edfawy M., Mansour A., Hamed AA., Antioxidant and antiapoptotic effects of capsaicin against carbon tetrachloride-induced hepatotoxicity in rats, Toxicology and Industrial Health, 2011; 28(5); 428-438.

30. Turkoglu I., Turkoglu S., Celik S., Kahyaoglu M. Anti-oxidant and anti-microbial activities of Turkish endemic Achillea species. African Journal of Microbiology Research, 2010; 4; 2034–2042.

31. Barış O., Güllüce M., Şahin F., Özer H., Kılıç H., Özkan H., Sökmen M., Özbek T., Biological activities of the essential oil and methanol extract of Achillea biebersteinii Afan. (Asteraceae), Turkish Journal of Biology, 2006; 30; 65-73.

32. Deniz B., Kızıl M., Aytekin Ç., Kızıl G., Yavuz M., Çeken B., Ertekin AS., In Vitro Antimicrobial and Antioxidant Activity of Ethanol Extract of Three Hypericum and Three Achillea Species From Turkey, International Journal of Food Properties, 2011; 14; 339-355.

JOTCSA Journal of the Turkish Chemical Society Section: A Chemistry

Turkish Chemical Society

Complementary Use of Raman and µ-XRF Spectroscopy for Non-destructive Characterization of an Oil Painting by Turkish Painter İbrahim Çallı

Özden ORMANCI, Meriç BAKİLER
Mimar Sinan University of Fine Arts, Istanbul, Turkey.

Abstract: The aim of the present work was to investigate the pigments used in oil painting "in the park" created in the first half of the 20th century, by Turkish painter and academician İbrahim Çallı (1882-1960). The non-destructive analyses were performed with a combination of µ-XRF and Raman Microscopy. Obtained results revealed following pigments on the investigated painting: Zinc white (ZnO), zinc yellow ($K_2O{\cdot}4ZnCrO_4{\cdot}3H_2O$), chrome yellow ($PbCrO_4$), strontium yellow ($SrCrO_4$), ultramarine ($Na_7Al_6Si_6O_{24}S_3$), prussian blue ($Fe_7C_{18}N_{18}$), hematite ($\alpha$-$Fe_2O_3$), cadmium red (CdSe), barite ($BaSO_4$), and carbon black. There is a great lack of knowledge about the materials used in Turkish painting and this non-destructive study provides the first systematic investigation into Çallı's palette.

Keywords: Micro-Raman, micro-XRF, pigment characterization, non-destructive analyses, Turkish painting.

Submitted: December 20, 2020. **Accepted:** March 11, 2021.

Cite this: Ormancı Ö., Bakiler M. Complementary Use of Raman and µ-XRF Spectroscopy for Non-destructive Characterization of an Oil Painting by Turkish Painter İbrahim Çallı. JOTCSA. 2021;8(2):491–500.

DOI: https://doi.org/10.18596/jotcsa.842525.

***Corresponding author.** E-mail: meric.bakiler@msgsu.edu.tr.

INTRODUCTION

There was a widespread assumption that art and technology were notions opposite to each other. However, during the recent years, a great awareness has been created across several disciplines that modern science and technology are crucial for a better insight into art and cultural heritage(1,2). The characterization of pigments on artworks is the major interest by reason of providing detailed historical and technological information. The identification of the chemical composition and degradation products of the pigments used, provide a remarkable contribution to the conservation method to be employed(3,4). This would also allow the detection of forgeries by the detection of anachronistic pigments due to well establishing chronology of most pigments(5). However, pigment analysis can be a challenging problem because of the extremely limited sampling of works of art. In such cases, the non-destructive techniques, which can be applied on the object itself, is obviously mostly desirable. In a detailed analysis of the different possible techniques for pigment analysis, it is reported that Raman microscopy is the best single technique for this purpose due to its specificity, sensitivity, spatial resolution, and providing spectra which are free from interference by the surrounding materials(6–9). Many authors have previously reported Raman studies of oil painting mainly focused on the palette composition and pigment admixtures and in some cases on the degradation of pigments(10–17). However, to the best of our knowledge it is not very likely to find scientific data on the Turkish paintings, except a work investigating a Feyhaman Duran painting, the contemporary of İbrahim Çallı(18).

In parallel with the westernization policies of the Ottoman Empire, a new style of art entered to Ottoman visual culture. The most important event regarding the history of Turkish painting was the foundation of Sanayi-i Nefise Mektebi (1882) in İstanbul (today, Mimar Sinan Fine Arts University), which was founded by Osman Hamdi Bey who

received education of painting in Paris. A group of young artists who graduated from the Academy of Fine Arts went to study abroad after the Second Constitutional Revolution. They returned to the empire with the beginning of World War I in 1914 and despite training in academic style, they started painting with an impressionistic palette. This younger generation rebelled against the academism of their teachers and introduced a new concept of painting to Turkey(19–21). İbrahim Çallı (1882-1960) is one of best known member of the group and has a more active position than the others. He is considered to be the pioneer of the Impressionist trend in Turkey, such that the group is also known as the “Çallı Generation”(20,21).

The paper here presented intends to display the analytical characterization results of the Çallı’s pigment palette which he used on the painting “in the park” (75 cm x 60 cm). It is understood from the artist's signature that the painting was created before 1934, when the surname law came out. Raman and µ-XRF spectrometers were used with the aim of characterizing the pigments used. For the first time in this study, an oil painting by a Turkish painter was analyzed non-destructively considering the importance of the painting and it is also crucial to state that, this work is the first to investigate a Çallı painting, regarding the pigment palette.

MATERIALS AND METHODS

All the studies were performed non-destructively using the facilities of Central Research Laboratory (MerLab), functioning under Materials Research Center for Cultural Property and Artworks in Mimar Sinan Fine Arts University, İstanbul, Turkey.

For elemental characterization, a Bruker ARTAX 800 micro X-Ray Fluorescence spectrometer (µ-XRF) with molybdenum source, at an electric accelerating potential of 40 kV and a current of 600 µA was used. The measuring head which consists of a central unit containing a Peltier-cooled silicon drift detector, the laser spot and the CCD camera, allowed us to focused on the different spots of the sample. Each spectrum was collected during 60s and evaluated by ARTAX software.

Raman microscopy measurements were made with a Bruker SENTERRA Dispersive Raman spectrometer, which is equipped with an Olympus confocal microscope mounted onto a crane (Figure 1). In this study, 20x and 50x magnification objectives were employed to focus the 785 nm laser beam onto the samples. The irradiating laser power (1-50 mW) and the exposure time has been changed during the study. The analysis were performed directly on the painting, and the signals recorded by a TE-cooled CCD detector. The band intensities are defined as vw: very weak; w: weak; m: medium; s: strong; sh: shoulder throughout the text.

Since, the analyses were based on the use of non-destructive techniques, no samples were removed from the painting. After the visual inspections on the artwork, the colors and points to be analyzed were selected considering their homogeneity and the analytical reproducibility, and they were shown in Figure 2.

Figure 1. The raman spectrometer, which was used in this study, equipped with a confocal microscope mounted onto a crane.

Figure 2.İbrahim Çallı's oil painting "in the park" (75 cm x 60 cm) and the points from which Raman and XRF spectra were collected.

RESULTS AND DISCUSSION

As shown in Figure 3, paint layers were applied directly onto the rough surface of a wooden panel support, no preparation layer was laid on.

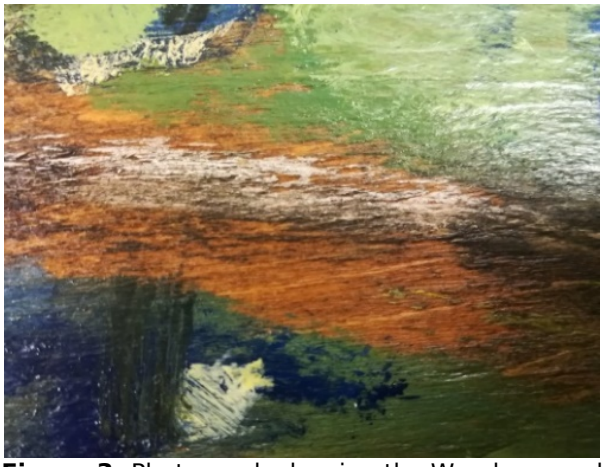

Figure 3. Photograph showing the Wooden panel support.

XRF analysis of the Spot 1 shows three elements which can be related to white color: zinc and lead. On the other hand, Raman analyses were carried out from a significant number of points and only one measurement yield a useful Raman spectrum (Figure 4) since zinc white is a poor Raman scatter(22). This spectrum confirmed the application of zinc white with the characteristic bands at 99, 320 and 435 cm^{-1}(23). However, white paint is likely a mixture of lead white and zinc white.

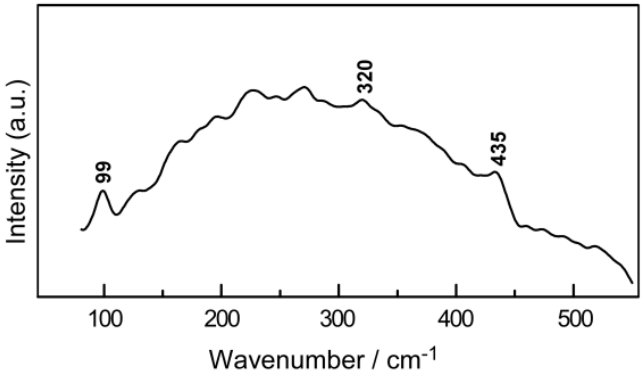

Figure 4. Raman spectrum of the white color (Spot 1).

Figure 5 shows the Raman spectrum of the green color, Spot 6. The green pigment was detected to be not a green chromophore but a mixture of Prussian blue $[Fe_4[Fe(CN)_6]_3 \cdot xH_2O]$ and chrome yellow ($PbCrO_4$). The intense peak at 2153 cm^{-1} and weaker bands at 2091, 534, and 277 cm^{-1} clearly indicate the presence of blue, while the band at 841 cm^{-1}, due to CrO_4^{2-} stretching, is assigned to chrome yellow(3,24,25). Prussian blue is reported as a compatible pigment which can be used in mixtures with lead chromate to produce green color and many studies have shown its predominant application as a blue pigment used to achieve green hues(22,24,26–28). Furthermore, the spectrum shows a band at 987 cm^{-1} which is

caused by barium sulfate ($BaSO_4$) and its presence may be related to Prussian blue since barium sulfate is reported to be detected in Prussian blue widely(29). It may also be intentionally added as an extender or a white pigment. The analysis of XRF spectra confirmed these findings and revealed the presence of Zn, Fe, Cr, Ba, Pb, and S. In addition to these elements Ca, which may be suggesting the application of a small amount of calcite ($CaCO_3$), was also detected.

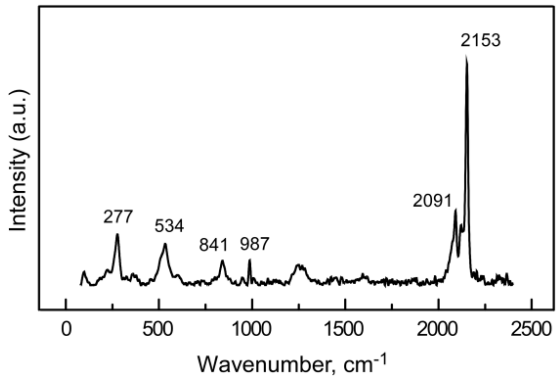

Figure 5. Raman spectrum of the green color (Spot 6).

Regarding the yellow color (Spot 4), characteristic Raman bands of zinc yellow at 114 (vw), 162 (vw), 346 (m), 358 (sh), 412 (vw), 776(vw), 874 (vs), 894 (sh), 942 (m) cm^{-1} were detected (Figure 6) (25,27,30). Zinc yellow was first synthesized in about 1800 cm^{-1} but it has not been used as a pigment until the second half of the 19th century. The basic zinc chromate has the composition $4Zn(OH)_2{\cdot}ZnCrO_4$, while most modern yellows are of the $K_2O{\cdot}4ZnCrO_4{\cdot}3H_2O$ composition(31–33). In this study, detection of K in XRF spectrum of the yellow color, indicating the application of a pigment having zinc potassium chromate hydrate composition. Besides these elements mentioned above, the XRF analysis revealed the presence of Sr, Pb, Fe, Ba, and S in Spot 4. The high amount of Sr detected in yellow area can be considered as an important clue indicating the application of strontium yellow (Strontium chromate, $SrCrO_4$) pigment, although it was not detected in the Raman spectra. The presence of Pb, Fe, Ba and S may not be unambiguously related to the yellow pigment, rather may be indicating the underlayer pigment, which we believe is a mixture of Prussian blue and chrome yellow as it is identified on Spot 6.

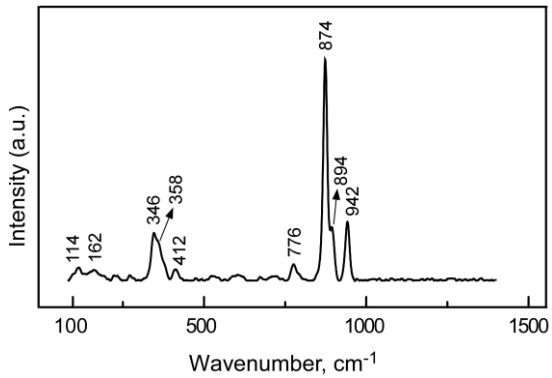

Figure 6. Raman spectrum of the yellow color (Spot 4).

As for the blue, the Raman spectra performed on the Spot 5 showed the use of ultramarine blue, which is a three-dimensional aluminosilicate complex with a sodalite structure containing sodium ions and sulfur groups ($(Na,Ca)_8(AlSiO_4)_6(O,S,SO_4)_{1-2}$) (3,25,32). The Raman spectra of the ultramarine blue obtained have bands at 268 (vw) 375 (w), 549 (vs), 584 (sh), 1096 (vw), cm^{-1} as shown in Figure 7(34–36). The elements regarding the underlying green color, Fe, Pb, Cr, Ba and S, were also detected in XRF spectra.

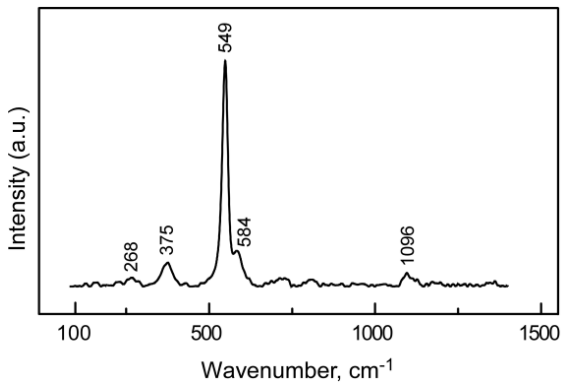

Figure 7. Raman spectrum of the blue color (Spot 5).

The Raman analysis of the black color (Spot 2) have given the spectra of a carbon-based black pigment distinguished by two broad bands at around 1320 and 1580 cm^{-1} as shown in Figure 8 (37,38). On the other hand, the detection of Ca and P in XRF spectra, can be associated with the presence of bone black.

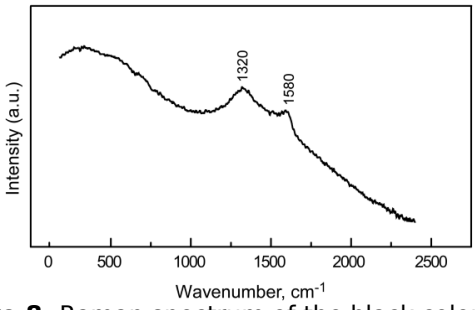

Figure 8. Raman spectrum of the black color (Spot 2).

For the red color (Spot 3), no useful Raman spectra could be collected. However, the detection of key elements such as Cd and Se in XRF spectrum was a clear indication of the presence of cadmium red pigment (CdSe) and allowed us to distinguish the pigment used from that of any other red pigments (Figure 9). It is also worth noting that the result is emphasized the importance of complementary using of the Raman and XRF techniques for identification purposes.

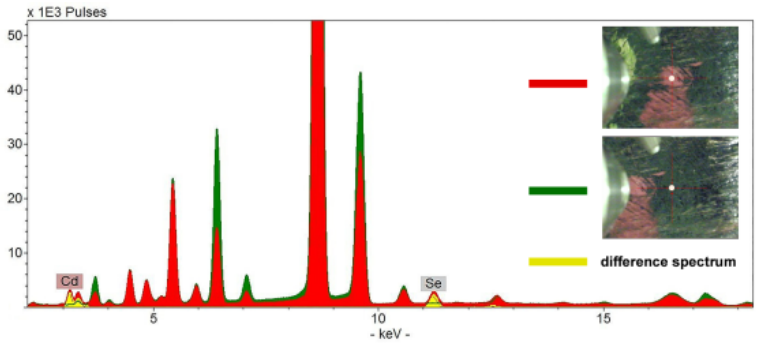

Figure 9. XRF spectra collected from the red and green colors and the difference spectrum.

As regards to artist signature (Spot 7), the color was identified as a mixture of pigments and obtained by adding carbon-based black pigment to hematite (α-Fe_2O_3) to produce a brown hue. Figure 10 shows the Raman spectrum and the bands at 230 (m-s), 297 (vs), 413 (m-s), 504 (w-m), 617 (m), 676 (w), 801 (vw) cm^{-1} were assigned to the presence of hematite, whereas those at 1318 and 1601 cm^{-1} were assigned to carbon-based black pigment (37–40). In addition, besides the elements arising from the under layer, Cd and Se were also detected in XRF spectrum. Thus, the analysis revealed that the occurrence of this brown pigment used for signature consisting of a mixture of at least three different pigment which are hematite, carbon black and cadmium red.

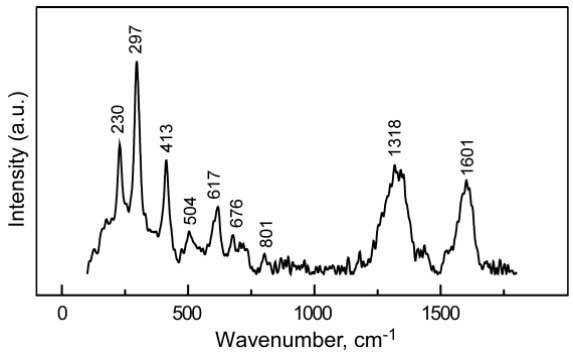

Figure 10. Raman spectrum of the brown signature (Spot 7).

There is another point to take into consideration that zinc was almost always detected in the colors analyzed. It is reported in the literature that treatises from the late medieval period recommended zinc sulfate, also known as zinc vitriol or white vitriol, as driers for varnishes and paints(41,42). The significant amount of zinc detected in this study was most probably incorporated in the form of zinc sulfate which like powdered glass. The detection of sulfur by XRF corroborates the idea of the usage of white vitriol. However, the addition of zinc may also be suggested its addition by manufacturers as a lightening agent(43).

An overview of the study, the measured points and results, is given in Table 1.

Table 1. Overview of the measured points, colors, analysis results, identified pigments, and chemical compositions.

Measuring Point	Color	μ-XRF Results (net peak area values in decreasing order)	Raman peaks (cm^{-1})	Chemical Composition	References
1	White	Zn, Pb, Fe, Cr, Ca, Ba, K, S	Zinc white: 99(w), 320(vw), 435(vw)	ZnO	(3,25)
2	Black	Zn, Pb, Fe, Ca, Cr, Ba, K, S, P	Carbon-based black: 1320(br), 1580(br)	carbon-based black	(37-40)
3	Red	Zn, Cr, Fe, Ba, Pb, Se, Cd, Ca, Sr, S	-	CdSe	
4	Yellow	Zn, Cr, K, Sr, Pb, Fe, S, Ba	Zinc yellow: 114(vw), 162(vw), 346(w-m), 358(sh), 412(vw), 776(w), 874(vs), 894(sh), 942(m)	$K_2O{\cdot}4ZnCrO_4{\cdot}3H_2O$ and $SrCrO_4$ (?)	(25,27,30)
5	Blue	Zn, Fe, Cr, Pb, Ca, Ba, S, K, Sr, Si	Ultramarine: 268(vw), 375(w), 549(vs), 584(sh), 1096(vw)	$Na_7Al_6Si_6O_{24}S_3$	(34-36)
6	Green	Zn, Pb, Ca, Ba, Cr, Fe, Sr, S	Prussian blue: 277(w-m), 534(w-m), 2091(m), 2153(vs) Chrome yellow: 841(w), Barite: 987(w)	$Fe_7C_{18}N_{18}$ $PbCrO_4$ $BaSO_4$	(24,25)
7	Signature (Brown)	Zn, Fe, Cr, Ca, Ba, Pb, Cd, Sr, S, Se	Hematite: 230(m-s), 297(vs), 413(m-s), 504(w-m), 617(m), 676(w), 801(vw) Carbon-based black: 1318(br), 1601(br)	α-Fe_2O_3,CdSe, and carbon-based black	(37-40)

CONCLUSIONS

The results of the present study once again emphasize the great potential of the complementary use of µ-XRF and Raman spectroscopy and the pigments used by İbrahim Çallı were successfully determined. The painter's palette includes zinc white, zinc yellow, chrome yellow, strontium yellow, ultramarine, Prussian blue, hematite, cadmium red, barite, and carbon-based black pigments.

The knowledge of his palette plays an substantial contribution to the knowledge of the pigments used in 20th century Turkish painting. In addition, one of the most important characteristic of this work was to be the first to investigate a Turkish painting non-destructively. Nevertheless, Çallı's paintings will continue to be analyzed to create an extensive database.

ACKNOWLEDGMENT

The authors would like to thank İpek-Ahmet Merey for allowing the investigation of the precious painting belonging their collection.

REFERENCES

1. Fotakis, C., Anglos, D., Zafiropulos, V., Georgiou, S., Tornari V. Lasers in the Preservation of Cultural Heritage: Principles and Applications. CRC Press. 2006.

2. Messina, G., Santangelo S. GNSR 2001: State of Art and Future Development in Raman Spectroscopy and Related Techniques. CRC Press. 2001. 290 p.

3. Burgio L, Clark RJH. Library of FT-Raman spectra of pigments, minerals, pigment media and varnishes, and supplement to existing library of Raman spectra of pigments with visible excitation. Vol. 57, Spectrochimica Acta - Part A: Molecular and Biomolecular Spectroscopy. 2001. 1491–1521 p.

4. Best SP, Clark RJH, Withnall R. Non-destructive pigment analysis of artefacts by Raman microscopy. Endeavour. 1992;16(2):66–73.

5. Chalmers JM, Edwards HGM, Hargreaves MD. Infrared and Raman spectroscopy in Forensic Science. Wiley; 2012.

6. Clark RJH. Raman microscopy: Application to the identification of pigments on medieval manuscripts. Chem Soc Rev. 1995;24(3):187–96.

7. Clark RJH. Pigment identification on medieval manuscripts by Raman microscopy. J Mol Struct. 1995;347:417–27.

8. Burgio L, Ciomartan DA, Clark RJH. Pigment identification on medieval manuscripts, paintings and other artefacts by Raman microscopy: Applications to the study of three German manuscripts. J Mol Struct. 1997;405(1):1–11.

9. Jurado-López A, Demko O, Clark RJH, Jacobs D. Analysis of the palette of a precious 16th century illuminated Turkish manuscript by Raman microscopy. J Raman Spectrosc. 2004;35(2):119–24.

10. Cazzanelli E, Platania E, De Santo G, Fasanella A, Castriota M. Micro-spectroscopic Raman investigation on the canvas oil painting "Rebecca at the well" of Neapolitan anonymous. J Raman Spectrosc. 2012;43(11):1694–8.

11. Antunes V, Candeias A, Mirão J, Carvalho ML, Dias CB, Manhita A, et al. Analytical characterization of the palette and painting techniques of Jorge Afonso, the great 16th century Master of Lisbon painting workshop. Spectrochim Acta - Part A Mol Biomol Spectrosc. 2018;193:264–75. Available from:https://doi.org/10.1016/j.saa.2017.12.027

12. Cristina L. Aibeo, Stien Goffin, Olivier Schalm, Geert van der Snickt, Nathalie Laquiere, Peter Eyskens KJ. Micro-Raman analysis for the identification of pigments from 19th and 20th century paintings. J Raman Spectrosc. 2008;39(May):1091–8. Available from: 10.1002/jrs.1990

13. Damjanović L, Gajić-Kvaščev M, Durdević J, Andrić V, Marić-Stojanović M, Lazić T, et al. The characterization of canvas painting by the Serbian artist Milo Milunović using X-ray fluorescence, micro-Raman and FTIR spectroscopy. Radiat Phys Chem. 2015;115:135–42.

14. Ricci C, Borgia I, Brunetti BG, Miliani C, Sgamellotti A, Seccaroni C, et al. The Perugino's palette: Integration of an extended in situ XRF study by Raman spectroscopy. J Raman Spectrosc. 2004;35(8–9):616–21.

15. Artesani A, Ghirardello M, Mosca S, Nevin A, Valentini G, Comelli D. Combined photoluminescence and Raman microscopy for the identification of modern pigments: explanatory examples on cross-sections from Russian avant-garde paintings. Herit Sci. 2019;7(1):1–13. Available from: https://doi.org/10.1186/s40494-019-0258-x

16. Giorgi L, Nevin A, Nodari L, Comelli D, Alberti R, Gironda M, et al. In-situ technical study of modern paintings part 1: The evolution of artistic materials and painting techniques in ten paintings from 1889 to 1940 by Alessandro Milesi (1856–1945). Spectrochim Acta - Part A Mol Biomol Spectrosc. 2019;219:530–8. Available from: https://doi.org/10.1016/j.saa.2019.04.083

17. Vermeulen M, Saverwyns S, Coudray A, Janssens K, Sanyova J. Identification by Raman spectroscopy of pararealgar as a starting material in the synthesis of amorphous arsenic sulfide pigments. Dye Pigment. 2018;149(October

2017):290–7.

18. Akyuz S, Akyuz T, Emre G, Gulec A, Basaran S. Pigment analyses of a portrait and paint box of Turkish artist Feyhaman Duran (1886-1970): The EDXRF, FT-IR and micro Raman spectroscopic studies. Spectrochim Acta - Part A Mol Biomol Spectrosc. 2012;89:74–81. Available from: http://dx.doi.org/10.1016/j.saa.2011.12.046

19. Yaban NT. Environment of Culture and Art in the Ottoman Empire in 19th Century. Online J Sci Technol. 2018;8(2):71–8.

20. Shaw WMK. Ottoman painting: reflections of Western art from the Ottoman Empire to the Turkish Republic. IB Tauris Publishers. 2010. 208 p.

21. Gültekin G. Western Trends in the Turkish Art of Painting.pdf. Ankara: T.C. Ziraat Bankası Cultural and Art Activities, Ajans Türk Publishing&Printing Co. Inc.; 1992. 216 p.

22. Veronika Košařová, David Hradil, Janka Hradilová, Zdeňka Čermáková, Ivan Němec MS. The efficiency of micro-Raman spectroscopy in the analysis of complicated mixtures in modern paints: Munch's and Kupka's paintings under study. Spectrochim Acta Part A Mol Biomol Spectrosc. 2016;156:36–46.

23. Marinho JZ, Romeiro FC, Lemos SCS, Motta F V., Riccardi CS, Li MS, et al. Urea-based synthesis of zinc oxide nanostructures at low temperature. J Nanomater. 2012;2012.

24. Rosi F, Miliani C, Borgia I, Brunetti B, Sgamellotti A. Identification of nineteenth century blue and green pigments by in situ x-ray fluorescence and micro-Raman spectroscopy. J Raman Spectrosc. 2004;35(8–9):610–5.

25. Bell IM, Clark RJH, Gibbs PJ. Raman spectroscopic library of natural and synthetic pigments (pre-~ 1850 AD). Spectrochim Acta - Part A Mol Biomol Spectrosc. 1997;53(12):2159–79.

26. Grim DM, Allison J. Identification of colorants as used in watercolor and oil paintings by UV laser desorption mass spectrometry. Int J Mass Spectrom. 2003;222(1–3):85–99.

27. Edwards HGM. Analytical raman spectroscopic discrimination between yellow pigments of the renaissance. Spectrochim Acta - Part A Mol Biomol Spectrosc. 2011;80(1):14–20. Available from: http://dx.doi.org/10.1016/j.saa.2010.12.023

28. Li XL, Sun CJ, Luo L Bin, He Y. Nondestructive detection of lead chrome green in tea by Raman spectroscopy. Sci Rep. 2015;5:1–9. Available from:http://dx.doi.org/10.1038/srep15729

29. Gautier G, Bezur A, Muir K, Casadio F, Fiedler I. Chemical fingerprinting of ready-mixed house paints of relevance to artistic production in the first half of the twentieth century. Part I: Inorganic and organic pigments. Appl Spectrosc. 2009;63(6):597–603.

30. Correia AM, Clark RJH, Ribeiro MIM, Duarte MLTS. Pigment study by Raman microscopy of 23 paintings by the Portuguese artist Henrique Pousão (1859-1884). J Raman Spectrosc. 2007;38(11):1390–405.

31. Simonsen KP, Christiansen MB, Vinum MG, Sanyova J, Bendix J. Single crystal X-ray structure of the artists' pigment zinc yellow. J Mol Struct. 2017;1141:322–7. Available from: http://dx.doi.org/10.1016/j.molstruc.2017.03.108

32. Nicholas Eastaugh, Valentine Walsh, Tracey Chaplin RS. Pigment Compendium. A Dictionary and Optical Microscopy of Historical Pigments. Butterworth-Heinemann. 2008.

33. Feller RL, editor. Artists' Pigments: A Handbook of Their History and Characteristics. Volume 1. Oxford University Press; 1986.

34. Osticioli I, Mendes NFC, Nevin A, Gil FPSC, Becucci M, Castellucci E. Analysis of natural and artificial ultramarine blue pigments using laser induced breakdown and pulsed Raman spectroscopy, statistical analysis and light microscopy. Spectrochim Acta - Part A Mol Biomol Spectrosc. 2009;73(3):525–31.

35. Frausto-Reyes C, Ortiz-Morales M, Bujdud-Pérez JM, Magaña-Cota GE, Mejía-Falcón R. Raman spectroscopy for the identification of pigments and color measurement in Dugès watercolors. Spectrochim Acta - Part A Mol Biomol Spectrosc. 2009;74(5):1275–9.

36. Colomban P. Lapis lazuli as unexpected blue pigment in Iranian Lâjvardina ceramics. J Raman Spectrosc. 2003;34(6):420–3.

37. Tomasini EP, Halac EB, Reinoso M, Di Liscia EJ, Maier MS. Micro-Raman spectroscopy of carbon-based black pigments. J Raman Spectrosc. 2012;43(11):1671–5.

38. Coccato A, Jehlicka J, Moens L, Vandenabeele P. Raman spectroscopy for the investigation of carbon-based black pigments. J Raman Spectrosc. 2015;46(10):1003–15.

39. Pięta E, Proniewicz E, Szmelter-Fausek B, Olszewska-wietlik J, Proniewicz LM. Pigment characterization of important golden age panel paintings of the 17th century. Spectrochim Acta - Part A Mol Biomol Spectrosc. 2015;136:594–600.

40. Lauridsen CB, Sanyova J, Simonsen KP. Raman analysis of complex pigment mixtures in 20th century metal knight shields of the Order of the Elephant. Spectrochim Acta - Part A Mol Biomol Spectrosc. 2015;150:54–62. Available from: http://dx.doi.org/10.1016/j.saa.2015.04.117

41. O'Donoghue E, Romero R, Dik loris. French eighteenth-century painting techniques. Stud Conserv. 1998;43(sup1):185–9.

42. Burgio L, Clark RJH, Hark RR. Raman microscopy and x-ray fluorescence analysis of pigments on medieval and Renaissance Italian manuscript cuttings. Proc Natl Acad Sci U S A. 2010;107(13):5726–31.

43. Osmond G, keune K, Boon J. A study of zinc soap aggregates in a late 19th century painting by R.G. Rivers at the Queensland Art Gallery. AICCM Bull. 2005;29(1):37–46.

JOTCS A
Journal of the Turkish Chemical Society
Section: A
Chemistry
TURKISH CHEMICAL SOCIETY

Synthesis and Characterization of Benzodioxinone-Bearing Methacrylate-Based Random Copolymer via Atom Transfer Radical Polymerization

Cumali Celik[1]*, Gokhan Acik[2]

[1]Property Protection and Security Department, Yalova Vocational School, Yalova University, Yalova, Turkey

[2]Department of Chemistry, Faculty of Sciences and Letters, Piri Reis University, Tuzla, Istanbul, Turkey

Abstract: Methacrylate-benzodioxinone (BDMA) as a monomer was firstly synthesized and then copolymerized with methyl methacrylate and 2-hydroxyethyl methacrylate via atom transfer radical polymerization (ATRP) in the presence of CuCl/pentamethyldiethylene triamine (PMDETA) catalytic system using ethyl 2-bromopropionate (EtBrP) as an initiator. Successful formation of the block copolymer was also confirmed in detail by proton nuclear magnetic resonance spectroscopy (^{1}H NMR), Fourier-transform infrared spectroscopy (FT-IR), and gel permeation chromatography (GPC) appropriately. Secondly, photochemical acylation of obtained copolymer through hydroxyl and benzodioxinone groups led to the release of benzophenone compound and ester-linkage on the polymer backbone. The formation of ester-linkage increases the glass transition temperature and the thermal stability of the obtained copolymer.

Keywords: Atom transfer radical polymerization, ketene chemistry, photochemical acylation, random copolymer.

Submitted: February 12, 2021. **Accepted:** March 20, 2021.

Cite this: Celik C, Acik G. Synthesis and Characterization of Benzodioxinone-Bearing Methacrylate-Based Random Copolymer via Atom Transfer Radical Polymerization. JOTCSA. 2021;8(2):501–10.

DOI: https://doi.org/10.18596/jotcsa.879021.

***Corresponding author. E-mail:** cumali.celik@yalova.edu.tr.

INTRODUCTION

Copolymers have attracted enormous interest ranging from many industrial fields to another applications in the past two decades (1-4). The development of controlled/living radical polymerizations provides many advantages for producing well-defined polymers (5, 6). The reversible addition-fragmentation chain transfer (RAFT), (7, 8) atom transfer radical polymerization (ATRP), (9-12) nitroxyl-mediated polymerization (NMP) (13, 14) are widely used CLRP methods over the past three decades. Among these methods, ATRP is the most powerful, versatile, and inexpensive method discovered by Matyjaszewski (5, 11, 15-18). Furthermore, the ATRP can be applied in various monomers under different conditions and provided control over molecular weight, polydispersity, and polymers' topology (9, 10, 14). This robust method also overcame a wide range of industrial problems, such as tolerance to solvents and impurities (9-11, 19).

Recently, benzodioxinone chemistry (20), which can easily form ketene and corresponding ketone intermediates upon UV irradiation (21-24) or temperature exposure thermolysis (25-27), has been utilized in synthetic polymer chemistry (28-30). Due to its chemical structure containing carbonyl and alkenyl groups and the possibility of their transformation into ketenes, benzodioxinone compounds are versatile organic reactive intermediates. Also, salicylate esters, one of the most important materials in the medical field (31), can be synthesized by the photochemical acylation process of benzodioxinone in the presence of either phenols or alcohols (32, 33). Recently, this photochemistry has been applied to synthesize various macromolecular architectures by combining various CLRP methods (34).

This study aims to synthesize photochemically sensitive random copolymer-bearing antagonist benzodioxinone and hydroxyl functionalities via atom transfer radical polymerization with a one-step procedure. For this purpose, methacrylated benzodioxinone was firstly synthesized by esterification reaction of 5-hydroxy-2,2-diphenyl-4H-benzo[d][1,3]dioxin-4-one with methacryloyl chloride. The methacrylated benzodioxinone monomer was copolymerized with methyl methacrylate and 2-hydroxylethyl methacrylate to get photochemically sensitive random copolymer, by using simple UV irradiation of the resulting copolymer led to photochemical acylation reaction between antagonist benzodioxinone and hydroxyl functionalities. Spectroscopic, chromatographic, and thermal analyses confirmed the formations of obtained copolymer and its acylated species.

MATERIALS AND METHODS

Materials

Monomers, methyl methacrylate (Aldrich, MMA, 99%,), and 2-hydroxyethyl methacrylate (Aldrich, HEMA, 99%) were purified to remove the inhibitor by passing through a basic alumina column. Copper(I) chloride (Aldrich, CuCl, 99.99%), ethyl 2-bromopropionate (99%, Aldrich), and methacryloyl chloride (Aldrich, 97%) were used without further purification. N,N,N',N",N''-pentamethyldiethylene triamine (PMDETA; 99%, Aldrich) was used as ligand and distilled before use. Toluene (99.7%, Aldrich) and other solvents were purified prior to use by conventional distillation and drying procedures.

Instrumentation

The ^{1}H-NMR analysis was conducted by Agilent NMR System VNMRS 500 spectrometer at room temperature in deuterated chloroform ($CDCl_3$) with tetramethylsilane (TMS) as the internal standard. Additionally, Perkin-Elmer FT-IR Spectrum One B spectrometer was used for Fourier transform infrared (FT-IR) spectroscopic analysis. The molecular weights and molecular weight distributions of the resulting polymers were determined by a Viscotek GPCmax. The GPC was equipped with an autosampler system consisting of a pump module (GPCmax, Viscotek, Houston, TX), a refractive index (RI) detector (VE 3580, Viscotek), and a combined light-scattering (Model 270 dual detector, Viscotek). The GPC system was equipped with two columns (LT5000L, Mixed, Medium Organic 300x8 mm and LT3000L and Mixed, Ultra-Low Organic 300x8 mm) with a guard column (TGuard, Organic Guard Column 10x4.6 mm) using tetrahydrofuran eluent at 35 ºC (flow rate, 1 mL min^{-1}). The polystyrene standards having narrow molecular weight distribution were used for the calibration of the refractive index detector. Two scattering angles, namely 90 and 7, were used in the light-scattering detector (λ_0 = 670 nm). The GPC data were analyzed using Viscotek OmniSEC Omni-01 software. Perkin-Elmer Diamond TA/ TGA thermogravimetric analysis (TGA) analyzed the thermal stability of obtained polymers with a heating rate of 10 °C/min under nitrogen flow (200 mL/min). Also, thermal transitions of obtained polymers were analyzed by Perkin-Elmer Diamond differential scanning calorimetry (DSC) with a heating rate of 10 °C/min under nitrogen flow (10 mL /min).

Synthesis of 4-oxo-2,2-diphenyl-4H-benzo[d][1,3]dioxin-5-yl methacrylate (BDMA)

Methacrylated benzodioxinone was synthesized with a modified two-step procedure. Firstly, the 5-hydroxy-2,2-diphenyl-4H-benzo[d][1,3]dioxin-4-one (1), was prepared as reported previously (35). In the second step, hydroxyl function of (1) was converted to methacrylate (2) by esterification using methacryloyl chloride according to the procedure given below (Scheme 1);

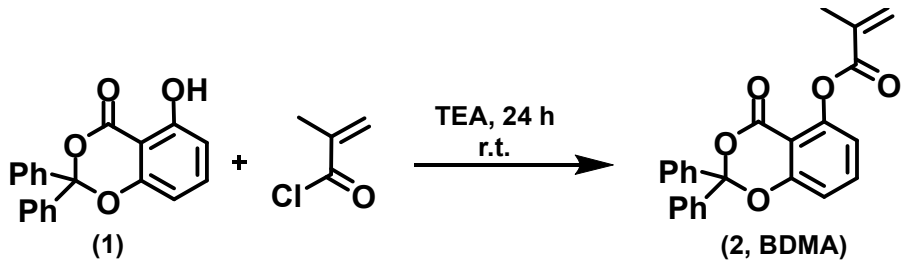

Scheme 1. Synthesis of 4-oxo-2,2-diphenyl-4H-benzo[d][1,3]dioxin-5-yl methacrylate (BDMA).

A solution of the above-obtained benzodioxinone, (1), (0.6 g, 1.88 mmol), and a 1.05 molar equivalent of triethylamine were added into dry acetone, and the solution was cooled to 0 ºC. Then, 1.05 mol of methacryloyl chloride per mol of alcohol was added drop-wise into the solution with vigorous stirring. After that, the suspension was stirred for 24 h at room temperature. The resulting salt firstly precipitated out, and then it was filtered off. The BDMA monomer was obtained by distillation of the acetone, unreacted methacryloyl chloride, and triethylamine under low pressure. Finally, the BDMA monomer yielded an oily yellow liquid (BDMA, 70%).

General procedure for Random Copolymerization by ATRP

Methacrylated benzodioxinone (BDMA, 0.1 g, 2.6×10^{-4}mol), 2-hydroxyethyl methacrylate (2.5 mL, 2×10^{-2} mol) and methyl methacrylate (9.25 mL, 9×10^{-2} mol) dissolved in deoxygenated solvent toluene (0.5 mL), PMDETA as a ligand (17 µL, 8×10^{-5} mol), ethyl 2-bromopropionate as an initiator (17 µL, 1.35×10^{-5} mol) and catalysts Cu(I), (0.016 g, $1.6\times10^{-}$

^{4} mol) were added to a Schlenk tube equipped with a magnetic stirring bar. The reaction tube was then degassed by three freeze-pump-thaw cycles and was placed in an oil bath (90 °C) for 48 h. The ATRP of BDMA, MMA, and HEMA was stopped by exposing to air. The reaction mixture was diluted with THF and passed through a short basic silica column to remove the copper catalyst. Then the reaction solution was concentrated by rotary evaporation and precipitated in 10-fold excess cold methanol. The obtained copolymer (PBDMA-*co*-PHEMA-*co*-PMMA) was filtered and dried under a vacuum oven at room temperature (yield: 20%; determined gravimetrically).

Photochemical acylation process of PBDMA-*co*-PHEMA-*co*-PMMA

Previously synthesized PBDMA-*co*-PHEMA-*co*-PMMA in THF (30 mL) were added to a quartz tube and irradiated for 48 h by a merry-go-round type UV-reactor equipped with 16 Philips 8W/06 lamps and a cooling system. All lamps emitted light at λ>350 nm. After the given time, the acylated copolymer first was precipitated in methanol, then collected by filtration. The filtrated copolymer was then dried under vacuum for 24 h at room temperature. Upon UV irradiation, benzophenone was released as a by-product removed by precipitation step using methanol as solvent.

RESULTS AND DISCUSSION

Based on previous literature studies that gave information about benzodioxinone photochemistry for various synthetic approaches, we synthesized copolymer including photosensitive benzodioxinone benefiting from ketene's chemoselective reactions intermediates toward hydroxyl groups in the copolymer backbone. For this purpose, firstly, methacrylated benzodioxinone (BDMA) was synthesized by esterification reaction of phenolic benzodioxinone 5-hydroxy-2,2-diphenyl-4H-benzo[d][1,3]dioxin-4-one with methacryloyl chloride (Scheme 1). The chemical structure of BDMA was confirmed by ^{1}H-NMR spectroscopy detecting characteristic protons of benzodioxinone (c, d, e, f, g, h, i, j) and methacrylate (a and b) at 6.5-7.6, 1.6, and 6.1 ppm (Figure 1).

In the second step, the random copolymerization of BDMA, 2-hydroxylethyl methacrylate, and methyl methacrylate was done by ATRP at 90 °C in toluene using EtBrP and CuCl/ PMDETA as initiator and catalyst, respectively (Scheme 2).

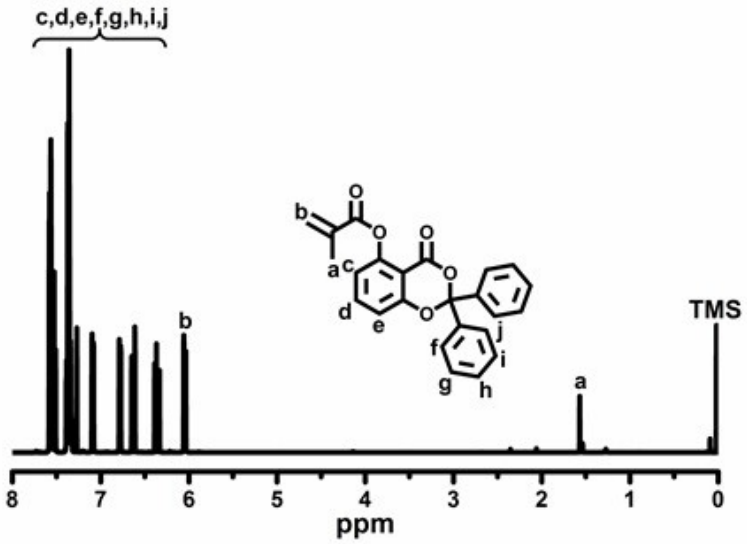

Figure 1. ^{1}H-NMR spectrum of BDMA.

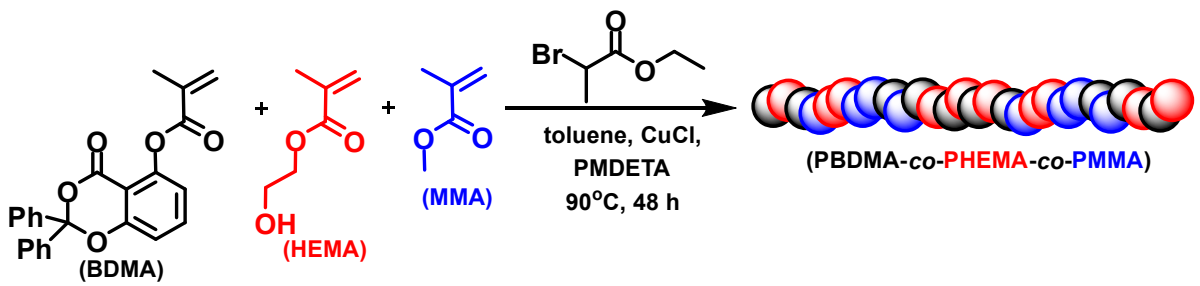

Scheme 2. Copolymerization of BDMA, HEMA and MMA via ATRP. (BDMA:HEMA:MMA:PMDETA:EtBrP:CuCl = 1:80:350:0.3:0.05:0.6 in 0.6 mL xylene)

The successful ATRP copolymerization led to photochemically active copolymer (PBDMA-*co*-PHEMA-*co*-PMMA), including benzodioxinone, which can absorb near UV light. In the final stage, the photochemical acylation process of the obtained PBDMA-*co*-PHEMA-*co*-PMMA was achieved throughout 48 h under UV light (Scheme 3).

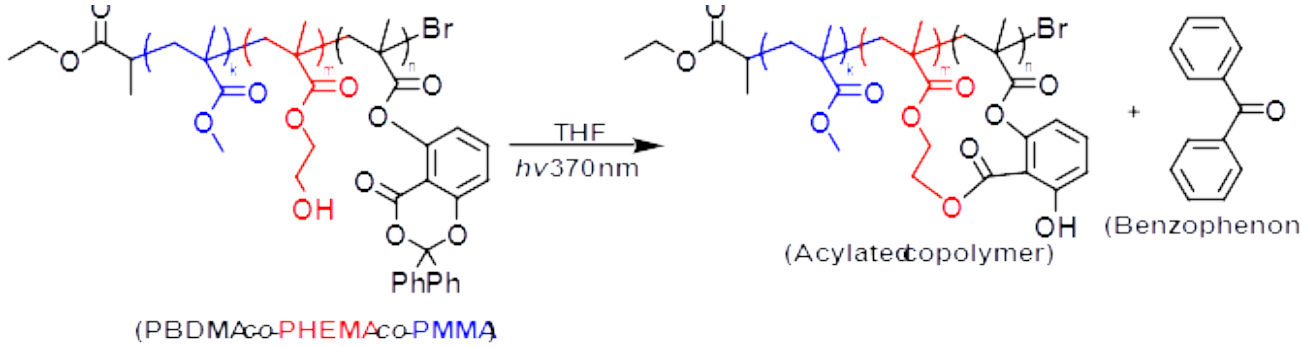

Scheme 3. Photochemical acylation of PBDMA-*co*-PHEMA-*co*-PMMA.

Based on spectroscopic (FT-IR and ^{1}H-NMR) and chromatographic (GPC) data of obtained copolymer by ATRP, the random copolymer was obtained with good yield as evaluated by acceptable monomer conversion (20%) and molecular weight (M_n= 73.730 g/mol) and molecular weight distribution (PDI= 1.26). The FT-IR spectra of untreated and UV-treated PBDMA-*co*-PHEMA-*co*-PMMA copolymer were shown in Figure 2. The spectrum for the neat PBDMA-*co*-PHEMA-*co*-PMMA displayed the characteristic bands such as broad O-H band at 3500 cm^{-1}, aromatic C-H band at 2950 cm^{-1}, sharp C=O band at 1700 cm^{-1}, aromatic C=C band at 1450 cm^{-1} at and C-O band at 1250 cm^{-1}. After the photochemical acylation process, all characteristic bands of PBDMA-*co*-PHEMA-*co*-PMMA were presented, whereas a new band at 1625 cm^{-1} attributed to the intramolecular hydrogen-bonded carbonyl group was formed.

Although FT-IR results confirmed the copolymer formation and acylation, the ^{1}H-NMR analysis provided a powerful indication. As can be seen, the Figure 3, the presence of aromatic protons belonging to PBDMA appear very clear between 6.10 and 7.50 ppm (**n, o, p, r, s, t, u and v**), PHEMA at 3.85 and 4.10 ppm (**k and j**), and PMMA at 3.58 ppm (**g**) prove the successful formation of copolymer bearing UV light-sensitive benzodioxinone. In addition, the chemical composition of the copolymer could be calculated from the integration ratio of methoxy protons of MMA (-O-CH_3, **g**) at 3.58 ppm, methylene protons (-CH_2-, **j and k**) of HEMA at 4.10 ppm and 3.95 ppm and the aromatic protons (**n, o, p, r, s, t, u and v**) of benzodioxinone at 6.10 and 7.50 ppm. According to the ^{1}H-NMR calculation, the copolymer composition was found as 8.7, 29.0, and 62.3% for PBDMA, PHEMA, and PMMA, respectively.

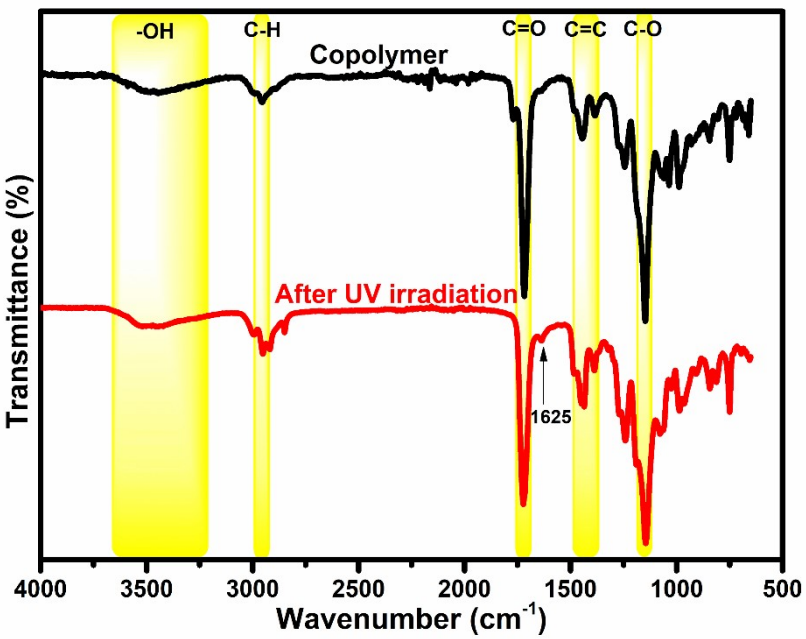

Figure 2. FT-IR spectra of PBDMA-*co*-PHEMA-*co*-PMMA and it's acylated species after UV irradiation.

The photoinduced acylation reaction antagonist benzodioxinone and hydroxyl groups of the PBDMA-*co*-PHEMA-*co*-PMMA led to the acylated product. After the acylation process, the aromatic peaks at 6.10 ppm and 6.18 ppm (**n, o, and p**) coming from benzodioxinone were remarkably decreased, whereas the aromatic peaks at 6.98 ppm and 7.08 ppm (**r, s, t, u and v**) belonging benzene rings of leaving benzophenone were almost disappeared. Additionally, the acylation process was monitored by gel permeation chromatography in the THF system (Figure 4). After the photoinduced acylation process, the molecular weight of PBDMA-*co*-PHEMA-*co*-PMMA was moderately decreased due to the leaving benzophenone compound as a by-product. Furthermore, the polydispersity indexes of both untreated and UV-treated PBDMA-*co*-PHEMA-*co*-PMMA copolymer displayed unimodal traces.

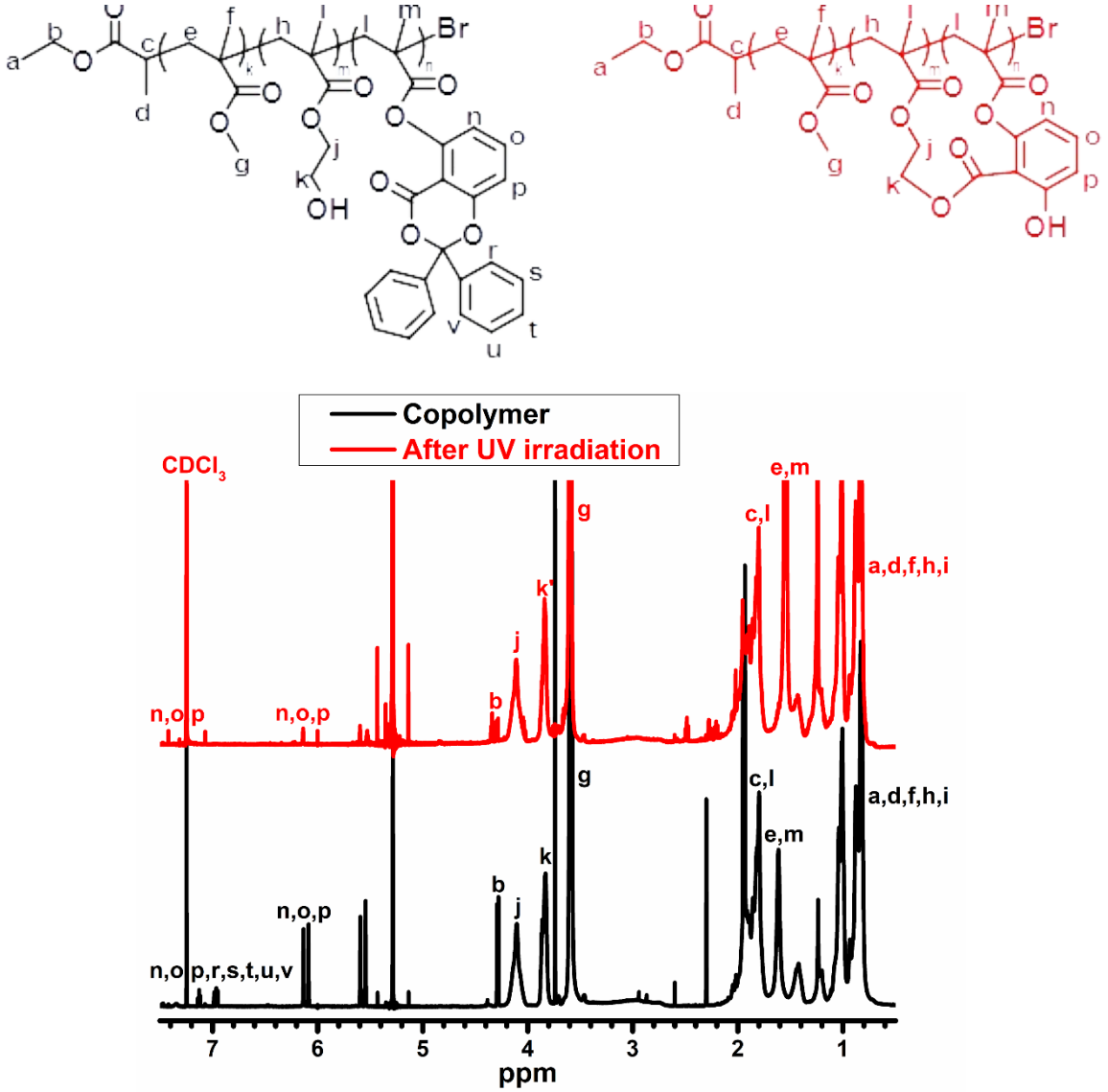

Figure 3. ^{1}H-NMR spectra of BDMA-*co*-PHEMA-*co*-PMMA and its acylated species after UV light irradiation. The random copolymer composition was calculated by ^{1}H-NMR analysis using the following formula: (Composition=(**n+o+p+r+s+t+u+v**)/(**n+o+p+r+s+t+u+v+g+j+k**)x100 and (**j+k**)/(**n+o+p+r+s+t+u+v+g+j+k**)x100, where **n+o+p+r+s+t+u+v** represents the integrated peak area at between 6.10 ppm and 7.50 ppm corresponding to aromatic protons of benzodioxinone, **j+k** represents the integrated peak area at 4.10 ppm and 3.95 ppm methylene protons (-CH_2-) of HEMA and **g** represents the integrated peak area at 3.58 ppm methoxy protons (-O-CH_3) of MMA).

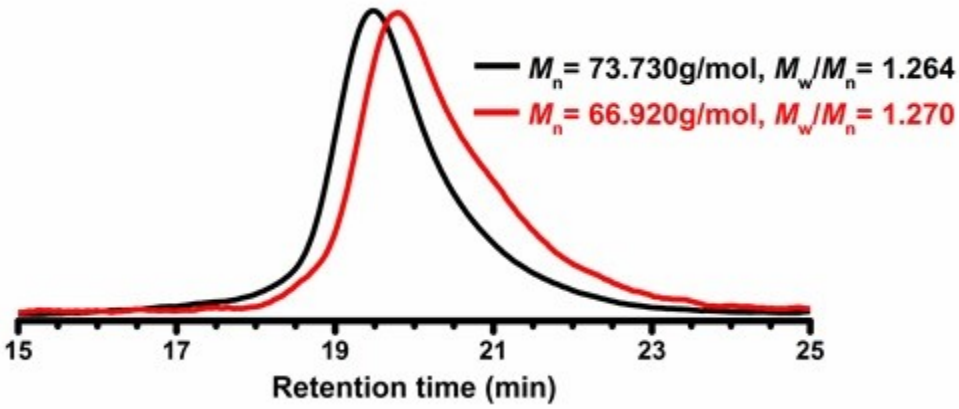

Figure 4. The GPC traces of PBDMA-*co*-PHEMA-*co*-PMMA and its acylated species after UV light irradiation (All GPC measurements were conducted using tetrahydrofuran as eluent with flow rate, 1 mL min^{-1} at 35 ^{0}C).

The thermal properties of the PBDMA-co-PHEMA-co-PMMA and its acylated species after esterification were determined by differential scanning calorimetric (DSC) analysis under a nitrogen atmosphere, and compared with pristine PHEMA-*co*-PMMA (Figure 5). The PHEMA-*co*-PMMA exhibited a glass transition temperature (T_g) at 88°C, whereas the obtained PBDMA-co-PHEMA-co-PMMA and its acylated species copolymers displayed higher T_g values at 98 and 109 °C, respectively. Due to the rigid benzodioxinone segments, the T_g value of PBDMA-*co*-PHEMA-*co*-PMMA higher than PHEMA-*co*-PMMA. After the acylation process, the linear polymer chains become entrapped within the particle, leading to decreased free volume. Therefore, the acylated species have the highest T_g value compared to the PBDMA-co-PHEMA-co-PMMA and PHEMA-*co*-PMMA (36-40).

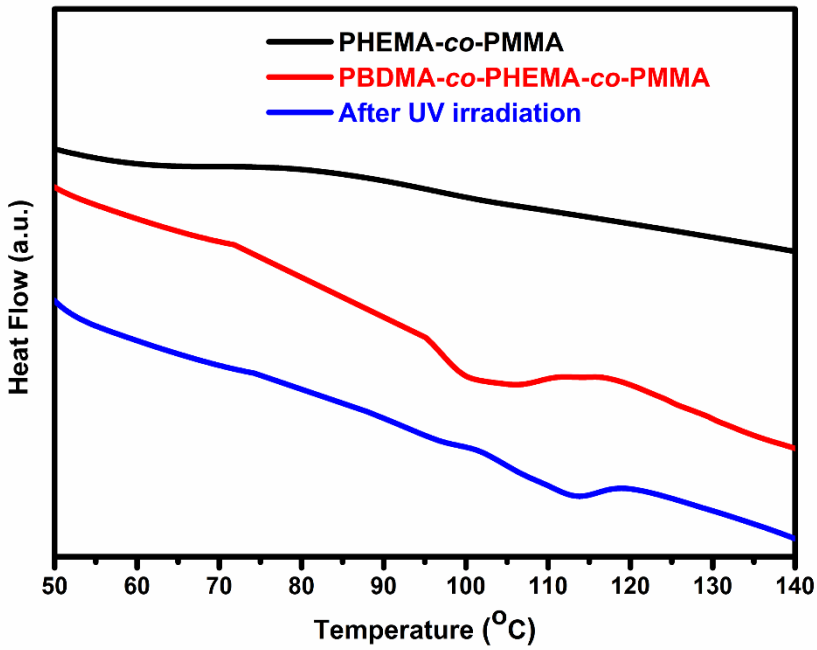

Figure 5. DSC thermogram of PHEMA-co-PMMA, PBDMA-co-PHEMA-co-PMMA, and its acylated species after UV light irradiation.

TGA further explored the thermal stabilities of the PHEMA-co-PMMA, PBDMA-co-PHEMA-co-PMMA, and its acylated species under nitrogen atmosphere. As shown in Figure 6, the weight loss of PHEMA-co-PMMA began at about 322 °C, reached its maximum at 440 °C, and displayed a single peak indicating one-step thermal degradation. The inclusion of benzodioxinone compounds on to polymer backbone, the rigid aromatic rings improved the thermal stability of the PBDMA-*co*-PHEMA-*co*-PMMA. However, the PBDMA-*co*-PHEMA-*co*-PMMA showed two-step degradations due to benzophenone's release and degradation of the polymer backbone. After the acylation process, the copolymer displayed one-step degradation and enhanced thermal stability again compared to the PBDMA-*co*-PHEMA-*co*-PMMA (40-42).

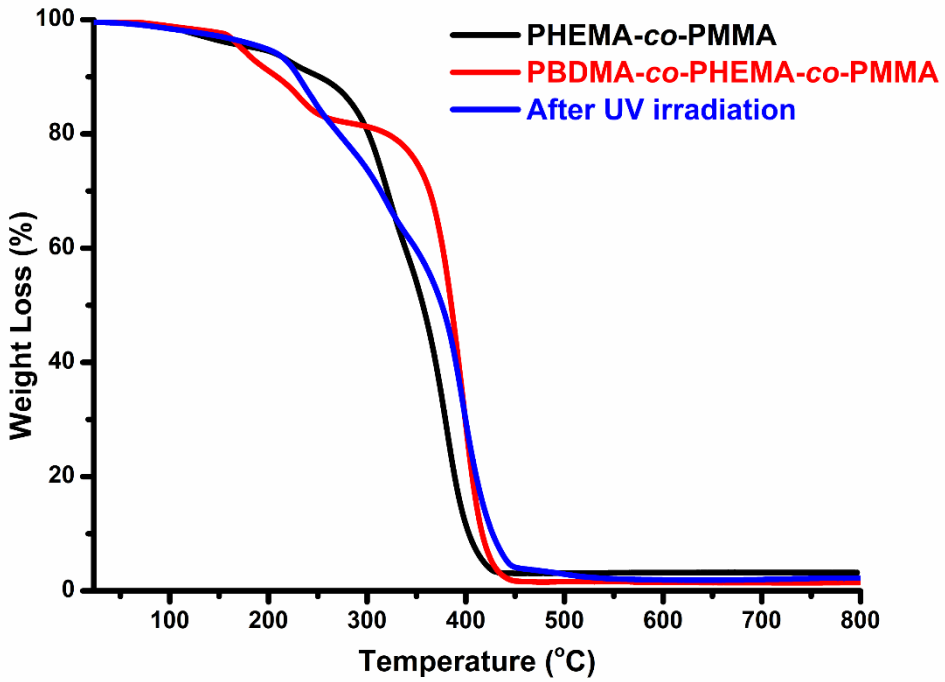

Figure 6. TGA thermogram of PHEMA-co-PMMA, BDMA-co-PHEMA-co-PMMA, and its acylated species after UV light irradiation.

CONCLUSION

In summary, a methacrylated benzodioxinone was synthesized under a mild condition and used as a co-monomer with 2-hydroxyethyl methacrylate and methyl methacrylate in the ATRP process to obtain random copolymer in one-step. The ester formation occurred through benzodioxinone's carbonyl group and the hydroxyl group of HEMA via acylation reaction upon UV photolysis. The formations of the obtained copolymer and its acylated species were confirmed by spectroscopic, chromatographic, and thermal analyses. The characteristic aromatic bands of benzodioxinone in the FT-IR and ^{1}H-NMR spectroscopies confirmed the chemical attachment of methacrylated benzodioxinone onto the linear polymer chain. In addition to this, the successful detection of ester bands in the FT-IR and ^{1}H-NMR spectroscopies was also proved the acylation process between antagonist benzodioxinone and hydroxyl groups of the PBDMA-*co*-PHEMA-*co*-PMMA. A slight decrease of the molecular weight after the photochemical acylation process was remarkably detected by gel permeation chromatography. Furthermore, thermal stabilities of the PBDMA-*co*-PHEMA-*co*-PMMA and its acylated product were also compared by DSC and TGA analyses. After the photochemical acylation process, thermal stability and glass transition temperature were clearly increased compared to the pristine PBDMA-*co*-PHEMA-*co*-PMMA.

REFERENCES

1. Klok HA, Lecommandoux S. Supramolecular materials via block copolymer self-assembly. Advanced Materials. 2001; 13(16): 1217-29.

2. Grayson SM, Frechet JM. Convergent dendrons and dendrimers: from synthesis to applications. Chemical Reviews. 2001; 101(12): 3819-68.

3. Cho I. New ring-opening polymerizations for copolymers having controlled microstructures. Progress in Polymer Science. 2000; 25(8): 1043-87.

4. Song A, Parker KA, Sampson NS. Synthesis of copolymers by alternating ROMP (AROMP). Journal of the American Chemical Society. 2009; 131(10): 3444-5.

5. Wang JS, Matyjaszewski K. "Living"/Controlled Radical Polymerization. Transition-Metal-Catalyzed Atom Transfer Radical Polymerization in the Presence of a Conventional Radical Initiator. Macromolecules. 1995; 28(22): 7572-3.

6. Kato M, Kamigaito M, Sawamoto M, Higashimuro T. Polymerization of methyl methacrylate with the carbon tetrachloride/dichlorotris-(triphenylphosphine) ruthenium (II)/methylaluminum bis (2, 6-di-tert-butylphenoxide) initiating system: possibility of living radical polymerization. Macromolecules. 1995; 28(5): 1721-3.

7. Rizzardo E, Chiefari J, Mayadunne R, Moad G, Thang S. Tailored polymer architectures by reversible addition-frasmentation chain transfer. Macromolecular Symposia. 2001; 174(1): 209-12.

8. Barner-Kowollik C, Davis PT, Heuts PAJ, Stenzel HM, Vana P, Whittaker M. RAFTing down under: Tales of missing radicals, fancy architectures, and mysterious holes. Journal of Polymer Science Part A: Polymer Chemistry. 2003; 41(3): 365-75.

9. Matyjaszewski K, Xia J. Atom transfer radical polymerization. Chemical Reviews. 2001; 101(9): 2921-90.

10. Kamigaito M, Ando T, Sawamoto M. Metal-catalyzed living radical polymerization. Chemical Reviews, 2001; 101(12): 3689-746.

11. Wang JS, Matyjaszewski K. Controlled/"living" radical polymerization. Atom transfer radical polymerization in the presence of transition-metal complexes. Journal of the American Chemical Society. 1995; 117(20): 5614-5.

12. Percec V, Barboiu B. "Living" Radical Polymerization of Styrene Initiated by Arenesulfonyl Chlorides and CuI (bpy) nCl. Macromolecules. 1995; 28(23): 7970-2.

13. Georges MK, Veregin RPN, Kazmaier PM, Hemer GK. Narrow molecular weight resins by a free-radical polymerization process. Macromolecules. 1993; 26(11): 2987-8.

14. Hawker CJ, Bosman AW, Harth E. New polymer synthesis by nitroxide mediated living radical polymerizations. Chemical Reviews. 2001; 101(12): 3661-88.

15. Patten TE, Xia J, Abernathy T, Matyjaszewski K. Polymers with very low polydispersities from atom transfer radical polymerization. Science. 1996; 272(5263): 866-8.

16. Wang JS, Matyjaszewski K. Controlled/"living" radical polymerization. Halogen atom transfer radical polymerization promoted by a Cu (I)/Cu (II) redox process. Macromolecules. 1995; 28(23): 7901-10.

17. Matyjaszewski K. New (co) polymers by atom transfer radical polymerization. Macromolecular Symposia. 1999; 143(1): 257-68.

18. Matyjaszewski K. General concepts and history of living radical polymerization. Handbook of Radical Polymerization. 2002; 361-406.

19. Patten TE, Matyjaszewski K. Copper (I)-catalyzed atom transfer radical polymerization. Accounts of Chemical Research. 1999; 32(10): 895-903.

20. Tasdelen MA, Yagci Y. Benzodioxinone Photochemistry in Macromolecular Science: Progress, Challenges, and Opportunities. ACS Macro Letters. 2017; 6(12): 1392-7.

21. Kumbaraci V, Talinli N, Yagci Y. Photoinduced synthesis of oligoesters. Macromolecules. 2006; 39(18): 6031-5.

22. Tasdelen MA, Kumbaraci V, Talinli N, Yagci Y. Photochemically masked benzophenone: Photoinitiated free radical polymerization by using benzodioxinone. Polymer. 2006; 47(22): 7611-4.

23. Kumbaraci V, Aydogan B, Talinli N, Yagci Y. Naphthodioxinone-1, 3-benzodioxole as photochemically masked one-component type II photoinitiator for free radical polymerization. Journal of Polymer Science Part A: Polymer Chemistry. 2012; 50(13): 2612-8.

24. Tasdelen MA, Kumbaraci V, Jockusch S, Turro NJ, Talinli N, Yagci Y. Photoacid generation by stepwise two-photon absorption: photoinitiated cationic polymerization of cyclohexene oxide by using benzodioxinone in the presence of iodonium salt. Macromolecules, 2008. 41(2): 295-7.

25. Leibfarth FA, Kang M, Ham M, Kim J, Campos LM, Gupto N, Moon B, Hawker CJ. A facile route to ketene-functionalized polymers for general materials applications. Nature Chemistry. 2010; 2(3): 207-12.

26. Leibfarth FA, Schneider Y, Lynd NA, Schultz A, Moon B, Kramer EJ, Bazan GC, Hawker CJ. Ketene functionalized polyethylene: Control of cross-link density and material properties. Journal of the American Chemical Society. 2010; 132(42): 14706-9.

27. Wolffs M, Kade MJ, Hawker CJ. An energy efficient and facile synthesis of high molecular weight polyesters using ketenes. Chemical Communications. 2011; 47(38): 10572-4.

28. Arslan M, Motallebzadeh A, Kiskan B, Demirel AL, Kumbaraci V, Yagci Y. Combining benzoxazine and ketene chemistries for self-healing of high performance thermoset surfaces. Polymer Chemistry. 2018; 9(15): 2031-9.

29. Alkan Goksu Y, Kumbaraci V, Yagci Y. Modular photoinduced grafting onto approach by ketene chemistry. Journal of Polymer Science Part A: Polymer Chemistry. 2019; 57(3): 274-80.

30. Aydogan C, Ciftci M, Kumbaraci V, Talinli N, Yagci Y. Hyperbranced Polymers by Photoinduced Self-Condensing Vinyl Polymerization Using Bisbenzodioxinone. Macromolecular Chemistry and Physics. 2017; 218(10): 1700045.

31. Cross SE, Anderson C, Roberts MS. Topical penetration of commercial salicylate esters and salts using human isolated skin and clinical microdialysis studies. British Journal of Clinical Pharmacology. 1998; 46(1): 29-35.

32. Durmaz YY, Kumbaraci V, Demirel AL, Talinli N, Yagci Y. Graft Copolymers by the Combination of

ATRP and Photochemical Acylation Process by Using Benzodioxinones. Macromolecules. 2009; 42(11): 3743-3749.

33. Soltani O, De Brabander JK. Synthesis of functionalized salicylate esters and amides by photochemical acylation. Angewandte Chemie International Edition. 2005; 44(11): 1696-9.

34. Tasdelen MA, Taskin OS, Celik C. Orthogonal Synthesis of Block Copolymer via Photoinduced CuAAC and Ketene Chemistries. Macromolecular Rapid Communications. 2016; 37(6): 521-6.

35. Kumbaraci V, Talinli N, Yagci Y. Photoinduced crosslinking of polymers containing pendant hydroxyl groups by using bisbenzodioxinones. Macromolecular Rapid Communications. 2007; 28(1): 72-7.

36. Patel M, Braden M, Davy K. Polymerization shrinkage of methacrylate esters. Biomaterials. 1987; 8(1): 53-6.

37. Levi G, Karel M. Volumetric shrinkage (collapse) in freeze-dried carbohydrates above their glass transition temperature. Food Research International. 1995; 28(2): 145-51.

38. Dewaele M, Asmussen E, Peutzfedt A, Munksgaard EC, Benetti AR, Finne G, Leloup G, Devaux J. Influence of curing protocol on selected properties of light-curing polymers: degree of conversion, volume contraction, elastic modulus, and glass transition temperature. Dental Materials. 2009; 25(12): 1576-84.

39. Caykara T, Özyürek C, Kantoğlu Ö. Investigation of thermal behavior of poly (2-hydroxyethyl methacrylate-co-itaconic acid) networks. Journal of Applied Polymer Science. 2007; 103(3): 1602-7.

40. Acevedo B, Martinez F, Olea A. Synthesis, thermal behavior, and aggregation in aqueous solution of poly (methyl methacrylate)-b-poly (2-hydroxyethyl methacrylate). Journal of the Chilean Chemical Society. 2013; 58(4): 2038-42.

41. Marcilla A, Beltran M. Kinetic study of the thermal decomposition of polystyrene and polyethylene-vinyl acetate graft copolymers by thermogravimetric analysis. Polymer Degradation and Stability. 1995; 50(1): 117-24.

42. Maurin MB, Dittert LW, Hussain AA. Thermogravimetric analysis of ethylene-vinyl acetate copolymers with Fourier transform infrared analysis of the pyrolysis products. Thermochimica Acta. 1991; 186(1): 97-102.

JOTCS A
Journal of the Turkish Chemical Society
Section: A
Chemistry
TURKISH CHEMICAL SOCIETY

Chemical compounds, antioxidant properties, and antimicrobial activity of olive leaves derived volatile oil in West Anatolia

Nilüfer Vural[1,2], M. Abdülkadir AKAY[3]

[1]*University of Ankara Yıldırım Beyazıt, Vocational School, Department of Food Processing-Food Technology, Çubuk, Ankara, Turkey*
[2]*University of Ankara Yıldırım Beyazıt, Institute of Public Health, Department of Traditional, Complementary and Integrative Medicine Practice and Research Center, Etlik, Ankara, Turkey*
[3]*University of Ankara, Faculty of Science, Department of Chemistry, Tandogan, Ankara 06100, Turkey*

Abstract: In this article, the chemical compounds, antimicrobial and antioxidant activity of the volatile oil from leaves of *Olea europaea* L. cultivar from Turkey (Ayvalık) has been studied. The essential oil was provided with a Clevenger apparatus and analyzed by GC-MS/FID. This analysis leads to the detection of 42 compounds representing 99.59±1.15% of the total oil. The major constituents were a-pinene (9.82±0.33%), benzylalcohol (8.83±0.27%), phenethylalcohol (8.52±0.25%), 2-monopalmitin (8.13±0.28%), palmitic acid (5.53±0.41%), octadecanoic acid 2,3-dihydroxypropylester (5.84±0.42%), phytol (4.22±0.17%), and benzaldehyde (4.21±0.38%). The antimicrobial activities of the dried leaves essential oils were assessed against seven bacterial and four fungal strains. Significantly, the essential oil has an efficient antibacterial activity toward to the bacterial strains such as *Bacillus cereus* ATCC 14579, *Candida albicans* ATCC 10231, *Enterococcus faecalis* ATCC 29212 and *Klebsiella pneumonia*e ATCC 13883. The olive a leaf essential oils showed significant antimicrobial and antioxidant effects. This study gives more knowledge for the development of this crucial therapeutic plant.

Keywords: *Olea europaea L. Leaves volatile oils, GC-MS/FID, Chemical composition, Antimicrobial activity, Antioxidant activity*

Submitted: November 29, 2020. **Accepted:** March 17, 2021.

Cite this: Vural N, Akay MA. Chemical compounds, antioxidant properties, and antimicrobial activity of olive leaves derived volatile oil in West Anatolia. JOTCSA. 2021;8(2):511–8.

DOI: https://doi.org/10.18596/jotcsa.833139.

***Corresponding author.** e-mail: nvural71@gmail.com, n.vural@ybu.edu.tr.

INTRODUCTION

Olea europaea L. is one of the most important fruit trees in Mediterranean countries, especially in Spain, Italy, France, Greece, Turkey, Tunisia, and Morocco (1). In Turkey, Ayvalık region of the Balıkesir province has the most plentiful olive variety representing more than 19% of in Turkey's whole olive trees.

Olive leaf is the origin of many phytochemicals such as polyphenolics and flavonoids, which accomplish many antioxidant, antibacterial, antifungal, and anti-inflammatory activity (2-10). In folk medicine, it is reported that the decoction prepared from the leaves is used for hypertension, arrhythmia, intestinal muscle spasms, and cancer treatment (11-14). In Turkey, congenital coronary artery anomalies are commonly seen at the rate of 0.2-1.2%. Coronary artery anomalies such as angina, significant hemodynamic abnormalities and myocardial infarction are essential because of the occurrence and sudden death (15).

Essential oils possess specific volatile odors or flavors obtained from various plant parts like

flowers, seeds, and leaves. Essential oils with various chemical components such as phenols, flavones, flavonoids, and terpenes, etc. show antibacterial, anti-cancer, antifungal, and anti-oxidant activities (16).

There are very few studies on the extract obtained by hydrodistillation of *Olea europaea* L. leaves and its essential oil content, antioxidant and antimicrobial effect in the literature. This study's primary purpose was to identify the constituents of *Olea europaea* L. essential oil by GC/MS spectrometric method and investigate the chemical characterization, antioxidant, and antimicrobial activities of the volatile oil from Ayvalık flora of Turkey.

EXPERIMENTAL SECTION

Plant material

Fresh leaves of *Olea europaea* L. cv. were picked up in October 2017 from Ayvalık (Turkey), a region in Balıkesir Province on the Aegean Sea coast located at 39°16′40.55N and 26°42′47.77E. The Mediterranean climate is dominant in this region, characterized by hot and dry summers and mild and rainy winters. The mean temperature is between 24-34 °C. West winds from the weather cool the region. The average annual rainfall is about 700 mm. The altitude of the region is 270 m.

The voucher specimen was described and stocked at Herbarium Turcicum, Ankara Herbarium Voucher No: 60542 (Department of Biology, Ankara University, Ankara, Turkey). Part of the leaves was washed, cleaned, and shade-dried at room temperature without an airflow (25 °C) for 15 days. After drying, olive leaf samples were milled and became ready for hydrodistillation.

Isolation of the volatile oils

The volatile oils were obtained by hydrodistillation in a Clevenger-type apparatus from *Olea europaea* L. leaves. To get a colorful oil with a yield of 0.06% (w/w), each dried sample (200 g) consisted of the leaves of upper branch parts of the plants were exposed to water (500 mL) distillation in a Clevenger apparatus for 3.5 h. The gained volatile oil was dried over anhydrous Na_2SO_4, then filtered, evaporated, and concentrated under a gentle stream of N_2 (nitrogen gas) and stored at 4 °C until analyzed.

Volatile oil analysis

GC analyses were made with a Shimadzu (Kyoto, Japan) GC17B instrument equipped with TC-5 capillary column (50 m×0.25 mm, film thickness 0.25 μm). The working conditions: oven temperature program consisted of a 10-min hold at 60 °C, followed by a 5 °C/min rise to 220 °C. The injector and FID detector temperature were maintained at 250 °C. The detector carrier gas was nitrogen (2 mL/min), FID split ratio was 1:25, and injection volume was 1 μL. The identification of the components was made by comparing their retention times with those of pure authentic samples. Simultaneously, linear retention indices (LRI) according to n-alkane series were also evaluated for component identification (1,17). Relative amounts of the individual components were calculated based on GC peak areas with FID response factor correction. The oil samples were analyzed by direct, splitless injection.

A Shimadzu (Kyoto, Japan) GC/MS QP2010 apparatus via the capillary column (TC-5/MS; 50 m x 0.25 mm i.d. film thickness 0.25 μm) equipped with electron ionization quadrupole detector (m/z 35-650) was used to determine the chemical composition of the samples. 1.2 mL/min flow rate for the carrier helium gas, 240 °C for injection heat, and 290 °C temperatures for the MS transfer line was selected. The column temperature was initially set at 50 °C and held for 3 min., then increased to 280 °C at the rate of 3 °C/min. and fit for 5 min at that temperature. Diluted samples (1:15 [v/v], in acetone) of 1.0 μL amounts were injected in a splitless manner.

The constituents were identified based on comparing their mass spectra with those of NBS75K, Wiley 7, NIST MS 2.0 library search data of the GC-MS system, standards of the main components, and literature data.

Total antioxidant activity (TAA)

DPPH (diphenylpicrylhydrazyl) assay

The TAA of the volatile fraction was measured by the reduction of alcoholic DPPH solutions in the existence of an electron-donating antioxidant (EDA) by modifying the method described by Gil et al. (18). Briefly, 100 μL aliquots of various concentrations of the volatile olive leaf extracts were added to 2.9 mL of a 2,2-diphenyl-1-picrylhydrazyl (DPPH; 6.10^{-5} M DPPH; 2.4 mg/100 mL of methanol). After a 40 min. incubation at 30 °C temperature in the dark, the absorbance was read at 520 nm. Percentage inhibition of free radical DPPH was calculated in the following manner:

$$\text{Inhibition \%} = [(A_{control}-A_{sample})/ A_{control}] \times 100$$

where $A_{Control}$ is the absorbance of the control and A_{sample} is the absorbance of the sample.

The volatile oil concentration providing 50% inhibition (IC_{50}) was calculated from the graph plotting of inhibition free radical DPPH in percentage (%) against essential oil concentration. As a positive control, butylated hydroxytoluene (BHT), a synthetic

antioxidant reagent, was used. All tests were carried out in triplicate.

Antimicrobial activity (AmA)

Source of Microorganisms

The bacterial strains tested were *Bacillus cereus* ATCC 14579, *Enterococcus faecalis* ATCC 29212, *Escherichia coli* ATCC 25922, *Klebsiella pneumoniae* ATCC 13883, *Lactobacillus plantarum* ATCC 8014, *Pseudomonas aeruginosa* ATCC 15442 and *Staphylococcus aureu*s ATCC 27950. In the case of yeasts, *Candida albicans* ATCC 10231, *Candida glabrata* ATCC 90030, *Candida kreusei* ATCC 34077, and *Candida parapsilosis* ATCC 22019. All these cultures were purchased from the culture collections of the National Type Culture disperse Collection Unit, Microbiology Reference Laboratory and Biological Products Department, Public Health General Directorate, Ministry of Health, (Ankara, Turkey).

Disc Diffusion Method

All method steps, including preparation conditions of test microorganisms, inoculation instructions, bacteria and yeast incubation times, were studied according to Vardar-Ünlü et al., (19). Briefly, a suspension of the test micro-organism (0.1 mL, 108 cells mL^{-1}) was spread on solid medium plates. Filter paper discs (6 mm in diameter) (Schleicher and Schüll, No.2668, Germany) were soaked with 30 µL of the oil and placed on the inoculated plates. After keeping the plates at 4 °C for 2 h, they were incubated at 37 °C for 24 h (bacteria) or at 30 °C for 48 h (yeasts). Following the incubation period, the diameters (mm) of the inhibition zones were measured. The diameters (mm) of the inhibition zones were quantified, and the results were classified into three categories according to the diameters obtained in the test: resistant (> 7 mm), medium (> 12 mm) and sensitive (> 18 mm) (20).

Minimum inhibitory concentration (MIC) Method

A microdilution broth susceptibility assay for bacteria and yeast was used to determine the MIC (21). Preparation, incubation, and counting of bacterial strains, yeasts, and test strains were performed consistent with the method of Ünlü et al. (22). All tests were performed in Mueller Hinton broth (MHB; BBL) supplemented with Tween 80 detergent (final concentration of 0.5%, v/v) to enhance the oil solubility. Bacterial strains were cultured overnight at 37 °C in MHA and the yeasts were cultured overnight at 30 °C in Sabouraud dextrose broth (SDB). Test strains were suspended in MHB to give a final density of 5 x 10^5 colony-forming units (CFU)/mL and were confirmed by viable counts. The essential oil's geometric dilutions were prepared in a 96-well microtiter plate, including one growth control (MHB + Tween 80) and one sterility control (MHB + Tween 80 + test oil). Plates were incubated under normal atmospheric conditions at 37 °C for 24 h for bacteria and at 30 °C for 48 h for the yeasts. British Society for Medical Mycology (BSMM) guidelines were used for broth microdilution testing for yeasts. The essential oil was resolved in Yeast Nitrogen Base Glucose (YNBG) supplemented with Tween 80 detergent (final concentration 0.5% v/v) and ultimate concentrations ranged from 100.00 mg/mL to 0.025 mg/mL (22).

Statistical Analysis

The data were statistically analyzed by ANOVA (n=3) and statistical significance was accepted at a level of $p< 0.05$ (23).

RESULTS AND DISCUSSION

Chemical Composition of volatile oil

The composition of *Olea europaea* L. volatile oil was analyzed by GC-MS. 42 compounds, representing 99.59±1.15% of the oil, were identified. The main components are α-pinene (9.82±0.33%), benzyl alcohol (8.83±0.27%), phenethyl alcohol (8.52±0.25%), 2-monopalmitin (8.13±0.28%), palmitic acid (5.53±0.41%), octadecanoic acid 2,3-dihydroxypropyl ester (5.84±0.42%), phytol (4.22±0.17%), benzaldehyde (4.21±0.38%) (Table 1). In our study, alcohols were characterized by the presence of eleven compounds (32.92±0.56 %), the most important of them were benzyl alcohol (8.83±0.27%), phenethyl alcohol (8.52±0.25%), followed by phytole (4.22±0.17%). The second priority group was aldehydes composed of five compounds (9.42%) mainly, benzaldehyde (4.21±0.38%) and, 2,4-heptadienal (2.91±0.23%). The ester group was characterized by 2-monopalmitin (8.13±0.28%).

Table 1. The main leaf volatiles (%) *of Olea europea L*. collected in the Ayvalık, Turkey.

	Constituents	LRI lit.	LRI cal.	%	Method of identification
Alcohols	1-penten-3-ol	683	678	1.81±0.09	MS
	2-ethoxyethanol	717	715	2.22±0.22	MS
	cis-3-hexene-1-ol	857	860	1.23±0.07	MS
	trans- 2-hexene-1-ol	868	870	2.62±0.24	CO, MS
	1-hexanol	884	881	1.21±0.09	CO, MS
	Benzyl alcohol	1007	1005	8.83±0.27	MS
	Phenethyl alcohol	1110	1112	8.52±0.25	MS
	p-cymen-8-ol	1183	1187	0.72±0.11	CO, MS
	Eugenol	1356	1350	0.33±0.02	CO, MS
	Isoeugenol	1384	1388	1.21±0.09	CO, MS
	Phytol	1840	1841	4.22±0.17	CO, MS
Aldehydes	n-Hexanal	784	785	0.73±0.12	CO, MS
	Benzaldehyde	996	998	4.21±0.38	MS
	2,4-heptadienal	1009	1008	2.91±0.23	MS
	n-octanal	1023	1022	0.23±0.02	MS
	Nonanal	1098	1100	1.34±0.08	CO, MS
Esters	2-Monopalmitin	2498	2493	8.13±0.28	CO, MS
Terpenes	α- pinene	941	968	9.82±0.33	CO, MS
	β- caryophyllene	1421	1420	2.01±0.18	MS
Carb. Acids	Hexanoic acid	1085	1092	0.42±0.03	MS
	Caprylic acid	1179	1182	0.64±0.05	MS
	Nonanoic acid	1280	1280	0.72±0.12	MS
	Myristic acid	1720	1718	0.71±0.11	MS
	Palmitic acid	1973	1968	5.53±0.41	MS
	Stearic acid	2124	2125	1.32±0.07	CO, MS
Hydrocarbons	2,2,6-trimethyloctane	1029	1030	2.44±0.22	CO, MS
	Undecane,5-methyl	1154	1157	0.23±0.02	CO, MS
	Dodecane,4,6-dimethyl	1285	1288	1.22±0.06	MS
	n-Tetradecane	1399	1400	1.53±0.06	MS
	n-Hexadecane	1600	1601	1.82±0.07	MS
	n-Heptadecane	1700	1700	0.82±0.11	MS
	1-chloro octadecane	2070	2068	1.47±0.09	MS
	Heneicosane	2100	2100	0.94±0.08	MS
	Tetracosane	2500	2501	0.88±0.05	MS
	Octadecanoic acid, 2,3-dihydroxypropyl ester	2689	2690	5.84±0.42	MS
Others	1-hydroxy-2-propanone	698	695	0.93±0.08	MS
	Trichloroethene	702	698	0.47±0.02	CO, MS
	4-Ethenylpyridine	1037	1040	2.25±0.18	MS
	Methyldiethanolamine	1053	1055	1.53±0.07	MS
	5-chloro-n- amylacetate	1129	1131	1.34±0.04	MS
	4-Ethenyl-2-methoxyphenol	1283	1284	1.32±0.05	MS
	Benzene, (2-propenyloxy) methyl	1405	1404	2.92±0.23	MS
	Total identified			**99.59±1.15**	

LRI: linear retention indices (HP5-MS column); MS, mass spectrometry; CO, co-injection with standards; LRI_{lit}, retention indices from the literature (10); LRI_{calc}, experimental retention indices calculated against a C_8–C_{32} n-alkanes mixture on the HP5-MS column
All values are mean ± standart deviation of triplicates.

We were able to find a limited number of articles associated with the essential oil compositions of *Olea europaea* L. (1, 24-28). In several previous studies, the chemical composition of the volatile fractions from *Olea europaea* L. cultivars was investigated. Most of these studies focused on the regions, showing similar climatic and geographic characteristics of the Mediterranean basin. In one of these researches, three Italian *Olea europaea* L. cultivars (Leccino, Frantoio, and Cipressino) were investigated in different years and months (July and November) by Campeol et al. (24, 25). In a Tunisian investigation, Chemlali cultivar was studied by Haloui et al. (26) and Nebjemel, Chemchali, Chemlali and Chetou cultivars were studied in October by Brahmi et al. (1, 27).

In the northern part of Algeria, olive leaves collected in September at an altitude of 800 m were investigated (28). The essential constituents in either plant were determined as (E)-2-hexenal, nonanal, kongol, benzene-acetaldehyde, (E)-β-

damascone, (E)-β-damascenone, (E,E)-a-farnesene and (E)-2-hexen-1-ol (24, 25). The main components were found as (E)-3-hexenol, 3-ethenylpyridine, (E)-β-damascenone, and phenylethyl alcohol (1).

Brahmi et al. (27) have identified the compounds forming 92.10% of the total volatile oil. Consistent with our study, Brahmi et al. (27) determined that there was the highest amount (6.10%) of phenylethyl alcohol in the alcoholic group, which was characterized by the presence of four compounds. Aldehydes were composed of nine compounds, primarily nonanal. Volatile compounds, characterizing at least 99.23% of the essential oils, were identified as a-pinene (52.70%), 2.6-dimethyl-octane (16.57%) being the most abundant components of the essential oil. The other chemical components were 2-methoxy-3-isopropylpyrazine (6.01%), tetracosane (4.38%) and docosane (3.58%). The following chemical components occurred in trace amounts: β-pinene (2.46%), z-3-hexanol (1.51%), (*E, Z*)- 2,6-nonadienal (1.46%), α-ionone (1.45%) and (*E*)-2-hexanol (1.26%) (26).

Boukhebti et al. (28) have analyzed and identified the volatile oil components of *Olea europaea* leaves which represent 94.10% of the total oil. The chemical composition of the essential oil is dominated by the compounds, palmitic acid (14.71%), Z-nerolidol (9.45%) and octacosane (6.32%).

Keskin et al. (29) reported that the chemical constitutions of aqueous extract (using a Soxhlet apparatus) from West Anatolia, Turkey were analyzed by GC/MS. GC/MS analysis of the extract resulted in the identification of fifteen constituents, representing 99.68% of the extracts; cyclotrisiloxane, hexamethyl (36.98%), cyclotetrasiloxane, octamethyl (15.18%) and cyclopentasiloxane, decamethyl (14.59%) being the main components.

In other articles focusing on the same cultivars or different cultivars growing in particular habitats, the role of environmental effects are studied and its importance is emphasized. Further investigations would probably explain and generalize the obtained data.

Total antioxidant activity (TAA) of volatile oil

The weakest TAA was exhibited by the volatile oil 70.68±2.4% and 3080±11.2 IC_{50} (µg/mL) (Table 2). The activities were compared with BHT. The volatiles of the dried leaves showed tolerable TAA and lower than the reference antioxidant, BHT (IC_{50}= 28.8 ±1.4 µg/mL; 85.12± 4.8%).

This observation is consistent with the other reports. In previous studies on the dried olive leaves, it is shown that DPPH IC_{50} (µg/mL) values vary in different cultivars. Brahmi et al. (1) reported that DPPH values were found 3430.70±51.36 (µg/mL), 3190.52±89.50 (µg/mL) and 3250.11±46.52 (µg/ml) respectively. Brahmi et al. (27) described that the essential oil exhibited the weakest TAA (49.92%), Haloui et al. (26) reported that the TAA was exhibited by the essential oil (74.44%±0.79).

Table 2. Antioxidant activity of the essential oil of *Olea europaea L.*

Sample	**DPPH radical scavenging activity, %**	**DPPH IC_{50}(µg/mL)**
Essential oil of *Olea europaea L* leaves	70.68 ± 2.40	3080.00 ±11.22
BHT	85.12 ± 4.80	28.20 ± 1.40

Results are means of three different experiments.

Antimicrobial activity (AmA) of volatile oil

The AmA of the volatile oil was examined for 7 bacteria and 4 Candida species using disk diffusion and MIC methods. (Table 3). Comparing the essential oils with the control antibiotic and control antifungal concluded that they could inhibit most bacterial growths with different effectiveness.

Table 3. Antimicrobial activity of essential oil from *Olea Europea* L. leaves.

	***Olea europaea L.* essential oil**			
Microorganisms	**Disc Diffusion[a]**	**MIC values (µg/mL)**	**Amphotericin** (Control Antifungal)	**Gentamicin** (Control Antibiotic)
Bacillus cereus ATCC 14579 (+)	29.00±0.50	1100	nd	1500
Enterococcus faecalis ATCC 29212	13.00±0.01	1750	nd	2100
Escherichia coli ATCC 25922	9.00±0.09	70	nd	1750
Klebsiella pneumoniae ATCC 13883	11.00±0.02	1500	nd	2250
Lactobacillus plantarum ATCC 8014 (+)	9.00±0.03	50	nd	750
Pseudomonas aeruginosa ATCC 15442	13.00±0.05	150	nd	1100
Staphylococcus aureus ATCC 27950 (+)	10.00±0.04	70	nd	2100
Candida albicans ATCC 10231	17.00±0.11	1250	600	nd
Candida glabrata ATCC 90030	9.00±0.15	150	550	nd
Candida kreusei ATCC 34077	7.00±0.06	250	500	nd
Candida parapsilosis ATCC 22019	7.00±0.21	-	450	nd

[a]DD, disc diffusion method; diameter of inhibition zone (mm) including disk diameter of 6 mm.
MIC, minimum inhibitory concentration; values given as µg mL^{-1} for the essential oils and antibiotics.
n.d. not determined
Disc diffusion values are expressed as mean±SD (n=3)
DMSO: Negative control

This study revealed that the volatile oil has efficient antibacterial activity toward bacterial strains, especially *Bacillus cereus* ATCC 14579, *Candida albicans* ATCC 10231, *Enterococcus faecalis* ATCC 29212, *Pseudomonas aeruginosa* ATCC 15442, *Klebsiella pneumoniae* ATCC 13883, *Staphylococcus aureus* ATCC 27950, *Candida glabrata* ATCC 90030. On the flip side, there is an inference that the essential oil's antimicrobial activity (resistant >7 mm) has no significant effect on *Candida kreusei* ATCC 34077 and *Candida parapsilosis* ATCC 22019. Susceptibility of the oil, amphotericin (control antifungal) and, gentamicin (control antibiotic) was expressed as a minimum inhibitory concentration (MIC) and, DMSO was used as a negative control.

Brahmi et al. (1) also analyzed the AmA of dried olive leaves. They found that essential oil has very remarkable antibacterial activity towards bacterial strains *E. faecali*s ATCC 29212 70 *S. aureus* ATCC 27950 *E. coli* ATCC 25922 *P. aeruginosa* ATCC27950 *C. Kreusei* ATCC6258 *C. parapsilosis* ATCC *C. albicans* ATCC90028 *C. glabrata* ATCC90030. While Boukhebti et al. (21) established similar results with *Citrobacter freundii* ATCC 8090, *Pseudomonas aeruginosa* ATCC 27853 and, *Staphylococcus aureus* ATCC 25923, while not having great antibacterial activity against *Bacillus subtilis* ATCC 6633 and *Escherichia coli* ATCC 25922.

CONCLUSION

Olive leaves are considered a by-product of the olive tree cultivation and oil industry. Interest in alternative uses of these agro-food by-products has increased significantly in recent years. Endowed with engaging biological activities, many studies focused on valorizing olive leaves in the food industry as a functional food or as a source of nutraceuticals.

In this study, to our knowledge, the antioxidant and antimicrobial activities of the essential oil obtained from the olive leaves in West Anatolia in Turkey were tested for the first time. According to the results obtained from this work, the volatile compounds of dried olive leaves have very high, antibacterial and antifungal properties that may benefit the pharmaceutical, food, and cosmetics industries. It has been determined that especially essential oils have a very impressive antibacterial activity against bacterial strains such as *Bacillus cereus* ATCC 14579, *Candida albicans* ATCC 10231, *Enterococcus faecalis* ATCC 29212 and *Klebsiella pneumoniae* ATCC 13883. However, the leaves' essential oil showed a lower, tolerable antioxidant activity than the reference antioxidant BHT. On the other hand, it can also be concluded that the changes in the Olea europea L. volatile oil chemical compositions, from different geographical areas, might have been based on different variables, climatic, seasonal, geographical, and geological differences.

COMPLIANCE WITH ETHICAL STANDARDS

Conflict of interest

The authors declare no conflict of interest.

REFERENCES

1. Brahmi F, Flamini G, Issaoui M, Dhibi M, Dabbou S, Mastouri M, Hammami M. Chemical composition and biological activities of volatile fractions from three Tunisian cultivars of olive leaves. Medicinal Chemistry Research. 2012; 21(10): 2863-72. Doi: 10.1007/s00044-011-9817-8

2. Borges A, Jose H, Homem V, Simoes M. Comparison of techniques and solvents on the antimicrobial and antioxidant potential of extracts from *Acacia dealbata* and *Olea europaea.* Antibiotics. 2020; 9(2): 48. Doi:10.3390/antibiotics9020048

3. Debib A, Boukhatem MN. Phenolic content, antioxidant and antimicrobial activities of "Chemlali" olive leaf (*Olea europaea* L.) extracts. International Journal of Pharmacology, Phytochemistry and Ethnomedicine. 2017; 6:38-46.Doi:10.18052/www.scipress.com/IJPPE. 6.38.

4. Vural N, Algan Cavuldak Ö, Akay MA. D-Optimal design and multi-objective optimization for green extraction conditions developed with ultrasonic probe for oleuropein. Journal of Applied Research on Medicinal and Aromatic Plants. 2021; 20: 100279. Doi: 10.1016/j.jarmap.2020.100279

5. Difonzo G, Squeo G, Pasqualone A, Summo C, Paradiso VM, Caponio F. The challenge of exploiting polyphenols from olive leaves: addition to foods to improve their shelf-life and nutritional value. Journal of the Science of Food and Agriculture. 2020. Doi: 10.1002/jsfa.10986

6. Nicolì F, Negro C, Vergine M, Aprile A, Nutricati E, Sabella E, Miceli A, Luvisi A, De Bellis L. Evaluation of phytochemical and antioxidant properties of 15 Italian *Olea europaea* L. Cultivar Leaves. Molecules. 2019; 24(10): 1998. Doi: 10.3390/molecules24101998

7. Chiaino E, Micucci M, Cosconati S, Novellino E, Budriesi R, Chiarini A, Frosini M. Olive leaves and *Hibiscus* flowers extracts-based preparation protect brain from oxidative stress-induced injury. Antioxidants. 2020; 9(9):806. Doi: 10.3390/antiox9090806

8. Samouh Y, Lemrani A, Mimouni H, Mohamad J, Said AAH. Ethnopharmacological Study of Herbal Medicines used to treat Cancer in Morocco. J Phytopharmacol 2019; 8(3):135-41. Doi:10.31254/phyto.2019.8309

9. Castillo JJ, Alcaraz M, Benavente-Garcia O. Antioxidant and radioprotective effects of olive leaf extract. Olives and olive oil in Health and Disease Prevention. 2010; 12: 951-8. Doi: 10.1016/B978-0-12-374420-3.00102-9

10. Venditti A, Serrilli AM, Rizza L, Frasca G, Cardile V, Bonina FP, Bianco A. Aromadendrine, a new component of the flavonoid pattern of Olea europaea L. and its anti-

inflammatory activity. Natural Product Research. 2013; 27(4):340-9. Doi: 10.1080/14786419.2012.693924
11. Khayyal MT, El-Ghazaly MA, Abdallah DM,.Nassar NN, Okpanyi SN, Kreuter MH. Blood pressure lowering effect of an olive leaf extract (*Olea europaea*) in L-NAME induced hypertension in rats. Arzneimittel-Forschung/Drug Research, 2002; 52(11):797–802.

12. Agalias A, Melliou E, Magiatis P, Mitaku S, Gikas E, Tsarbopoulos A. Quantitation of oleuropein and related metabolites in decoctions of Olea leaves from ten Greek cultivated varieties by HPLC with diode array detection (HPLC-DAD). Journal of Liq. Chr. & Related Tech. 2005; 28: 1557-71. Doi: 10.1081/JLC-200058355

13. Merrouni IA, Elachouri M. Anticancer medicinal plants used by Moroccan people: Ethnobotanical, preclinical, phytochemical and clinical evidence. Journal of Ethnopharmacology. 2021; 266:113435. Doi:10.1016/j.jep.2020.113435

14.Özcan MM, Matthäus B. A review: benefit and bioactive properties of olive (*Olea europaea* L.) leaves. European Food Research and Technology. 2017; 243(1): 89-99. Doi: 10.1007/s00217-016-2726-9
15. Çilingiroğlu S. Evaluation of coronary artery anomalies with angiography in Turkish adult population. Turkiye Klinikleri J Cardiovasc Sci. 2009; 21(3):363-9.

16. Upadhyay RK. Evaluation of antibacterial and antifungal activities of olive *(Olea europaea)* essential oil. International Journal of Green Pharmacy. 2014; 8(3): 180-6. Doi: 10.22377/ijgp.v8i3.382

17. Adams RP. Identification of essential oil components by Gas Chromatography/Quadrupole Mass Spectroscopy. 4th ed. Allured Publishing Corp, Carol Stream, IL. ISBN-10:1932633219. 2007.

18. Gil MI, Tomás-Barberán F A, Hess-Pierce B, Kader AA. Antioxidant capacities, phenolic compounds, carotenoids, and vitamin C contents of nectarine, peach, and plum cultivars from California. Journal of Agricultural and Food Chemistry. 2002; 50(17): 4976–82. Doi:10.1021/jf020136b

19. Vardar-Ünlü G, Ünlü M, Dönmez E, Vural N. Chemical composition and in vitro antimicrobial activity of the essential oil of *Origanum minutiflorum* O Schwarz & PH Davis. Journal of the Science of Food and Agriculture. 2007; 87(2): 255-9. Doi: 10.1002/jsfa.2708

20. Upadhyay RK. GC-MS analysis and in vitro antimicrobial susceptibility of *Foeniculum vulgare* seed essential oil. American Journal of Plant Sciences. 2015; 6: 1058-68. Doi: 10.4236/ajps.2015.67110.

21. NCCLS (National Committee for Clinical Laboratory Standards). Performance Standards
for Antimicrobial Susceptibility Testing, 9th International Supplement, M100-S9, Wayne, PA. 1999.

22. Ünlü M, Ergene E, Ünlü G V, Zeytinoglu H. S, Vural N. Composition, antimicrobial activity and in vitro cytotoxicity of essential oil from *Cinnamomum zeylanicum Blume* (Lauraceae). Food and Chemical Toxicology. 2010; 48(11): 3274-80. Doi: 10.1016/j.fct.2010.09.001

23. SAS/STAT® 9.1, SAS Institute, SAS User's Guide. SAS Institue Inc.,Cary, NC. 2004.

24. Campeol E, Flamini G, Chericoni S, Catalano S, Cremonini R. Volatile compounds from three cultivars of *Olea europaea* from Italy. Journal of Agricultural and Food Chemistry. 2001; 49(11): 5409-11. Doi: 10.1021/jf010455n

25. Campeol E, Flamini G, Cioni P. L, Morelli I, Cremonini R, Ceccarini L. Volatile fractions from three cultivars of *Olea europaea* L. collected in two different seasons. Journal of Agriculture Food Chem. 2003; 51: 1994−9. Doi: 10.1021/jf026025u

26. Haloui E, Marzouk Z, Marzouk B, Bouftira I, Bouraoui A, Fenina N. 2010. Pharmacological activities and chemical composition of the *Olea europaea* L. leaf essential oils from Tunisia. *Journal of Food Agriculture & Environment*. 8(2): 204-8.

27.Brahmi F, Flamini G, Mechri B, Dhibi M, Hammami M. Antioxidant activity of the leaf volatile oil and extracts of *Olea europaea* L.cv. Chetoui from N. Tunisia. Journal of Agricultural and Food Chemistry. 2015; 4(3):1-5. Doi: 10.4172/2324-9323.1000171

28. Boukhebti H, Chaker AN, Lograda T, Ramdani M. Chemical and antimicrobial properties of essential oils of *Olea europea* L. International Journal of Pharmacology & Toxicology. 2015; 5(1): 42-6.

29. Keskin D, Uğur A, Ceyhan N, Dbeys AD. Antimicrobial activity and chemical constitutions of West Anatolian olive (Olea europaea L.) leave. Journal of Food, Agriculture & Environment. 2012; 10(2): 99-102.

JOTCS A
Journal of the Turkish Chemical Society
Section: A
Chemistry
TURKISH CHEMICAL SOCIETY

Enhancement of Mechanical Property of Modified Polyurethane with bis-butyl succinate

Thi Sinh Vo[1]*, Tran Thi Bich Chau Vo[2], Tran Trung Tien[1], and Nguyen Truong Sinh[1]

[1]School of Mechanical Engineering, Sungkyunkwan University, Suwon 16419, Korea.
[2]Department of Industrial Management, Can Tho University, Can Tho, Vietnam.

Abstract: A new crosslinker (bis-butyl succinate, BBS) with terminal alkyne group has been explored in this study that can react with glycidyl azide polymer-based polyurethane (original PU) via "azide-alkyne" click reaction, which has supported enhanced mechanical properties and cross-link densities of modified PUs with BBS. Besides, this crosslinker has been designed and synthesized successfully via an esterification to incorporate with the original PU through the formation of 1,2,3-triazole groups. Notably, the mechanical properties of resultant modified PUs are investigated to indicate a relationship of mole ratio of $[C\equiv C]/[N_3]$ and cross-link density. Specifically, the stress and Young's modulus of the modified PUs increase (δ = 0.361–1.681 MPa, and E = 0.254–5.453 MPa), whereas their strain decrease (ε = 320.8–36.6%) on increasing the synthesized BBS content (mole ratio of $[C\equiv C]/[N_3]$ = 0–0.10) regarding to the increased rigid 1,2,3-triazole networks, as well as the cross-link densities of the modified PUs increase (v_e = 0.175–5.221 $mol\cdot cm^{-3}\cdot 10^4$, or v_e = 0.131–3.842 $mol\cdot g^{-1}\cdot 10^4$) with the BBS content (mole ratio of $[C\equiv C]/[N_3]$ = 0–0.10) through the Mooney-Rivlin equation. Resulting that there is an enhancement in the mechanical behaviors of the original PU cross-linked with BBS; concomitantly, the different mole ratio of $[C\equiv C]/[N_3]$ prepared in the present study can reveal new approaches for the design and future application of the original PU with alkyne compounds, as well as their desired cross-link densities can be controlled easily for powerful and selective reactions.

Keywords: Polyurethane, Crosslinker, Glycidyl azide polyol, Azide-alkyne click.

Submitted: February 11, 2021. **Accepted:** March 24, 2021.

Cite this: Vo TS, Vo TTBC, Tran TT, Nguyen TS. Enhancement of mechanical property of modified polyurethane with bis-butyl succinate. JOTCSA. 2021;8(2):519–26.

DOI: https://doi.org/10.18596/jotcsa.878515.

***Corresponding author. E-mail:** vtsinh92@skku.edu.

INTRODUCTION

As known, owing to lots of desirable and outstanding characterizations of polymeric materials such as softness, transparency, lightness, etc., there were a large number of polymers applied in various industrial materials. Among them, polyurethane (PU) is concerned to be a contender to other synthetically polymeric materials have been attracted attention recently in various applications (1-3). For a common synthesis of PU, it is based on a polycondensation between a segment with low molecular weight (named as pre-polymer) containing terminal hydroxyl groups and a diisocyanate (or a polyisocyanate). Besides, to reach desired PUs, it also depends on features of each reactant and polymeric material utilized in the different study purposes. For instance, Acik et al. (1) synthesized the biodegradable PU by a

step-growth polymerization of cholic acid with various loading ratios of L-lysine diisocyanate ethyl ester that could apply in several potential applications of drug delivery and tissue engineering technologies. Concomitantly, Acik et al. (3) also conducted a synthesis of another environmentally friendly PU based on ring-opening polymerization of ε-caprolactone with the presence of cholic acid – an initiator that could utilize in particularly tissue engineering and wound dressing applications.

Herein, a "azide-alkyne" click reaction is considered a significant classification for powerful and selective reactions. Specifically, 1,2,3-triazole networks between azide and alkyne groups have been appeared to be the most reported "azide-alkyne" click reaction (4-7). It obtained some useful advantages from high reaction yields, good functional group compatibility, strong reliability, as well as in mechanical behavior improvement. Although the crosslinkers have been wildly applied in different fields, a new crosslinker with terminal alkyne group (bis-butyl succinate, BBS) has been designed and synthesized to be employed reacting with glycidyl azide polymer-based polyurethane (original PU) via the "azide-alkyne" click reaction in this study. Interestingly, the crosslinker with terminal alkyne (-C≡C-) group can be synthesized by one-step method with an appropriate mole ratio of cheap reactants (Scheme 1), while glycidyl azide polyol with commercial availability is considered an azide compound containing terminal hydroxyl group is utilized in this study. Notably, this pre-polymer can bind with isocyanate (-N=C=O) compound that create the original PU (Scheme 2) owing to the available hydroxyl (-OH) groups on the pre-polymer chain. Concomitantly, the available azide ($-N_3$) groups on the original PU chain can also contribute binding with alkyne (-C≡C-) compound that create modified PU (Scheme 3) basing on the "azide-alkyne" click reaction. In particular, the modified PU's mechanical properties with BBS are also studied to manifest the effect of mole ratio of [C≡C]/[N_3] and cross-link density in this study.

MATERIALS AND METHODS

Materials

Toluene and dichloromethane (MC, +99.0%) were provided from Samchun Company. Magnesium sulfate ($MgSO_4$, +99.0%) was purchased from Junsei Company. Succinic anhydride (SA, ~99.0%), 3-butyn-1-ol (BTO, +98.0%), 4-(dimethylamino)pyridine (DMAP, ~99.0%), and N-N'-dicyclohexylcarbodiimide (DCC, ~99.0%) were procured from Alfa Aesar. Chloroform-d_1 ($CDCl_3$) was received from Merck. Glycidyl azide polyol was supplied by a Korean Company (the possible information of glycidyl azide polyol was shortly summarized in Table 1). The utilized water was obtained from a Milli-Q ultrapure water purification system.

Table 1. Possible information of glycidyl azide polyol.

Characterization	Details
Appearance	Amber liquid
Viscosity	12 Pa·s
Density	1.3 g/mL
Hydroxyl equivalent weight	2000
Water content	0.02 %
Functionality	Between 2.5 to 3 hydroxyl groups per molecule.
Reactivity	Gum stocks with 1:1 -NCO/-OH typically require added catalyst at 58 °C in a reasonable time.

Synthesis of bis-butyl succinate (BBS)

A mixture of SA, BTO, DMAP, DCC, and MC solvent was stirred in a two-necked round-bottomed flask at room temperature (24 h) and filtered through filter paper. The solution was washed with distilled water three times. The organic extracts were dried over $MgSO_4$ and the solvent was removed by rotary evaporator. The final crude product was purified by column chromatography (silica gel, ethyl acetate/hexane (v/v) = 5/5). The esterification scheme of BBS synthesis is shown in Scheme 1.

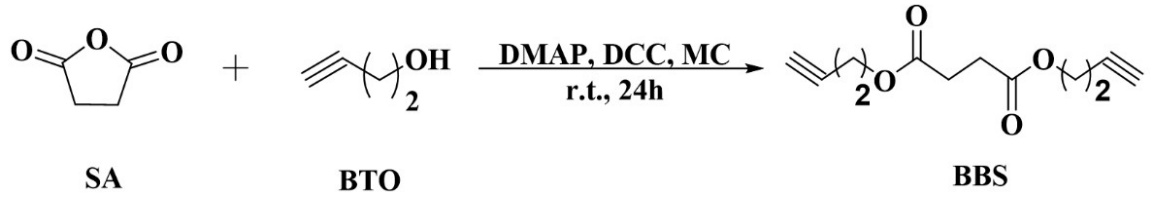

Scheme 1. Esterification scheme for the synthesis of BBS.

Bis-butyl succinate (BBS): ^{1}H NMR ($CDCl_3$, ppm): δ = 4.07 (t, 4H, -C***H₂***-O-); 2.53 (s, 4H, -C***H₂***-CO-); 2.40 (dt, 4H, ≡C-C***H₂***-); 1.95 (t, 2H, ***H***C≡C-). ^{13}C NMR ($CDCl_3$, ppm): δ = 172.04; 80.12; 70.17; 62.48; 29.01; 19.00.

Preparation of the Original PU

Glycidyl azide polyol (85.858 mmol) was dried at 60 °C under vacuum for 1 h and cooled down to 25–30 °C for 0.5 h. Next, IPDI (2.160 mmol) was rapidly added into the above glycidyl azide polyol and stirred at 25–30 °C. After 0.5 h, 20.0 wt% – TPB solution and 12.5 wt% – DNS solution were added and continued stirring (t = 0.5 h). Next, the above mixture was pulled into mold (3 cm x 8 cm) and put in the oven at 30 °C to remove the bubble under vacuum for 3 h; the curing process was carried out in the oven at 60 °C for 7 days (7). The reaction scheme of the original PU without BBS is shown in Scheme 2.

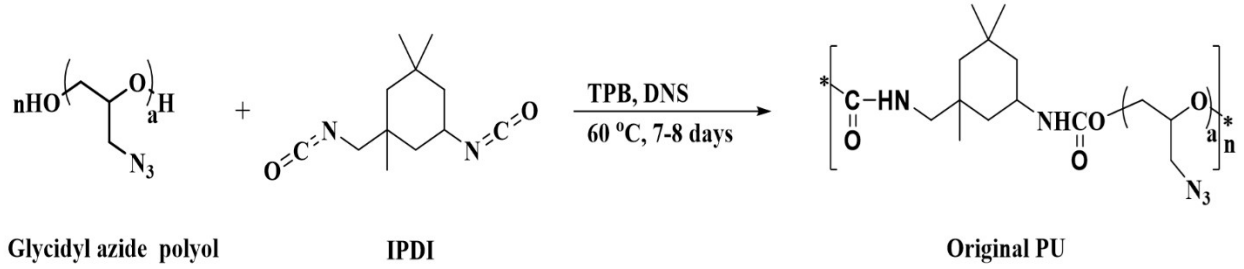

Scheme 2. Reaction scheme of original PU without BBS.

Preparation of the Modified PU

Glycidyl azide polyol (80.808 mmol) was dried at 60 °C under vacuum for 1 h and cooled down to 25–30 °C for 0.5 h. Then, PDI (2.270 mmol) was rapidly added into the above glycidyl azide polyol and stirred at 25–30 °C. After 0.5 h, the synthesized BBS with various molar ratios of [C≡C]/[N_3], 20.0 wt% – TPB solution, and 12.5 wt% – DNS solution was added and continued stirring (t = 0.5 h). Next, the mixture was pulled into mold (3 cm x 8 cm) and kept in the oven at 30 °C to remove the bubble under vacuum for 3 h; the curing process was carried out in the oven at 60 °C for 7 days. The reaction scheme of the original PU with BBS (modified PU) is shown in Scheme 3.

Analysis Instruments

The synthesized BBS structure was confirmed by NMR spectrometer (300 MHz, Varian Mercury Co.), which has been dissolved in $CDCl_3$. Fourier-transform infrared spectroscopy (FT-IR) was scanned in a wavenumber range of 4000–600 cm^{-1} through a Nicolet 380 spectrometer. The tensile test of original and modified PUs was measured on a universal test machine (TO-100-IC, Test One) with a 20 kg load cell (ramp rate = 0.8 mm/s) at room temperature. All results for tensile tests were an average of 3 measured values.

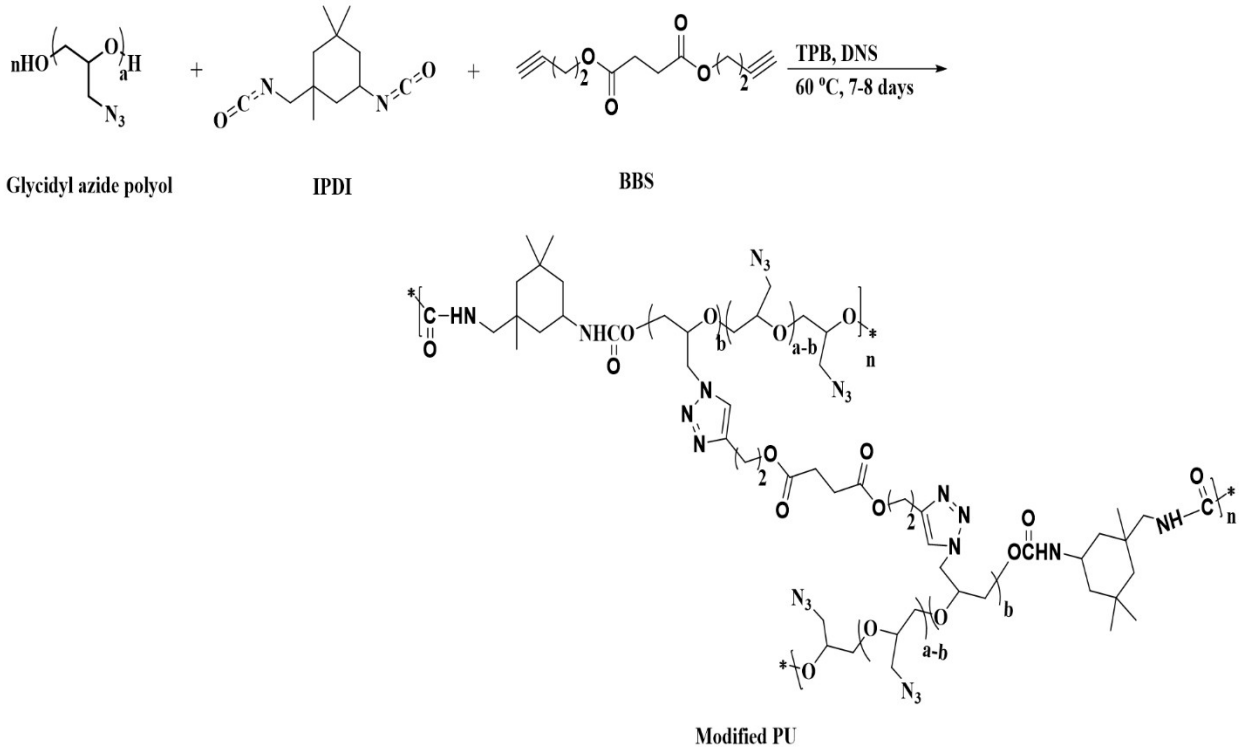

Scheme 3. Reaction scheme of original PU with BBS (modified PU).

RESULTS AND DISCUSSION

Chemical Structure of BBS

To determine the synthesized crosslinker's chemical structure – BBS, NMR instrument (^{1}H and ^{13}C NMR) was employed to analyze. In the ^{1}H NMR spectrum (Figure 1A), a peak of the acetylenic proton (***H***-*C*≡*C*-) is regarded at 1.95 ppm; concomitantly, new peaks of two protons adjacent to oxygen (-*C**H₂**-O*-) and (-*C**H₂**-CO*-) are a characteristic resonance of the synthesized BBS corresponding at 4.07 ppm and 2.53 ppm after esterification reaction. Moreover, in the ^{13}C NMR spectrum (Figure 1B), peaks of carbons of the alkyne (*H-C*≡***C***-) and (*H-**C***≡*C*-), carboxyl oxygen (-***C***H_2-*O-CO*-), and adjacent carbon to alkyne (*H-C*≡*C-**C***H_2-) are also observed at 80.12 ppm, 70.17 ppm, 62.48 ppm and 19.00 ppm, respectively. Thereby, based on resultant new peaks in both the ^{1}H-NMR and ^{13}C-NMR spectra, it indicates that the esterification has been well used to synthesize BBS successfully – a crosslinker with terminal alkyne group through anhydride (SA) and alcohol (BTO) compounds. Furthermore, the chemical characterization of BBS was confirmed by FTIR spectra (Figure 1C) that can be focused on the new presences of carboxyl (-COO^{-}) and alkyne (-C≡C-) groups on the synthesized BBS; in particular, the peaks of stretching vibration bands of alkyne groups (HC≡C-, and -C≡C-) and carboxyl groups (-C=O) were specifically observed at 3244 cm^{-1}, 2172 cm^{-1} and 1745 cm^{-1}, respectively. Thereby, the acetylene groups were successfully combined on BBS molecules, as well as which was appropriate with NMR results.

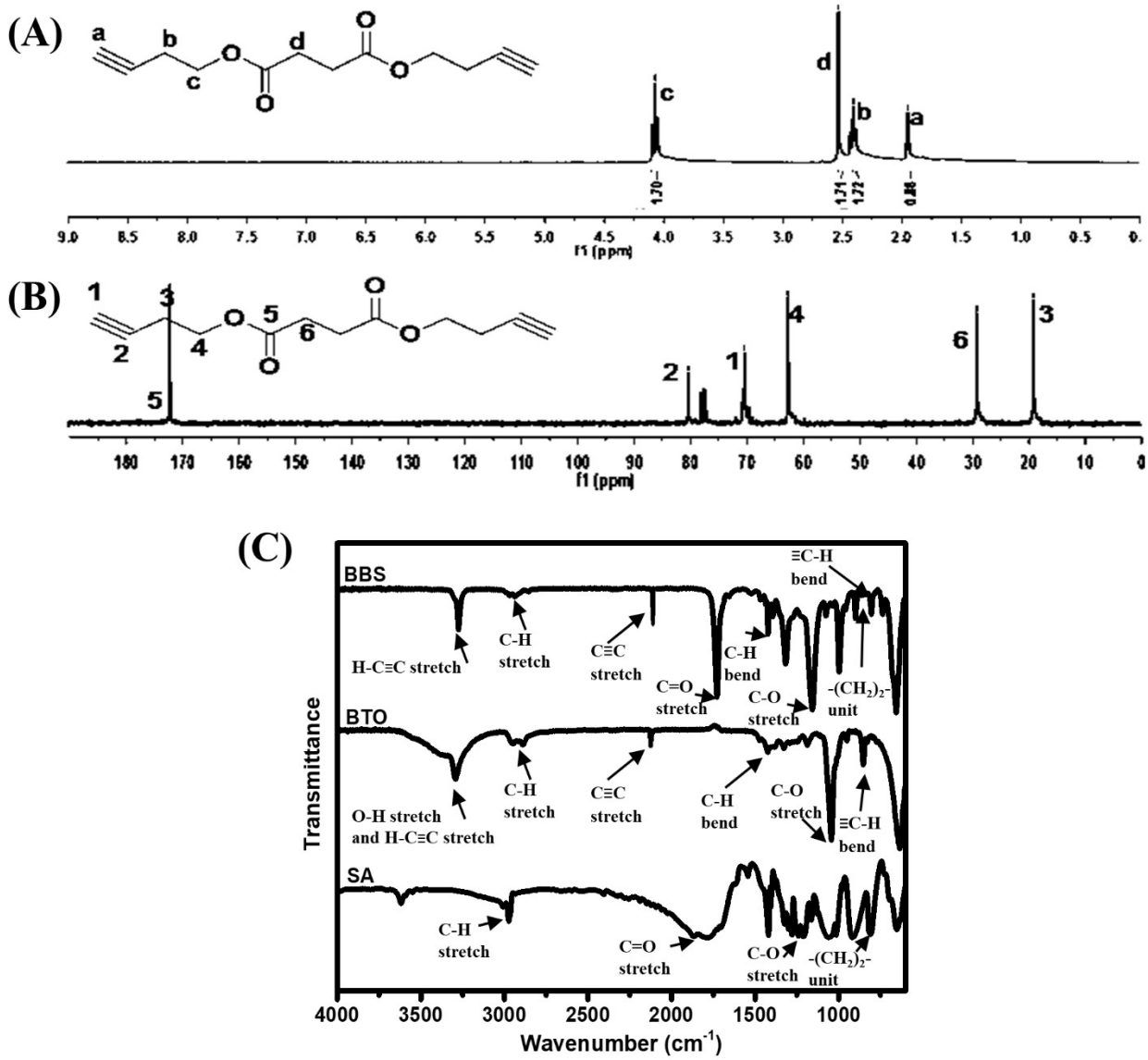

Figure 1. ^{1}H-NMR (A), ^{13}C-NMR (B) and FT-IR (C) of the synthesized BBS.

Mechanical Properties of the Modified PU

Mechanical properties of original and modified PUs were investigated through stress, strain, and Young's modulus. In stress-strain curves of the original and modified PUs (Figure 2A) were listed in Table 2, it is obvious that the modified PUs (P1 – P4) the mechanical properties were improved better than the original PU (P0). Specifically, the stress and Young's modulus of modified PUs (P1 – P4) were higher than those of the original PU (P0), whereas the strain of modified PUs (P1 – P4) is lower than that of the original PU (P0). This means that the modified PUs are harder than P0 regarding the "azide-alkyne" click reaction between azide groups (original PU) and terminal alkyne group (BBS – crosslinker), as well as there is an enhancement in mechanical property of original PU cross-linked with BBS.

Moreover, compared between the modified PUs with various content of the synthesized BBS (molar ratio of [C≡C]/[N_3] = 0.01–0.10), it reveals that a sudden increase in stress and Young's modulus displays harder and more ductile behaviors, which induces a transition in the intermolecular interaction of the original PU and the synthesized BBS, as well as the polymer chain stretching with external force support, which can be leading to a change in the polymer chain motion and structure variation. As a result, the

orientation arrangement of molecular chains and stretching forces gradually increases their stress values until fracturing (8-10). As such, these suggest that the raised content of resultant 1,2,3-triazole groups basing on the "azide-alkyne" click reaction has increased the steric hindrance and lowered the torsion of the backbone chains in the modified PUs (8, 9), inducing an increase in their rigidity (11). Basically, these results can also support improving the desired mechanical properties of the modified PU systems by adjusting a suitable [C≡C]/[N_3] ratio (12).

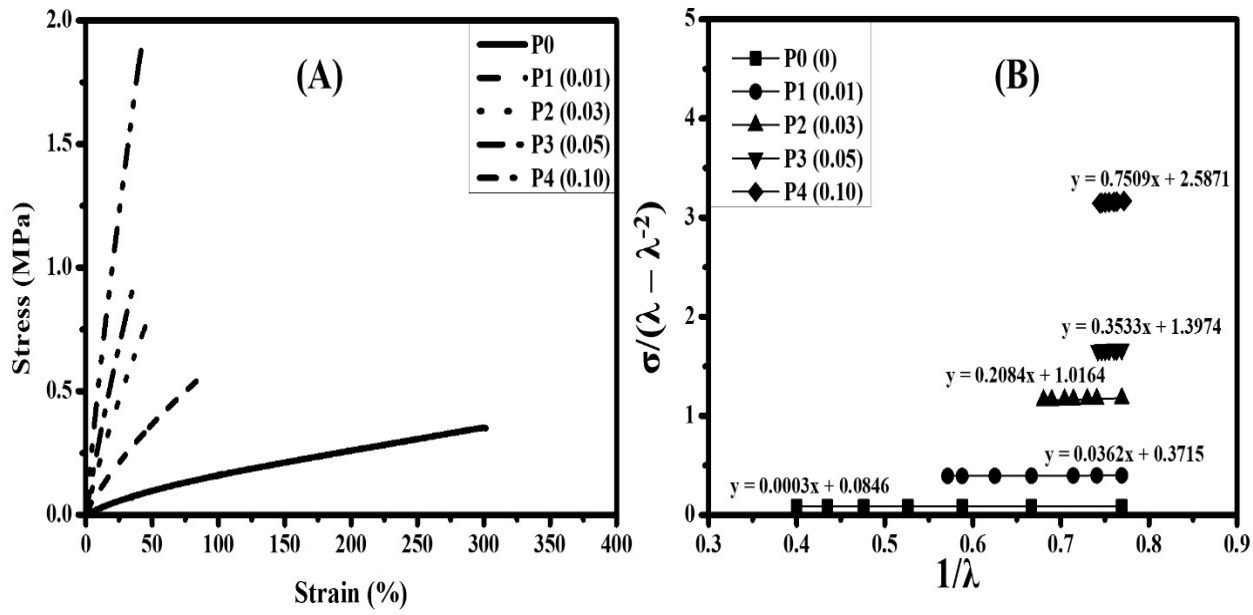

Figure 2. Stress-strain curves (A) and fitting curves for calculating cross-link density (B) of the modified PUs.

Additionally, the modified PUs with the above-obtained mechanical properties can also be used to determine their cross-link density (v_e) through the Mooney-Rivlin equation (Equation 3) (13, 14), as well as it contributes explaining further for a suitable relationship of cross-link density and mole ratio of [C≡C]/[N_3] in the modified PUs. Precisely, the cross-linking degree is calculated by plotting of $\sigma/(\lambda - \lambda^{-2})$ and $1/\lambda$ (Figure 2B). The intercept of each curve on the $\sigma/(\lambda - \lambda^{-2})$ plot regards the $2C_1$ value, whereas its slope corresponds to the $2C_2$ value. The below equations (Equations 1 – 3) show a relationship as follows (15):

$$F = 2A(\lambda - \lambda^{-2})(C_1 + C_2\lambda^{-1}) \quad \text{(Eq. 1)}$$

$$\frac{\sigma}{\lambda - \lambda^{-2}} = 2C_1 + 2\frac{C_2}{\lambda} \quad \text{(Eq. 2)}$$

$$v_e = \frac{C_1}{RT} \quad \text{Or} \quad v_e = \frac{C_1}{\rho RT} \quad \text{(Eq. 3)}$$

where σ is identified by F/A (Force/Area), v_e is a physical cross-link density based on the stress-strain test, λ is a strain range of 30.0–150.0%, R is a gas constant (8.314 $J \cdot mol^{-1} \cdot K^{-1}$ at 25 °C), and T is an absolute temperature. Herein, the v_e values of original and modified PUs are summarized in Table 2, their cross-link density increase as the mole ratio of [C≡C]/[N_3] stoichiometry be varied from 0.01 to 0.10. This is seen as a natural consequence of the cross-linked PUs with increasing cross-link density. Overall, the relationship of cross-link density and mole ratio of [C≡C]/[N_3] in the modified PUs are genuinely suitable to the above-suggested mechanical properties.

Table 2. Cross-link density and mechanical properties of the modified PUs.

PUs	Molar ratio of [C≡C]/[N_3]	Cross-link density		Mechanical properties		
		v_e (mol/cm^3) *10^4	v_e (mol/g) *10^4	Stress (MPa)	Strain (%)	Young's modulus (MPa)
P0	0	0.175	0.131	0.361±0.016	320.8±26.9	0.254±0.013
P1	0.01	0.750	0.561	0.546±0.003	88.4±2.4	0.865±0.017
P2	0.03	2.051	1.508	0.756±0.057	45.1±3.7	2.024±0.010
P3	0.05	2.820	2.057	0.914±0.007	35.8±0.6	2.997±0.015
P4	0.10	5.221	3.842	1.681±0.198	36.6±5.2	5.453±0.197

CONCLUSION

In summary, BBS – a new crosslinker with terminal alkyne group, has been synthesized successfully from the esterification of anhydride (SA) and alcohol (BTO) compounds incorporated with original PU well as the formation of 1,2,3-triazole groups. Besides, the original PU cross-linked with the above-synthesized BBS has achieved a significant improvement in their mechanical properties. Significantly, the stress and Young's modulus of the modified PUs increase, whereas their strain decreases on increasing the content of the synthesized BBS to the original PU matrix involving the increased rigid triazole networks. Moreover, the cross-link densities of the modified PUs increase with the BBS content through the Mooney-Rivlin equation, as well as there is an enhancement in the mechanical property of the original PU cross-linked with BBS. Thereby, the different mole ratio of [C≡C]/[N_3] prepared in the present study can reveal new approaches for the design and future application of the original PU with alkyne compounds, as well as their desired cross-link densities can be controlled easily for powerful and selective reactions.

ACKNOWLEDGMENTS

The authors thank the support of Can Tho University.

REFERENCES

1. Acik G, Karabulut HRF, Altinkok C, Karatavuk AO. Synthesis and characterization of biodegradable polyurethanes made from cholic acid and L-lysine diisocyanate ethyl ester. Polymer Degradation and Stability. 2019; 165: 43-8.

2. Caraculacu AA, Coseri S. Isocyanates in polyaddition processes. Structure and reaction mechanisms. Prog Polym Sci. 2001; 26: 799-851.

3. Acik B, Acik G, Erdemi H. Synthesis and characterization of bile acid, poly (ε-caprolactone) and L-lysine diisocyanate ethyl ester based polyurethanes and investigation of their biodegradability properties. Eur Polym J. 2021; 146: 110247.

4. Binder WH, Sachsenhofer R. 'Click' chemistry in polymer and material science: An update. Macromol Rapid Comm. 2008; 29: 952-81.

5. Diaz DD, Punna S, Holzer P, Mcpherson AK, Sharpless KB, Fokin VV, Finn MG. Click chemistry in materials synthesis. 1. Adhesive polymers from copper-catalyzed azide-alkyne cycloaddition. J Polym Sci Pol Chem. 2004; 42: 4392-403.

6. Rostovtsev VV, Green LG, Fokin VV, Sharpless KB. A stepwise Huisgen cycloaddition process: Copper(I)-catalyzed regioselective "ligation" of azides and terminal alkynes. Angew Chem Int Ed. 2002; 41: 2596-9.

7. Vo TS, Vo TTBC. Preparation and Characterization of Bis-Propargyl-Succinate, and its Application in Preliminary Healing Ability of Crosslinked Polyurethane using" Azide-Alkyne" Click. Journal of Engineering Science & Technology Review. 2020; 13.

8. Wool RP. Mechanisms of frequency shifting in the infrared spectrum of stressed polymer. Journal of Polymer Science, Polymer Physics Edition. 1975; 13: 1795-808.

9. Wool RP. Infrared studies of deformation in semicrystalline polymers. Polymer Engineering and Science. 1980; 20: 805-15.

10. Cifre JGH, de la Torre JG. Orientation of polymer chains in dilute solution under shear: Effect of chain

model and excluded volume. Macromol Theor Simul. 2004; 13: 273-9.

11. Ward IM, Hadley DW. An introduction to the mechanical properties of solid polymers. John Wiley & Sons, Chichester,. 2004; ISBN: 0-471-93887-4.

12. Keicher T, Kuglstatter W, Eisele S, Wetzel T, Krause H. Isocyanate-Free Curing of Glycidyl Azide Polymer (GAP) with Bis-Propargyl-Succinate (II). Propellants, Explosives, Pyrotechnics. 2009; 34: 210-7.

13. Flory PJ. Statistical mechanics of swelling of network structures. J Chem Phys. 1950; 18: 108 – 11.

14. Mullins L. Determination of degree of crosslinking in natural rubber vulcanizates (Part 3). Journal of Applied Polymer Science. 1959; 1: 1 – 7.

15. Hagen R, Salmen L, Stenberg B. Effects of the type of crosslink on viscoelastic properties of natural rubber. J Polym Sci Polym Phys. 1996; 34: 1997-2006.

JOTCS A
Journal of the Turkish Chemical Society
Section: A
Chemistry
TURKISH CHEMICAL SOCIETY

Investigation of the Acquisition Conditions of Tl_3AsS_4 Compound in the Aquatic Environment

Huseyn Imanov[1*], Gorkhmaz Huseynov[1]

Institute of Natural Resources of Nakhchivan Branch of Azerbaijan National Academy of Sciences, Nakhchivan city, H. Aliyev street 35, AZ7000, Azerbaijan

Abstract: The condition for obtaining the Tl_3AsS_4 compound was investigated based on $TlNO_3$ and As_2S_5 compounds in hydrothermal conditions in the aquatic environment. It was found that Tl_3AsS_4 compound has been obtained from a mixture of the primary components (As_2S_5 and $TlNO_3$) in a ratio of 4:15 mol at 80 °C in the range of pH = 7 – 8. The individuality of the obtained Tl_3AsS_4 compound was confirmed by the XRD method and DTA, and TG analyses. The thermally processed Tl_3AsS_4 compound crystallizes in an orthorhombic structure at 220 °C. Based on the results of TG analysis, the temperatures of the phase transitions that occur during the oxidation of the compound were determined and the stoichiometric composition of the compound was specified. The SEM results of the compound showed that the Tl_3AsS_4 precipitate obtained from the solution at 80 °C is composed of aggregates of highly adherent nanoparticles and the size of the nanoparticles varies from ~60 to 120 nm. The effect of pH of the medium and the amount of the primary components on the yield of Tl_3AsS_4 was studied. It was determined that when T > 100 °C, $(Tl_2S)_x(As_2S_3)_{1-x}$ (x=0.1-0.9) – containing sediments are obtained from different molar ratios of the primary components (As_2S_5 and $TlNO_3$).

Keywords: Functional materials, sediments, chemical analysis, thermogravimetric analysis, micromorphology.

Submitted: January 05, 2021. **Accepted:** March 31, 2021.

Cite this: Imanov H, Huseynov G. Investigation of the Acquisition Conditions of Tl3AsS4 Compound in the Aquatic Environment. JOTCSA. 2021;8(2):527-34.

DOI: https://doi.org/10.18596/jotcsa.854210.

***Corresponding author. E-mail:** huseyn.imanov1991@gmail.com.

INTRODUCTION

Thio-compounds created from thallium with arsenic and glass-like alloys obtained based on them are valuable functional materials of semiconductor, photoelectric, acousto-optical properties, etc. The phase equilibrium and glass formation in the Tl-As-S system, as well as the physicochemical properties of the intermediate phases, have been studied in a number of studies (1-7, 13-17, 19, 22). The compounds and alloys in the system are mainly obtained by the direct synthesis method.

The Tl-As-S system was first studied by Prerichs, and glass formation was observed in the polythermal incision of As_2S_3 – Tl_2S_3 in the area of 15 and 50% (w) Tl_2S_3 concentration (19). The synthesis was performed in H_2S flux in open quartz ampoules.

Glass formation on the incision of As_2S_3 – Tl_2S was studied by Goryunov, Kolomiych and Shilov (5, 6, 12). The glass formation was carried out by vacuum synthesis method at a temperature of 900 °C, cooling was carried out at a slow speed (1 deg/sec). Glass formation was observed in areas of 50-70 mol % Tl_2S concentration.

The boundaries of glass formation and properties in the Tl-As-S system were studied by Flashchen (3,4).

The glasses were obtained by the method of direct synthesis in quartz ampoules based on elemental (Tl, As, S) components. The cooling process was conducted slowly. In the system, stratification was observed in sulfur-rich areas. The melting temperature of the glass was determined by the dilatometric method. It was found that the melting point decreases as the amount of Tl in the glass increases.

The boundaries of glass formation in the Tl-As-S system have been repeatedly studied by Markova (16). The glasses were obtained by vacuum synthesis method based on elemental components at 850 °C for 1 – 2 hours. Hardening is completed in 10 – 12 hours with slow cooling. Alloys riched with Tl were hardened in air or water. It was found that stratification was observed in alloys under such conditions. During slow cooling, glasses are obtained up to 15% Tl concentration areas. The results of the (16) study are slightly different from the results of Flashchen (3,4). The glass obtained from the Tl-As-S system is resistant to weather conditions. It was found that when the amount of Tl_2S in glass increases from 7.2 to 50 mol%, the melting temperature decreases from 147 to 96 °C, respectively (13, 14).

The phase equilibrium in the As_2S_3-Tl_2S system was investigated and 4 chemical compounds (Tl_3AsS_3, $Tl_4As_2S_5$, $Tl_6As_4S_9$ and $TlAsS_2$) were found (2). The phase diagram of this system was created by the authors (13, 14). A long-term (400 hours) thermal process was performed to crystallize glass-like alloys. The $TlAsS_2$ triple compound observed in the system melts congruent at 280 °C while the Tl_3AsS_3 and $TlAs_3S_5$ compounds melt incongruent at 290 and 220 °C, respectively. It was found that the As_2S_3-$TlAsS_2$ system has formed a eutectic-type phase diagram. Eutectic is in the area of ~70 mol% As_2S_3 concentration and melts at 190 °C. Stratification is observed in the $TlAsS_2$-Tl_2S system and the monotectic temperature is 300 °C. Between $TlAsS_2$ and Tl_3AsS_3 compounds, eutectic is formed in the 35 mol% compositions of As_2S_3 and the melting point is 220 °C. Solid solutions based on Tl_2S were obtained in the As_2S_3-Tl_2S system (13, 14). $TlAsS_2$ is found in nature as a lorandite mineral and crystallizes in monoclinic syngony (21).

Recent literature shows that Tl_3AsS_4, $TlAsS_2$, Tl_3AsS_3, $TlAs_3S_5$, $Tl_3As_5S_{10}$, $Tl_9As_5S_{15}$, $Tl_9As_3S_{13}$, Tl_3AsS_6 and $Tl_8As_2S_9$ compounds are available in the Tl-As-S system (1, 17).
The interaction between Tl_2S-As_2S_3 with the co-precipitation method from aqueous solutions was studied by the microscopic method in 1907 (9). Homogeneous precipitates were obtained based on Tl^+ and As^{3+} salts in acidic and alkaline solutions by co-precipitation with H_2S. It was found that only sediment which is composed of 62 mol% As_2S_3 is a two-phase. According to the authors, solid solutions are obtained up to 62 mol% As_2S_3 concentration area in the As_2S_3-Tl_2S system. Tl_3AsS_4 compounds were obtained by the co-deposition method using aqueous solutions of Tl^+ and As^{5+} salts and alkali metal sulfides as sulfidation reagents (2). It was found that the compound Tl_3AsS_4 melts incongruently, its decomposition temperature is 250 °C.

In modern times, the production of a number of binary and triple sulfides from aqueous solutions is one of the most pressing issues, because the compounds obtained in aqueous solutions are in the form of nano- and microparticles. By controlling the size and shape of particles of known materials, it is possible to change their properties and identify new areas of application. In this regard, the acquire of very small-sized and new featured materials is of great interest. The literature provides information on the study of micromorphology of $AgAsS_2$, Ag_3AsS_3, $CuAsS_2$ and Cu_3AsS_3 compounds obtained by hydrochemical and hydrothermal methods (7,8).

The aim was to study the interaction between $TlNO_3$ and As_2S_5 in the aquatic environment and to obtain the Tl_3AsS_4 compound individually. The article presents the results of the study of the conditions for the acquisition of Tl_3AsS_4 in the aquatic environment and some physical-chemical properties.

EXPERIMENTAL SECTION

Chemicals

Arsenic(V) sulfide for this research was initially obtained using chemicals sodium arsenate, hydrochloric acid, hydrogen sulfide gas. Furthermore, arsenic(V) sulfide which is obtained in high purity and thallium nitrate were used to obtain the thallium tetrathioarsenate compound. All chemicals used in experimental studies were provided as high purity products, and whole reactions were conducted in ultra-clean water. Besides, distilled water and ethanol were used to wash the obtained precipitate. Moreover, ammonium molybdate and hydrazine solutions were used to analyze arsenic in sediment samples and leachate. All of the chemicals used during this study are of analytical grade.

Instrumental techniques

The following instruments were used for measurement and characterization: X-ray Diffraction (XRD) analysis of samples was performed by a Bruker D2 Phaser XRD. Thermogravimetric (TG) and differential thermal analysis (DTA) data were recorded using the NETZSCH STA 449F3 instrument. Scanning Electron Microscopy (SEM)

image for the investigation of the surface morphology is taken by the HITACHI TM3000 microscope. Glassco 710.AG.01 magnetic heater&stirrer (350 °C/1600 RPM) have been used for heating and stirring reaction solution. The pH measurements were carried out with an "аквилон" pH – 410 at room temperature. "КФК – 2 – УХЛ 4.2" photo calorimeter was used to determine the arsenic content of the initial reaction filtrate and the precipitate obtained. KD (WBFY-201) professional chemical microwave oven has been used for the formation of sediment.

Synthesis of Tl_3AsS_4 Compound

According to the known methodology, as an initial component to obtain the Tl_3AsS_4 compound, the As_2S_5 compound was obtained by mixing a 0.5 g Na_3AsO_4 compound acidified with 10 N hydrochloric acids and releasing H_2S gas in a temperature range of 0 – 10 °C for 2 hours (11). The system was cooled with ice water. In this case, the following reaction occurs:

$$2Na_3AsO_4 + 5H_2S + 6HCl \rightarrow As_2S_5 + 6NaCl + 8H_2O \quad (1)$$

0.35 g of As_2S_5 and 1.12 g of $TlNO_3$ were mixed to obtain the Tl_3AsS_4 compound in the aquatic environment. The reaction mixture was stirred in a magnetic stirrer for 3 hours, then the precipitate was filtered, after which it first washed with distilled water and then with ethanol. The sediment kept in a microwave oven under hydrothermal conditions (80 °C) for 78 hours by adding ultra-clean water again. The pH of the condition was kept in the range of 7 - 8. The equation of the reaction can be summarized as follows:

$$4As_2S_5 + 15TlNO_3 + 12H_2O \rightarrow 5Tl_3AsS_4 + 3H_3AsO_4 + 15HNO_3 \quad (2)$$

After thermal processing, the sediment was filtered, washed, and dried at 100 °C under vacuum (~10^{-1} Pa).

RESULTS AND DISCUSSION

Chemical Analysis

Obtaining the Tl_3AsS_4 compound was carried out based on the results of a number of experimental studies. The sample taken from the precipitate of the Tl_3AsS_4 compound was dissolved in concentrated HNO_3 and completely evaporated. Upon completion of the complete evaporation process, the volume of the dry residue was clarified to 100 mL. A sample was taken from the diluted solution and then ammonium molybdate and hydrazine solution were added to it. This solution was heated in a water bath for 10 minutes. In this case, arsenomolybdate blue has been formed. The amount of arsenic in the sediment was determined by the colorimetric method in a sample taken from the blue solution (18). Besides, the amount of arsenic in the filtrate after the initial reaction was determined by the same method. The table below shows the results of 8 experiments (Table 1.). Chemical analysis methods determined (20) that the amount of precipitate obtained and the amount of As^{+5} ion transferred to the solution during the interaction of the initial components taken in the amount corresponding to the stoichiometric composition of Tl_3AsS_4 between pH = 7 and 8 corresponds well to the reaction (2).

Table 1. The amount of obtained Tl_3AsS_4 sediment and passed components to the solution during the reactions.

Experiment	As_2S_5, g	$TlNO_3$, g	Tl_3AsS_4 sediment, g	The amount of As^{+5} ion transferred to the solution, g
1	0.3500	1.1278	1.0251	0.0631
2	0.4011	1.2925	1.3199	0.0704
3	0.5002	1.6118	1.6325	0.0896
4	0.4922	1.5860	1.6095	0.0883
5	0.3944	1.2709	1.2703	0.0604
6	0.3539	1.1404	1.1315	0.0589
7	0.3098	0.9983	0.9968	0.0476
8	0.3321	1.0701	1.0658	0.0518

XRD Analysis

The obtained Tl_3AsS_4 sediment was thermally processed at a temperature of 220 °C in a vacuum (~ 10^{-2} Pa) for 2 hours and its composition was checked by XRD. It was found that the sediment consists of the Tl_3AsS_4 compound and has an orthorhombic structure (Space gr.: Pnma; lattice. par.: *a = 0.9268 nm, b = 0.9334 nm, c = 1.1123 nm,* $\alpha = \beta = \gamma = 90^0$). The values of the intensity peaks in the diffractogram were well matched with the results of other studies (1, 17, 22) (Fig. 1).

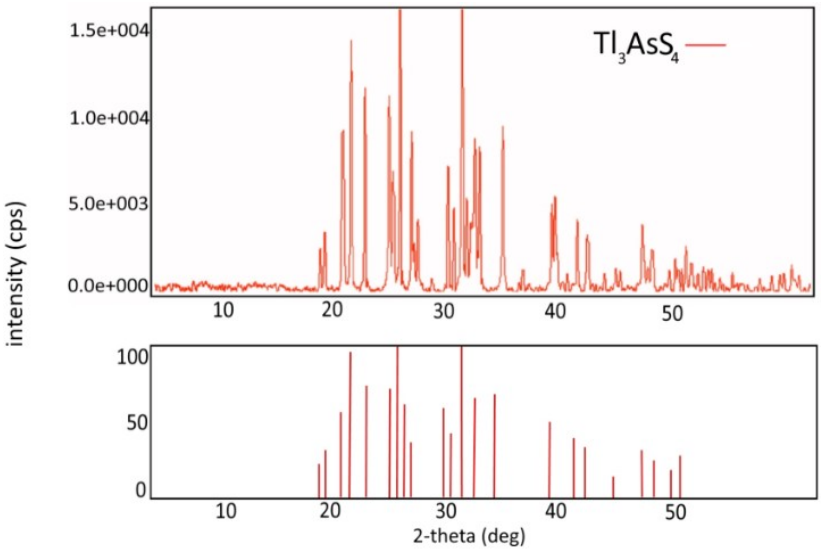

Figure 1. Diffractogram of the Tl_3AsS_4 compound.

TG Analysis

A thermogravimetric (TG) analysis was performed to determine the stoichiometric composition of the obtained Tl_3AsS_4 compound (Fig. 2). The heating process was carried out in a flow of oxygen. As can be seen from the thermogravimetric curve of the compound, the decomposition of the compound begins at 180 °C. Melting of the sulfur separated from the sample occurs in the temperature range of 260-300 °C. The As_2S_3 compound formed in the temperature range of 310-360 °C melts. The exact decomposition of the Tl_3AsS_4 compound is completed at 680 °C, and the maximum mass loss in a 36 mg of sample is 3.61 mg. This is well compatible with the stoichiometric composition of the Tl_3AsS_4 compound. Oxidation of decomposition products occurs when was T > 680 °C and exact oxidation ends at 810 °C. 1.91 mg of oxygen combined with 32.39 mg of the decomposition product. Complete decomposition of oxidation products was observed at 900 °C. After TG analysis, the X-ray results of the remaining residues showed that the sample residue obtained in the temperature range 180-300 °C contains Tl_3AsS_3 + S compounds, in the range of 300-680 °C contains Tl_3AsO_3 compound, in the range of 690-810 °C contains Tl_3AsO_4 compound, finally, in the range of 810-900 °C contains Tl_3AsO_3 compound. The reaction equations based on the X-ray results can be written as follows:

$Tl_3AsS_4 \rightarrow Tl_3AsS_3 + S$ (180-300 °C);

$2Tl_3AsS_3 + 9O_2 \rightarrow 2Tl_3AsO_3 + 6SO_2$ (300-680 °C);

$2Tl_3AsO_3 + O_2 \rightarrow 2Tl_3AsO_4$ (690-810 °C);

$2Tl_3AsO_4 \rightarrow 2Tl_3AsO_3 + O_2$ (810-900 °C).

DT Analysis

DT analysis of Tl_3AsS_4 was conducted in an inert (N_2 gas flow) environment. Thermal effects were observed in the DTA curve of Tl_3AsS_4 at 265 °C and 419.8 °C (Fig. 3). The weak thermal effect observed at 265 °C can be considered as the attenuation or polymorphic conversion temperature of Tl_3AsS_4. The thermal effect at 419.8 °C corresponds to its melting point. The reason for the relatively low melting point can be explained by the fact that the compound is in nanoparticle form. It is known that the melting point of nanoparticles of the same substance is lower than the melting point of its monocrystals (10).

SEM Imaging

The micromorphology of the Tl_3AsS_4 compound obtained at 80 °C was studied. The size and shape effects of particles in an area of 10 micrometers were determined. As can be seen from the SEM image of the compound, the sediment from the solution is composed of aggregates of highly adhesive nanoparticles (Fig. 4). The size of nanoparticles varies in the range of ~ 60 - 120 nm. It has been found that the particle size increases as the crystallization degree increases when the temperature increases (T > 80 °C).

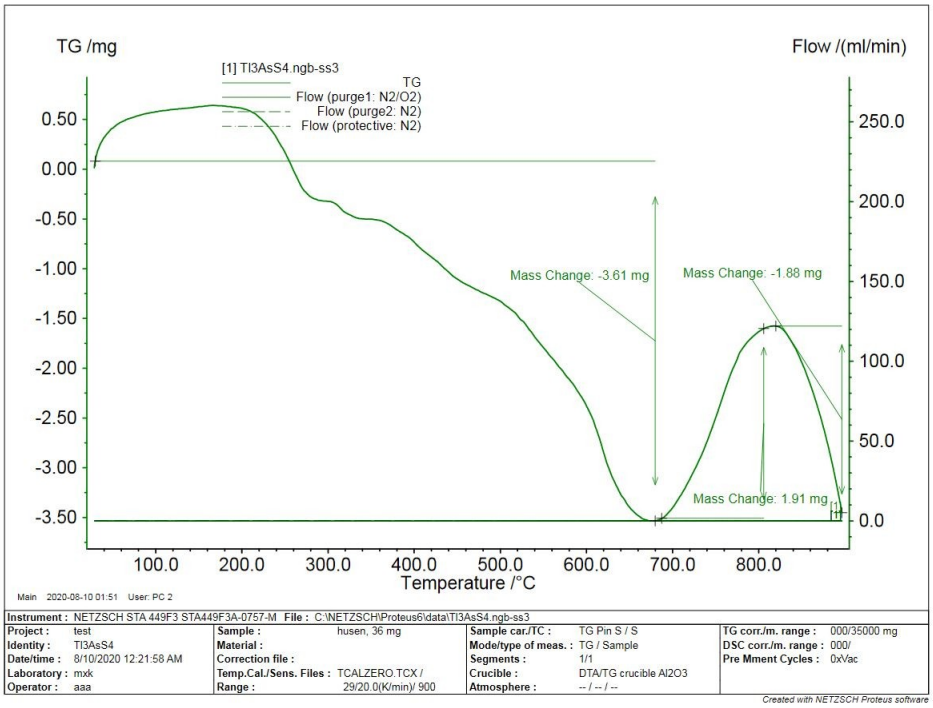

Figure 2. Thermogram of the compound Tl_3AsS_4.

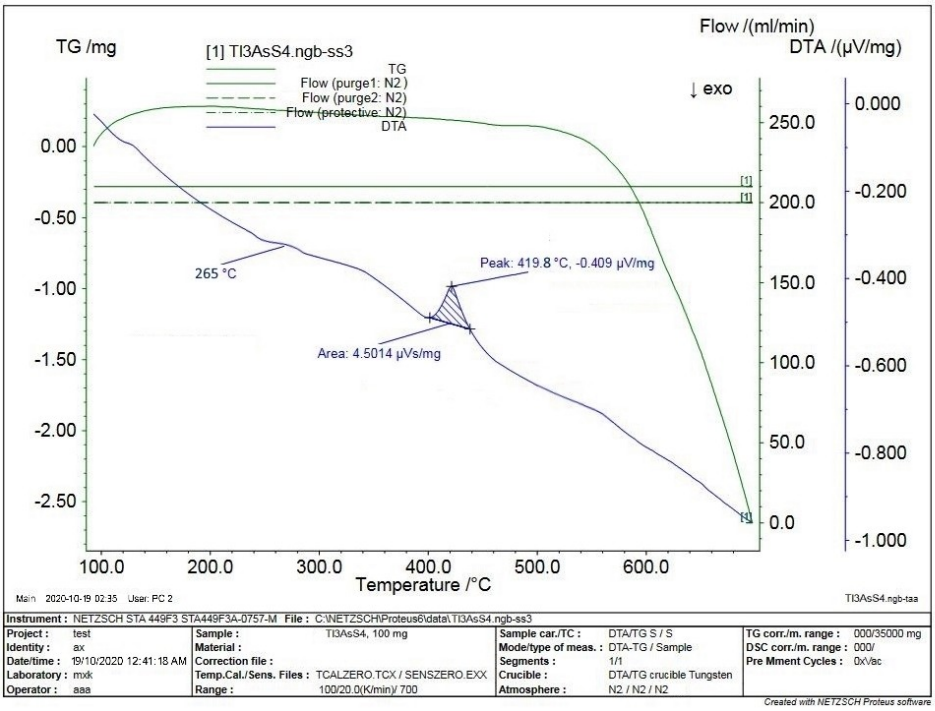

Figure 3. DTA curve of Tl_3AsS_4 compound.

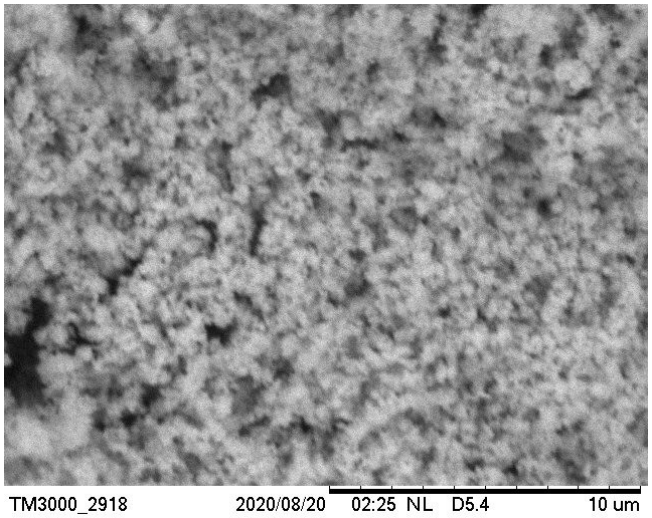

Figure 4. SEM image of the Tl_3AsS_4 compound.

Effect of the pH of the solution

Physical-chemical analysis methods (XRD, DTA) have shown that the yield of Tl_3AsS_4 depends on the pH of the condition. Thus, there is no reaction between the primary components ($TlNO_3$ and As_2S_5) between pH = 1 and 4. The reaction occurs weakly between pH = 4 and 7 and becomes fast between pH = 7 and 8. A mixture of thio- and oxysalts are obtained when was pH > 8.

It was found that when was pH = 7 – 8, depending on the amount of the primary components (As_2S_5 and $TlNO_3$), $(Tl_2S)_x(As_2S_3)_{1-x}$ (x=0.1-0.9) – containing sediments were obtained in the solution. It is known that when the temperature is T > 90 °C, As_2S_5 decomposes by the reaction $As_2S_5 \rightarrow As_2S_3 + 2S$. When the temperature is T < 90 °C, Tl_3AsS_4 is obtained from the amount taken in the appropriate ratio (4:15 mol) corresponding to reaction (2).

CONCLUSION

Tl_3AsS_4 was obtained by hydrothermal method (T = 80 °C and pH = 7 – 8) based on $TlNO_3$ and As_2S_5 compounds and formation conditions have been studied. It was found that the reaction between As_2S_5 and $TlNO_3$ at 80 °C was completed within 3 hours. As_2S_5 decomposes when the synthesis temperature was T > 100 °C and therefore a mixture of thioarsenites ($TlAsS_2$, Tl_3AsS_3) was obtained. The individuality of the obtained Tl_3AsS_4 compound was confirmed by the XRD method. It was found that the thermally processed Tl_3AsS_4 compound crystallized in the orthorhombic structure at 220 °C. It was determined by the TG analysis method that the exact decomposition of the Tl_3AsS_4 compound was completed at 680 °C. The stoichiometric composition of the compound was determined based on the decomposition and oxidation products. The SEM results showed that the Tl_3AsS_4 sediment obtained from the solution was composed of aggregates of highly adhesive nanoparticles. The complete formation of the particles was completed in 78 hours at a temperature of 80 °C. The effect of pH of the medium and the amount of the primary components on the yield of Tl_3AsS_4 were studied. Between pH 7 and 8, Tl_3AsS_4 compound was obtained from a mixture taken at a ratio of 4:15 mol, depending on the amount of the primary components (As_2S_5 and $TlNO_3$). When T > 100 °C, $(Tl_2S)_x(As_2S_3)_{1-x}$ (x=0.1-0.9) – containing sediments were obtained from mixtures of different mole ratios.

ACKNOWLEDGEMENT

The authors are very thankful to the Institute of Natural Resources of Nakhchivan Branch of Azerbaijan National Academy of Sciences for supporting this study.

CONFLICT OF INTEREST

The authors declare that they have no conflict of interest.

REFERENCES

1. Babanly M.B., Il'jasly T.M., Muradova G.V., Babanly D.M. Tverdofaznye ravnovesija v sisteme Tl_2-As_2S_3-S i termodinamičeskie svojstva trojnyh soedinenij. Vestnik Bakinskogo Universiteta. 2011;№4:c 203-5.

2. Canneri G., Fernandes L. Contributo allo studio di alcun minerali contenenti tallio. Analisi termica dei systemi Tl_2S-As_2S_3, Tl_2S-PbS. Atti accad. naz. Lincei. 1925;ser 6:vol.32:II:p 671-6.

3. Flashchen S.S., Pearson A.D., Northover W.R. Low-melting inorganic glasses with high melt

fluidities below 400 °C. J. Amer Ceram. Soc. 1959;vol.42:N9:p 450-450.

4. Flashchen S.S., Pearson A.D., Northover W.R. Formation and properties of low-melting glasses in the ternary systems As – Tl – S, As – Tl – Se and As – Se – S. J.Amer Ceram. Soc. 1960;vol.43:p 274-5.

5. Gorjunova N.A., Kolomiec B.T., Šilo V.P. Stekloobraznye poluprovodniki. Žurn. tehn. Fiziki. 1958;t. 28:№5:s 981-5.

6. Gorjunova N.A., Kolomiec B.T., Šilo V.P. Stekloobraznye poluprovodniki. 9. Stekloobraznie v složnyh halʹkogenidah na osnove sulfida i selenida myšʹjaka. FTT 1960;t.2:№2:s 280-3.

7. Gusejnov G.M. Issledovanie uslovija polučenija tetratioarsenita medi(I) gidrohimičeskim metodom. VI Meždunarodnyj Naučnye Konfrans Novye funkcionalʹnoe materialy i vysokie tehnologii. Tivat, Černogorija. 2018;s 194-5.

8. Gusejnov G.M. Sulejmanova T.I. Polučenie soedinenij $AgAsS_2$ i Ag_3AsS_3 gidrotermalʹnym metodom. Meždunarodnyj žurnal prikladnyh i fundamen-talnyh issledovanija. Moskva, Akademija estestvoznanija. 2017;№3(2):s 341-167.

9. Hawley L.F. Contributions to the chemistry of thallium. J. Amer Chem. Soc. 1907;vol.29:p 300-4.

10. Huseynov G.M. Methods of obtaining nanomaterials. Nakhchivan, Ajami Publishing and Printing Association. 2017;256 p.

11. Imanov H.A. Investigation of conditions for obtaining arsenic(V) sulfide in an aquatic environment. Nakhchivan Branch of ANAS, Scientific works. 2018;№2:p 312-3.

12. Kolomiec B.T., Gorjunova N.A., Šilo V.P. Stekloobraznov sostojanie v halʹkogenidah. – V kn.: Stekloobraznoe sostojanie. M.: L Izd-vo AN SSSR. 1960;s 456-60.

13. Kirilenko V.V., Demboeskij S.A., Poljakov Ju.A. Optičeskie svojstva stekol v sistemah As_2S_3 – Tl_2S i As_2Se_3 – Tl_2Se. Izv. AN SSR. Neorgan. Materialy. 1975;t. 11:№11:s 1923-8.

14. Kirilenko V.V., Nikitina V.K., Demboeskij S.A. Stekloobrazovanie i osobennosti himičeskogo vzaimodejstvija v halʹkogenidnyh sistemah As_2X_3 – Tl_2X. Izv. AN SSR. Neorgan. Materialy. 1975;t. 11:№11:s 1929-35.

15. Lazareva V.B., Kiš Z.Z. Pereš E.Ju., Semrad E.E. Složnye halʹkogenidy v sistemah $A^IB^{III}C^{VI}$. Izdatelʺstvo Metallurgija. 1993;s 230.

16. Markova T.P. Èlektroprovodnostʹ stekloobraznoj sistemy myšʹjak – sera – tallij. Vestn. LGU. Fizika i himija. 1962;№22:vyp. 4:s 96-104.

17. Muradova G.V., T.M.Ilʹjasly, Ju.A.Jusibov, M.B.Babanly. Fazovye ravnovesija v sistemah TlS–$TlAsS_2$ i Tl_3AsS_3–S. Azerbajdžanskij Himičeskij Žurnal. 2012;№3:s 109-3.

18. Nemodruk A.A. Analitičeskaja himija myšʹjaka. Izdatelstvo Nauka Moskva. 1976;s 244.

19. Prerichs R. New optical glasses with good transparency in the infrared. J.Opt. Soc. Amer. 1953;vol.43: issue 5;p.339-431.

20. Šarlo.G. Metody analitičeskoj himii. Kličestvennyj analiz neorganičeskih soedinenij. Moskva Izdatelʺstvo Himija. 1965;976 s.

21. Solovʹev P.P. Spravočnik po mineralogi. M.; L.: GNTI po černoj i cvetnoj metallurgii 1948;s 517.

22. Vinogradova G.Z. Stekloobrazovanie i fazovye ravnovesija v halʹkogenidnyh sistemah. Izdatelʹstvo Nauka Moskva. 1984;s 172.

JOTCS A
Journal of the Turkish Chemical Society
Section: A
Chemistry
TURKISH CHEMICAL SOCIETY

2-Naphthylthio Cyclotriphosphazene Derivatives: Synthesis, Characterization, Crystallographic and Fluorescence Properties

Ceylan MUTLU BALCI[1]*

[1]Department of Chemistry, Gebze Technical University, Gebze 41400, Kocaeli, Turkey.

Abstract: In this study, new cyclotriphosphazene derivatives bearing 2-naphthylthio group were reported. The reactions of hexachlorocyclotriphosphazene (**1**) with 2-naphthalenethiol (**2**) were carried out with NaH base in tetrahydrofuran solution under inert (Ar) atmosphere in (1:2), (1:4) and (1:6) molar ratios. As a result of the reactions, bis geminal (**3**), tetrakis (**4**) and hexakis (**5**) 2-naphthylthio substituted cyclotriphosphazene derivatives formed and isolated. These new compounds were characterized with elemental analysis, mass (MALDI-TOF) analysis, $^{31}P\{H\}$ and ^{1}H NMR spectroscopies. The molecular structure of compound **3** was illuminated by single-crystal X-Ray diffraction technique. Furthermore, the fluorescence properties of the newly designed and synthesis compounds (**3**-**5**) were examined.

Keywords: Cyclotriphosphazene, Synthesis, Crystal Structure, Spectroscopy, X-Ray.

Submitted: January 08, 2021. **Accepted:** March 29, 2021.

Cite this: Mutlu Balcı C. 2-Naphthylthio Cyclotriphosphazene Derivatives: Synthesis, Characterization, Crystallographic and Fluorescence Properties. JOTCSA. 2021;8(2):535-52.

DOI: https://doi.org/10.18596/jotcsa.856600.

***Corresponding author.** E-mail: (ceylanmutlu@gtu.edu.tr), Tel: (90 262 6053111), Fax: (90 262 6053005).

INTRODUCTION

Cyclophosphazenes are the most important members of inorganic heterocyclic compounds (1–9). The most well-known and studied derivatives of cyclophosphazenes are trimer (hexachlorocyclotriphosphazene) and tetramer (octachlorocyclotetraphosphazene). Thanks to their active phosphorus-chlorine bonds, they can be used with many different groups and easily give chlorine displacement reactions (10–16). Another reason these compounds are preferred is to be used as the starting material in the preparation of polyphosphazenes which is the largest class of known inorganic polymers (12). Also, they can be used as ligand in coordination chemistry and organometallic chemistry (10–14). Six-membered trimer (P_3N_3) is more preferred and studied than eight-membered tetramer (P_4N_4) because it is planar, stable, rigid, and its product range is less than tetramer (17–20). Thus, an easily functionalized platform is created for the preparation of compounds suitable for different and new application areas such as biologically active materials, liquid crystallinity, anticancer agents, fluorescent chemosensors and organic light emitting diodes (21–26).

In order to synthesize materials with intended properties, one must know the reaction mechanism (S_N1 and S_N2) by which nucleophiles proceed. This is very important in controlling the progress of the reaction. For example, some nucleophiles prefer the non-geminal (S_N2) reaction pathway like alcohols (27–30), while others move through the geminal (S_N1) reaction pathway like some primary amines (31,32) and thiol groups (33,34). The replacement of Cl atoms in P-Cl bonds of hexachlorocyclotriphosphazene with thiolate groups follow the geminal (S_N1) reaction mechanism due to

the low donor ability of the sulfur atom (35). Therefore, geminal product formation is observed (33,34,36). Reactions of cyclotriphosphazenes and thiol group-containing nucleophiles are very rare in the literature (33–37).

Considering the industrial and current uses of luminescent compounds, aromatic groups such as naphthalene are of interest to researchers due to their fluorescence and colorimetric sensor features. Since the cyclotriphosphazene skeleton alone does not show fluorescence-like properties, it can allow the synthesis of molecules with different and tuneable properties depending on the number of substitutions. Nucleophilic substitution studies and fluorescence properties of 2-naphthylamine (38) and 2-naphthol (39) derivatives with hexachlorocyclotriphosphazene have been previously studied. Although 1-naphthylthio cyclotriphosphazene derivatives were seen in the literature (37), there is no report so far about 2-naphthylthio cyclotriphosphazene derivatives. In addition, the fluorescence properties of naphthylthio derivatives have not been investigated before.

In this study, nucleophilic substitution reactions of hexachlorocyclotriphosphazene (**1**) with 2-naphthelenethio (**2**) in 1: 2, 1: 4 and 1: 6 mole ratios were performed in order to determine their product diversity and reaction pathways (Scheme 1). Compounds **3**, **4** and **5** were isolated in pure, and characterized by different characterization methods such as mass analysis and nuclear magnetic resonance spectroscopy. Molecular structure of compound **3** was confirmed by X-Ray (single crystal) diffraction technique. And therewithal, fluorescence properties of all these new compounds (**3**-**5**) were investigated first time.

EXPERIMENTAL SECTION

Materials and Instrumentation

The reagents {hexachlorocyclotriphosphazene (Aldrich) and 2-naphthalenethiol (Aldrich)} and solvents {Dichloromethane, DCM, (Merck), *n*-hexane (Merck), tetrahydrofuran, THF, (Merck)} which are used for synthesis of compounds **3**-**5** were purchased commercially. Before using sodium hydride (60% dispersion in mineral oil, Merck), the oil was removed by washing with dry *n*-hexane. Deuterated chloroform for NMR spectroscopy was also received from Merck commercially. Column chromatography was realized by using Merck, Kieselgel 60, 230-400 mesh silica gel. Again, Merck silica gel plates (Merck, Kieselgel 60, 0.25 mm thickness) with F254 indicator were used for Thin Layer Chromatography (TLC).

Elementar Vario MICRO Cube was used for elemental analyses. Molecular masses were measured by Bruker Daltonics Microflex MALDI-TOF (Matrix-Assisted Laser Desorption/Ionization-Time-Of-Flight) spectrometer and 1,8,9-trihydroxyanthracene was used as a matrix. ^{1}H and ^{31}P NMR spectra were analyzed for all compounds in $CDCl_3$ on a Varian INOVA 500 MHz spectrometer. Melting point analyses were performed by Stuart SMP3 melting point apparatus. Varian Eclipse spectrofluorometer and Shimadzu 2101 UV spectrophotometer were used for recording fluorescent and the electronic absorption spectra of compounds **3**-**5** in the UV-Vis region. Measurements were taken at 25 °C using 1 cm-wide quartz cuvettes.

Single crystals were obtained at ambient temperature. Appropriate single crystals of compounds **3** and **5** were selected under a polarized microscope. Then it was cleaned in perfluoro polyether oil and taken to the goniometer to be attached to the single crystal X-Ray diffraction device. Although the data of both compounds were collected, only the data of compound **3** could be refined. Data were obtained with a Bruker APEX II QUAZAR three-circle diffractometer using mono-chromatized Molybdenum X-radiation (λ=0.71073 Å). Absorption correction was performed by the multi-scan method implemented in SADABS (40) and space groups were assigned using XPREP implemented in APEXII (41). Structures were identified using the direct methods procedure in SHELXS-97 and refined by full-matrix least squares on F^2 using SHELXL-97 (42). Aromatic C-bound H atoms were positioned geometrically and refined using a riding mode. Crystal structure validations and geometrical calculations were performed using PLATON software (43). MERCURY software (44) was used for visualization of the cif file. The DIAMOND (45) program was used for molecular drawing. Crystallographic data with Cambridge Crystallographic Data Centre reference number 2052687 for compound **3** has been deposited.

Synthesis of the compounds 3, 4 and 5

Reaction of hexachlorocyclotriphosphazene (1) with 2-naphthalenethiol (2) at a 1:2 molar ratio

Hexachlorocyclotriphosphazene [$P_3N_3Cl_6$] **1**, (1.74 g, 5 mmol) was dissolved in 80 mL of THF in a 250 mL three-necked reaction flask. 2-Naphthalenethiol (1.60 g, 10 mmol) in 20 mL of dry THF was added into the stirred solution. Then, the reaction mixture was cooled on an ice bath and NaH (60% oil suspension, 0.4 g, 10 mmol) in 20 mL of dry THF was quickly added under an inert (Ar) atmosphere. The reaction was continued during a day at ambient temperature. At the end of the reaction, one new product was observed by using TLC solvent system, *n*-hexane-THF (30:1). The crude product was subjected to column chromatography using same

solvent system. Bis geminal naphthylthio compound **3** was eluted from the column. The colorless crystals were obtained from *n*-hexane:DCM (3:1) system.
Anal Calc. for **3**; $C_{20}H_{14}Cl_4N_3P_3S_2$: 40.36 (C); 2.37 (H); 7.06 (N) %, M, 595.2 m/z.

Compound 3 (2.44 g, yield: 82%, m.p. 167 ºC), Found %: 40.66 (C), 2.59 (H), 6.98 (N), $[M]^+$: 595.7 m/z (Figure S1). ^{1}H NMR, in $CDCl_3$ at 25 ºC, δppm; 8.17–7.54 ppm (m, 14H, Ar-*H*). ^{31}P NMR{^{1}H}, $CDCl_3$, 25 ºC, AX_2 spin system, δ(ppm); 11.8 (d, 2xPCl_2, ^2J= 8.30 Hz) and 47.8 [t, $P(SC_{10}H_7)_2$, $^2J_{AX}$ = 8.30 Hz].

Reaction of hexachlorocyclotriphosphazene (1) with 2-naphthalenethiol (2) at a 1:4 molar ratio
The general reaction medium and procedure is the same as in the previous experimental part. In here, hexachlorocyclotriphosphazene [$P_3N_3Cl_6$] **1**, (1.74 g, 5 mmol), 2-naphthalenethiol (3.21 g, 20 mmol) and NaH (60% oil suspension, 0.8 g, 20 mmol) were used. Products were purified again by column chromatography using *n*-hexane-THF (10:1) solvent system. Firstly, bis geminal naphthylthio compound **3** (0.65 g, 21%) was eluted from the column and secondly, tetrakis naphthylthio substituted compound **4** was isolated as a white solid. Although many solvent systems and crystallization techniques were tried, suitable single crystals could not be obtained.
Anal Calc. for **4**; $C_{40}H_{28}Cl_2N_3P_3S_4$: C, 57.01; H, 3.35; N, 4.99 %, M, 842.7 m/z.

Compound 4 (2.78 g, yield: 65%, m.p. 156 °C), Found: C, 57.41; H, 3.59; N, 4.68 %, $[M]^+$, 842.1 m/z (Figure S2). ^{1}H NMR, in $CDCl_3$ at 25 ºC, δppm; 7.99–7.49 ppm (m, 28H, Ar-*H*). ^{31}P NMR{^{1}H}, $CDCl_3$, 25 ºC, A_2X spin system, δ(ppm); 17.9 [s, PCl_2] and 45.6 [s, 2x$P(SC_{10}H_7)_2$].
Reaction of hexachlorocyclotriphosphazene (1) with 2-naphthalenethiol (2) at a 1:6 molar ratio
The general reaction medium and procedure is the same as in the previous experimental parts. In here hexachlorocyclotriphosphazene [$P_3N_3Cl_6$] **1**, (0.44 g, 1.25 mmol), 2-naphthalenethiol (1.20 g, 7.5 mmol) and NaH (60% oil suspension, 0.3 g, 7.5 mmol) were used. Column chromatography solvent system is *n*-hexane-THF (4:1). Firstly, tetrakis naphthylthio compound **4** (0.29 g, 45%) was eluted from the column and secondly, hexakis naphthylthio (full) substituted compound **5** was isolated as a white solid. Compound **5** was re-crystallized from *n*-heptane:DCM (3:1) and obtained as colorless very weak, thin and plate crystals.
Anal Calc. for **5**; $C_{60}H_{42}N_3P_3S_6$: 66.10 (C); 3.88 (H); 3.85 (N) %, M, 1090.3 m/z.

Compound 5 (0.14 g, yield: 10%, m.p. 212 ºC), Found: C, 57.41; H, 3.59; N, 4.68 %, $[M+H]^+$, 1091.8 m/z (Figure S3). ^{1}H NMR, in $CDCl_3$ at 25 ºC, δppm; 7.80–7.28 ppm (m, 42H, Ar-*H)* ^{31}P NMR{^{1}H}, $CDCl_3$, 25 °C, A_3 spin system, δ(ppm); 43.3 [s, 3x$P(SC_{10}H_7)_2$].

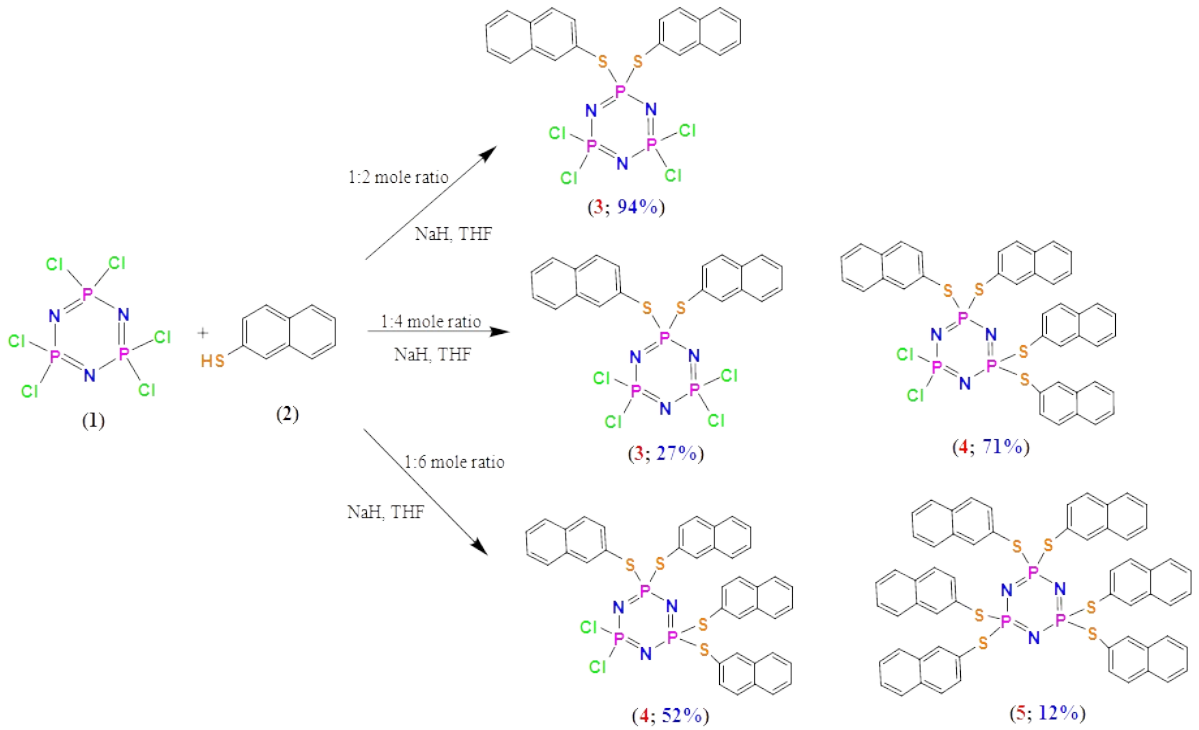

Scheme 1: The synthesis and relative amounts of compounds **3**, **4** and **5**.

RESULTS AND DISCUSSION

Structural Characterization

The reactions of hexachlorocyclotriphosphazene and 2-naphthalenethiol were performed under inert (Ar) atmosphere using THF solvent in the presence of NaH base. Reactions at three different molar ratios (1: 2, 1: 4 and 1: 6) were performed to determine the variety of products. As a result of the reactions; geminal bis (**3**), tetrakis (**4**) and hexakis (**5**) naphthylthio substituted cyclotriphosphazene derivatives were isolated. Formation and diversity of product quantities were determined by detailed examination of $^{31}P\{H\}$ NMR of the reaction mixture. The structures of cyclotriphosphazene derivatives were confirmed by elemental analysis, mass spectroscopy (MALDI-TOF), ^{1}H and ^{31}P NMR spectroscopies. The elemental analyses, mass analysis results and the phosphorus chemical shifts of each new compound are given in the experimental section.

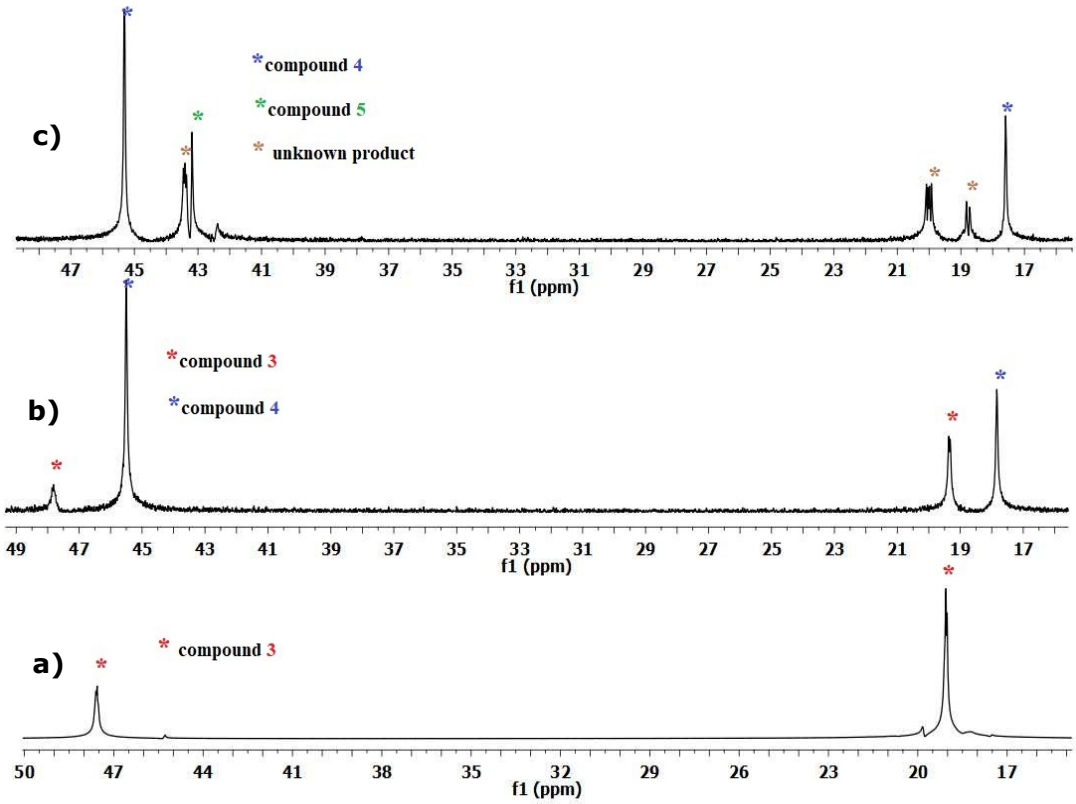

Figure 1. Proton-decoupled ^{31}P NMR spectra of the product of reaction of compound **1** with **2 a)** 1:2 molar ratio **b)** 1:4 molar ratio and **c)** 1:6 molar ratio, in THF solution; the reaction mixture was filtered, and the solvent removed prior to dissolving in $CDCl_3$ solution.

The examination of the $^{31}P\{H\}$ NMR of the reaction mixture allowed for the assignment of the relative amounts of each compound. The proton decoupled ^{31}P NMR spectrum of the reaction mixture, which was carried out at a 1: 2 mole ratio, was examined (Figure 1a), it was observed that the one major product (**3**), which had AX_2 spin system, with 94% yield was formed. At the same time, a product thought to be a trace amount of tetrakis compound was seen in $^{31}P\{H\}$ NMR of the reaction mixture. After purification, when evaluating the mass and elemental analysis of compound **3**, it was determined two naphthylthio groups were attached to the cyclotriphosphazene ring. It actually reveals the geminal or non-geminal bonding possibilities of naphthylthio groups to cyclotriphosphazene core. It is known that the phosphorus atom in thiol group substituted cyclotriphosphazene derivatives shifts to high frequency (downfield) about between 43.0 and 48.0 ppm (32,37). Therefore, it was determined that the group resonating at 48.0 ppm (the integral value of the P atom is one) is naphthylthio substituted phosphorus atom, and the group resonating around 12.0 (the integral value of the P atom is two) ppm belongs to the PCl_2 group. When the spectrum as a whole is evaluated, it is determined that structure is bis-geminal. It is seen $[P(SC_{10}H_7)_2]$ group is split into three due to two PCl_2 groups having the same chemical environment, and double splitting of PCl_2 groups were assigned because of phosphorus atom with naphthylthio group (Figure 2a). Therefore, it is understood from

this point that it follows the S_N1 reaction mechanism as expected. Also, the molecular structure of the bis geminal compound **3** has been confirmed by single crystal X-Ray diffraction.

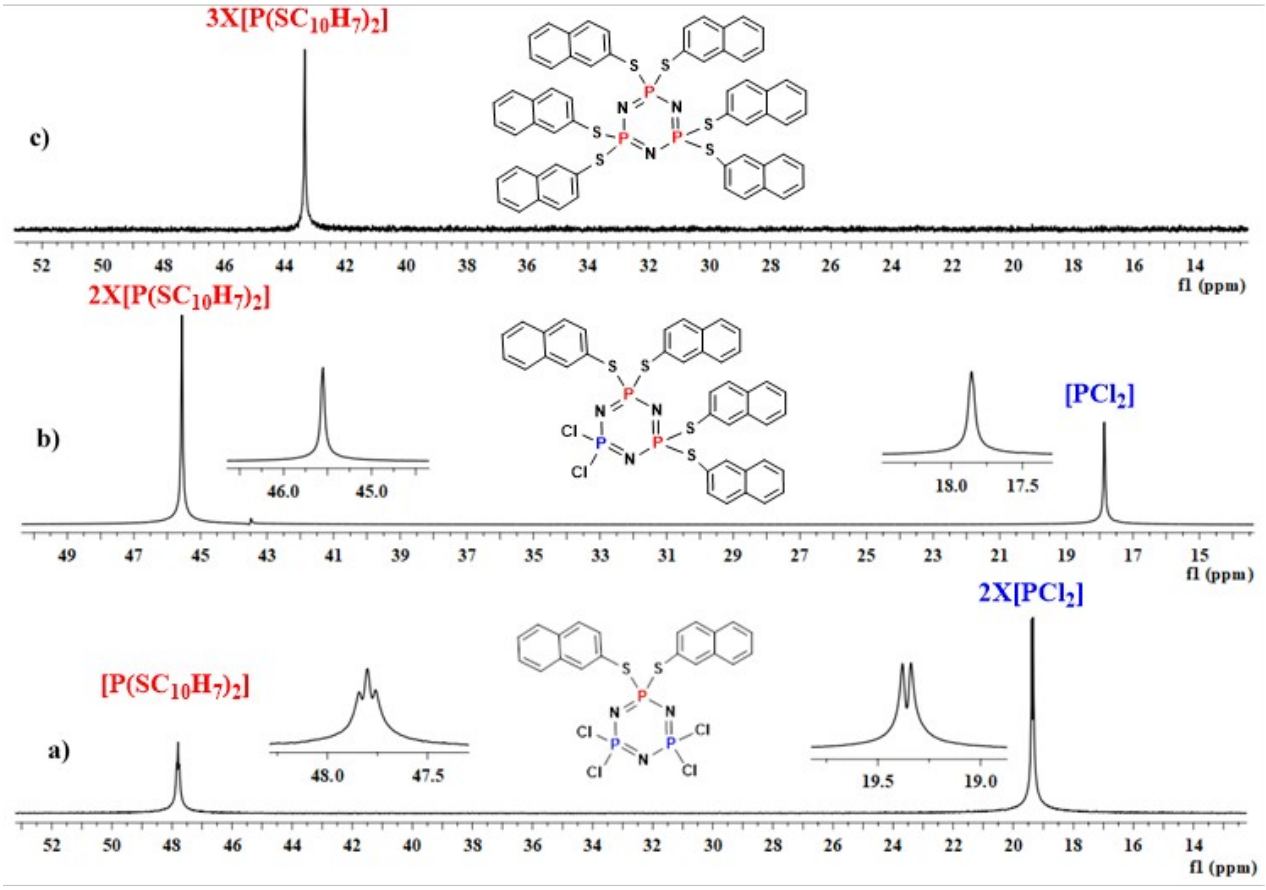

Figure 2. Proton-decoupled ^{31}P NMR spectra of the **a)** compound **3** and **b)** compound **4 c)** compound **5**.

When the ^{31}P NMR spectrum of the reaction mixture was examined at 1: 4 molar ratios, it was seen that two products with spin system AX_2 (27%), belongs to compound **3**, and A_2X (71%) were formed (Figure 1b). When the integral values and locations of the peak groups belonging to the A_2X system were evaluated, it was thought that the structure could be a geminal tetrakis product (**4**). Mass and elemental analyses also confirm this situation. In the ^{31}P NMR spectrum of compound **4**, the peaks of the PCl_2 group and the $[P(SC_{10}H_7)_2]$ group are not split and they are in single peak form (Figure 2b) (32). The Gaussian of the spectrum has been carefully studied. It was observed that the groups $[P(SC_{10}H_7)_2]$ and $[PCl_2]$ did not split again. When $^{31}P\{1H\}$ NMR spectrum was taken in other d-solvent (toluene-d8) may be peak splitting in this group can be observed (32).

When the reaction was carried out at a ratio of 1: 6 moles, it was observed that in $^{31}P\{H\}$ NMR of the reaction mixture, 12% of the hexakis (full) substituted product (**5**) (Figure 1c), which had A_3 spin system (due to the chemical equivalent phosphorus atoms) shown in Figure 2c, 52% of geminal tetrakis product (**4**), which had A_2X spin system, and 36% of unknown products formed in the reaction mixture (Figure 1c).

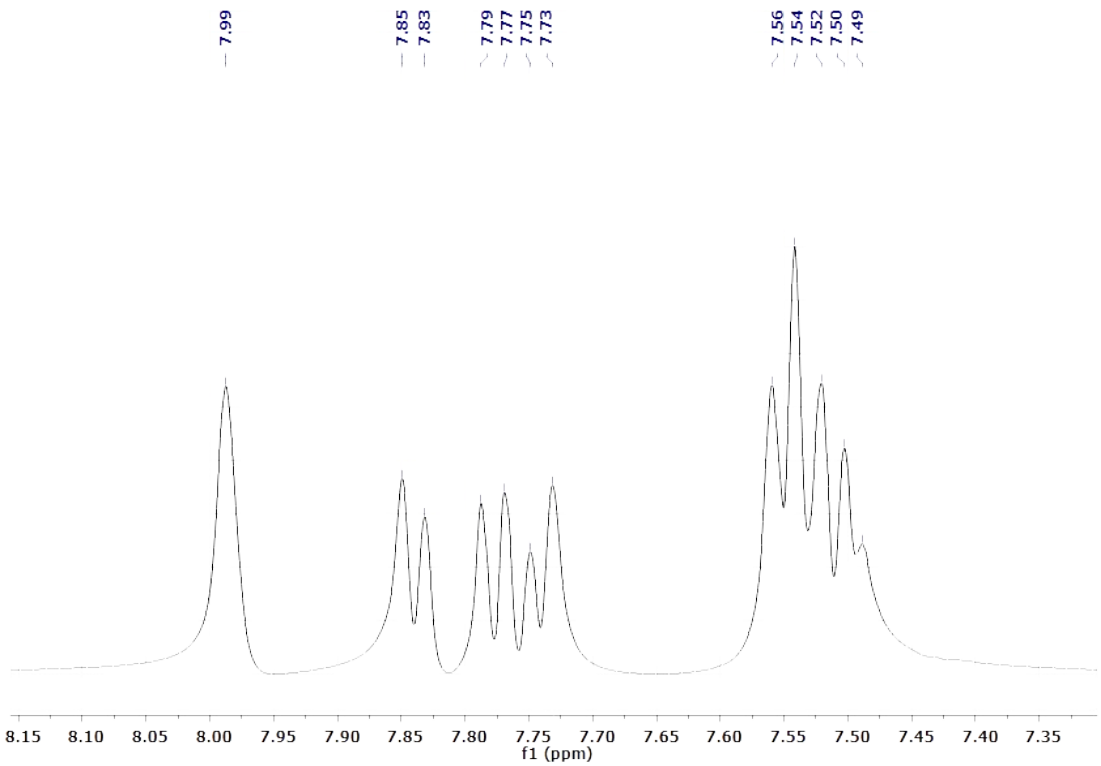

Figure 3. ^{1}H NMR spectrum of the compound **4.**

The ^{1}H NMR spectra of all three compounds (**3**-**5**) are very similar. Aromatic protons in naphthyl groups resonate in the range 7.28-8.17 ppm. Since the protons in the synthesized compounds are all aromatic protons, the spectra are quite similar to each other. Therefore, only the ^{1}H NMR spectrum of compound **4** is given as an example (Figure 3). ^{1}H NMR spectra of compounds **3** and **5** were also given supplementary material (Figure S4 and S5).

X-Ray Structure Analysis for Compound 3

The crystal structure of **3** was illuminated by single crystal X-Ray diffraction. The molecular structure of **3** along with the atom-numbering scheme is shown in Figure 4. The crystal structure of compound **5** was also approved by single crystal X-ray diffraction. But the crystal structure could not be fully elucidated due to crystallographic problems. Although different crystallization systems and methods were tried, suitable crystals could not be obtained. The X-Ray crystallographic data collection and refinement parameters for compound **3** are summarized in Table 1.

The crystal structure of compound **3** showed that it contains a 6-membered cyclotriphosphazene (P_3N_3) ring, substituted with two 2-naphtalenethio groups on the same phosphorus atom (P1) (Figure 4). Compound **3** has orthorhombic system, space group P*ccn*, and molecule sits on inversion centre [symmetry code (#): 1/2-x,3/2-y, z] (Table 1).

Table 1. X-ray crystallographic parameters for compound **3**.

Compound	**3**
Empirical formula	$C_{20}H_{14}Cl_4N_3P_3S_2$
Formula weight (g/mol)	595.17
Temperature (K)	296(2)
Crystal system	orthorhombic
Space group	P c c n
a(Å)	6.9214(5)
b(Å)	13.6686(8)
c(Å)	26.4880(16)
α (°)	90
β (°)	90

γ (°)	90
Volume (Å^3)	2505.9(3)
Z	4
Density (calc, Mg/m^3)	1.578
Absorption Coefficient (mm^{-1})	0.847
F(000)	1200
Crystal size (mm^3)	0.18 x 0.20 x 0.31
θ_{max} (°)	25.00
Reflections collected	32937
Independent reflections	2207
R_{int} (merging R value)	0.0351
Parameter	146
R (F^2>2ΘF^2)	0.0377
wR (all data)	0.1046
Goodness-of-fit on F^2	1.057
Θ× max / min (eÅ^{-3})	0.574 and -0.476

Table 2. Some bond and conformational parameters of compound **3**

	3		**3**
P1-N1	1.600(2)	**N1-P2-N2**	119.52(13)
N1-P2	1.557(2)	**P1-N1-P2**	122.31(14)
P2-N2	1.5771(17)	**N1-P1-N1**	116.06(16)
P1-S1	2.0574(8)	**P2-N2-P2**	120.2(2)
P2-Cl1	1.9794(13)	**N1-P1-S1**	101.26(9)
P2-Cl2	1.9977(12)	**N1-P1-S1**	114.19(10)
S1-C1	1.778(2)	**N2-P2-Cl1**	108.52(8)
P1-N1-P2-N2	3.4(2)	**N2-P2-Cl2**	108.21(7)
N1-P2-N2-P2	-1.66(12)	**C1-S1-P1**	103.59(8)
P2-N1-P1-N1	-1.72(13)	**S1-P1-S1**	110.33(5)
Cl2-P2-N1-P1	-121.55(17)	**Cl1-P2-N1-P1**	129.62(16)
S1-P1-N1-P2	-118.97(17)	**S1-P1-N1-P2**	122.50(18)
Cl2-P2-N2-P2	123.58(6)	**Cl1-P2-N2-P2**	-128.46(7)
P1-S1-C1-C2	61.1(2)	**P1-S1-C1-C10**	-124.00(18)
Max. Deviation for P_3N_3 ring	-0.020(2) (N1)	**Puckering amplitude,Q for P_3N_3**	Planar

There have been some changes in P-N bond lengths and P-N-P bond angles as a result of the replacement of 2-naphthylthio groups with Cl atoms. The P1-N1 bond length [1.600 (2) Å] is slightly greater than the bond length of P2-N2 [1.5771 (17) Å] (Table 2). Also, the P1-S1 bond length [2.0574(8) Å] is slightly greater than the P-Cl bond lengths [av.1.9885 Å]. When the N-P-N angles were examined, it was determined that the N1-P1-N1 bond angle [116.06 (16) Å] containing the P1 phosphorus atom (naphthylthio group substituted) was smaller than the N1-P2-N2 bond angle [119.52 (13) Å] (Table 2). In compound **3**, 6-membered cyclophosphazene ring is planar and the max. deviations from the main plane is -0.020(2) (N1) (Table 2). The found values are similar and compatible with the bis geminal 1-naphthylthio substituted cyclotriphosphazene compound (37), as well as with other substituted cyclotriphosphazene compounds (46–49). The crystal structures of bis geminal 1-naphthalenethio cyclotriphosphazene compound, which was previously synthesized (37), and the compound **3** which was synthesized in this study were compared. Crystal structures of bis geminal 1- and 2-naphthylamino cyclotriphosphazenes (37,38) were also examined in CCDC (Cambridge Crystallographic Data Centre) in order to investigate this difference, but it was seen that there was not such a big difference as in thiol groups. Interestingly, it was observed that the naphthylthio groups in these two isomers crystallized at very different positions (Figure 5).

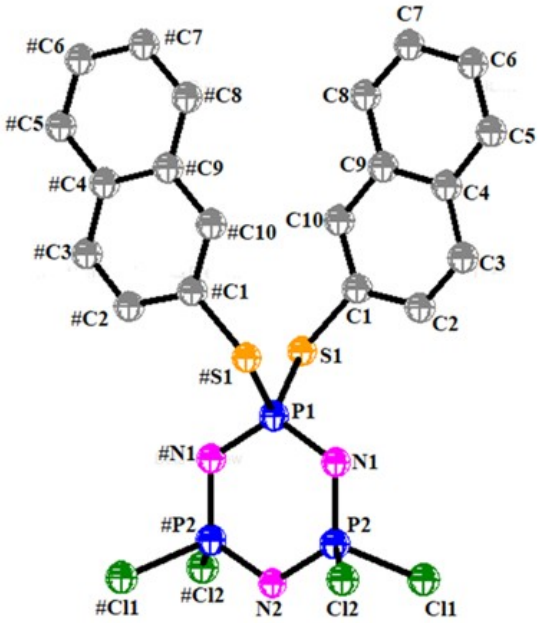

Figure 4. Molecular structure of compound **3** (ellipsoids were drawn 50% probability level). All hydrogen atoms were omitted for clarity.

In the 1-naphthylthio group substituted cyclotriphosphazene compound, the distance between S-S was 3.150 Å, while this value was 3.377 Å in the 2-naphthylthio substituted cyclotriphosphazene (**3**). Also, the S-P-S angle of compound **3** (110.33º) is also greater than the S-P-S (98.45º) in the 1-naphthylthio isomer (Figure 5). The different position of the naphthyl groups naturally resulted in the differences between intra and inter molecular interactions. While in 1-naphthylthio cyclotriphosphazene compound, the N atom and Cl atom in the P_3N_3 ring play a role in intermolecular interactions (Figure 6a), in compound **3**, the C, H and S groups on the naphthyl groups are predominantly involved in the interactions (Figure 6b). Crystal-packing give very important and valuable information about the arrangement of the molecules in the crystal. Therefore, in order to investigate the contributions of the interactions of aromatic rings on cyclotriphosphazene ring, crystal packing of compound **3** was examined. The packing of both isomers along the *b* axis is shown in Figure 6. Compound **3** has π-π interactions (Figure 6c) in the crystalline structure ranging from 3.6725 (15) Å (Cg2-Cg2; Cg2 is the centroids of the C4-C9 ring) to 5.8031 (14) Å (Cg2-Cg4; Cg2 and Cg4 are the centroids of the C4-C9 and C1-C10 rings, respectively).

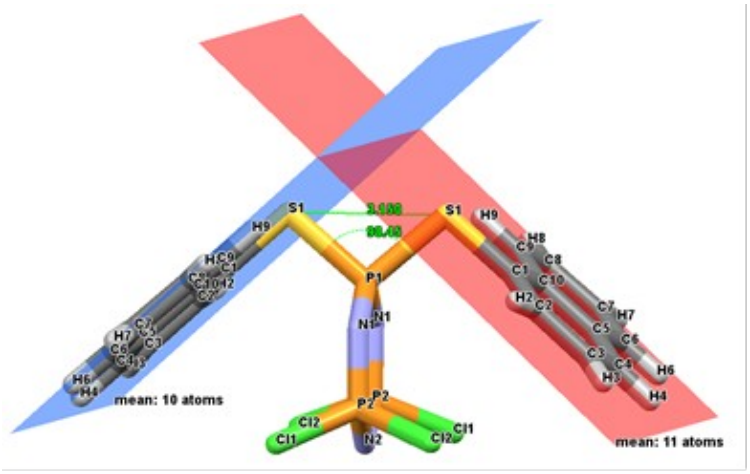

a)

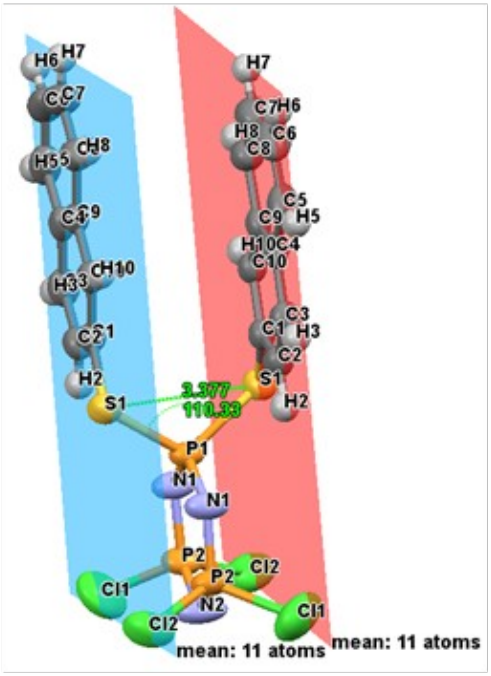

b)

Figure 5. Position of naphthylthio groups on main plane and representation of P-S and S-S distances a) 1-naphthylthio groups (37) b) 2- naphthylthio groups.

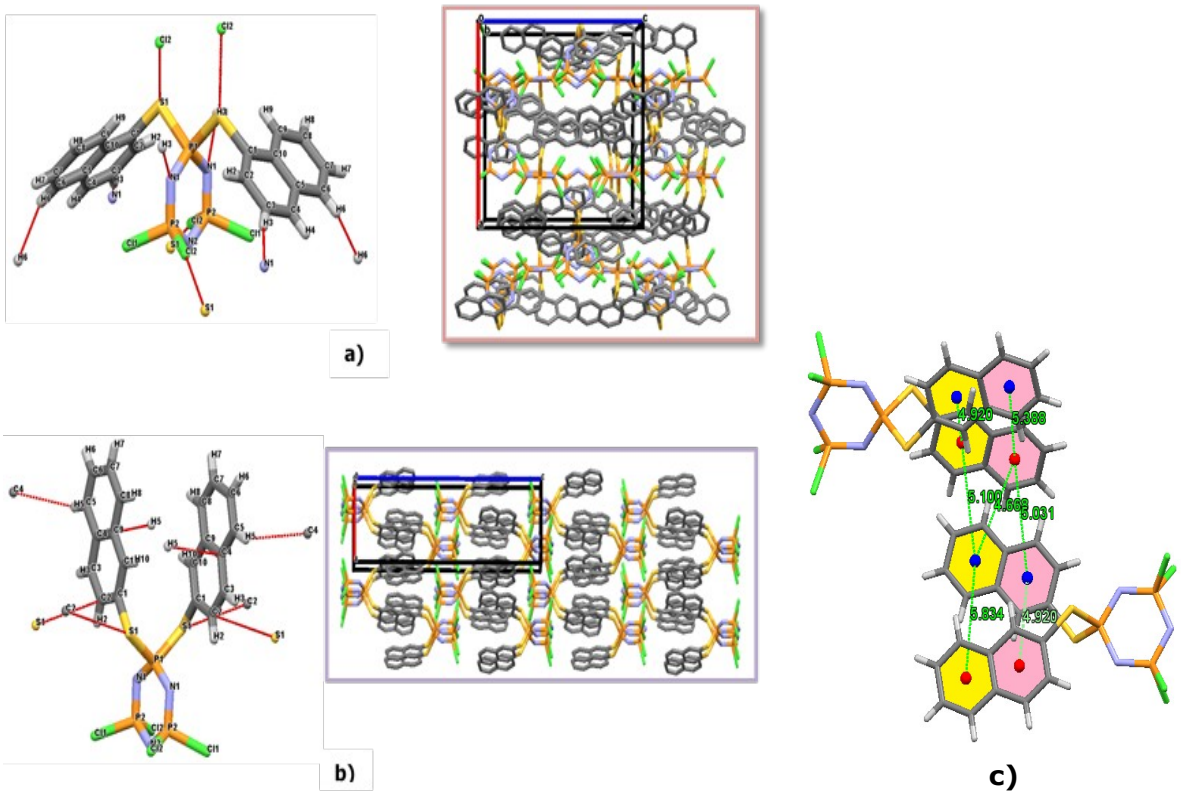

Figure 6: Representation of inter molecular interactions and the arrangement / packaging of molecules along the *b* axis **a)** bis geminal 1-naphthylthio (38) **b)** bis geminal 2-naphthylthio cyclotriphosphazene (**3**) **c)** π-π interactions in compound **3**

Fluorescence Properties

The hexachlorocyclotriphosphazene can be used as a suitable scaffold for optical materials because the six membered $(PN)_3$ skeleton does not have any absorption or emission properties in UV–Vis region (46). In this work, after structural characterization of **3**, **4** and **5**, it was examined the absorption and emission properties of 2-naphthalenethiol-substituted cyclotriphosphazene derivatives in solution state by UV–Vis absorption and florescence emission experiments.

Fluorescence studies of naphthol and naphthylamine substituted cyclotriphosphazene (38,39) compounds have been previously conducted in the literature. However, there is no information about on fluorescence studies of naphthylthio cyclotriphosphazene derivatives. Electronic absorbance and fluorescence measurements of these new compounds (**3**-**5**) were carried out under three different concentrations ($1x10^{-6}$ M, $5x10^{-6}$ M and $1x10^{-5}$ M) in tetrahydrofuran (THF). UV absorption bands in compound **3**-**5** were observed in the range of 270-280 nm, except for small changes in peak intensities. Fluorescence emission peaks were observed around 310 nm. It was determined that the fluorescence intensity was approximately the same in the three compounds at $1x10^{-6}$ M and $5x10^{-6}$ M THF. Fluorescence emission spectra are given in Figure 7.

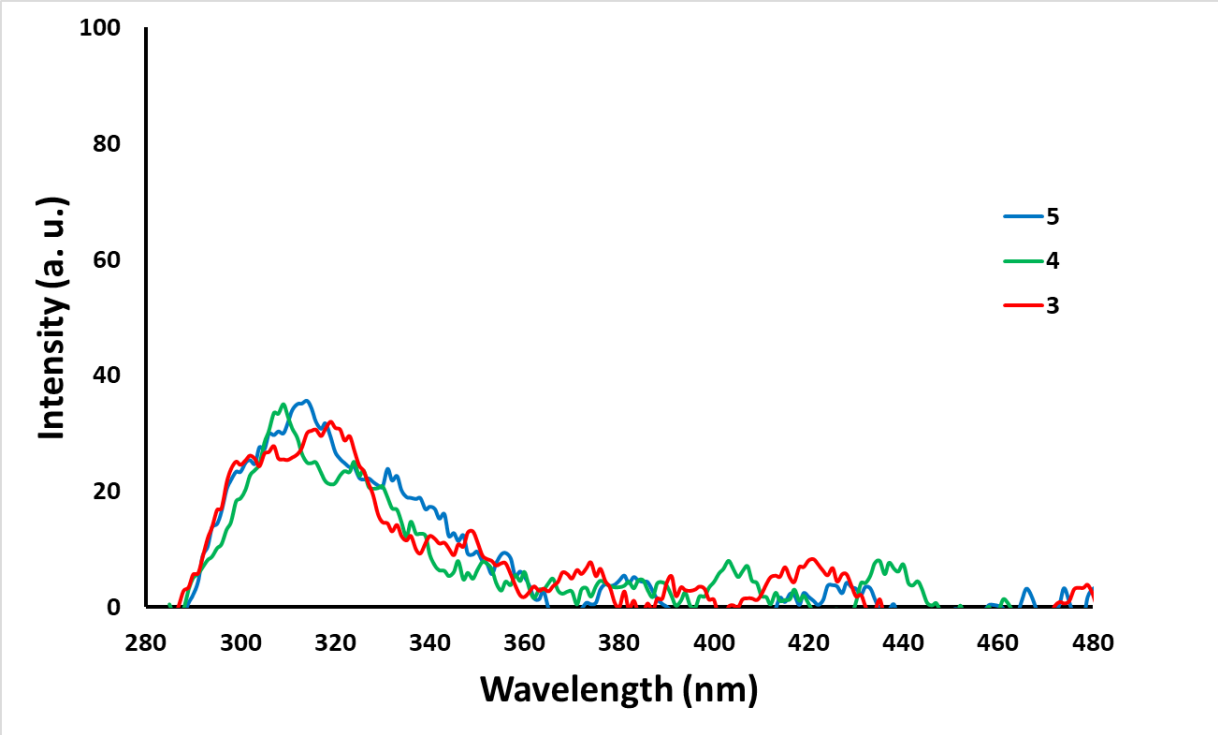

Figure 7: Fluorescence emission spectra of compounds **3**-**5** in THF. (Concentration:1x10^{-6} mol dm^{-3}; λ_{ex}: 270 nm).

It was determined that 2-naphthylthio cyclotriphosphazene derivatives showed weak fluorescence especially when compared to full naphthylamine substituted cyclotriphosphazene derivative. When the fluorescence properties in 1x10^{-5} M THF were examined, emission bands around 310 nm were observed again in all three compounds. But there have been changes in emission band strengths. Emission intensity was determined as 3> 4> 5 (Figure 8). The reason for the difference here may be self-quenching depending on the increase in concentration.

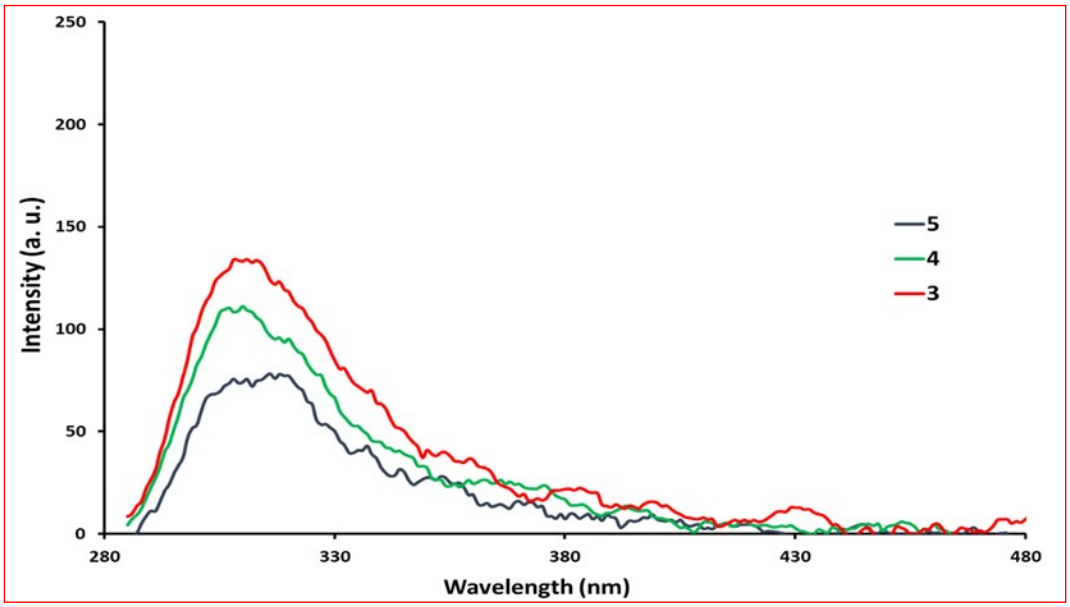

Figure 8: Fluorescence emission response of compounds **3**-**5** in THF solutions. (Concentration:1x10^{-5}mol dm^{-3}; λex : 270 nm).

CONCLUSION

In this study, three new cyclotriphosphazene derivatives bearing with 2-naphthylthio groups (**3**-**5**) were synthesized. Their structures have been elucidated using various analysis methods (^{1}H, ^{31}P NMR, MALDI-TOF and elemental analysis). Moreover, the molecular structure of compound **3** was illuminated with single crystal X-Ray diffractometer. The crystal structure of bis geminal 1-naphthylthio cyclotriphosphazene, which is the binding isomer of each other and previously synthesized, and the crystal structure of compound **3** in this study were compared with previous work in the literature. While the naphthalene groups in compound **3** are parallel to the cyclotriphosphazene ring, in the 1-naphthylthio group, unlike this structure, the naphthalene groups diverged from each other and turned downward. Fluorescence spectral properties of **3**-**5** compounds were studied for the first time. It was determined that cyclotriphosphazenes containing 2-naphthylthio group gave fluorescence signal around 310 nm. This study will provide a guide for future studies, because of the examination of fluorescence properties of 2-naphthylthio groups.

Appendix A. Supplementary Data

CCDC 2052687 contains the supplementary crystallographic data for compound **3**. This data can be obtained free of charge via http://www.ccdc.cam.ac.uk/conts/retrieving.html, or from the Cambridge Crystallographic Data Centre, 12 Union Road, Cambridge CB2 1EZ, UK; fax: (+44) 1223-336-033; or e-mail: deposit@ccdc.cam.ac.uk

REFERENCES

1. Gleria M, Jaeger RD, editors. Applicative aspects of cyclophosphazenes. New York: Nova Science Publishers; 2004. 371 p.

2. Allcock HR. Chemistry and applications of polyphosphazenes [Internet]. Hoboken, N.J: Wiley-Interscience; 2003. 725 p. Available from: https://www.wiley.com/en-us/Chemistry+and+Applications+of+Polyphosphazenes-p-9780471443711

3. Bowers DJ, Wright BD, Scionti V, Schultz A, Panzner MJ, Twum EB, et al. Structure and Conformation of the Medium-Sized Chlorophosphazene Rings. Inorg Chem. 2014 Sep 2;53(17):8874–86.

4. Uslu A, Mutlu Balcı C, Yuksel F, Özcan E, Dural S, Beşli S. The investigation of thermosensitive properties of phosphazene derivatives bearing amino acid ester groups. J Mol Struct. 2017 May;1136:90–9.

5. Liu X, Breon JP, Chen C, Allcock HR. Substituent exchange reactions of trimeric and tetrameric aryloxycyclophosphazenes with sodium 2,2,2-trifluoroethoxide. Dalton Trans. 2012;41(7):2100–9.

6. Jiménez J, Callizo L, Serrano JL, Barberá J, Oriol L. Mixed-Substituent Cyclophosphazenes with Calamitic and Polycatenar Mesogens. Inorg Chem. 2017 Jul 17;56(14):7907–21.

7. Kumar D, Singh N, Keshav K, Elias AJ. Ring-Closing Metathesis Reactions of Terminal Alkene-Derived Cyclic Phosphazenes. Inorg Chem. 2011 Jan 3;50(1):250–60.

8. Mukundam V, Dhanunjayarao K, Mamidala R, Venkatasubbaiah K. Synthesis, characterization and aggregation induced enhanced emission properties of tetraaryl pyrazole decorated cyclophosphazenes. J Mater Chem C. 2016;4(16):3523–30.

9. Allen CW, Brown DE, Worley SD. Synthesis and Spectroscopy of $N_3P_3X_5OCHCH_2$ (X = Cl, F, OCH_3, OCH_2CF_3, $N(CH_3)_2$) and $N_3P_3X_4(OCHCH_2)_2$ (X = Cl, $N(CH_3)_2$). Correlations of Ultraviolet Photoelectron Spectroscopy and Nuclear Magnetic Resonance Data to Electronic and Geometrical Structure. Inorg Chem. 2000 Feb;39(4):810–4.

10. Ainscough EW, Brodie AM, Davidson RJ, Moubaraki B, Murray KS, Otter CA, et al. Metal−Metal Communication in Copper(II) Complexes of Cyclotetraphosphazene Ligands. Inorg Chem. 2008 Oct 20;47(20):9182–92.

11. Keshav K, Singh N, Elias AJ. Synthesis and Reactions of Ethynylferrocene-Derived Fluoro- and Chlorocyclotriphosphazenes. Inorg Chem. 2010 Jun 21;49(12):5753–65.

12. Carriedo GA, García Alonso FJ, Gómez Elipe P, Brillas E, Labarta A, Juliá L. Macromolecular Polyradicals with Cyclic Triphosphazene as a Core. Spectral and Electrochemical Properties. J Org Chem. 2004 Jan;69(1):99–104.

13. Liang W-J, Li Y-L, Zhao P-H, Zhao G-Z. Facile synthesis, spectroscopic characterization, and crystal structures of dioxybiphenyl bridged cyclotriphosphazenes. Polyhedron. 2017 Jun;129:30–7.

14. Zhu X, Liang Y, Zhang D, Wang L, Ye Y, Zhao Y. Synthesis and Characterization of Side Group–Modified Cyclotetraphosphazene Derivatives.

Phosphorus Sulfur Silicon Relat Elem. 2011 Jan 31;186(2):281–6.

15. Okutan E, Çoşut B, Beyaz Kayıran S, Durmuş M, Kılıç A, Yeşilot S. Synthesis of a dendrimeric phenoxy-substituted cyclotetraphosphazene and its non-covalent interactions with multiwalled carbon nanotubes. Polyhedron. 2014 Jan;67:344–50.

16. Okumuş A, Elmas G, Cemaloğlu R, Aydın B, Binici A, Şimşek H, et al. Phosphorus–nitrogen compounds. Part 35. Syntheses, spectroscopic and electrochemical properties, and antituberculosis, antimicrobial and cytotoxic activities of mono-ferrocenyl-spirocyclotetraphosphazenes. New J Chem. 2016;40(6):5588–603.

17. Akbaş H, Karadağ A, Destegül A, Çakırlar Ç, Yerli Y, Tekin KC, et al. Synthesis, and spectroscopic, thermal and dielectric properties of phosphazene based ionic liquids: OFET application and tribological behavior. New J Chem. 2019;43(5):2098–110.

18. Beşli S, Mutlu Balcı C, Doğan S, Allen CW. Regiochemical Control in the Substitution Reactions of Cyclotriphosphazene Derivatives with Secondary Amines. Inorg Chem. 2018 Oct;57(19):12066–77.

19. Yıldırım T, Şenkuytu E, Ergene E, Bilgin K, Uludağ Y, Çiftçi GY. Biological Activity of New Cyclophosphazene Derivatives Including Fluorenylidene-Bridged Cyclophosphazenes. ChemistrySelect. 2018 Sep 14;3(34):9933–9.

20. Ün İ, İbişoğlu H, Kılıç A, Ün ŞŞ, Yuksel F. Nucleophilic substitution reactions of adamantane derivatives with cyclophosphazenes. Inorganica Chim Acta. 2012 May;387:226–33.

21. Yenilmez Çiftçi G, Şenkuytu E, Durmuş M, Yuksel F, Kılıç A. Fluorenylidene bridged cyclotriphosphazenes: 'turn-off' fluorescence probe for Cu2+ and Fe3+ ions. Dalton Trans. 2013;42(41):14916.

22. Elmas (nee Egemen) G, Okumuş A, Kılıç Z, Hökelek T, Açık L, Dal H, et al. Phosphorus–Nitrogen Compounds. Part 24. Syntheses, Crystal Structures, Spectroscopic and Stereogenic Properties, Biological Activities, and DNA Interactions of Novel Spiro-ansa-spiro- and Ansa-spiro-ansa-cyclotetraphosphazenes. Inorg Chem. 2012 Dec 3;51(23):12841–56.

23. Yıldırım T, Bilgin K, Çiftçi GY, Eçik ET, Şenkuytu E, Uludağ Y, et al. Synthesis, cytotoxicity and apoptosis of cyclotriphosphazene compounds as anti-cancer agents. Eur J Med Chem. 2012 Jun;52:213–20.

24. Çiftçi GY, Eçik ET, Yıldırım T, Bilgin K, Şenkuytu E, Yuksel F, et al. Synthesis and characterization of new cyclotriphosphazene compounds. Tetrahedron. 2013 Feb;69(5):1454–61.

25. Davarcı D, Beşli S, Demirbas E. Synthesis of a series of triple-bridged cyclotriphosphazene hexa-alkoxy derivatives and investigation of their structural and mesomorphic properties. Liq Cryst. 2013 May 1;40(5):624–31.

26. Bolink HJ, Santamaria SG, Sudhakar S, Zhen C, Sellinger A. Solution processable phosphorescent dendrimers based on cyclic phosphazenes for use in organic light emitting diodes (OLEDs). Chem Commun. 2008;(5):618–20.

27. Dell D, Fitzsimmons BW, Shaw RA. 752. Phosphorus–nitrogen compounds. Part XIII. Phenoxy- and p-bromophenoxy-chlorocyclotriphosphazatrienes. J Chem Soc. 1965;0(0):4070–3.

28. Schmutz JL, Allcock HR. Phosphorus-nitrogen compounds. XXIII. Reaction of sodium 2,2,2-trifluoroethoxide with hexachlorocyclotriphosphazene. Inorg Chem. 1975 Oct;14(10):2433–8.

29. Carter KR, Calichman M, Allen CW. Stereodirective Effects in Mixed Substituent Vinyloxycyclotriphosphazenes. Inorg Chem. 2009 Aug 3;48(15):7476–81.

30. Nataro C, Myer CN, Cleaver WM, Allen CW. Synthesis and characterization of ferrocenylalcohol derivatives of hexachlorocyclotriphosphazene. X-ray crystal structure of N3P3Cl5OCH2CH2C5H4FeCp. J Organomet Chem. 2001 Dec;637–639:284–90.

31. Coles SJ, Davies DB, Hursthouse MB, İbişoğlu H, Kılıç A, Shaw RA. 4,4,6,6-Tetrachloro-2-[(2,4-dimethylphenyl)sulfanyl]- *N* -[4-(2,2,4,4-tetrachloro-1,3,5,7,11-pentaaza-2λ ^{5} ,4λ ^{5} ,6λ ^{5} -triphosphaspiro[5.5]undeca-1,3,5-trien-7-yl)butyl]-1,3,5,2λ ^{5} ,4λ ^{5} ,6λ ^{5} -triazatriphosphinin-2-amine. Acta Crystallogr Sect E Struct Rep Online. 2007 Sep 15;63(9):o3753–o3753.

32. İbişoğlu H, Dal H, Hökelek T, Kılıç A, Ün İ, Vardı S. The reaction of thiophenoxide with amino-substituted chloro-cyclotriphosphazenes. Polyhedron. 2009 Sep;28(14):2863–70.

33. Carroll AP, Shaw RA. Phosphorus–nitrogen compounds. Part XXI. Alkylthio- and phenylthio-

cyclotriphosphazatrienes. J Chem Soc A. 1966;0(0):914–21.

34. Jung O-S, Park SH, Lee Y-A, Cho Y, Kim KM, Lee S, et al. Unique Intramolecular Interaction in Cyclotriphosphazene Molecule. Synthesis, Structure, and Properties of 1,1-Bis(pyridyl-2-thio)-3,3,5,5-tetrachlorocyclotriphosphazene. Inorg Chem. 1996 Jan;35(23):6899–901.

35. Allen CW. Regio- and stereochemical control in substitution reactions of cyclophosphazenes. Chem Rev. 1991 Mar;91(2):119–35.

36. Allcock HR. Recent advances in phosphazene (phosphonitrilic) chemistry. Chem Rev. 1972 Aug;72(4):315–56.

37. İbişoğlu H, Güzel AM. Syntheses and characterizations of cyclotriphosphazenes containing 1-naphthyl derivatives. Polyhedron. 2015 Nov;100:139–45.

38. Yenilmez Çiftçi G, Şenkuytu E, Durmuş M, Yuksel F, Kılıç A. Structural and fluorescence properties of 2-naphthylamine substituted cyclotriphosphazenes. Inorganica Chim Acta. 2014 Nov;423:489–95.

39. Çoşut B, Yeşilot S. Synthesis, thermal and photophysical properties of naphthoxycyclotriphosphazenyl-substituted dendrimeric cyclic phosphazenes. Polyhedron. 2012 Mar;35(1):101–7.

40. Bruker AXS Inc. SADABS. Madison, WI, USA; 2005.

41. Bruker AXS Inc. APEX2, version 2014.1-1. Madison, WI, USA; 2014.

42. Sheldrick GM. A short history of *SHELX*. Acta Crystallogr A. 2008 Jan 1;64(1):112–22.

43. A.L.Spek. PLATON. Netherlands: Utrecht University, Padualaan 8, 3584 CH Utrecht;

44. Macrae CF, Bruno IJ, Chisholm JA, Edgington PR, McCabe P, Pidcock E, et al. *Mercury CSD 2.0* – new features for the visualization and investigation of crystal structures. J Appl Crystallogr. 2008 Apr 1;41(2):466–70.

45. Brandenburg, K., Berndt, M. Diamond. Bonn, Germany: Crystal impact Gb R; 1999.

46. Çoşut B, Durmuş M, Kılıç A, Yeşilot S. Synthesis, thermal and photophysical properties of phenoxy-substituted dendrimeric cyclic phosphazenes. Inorganica Chim Acta. 2011 Jan;366(1):161–72.

2-Naphthylsulfanyl Cyclotriphosphazene Derivatives: Synthesis, Characterization, Crystallographic and Fluorescence Properties

Ceylan MUTLU BALCI[1]*

[1]Department of Chemistry, Gebze Technical University, Gebze 41400, Kocaeli, Turkey
Corresponding author e-mail: ceylanmutlu@gtu.edu.tr

Supplementary Material

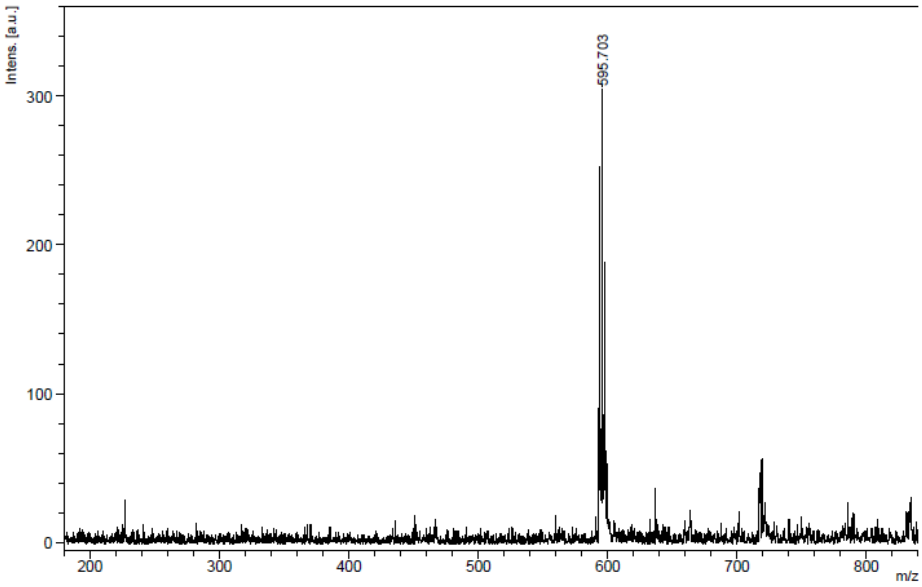

Figure S1. Mass spectrum (MALDI-TOF) of compound **3**

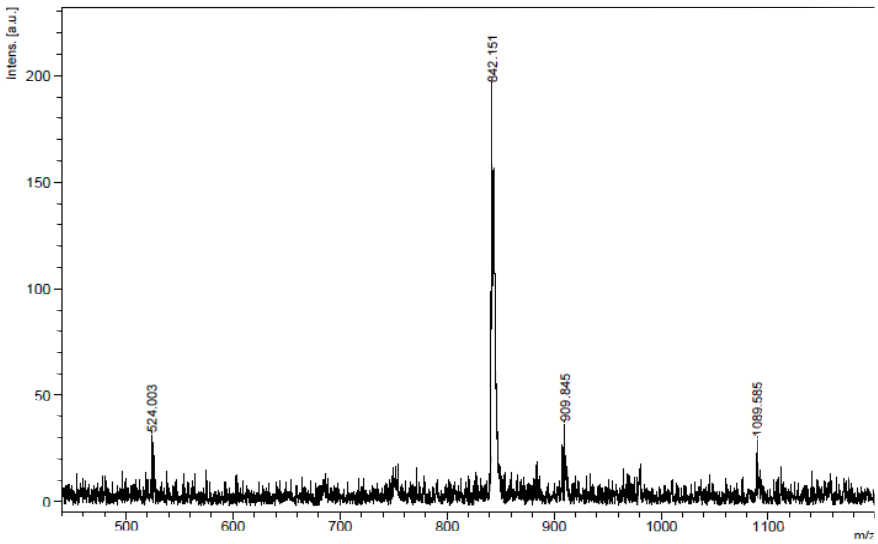

Figure S2. Mass spectrum (MALDI-TOF) of compound **4**

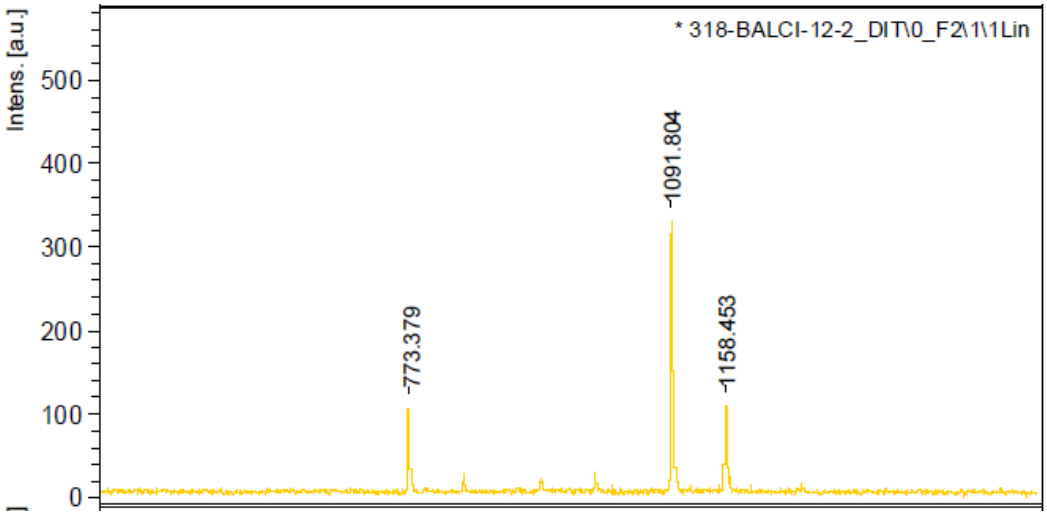

Figure S3. Mass spectrum (MALDI-TOF) of compound **5**

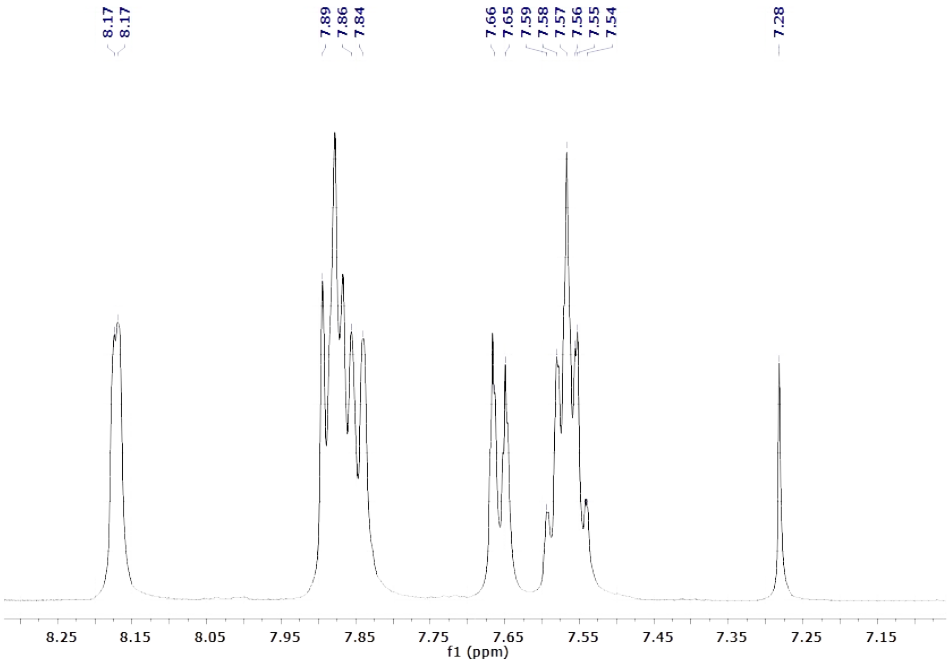

Figure S4. ^{1}H NMR spectrum of the compound **3.**

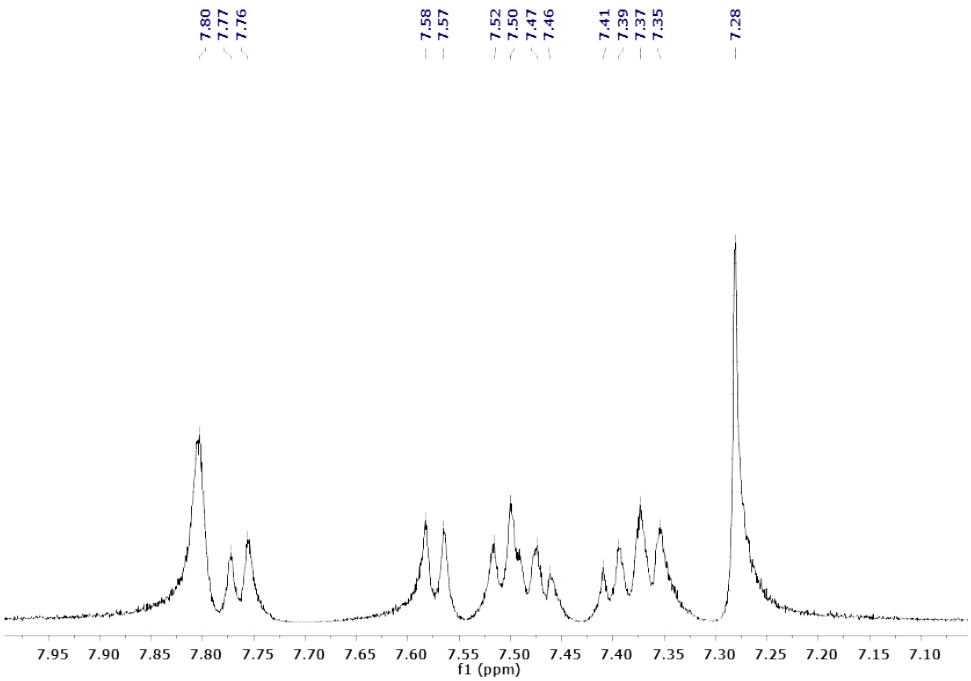

Figure S5. ^{1}H NMR spectrum of the compound **5**.

JOTCS A
Journal of the Turkish Chemical Society
Section: A
Chemistry
TURKISH CHEMICAL SOCIETY

Preparation and characterization of Co-doped TiO_2 for efficient photocatalytic degradation of Ibuprofen

Hatice Çağlar Yılmaz*, Ceren İlhan, Emrah Akgeyik, Sema Erdemoğlu

İnönü University, Department of Chemistry, Art and Science Faculty, Malatya, Turkey.

Abstract: Photocatalytic degradation of Ibuprofen (IBU) which is an anti-inflammatory drug was investigated in aqueous solution by Co-doped TiO_2 and bare TiO_2 synthesized by reflux route. The prepared catalyst powders were fully characterized using X-ray diffraction (XRD), FT-IR spectroscopy, scanning electron microscopy (SEM), BET surface areas, X-ray Fluorescence Spectroscopy (XRF), dynamic light scattering (DLS). Efficiency of photocatalytic activity for synthesized Co-doped and bare TiO_2 was evaluated for the degradation of IBU under UV-C and visible irradiation by investigating the effects of cobalt doping percentage, amount of catalyst, irradiation time, initial IBU concentration, pH and also the effect of organic and inorganic matrix. At optimum degradation conditions under UV-C light and visible light, photocatalytic degradation rates were monitored using UV/Vis spectrophotometer, HPLC and Total Organic Carbon (TOC) analysis. The results showed up the degradation of IBU was improved upon Co doping. It was detected that complete removal was achieved within 240 min of irradiation under UV-C and 98% of IBU was decomposed under visible light in 300 min.

Keywords: Co-doped TiO_2, wastewater, veterinary drugs, ibuprofen, advanced oxidation techniques.

Submitted: January 25, 2021**. Accepted:** April 07, 2021**.**

Cite this: Çağlar Yılmaz H, İlhan C, Akgeyik E, Erdemoğlu S. Preparation and characterization of Co-doped TiO2 for efficient photocatalytic degradation of Ibuprofen. JOTCSA. 2021;8(2):553–66.

DOI: https://doi.org/10.18596/jotcsa.855107.

Corresponding author. E-mail: hatice.caglar@inonu.edu.tr

INTRODUCTION

Marine pollution results from several causes, such as wastewater discharge from industrial and commercial sources, products that contain chemical substances, and widespread usage of medical and cosmetic products by human beings (1). Pharmaceutical pollution has attracted particular attention both due to limited information on its effects on the environment and its possible deadly impacts on wildlife, humans, and aquatic ecosystems (2). One of the pharmaceuticals with a wide range of usage is ibuprofen, an NSAID (a non-steroidal anti-inflammatory drug) with low solubility in water (0.021 mg/mL at 20 °C) but is quite soluble in most organic solvents. Its usage areas include the treatment of fever, pain and inflammation, migraines, and rheumatoid arthritis. Ibuprofen's direct and indirect use in everyday life can lead to leaching into groundwater and soil, just like other pharmaceuticals. The elimination of pharmaceuticals is important as drug degradation is not widely included in traditional wastewater treatment facilities (3).

The elimination of resistant toxic chemicals is necessary to degrade pharmaceutical organic pollutants found at different amounts in various water sources and ensure quality drinking water is available. To this end, various methods, including chemical oxidation through chemical-physical and biological processes, are used. Since persistent organic pollutants (POPs), which have toxic impacts on microorganisms, are resistant to known environmental degradation processes, biological processes fail to eliminate such pollutants in

wastewater. For this reason, more effective degradation techniques must be developed (4). The process of chemical oxidation, which is not a cost-effective method for the degradation of pollutants at high concentrations, is not appropriate for eliminating all organic pollutants. For this reason, the removal or degradation of persistent organic pollutants required the development of a number of oxidative degradation processes. Degradation and removal methods are classified into two groups: Photochemical Advanced Oxidation Processes and Ozonation Processes. Many studies conducted in recent years on advanced oxidation techniques aimed to achieve the degradation of persistent organic pollutants by using heterogeneous semiconductor photocatalysts such as ZnO, Fe_2O_3, TiO_2. These studies focused especially on removing textile dyes from wastewater. Free hydroxyl radicals are formed by heterogeneous photocatalysis, particularly the absorption of under 400 nm light. The formed free radicals are later used in the degradation of organic pollutants. With its high photocatalytic activity, superior functionality, and low cost, TiO_2 has an important place in advanced oxidation technology.

Nevertheless, the rapid electron-hole recombination has a decreasing effect on the photocatalytic activity of TiO_2 (5). The introduction of extra components, including metallic and non-metallic doping elements into TiO_2, would reduce the bandgap of TiO_2 and shift the light absorption ability to the visible region (6). Furthermore, because of its large bandgap (3.2 eV), TiO_2 has no activity under visible light. Various methods have been used to make use of sunlight. This can be achieved by doping transitional metal ions such as Ni, Co, Fe, Cu, V, or non-metal doping such as S, N (7,8,9,10). Hence, some of the major concerns for enhancing the photocatalytic activity of TiO_2 include a decrease in the work function for reaction, suitable bandgap to seize visible light, and higher carrier mobility for lower rates of recombination of electrons and holes. Co-doped TiO_2 has drawn particular attention among these metals because cobalt has electrical, catalytic, magnetic, and optical characteristics. Therefore, it is widely utilized in electromagnetic and photocatalysis applications (11). In many studies, advanced oxidation processes (AOP) have been used for the degradation of NSAID. In order to increase these degradation rates, the studies in which H_2O_2 or O_2 (by pumping) is added to the medium where photocatalysts are found (12). However, in this study, although H_2O_2 or O_2 was not added to the medium, quite high photoactivity was achieved with the synthesized Co-TiO_2. Many study in the literature have mostly focused on the use of commercial TiO_2, known as Degussa P25 and Hombikat UV-100, in suspension form. These commercial catalysts have disadvantages such as having low surface area of 40-60 m^2/g, being excited by UV light and only 5% of the sun (13). In the present study, the reflux technique was used to synthesize Co-doped TiO_2 for Ibuprofen's photocatalytic degradation in aqueous solutions under UV-A or UV-C light.

EXPERIMENTAL SECTION

Materials

Titanium isopropoxide ($Ti(OPri)_4$) $C_{12}H_{28}O_4Ti$ (97 wt. %) was provided from Alfa Aesar. 2-propanol (≥99.5 wt.%), ethanol (99 wt.%), cobalt acetate tetrahydrate, methanol (HPLC grade), potassium hydrogen phosphate, tannic acid, gallic acid, and Ibuprofen (IBU) were provided by Sigma Aldrich. Hydrochloric acid (37 wt.%) was purchased from Riedel de Haën. Potassium nitrate, magnesium chloride, sodium phosphate, calcium sulfate, potassium carbonate, sodium hydroxide, and potassium chloride were purchased by Merck.

Catalyst synthesis

Bare and Co-doped TiO_2 nanoparticles (NPs) were synthesis by a reflux method (14). Applied synthesis stages are given in Figure 1. For the preparation of bare TiO_2 NPs, the processes were the same as the method described below in the absence of doping Co^{2+} ion.

Characterization of the catalyst

The NPs were characterized by X-ray diffraction (XRD) pattern recorded using the Rigaku RadB-DMAX II diffractometer. The prepared NPs were determined with Cu Kα (λ = 1.5418 A) radiation at room temperature to characterize the crystalline phase of nanoparticles. Bragg angle is 2θ=25.3° in the region. The crystallite size of nanoparticles was determined from XRD peak of spacing according to the Scherrer's equation given below.

$$D=\frac{K\times\lambda}{\beta\,½\times\cos Q} \qquad \text{(Eq. 1)}$$

The adsorption-desorption isotherms using liquid nitrogen (77 K) were acquired in a Micromeritics Tristar 3030 model equipment to define the specific surface area (S_{BET}) and average pore diameter of all synthesized samples. The NPs specific surface areas and pore size distributions were determined by BET (Brunauer–Emmett–Teller) methodology.

The morphology, size, and size distribution of samples were investigated by Leo Evo 40 Model scanning electron microscopy (SEM) equipped with energy-dispersive X-ray spectroscopy (EDX) was used. Hydrodynamic diameter, zeta potential, and particle size distribution of the NPs were defined by a Malvern Zetasizer Nano-ZS model using the dynamic light scattering (DLS) method. Elemental

analysis and chemical composition of NPs was determined using PANalytical Axios^{MAX} model energy-dispersive X-ray spectroscopy. X-ray Fluorescence Spectroscopy (XRF) was employed to determine the atomic percentage of the Co^{2+} with respect to titanium. The phase purity and monitoring functional groups of NPs were defined by Fourier-Transform Infrared (FT-IR) spectra. The infrared spectra were acquired on an FT-IR spectrometer (Spectrum 1000, Perkin Elmer).

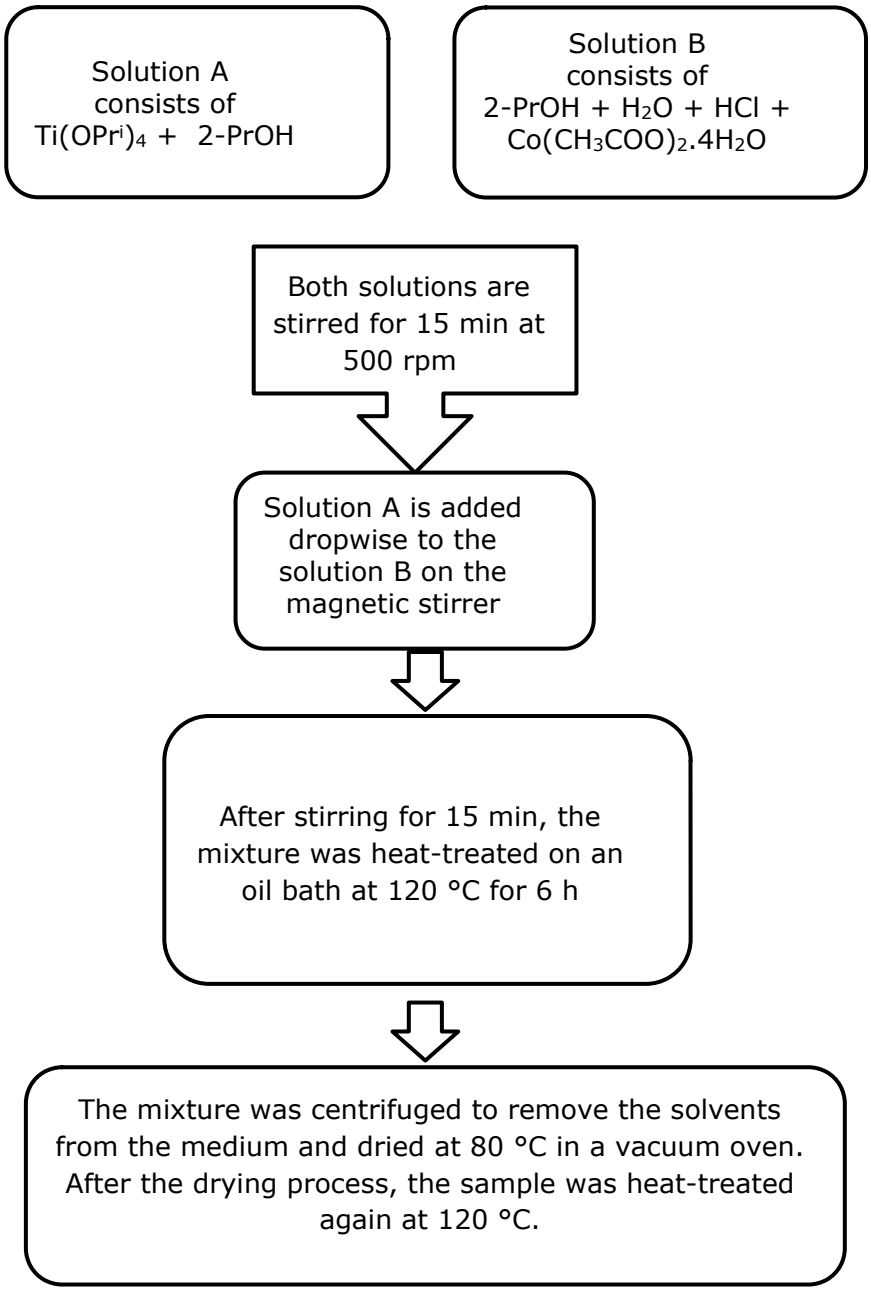

Figure 1: The schema of synthesis of Co-doped TiO_2 NPs.

Evaluation of the photocatalytic performance of IBU

To use in the degradation experiments for IBU, the stock IBU solution was prepared at 100 mg/L in ultrapure water and held in an ultrasonic bath for complete dissolution. Deionized water used in all experimental studies was provided from the Elga Purelab distillation unit. All standard solutions were diluted from the stock solution, and all solutions were stored at -5°C in dark glass bottles for one month. Photocatalytic degradation studies were performed in an Erichsen 1500 model solar box unit

with a Xe lamp (Erichsen, Germany) and controllers for irradiation time and intensity of light. UV light transmission was interrupted with a cut-off filter (yellow filter), and photocatalytic studies were performed under visible light. At first, the predetermined amount of catalyst was added into a dilute solution of IBU in a 50 mL polystyrene transparent beaker placed in the dark to ensure adsorption-desorption equilibrium for 90 minutes at room temperature. According to UV-Vis spectrophotometric measurements, no significant change in the IBU concentration in the solution was observed when the adsorption-desorption equilibrium was reached.

The solution was irradiated immediately. After irradiation, the solution was filtered with a 0.45 µm membrane filter. Degradation of IBU by photolysis without catalysts was also irradiation under UV-C light in the solar box. Change of the IBU concentration in the solution during the degradation process was measured by a UV-Vis spectrophotometer (Varian Cary 50, λmax=224 nm for IBU), and total organic carbon (TOC) in the solution before and after the irradiation was determined using a TOC analyzer (Teledyne Tekmar TOC Torch).

To determine the experimental conditions for degradation of IBU, the influence of the parameters such as the amount of catalyst, percentage of Co-doped TiO_2, pH, irradiation time, and initial concentration of IBU were investigated. The degradation efficiency was calculated using the following equation,

$$Degradation\,efficiency\,(\%)=\frac{(C_t-C_0)}{C_0}\times 100 \quad \text{(Eq. 2)}$$

where C_0 represents the first concentration, C_t is the residual concentration of after irradiation at the time (t). The correlation of ln C_0/C_t with irradiation time (t) was used to determined degradation kinetics.

In order to define the effect of the matrix on the photocatalytic degradation process, various anions and cations, as well as organic substances such as gallic and tannic acid, were added to the irradiation medium. The concentration of IBU before and after the photocatalytic degradation process was determined using an Agilent 1100 series HPLC equipped with a photodiode array detector and Zorbax Eclipse XDB-C_{18} column. The mobile phase consists of 20% MeOH and 80% KH_2PO_4 (pH:3) mixture. Dynamic calibration range was 0.5-30 mg/L, LOD was 0.15 mg/L, and R^2=0.9992 by HPLC-DAD for IBU. Every photocatalytic experiment was done in triplicate.

RESULTS AND DISCUSSION

Characterization of bare and Co-doped TiO_2

Figure 2 shows XRD diffraction patterns for reflux-synthesized bare TiO_2 and Co-doped TiO_2, XRD patterns exhibit strong diffraction peaks at 25.24°, 37.62°, 48.22° and 54.72° 2θ indicating the presence of TiO_2 in the anatase phase, rutile and brookite phases were not detected, no peaks associated with separated cobalt oxide phases such as Co_3O_4 were detected. This could be either explained by the fact that the Co^{2+} ions have been doped into the TiO_2 lattice since the Co^{2+} ions (0.65 Å) are smaller than that of Ti^{4+} (0.69 Å) (15), or due to the low concentration of cobalt ions to be detected.

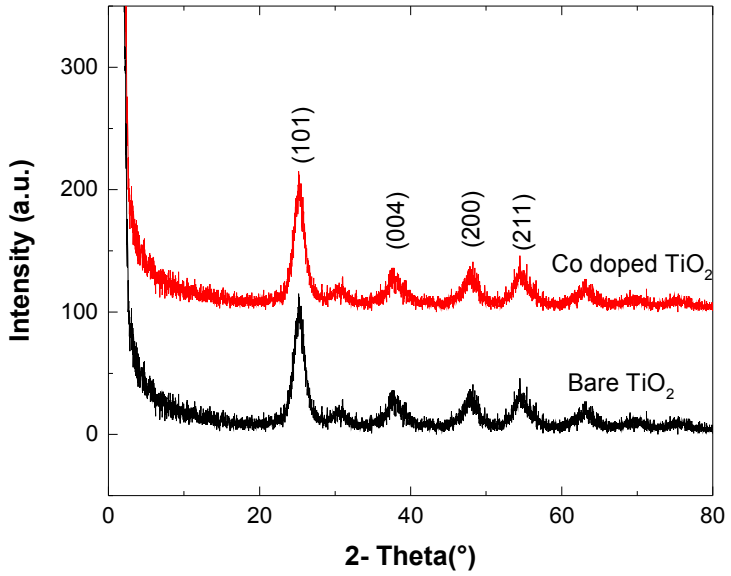

Figure 2: XRD patterns of bare and Co-doped TiO_2 catalysts.

According to the calculations obtained in the Scherrer's equation, the average crystallite size of the bare TiO_2, Co-doped TiO_2 is much lower compared to commercial Degussa P25. It was estimated to be 9.3, 9.2, and 30 nm, respectively. The specific surface area of bare and Co-doped TiO_2 was determined by the Brunauer-Emmett-Teller (BET) method. It was demonstrated that de Co-doped titanium dioxide has a higher specific surface area with 209 m^2/g compared to the bare titanium dioxide and Degussa P25 with 198 and 56 m^2/g, respectively. The synthesized samples' microstructure and external morphology can be explained by the SEM characterization technique presented in Figure 3. The particle shape shows similarities and irregular blocks due to agglomeration. These results were in good agreement with the XRD pattern, which did not show any clear cobalt oxide peaks in the composite.

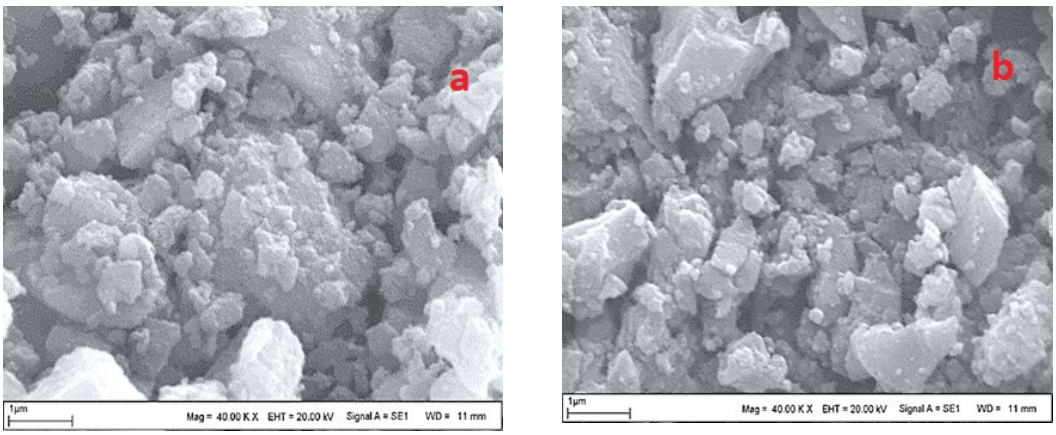

Figure 3: SEM images of bare TiO_2 (a) and Co doped TiO_2 (b).

To confirm the cobalt oxide concentration in the synthesized materials, a full elemental analysis was carried out after the synthesis. EDX results of elemental analysis of Co-doped TiO_2 verified Ti, O, Co, and Cl elements with elements contents of 31.76%, 65.61%, and 0.29% 2.34% (by weight), respectively compared to bare TiO_2 that confirmed the absence of cobalt ions. The chemical composition of TiO_2 samples was identified with X-ray fluorescence (XRF) analysis. The XRF results are summarized in Table 1.

Table 1: Results of XRF of the synthesized bare TiO_2 and Co-doped TiO_2 catalysts.

	Bare TiO_2 (wt. %)	Co-doped TiO_2 (wt. %)
TiO_2	97.42	97.03
Co_3O_4	-	0.2115
Cl	2.37	2.41

The XRF results were compatible with EDX results, which approximately show the same cobalt oxide ingredient into the TiO_2 matrix.

It is also significant the agreement between Cobalt content measured by DLS presented in Figure 4 and XRF for the bare and Co-doped TiO_2 indicating the good dispersion of cobalt into TiO_2 matrix and the similar dimension of agglomerates for Co-doped TiO_2.

Figure 5 exhibits the FT-IR spectra of the bare and Co-doped TiO_2 samples. The broad and strong peaks in the range of 400–1000 cm^{-1} can be ascribed to the Ti–O and Ti–O–Ti bonds in the sample. The peak at 3000–3400 cm^{-1} is attributed to the O-H stretching vibration of Ti-OH and water that corroborate hydroxyl groups' presence in the modified TiO_2 catalysts. The broad absorption peak observed at 1620 cm^{-1} corresponds to water -OH bending and C=C stretching.

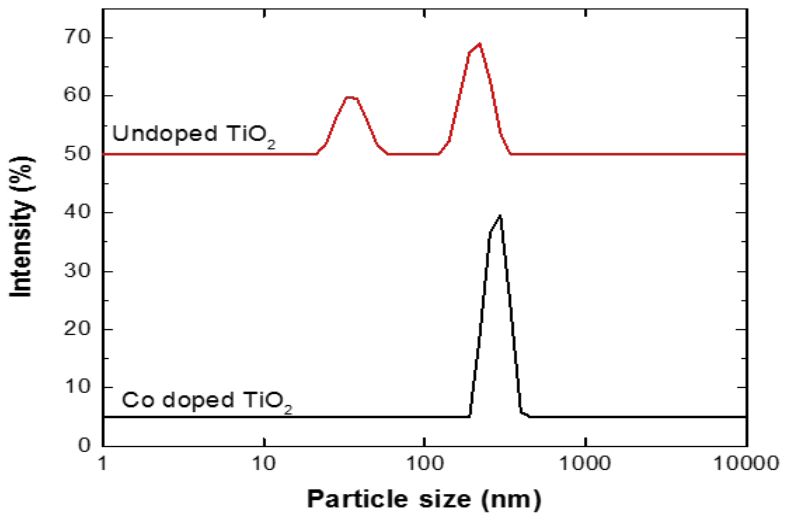

Catalyst	Size (nm)
Co doped TiO_2	295
Bare TiO_2	82.8; 255

Figure 4: Particle size distributions of the catalysts according to DLS measurements.

In order to better understand the stability and surface electrostatic charge of the suspended materials, zeta potential values and isoelectric point of bare and Co-doped TiO_2 were determined in aqueous solution at different pH values, using a Zetasizer apparatus. The results are presented in Figure 6 and Table 2. If the systems have a zeta potential higher than ±30 mV in colloidal systems, it is considered stable. As shown in Table 2 and Figure 6, the catalysts' zeta potential is nearly 35 mV up to pH values of 4.

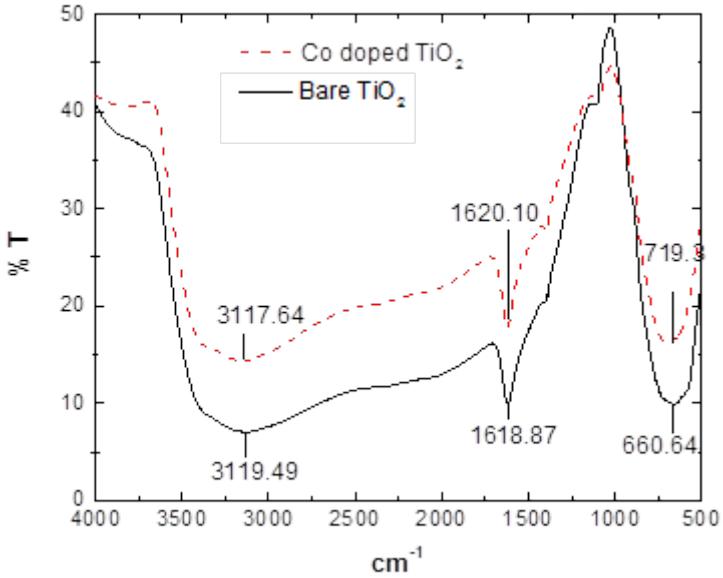

Figure 5: FTIR spectra of bare TiO_2 and Co-doped TiO_2 catalysts.

Table 2: The native pH value, isoelectric point, and zeta potential of bare and Co doped TiO_2.

Catalyst	Zeta potential (mV)	Medium pH	Isoelectric point, pH
Bare TiO_2	35.3 ± 0.3	3.14	6.93
Co doped TiO_2	34.23 ± 1.0	3.07	6.38

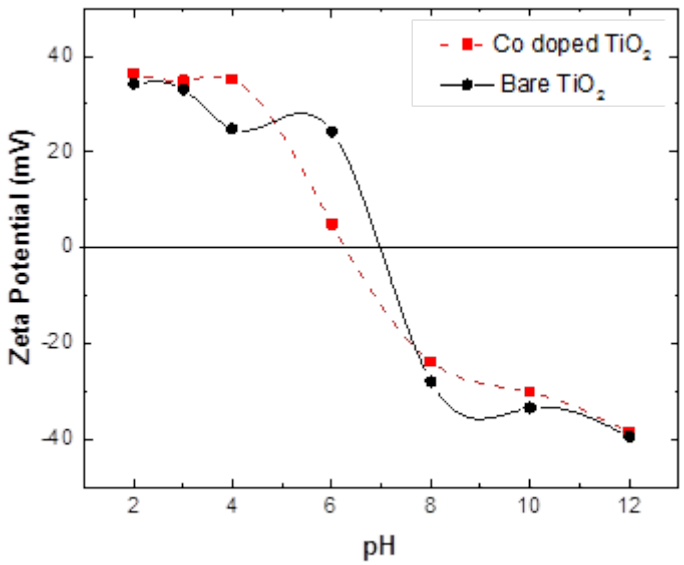

Figure 6: Zeta potentials at different pHs in the 10^{-3} M KCl medium of bare TiO_2.

Effects of parameters on the degradation of IBU

Effect of adsorption and photolysis

Before irradiation, the mixture of catalyst and IBU was soaked in the dark for 90 min at room temperature to reach adsorption equilibrium on the surface catalyst; no significant adsorption effects were observed. The photolysis effect was also investigated and solutions of IBU were irradiated with UV-C radiation at 240 min for the photocatalytic test. After 180 min irradiation under UV-C light, only 2.50% of IBU was degraded.

Effect of cobalt doping percentage

Several tests were performed to observe the effect of cobalt doping percentage on the photodegradation of IBU (Figure 7). The activities were investigated in the range of 0.25–1.0%. It can be observed that the degradation increases with doping concentration from 0.25% (n/n) to achieve

maximum degradation at 0.5% of cobalt doping, but further cobalt concentration increase does not improve degradation, a possible explanation resides in the fact that when the dopants are excessive, cobalt ions may not enter TiO_2 lattice but cover the surface of TiO_2 and form heterogeneity junction so photocatalytic activity is reduced. Furthermore, as the concentration of dopant increases, electron-hole pairs captured overcome the barrier and recombine. On the other hand, 0.5% Co concentration considered as the suitable amount dopant since it can capture photogenerated electrons and decrease the rate of recombination of electron-hole and therefore accelerate the photocatalytic reaction. This result is quite comparable to other reports (16,17) for sprayed Mo/TiO_2 films for similar doping range.

Effect of photocatalyst dosage

The effect of the amount of catalyst on IBU degradation was studied in the range 0.1-0.4 % under pH 4.0, and the results are shown in Figure 8. As seen, IBU degradation increase from 50.33% to 99.7% by increasing catalyst concentration from 0.1 to 0.4%, beyond which the effect is less pronounced. Thus, a solid to liquid ratio of 0.4% could be considered the optimum concentration of catalyst for IBU degradation.

This improvement can be attributed to increasing active sites on the catalyst surface and the light penetration of photo activating light into the solution. Consequently, the formation of electron-hole pairs and reactive hydroxyl radicals on the semiconductor's surface increased, which improved the oxidation of IBU into other intermediates.

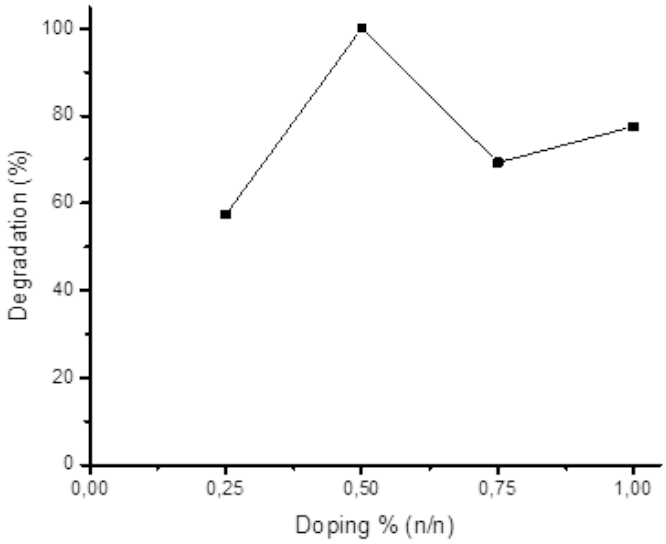

Figure 7: Effect of Co doped on photocatalytic degradation of IBU (20 mg/L, 180 min UV-C irradiation, 670 W/m^2).

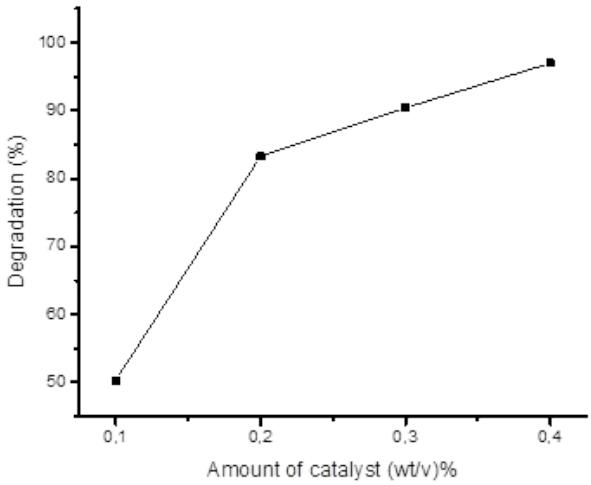

Figure 8: Effect of amount of catalyst on photocatalytic degradation of IBU (20 mg/L IBU, 180 min UV-C irradation, 670 W/m^2).

Effect of irradiation time

The degradation profiles of IBU as a function of irradiation time in the presence of Co-doped TiO_2 is shown in Figure 9. The complete removal of the drug with the initial concentration of 20 mg/L was reached nearly within 240 min of irradiation. It was observed that IBU photodegradation augmented with longer irradiation time directly affects degradation efficiency. After 240 min of irradiation, 99% of IBU was degraded by catalyst under UV light.

In order to determine the kinetics of photodegradation, the correlation between ln C/C_0 and irradiation time was plotted (as inset in Figure 9). As can be seen, a good linear correlation existed between ln C/C_0 and irradiation time, and the degradation reaction obeys the first-order reaction kinetics.

Many authors have reported that the kinetic behavior of photocatalytic reaction can be explained by a modified Langmuir–Hinshelwood model (18). At low concentration, the number of catalytic sites is not a limiting factor, and the rate of degradation is proportional to the substrate concentration, in accordance with apparent first-order kinetics.

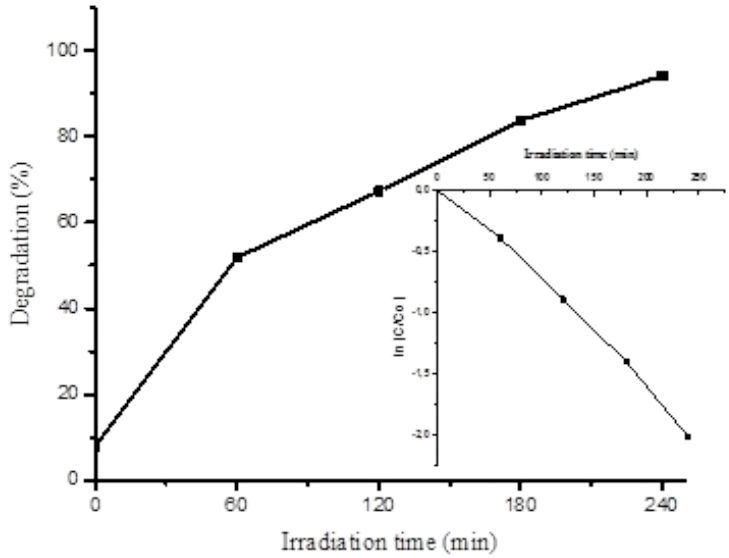

Figure 9: Effect of irradiation time on photocatalytic degradation of IBU (0.4% wt/v catalyst, 20 mg/L IBU, pH: 4.0, UV-C irradation, 670 W/m^2).

Effect of IBU concentration

The effect of the initial concentration on photocatalytic degradation of IBU was studied for six different concentrations of IBU. For this series of experiments, 0.5% Co-doped TiO_2 was dispersed in 0.4% w/v added into 5, 10, 20, 40, 60, and 80 mg/L IBU solutions, respectively and irradiated under UV-C light during 240 min. Figure 10 illustrates the degradation profile of IBU as a function of the initial concentration. Even at high concentrations of IBU, the photocatalyst activity is high.

Effect of pH

pH is considered an important factor since it affects the surface charge properties of the semiconductor. To study the effect of initial pH on the degradation of IBU with Co doped TiO_2, experiments were conducted by changing the pH in the range 2–10.

As shown in Figure 11, the degradation of IBU strongly depended on the pH solution in the oxidation process. Increased degradation of IBU was observed up to pH 4.0, after which degradation was significantly less effective. When the results are evaluated, the optimum pH for degradation of IBU in an aqueous solution is pH 4. TiO_2 particles tend to form agglomerates when dispersed in alkaline aqueous media. When studied in acidic conditions, agglomeration is reduced, thus increasing the catalyst's effective surface area.

Effect of organic and inorganic water matrix

Wastewater may contain various pollutants; organic solvents and inorganic substances are in general present in industrial water. In order to determine the effect of the organic matrix, gallic acid (170.12 g/mol) as low molecular weight and tannic acid (1701.19 g/mol) as high molecular weight were added as organic compounds commonly found in

real waters. In this study, 0.5% Co-doped TiO_2 was added to 20 mg/L of IBU solution, and the final concentration of the above organic acids was added to the solution as 10, 20, and 30 mg/L; the mixture was maintained over 90 min in the dark to ensure adsorption-desorption equilibrium. Immediately following this, the irradiation experiments were carried out under UV-C light for 240 min. As seen in Figure 12, the presence of organic compounds slightly affects the photocatalytic activity of Co-doped TiO_2 in the degradation of IBU. Thus, the higher the organic compound concentration, the more the deactivation effect, degradation percentage of IBU decreases about 8.11% and 7.25% in the presence of 30 mg/L of tannic acid and gallic acid considered as the large and small molecular weight of organic compounds.

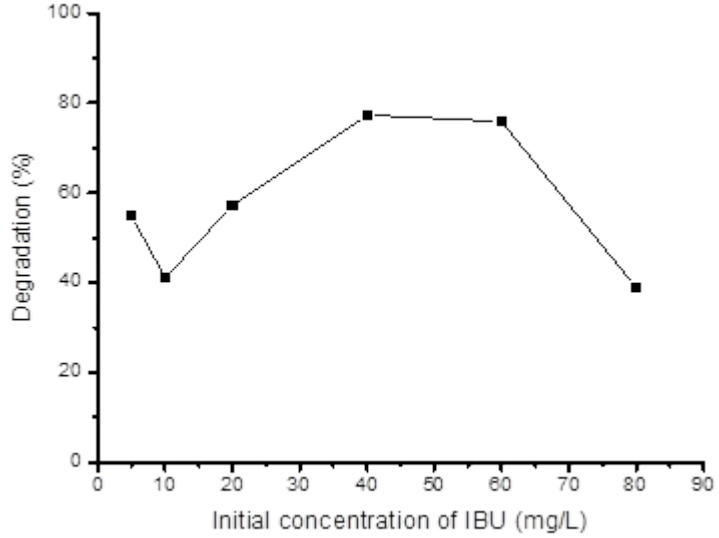

Figure 10: Effect of the initial concentration on photocatalytic degradation of IBU (0.4% wt/v catalyst, pH: 4.0, 240 min UV-C irradiation, 670 W/m^2).

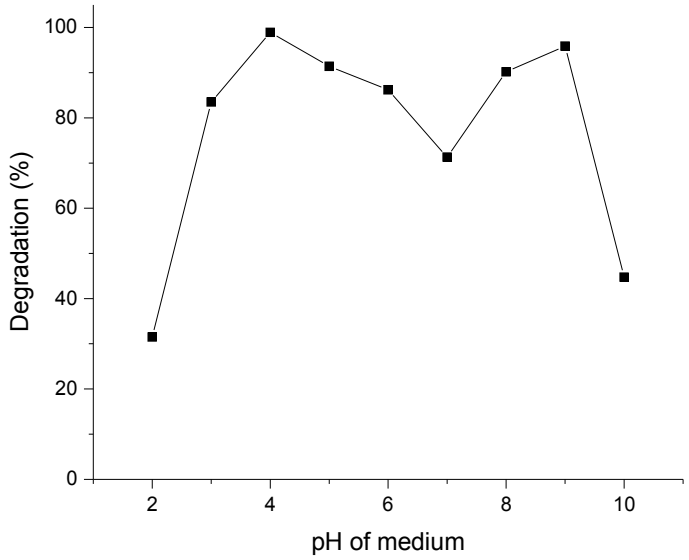

Figure 11: Effect of pH on photocatalytic degradation of IBU (0.4% w/v catalyst, 20 mg/L IBU, 240 min UV-C irradiation, 670 W/m^2).

As can be deduced from Figure 13, the inorganic matrix apparently caused a stronger deactivation effect than the organic matrix. In the presence of inorganic acting as hydroxyl radical scavengers, competition for free radicals and blockage of catalyst active sites by adsorption of anions such as Cl^-, PO_4^{3-}, NO^+, SO_4^{2-}, CO_3^{2-} and cations such as Mg^{2+}, K^+, Ca^{2+}, and Na^+ to form a surrounding layer

that may also be responsible for decreased efficiency of catalyst directly affecting photocatalytic efficiency.

The optimal photocatalytic degradation conditions for IBU are summarized in Table 3.

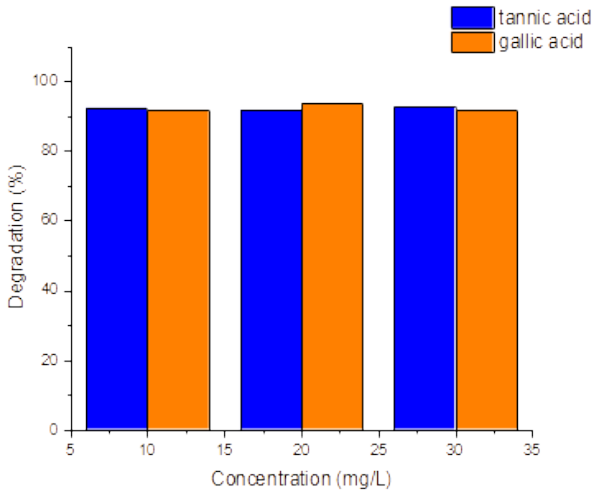

Figure 12: Effect of organic matrix on photocatalytic degradation of IBU (0.4% w/v catalyst, 20 mg/L IBU, 240 min UV-C irradation, 670 W/m^2).

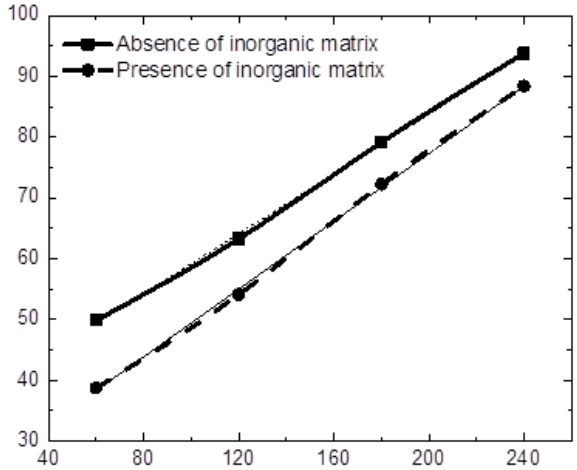

Figure 13: Effect of inorganic matrix on photocatalytic degradation of IBU (0.4% wt/v catalyst, 20 mg/L IBU, 240 min UV-C irradation, 670 W/m^2).

Table 3: The optimum conditions of photocatalytic degradations for IBU.

Conditions	IBU
Initial concentration, mg/L	20
Adsorption-desorption equilibrium ,min	90
Amount of catalyst, w/v	0.4
UV light intensity, W/m^2	670
pH	4.0
Illumination time (UV-C), min	240
Illumination time (Vis), min	300

Results of photocatalytic degradation of IBU

The photocatalytic degradation of IBU was studied by liquid chromatographic analysis, UV-Vis analysis, and total organic carbon elimination. The evolution of IBU degradation as a function of time is almost similar for different analytic techniques that confirm the used methods' viability. The maximum degradation rate was obtained at 224 min of

irradiation time with an average degradation rate with different methods of 99.43%.
Maximum IBU absorbance is observed at 224 nm, and with increasing irradiation time from 60 to 240 min, the absorption decreased gradually to a value near blank (Figure 13). The same results were confirmed by HPLC analysis presented in Figure 14 and performed with the same protocol of UV-Vis analysis in order to compare the performance of both analytical methods.

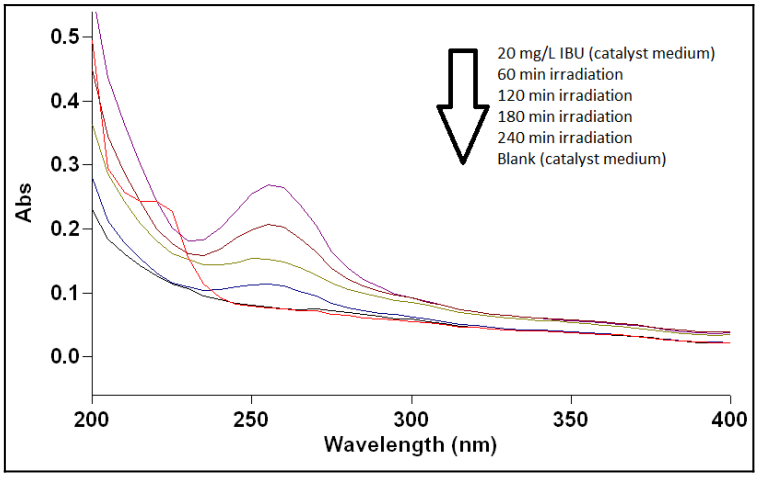

Figure 14: UV-Vis spectrum of the effect of irradiation time on photocatalytic activity of IBU.

The limitation of detection (LOD) and quantification (LOQ) values for IBU degradation are 0.05 and 0.2 mg/L, respectively, according to HPLC analysis and 0.38 and 1.28 mg/L respectively, with the UV-Vis spectrophotometric measurements. The values enable us to evaluate the suitability of the used analytical technique and compare both analytic methods (Table 4).

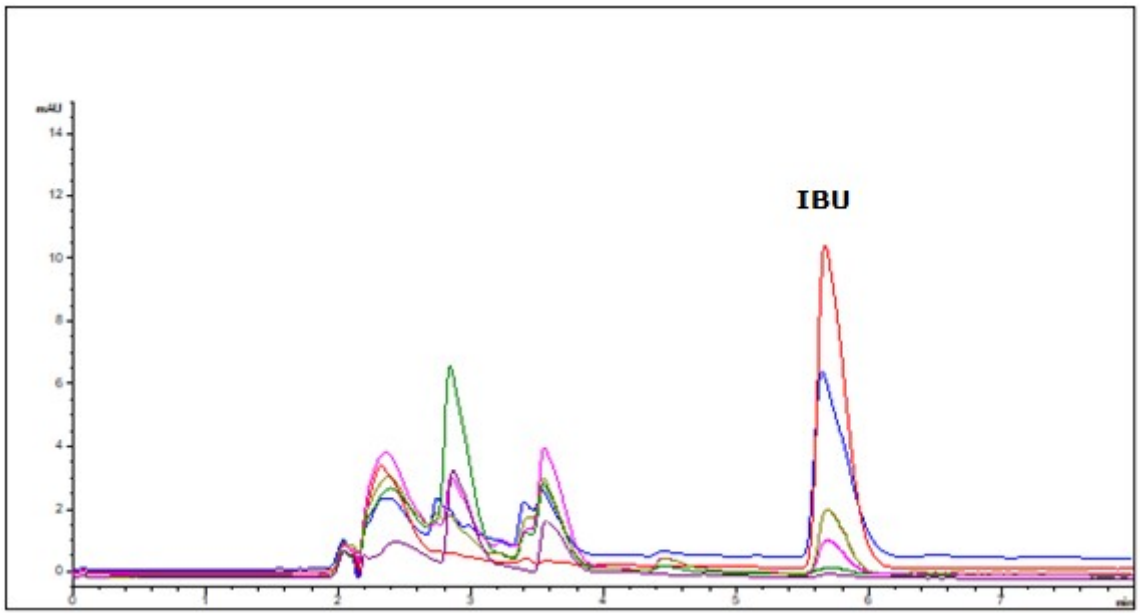

Figure 15. HPLC chromatogram of the effect of UV-C irradiation time on photocatalytic activity (---- 20 ppm IBU (catalyst medium), ----60 min irradiation, ----120 min irradiation, ----180 min irradiation, ----240 min irradiation, ----Blank (catalyst medium).

Table 4: Results of IBU degradation according to different analysis methods.

Catalyst	Degradation ($\bar{x}$ %± sd), n=3					
	UV/Vis Spect. analysis		TOC analysis		HPLC analysis	
	UV-C light, 240 min	Vis light, 300 min	UV-C light, 240 min	Vis light, 300 min	UV-C light, 240 min	Vis light, 300 min
Co-doped TiO_2	100±0.75	98.06±1.12	98.76±2.15	97.04±1.94	99.54±1.14	98.16±2.44
TiO_2	97.56±1.06	24.96±1.99	91.07±2.01	21.97±2.16	93.11±0.99	21.82±1.73
Degussa P25	96.42±2.04	22.25±0.58	90.95±2.26	17.03±2.66	95.47±0.85	19.78±2.13

CONCLUSION

Under UV-C light, the photocatalytic efficiency of Co-doped TiO_2 was found to be as efficient as bare TiO_2 and Degussa P25. Degradation percentage does not present any significant difference between all of them, achieving more than 98% of degradation after 240 min. Under visible illumination, the degradation of IBU shows noteworthy differences with what we observed under UV–C illumination. First, the degradation ratio of bare TiO_2 and Degussa P25 decreases drastically to 24.96% and 22.25% respectively, the low activity of P25 could be explained by the low adsorption of IBU particles on the surface of P25 due to its high pore volume and pore diameter resulting with a decrease in degradation ratio.

The results indicate that the photocatalytic activity of TiO_2 in the visible range is greatly improved by cobalt doping; firstly, Co-doped TiO_2 presents a BET surface area of 209 m^2/g that is fourfold the value of the Degussa P25 (56 m^2/g) and higher than bare TiO_2 198 m^2/g and since the photocatalytic activity increases with increasing BET area which reveals the higher activity. On the other hand, the presence of cobalt can efficiently inhibit the agglomeration of TiO_2 particle, so that Co-doped TiO_2 possesses more active sites than bare TiO_2 and exhibits a higher degradation ratio, it's at least factor 4.5 compared to the other catalyst.

Photodegradation of IBU in aqueous solutions with the catalysis of reflux-synthesized Co-doped TiO_2 with nanocrystalline size (9 nm) was studied. Anatase was the only crystalline phase.

Performance of synthesized bare and Co-doped TiO_2 in photocatalytic degradation under UV-C and visible irradiation was studied by investigating the effects of cobalt doping percentage and catalyst irradiation time, initial IBU concentration pH, and also the effect of inorganic and organic water matrix. The results showed that the degradation of IBU was improved upon Co doping. It was observed that 0.5% Co doping TiO_2 and 0.4% w/v sol could degrade 20 mg/L of IBU within 240 min under UV-C irradiation and 300 min visible irradiation at pH=4.0. The degradation reaction of IBU basically followed the first-order reaction kinetics. Effects of the inorganic and organic matrix on the degradation were examined, and it was found that the inorganic matrix apparently caused a stronger deactivation effect than the organic matrix. Thus, decreases in IBU degradation was observed after 240 min of treatment with 88% of degradation compared to the absence of water matrix with degradation ratio who reaches 93%, whereas organic matrix slightly decreases the degradation ratio.

The results were compared with Degussa P25 TiO_2 at the same degradation conditions; it was found that the synthesized Co-doped TiO_2 showed higher photocatalytic activity than bare TiO_2 and Degussa P25 under visible irradiation.

REFERENCES

1. Gu Y, Yperman J, Carleer R, D'Haen J, Maggen J, Vanderheyden S, et al. Adsorption and photocatalytic removal of Ibuprofen by activated carbon impregnated with TiO_2 by UV–Vis monitoring. Chemosphere. 2019 Feb;217:724–31.

2. Khedr TM, El-Sheikh SM, Ismail AA, Bahnemann DW. Highly efficient solar light-assisted TiO_2 nanocrystalline for photodegradation of ibuprofen drug. Optical Materials. 2019 Feb;88:117–27.

3. Hernando M, Mezcua M, Fernandezalba A, Barcelo D. Environmental risk assessment of pharmaceutical residues in wastewater effluents, surface waters and sediments. Talanta. 2006 Apr 15;69(2):334–42.

4. Sahoo C, Gupta AK. Optimization of photocatalytic degradation of methyl blue using silver ion doped titanium dioxide by combination of experimental design and response surface approach. Journal of Hazardous Materials. 2012 May;215–216:302–10.

5. Park D-W, Choi Y-K, Hwang K-J, Lee J-W, Park JK, Jang HD, et al. Nanocrystalline TiO_2 films treated with acid and base catalysts for dye-sensitized solar cells. Advanced Powder Technology. 2011 Nov;22(6):771–6.

6. Senthilnathan J, Philip L. Photocatalytic degradation of lindane under UV and visible light using N-doped TiO_2. Chemical Engineering Journal. 2010 Jul;161(1–2):83–92.

7. Gar Alalm M, Tawfik A, Ookawara S. Enhancement of photocatalytic activity of TiO_2 by immobilization on activated carbon for degradation of pharmaceuticals. Journal of Environmental Chemical Engineering. 2016 Jun;4(2):1929–37.

8. Hosseini-Zori M. Co-doped TiO_2 nanostructures as a strong antibacterial agent and self-cleaning cover: Synthesis, characterization and investigation of photocatalytic activity under UV irradiation. Journal of Photochemistry and Photobiology B: Biology. 2018 Jan;178:512–20.

9. Siddiqa A, Masih D, Anjum D, Siddiq M. Cobalt and sulfur co-doped nano-size TiO_2 for photodegradation of various dyes and phenol. Journal of Environmental Sciences. 2015 Nov;37:100–9.

10. Sarkar D, Mukherjee S, Chattopadhyay KK. Synthesis, characterization and high natural sunlight photocatalytic performance of cobalt doped TiO_2 nanofibers. Physica E: Low-dimensional Systems and Nanostructures. 2013 May;50:37–43.

11. Hamadanian M, Karimzadeh S, Jabbari V, Villagrán D. Synthesis of cysteine, cobalt and copper-doped TiO_2 nanophotocatalysts with excellent visible-light-induced photocatalytic activity. Materials Science in Semiconductor Processing. 2016 Jan;41:168–76.

12. Lee S-Y, Park S-J. TiO_2 photocatalyst for water treatment applications. Journal of Industrial and Engineering Chemistry. 2013 Nov;19(6):1761–9.

13. Nakashima T, Ohko Y, Tryk DA, Fujishima A. Decomposition of endocrine-disrupting chemicals in water by use of TiO_2 photocatalysts immobilized on polytetrafluoroethylene mesh sheets. Journal of Photochemistry and Photobiology A: Chemistry. 2002 Aug;151(1–3):207–12.

14. Çağlar Yılmaz H, Akgeyik E, Bougarrani S, El Azzouzi M, Erdemoğlu S. Photocatalytic degradation of amoxicillin using Co-doped TiO_2 synthesized by reflux method and monitoring of degradation products by LC–MS/MS. Journal of Dispersion Science and Technology. 2020 Feb 23;41(3):414–25.

15. Colón G, Maicu M, Hidalgo MC, Navío JA. Cu-doped TiO_2 systems with improved photocatalytic activity. Applied Catalysis B: Environmental. 2006 Sep;67(1–2):41–51.

16. Putra EK, Pranowo R, Sunarso J, Indraswati N, Ismadji S. Performance of activated carbon and bentonite for adsorption of amoxicillin from wastewater: Mechanisms, isotherms and kinetics. Water Research. 2009 May;43(9):2419–30.

17. Klauson D, Babkina J, Stepanova K, Krichevskaya M, Preis S. Aqueous photocatalytic oxidation of amoxicillin. Catalysis Today. 2010 Apr;151(1–2):39–45.

18. Li T, Yang S, Huang L, Gu B, Du Y. A novel process from cobalt nanowire to Co_3O_4 nanotube. Nanotechnology. 2004 Sep;15(11):1479–82.

JOTCSA Journal of the Turkish Chemical Society Section: A Chemistry

TURKISH CHEMICAL SOCIETY

A Near-infrared Benzothiazole-based Chemodosimeter for Rapid and Selective Detection of Hydrogen Sulfide

Safacan KOLEMEN[1,2,3*]

[1]Department of Chemistry, Faculty of Science, Koc University, Sariyer, Istanbul 34450, Turkey
[2]Surface Science and Technology Center (KUYTAM), Koc University, Sariyer, Istanbul 34450, Turkey
[3]Boron and Advanced Materials Application and Research Center, Koc University, Sariyer, Istanbul 34450, Turkey

Abstract: Hydrogen sulfide (H_2S) is a biologically relevant gaseous molecule, which involves in a wide variety of physiological and pathological processes. Thus, detection of H_2S is highly valuable in order to clarify its complex roles. In this study, a new benzothiazole-based donor-acceptor type H_2S selective chemodosimeter (**HP-1**) was synthesized and its H_2S detection capabilities were investigated in aqueous solutions. **HP-1** exhibited a red-shifted absorption signal at 530 nm and a near-infrared (NIR) fluorescence peak at 680 nm as a result of enhanced intramolecular charge transfer (ICT) in the presence of H_2S, which enabled a selective and very rapid ratiometric fluorescent detection. **HP-1** was also showed to be highly sensitive toward H_2S with a very low limit of detection value.

Keywords: Fluorescence, hydrogen sulfide, benzothiazole, near-infrared imaging chemodosimeters.

Submitted: January 05, 2021. **Accepted:** April 12, 2021.

Cite this: Kolemen S. A near-infrared benzothiazole-based chemodosimeter for rapid and selective detection of hydrogen sulfide. JOTCSA. 2021;8(2):567–78.

DOI: https://doi.org/10.18596/jotcsa.853370.

***Corresponding author. E-mail:** skolemen@ku.edu.tr.

INTRODUCTION

Hydrogen sulfide (H_2S) is an important gasotransmitter along with carbon monoxide and nitric oxide in living cells, which is endogenously produced from cysteine and cysteine derivatives in reactions that are catalyzed by cystathionine β-synthase (CBS), cystathionine γ-lyase (CSE) and 3-mercaptopyruvate sulfurtransferase (MST) (1-4). H_2S involves in fundamental signaling pathways and consequently plays crucial roles in various physiological processes such as cell growth, neurotransmission, insulin secretion, regulation of the redox balance, inflammation, angiogenesis and apoptosis (3,5). However, mismanagement of intracellular H_2S level is directly associated with the formation of serious health problems including Alzheimer's disease, Down syndrome, diabetes, hepatic cirrhosis, and cardiovascular disorders (5-8). It is also well-established that CSE and CBS enzymes are overexpressed in certain cancer cells, which makes H_2S a significant marker for cancer diagnosis (9,10). Thus, it is critical to detect and track dynamic H_2S fluxes with high selectivity and sensitivity in their native environment. Conventional detection approaches mostly rely on electrochemical analyses, gas chromatography, and metal-induced precipitation techniques, which are limited mainly due to the low sensitivity and lack of real-time imaging capability (11-13). To that end, fluorescence imaging is a highly promising tool as it offers spatial and temporal resolution, high selectivity/sensitivity, non-destructive nature, in situ detection, and cheap instrumentation (14-16). In the design of H_2S selective fluorescent agents, the most popular

approach is to employ reaction-based probes (chemodosimeters) as a result of high reactivity of H_2S. Accordingly, plenty of chemodosimeters utilizing a wide variety of reactions such as reduction of azide or nitro to amine, nucleophilic addition, thiolysis of *m*-dinitrophenyl ether and cleavage of dinitrobenzenesulfonyl moiety have been successfully reported so far in order to satisfy selective optical detection (15-19). However, majority of the reaction-based probes still suffer from the emission signals below 650 nm, which can be absorbed by biomolecules and results in autofluorescence. On the other side, near-IR (NIR) emitting probes are quite attractive as the NIR signal does not interfere with the biological fluorophores as well as allows deeper tissue penetration (20). Thus, a great deal of effort has been put to develop H_2S-selective NIR chemodosimeters, (15,20-23), however there are still some challenges need to be addressed in order to improve the impact of NIR probes such as slow response rates, low fluorescence quantum yields and small Stokes shifts.

Donor-π-acceptor (D-π-A) dyes have attracted great interest as fluorescent probes in recent years since they possess strong NIR emission signals and large Stokes' shifts in aqueous solutions, and they can be easily obtained through a well-established chemistry (24-27). In a typical design approach, a phenol group, which acts as a donor, is attached to acceptor moieties, which results in a π-conjugated system. Deprotonation of the phenol in physiological conditions or removing the cage group on the phenol with an analyte of interest yields a phenolate that initiates intramolecular charge transfer (ICT) process by triggering the donation of π-electrons from phenolate to conjugated acceptor units (24). This causes a remarkable red-shift in the absorption signal of the probe and generates a strong NIR emission, which allows both ratiometric and OFF-ON type detection (24). Benzothiazole is among the promising acceptor units, which have been used successfully in the design of D-π-A type chemodosimeters for imaging of several analytes (23,28,29). In this study, a H_2S selective benzothiazole-based chemodosimeter (**HP-1**) (Figure 1) was developed as a (D-π-A) type probe and its H_2S detection capabilities were evaluated in detail by UV-Vis and fluorescence spectroscopies in aqueous solutions.

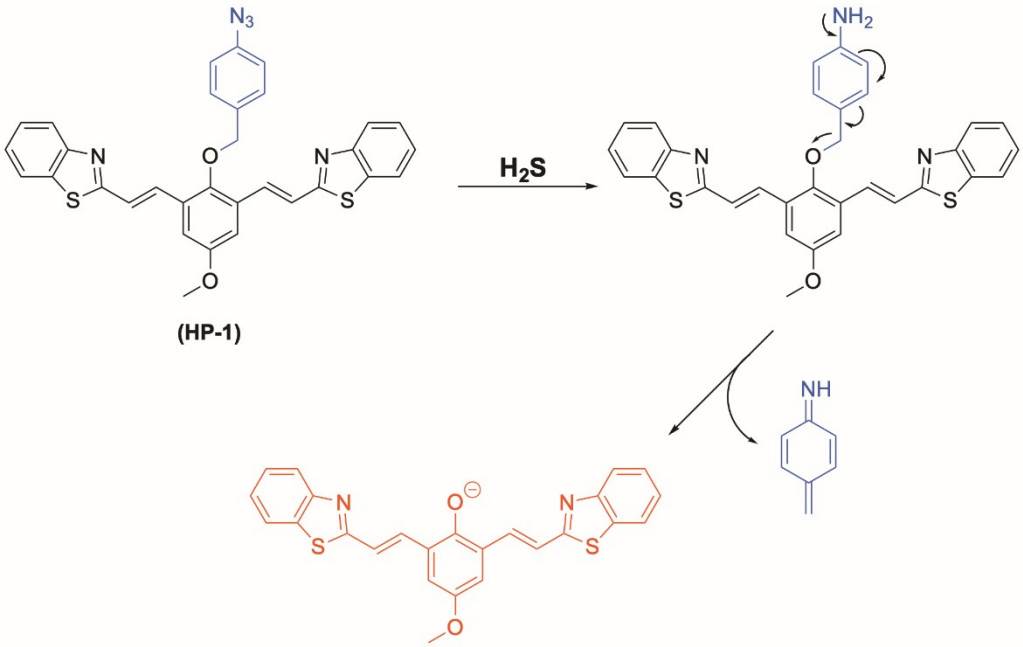

Figure 1. Structure of **HP-1** and its activation mechanism in the presence of H_2S.

EXPERIMENTAL

Chemicals and Apparatus

Reagents were purchased from Sigma-Aldrich or Merck and used without further purification. All dry solvents used in reactions were directly obtained from the Mbraun MBSPS5 solvent drying system. Sodium sulfide nonahydrate $Na_2S{\cdot}9H_2O$ was purchased from Sigma-Aldrich and stored at 2-8 °C. Deuterated solvents were purchased from Eurisotop and used as received. Column chromatography was performed by using thick-walled glass columns and silica gel (Merck 230-400 mesh). Thin layer chromatography (TLC Merck Silica Gel 60 F254) was performed by using commercially prepared 0.25 mm silica gel plates

and visualization was provided by UV lamp. The relative proportions of solvents in chromatography solvent mixtures refer to the volume: volume ratio.

Instruments

^{1}H and ^{13}C NMR spectra were recorded on a Bruker Avance III Ultrashield 500 MHz NMR spectrometer using $CDCl_3$ or d_6-DMSO as the solvents. Chemical shifts are reported in ppm. Coupling constants (J) are reported in hertz (Hz), and the spin multiplicities were specified by the following symbols: s (singlet), d (doublet), t (triplet), and m (multiplet). NMR spectra were processed with MestReNova software. UV−Visible spectra were acquired on a Shimadzu UV-3600 UV-Vis-NIR spectrophotometer. Fluorescence spectra were collected on an Agilent Cary Eclipse spectrophotometer. Fluorescence quantum yield of the samples were investigated by using a fluorescence spectrometer (FLS 1000, Edinburgh Instruments) with an integrating sphere accessory. Mass spectra were recorded on Waters Synapt G1 High-Definition mass spectrometer.

Synthesis

1-azido-4-(bromomethyl)benzene **(2)** (30) and compound **(4)** (23) were synthesized according to literature reports (Figure 2).

Synthesis of HP-1

Compound **4** (50 mg, 0.12 mmol) was dissolved in dry ACN (10 mL) and K_2CO_3 (636 mg, 4.6 mmol) was added to the resulting solution. The solution was stirred at room temperature for 15 minutes and compound **2** (31 mg, 0.15 mmol) was added to the reaction mixture. The reaction was stirred overnight at room temperature. The crude mixture was diluted with DCM (100 mL) and washed with brine (100 mL). Organic layer was separated and dried over Na_2SO_4. The crude product was purified by column chromatography on silica gel (*n*-hexane/EtOAc, 2/1) to give yellow-white solid (58% yield, 38 mg). ^{1}H NMR (500 MHz, $CDCl_3$, ppm) δ 8.02 (d, *J* = 8.1 Hz, 2H), 7.89 (d, *J* = 8.0 Hz, 2H), 7.74 (d, *J* = 16.3 Hz, 2H), 7.51 – 7.39 (m, 8H), 7.20 (s, 2H), 7.03 (d, *J* = 8.1 Hz, 2H), 4.87 (s, 2H), 3.89 (s, 3H). ^{13}C NMR (126 MHz, $CDCl_3$, ppm) δ 166.9, 156.3, 153.9, 149.6, 140.5, 134.3, 132.7, 132.1, 130.9, 130.7, 126.4, 125.7, 124.2, 123.1, 121.6, 119.4, 112.8, 77.7, 55.7. HRMS m/z calc. for $C_{32}H_{23}N_5O_2S_2$: 574.1293 $[M+H]^+$; found: 574.1371.

Photophysical measurements

Stock solution of **HP-1** was prepared in DMF and then diluted with PBS (pH 7.4) to final concentrations before each measurement. $Na_2S{\cdot}9H_2O$ stock solution was prepared in PBS (pH 7.4). 3 mL quartz cells were used, and the slit widths were set up as 10 nm for both emission and excitation.

Fluorescence quantum yield calculation

Fluorescence quantum yield of the sample was investigated by using a fluorescence spectrometer with an integrating sphere accessory. A continuous-wave xenon lamp was used as the excitation source and the emitted fluorescence was detected with a standard photomultiplier (PMT-900) covering a wavelength range of 200-900 nm. During the measurements, the PMT was cooled down to -20 °C by using a built-in housing to reduce the undesired dark current noise.

For quantum yield measurement, an integrating sphere was placed inside the sample compartment of the spectrometer. Internal cavity of the sphere was coated with a PTFE-like material to enable a reflectance of approximately >95% over the wavelength range between 400 and 1500 nm (250 and 2500 nm). Prior to the experiments performed with the sample, the blank spectrum was measured by using the reference solvents (PBS (pH 7.4, 50% DMF)). In order to cover a scattering range, the emission scans were started from 20 nm below the actual excitation wavelength (510 nm) and finished at 900 nm. Furthermore, the step size and the integration time of the measurements were set to 1 nm and 0.2 seconds, respectively. After all the emission measurements of the samples and references were complete, the quantum yield of the sample was determined by using the Fluoracle® software. The built-in analysis tool calculated the quantum yield (QY) by following Eq. (1).

$$QY = \frac{E_s - E_B}{S_B - S_s} \quad (1)$$

where E_s (E_B) and S_S (S_B) are the selected areas for the emitted and scattered signals of the sample (blank).

Limit of detection (LOD) calculation

The limit of detection was calculated according to formula given below, where m is the slope of the emission intensity at 680 nm versus Na_2S concentration graph and s is the standard deviation of the 6 blank measurements. LOD was calculated according to Eq. (2).

$$LOD = 3s/m \quad (2)$$

RESULTS AND DISCUSSION

In the design of **HP-1**, two benzothiazole acceptor units were conjugated to donor *p*-methoxyphenol core and a H_2S-cleavable azido group was used as a cage moiety to mask the phenol. Removal of the cage group upon H_2S-induced selective reduction of azide to amine causes a red-shift in both absorption and emission signals of **HP-1**, which reveals a ratiometric fluorescence sensor for detection of H_2S (Figure 1). Synthesis of **HP-1** was depicted in Figure 2. Initially, 4-aminobenzyl alcohol was treated with NaN_3 in the presence of $NaNO_2$ to get 4-azidobenzylalcohol **(1)**. Then **(1)** was reacted with PBr_3 and the cage unit 4-azidobenzyl bromide **(2)** was obtained. For the probe core synthesis, commercially available 4-methoxyphenol was formylated by running a Duff reaction to give 2,6-diformyl-4-methoxyphenol **(3)**, which was then converted to **(4)** via Knoevenagel condensation. Finally, the cage unit **(2)** was attached to **(4)** in dry acetonitrile and **HP-1** was attained in a moderate yield. **HP-1** was characterized by ^{1}H NMR, ^{13}C NMR and high-resolution mass spectrometry (HR-MS) (Figure S1-S3).

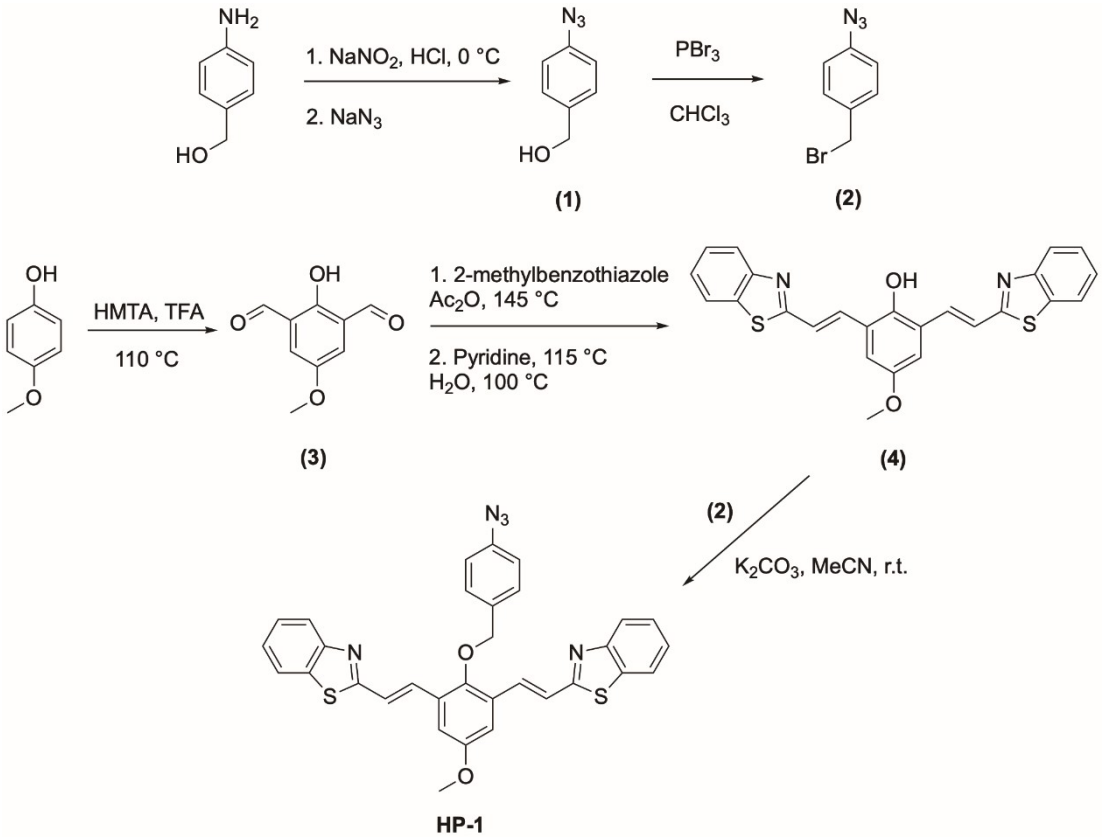

Figure 2. Synthetic pathway for **HP-1**.

After completing the synthesis, the optical responses of **HP-1** to H_2S were investigated with UV-Vis and fluorescence spectrophotometers in aqueous PBS solution (pH 7.4, 50% DMF) (Figures 3 and 4). In all the experiments, H_2S was generated *in situ* by adding Na_2S into a PBS buffered solution (pH 7.4) as in the case of literature examples (15). The pKa of H_2S is 7, thus the Na_2S solution in PBS at pH 7.4 contains HS^- and S^{2-} anions in addition to H_2S, which, in fact, mimics the speciation in the cellular environment (15). **HP-1** exhibited strong but short wavelength absorption peak centered at 335 nm (ε = 23100 $M^{-1}cm^{-1}$) as a result of blocked electron donation from donor core to acceptor units (Figure 3a). Upon treating **HP-1** (20 μM) with Na_2S (200 μM), absorption peak at 335 nm was slightly decreased and a concomitant red-shifted peak appeared at 530 nm (ε = 6600 $M^{-1}cm^{-1}$) with an isosbestic point at 420 nm, which can be also detected by naked eye as colorless **HP-1** solution turned to pale pink after the addition of Na_2S. This result indicates that **HP-1** reacts readily with H_2S and uncages the phenol, which switches on the ICT process. A gradual increase in the absorption signal at 530 nm was also determined when **HP-1** was titrated with increasing concentrations of Na_2S (0-200 μM) (Figure 3b, Figure S5a).

In the case of fluorescence measurements, a characteristic NIR emission signal at 680 nm appeared gradually as the Na_2S concentration (0-200 μM) increased (up to 130-fold, φ_F = 11%) upon excitation at newly formed absorption peak at 530 nm (Figure 4 a,b, Figure S5b). When the excitation wavelength was adjusted to 420 nm (isosbestic point), emission peak of the parent **HP-1** at 470 nm was decreased and broad NIR fluorescence signal was observed between 650-750 nm with a maximum at 680 nm (Figure 4c), suggesting that **HP-1** can act as a NIR ratiometric probe. Both changes in absorption and emission signals were accomplished in seconds, clearly indicating that **HP-1** works much faster than most of the current H_2S selective probes and can rapidly detect H_2S. It is also important to note that **HP-1** exhibited a large Stokes' shift (~150 nm) (Figure 4d), which is another critical parameter for a fluorescent probe.

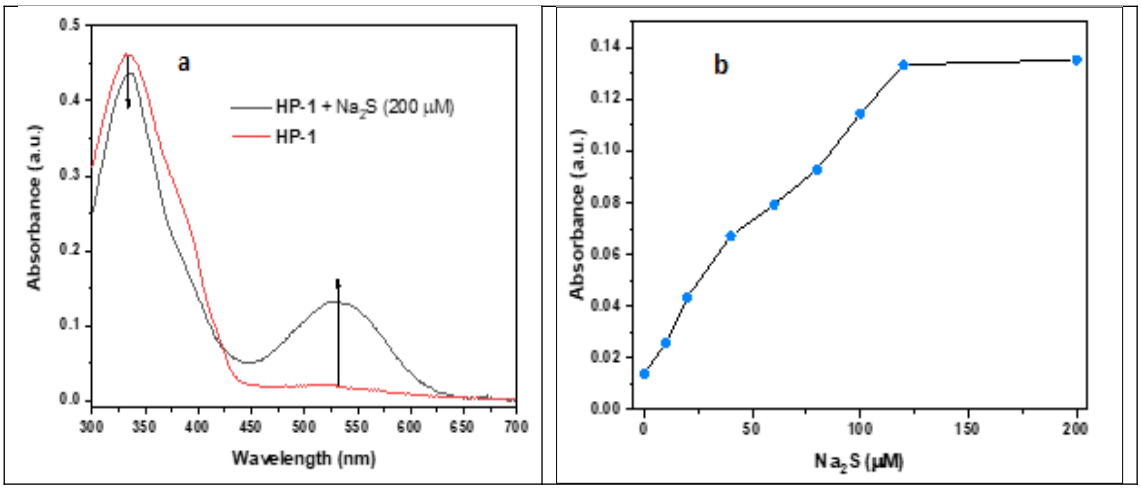

Figure 3. (a) Absorption spectra of **HP-1** (20 μM) before and after addition of Na_2S (200 μM) and (b) absorption signal of **HP-1** (20 μM) at 530 nm in increasing Na_2S concentrations in PBS (pH 7.4, 50% DMF).

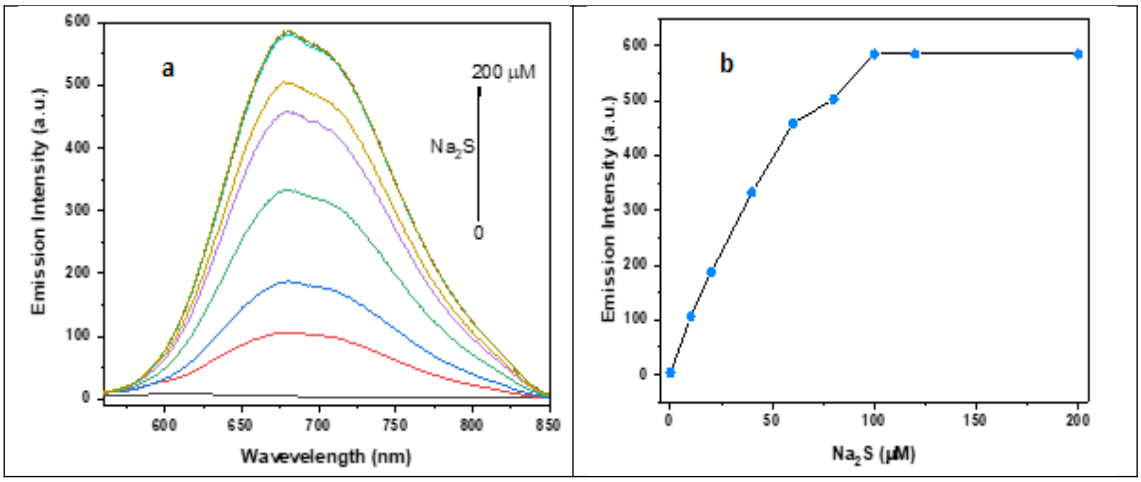

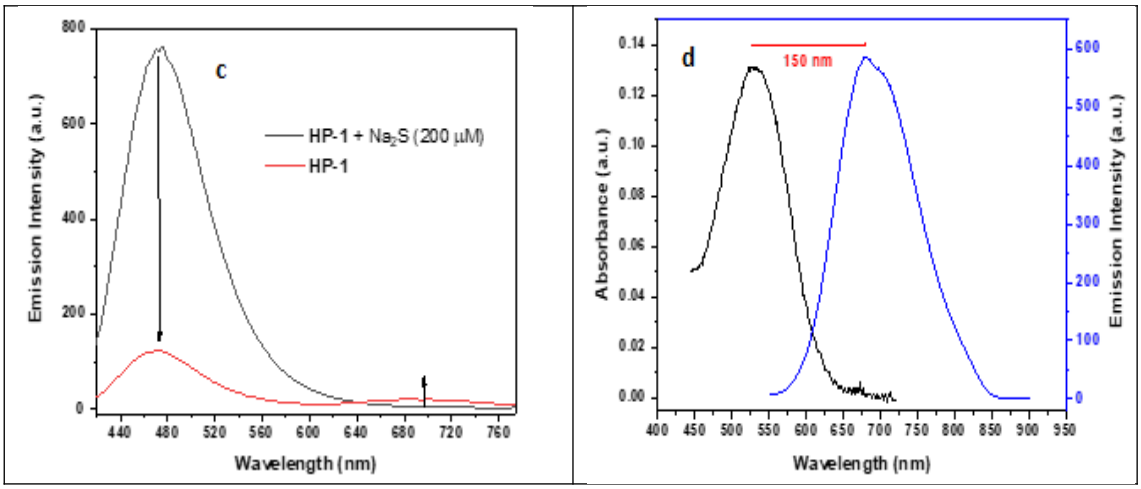

Figure 4. (a) Emission spectra of **HP-1** (20 μM) upon addition of increasing Na_2S concentrations and (b) the relationship between the emission intensities of **HP-1** (20 μM) at 680 nm and the concentration of Na_2S. Excitation wavelength is 530 nm. (c) Emission spectra of **HP-1** (20 μM) before and after addition of Na_2S (200 μM). Excitation wavelength is 420 nm. (d) The Stokes' shift of **HP-1** (20 μM) after addition of Na_2S (200 μM). Excitation wavelength is 530 nm. All experiments were done in PBS (pH 7.4, 50% DMF).

Next, the selectivity of **HP-1** towards H_2S was checked by using biologically relevant nucleophilic species including bio-thiols such as glutathione (GSH), cysteine (Cys) and homocysteine (Hcy) as well as different metal ions. No detectable change was observed both in absorption and emission spectra (Figure 5), proving the high selectivity of **HP-1** for H_2S over other species. The sensitivity of **HP-1** was measured by calculating the limit of detection (LOD) value and found to be as low as 0.64 μM. Finally, H_2S-induced removal of the cage group and the release of compound **4** was confirmed by acquiring a high-resolution mass spectrum (Figure S4).

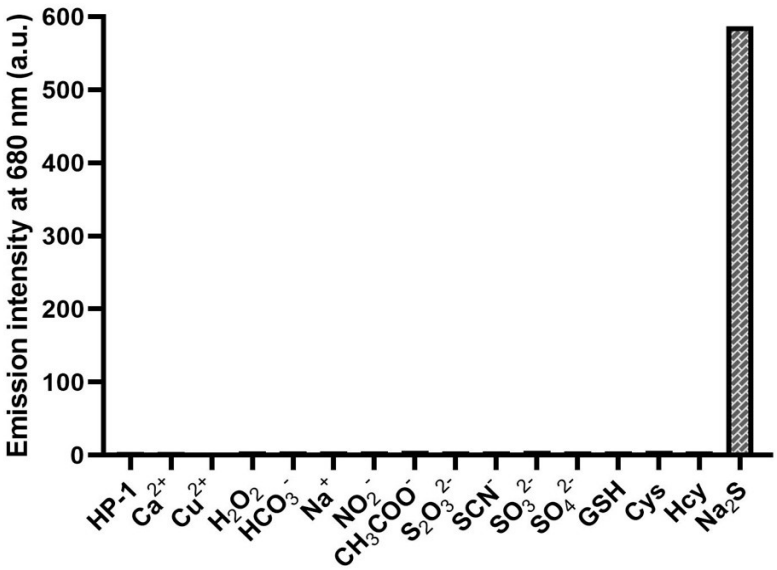

Figure 5. Emission intensities of **HP-1** (20 μM) in the absence and presence of different analytes in PBS (pH 7.4, 50% DMF). Na_2S concentration was 200 μM. All other analyte concentrations were set to 1 mM.

CONCLUSION

In summary, an easily accessible H_2S-selective benzothiazole-based chemodosimeter (**HP-1**) was synthesized and its molecular structure as well as optical responses to H_2S were characterized. Upon addition of Na_2S, **HP-1** exhibited a 195 nm bathochromic shift in the absorption signal and a

noticeable concentration dependent increase in the NIR emission at 680 nm as a result of enhanced ICT process, which was triggered by the removal of the azido cage group. Remarkably, all of these changes in photophysical parameters were realized in seconds with high sensitivity and selectivity towards H_2S.

CONFLICT OF INTEREST

The author declares no conflict of interest.

ACKNOWLEDGEMENTS

S. Kolemen thanks Koç University for the financial support. The author also acknowledges the researchers in Koç University Surface Science and Technology Center (KUYTAM) for fluorescence quantum yield measurements.

REFERENCES

1. Qian Y, Karpus J, Kabil O, Zhang S-Y, Zhu H-L, Banerjee R, et al. Selective fluorescent probes for live-cell monitoring of sulphide. Nat Commun. 2011 Sep;2(1):495.

2. Olas B. Hydrogen sulfide in signaling pathways. Clinica Chimica Acta. 2015 Jan;439:212–8.

3. Rose P, Moore PK, Zhu YZ. H2S biosynthesis and catabolism: new insights from molecular studies. Cell Mol Life Sci. 2017 Apr;74(8):1391–412.

4. Wang R. The Gasotransmitter Role of Hydrogen Sulfide. Antioxidants & Redox Signaling. 2003 Aug;5(4):493–501.

5. Papapetropoulos A, Pyriochou A, Altaany Z, Yang G, Marazioti A, Zhou Z, et al. Hydrogen sulfide is an endogenous stimulator of angiogenesis. Proceedings of the National Academy of Sciences. 2009 Dec 22;106(51):21972–7.

6. Wei H-J, Li X, Tang X-Q. Therapeutic benefits of H2S in Alzheimer's disease. Journal of Clinical Neuroscience. 2014 Oct 1;21(10):1665–9.

7. Szabó C. Hydrogen sulphide and its therapeutic potential. Nature Reviews Drug Discovery. 2007 Nov 1;6(11):917–35.

8. Kamoun P, Belardinelli M-C, Chabli A, Lallouchi K, Chadefaux-Vekemans B. Endogenous hydrogen sulfide overproduction in Down syndrome. American journal of medical genetics. 2003;116(3):310–1.

9. Wang L, Cai H, Hu Y, Liu F, Huang S, Zhou Y, et al. A pharmacological probe identifies cystathionine β-synthase as a new negative regulator for ferroptosis. Cell Death Dis. 2018 Oct;9(10):1005.

10. Breza J, Soltysova A, Hudecova S, Penesova A, Szadvari I, Babula P, et al. Endogenous H2S producing enzymes are involved in apoptosis induction in clear cell renal cell carcinoma. BMC Cancer. 2018 May 24;18(1):591.

11. Lawrence NS, Davis J, Jiang L, Jones TGJ, Davies SN, Compton RG. The Electrochemical Analog of the Methylene Blue Reaction: A Novel Amperometric Approach to the Detection of Hydrogen Sulfide. Electroanal. 2000;12(18):1453–60.

12. Choi MG, Cha S, Lee H, Jeon HL, Chang S-K. Sulfide-selective chemosignaling by a Cu2+ complex of dipicolylamine appended fluorescein. Chem Commun. 2009;(47):7390.

13. Furne J, Saeed A, Levitt MD. Whole tissue hydrogen sulfide concentrations are orders of magnitude lower than presently accepted values. American Journal of Physiology-Regulatory, Integrative and Comparative Physiology. 2008 Nov;295(5):R1479–85.

14. Qian Y, Zhang L, Ding S, Deng X, He C, Zheng XE, et al. A fluorescent probe for rapid detection of hydrogen sulfide in blood plasma and brain tissues in mice. Chem Sci. 2012;3(10):2920.

15. Lin VS, Chen W, Xian M, Chang CJ. Chemical probes for molecular imaging and detection of hydrogen sulfide and reactive sulfur species in biological systems. Chem Soc Rev. 2015;44:4596–618.

16. Liu C, Pan J, Li S, Zhao Y, Wu LY, Berkman CE, et al. Capture and Visualization of Hydrogen Sulfide by a Fluorescent Probe. Angew Chem. 2011 Oct 24;123(44):10511–3.

17. Lippert AR, New EJ, Chang CJ. Reaction-Based Fluorescent Probes for Selective Imaging of Hydrogen Sulfide in Living Cells. J Am Chem Soc. 2011 Jul 6;133(26):10078–80.

18. Liu Y, Feng G. A visible light excitable colorimetric and fluorescent ESIPT probe for rapid and selective detection of hydrogen sulfide. Org Biomol Chem. 2014;12:438–45.

19. Guo Z, Park S, Yoon J, Shin I. Recent progress in the development of near-infrared fluorescent probes for bioimaging applications. Chem Soc Rev. 2014;43(1):16–29.

20. Gong S, Zhou E, Hong J, Feng G. Nitrobenzoxadiazole Ether-Based Near-Infrared Fluorescent Probe with Unexpected High Selectivity for H 2 S Imaging in Living Cells and Mice. Anal Chem. 2019 Oct 15;91(20):13136–42.

21. Ozdemir T, Sozmen F, Mamur S, Tekinay T, Akkaya EU. Fast responding and selective near-IR Bodipy dye for hydrogen sulfide sensing. Chem Commun. 2014;50:5455–7.

22. Zheng Y, Zhao M, Qiao Q, Liu H, Lang H, Xu Z. A near-infrared fluorescent probe for hydrogen sulfide in living cells. Dyes and Pigments. 2013 Sep 1;98(3):367–71.

23. Zhang X, Zhang L, Ma W-W, Zhou Y, Lu Z-N, Xu S. A Near-Infrared Ratiometric Fluorescent Probe for Highly Selective Recognition and Bioimaging of Cysteine. Frontiers in Chemistry. 2019;7:32.

24. Karton-Lifshin N, Albertazzi L, Bendikov M, Baran PS, Shabat D. "Donor–Two-Acceptor" Dye Design: A Distinct Gateway to NIR Fluorescence. J Am Chem Soc. 2012 Dec 19;134(50):20412–20.

25. Chen C, Fang C. Devising Efficient Red-Shifting Strategies for Bioimaging: A Generalizable Donor-Acceptor Fluorophore Prototype. Chem Asian J. 2020;15:1514–23.

26. Jaswal S, Kumar J. Review on fluorescent donor–acceptor conjugated system as molecular probes. Materials Today: Proceedings. 2020;26:566–80.

27. Woo S-J, Kim Y, Kim M-J, Baek JY, Kwon S-K, Kim Y-H, et al. Strategies for the Molecular Design of Donor–Acceptor-type Fluorescent Emitters for Efficient Deep Blue Organic Light Emitting Diodes. Chem Mater. 2018 ubat;30(3):857–63.

28. Gong Y, Feng D, Liu W, Fang J, Feng S. A self-immolative near-infrared probe based on hemi-benzothiazolecyanine for visualizing hydrogen peroxide in living cells and mice. Dyes and Pigments. 2021 Feb;186:108954.

29. Zhang X, Liu J-Y. Solvent dependent photophysical properties and near-infrared solid-state excited state intramolecular proton transfer (ESIPT) fluorescence of 2,4,6-trisbenzothiazolylphenol. Dyes and Pigments. 2016 ubat;125:80–8.

30. Li S-J, Li Y-F, Liu H-W, Zhou D-Y, Jiang W-L, Ou-Yang J, et al. A Dual-Response Fluorescent Probe for the Detection of Viscosity and H 2 S and Its Application in Studying Their Cross-Talk Influence in Mitochondria. Anal Chem. 2018 Aug 7;90(15):9418–25.

SUPPLEMENTARY INFORMATION

A Near-infrared Benzothiazole-based Chemodosimeter for Rapid and Selective Detection of Hydrogen Sulfide

Safacan KOLEMEN[1,2,3]*

[1]Department of Chemistry, Faculty of Science, Koc University, Sariyer, Istanbul 34450, Turkey
[2]Surface Science and Technology Center (KUYTAM), Koc University, Sariyer, Istanbul 34450, Turkey
[3]Boron and Advanced Materials Application and Research Center, Koc University, Sariyer, Istanbul 34450, Turkey

NMR Spectra

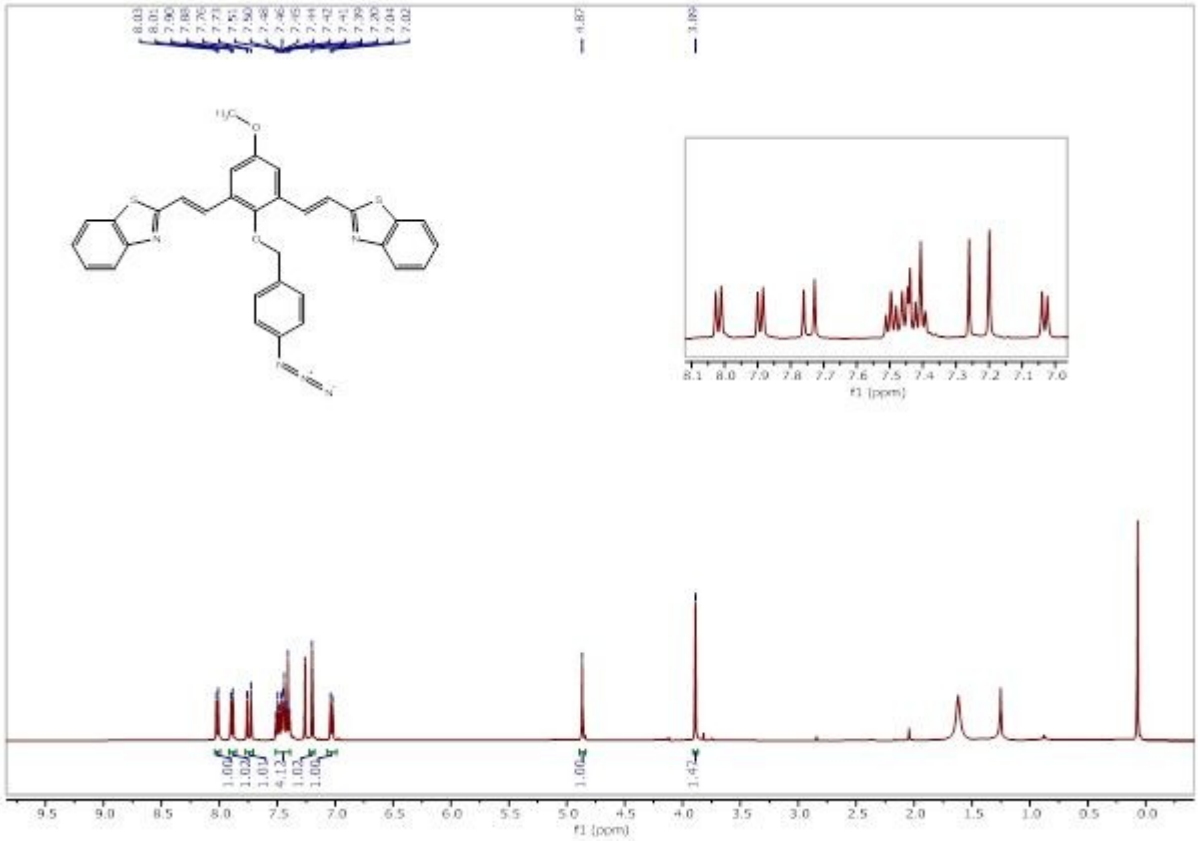

Figure S1. ^{1}H NMR spectrum of **HP-1**.

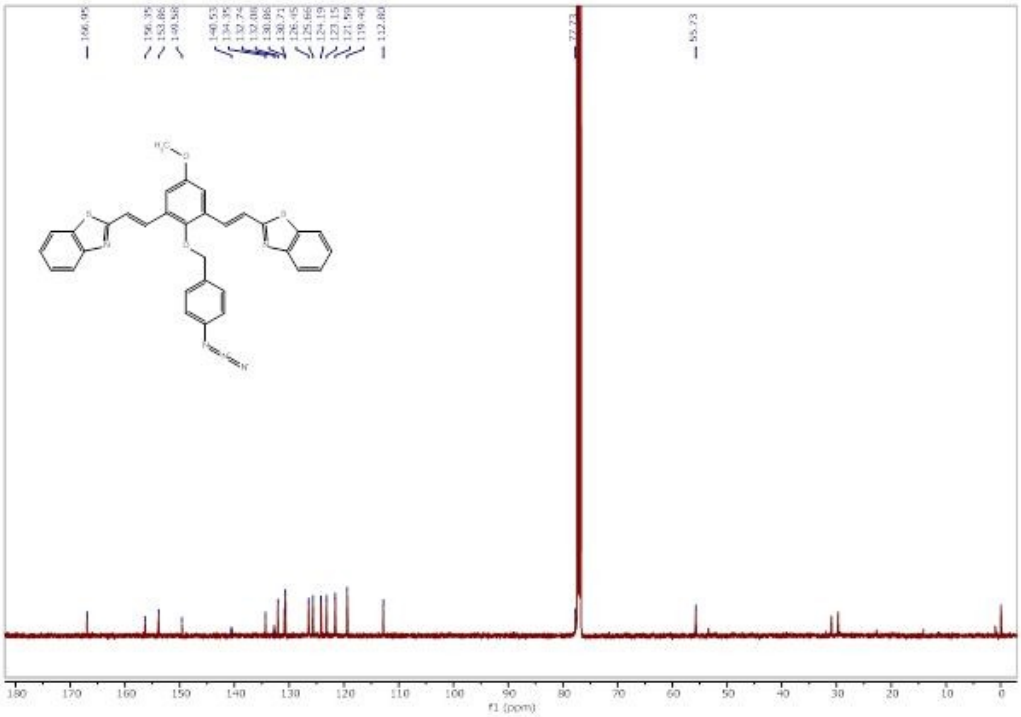

Figure S2. ^{13}C NMR spectrum of HP-1.

Mass Spectra

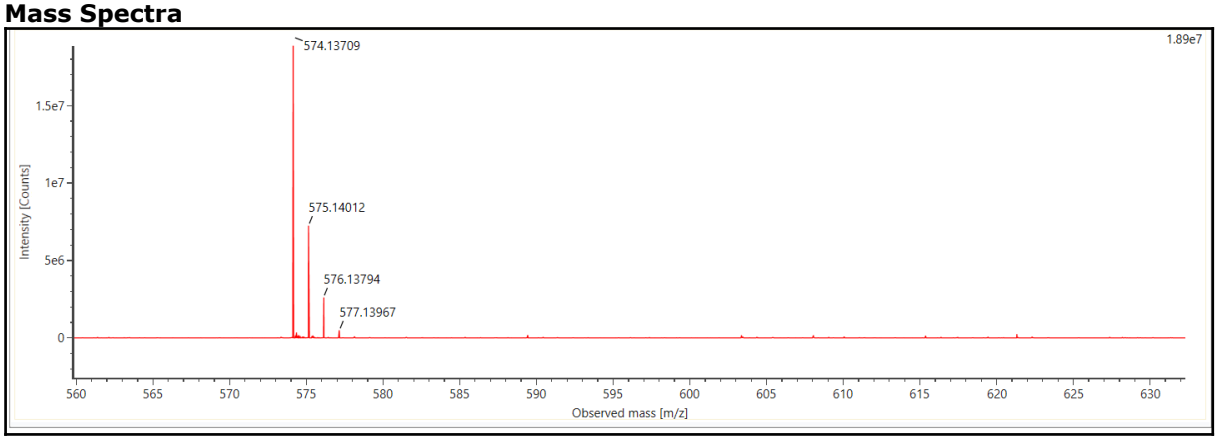

Figure S3. HR-MS spectrum of **HP-1**.

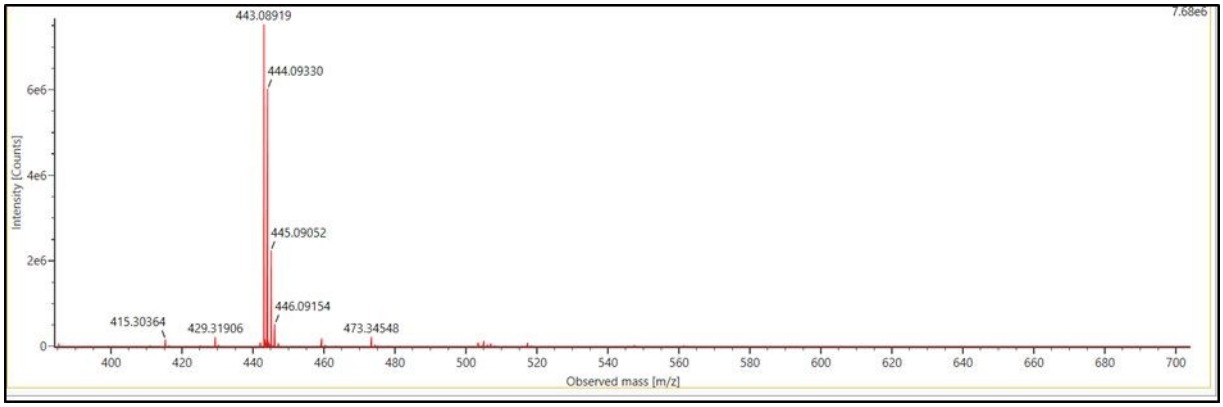

Figure S4. HR-MS spectrum of **HP-1** + Na_2S. Calc. for $C_{25}H_{18}N_2O_2S_2$ 443.0810 $[M+H]^+$; found: 443.0892.

Photophysical characterization

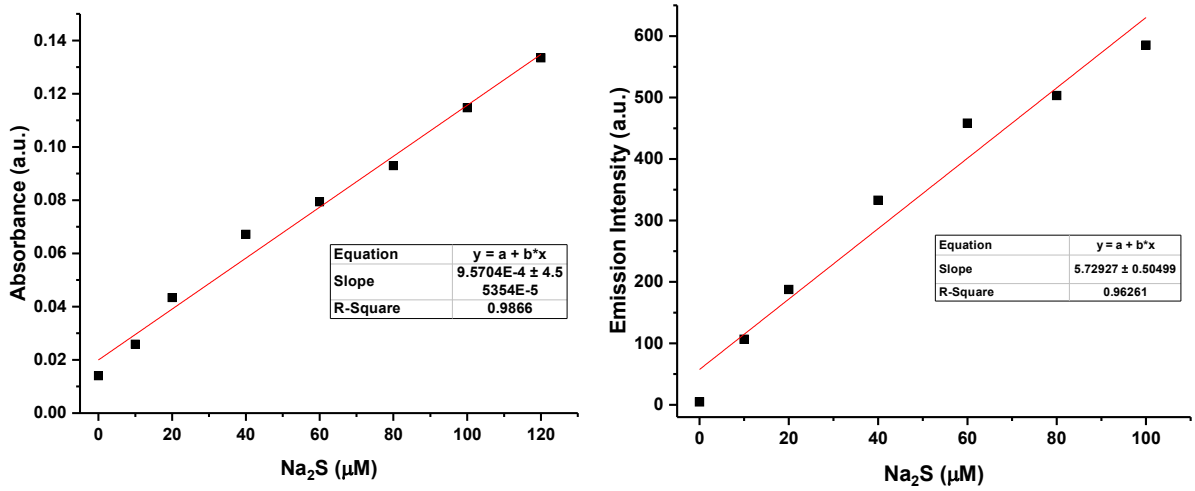

Figure S5. Increase of the absorption signal (left) of **HP-1** (20 μM) at 530 nm and emission signal (right) at 680 nm in increasing Na_2S concentrations in PBS (pH 7.4, 50% DMF) in the linear concentration range.

JOTCS A
Journal of the Turkish Chemical Society
Section: A
Chemistry
TURKISH CHEMICAL SOCIETY

The Compound Specific Antibacterial Activities of Major Urolithins and Their Methyl Ethers

Hayrettin Ozan Gülcan[1]*, Mehmet İlktaç[1], Bahareh Noshadi[1], Karar Tawfeeq Shukur[1], and Mustafa Gazi[2]

[1]Eastern Mediterranean University, Faculty of Pharmacy, Gazimağusa, TR. Northern Cyprus, via Mersin 10, Turkey.
[2]Eastern Mediterranean University, Faculty of Arts and Sciences, Department of Chemistry, Gazimağusa, TR. Northern Cyprus, via Mersin 10, Turkey.

Abstract: The investigation of biological activities of natural products, particularly considering the secondary metabolites, continuously receives attention. Urolithins, the bioavailable metabolites of ellagitannins, were shown to possess enzyme inhibitor, antioxidant, and anti-inflammatory compounds in scientific studies conducted in the last two decades. Regarding the limited number of studies related to their antimicrobial activity, this study aimed to synthesize major urolithins (Urolithin A and B) concomitant to their methyl ether derivatives and screen their antibacterial activity against some Gram positive and Gram negative bacteria. In parallel to the antibacterial activity, the synergistic and antagonist properties of the compounds were also analyzed in the presence of reference beta-lactam antibiotics. The results displayed the improvable characteristics of urolithin scaffold to be employed in antibiotic drug design studies. In addition, the antagonist effect of some compounds on the antibacterial action of standard molecules also pointed out the compound specific activities of the title molecules.

Keywords: Urolithin, synthesis, antibacterial activity, antagonism, synergism.

Submitted: January 15, 2021. **Accepted:** April 12, 2021.

Cite this: Gülcan HO, İlktaç M, Noshadi B, Shukur KT, Gazi M. The Compound Specific Antibacterial Activities of Major Urolithins and Their Methyl Ethers. JOTCSA. 2021;8(2):579–84.

DOI: https://doi.org/10.18596/jotcsa.861808.

***Corresponding author.** E-mail: (ozan.gulcan@emu.edu.tr), Tel: (+903926302401).

Note: Hayrettin Ozan Gülcan and Mehmet İlktaç have contributed equally to this article.

INTRODUCTION

Natural compounds, generally referred to as secondary metabolites of living things, have always attracted the curiosity of scientists to discover alternative strategies for the treatment of many states of disease (1,2). Indeed, there are many natural product-based drugs still used today. This type of research studies also guide to understand the possible biological activities of secondary metabolites, particularly in case of routine exposure to them via different sources (2,3). For instance, papaver somniferum alkaloids (e.g., morphine, codeine) have been used in different preparations either for treatment of pain or abuse purposes for centuries, however, the motivation on research for natural product chemistry, and biological activity screening of natural products have led to the discovery of opioid receptors and synthetic opioid molecules throughout the 20th century (4). As another example, the work of Alexander Fleming on the discovery of beta-lactam antibiotics from mold still has life-saving effects in the treatment of many life-threatening infectious diseases (5).

Urolithins, the hydroxyl substituted benzo[c] chromen-6-one derivatives, have attracted attention as natural compounds in the last two decades. In fact, these compounds are metabolism products in many mammalian species following exposure to ellagitannins (6,7). Nuts, berries, and particularly pomegranate are rich sources of ellagitannins. Many mammalians like humans regularly eat these diets. As seen in Figure 1, ellagitannins, the ester bond connected gallic acid derivative macromolecules, are subject to the gastrointestinal system microflora-catalyzed biotransformation reactions to yield out urolithin molecules, mainly as mono-, di-, tri-, and tetra-hydroxy substituted benzo [c] chromen-6-ones (8). The metabolism studies indicated that ellagitannins and their metabolism precursor molecule ellagic acid have negligible absorption from the gastrointestinal tract (9). However, the urolithins are bioavailable compounds. Indeed, urolithins appear in systemic circulation in two to three hours following the oral exposure to ellagitannin rich diet, particularly pomegranate (10).

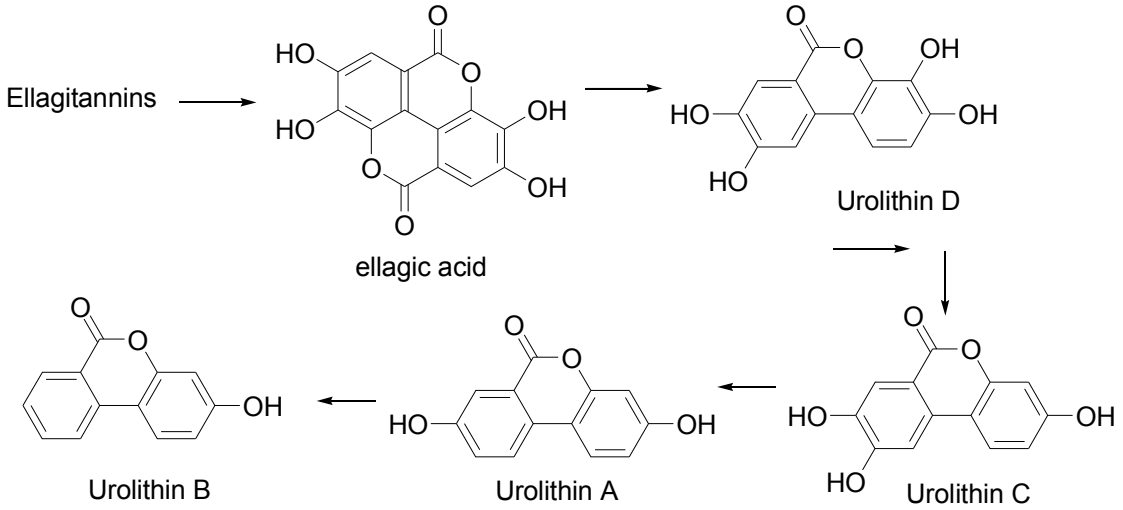

Figure 1: The formation of major urolithins, Urolithin A and B, through metabolism.

So far, many biological activities of ellagitannins have been shown under *in vivo* conditions (11). These were attributed to the urolithins, since a systemic effect can be seen only for bioavailable compounds. Among these activities, the antimicrobial activity gathered limited attention, since the main focus has been provided on ellagitannins (12). In one study, it was shown that urolithins A and B displayed antibacterial effects in the colon against *Yersinia enterocolitica* (13).

From this perspective, within this study, we have aimed to synthesize major urolithins (Urolithin A and B) and their methyl ether metabolites, formed through the catechol-O-methyl transferase activity. The antibacterial activities of the title compounds have been planned to be screened against several bacterial strains [i.e., *Escherichia coli*, *Staphylococcus aureus*, *Enterococcus faecalis*, and methicillin resistant *Staphylococcus aureus* (MRSA)]. Besides, the antagonist or synergistic activities of the compounds with a beta-lactam antibiotic have been aimed to be analyzed. To our knowledge, this has been the first study conducted on the total evaluation of urolithins in terms of their antibacterial activities in different Gram(+) and Gram(−) bacteria.

EXPERIMENTAL SECTION

Materials and instruments

All the chemicals and biologicals were purchased from local chemical suppliers of Turkish Republic of Northern Cyprus. They were used without purification unless otherwise stated. Thin layer chromatography studies were performed using Merck aluminum-packed silica gel plates to monitor the reactions. Ethyl acetate – n-hexane (1:1, v/v) was used as the mobile phase. Infrared spectra were obtained through a Shimadzu FT-IR Prestige spectrometer. Proton and carbon 13 NMR spectra of the title compounds were obtained via a Bruker-400 NMR spectrometer. Tetramethylsilane (TMS) was used as internal standard and deuterated dimethylsulfoxide (DMSO-d_6) was employed to dissolve the samples. The chemical shifts were reported in ppm. A Thermo Fisher Flash Smart CHNS elemental analyzer was employed for elemental analysis.

Chemistry

General synthesis protocols

Previously known procedures were followed for the synthesis of the title molecules (Figure 2) (14). Accordingly, the hydroxy substituted urolithin analogues (i.e., Urolithin A and B), and 3-hydroxy-8-methoxy-6H-benzo[c]chromen-6-one were

synthesized through reacting 15 mmol of resorcinol either with 5 mmol of 2-bromobenzoic acid (to obtain Urolithin B), or 5 mmol of 2-bromo-5-hydroxybenzoic acid (to obtain Urolithin A), or 5 mmol of 2-bromo-5-methoxybenzoic acid (to obtain 3-hydroxy-8-methoxy-6H-benzo[c]chromen-6-one) in 18 mmol NaOH dissolved distilled water. The mixtures were refluxed for 1 h and added 22% of $CuSO_4$ solution in 15 mL distilled water at the end of the time. The products precipitated were filtered off and washed with 0.01 N 50 mL hydrochloric acid solution.

The alternative methoxy-substituted analogues (i.e., methyl ether of Urolithin B, and dimethyl ether of Urolithin A) were synthesized respectively treating Urolithin B and A with methyl iodide. Briefly, 5 mmol of urolithin A or B was treated with 5.5 mmol of NaH in DMF. Following stirring at rt for 3 min, the solutions were added appropriate amount of methyl iodide (i.e., 5.5 mmol methyl iodide to obtain the methyl ether of Urolithin B, and 10.5 mmol methyl iodide to obtain the dimethyl ether of Urolithin A). After stirring at rt for 3h, the reaction mixtures were poured into 50 mL of distilled water. The mixture was extracted with 3 times of 30 mL of ethyl acetate. Following the evaporation of collected organic phases, the compounds were purified through column chromatography employing ethyl acetate – n-hexane (1:1) as the mobile phase. Spectral characterizations of the molecules have also been previously stated (14).

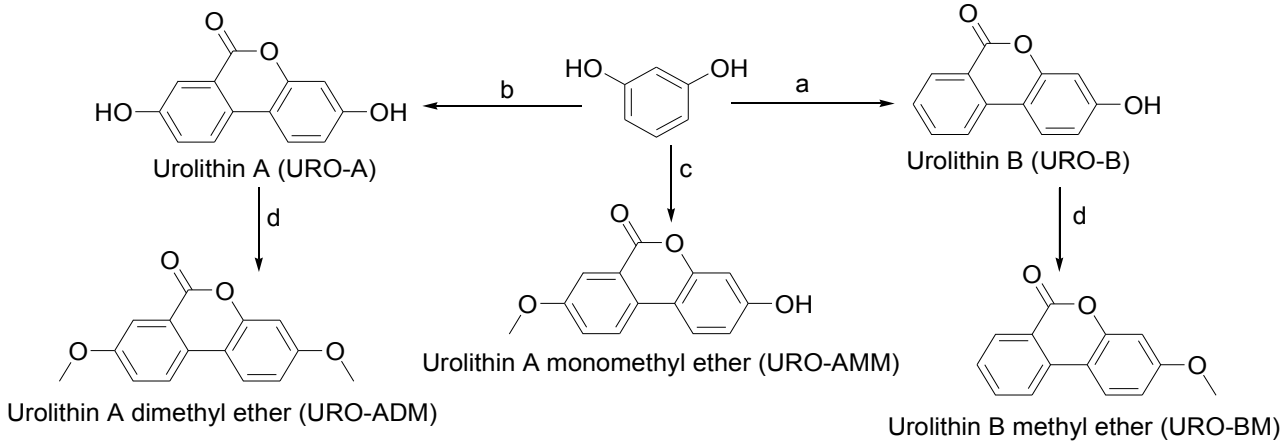

Figure 2: The synthetic protocol followed. a: 2-Bromobenzoic acid, NaOH, H_2O; b: 5-Hydroxy-2-bromobenzoic acid, NaOH, H_2O; c: 5-Methoxy-2-bromobenzoic acid, NaOH, H_2O; d: NaH, Methyl iodide, DMF

Antibacterial Activity

Bacterial strains

The antibacterial activity of the compounds was investigated against quality control strains of American Type Culture Collection (ATCC). *Staphylococcus aureus* ATCC 25923 (methicillin susceptible) and *Enterococcus faecalis* ATCC 29212 were used as representatives of Gram(+) whereas *Escherichia coli* ATCC 25922 was used as the representative of Gram(−) bacteria. MRSA strain that was isolated from the nose of a carrier and identified as *Staphylococcus aureus* by Gram characteristics, catalase and coagulase test was included in the study. The methicillin resistance of the strain was identified by disk diffusion method using cefoxitin disk (30 µg) as suggested by European Committee on Antimicrobial Susceptibility Testing (EUCAST) (15).

Bacteria were inoculated on Mueller Hinton agar (MHA) (Merck, Germany) by spread plate method and incubated at 37 °C for 24 hours under aerobic atmosphere. After incubation period, pure culture was derived by sub-culturing the single colony of each strain onto MHA and incubating under the same conditions mentioned above. Each of four strains was suspended in Mueller Hinton broth (MHB) and the suspensions were adjusted to the turbidity of 0.5 McFarland that are equivalent to the microorganism density of 1.5 x 10^8 cfu/mL. The inoculum of each strain was diluted using MHB to give an inoculum of 1 x 10^6 cfu/mL.

Preparation of the compounds

32.77 g/L of each of the compounds was prepared in dimethyl sulfoxide (DMSO), diluted 1:16 using MHB to obtain the concentration of 2048 mg/L and filtered using 0.45 µm pore sized syringe filters.

Determination of Minimum Inhibitory Concentrations (MICs)

The MICs of the compounds were investigated by broth microdilution method (16). Briefly, 50 µL of two fold diluted concentrations of the compounds were mixed in individual wells of 96 round bottom well plates with 50 µL of inoculum containing 1 x 10^6 cfu/mL of each strain. The final concentrations

of the compounds ranged from 1024 mg/L to 2 mg/L and the final concentration of DMSO in each well is ≤ 3%. For each run, a well containing 50 µL 3% DMSO with 50 µL inoculum of the respective strain was used as a positive control and a well including 50 µL 1024 mg/L with 50 µL MHB (instead of the bacterium) was used as a negative control. Ampicillin was used as internal control for *Enterococcus faecalis* ATCC 29212 and *Escherichia coli* ATCC 25922. On the other hand, penicillin G was used internal control for *Staphylococcus aureus* ATCC 25923 and MRSA. The microplates were incubated at 37 °C under aerobic atmosphere for 16 hours. MIC was regarded as the minimum concentration of the compound that inhibited the growth of the strain.

Effects of the compounds on MIC values of antibiotics

The effects of the compounds on ampicillin (Sigma-Aldrich) against *Escherichia coli* ATCC 25922 and *Enterococcus faecalis* ATCC 29212 and on penicillin G (Sigma-Aldrich) against *Staphylococcus aureus* ATCC 25923 and MRSA were investigated by broth microdilution checkerboard method (17). The compounds were prepared as described in the preparation of compounds and the antibiotics were prepared as suggested by the manufacturer. The final concentrations of the antibiotics ranged from eight times higher and sixteen times lower than expected MICs. The concentrations of the compounds eight times lower and higher than the MICs calculated by microdilution method were tested. 50 µL of the two fold increasing antibiotic concentrations was mixed with equal volume of two fold increasing concentrations of the compounds. The final organism concentration was 3×10^5 – 5×10^5 cfu/mL in each well. The individual MICs of the antibiotics and the compounds were confirmed in the first row and column, respectively, of the microplate for each run. The plates were incubated under aerobic atmosphere at 37 °C for 16-20 hours.

For the combination of the compound with the antibiotic tested, summation of fractional inhibitory concentration (∑FIC) was calculated as the sum of FIC of compound and FIC of antibiotic formula; where FIC of a compound is the ratio of MIC of a compound in combination over the MIC of compound alone, and the FIC of an antibiotic is the MIC of antibiotic in combination divided by the MIC of the antibiotic alone. The interaction between the compound and the antibiotic was regarded as; Synergism, where ∑FIC ≤ 0.5, Indifference, where 0.5 < ∑FIC ≤ 4, and Antagonism, where ∑FIC >4.

RESULTS AND DISCUSSION

The antibacterial activities of the title compounds have been assessed against several Gram(+) and Gram(−) bacterial strains (i.e., *Escherichia coli* as Gram(−), and *Staphylococcus aureus*, *Enterococcus faecalis*, and MRSA as Gram(+) strains) and the MIC values measured are shown in Table 1. Accordingly, none of the urolithins displayed activity against the Gram(−) strain *Escherichia coli*. Beside the inactivity of URO-AMM, the rest four urolithin derivatives displayed some activity against MRSA. In addition, all the compounds displayed weak to moderate activity against *Enterococcus faecalis*. On the other hand, beside the weak activity of URO-A, none of the compounds was found to be active against *Staphylococcus aureus*. The MIC values of the title molecules were also found weaker in comparison to the activities of reference molecules, ampicillin and penicillin G, against the strains employed in the study. Among the compounds tested, URO-A has been found as the only molecule that displays activity against the strains tested. This outcome is significant considering the fact that URO-A is one of the major metabolites found in systemic circulation following exposure to ellagitannin rich diet (18). URO-B, another major metabolite, was found to be inactive in general, beside its activity against *Enterococcus faecalis*.

On one hand, the results obtained pointed out the significance of URO-A molecule to be employed in antibacterial drug design studies as a scaffold to be developed to obtain more active antibacterial compounds. On the other hand, as methyl ether analogs typically exhibited weaker activities, phenolic hydroxyls appear to be important substitutions for the antibacterial activities obtained.

Table 1: MIC values (mg / L) of the title urolithin derivatives.

Title compound	*E. coli*	*S. aureus*	*E. faecalis*	MRSA
URO-B	> 512	> 512	32	256
URO-BM	> 512	> 512	128	64
URO-A	> 512	64	32	64
URO-ADM	> 512	> 512	128	64
URO-AMM	> 512	> 512	128	> 512
Ampicillin	4	NT	0.5	NT
Penicillin G	NT	0.03	NT	8

NT: Not tested

One of the important research fields in the action of antibacterials is the investigation of the effect of the natural products on the antibacterial activity of known and used antimicrobial agents (19,20). From this perspective, the effect of title urolithin compounds on the antimicrobial action of reference molecules (i.e., ampicillin, penicillin G) against the bacterial strains employed was tested. The results obtained are shown in Table 2.

Accordingly, none of the compounds tested caused a change on the MIC of ampicillin over *Escherichia coli*. URO-AMM (i.e., the monomethyl ether of Urolithin A) increased the MIC of penicillin G against *Staphylococcus aureus* more than 4 fold. Therefore, its action was characterized as antagonist on the activity of penicillin G. Although URO-AMM doubled the MIC of penicillin G against MRSA, since ∑FIC was less than 4, the net effect was evaluated as indifferent.

One of the major urolithin metabolites, URO-B, also displayed considerable effects. At one hand, it lowered the MIC of ampicillin against *Enterococcus faecalis*. Since ∑FIC was not less than 0.5, the overall effect was assessed as indifference. However, URO-B increased the MIC of penicillin G for more than 4 fold against MRSA, and therefore, its activity was found to be antagonist for the activity of penicillin G over MRSA.

Besides, the URO-A, URO-BM, and URO-ADM have been found not to have any effect on the MIC values of ampicillin and penicillin on *Staphylococcus aureus* and *Enterococcus faecalis*. On the other hand, URO-BM and URO-ADM combination with penicillin G was found to have two times higher MICs than the MIC of penicillin G alone against MRSA. Since the ∑FIC was less than 4, these activities were evaluated as indifferent. Finally, the other major metabolite of ellagitannin metabolism, URO-A, displayed almost no activity in combination studies, beside its negligible effect on the MIC of penicillin G against MRSA.

Table 2: The effect of title urolithins on the MICs of reference molecules.

Reference Drug/Combination	Bacterial strain / MIC	∑FIC
	S. aureus	
Penicillin G (alone)	0.03	
Penicillin G + URO-AMM (64-512 mg/L)	0.125	> 4
	E. faecalis	
Ampicillin (alone)	0.5	
Ampicillin + URO-B (8-16 mg/L)	0.25	0.75-1
	MRSA	
Penicillin G (alone)	8	
Penicillin G + URO-B (16-128 mg/L)	32	>4
Penicillin G + URO-BM (8-32 mg/L)	16	2
Penicillin G + URO-ADM (8-16 mg/L)	16	2
Penicillin G + URO-AMM (8-512 mg/L)	16	2

CONCLUSION

There are limited number of studies conducted on the antibacterial activity of urolithins. From this perspective, this study for the first time, analyzed the antibacterial activity of major urolithins (Urolithins A and B) concomitant to their methyl ether derivatives against some Gram(+) and Gram(−) strains. In general, it was found that the antibacterial activity of urolithins was compound- and the bacterial strain-specific. Furthermore, the synergistic and antagonist activity results also depicted that some urolithins (URO-B and URO-AMM) might act as antagonist, since they were able to lower the MIC of reference drugs more than four-fold.

The study outcomes also warrant future research studies. At first hand, the activities obtained against *Enterococcus faecalis* and MRSA points out that the

urolithin scaffold is improvable to design alternative urolithin based antibacterial compounds. On the other hand, depending on the exposure level to ellagitannin-rich diet, particularly involving pomegranate juice, the urolithins, formed through metabolism and present in systemic circulation, can interfere with antibacterial drug treatment. From this perspective, the findings regarding the effects of URO-B and URO-AMM might be enlarged in future research studies to see the extrapolation of antagonist effects to other beta lactam antibiotics.

REFERENCES

1. Koehn FE, Carter GT. The evolving role of natural products in drug discovery. Nature reviews Drug discovery. 2005 Mar;4(3):206-20.

2. Ji HF, Li XJ, Zhang HY. Natural products and drug discovery: can thousands of years of ancient medical knowledge lead us to new and powerful drug combinations in the fight against cancer and dementia?. EMBO reports. 2009 Mar;10(3):194-200.

3. Wöll S, Kim SH, Greten HJ, Efferth T. Animal plant warfare and secondary metabolite evolution. Natural products and bioprospecting. 2013 Feb 1;3(1):1-7.

4. Pathan H, Williams J. Basic opioid pharmacology: an update. British journal of pain. 2012 Feb;6(1):11-6.

5. Demain AL, Sanchez S. Microbial drug discovery: 80 years of progress. The Journal of antibiotics. 2009 Jan;62(1):5-16.

6. Gulcan HO, Unlu S, Esiringu İ, Ercetin T, Sahin Y, Oz D, Sahin MF. Design, synthesis and biological evaluation of novel 6H-benzo [c] chromen-6-one, and 7, 8, 9, 10-tetrahydro-benzo [c] chromen-6-one derivatives as potential cholinesterase inhibitors. Bioorganic & medicinal chemistry. 2014 Oct 1;22(19):5141-54.

7. Selma MV, Beltrán D, García-Villalba R, Espín JC, Tomás-Barberán FA. Description of urolithin production capacity from ellagic acid of two human intestinal Gordonibacter species. Food & function. 2014;5(8):1779-84.

8. Gonzalez-Barrio R, Truchado P, Ito H, Espin JC, Tomas-Barberan FA. UV and MS identification of urolithins and nasutins, the bioavailable metabolites of ellagitannins and ellagic acid in different mammals. Journal of Agricultural and Food Chemistry. 2011 Feb 23;59(4):1152-62.

9. Landete JM. Ellagitannins, ellagic acid and their derived metabolites: a review about source, metabolism, functions and health. Food research international. 2011 Jun 1;44(5):1150-60.

10. Seeram NP, Henning SM, Zhang Y, Suchard M, Li Z, Heber D. Pomegranate juice ellagitannin metabolites are present in human plasma and some persist in urine for up to 48 hours. The Journal of nutrition. 2006 Oct 1;136(10):2481-5.

11. Lipińska L, Klewicka E, Sójka M. The structure, occurrence and biological activity of ellagitannins: a general review. Acta Scientiarum Polonorum Technologia Alimentaria. 2014 Sep 30;13(3):289-99.

12. Ammar OM, Ilktac M, Gulcan HO. Urolithins and their antimicrobial activity: A short review. EMU Journal of Pharmaceutical Sciences. 2019;3(2):117-24.

13. Giménez-Bastida JA, Truchado P, Larrosa M, Espín JC, Tomás-Barberán FA, Allende A, García-Conesa MT. Urolithins, ellagitannin metabolites produced by colon microbiota, inhibit quorum sensing in Yersinia enterocolitica: phenotypic response and associated molecular changes. Food chemistry. 2012 Jun 1;132(3):1465-74.

14. Noshadi B, Ercetin T, Luise C, Yuksel MY, Sippl W, Sahin MF, Gazi M, Gulcan HO. Synthesis, Characterization, Molecular Docking, and Biological Activities of Some Natural and Synthetic Urolithin Analogs. Chemistry & Biodiversity. 2020 Aug;17(8):e2000197.

15. The European Committee on Antimicrobial Susceptibility Testing (EUCAST). Breakpoint tables for interpretation of MICs and zone diameters. Version 11.0, 2021. http://www.eucast.org.

16. Leber A. Broth Microdilution Test. In: Clinical Microbiology Procedures Handbook, Fourth Edition. ASM Press, Washington, DC. 2016. pp. 5.2.1.1-5.2.2.10. doi: 10.1128/9781555818814.ch5.2.1.

17. Leber A. Synergism Testing: Broth Microdilution Checkerboard and Broth Macrodilution Methods. In: Clinical Microbiology Procedures Handbook, Fourth Edition. ASM Press, Washington, DC. 2016. pp. 5.16.1-5.16.23. doi: 10.1128/9781555818814.ch5.16.

18. Ishimoto H, Shibata M, Myojin Y, Ito H, Sugimoto Y, Tai A, Hatano T. In vivo anti-inflammatory and antioxidant properties of ellagitannin metabolite urolithin A. Bioorganic & medicinal chemistry letters. 2011 Oct 1;21(19):5901-4.

19. Moghaddam KM, Iranshahi M, Yazdi MC, Shahverdi AR. The combination effect of curcumin with different antibiotics against Staphylococcus aureus. International Journal of Green Pharmacy (IJGP). 2009;3(2).

20. Hemaiswarya S, Kruthiventi AK, Doble M. Synergism between natural products and antibiotics against infectious diseases. Phytomedicine. 2008 Aug 1;15(8):639-52.

JOTCSA Journal of the Turkish Chemical Society Section: A Chemistry

TURKISH CHEMICAL SOCIETY

Microwave Assisted Green Synthesis of Ag, Ag_2O, and Ag_2O_3 Nanoparticles

Nesrin KORKMAZ[1]*, Ahmet KARADAĞ[2]

[1]Department of Basic Sciences and Health, Hemp Research Institute, Yozgat Bozok University, 66200, Yozgat, Turkey.

[2]Department of Chemistry, Faculty of Arts and Sciences, Yozgat Bozok University, 66200, Yozgat, Turkey.

Abstract: In this study, nanoparticles containing Ag, Ag_2O, and Ag_2O_3 mixture were synthesized by using a microwave-assisted green synthesis method. For the reduction of Ag^+ to Ag^0, *Rhododendron ponticum* plant extract was used while the microwave synthesis method was used for the formation of silver oxides. Nanoparticles synthesized under 90 °C, 450 W, and 30-minute microwave synthesis conditions were characterized by UV-Vis, XRD, and STEM. As a result of characterization, Ag-NPs were found to show maximum absorbance peak at 432 nm in the UV-Vis spectrum, crystallite size was 46 nm according to XRD analysis, and nanoparticles showed in a spherical_homogeneous distribution by STEM analysis. Our results showed that the phytochemicals in the plant extract of *R. ponticum* reduce Ag^+ ions to Ag-NPs and that the mixture of silver and silver oxide can be synthesized quickly and easily with microwave heating support. This study is important to increase the use of Ag_2O and Ag_2O_3 nanoparticles in industrial production and medical applications. In particular, nanoparticles of silver and silver(I) oxide show great promise for widespread usage in medical polymers and nanodrugs. Because in this study, toxic chemicals were not used in the synthesis of silver oxide nanoparticles and it is a safe synthesis because there is no risk of explosion.

Keywords: Silver oxide nanoparticles, Green synthesis, Microwave synthesis, Ag_2O_3 nanoparticles, Ag_2O nanoparticles.

Submitted: August 22, 2020. **Accepted:** April 14, 2021.

Cite this: Korkmaz N, Karadağ A. Microwave Assisted Green Synthesis of Ag, Ag_2O, and Ag_2O_3 Nanoparticles. JOTCSA. 2021;8(2):585–92.

DOI: https://doi.org/10.18596/jotcsa.784065.

***Corresponding author. E-mail:** nesrin.korkmaz@bozok.edu.tr, nesrinokumus@gmail.com.

INTRODUCTION

Nanotechnology involves the adaptation of atomic materials at the nanometer level to achieve the desired shape and properties according to the field of application (1). Recently, there has been an increase in studies aimed at developing rapid, inexpensive, and environmentally friendly methods in nanoparticle synthesis methods (2). These studies focused on using everything from plants to bacteria as a reducing agent in reducing noble metal ions. The green synthesis method has been developed as a product of this orientation (4-10). Compared with traditional methods; In addition to being inexpensive, easily available, it does not contain toxicity against human and ecological systems (4,5,11). On the other hand, the mechanism of action is not fully known, and shape and size control has not been achieved in metal nanoparticle synthesis.

Similarly, many plant extracts have been used in the synthesis of metal nanoparticles and similar results have been obtained. Plant extracts such as Artocarpus hetrophyllus, *Azadirechta indica, Callistemon lanceolatus, Centella asiatica, Lippia citriodora, Fenugreek, Paeonia emodi, and Pinus longifolia* play an important role in reducing toxicity during the reduction of metal ions (12-19). Studies on Ag2O nanoparticles synthesized using these plants are summarized in Table 1. Bio-synthesized Ag-nanoparticles have many application areas such as solar energy systems, coatings, battery production, sensors, medical devices, biological studies, and biotagging (20-23).

Silver has three different oxidative forms: Ag_2O, AgO, and Ag_2O_3. Silver oxides are widely used in the production of medical devices, in the production of zinc-mixed alkaline batteries (22,24). Although AgO and Ag_2O oxidative forms of silver are easily obtained, the industrial production of Ag_2O_3 is quite difficult. Generally; although $AgClO_4$ is frequently used in the chemical synthesis method, the presence of ClO_4^- ion is very harmful to both human health and the environment. In addition, there is a high risk of explosion during the synthesis.

In this study, *Rhododendron ponticum* plant, a forest waste, was used as a reducing agent. Although green synthesis has been used for nanoparticle synthesis in the last two decades, the microwave-assisted synthesis method has been preferred for the first time for oxide formation. As a result, the use of environmentally friendly, rapid microwave synthesis method for oxide formation adds innovation to this study.

Characterization of the synthesized silver and silver oxide mixture was done by UV-Vis, X-Ray diffractometry, and STEM (Scanning Transmission Electron Microscopy) analysis. As a result of these, by combining two different synthetic methods (green synthesis method, microwave synthesis method), it attracts attention with its ease of use advantage compared to other studies in the literature with a cheap, easy, healthy, and safe synthesis method.

MATERIALS and METHODS

Plant selection and preparation

Located about 150 genera and 4.000 species of shrubs in Turkey is a cosmopolitan family *Ericaceae* including the small tree-like community (25). *R. ponticum* is a species of this family. Turkey's Black Sea coast, at the edge reach that level up to 2500 m altitude, lovers of the acidic growing conditions, evergreen, is a perennial shrub species (26). *R. ponticum* has been used as medicinal plants in treatments due to its pain-relieving properties (tooth, back, joint and rheumatic pain) (27,28).
R. ponticum was collected and washed thoroughly and dried in a non-direct sunlight environment. The dried leaves of the plant are dried into a fine powder with the help of a grinder and stored at +4 °C for use in the synthesis process.

Silver and silver oxide synthesis

On the one hand, 20 mg of plant powder was mixed in 20 mL of pure water at 70 °C for 6 hours, then filtered. On the other hand, $AgNO_3$ solution was prepared with a concentration of 1 mM. It was taken from 10 mL of plant extract stock and 50 mL of $AgNO_3$ solution and mixed in a beaker. The mixture in the beaker was then placed in 20 mL of microwave synthesizer containers and subjected to experimental conditions of 30 min, 90 °C, 450 W. As a result of the synthesis, particles settled to the bottom of the containers were observed. The collapsed part is washed several times with pure water, then was centrifuged at 10.000 rpm for 20 min.

Physical characterization

To achieve physical characterization of silver nanoparticles, we first determined the UV-Vis spectrometric analysis (TERMO, Model Multiscanner spectrophotometer) for obtaining the maximum absorbent peak between 300 and 700 nm, then powder X-ray analysis for calculating the average silver nanoparticle size (Brand name-Panalytical, Model-Empyrean Advance, made in the Netherlands). It was then characterized by scanning transmission electron microscopy (TESCAN, MAIA3 XMU) analysis, which is one of the most commonly used methods to analyze the morphology and size of the vacuum-dried sample.

RESULTS AND DISCUSSION

In this synthetic reaction, Ag^+ ions are reduced to Ag^0 (AgNP formation) thanks to the phytochemicals contained in the plant extract. Afterward, silver oxide mixtures were obtained as a result of exposure to microwaves of 90 °C and 450 W for 30 minutes.

Generally, it is very difficult to give a formation mechanism for metal nanoparticles obtained by green synthesis. While the reducing agent is clearly known in the chemical synthesis method, it is not known which phytochemicals in the plant have a reducing effect in green synthesis. Scheme 1. will be a reasonable representation for the AgNPs to be obtained in this study.

Table 1. Biosynthesis of Ag_2O NPs using various plant extracts with size and shape.

Plant's name	**Morphology**	**Size (nm)**	**Characterization Techniques**	**Refs.**
Artocarpus hetrophyllus	Spherical	14	XRD, UV-Vis, FTIR, DLS, TEM	12
Azadirechta indica	Spherical and sheet	60-100	UV-Vis, FTIR, XRD, SEM, Zeta potential	13
Callistemon lanceolatus	Spherical and hexagonal	3-30	UV-Vis, FTIR, XRD, SEM, HRTEM	14
Centella asiatica	Spherical	11-12	XRD, UV-Vis, SEM, EDS, FTIR	15
Lippia citriodora	Spherical	20	XRD, TEM, EDS, FTIR, TGA	16
Fenugreek	Spherical	31.5	UV-Vis, FTIR, TEM, Zeta potential	17
Paeonia emodi	Spherical	38.29	XRD, TEM, SEM, EDX, FTIR, UV-Vis	18
Pinus longifolia	Spherical and sheet	1-100	UV-Vis, SEM	19

$$\text{Plant phytochemicals} \xrightarrow{e^-} Ag^+ \longrightarrow Ag^0 \text{ (AgNPs and AgONPs)}$$

Scheme 1. Mechanism of AgNPs and AgONPs synthesis.

Many attempts have been made in the microwave synthesis system, especially for Ag_2O_3 synthesis. In most of the trials, only Ag_2O form nanoparticles were synthesized at high temperatures. Ag_2O-Ag_2O_3 mixtures were obtained by subjecting only the plant extract-$AgNO_3$ mixture solution to 450 W microwave at 90 °C for 30 minutes. These optimized synthesis conditions are of great importance for the reproducibility of the experiment.

UV-Vis Absorption Analysis

UV-Vis analysis is the most widely used technique for the determination of different materials such as transition metal ions, organic compounds, and biological molecules. The first evidence that the synthesis reaction took place; it was understood that the color of the colorless $AgNO_3$ solution turned brown by the addition of *R. ponticum* extract. After this evidence, the primary characterization of silver and silver oxide nanoparticles was done by UV-Vis analysis. In the UV-visible spectrophotometric observations of silver nanoparticles synthesized using *R. ponticum* extract, a maximum absorbance was observed at 432 nm (Figure 1). According to previous papers, it can be said that the spectrum values for Ag nanoparticles vary between 420-450 nm depending on the particle size, plant extraction concentration, chemical environment, and dielectric medium (20-23). For the nanoparticles that are stable and monodisperse, the spectral peak is narrower and sharp whereas for colloidal aggregates (or agglomerates of AgNPs) a much broader peak, usually the visible in the spectrum can be observed.

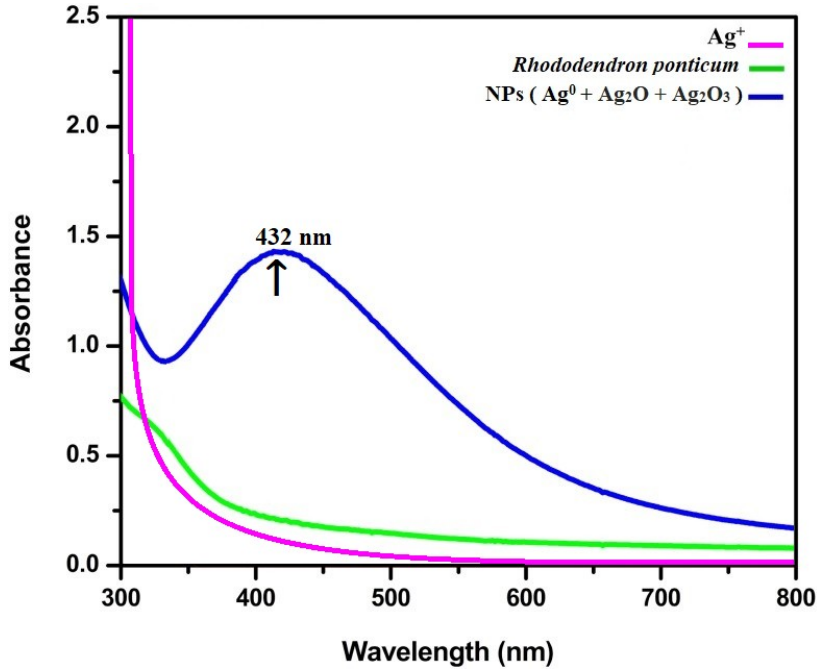

Figure 1. UV–Vis absorption spectra.

XRD analysis

XRD analysis data of pure Ag^0, Ag_2O, and Ag_2O_3 nanoparticles in mixture form synthesized by microwave synthesis method are shown in Figure 2. As seen from the powder X-ray analysis data, six 2θ values that were intensely seen from 20 to 80 were seen. Evaluation of the powder X-ray analysis is important to clearly learn the nature of the nanoparticles formed. The standard 2θ values for silver nanoparticles given in the literature were confirmed to be in the form of nanocrystals as a result of overlapping with the 2θ values (38.23°, 46.36°, 64.62° and 77.57°) we obtained as a result of synthesis. It is also clearly seen that other peaks other than 38.23° seen in the XRD spectrum are a mixture of silver and silver oxides.

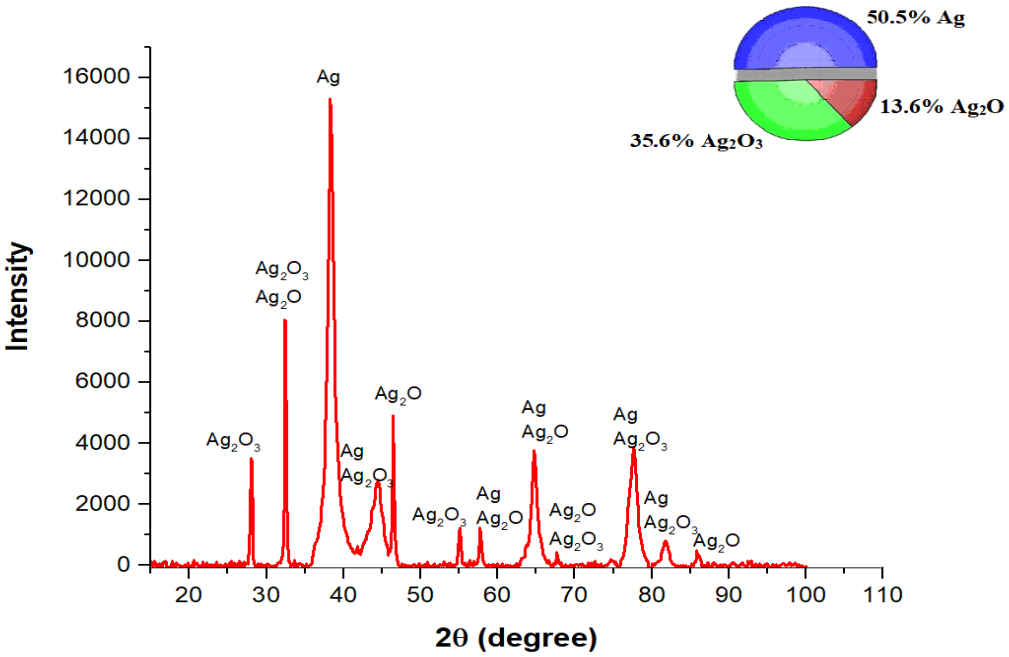

Figure 2: XRD analysis of silver and silver oxide nanoparticles.

This study involving the synthesis of Ag nanoparticles, Ag_2O_3 and Ag_2O nanoparticles with pure Ag nanoparticles were observed together. Semaltianos et al. conducted a study involving silver nanoparticle synthesis by laser ablation from the material in pure water. As a result of the synthesis, they observed Ag_2O_3 nanoparticle mass in addition to pure silver (29).

In another study, they suggested that the formation of AgONP was caused by the interaction of Ag atoms with oxygen atoms or radicals during their decomposition in water. They also stated that the type of oxide formed depends on the partial pressure of oxygen and temperature (30). Sajti et al. stated that AgO formed at low partial oxygen pressure, remained stable in the large temperature range and Ag_3O_4 and Ag_2O_3 formed at higher partial pressures (31).

The Scherrer equation was used to calculate the crystal size of nanoparticles composed of silver and silver oxide mixtures.

$$D = (K\,\lambda) / (\beta \cos\theta) \qquad \text{(Eq. 1)}$$

In the equation, λ is the X-ray wavelength, β is the half-height width of the X-ray peak, the K shape factor constant (0.9), and the angle θ denotes the reference peak width. As a result of this equation, the crystal size of Ag-ONPs was calculated as 46 nm. It was noted that the result obtained was close to the silver oxide values synthesized in the literature as well as the results of the STEM analysis (13,14,18,19,32).

STEM (SEM) study of the AgNPs and AgONPs

STEM images of the synthesized nanoparticles were made to determine the particle size, shape, in short, their morphology of the nanoparticles. Figure 3 shows that the synthesized particles are nano-spheres and the particle size variation is widely distributed. Also from the particle size distribution, it indicates that the nanoparticle sizes generally vary between 40 and 60 nm. As a result, it is possible to say that the average of the particle size variation coincides with the crystal size obtained as a result of X-ray.

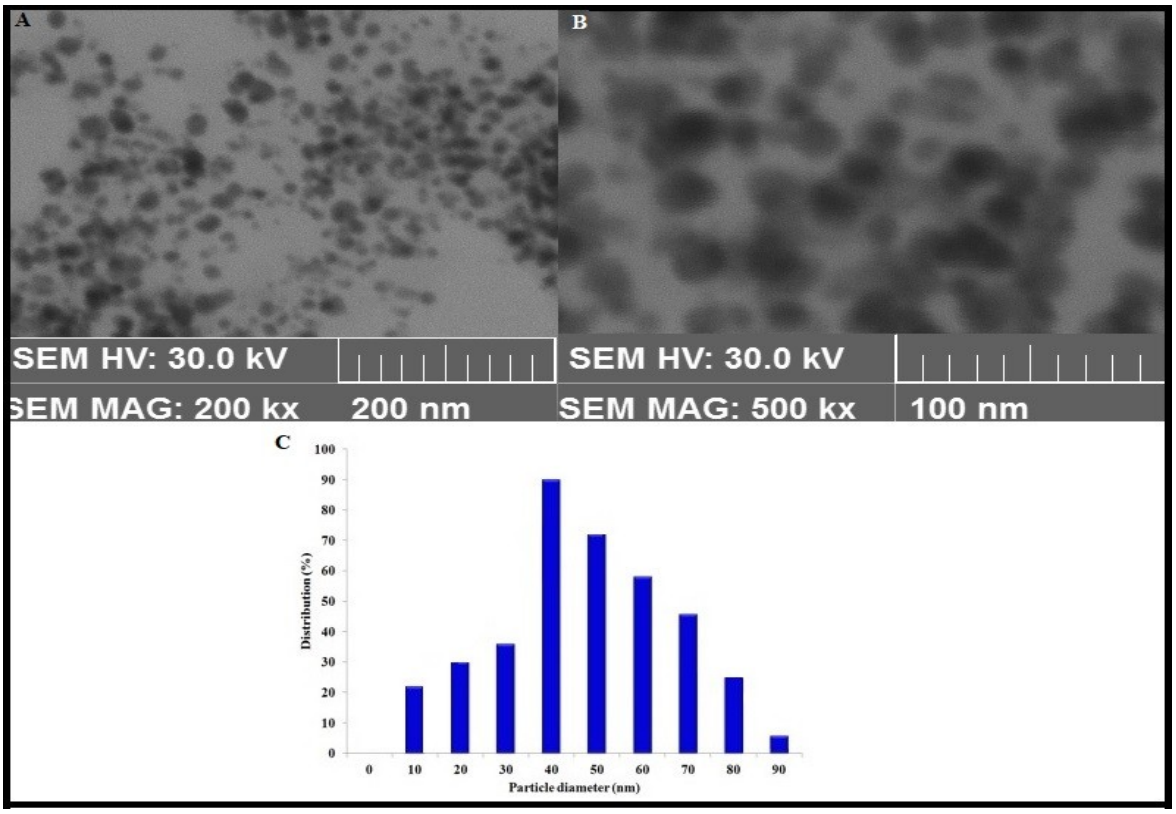

Figure 3. STEM images of the nanoparticles synthesized by *R. ponticum* plant extracts.

CONCLUSION

Easy, fast, cheap, and non-toxic green synthesis method was used in the synthesis of Ag_2O and Ag_2O_3 nanoparticles. In this method, the synthetic reaction was supported by the microwave method using *R. ponticum* plant extract as a substrate. The combination of two separate synthesis methods allowed the rare synthesized Ag_2O_3 nanoparticles to be obtained easily and safely. Silver oxide is a well-known semiconductor metal oxide having vast applications, in the field of electrochemical, electronic, optical properties, oxidation catalysis, sensors, fuel cells, photovoltaic cells, all-optical switching devices, optical data storage systems, and as a diagnostic biological probe, anticancer chemotherapy, antibiotics, and cosmetics. In the study the nanoparticles obtained were physically (UV-Vis analysis, XRD analysis, and STEM analysis) examined; the nanoparticles were found to exhibit a homogeneity in shape and size, and the crystallite size was 46 nm.

Microwave-assisted Ag_2O-Ag_2O_3 NPs are stable due to the presence of vegetable capping agents such as flavonoids, proteins, and phenols whose NPs are resistant to agglomeration. Biomimetic synthesis of Ag_2O-Ag_2O_3 NPs using plant extract and microwave has many advantages such as non-harmfulness, environmentally friendliness, sustainability, biocompatibility, simplicity, and cost-effectiveness. Because of these properties, it is concluded that Ag_2O NPs will have an important and mandatory role in most nanotechnology-based protocols.

In the future, if the biosynthetic experimental conditions are optimized to control the size and shape parameters of silver oxide NPs, photocatalytic performance applications and growth towards more biomedical fields are expected.

REFERENCES

1. Korkmaz N, Ceylan Y, Hamid A, Karadağ A, Bülbül AS, Aftab MN, Şen F, Biogenic silver nanoparticles synthesized via Mimusops elengi fruit extract, a study on antibiofilm, antibacterial, and anticancer activities. Journal of Drugs Delivery Science and Technology, 59, (2020) 101864, 1-7.

2. Whitesides GM. The 'right' size in nanobiotechnology. Nature Biotechnology. 2003; 21 (10): 1161-1165.

3. Korkmaz N, Berkil Akar K, İmamoğlu R, Kısa D, Karadağ A, Synthesis of silver nanowires in a two-phase system for biological Applications. Applied Organometallic Chemistry, 2021; e6213.

4. Mukherjee P, Senapati S, Mandal D, Ahmad A, Khan MI et al. Extracellular synthesis of gold nanoparticles by the fungus Fusarium oxysporum. ChemBioChem 2002; 3 (5): 461–463

5. Ahmad A, Mukherjee P, Senapati S, Mandal D, Khan MI et al. Extracellular biosynthesis of silver nanoparticles using the fungus Fusarium oxysporum. Colloids Surf B: Biointer 2003; 28 (4): 313–318.

6. Kumar V, Yadav SK. Plant-mediated synthesis of silver and gold nanoparticles and their applications. Journal of Chemical Technology & Biotechnology: International Research in Process, Environmental Clean Technology 2009; 84 (2): 151-157.

7. Bhambure R, Bule M, Shaligram N, Kamat M, Singhal R. Extracellular biosynthesis of gold nanoparticles using Aspergillus niger – its characterization and stability. Chemical Engineering & Technology 2009; 32 (7): 1036–1041.

8. Das SK, Das AR, Guha AK. Gold nanoparticles: microbial synthesis and application in water hygiene management. Langmuir 2009; 25 (14): 8192–8199.

9. Kalishwaralal K, Deepak VS, Kumar PR, Gurunathan S. Biological synthesis of gold nanocubes from Bacillus licheniformis. Bioresour Technol 2009; 100 (21): 5356–5358.

10. Kalishwaralal K, Deepak V, Pandian SRK, Kottaisamy M, BarathmaniKanth S, et al. Biosynthesis of silver and gold nanoparticles using Brevibacterium casei. Colloids Surf B: Biointerf 2010; 77 (2): 257–262.

11. Klaus T, Joerger R, Olsson E, Granqvist CG, Silver-based crystalline nanoparticles, microbially fabricated. Proc Natl Acad Sci USA, 1999; 96 (24): 13611–13614.

12. Sharma SN, Srivastava R, Silver oxide nanoparticles synthesized by green method from Artocarpus Hetrophyllus for antibacterial and antimicrobial applications, Materials Today: Proceedings, 2020.

13. Muruganatham N, Givindharaju R, Jayaseelan R, Sundararajan G. Green synthesis and characterization of silver oxide nanoparticles using plant extract. J. Appl. Sci. Comp, 2019; 6, 987-1004.

14. S. Ravichandran, V. Paluri, G. Kumar, K. Loganathan, B.R. Kokati Venkata, A novel approach for the biosynthesis of silver oxide nanoparticles using aqueous leaf extract of Callistemon lanceolatus (Myrtaceae) and their therapeutic potential, Journal of Experimental Nanoscience, 11 (2016) 445-458.

15. B.N. Rashmi, S.F. Harlapur, B. Avinash, C.R. Ravikumar, H.P. Nagaswarupa, M.A. Kumar, K. Gurushantha, M.S. Santosh, Facile green synthesis of silver oxide nanoparticles and their electrochemical, photocatalytic and biological studies, Inorganic Chemistry Communications, 111 (2020) 107580.

16. R. Li, Z. Chen, N. Ren, Y. Wang, Y. Wang, F. Yu, Biosynthesis of silver oxide nanoparticles and their photocatalytic and antimicrobial activity evaluation for wound healing applications in nursing care, Journal of Photochemistry and Photobiology B: Biology, 199 (2019) 111593.

17. C. Ashokraja, M. Sakar, S. Balakumar, A perspective on the hemolytic activity of chemical and green-synthesized silver and silver oxide nanoparticles, Materials Research Express, 4 (2017) 105406.

18. A. Shah, S. Haq, W. Rehman, M. Waseem, S. Shoukat, M. ur Rehman, Photocatalytic and antibacterial activities of paeonia emodi mediated silver oxide nanoparticles, Materials Research Express, 6 (2019) 045045.

19. Z. Khatun, R.S. Lawrence, M. Jalees, K. Lawerence, Green synthesis and Anti-bacterial activity of Silver Oxide nanoparticles prepared from Pinus longifolia leaves extract, International Journal, 3 (2015) 337-343.

20. Kumar A, Chisti Y, Banerjee U. Synthesis of metallic nanoparticles using plant extracts: Biotechnology Advances 2013; 31: 346–356

21. Durán N, Marcato PD, Alves OL, De Souza GI, Esposito E. Mechanistic aspects of biosynthesis of silver nanoparticles by several Fusarium oxysporum strains. Journal of Nanobiotechnology 2005; 3 (1): 8.

22. Korkmaz N. Antibacterial Activity and Biofilm Property of Silver Nanoparticles Synthesized by Using Saintpaulia Aqueous Leaf Extract, Journal of the Institute of Science and Technology 2019; 9 (4): 2225-2234. doi: 10.21597/jist.561197

23. Korkmaz N, Ceylan Y, Karadağ A, Bülbül AS, Aftab MN, et al. Biogenic silver nanoparticles synthesized from Rhododendron ponticum and their antibacterial, antibiofilm and cytotoxic activities. Journal of Pharmaceutical and Biomedical Analysis 2020; 179 (112993): 1-8. doi:10.1016/j.jpba.2019.112993

24. Ando S, Hioki T, Yamada T, Watanabe N, Higashitani A. Ag2O3 clathrate is a novel and effective antimicrobial agent. Journal of Materials Science 2012; 47 (6): 2928-2931. doi: 10.1007/s10853-011-6125-0

25. Stevens PF, Rhododendron L. Davis PH (Ed.). Flora of Turkey and the East Aegean Islands, Edinburgh University Press, Edinburgh, 1978; 6: 90–94.

26. Avcı M, Ormangülleri (Rhododendron L.) Ve Türkiye'deki Doğal Yayılışları. Coğrafya Dergisi. 2004(12): 13–29.

27. Yesilada E, Sezik E, Honda G, Takasihi Y, Takeda Y. et al. Traditional medicine in Turkey IX. Folk medicine in Noth-West Anatolia. Journal of Ethnopharmacology 1999; 64: 195–210.

28. Baytop T. Therapy with Medicinal Plants in Turkey: Past and Present, Second edition. Nobel Tıp Kitabevleri, Istanbul. 1999.

29. Semaltianos NG, Perrie W, Romani S, Potter RJ, Dearden G. Watkins, Polymer-nanoparticle composites composed of PEDOT: PSS and nanoparticles of Ag synthesised by laser ablation. Colloid and Polymer Science, 2012; 290: 213-220.

30. Suzuki RO, Ogawa T, Ono K. Use of ozone to prepare silver oxides. Journal of the American Ceramic Society, 1999; 82(8): 2033-2038.

31. Sajti CL, Sattari R, Chichkov BN, Barcikowski S. Gram scale synthesis of pure ceramic nanoparticles by laser ablation in liquid. The Journal of Physical Chemistry 2010; 114 (6): 2421-2427.

32. Yong NL, Ahmad A, Mohammad AW. Synthesis and characterization of silver oxide nanoparticles by a novel method. International Journal of Scientific & Engineering Research, 2013; 4:155-158.

JOTCS A
Journal of the Turkish Chemical Society
Section: A
Chemistry
TURKISH CHEMICAL SOCIETY

Oxovanadium(IV) Template Derived from Benzophenone S-allyl Thiosemicarbazone: Synthesis, Crystal Structure, Antioxidant Activity and Electrochemistry

Berat İlhan-Ceylan*

Istanbul University-Cerrahpasa, Engineering Faculty, Department of Chemistry, Inorganic Chemistry Division, 34320, Avcılar, Istanbul, Turkey.

Abstract: The oxovanadium(IV) template was formed with the reaction between vanadyl sulfate pentahydrate, 2-hydroxybenzophenone-S-allylthiosemicarbazone, and 3-methoxysalicylaldehyde. The synthesized template complex, along with the starting ligand, was subjected to UV-Vis, FTIR, ESI-mass, and magnetic measurement. The square pyramidal structure was proven with the single-crystal X-ray diffraction method. Stronger crystals were formed with π- π interactions, which was also supported by the corresponding peak in the mass spectrum. Electrochemical measurements was performed using a conventional three-electrode cell with cyclic voltammetry (CV) method. CV results show that complex **2** gives one-electron reduction ($V^{IV}O$ –$V^{III}O$) couple and one-electron oxidation ($V^{IV}O$ –$V^{V}O$) couple at the vanadium center. The total antioxidant capacity of the template compound and the starting ligand was performed by the CUPRAC method, yielding that the complex was more potent than the control compound, ascorbic acid.

Keywords: Thiosemicarbazone, oxovanadium(IV), antioxidant capability, electrochemistry, X-ray crystallography.

Submitted: April 07, 2021. **Accepted:** April 23, 2021.

Cite this: İlhan-Ceylan B. Oxovanadium(IV) Template Derived from Benzophenone S-allyl thiosemicarbazone: Synthesis, Crystal Structure, Antioxidant Activity and Electrochemistry. JOTCSA. 2021;8(2):593–608.

DOI: https://doi.org/10.18596/jotcsa.911318.

***Corresponding author. E-mail:** beril@istanbul.edu.tr.

INTRODUCTION

Complexes of vanadium have antimicrobial, antibacterial, antitumoral, and catalytic activity and insulin-enhancing effects. Vanadium has the potential of displaying oxidation states of III, IV, and V, and readily forming V-O bonds and binding nitrogen and sulfur. Nitrogenase and haloperoxidases are important vanadium-containing enzymes (1-3).

Vanadium salts act as insulin-like behavior in the cells and in diabetic animals, and this has been known since the 80s. Frequently, diabetic patients have abnormal levels of glucose and lipids in the blood, and insulin treatment can normalize this abnormality. It has been shown that, in animal model systems and human beings, treatment with vanadium complexes and vanadium salts could alleviate the symptoms of diabetes (1, 4, 5). In vivo insulin-like activity (6, 7) and in vitro insulin-mimetic activities of oxovanadium(IV) complexes with thiosemicarbazones are also reported (8, 9).

Thiosemicarbazones and related metal complexes display important biological and therapeutic properties, such as catalytic applications (10-12), sensors (13), antioxidant (14, 15), cytotoxic (16,

17), antidiabetic (18), antimalarial (19), antiviral (20, 21), antimicrobial (17, 22), antifungal (23, 24), antibacterial (25, 26), anticancer (27), and antitumoral (16, 28, 29) activities.

In this work, an oxovanadium(IV) thiosemicarbazone (**2**) template structure was prepared with 2-hydroxybenzophenone S-allylthiosemicarbazone (**1**) and 3-methoxysalicylaldehyde. The single crystals of compound **2** were obtained, and cyclic voltammetry (CV), thermogravimetric analysis (TGA), and antioxidant efficiency (with the CUPRAC method) were studied. It was found that compound **2** was more active than compound **1**. Also, the crystalline structure revealed that there were interactions of π- π and C- π nature in the X-ray crystal determination.

EXPERIMENTAL

General Remarks

All chemicals were of reagent grade and they were used as received. For elemental analyses, a Thermo Finnigan Flash EA 1112 device and for molar conductivity measurements, a Therma conductivity meter was employed. Fourier transform infrared spectral measurements were performed with an Agilent Cary 630 FT-attenuated total reflectance (ATR) spectrometer between 4000 and 600 cm^{-1}. For antioxidant capacity measurements, a Shimadzu brand UV-2600 spectrophotometer working in the ultraviolet-visible range was used, and a matched pair of quartz cuvettes with 10 mm path length were equipped. All determinations were done at room temperature.

For X-ray crystallography, data collection was carried out with a Bruker brand, APEX2 CCD diffractometer and data were reduced with Bruker SAINT (30). Solving and refinement of the structure were performed with SHELXT 2018/2 and SHELXL-2018/3 (31, 32). Direct methods were used for the solvation of the structure, which was refined on F^2 using all the reflections.

Synthesis

2-hydroxybenzophenone-S-allylthiosemicarbazone (**1**) was synthesized by applying slight modifications to the literature procedure. Briefly, the compound was stirred in ethanol to get rid of sticky substances, and then 5% sodium hydrogen carbonate solution was added and therefore the synthetic yield was increased (14, 33).

Triethyl orthoformate (1.0 mL) and vanadyl sulfate pentahydrate (1.0 mmol) in 5.0 mL of ethanol were reacted overnight at room temperature. The solution was treated with a mixture of compound **1** (1.0 mmol) and 3-methoxysalicylaldehyde (1.0 mmol) in ethanol (5.0 mL). For a few days, the mixture was kept at room temperature, and the black-colored product obtained (**2**) was washed with cold ethanol. The template complex yielded the following experimental data which were described below.

Oxovanadium(IV) complex (**2**): Black, m.p. 284.8-285.3 °C, yield 12%. Molar Conductivity (DMSO, $\Omega^{-1}cm^2mol^{-1}$): 8.2. Anal. Calc. for $C_{25}H_{23}N_3O_5SV$ (528.47 g/mol): C, 56.82; H, 4.39; N, 7.95; S, 6.07. Found: C, 56.43; H, 4.55; N, 7.44; S, 5.79%. UV–Vis ($CHCl_3$) [λ_{max} (nm), log ε (dm^3 cm^{-1} mol^{-1})]: 239(5.03) 258(4.99) 333(4.83) 359(4.77) 434(4.52). IR (cm^{-1}): v(C=N^1) 1608, 1601; v(C=N^2) 1574; v(N^4=C) 1519; v(C_{ar}–O) 1149, 1104; v(N–N) 1025; v(V=O) 966, v(C–S) 746. MS m/z (%): $[(M-H_2O)+Na]^+$ 533.1 (22.91), $[(2M+H_2O)+Na]^+$ 1042.8 (100).

Cyclic Voltammetry

A conventional three-electrode cell system was employed for the electrochemical measurements. A glassy carbon electrode (GCE) having a diameter of 3.0 mm was used as the working electrode. A Ag/AgCl reference electrode and a platinum wire counter electrode were also used to complete the circuit. The working electrode, before each run, was polished with an alumina slurry, obtained from Buehler Micropolish, on a Buehler-102 mm polishing pad and rinsed with distilled water.

The electrochemical measurements were performed for compound (**2**) at 1.0 x 10^{-3} M concentration in electrochemically pure dimethyl sulfoxide, along with, as the supporting electrolyte, 0.1 M $Bu_4N^+ClO_4^-$ (TBAP) under nitrogen atmosphere.

CUPRAC study

To study the total antioxidant capacity of the compounds, CUPRAC (CUPric Reducing Antioxidant Capacity) was employed (34). Under identical conditions, calculations of the molar absorption coefficients were performed for every compound. By taking the selected compound's molar absorptivity as a fraction of trolox, TEAC (trolox-equivalent antioxidant capacity) values were computed. Into a test tube were placed, in this very order, copper(II) chloride dihydrate (1.0 mL, 10 mM), neocuproine (Nc; 1.0 mL, 7.5 mM), pH = 7 ammonium acetate buffer (1.0 mL, 1.0 M), antioxidant sample solution (x mL), and distilled water (1.1 – x mL). The total volume was 4.1 mL, and after an incubation period of half an hour, the absorbance at 450 nm was recorded against a blank, which does not include the reagents. The computation of TEAC coefficients was performed with the following equation:

$$TEAC\ coefficient = \frac{molar\ absorptivity\ of\ the\ compound}{molar\ absorptivity\ of\ trolox\ \left(1.67 \times 10^{4}\ L\ mol^{-1} cm^{-1}\right)} \quad \text{(Eq. 1)}$$

RESULT AND DISCUSSION

Synthesis

The yield of synthesis was poor; it was because the complexation reaction was conducted at room temperature, and suitable single crystals were attempted to isolate, in a dark environment with no stirring at all, for 3-4 days. Otherwise, X-ray-suitable crystals could not be obtained. Template condensations require the presence of a metal ion; in our case, the oxovanadium(IV) ion was used to conduct the complexation and provide the Schiff base condensation of the N^4 thioamide moiety, which is unable to react without a template condensation. The template complexes, as well as the reagents, are stable in the air, which increases the application of them.

Molar Conductivity

Compound (**2**) had a molar conductivity of 8.2 Ω^{-1} cm^2 mol^{-1} in a 10^{-3} M DMSO solution at room temperature. This value is indicative of the non-electrolytic nature of the complex; according to references, this means the absence of anions (35-37).

Crystallographic Studies

The oxovanadium(IV) complex (**2**) crystallized in the triclinic space group P-1 (2) with Z = 2. Compound **2**'s several properties are displayed in Table 1 (bond lengths), Table 2 (bond angles) and Table 3 (torsion angles) and Tables S1a (atomic coordinates) and S2a (hydrogen bonds). Figures 1, 2, and 3 summarize structural refinement parameters and principal crystalline data.

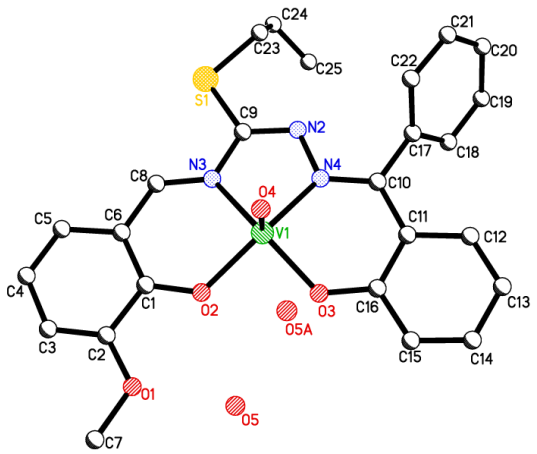

Figure 1: Perspective view of oxovanadium(IV) complex (**2**) with atom numbering.

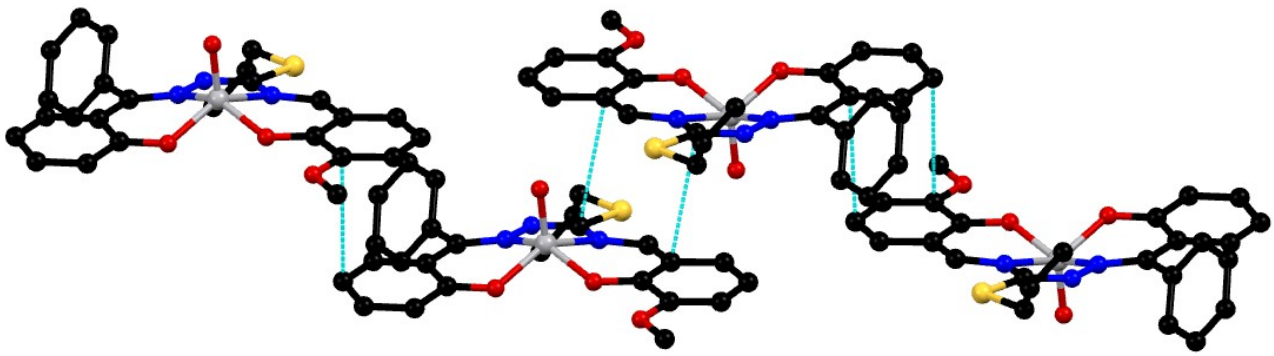

Figure 2: π- π stacking interactions for the oxovanadium(IV) complex (**2**).

Table 1: Crystalline data and structure refinement for the oxovanadium(IV) complex (**2**).

Identification code	Oxovanadium(IV) complex (**2**)
Empirical formula	C_{25} H_{25} N_3 O_5 S V
Formula weight	530.45
Temperature	293(2) K
Wavelength	0.71073 Å
Crystal system	Triclinic
Space group	P-1
Unit cell dimensions	a = 9.5801(10) Å, α= 100.737(10)°
	b = 11.9561(14) Å, β= 100.758(9)°
	c = 12.1053(14) Å, γ = 111.107(10)°
Volume	1221.2(3) $Å^3$
Z	2
Density (calculated)	1.443 mg/m^3
Absorption coefficient	0.536 mm^{-1}
F(000)	546
Crystal size	0.16 x 0.11 x 0.08 mm^3
Theta range for data collection	3.339 to 27.779°.
Index ranges	-8<=h<=11, -15<=k<=13, -13<=l<=15
Reflections collected	7210
Independent reflections	4774 [R(int) = 0.0344]
Completeness to theta = 25.242°	98.4 %
Max. and min. transmission	0.7457 and 0.5092
Refinement method	Full-matrix least-squares on F^2
Data / restraints / parameters	4774 / 1 / 328
Goodness-of-fit on F^2	1.024
Final R indices [I>2sigma(I)]	R1 = 0.0785, wR2 = 0.1929
R indices (all data)	R1 = 0.1335, wR2 = 0.2305
Extinction coefficient	n/a
Largest diff. peak and hole	0.722 and -0.657 e.$Å^{-3}$

Table 2: Selected bond distances [Å] and angles [°] for oxovanadium(IV) complex (**2**).

Atoms	**Distances [Å]**	**Atoms**	**Angles [°]**
V(1)-O(4)	1.603(4)	O(4)-V(1)-O(3)	111.6(2)
V(1)-O(3)	1.894(4)	O(4)-V(1)-O(2)	108.35(17)
V(1)-O(2)	1.947(3)	O(3)-V(1)-O(2)	87.82(15)
V(1)-N(3)	2.036(5)	O(4)-V(1)-N(3)	108.07(19)
V(1)-N(4)	2.043(4)	O(3)-V(1)-N(3)	139.47(17)
S(1)-C(9)	1.758(6)	O(2)-V(1)-N(3)	87.40(16)
S(1)-C(23)	1.787(7)	O(4)-V(1)-N(4)	103.90(18)
O(1)-C(2)	1.343(7)	O(3)-V(1)-N(4)	86.67(16)
O(1)-C(7)	1.423(6)	O(2)-V(1)-N(4)	147.02(18)
O(2)-C(1)	1.306(6)	N(3)-V(1)-N(4)	76.12(17)
O(3)-C(16)	1.319(6)	C(1)-O(2)-V(1)	128.9(3)
N(2)-C(9)	1.295(7)	C(16)-O(3)-V(1)	127.1(3)
N(2)-N(4)	1.405(6)	C(8)-N(3)-V(1)	126.1(4)
N(3)-C(8)	1.326(6)	C(9)-N(3)-V(1)	112.9(4)
N(3)-C(9)	1.410(6)	C(10)-N(4)-V(1)	128.0(4)
N(4)-C(10)	1.317(6)	C(10)-N(4)-N(2)	114.5(4)

Symmetry transformations used to generate equivalent atoms.

Table 3: Hydrogen bonds for oxovanadium(IV) complex (**2**) [Å and °].

D-H...A	d(D-H)	d(H...A)	d(D...A)	<(DHA)
C(4)-H(4)...O(4)#1	0.93	2.65	3.483(7)	149.3
C(8)-H(8)...O(4)#2	0.93	2.61	3.371(7)	139.4
C(18)-H(18)...O(3)#3	0.93	2.43	3.295(7)	153.8
O(5^a)-H(5A^a)...O(1)	0.85	2.41	2.988(14)	126.2
O(5^a)-H(5A^a)...O(2)	0.85	2.58	3.354(13)	152.8
_O(5A^b)-H(5AA^b)...O(4)	0.85	2.39	2.991(13)	128.3

Symmetry transformations used to generate equivalent atoms:
#1 x-1,y, z #2 -x+1,-y,-z+1 #3 -x+2,-y+1,-z+1

Vanadium template complex forms two six- and one five-membered rings. In the six-membered rings, the bond angles are very close with O(3)-V(1)-N(4) being 86.67 Å while O(2)-V(1)-N(3) is 87.40 Å. The five-membered ring has a N(3)-V(1)-N(4) angle of 76.12°. When dealing with bond distances, the shortest bond was 1.603 Å for V(1)-O(4) while the longest bond was 2.043 Å for V(1)-N(4). Experimental results show that vanadium-oxygen bonds are shorter than vanadium-nitrogen bonds (38, 39). The previous publication could be accessed for detailed crystalline data and related comments about S-allyl thiosemicarbazone (**1**) (14).

A disordered water molecule (O5 and O5A) is present in the asymmetric unit and this was computed over two positional site occupancies, 0.576 and 0.424, respectively. Moreover, the allyl group C23-C24-C25 is quite a lot disordered and the modeling of this disorder did not give better refinement values; therefore it was left as it is.

The stacking-type π- π interactions forge a link for compound **2**. In these interactions, complexes' aromatic rings are linked on adjacent parallel planes containing the other complex's ligand portion. Figure 2 shows the π- π stacking for compound **2**. It is concluded that the π- π stacking works in the stabilization of the structure (40).

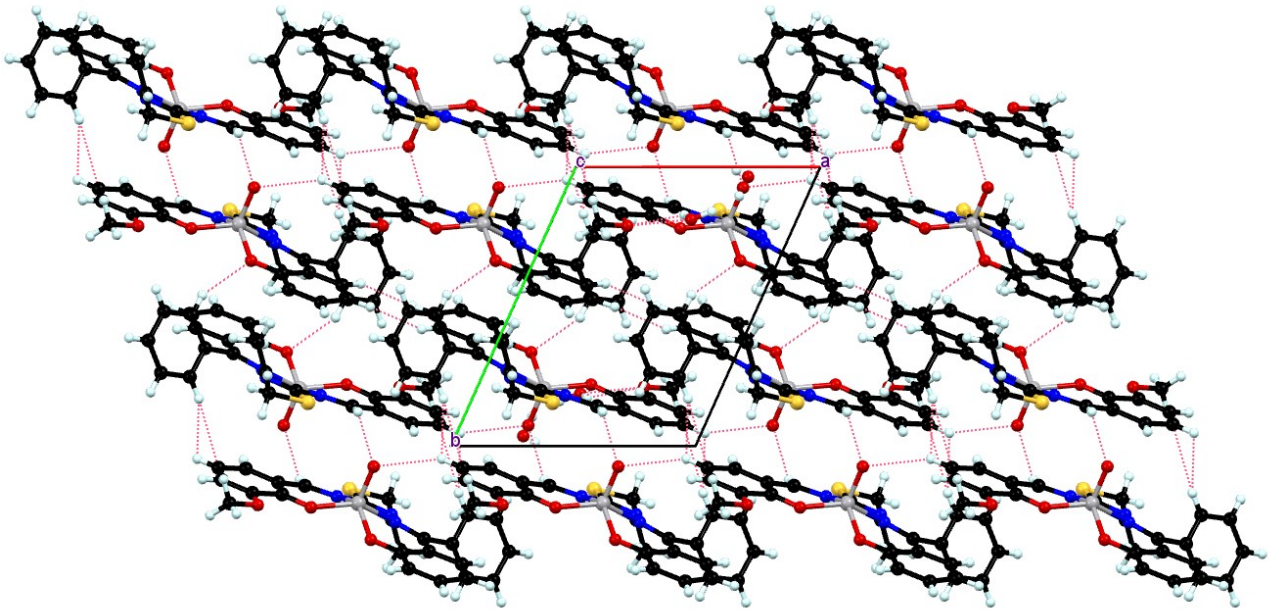

Figure 3: The CH····O hydrogen bonds forming a 2D hydrogen bond network for (**2**).

Addison tau parameter (39) gives an indication of the closeness of the structure, either to the ideal square pyramidal or to the trigonal bipyramidal geometry. Equation (1) was computed with O(2)-V(1)-N(4) as β (147.02°) and O(3)-V(1)-N(3) as α (139.47°) (Table 3) for compound (**2**) to find the Addison tau parameter. Tau parameter being equal to zero leads to the ideal square pyramidal geometry, and the result is very close to zero (τ =0.13) (41).

$$\tau = \frac{(\beta - \alpha)}{60} \qquad \text{(Eq. 2)}$$

Electrochemistry

Cyclic voltammetry was performed, for getting information about the electrochemical behavior of the compound (**2**), within -1.4 to +1.4 V versus

Ag/AgCl reference electrode in TBAP/DMSO electrolyte system (Figure 4). In DMSO, complexes containing different metal ions displayed excellent behaviors of voltammetry, with redox processes of the metal and ligand centers. To characterize all the electrode processes, peak-to-peak separation (Δ_{ep}) and the ratio of anodic to cathodic peak currents (I_{pa} / I_{pc}) were used. Table 4 lists the electrochemical parameters from the CV at 0.1 V s^{-1} scan rate.

Cyclic voltammogram of the complex (**2**) in electrochemically pure DMSO containing TBAP as electrolyte demonstrated a wave at 0.56 V (reversible) and another wave at -0.77 V (irreversible) vs. Ag/AgCl reference electrode (43). The cathodic redox couple is assignable to the $V^{IV}O$ to $V^{V}O$ oxidation process at a scan rate of 100 mVs^{-1}. ΔEp value of this redox couple was 80 mV and the i_{pa}/i_{pc} value was almost unity, which is indicative of the reversible character of this process. An irreversible redox couple (ΔE_p, 100 mV and I_{pa}/I_{pc}, 0.20) was attributable to the reduction of $V^{IV}O$ to $V^{III}O$ at -0.77 V. Although the ΔEp value of the reduction couple seemed to be a quasi-reversible redox process, the tiny I_{pa}/I_{pc} ratio (0.2) explains the irreversibility (44). There is a shoulder at -0.65 V and this value was mentioned of in a previous report (38), which is possibly indicative of an electrode/electrolyte interface adsorption process (45, 46).

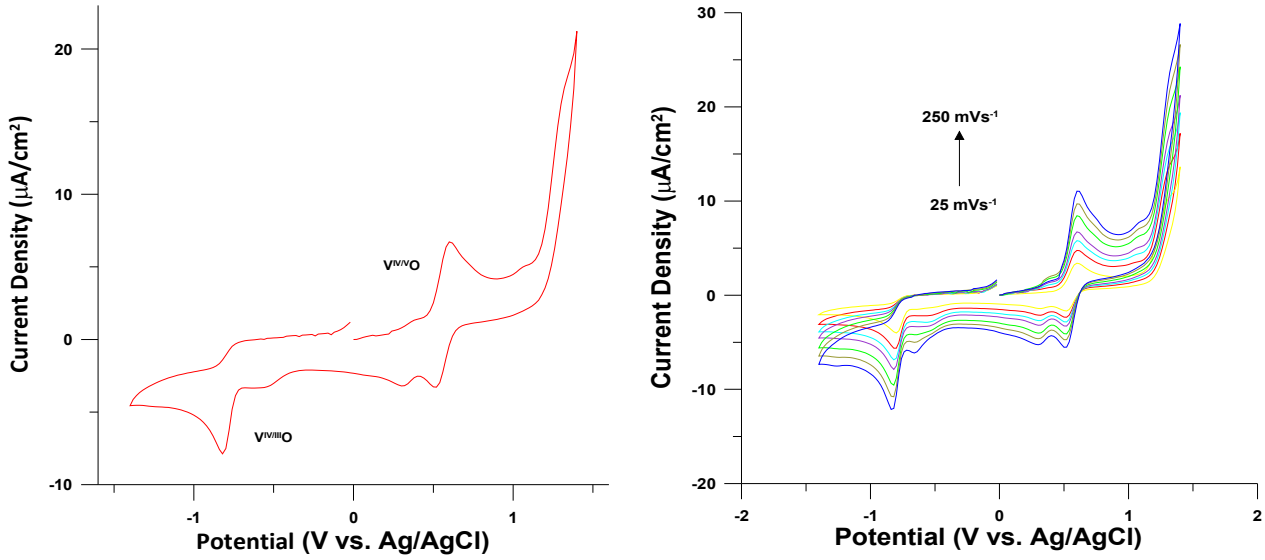

Figure 4: CV of the oxovanadium(IV) complex (**2**) in 0.1 M TBAP/DMSO solution at 0.1 Vs^{-1} scan rate (left) and other different scan rates (right).

Table 4: Electrochemical parameters of 1.0 x 10^{-3}M oxovanadium(IV) complex (**2**) in DMSO/TBAP at 0.1 Vs^{-1} scan rate.

		Peak Parameters		
Complex	**Redox Process**	**[a]$E_{1/2}$(V)**	**[b]i_{pa}/i_{pc}**	**[c]ΔE_p (mV)**
2	$V^{IV/V}O$	0.56	1.1	80
	$V^{IV/III}O$	-0.77	0.2	100

[a] $E_{1/2} = (E_{pa} + E_{pc})/2$ E_{pa} and E_{pc} are the cathodic and anodic peak potentials, respectively.
[b] i_{pa} and i_{pc} are the anodic and cathodic peak currents, respectively.
[c] ΔE_p is peak-to-peak separation ($\Delta E_p = |E_{pa} - E_{pc}|$).

Thermogravimetric data

Table 5, Figure 5, and Figure S1-S2 present the TGA and DTG results for the starting compound (**1**) and the vanadium complex (**2**) in detail. The starting compound (**1**) underwent degradation in two steps, and sulfur (S) remained intact. First, allyl group ($-CH_2-CH=CH_2$) left, then 2-OH-$(C_6H_5)_2$-C=N-N=C-NH_2 degraded.

The vanadium complex (**2**) underwent degradation in two steps, and VO + S remained intact. First, -CH_2-CH=CH_2 + O-CH_3 and coordinated water left the compound, then 2-OH-$(C_6H_5)_2$-C=N-N=C-N=C-(C_6H_5) degraded. Both structures are stable at room temperature, and they degrade at high temperatures (38, 47). Thermogravimetric analysis shows that the oxovanadium(IV) complex (**2**) is stable even in high temperatures.

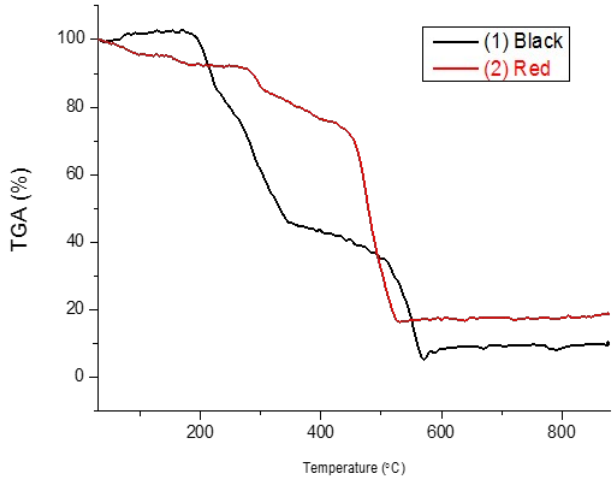

Figure 5: TGA-DTGA curves of S-allyl thiosemicarbazone (black, **1**) and oxovanadium(IV) complex (red, **2**).

Table 5: Thermogravimetric data for compound **1** and **2**.

Compound	Step	Temperature Range (°C)	DTG (°C)	Weight loss (%) Found (Calcd.)	Residue
1	1st	153-223	171	13.07(13.18)	
	2nd	460-581	553	76.74(76.84)	10.19(10.27)
2	1st	240-321	279	17.13(17.05)	
	2nd	402-531	501	64.15(64.21)	18.79(18.72)

Electronic spectra

Ultraviolet-visible spectra were obtained between 200-900 nm in a chloroform solution. At 260 nm, there was the starting material's (**1**) π-π* transition. For the oxovanadium complex, this transition was spotted at 266 nm. This is caused by the presence of the benzophenone ring system. The azomethine- and thioamide-originated n-π* transitions were observed at 306 and 340 nm, while in compound **2,** these transitions were observed at 338 and 361 nm. In addition, the vanadium complex featured a ligand-to-metal transition (LMCT) at 440 nm in the Figure 6. These transitions support the square pyramidal structure (42, 48).

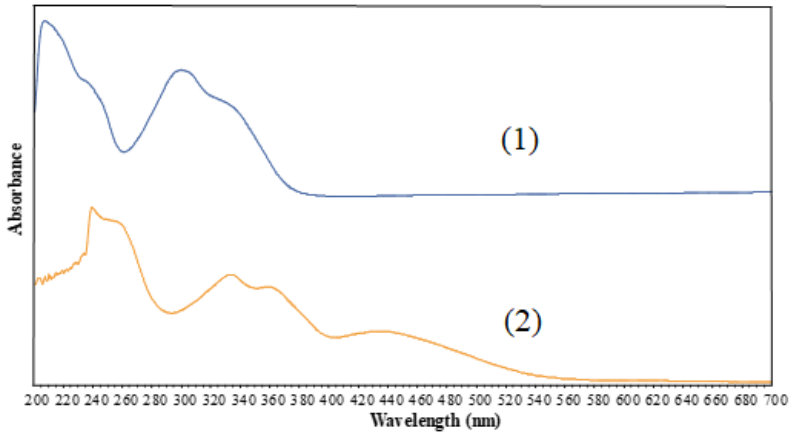

Figure 6: UV spectra of S-allyl-thiosemicarbazone (**1**), oxovanadium(IV) complex (**2**).

Infrared spectra

The v(OH) stretching vibration for compound (**1**) was observed at 3468 cm^{-1}. Asymmetric NH_2 vibration, symmetric NH_2 vibration, and NH_2 deformation peaks were seen at 3329, 3284, and 1630 cm^{-1}, respectively. Azomethine ($C=N^1$) and ($C=N^2$) vibrations were observed at 1600 and 1561 cm^{-1}, respectively. At the end of template reaction, the OH, asymmetric NH_2, and symmetric NH_2 vibrations disappeared, as expected. In addition, v(N^4=C) was observed at 1519 cm^{-1} as a new band, which confirmed the template synthesis. v(V=O) band was seen at 966 cm^{-1}. This could be used as an indicator of template complexation. Disappearance or appearance of the aforementioned peaks serve as a confirming entity of the template reaction and thus, the template complex (**2**) in the Figure 7 (14, 38). The infrared spectrum of compound (**1**) is available in the supplementary material (Fig. S3).

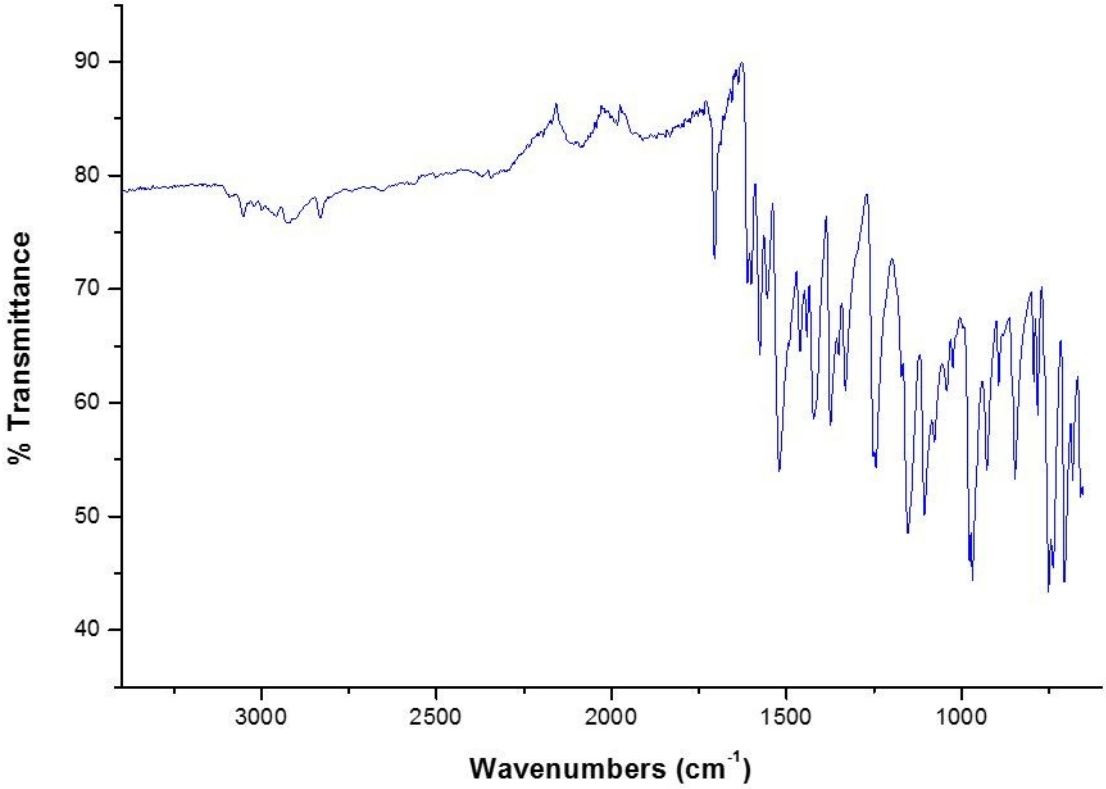

Figure 7: FT-IR spectrum of the oxovanadium(IV) complex (**2**).

Mass Spectrometry

The electron spray ionization (ESI) mass spectrum of compound **2** showed the molecular ion peak at m/z 528.47, featuring a molecular formula of $C_{25}H_{25}N_3O_5SV$. In the spectrum, the molecular ion peak relative ratio was 22.91 for 533.1 [(M-H_2O) + Na]. The (M-H_2O) peak's ratio was 9.46 and the position was at 511.1 [(2M-2H_2O) + Na] peak supported the π- π interaction in the molecule, with a relative ratio of 100% and relative m/z of 1042.8. During the recording of the mass spectrum, coordinated water molecule left the complex (38). The detailed mass spectrum is available in the supplementary material (Fig. S4).

Antioxidant efficiency

The antioxidant efficiency was referenced against trolox, which is the water-soluble analog of Vitamin E. CUPRAC method was applied in this determination, and the results were reported as µmol trolox equivalent per gram of sample. In the determination, the redox chemistry of copper(II) to copper(I) in a neocuproine complex was assayed and reported. The trolox-equivalent antioxidant capacity (TEAC) value of the oxovanadium(IV) complex ($TEAC_{CUPRAC}$ = 3.10 ± 0.01) was higher than the starting material, (**1**) ($TEAC_{CUPRAC}$ = 0.30 ± 0.01) and ascorbic acid ($TEAC_{ascorbic\ acid}$=1.00 ± 0.01). Therefore, the compound **2** could serve as a powerful antioxidant. Benzophenone thiosemicarbazone-based oxovanadium(IV) complexes have higher antioxidant activities than those containing naphthaldeyhde-based oxovanadium(IV) complexes (14, 38, 49).

CONCLUSION

2-Hydroxybenzophenone S-allylthiosemicarbazone (**1**) was reacted with vanadyl sulfate to obtain the template complex (**2**), and UV-Vis, FTIR, electrochemistry, and copper ion reducing antioxidant capacity measurements were conducted. The UV-Vis spectra showed π-π* and n-π* transitions for the ligand and LMCT peak for the complex. FTIR was useful to point to the vibrations present before complexation, and they disappeared after the formation of the template structure. Similarly, new bands were obtained after template complex formation. Thermogravimetric analysis of compounds **1** and **2** revealed that they were stable at high temperatures. Mass spectra showed that the π- π and C- π interactions were present in the complex.

Electrochemistry of the complex, supplied valuable information for the redox chemistry of vanadium-centered template; an oxidation couple from V^{IV} to V^{V} were clearly identified. A further reduction from V^{IV} to V^{III} was also recorded. Oxidation of the ligand was not observed.

Copper ion reducing antioxidant capacity experiment showed that the complex **2** is a potent antioxidant and its trolox-equivalent antioxidant capacity is at least three times more powerful than ascorbic acid. A less positive oxidation potential is a requirement for a powerful reducing agent, as shown by electrochemical measurements. Oxovanadium(IV) complex (**2**) has this requirement and it is a better reducing agent. CUPRAC results are confirmed by a high ligand-based reduction potential and complex **2** is suitable as an antioxidant agent (14).

ACKNOWLEDGEMENTS

This manuscript is dedicated to Dr. Bahri ÜLKÜSEVEN and Dr. Yasemin KURT as being my prime directors of my career.

Supplementary crystallographic data are deposited with the CCDC number of 2075485 for compound (2) ($C_{25}H_{25}N_3O_5SV$). It is free of charge to obtain the data from Cambridge Crystallographic Data Center at http://www.ccdc.cam.ac.ac.uk/conts/retrieving.html website or from the postal address of Cambridge Crystallographic Data Center, 12, Union Road, Cambridge CB2 1EZ, UK; fax: +44 1223 336 033 or from the e-mail deposit@ccdc.cam.ac.uk.

The Research Fund of Istanbul University-Cerrahpasa supported this work, with Project numbers 24195 and 34846.

REFERENCES

1. Mendes IC, Botion LM, Ferreira AVM, Castellano EE, Beraldo H. Vanadium complexes with 2-pyridineformamide thiosemicarbazones: In vitro studies of insulin-like activity. Inorganica Chimica Acta. 2009 Jan;362(2):414–20.

2. Far BS, Grivani G, Khalaji AD, Khorshidi M, Gholizadeh A. A new six coordinated oxidovanadium(IV) Schiff base complex: Synthesis, characterization, crystal structure, thermal study and antibacterial activity. Journal of Molecular Structure. 2019 Dec;1197:361–8.

3. Bhattacharjee CR, Goswami P, Sengupta M. Synthesis, electrochemical and antimicrobial studies of mono and binuclear iron(III) and oxovanadium(IV) complexes of [ONO] donor tridentate Schiff-base ligands. Journal of Coordination Chemistry. 2010 Nov 20;63(22):3969–80.

4. Akhter S, Zaman HU, Mir S, Dar AM, Shrivastava S. SYNTHESIS OF SCHIFF BASE METAL COMPLEXES: A CONCISE REVIEW. ECB. 2017 Dec 19;6(10):475.

5. Meng X-F, Liu Q-F, Liu J-L, Sun M-H, Ma J-J. Synthesis, crystal structure, and insulin-like activity of [*N′* -(2-hydroxy-3-methoxybenzylidene)-2-methoxybenzohydrazonato](1,10-phenanthroline)oxovanadium(IV) methanol solvate. Inorganic and Nano-Metal Chemistry. 2017 Nov 2;47(11):1585–9.

6. Saatchi K, Thompson KH, Patrick BO, Pink M, Yuen VG, McNeill JH, et al. Coordination Chemistry and Insulin-Enhancing Behavior of Vanadium Complexes with Maltol $C_6H_6O_3$ Structural Isomers. Inorg Chem. 2005 Apr;44(8):2689–97.

7. Storr T, Mitchell D, Buglyó P, Thompson KH, Yuen VG, McNeill JH, et al. Vanadyl−Thiazolidinedione Combination Agents for Diabetes Therapy. Bioconjugate Chem. 2003 Jan;14(1):212–21.

8. Bharathi S, Mahendiran D, Senthil Kumar R, Kalilur Rahiman A. In Vitro Antioxidant and Insulin Mimetic Activities of Heteroleptic Oxovanadium(IV) Complexes with Thiosemicarbazones and Naproxen. ChemistrySelect. 2020 Jun 8;5(21):6245–54.

9. Tunali S, Gezginci-Oktayoglu S, Bolkent S, Coskun E, Bal-Demirci T, Ulkuseven B, et al. Protective Effects of an Oxovanadium(IV) Complex with N_2O_2 Chelating Thiosemicarbazone on Small

Intestine Injury of STZ-Diabetic Rats. Biol Trace Elem Res. 2021 Apr;199(4):1515–23.

10. Kanchanadevi A, Ramesh R, Semeril D. Synthesis of Ru(II) pyridoxal thiosemicarbazone complex and its catalytic application to one-pot conversion of aldehydes to primary amides. Inorganic Chemistry Communications. 2015 Jun;56:116–9.

11. Paul P, Sengupta P, Bhattacharya S. Palladium mediated C–H bond activation of thiosemicarbazones: Catalytic application of organopalladium complexes in C–C and C–N coupling reactions. Journal of Organometallic Chemistry. 2013 Jan;724:281–8.

12. Prabhu RN, Ramesh R. Synthesis and structural characterization of palladium(II) thiosemicarbazone complex: application to the Buchwald–Hartwig amination reaction. Tetrahedron Letters. 2013 Feb;54(9):1120–4.

13. Quiroga-Campano C, Gómez-Machuca H, Moris S, Pessoa-Mahana H, Jullian C, Saitz C. Synthesis of calix[4]arenes bearing thiosemicarbazone moieties with naphthalene groups: Highly selective turn off/on fluorescent sensor for Cu(II) recognition. Journal of Molecular Structure. 2021 Feb;1225:129125.

14. İlhan Ceylan B, Yilmaz A, Bölükbaşı O, Acar ET, Özyürek M, Kurt Y, et al. A square-pyramidal iron(III) complex obtained from 2-hydroxy-benzophenone- *S* -allyl-thiosemicarbazone: synthesis, characterization, electrochemistry, quantum chemical studies and antioxidant capability. Journal of Coordination Chemistry. 2020 Jan 2;73(1):120–36.

15. Poladian Q, Şahin O, Karakurt T, İlhan-Ceylan B, Kurt Y. A new zinc(II) complex with N2O2-tetradentate schiff-base derived from pyridoxal-S-methylthiosemicarbazone: Synthesis, characterization, crystal structure, DFT, molecular docking and antioxidant activity studies. Polyhedron. 2021 Jun;201:115164.

16. Jia X, Liu Q, Wang S, Zeng B, Du G, Zhang C, et al. Synthesis, cytotoxicity, and in vivo antitumor activity study of parthenolide semicarbazones and thiosemicarbazones. Bioorganic & Medicinal Chemistry. 2020 Jul;28(13):115557.

17. Aly MM, Mohamed YA, El-Bayouki KAM, Basyouni WM, Abbas SY. Synthesis of some new 4(3H)-quinazolinone-2-carboxaldehyde thiosemicarbazones and their metal complexes and a study on their anticonvulsant, analgesic, cytotoxic and antimicrobial activities – Part-1. European Journal of Medicinal Chemistry. 2010 Aug;45(8):3365–73.

18. Yanardag R, Demirci TB, Ülküseven B, Bolkent S, Tunali S, Bolkent S. Synthesis, characterization and antidiabetic properties of N1-2,4-dihydroxybenzylidene-N4-2-hydroxybenzylidene-S-methyl-thiosemicarbazidato-oxovanadium(IV). European Journal of Medicinal Chemistry. 2009 Feb;44(2):818–26.

19. Biot C, Castro W, Botté CY, Navarro M. The therapeutic potential of metal-based antimalarial agents: Implications for the mechanism of action. Dalton Trans. 2012;41(21):6335.

20. Genova P, Varadinova T, Matesanz AI, Marinova D, Souza P. Toxic effects of bis(thiosemicarbazone) compounds and its palladium(II) complexes on herpes simplex virus growth. Toxicology and Applied Pharmacology. 2004 Jun;197(2):107–12.

21. Fonteh PN, Keter FK, Meyer D. New bis(thiosemicarbazonate) gold(III) complexes inhibit HIV replication at cytostatic concentrations: Potential for incorporation into virostatic cocktails. Journal of Inorganic Biochemistry. 2011 Sep;105(9):1173–80.

22. Yildirim H, Guler E, Yavuz M, Ozturk N, Kose Yaman P, Subasi E, et al. Ruthenium (II) complexes of thiosemicarbazone: Synthesis, biosensor applications and evaluation as antimicrobial agents. Materials Science and Engineering: C. 2014 Nov;44:1–8.

23. de Araújo Neto LN, de Lima M do CA, de Oliveira JF, de Souza ER, Feitosa Machado SE, de Souza Lima GM, et al. Thiophene-thiosemicarbazone derivative (L10) exerts antifungal activity mediated by oxidative stress and apoptosis in C. albicans. Chemico-Biological Interactions. 2020 Apr;320:109028.

24. de Araújo Neto LN, do Carmo Alves de Lima M, de Oliveira JF, de Souza ER, Buonafina MDS, Vitor Anjos MN, et al. Synthesis, cytotoxicity and antifungal activity of 5-nitro-thiophene-thiosemicarbazones derivatives. Chemico-Biological Interactions. 2017 Jun;272:172–81.

25. Li J-Q, Sun L-Y, Jiang Z, Chen C, Gao H, Chigan J-Z, et al. Diaryl-substituted thiosemicarbazone: A potent scaffold for the development of New Delhi metallo-β-lactamase-1 inhibitors. Bioorganic Chemistry. 2021 Feb;107:104576.

26. Bisceglie F, Bacci C, Vismarra A, Barilli E, Pioli M, Orsoni N, et al. Antibacterial activity of metal complexes based on cinnamaldehyde thiosemicarbazone analogues. Journal of Inorganic Biochemistry. 2020 Feb;203:110888.

27. Singh NK, Kumbhar AA, Pokharel YR, Yadav PN. Anticancer potency of copper(II) complexes of thiosemicarbazones. Journal of Inorganic Biochemistry. 2020 Sep;210:111134.

28. Subasi E, Atalay EB, Erdogan D, Sen B, Pakyapan B, Kayali HA. Synthesis and characterization of thiosemicarbazone-functionalized organoruthenium (II)-arene complexes: Investigation of antitumor characteristics in colorectal cancer cell lines. Materials Science and Engineering: C. 2020 Jan;106:110152.

29. de Oliveira JF, da Silva AL, Vendramini-Costa DB, da Cruz Amorim CA, Campos JF, Ribeiro AG, et al. Synthesis of thiophene-thiosemicarbazone derivatives and evaluation of their in vitro and in vivo antitumor activities. European Journal of Medicinal Chemistry. 2015 Nov;104:148–56.

30. Anonymous. Bruker, APEX2 & SAINT. AXS Inc., Madison, WI; 2004.

31. Sheldrick G. Program for Crystal Structure Refinement. University of Göttingen, Germany; 2014.

32. Sheldrick GM. *SHELXT* – Integrated space-group and crystal-structure determination. Acta Crystallogr A Found Adv. 2015 Jan 1;71(1):3–8.

33. Yamazaki C. The Structure of Isothiosemicarbazones. Can J Chem. 1975 Feb 15;53(4):610–5.

34. Apak R, Güçlü K, Özyürek M, Karademir SE. Novel Total Antioxidant Capacity Index for Dietary Polyphenols and Vitamins C and E, Using Their Cupric Ion Reducing Capability in the Presence of Neocuproine: CUPRAC Method. J Agric Food Chem. 2004 Dec;52(26):7970–81.

35. Dekar S, Ouari K, Bendia S, Hannachi D, Weiss J. Mononuclear oxovanadium(IV) Schiff base complex: Synthesis, spectroscopy, electrochemistry, DFT calculation and catalytic activity. Journal of Organometallic Chemistry. 2018 Jul;866:165–76.

36. Jeyaraman P, Alagarraj A, Natarajan R. *In silico* and *in vitro* studies of transition metal complexes derived from curcumin–isoniazid Schiff base. Journal of Biomolecular Structure and Dynamics. 2020 Jan 22;38(2):488–99.

37. Abu-Dief AM, Nassr LAE. Tailoring, physicochemical characterization, antibacterial and DNA binding mode studies of Cu(II) Schiff bases amino acid bioactive agents incorporating 5-bromo-2-hydroxybenzaldehyde. J IRAN CHEM SOC. 2015 Jun;12(6):943–55.

38. İlhan-Ceylan B. Oxovanadium(IV) and Nickel(II) complexes obtained from 2,2′-dihydroxybenzophenone-S-methyl-thiosemicarbazone: Synthesis, characterization, electrochemistry, and antioxidant capability. Inorganica Chimica Acta. 2021 Mar;517:120186.

39. Ilhan Ceylan B. Oxovanadıum(IV)-containing N_2O_2 chelate complex; crystal structure determination and DFT. J Turk Chem Soc, Sect A: Chem [Internet]. 2016 Sep 30 [cited 2021 Apr 7];3(3). Available from: http://dergipark.gov.tr/doi/10.18596/jotcsa.33245

40. Ze-hua L, Chun-ying D, Ji-hui L, Yong-jiang L, Yu-hua M, Xiao-zeng Y. Structural dependence of π–π interactions in dithiocarbazato and thiosemicarbazato nickel complexes. New J Chem. 2000;24(12):1057–62.

41. Addison AW, Rao TN, Reedijk J, van Rijn J, Verschoor GC. Synthesis, structure, and spectroscopic properties of copper(II) compounds containing nitrogen–sulphur donor ligands; the crystal and molecular structure of aqua[1,7-bis(N-methylbenzimidazol-2′-yl)-2,6-dithiaheptane]copper(II) perchlorate. J Chem Soc, Dalton Trans. 1984;(7):1349–56.

42. Menati S, Rudbari HA, Khorshidifard M, Jalilian F. A new oxovanadium(IV) complex containing an O,N-bidentate Schiff base ligand: Synthesis at ambient temperature, characterization, crystal structure and catalytic performance in selective oxidation of sulfides to sulfones using H_2O_2 under solvent-free conditions. Journal of Molecular Structure. 2016 Jan;1103:94–102.

43. Dekar S, Ouari K, Bendia S, Hannachi D, Weiss J. Mononuclear oxovanadium(IV) Schiff base complex: Synthesis, spectroscopy, electrochemistry, DFT calculation and catalytic activity. Journal of Organometallic Chemistry. 2018 Jul;866:165–76.

44. Kurt Y, İlhan-Ceylan B, Açıkgöz M, Tüzün E, Atun G, Ülküseven B. N_2O_2-complexes of oxovanadium(IV) with 2,2′-dihydroxybenzophenone thiosemicarbazones: Synthesis, EPR and electrochemical studies. Polyhedron. 2013 Nov;65:67–72.

45. Kurt Y, Koca A, Akkurt M, Ülküseven B. Iron(III) and nickel(II) complexes of O,N,N,O-chelating benzophenone thiosemicarbazone: Electrochemistry and in situ spectroelectrochemistry. Inorganica Chimica Acta. 2012 Jun;388:148–56.

46. Aranha PE, Souza JM, Romera S, Ramos LA, dos Santos MP, Dockal ER, et al. Thermal behavior of vanadyl complexes with Schiff bases derived from trans-N,N′-bis(salicylidene)-1,2-cyclohexadiamine (t-Salcn). Thermochimica Acta. 2007 Jan;453(1):9–13.

47. Asadi M, Asadi Z, Savaripoor N, Dusek M, Eigner V, Shorkaei MR, et al. Structural investigation of oxovanadium(IV) Schiff base complexes: X-ray crystallography, electrochemistry and kinetic of thermal decomposition. Spectrochimica Acta Part A: Molecular and Biomolecular Spectroscopy. 2015 Feb;136:625–34.

48. Maurya MR, Kumar A, Abid M, Azam A. Dioxovanadium(V) and μ-oxo bis[oxovanadium(V)] complexes containing thiosemicarbazone based ONS donor set and their antiamoebic activity. Inorganica Chimica Acta. 2006 May;359(8):2439–47.

49. Ilhan-Ceylan B, Tuzun E, Kurt Y, Acikgoz M, Kahraman S, Atun G, Ulkuseven B, "Oxovanadium(IV) complexes based on S-alkyl-thiosemicarbazidato ligands. Synthesis, characterization, electrochemical, and antioxidant studies", Journal of Sulfur Chemistry. 2015; 36: 434–449.

Oxovanadium(IV) template derived from benzophenone S-allyl thiosemicarbazone: Synthesis, crystal structure, antioxidant activity and electrochemistry

Berat İlhan-Ceylan

Istanbul University-Cerrahpasa, Engineering Faculty, Department of Chemistry, Inorganic Chemistry Division, 34320, Avcılar, Istanbul, Turkey

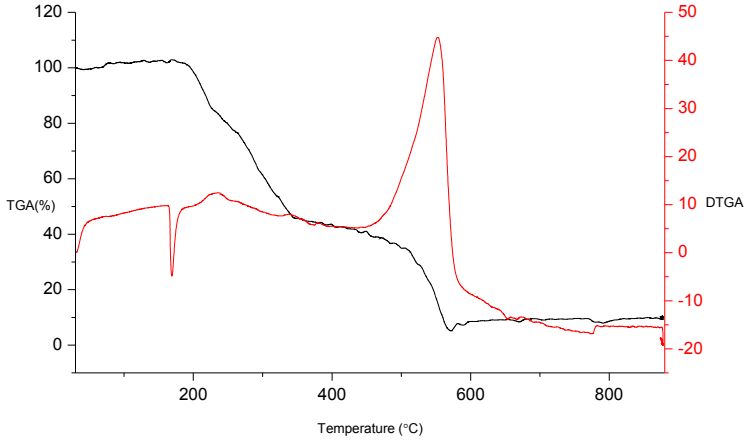

Figure S1: TGA-DTGA curves of S-allyl-thiosemicarbazone (**1**).

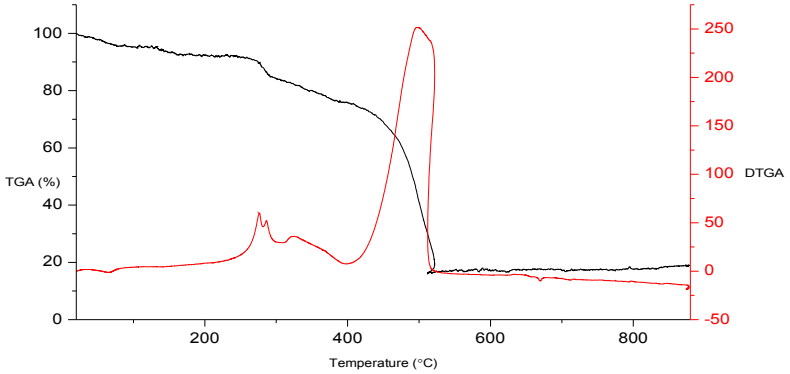

Figure S2: TGA-DTGA curves of oxovanadium(IV) complex (**2**).

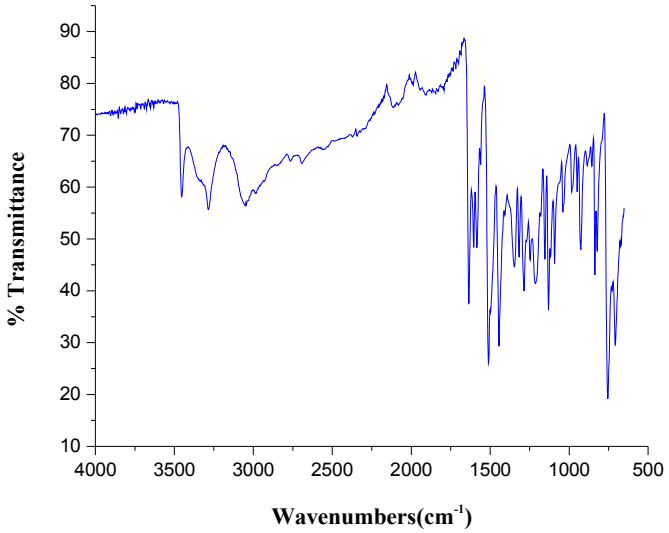

Figure S3: FT-IR spectra of S-allyl-thiosemicarbazone (**1**).

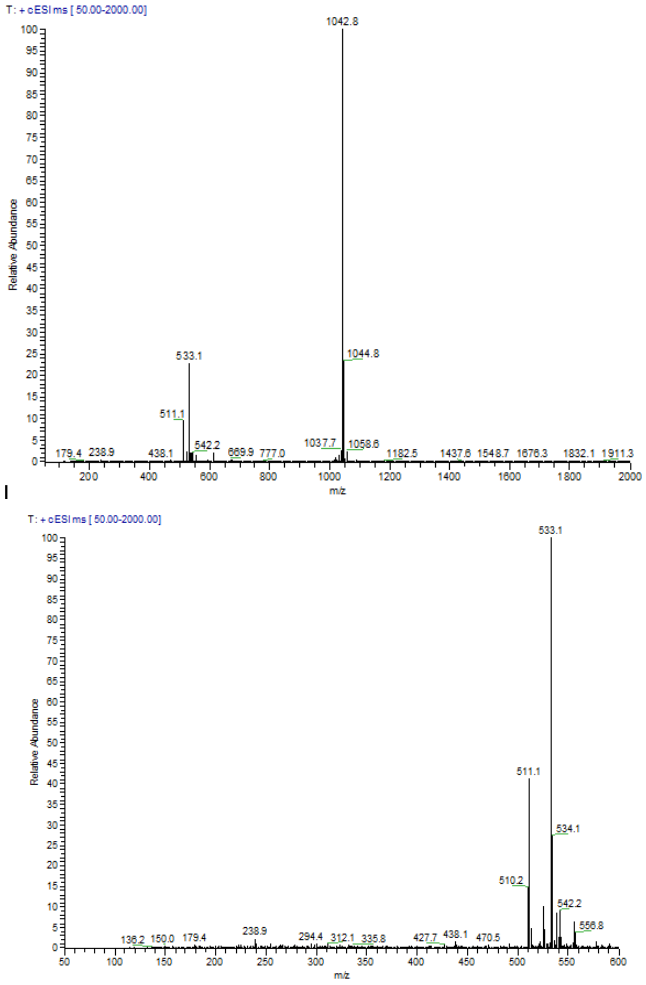

Figure S4: Mass spectra of the oxovanadium(IV) complex (**2**).

Table S1: Anisotropic displacement parameters ($Å^2$x 10^3) for the oxovanadium (IV) complex. The anisotropic displacement factor exponent takes the form: $-2\pi^2[h^2 a^{*2}U^{11} + ... + 2 h k a^* b^* U^{12}]$

	U^{11}	U^{22}	U^{33}	U^{23}	U^{13}	U^{12}
V(1)	32(1)	51(1)	47(1)	18(1)	2(1)	13(1)
S(1)	56(1)	88(1)	53(1)	35(1)	10(1)	20(1)
O(1)	45(2)	94(3)	59(3)	35(2)	1(2)	21(2)
O(2)	36(2)	70(2)	50(2)	28(2)	7(2)	17(2)
O(3)	38(2)	61(2)	64(3)	32(2)	6(2)	15(2)
O(4)	45(2)	55(2)	60(2)	12(2)	6(2)	17(2)
N(2)	36(2)	54(3)	49(3)	18(2)	3(2)	11(2)
N(3)	39(2)	44(2)	46(3)	17(2)	-2(2)	11(2)
N(4)	35(2)	48(3)	46(3)	16(2)	5(2)	9(2)
C(1)	34(3)	44(3)	54(3)	10(3)	3(2)	11(2)
C(2)	37(3)	53(3)	54(3)	18(3)	7(2)	17(2)
C(3)	36(3)	60(3)	66(4)	24(3)	0(3)	15(3)
C(4)	36(3)	60(4)	85(5)	30(3)	15(3)	18(3)
C(5)	45(3)	58(3)	66(4)	31(3)	17(3)	21(3)
C(6)	42(3)	48(3)	55(3)	17(3)	13(3)	19(2)
C(7)	59(4)	116(6)	68(4)	41(4)	-10(3)	27(4)
C(8)	45(3)	48(3)	46(3)	21(2)	10(2)	15(2)
C(9)	44(3)	45(3)	48(3)	12(2)	3(2)	14(2)
C(10)	35(3)	40(3)	51(3)	12(2)	5(2)	10(2)
C(11)	35(3)	52(3)	47(3)	9(3)	0(2)	10(2)
C(12)	36(3)	98(5)	53(4)	24(3)	2(3)	18(3)
C(13)	38(3)	113(6)	62(4)	24(4)	12(3)	6(3)
C(14)	50(3)	74(4)	62(4)	26(3)	15(3)	11(3)
C(15)	45(3)	57(3)	55(4)	22(3)	6(3)	15(3)
C(16)	37(3)	38(3)	51(3)	9(2)	2(2)	12(2)
C(17)	38(3)	50(3)	45(3)	14(2)	3(2)	16(2)
C(18)	41(3)	54(3)	53(3)	17(3)	2(3)	8(3)
C(19)	51(3)	72(4)	53(4)	12(3)	-2(3)	7(3)
C(20)	53(4)	101(5)	55(4)	29(4)	-2(3)	34(4)
C(21)	67(4)	83(5)	69(4)	34(4)	10(3)	42(4)
C(22)	51(3)	56(3)	63(4)	22(3)	8(3)	19(3)
C(23)	81(5)	109(6)	58(4)	40(4)	8(4)	33(4)
C(24)	1900(80)	2030(80)	430(40)	-400(70)	-400(70)	1960(80)
C(25)	880(60)	360(20)	80(9)	79(13)	-21(19)	410(30)
O(5)	163(12)	169(12)	124(10)	55(8)	55(9)	78(9)
O(5A)	111(11)	147(12)	83(9)	8(8)	33(8)	81(10)

Table S2: Hydrogen coordinates (x 10^4) and isotropic displacement parameters ($Å^2$x 10^3) for the oxovanadium (IV) complex.

	x	y	z	U(eq)		x	y	z	U(eq)
H(3)	440	1192	1980	67	H(20)	15143	3873	9072	84
H(4)	-141	464	3541	72	H(21)	13267	1921	8056	83
H(5)	1778	510	5002	65	H(22)	11175	1691	6579	70
H(7A)	2474	2435	94	129	H(23A)	8286	1110	8894	100
H(7B)	1418	2489	931	129	H(23B)	9212	2079	8319	100
H(7C)	1314	1198	250	129	H(24)	8786	2524	10334	1584
H(8)	4430	1220	5983	57	H(25A)	9519	3652	8618	626
H(12)	13339	4184	5204	79	H(25B)	10880	3869	9693	626
H(13)	14149	5014	3779	95	H(25C)	9621	4383	9869	626
H(14)	12397	5241	2341	78	H(5A)	5313	1723	1094	217
H(15)	9812	4453	2242	65	H(5B)	6371	1605	488	217
H(18)	12929	5400	7095	65	H(5AA)	6626	121	1356	162
H(19)	14924	5609	8654	81	H(5BB)	7215	1048	872	162

JOTCS A
Journal of the Turkish Chemical Society
Section: A
Chemistry
TURKISH CHEMICAL SOCIETY

Synthesis and Characterization of the Molecularly Imprinted Composite as a Novel Adsorbent and its Competition with Non-Imprinting Composite for Removal of Dye

Ayfer Yildirim[a]*, Hilal Acay[b], Ayse Baran[c]

[a*]*Mardin Artuklu University, Vocational School of Health Services, 47200 Mardin/Turkey*
[b]*Department of Nutrition and Dietetics, School of Health, Mardin/Turkey*
[c]*Mardin Metropolitan Municipality, Artuklu, Mardin/Turkey*

Abstract: Due to its high visibility, high resistance, and toxic effects, colored substances in the textile and other dyeing industries waste-water cause great damage to biological organisms and ecology. Therefore, current research efforts to develop high selectivity, specificity, and efficient water treatment technologies are very intense, and molecularly imprinting methods (MIM) constitute a category of functional materials to meet these criteria. Polymethylmethacrylate-chitosan molecularly imprinted composite (PMMAC-MIC) and non-imprinted composite (PMMAC-NIC) were successfully prepared by MIM. Dye adsorption performance of MIC and NIC composites was investigated by comparison. The obtained adsorbents were characterized by Fourier transform infrared spectroscopy (FTIR), X-ray diffraction (XRD), field-emission scanning electron microscopy (FE-SEM), differential scanning calorimetry (DSC), thermogravimetric analysis (TGA), and zeta potential techniques. The kinetics of adsorption followed a pseudo-first-order model while the Langmuir adsorption isotherm provided the best fit. The maximum adsorption capacity of dye was found as 93.78 mg/g for PMMAC-MIC and 17.70 mg/g for PMMAC-NIC at 298 K temperature, the initial dye concentration was 100 mg/L. Thermodynamic parameters indicated that the removal of dye from PMMAC-MIC was endothermic and spontaneous. Besides, the regeneration of composite was recycled four times.

Keywords: Molecular imprinting, adsorption, composite, regeneration, selectivity.

Submitted: January 25, 2021. **Accepted:** April 30, 2021.

Cite this: Yildirim A, Acay H, Baran A. Synthesis and Characterization of the Molecularly Imprinted Composite as a Novel Adsorbent and its Competition with Non-Imprinting Composite for Removal of Dye. JOTCSA. 2021;8(2):609–22.

DOI: https://doi.org/10.18596/jotcsa.868054.

***Corresponding author. E-mail:** ayferyildirim@artuklu.edu.tr.

INTRODUCTION

With the development of industrialization, the use of dyes, which endangers the living organisms, in textile and other dyeing sectors e.g. plastic, paper, foods, pulp, color photographs, cosmetics has been increasing in recent years. As a result of textile wastes being released, the waters are rapidly exposed to pollution day by day (1). Also, dyes are the most dangerous pollutants in wastewater because of their permanence and high hazardous properties. Malachite green (MG) is an important cationic textile dye that is widely used because of its strong effect on antimicrobial, antifungal, antiparasitic, and antibacterial effects. However, due to its acute and persistent toxicity, this dyestuff exposes aquatic and territorial organisms to mutagenic, teratogenic, and carcinogenic effects (2). At this point, drinking water industries focus their efforts on the development of new technologies to remove various persistent pollutants from water sources. Many physical and physicochemical methods such as coagulation/flocculation, chemical oxidation,

ozonation, ultra-filtration, membrane, and photo-separation processes have been developed for the removal of dyes from aqueous solution (3). However, adsorption is a highly effective and low-cost preferred technique for removing dyestuff from contaminated water. A recent study focuses on both efficient composites and recognized methods (4).

The molecular imprinting method (MIM) for dyes is mainly used as adsorbents for solid-phase extraction due to their high selectivity in complex samples. MIM ensures cost-effective and easy-handling for the selective removal of certain water pollutants. Owing to these pressure holes, the target pollutant molecules are adsorbed very easily since they are defined according to the structure of the template molecule (5). Recently, the imprinting method has been of great interest in the development of chromatographic adsorbents, sensors, membranes, enzymes, and receptor mimetics.

Chitosan is one of the most abundant biological substances (natural polysaccharides) in nature. It has great biological and chemical properties as non-toxicity, low-cost, intelligent, biocompatible, biodegradable, and hydroxyl and amine functional groups on its structure. All these important features make chitosan a very interesting ingredient that can be preferred in removing dyes from the aqueous wastewater system (6,7). A lot of dye-imprinted chitosan have shown great promise for preparing materials and recognition of target dyes in the past regarding the economic feasibility and environmental importance of it. Because of the easy dissolution in acidic media (pH<6.0), weak mechanical strength, and low surface area of chitosan, innovative physical and chemical modifications like crosslinked or composite formation can be developed to overcome these limitations. Thus, higher adsorption capacity and better mechanical properties can be achieved by different composite material formations. The preference of polymethylmethacrylate (PMMA) in this study is that it can easily interact with chitosan by forming hydrogen bonds, and it is a common polymer that has high mechanical strength and good acid fastness that will increase the strength and stability of the composite.

There are many studies reported in the literature about the MIM method for the adsorption of dyes with composites based on chitosan. For example, Deng et al., (8) prepared the Lewis acid-functionalized-crosslinked chitosan as a sorbent for active brilliant red (X-3B) dye. Crosslinked-chitosan and β-cyclodextrin were used as an adsorbent for Remazol Red (9). Epichlorohydrin and glutaraldehyde magnetic chitosan were prepared for the adsorption of chalcone dye (10). Chitosan-TiO_2 nanocomposite was prepared for the selective and quantitative removal of Rose Bengal dye (11). The adsorption performance of Acid Blue 113 was investigated by cross-linked polyacrylamide grafted /chitosan hydrogels (12). In another previous study, zeolitic imidazolate framework /chitosan/polyvinyl alcohol composite membrane adsorbents were performed for the removal of malachite green dye (13). Lulu et al. have prepared a chitosan/magnetite and used alizarin red as template dye (14).

The main purpose of this study is to synthesize the polymethylmethacrylate-chitosan composite to join the selectivity advantages of MIM and investigate the removal of malachite green (MG) dye using the molecular imprinting method with a comparison with the non-imprinting method. In the adsorption studies, kinetic studies were carried out by using pseudo-first and pseudo-second kinetic models with the effects of initial dye concentration, pH, and temperature. Besides, thermodynamic parameters were predicted by using Langmuir and Freundlich isotherms. The regeneration feature was made to provide an economic contribution to the study. Also, the selectivity experiment for PMMAC-MIC-MG was analyzed with methylene blue (MB) as a cationic dye and reactive orange 25 (RO16), acid blue 25 (AB25) as anionic dyes.

MATERIALS AND METHODS

Materials and Chemicals

The methylmethacrylate (MMA, Mw:100.12 g/mol), ethylene glycol dimethacrylate (EGDMA, M_w: 198.22 g/mol), ammonium persulfate (APS, Mw: 228 g/mol), malachite green oxalate (MG, $C_{52}H_{54}N_4O_{12}$, M_w: 927 g/mol) and chitosan (C, medium molecular weight) were supplied by Sigma-Aldrich.

Synthesis of PMMAC-MIC and PMMAC-NIC Composites

In the initial process of preparing the PMMAC-MIC, briefly, 200 mg of chitosan was dissolved by 1%, 30 mL acetic acid in a flask for 2 hours. Then, 49.35 mg of MG, 0.42 mL of MMA was dissolved in 10 mL of ethanol and 0.4 mL of EGDMA was added. After the substances were dissolved in ethanol completely, then it was poured into chitosan solution. Later, 148 mg APS was transferred into the mixture and then stirred for 4 h at 80 ^oC. The obtained solution was added dropwise into 0.1 M HCl and filtered to remove the MG ions. Finally, the unreacted materials were removed by washing the composite with distilled water and ethanol, and the resulting composite particles were dried at about 90-100 ^oC. The nonimprinted composite (PMMAC-NIC) was prepared in the same way, but without the addition of MG during preparation.

Characterization of Composites

To examine the characterization of composite, FTIR analysis of PMMAC-MIC and PMMAC-NIC, Perkin-Elmer Spectrum 100 model ATR-FTIR apparatus

(wavenumber range: 4000-400 cm^{-1}) was used. XRD patterns of the composites were examined by Rigaku Ultima-IV model device. FE-SEM was used for the investigation of the morphological structure of composites with the model Quanta 400F apparatus. Thermal behavior of composites was employed by DSC measurements on a DSC250 TA instrument with 10 °C min^{-1} heating rate under a nitrogen atmosphere and TGA on SDT650 model with the analyzes performing in the range from 25 to 950 °C, the heating rate of 10 °C 1/min, nitrogen atmosphere with a flow rate of 100 mL/min. The Zeta potential was analyzed by a Zetasizer (Malvern Nano ZS90 Zetasizer).

Adsorption Experiments

The adsorption ability of PMMAC-MIC and PMMAC-NIC was investigated by batch adsorption technique. The contact time, effect of pH and temperature, kinetics and isotherms of adsorption were studied. For the preparation of the stock dye solution, 100 mg of MG dye was dissolved in 1 L of distilled water. To make batch experiments, 10 mg of composites were shaken with a 20 mL dye solution with a shaking speed of 120 rpm (GFL 1083) and pH (5) at 298 K for 300 min. The concentration of dye solution was examined by PG T80+ model UV–Vis spectrophotometer at 617 nm. The adsorption capacity and percent adsorption were calculated with the below equations (Eq. 1,2), respectively (15).

$$q=(Co-Ce)*\frac{V}{m} \quad \text{(Eq. 1)}$$

$$\%\ adsorption=\frac{Co-Ce}{Co}*100 \quad \text{(Eq. 2)}$$

Where q (mg/g) presents the adsorption capacity, C_o and C_e (mg/L) are the initial and equilibrium concentrations of MG, V (L) refers to the volume of the solution, and m (mg) is the amount of the composites. Experimental studies were made in 2 repetitions and error bars were shown in the figures.

Regeneration Studies

Some of the conditions for the composite regeneration mentioned in the literature (16) were carried out with a little modification as follows: 20 mL, 100 mg/L MG dye solution was contacted with 10 mg of PMMAC-MIC composite for 180 min at 298 K and pH 8. The composite particles were filtered and the amount of adsorbed dye was analyzed by a UV-spectrophotometer (617 nm). The charged adsorbent was completely washed with distilled water, filtered, and transferred to a flask involving the 0.1 M HCl desorbing agent and shaken for 180 min at 298 K. This study was repeated four times. The amount of desorbed MG dye was calculated by the following equation (Eq. 3):

$$Dye\ ads.\% = \frac{\text{amt. desorbed from ads}}{amt\ desorbed\ onto\ ads} \times 100 \quad \text{(Eq. 3)}$$

Selectivity Experiments

To investigate the selectivity of the MG dye, a cationic dye MB and two anionic dyes RO16, AB25 were used (structures are shown in Figure 1). Besides, the percentages of binding of these dyes were investigated by comparison with the MG dye and plotted graphically. For the experimental studies, 20 mL of the initial concentration of 50 mg/L of each dyestuff was prepared and poured into a 100 mL flask, 10 mg of adsorbent was then added to each flask and shaken at 120 rpm in the shaking water bath for 180 minutes. The final supernatants of MB, RO16, AB25 dyes were performed by a UV-Vis spectrophotometer at the maximum absorption wavelengths at 664 nm, 505 nm, 610 nm, respectively.

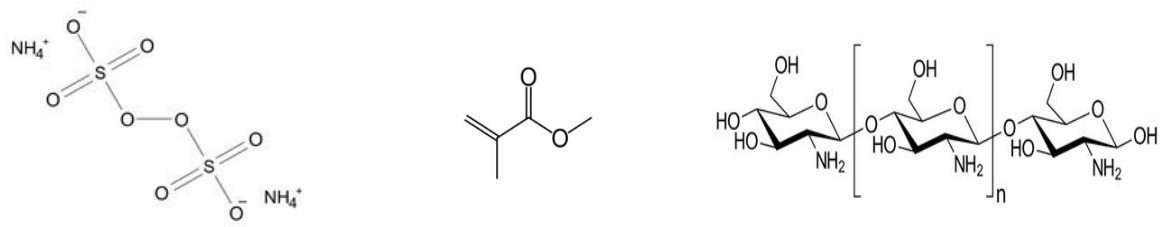

(a) (b) (c)

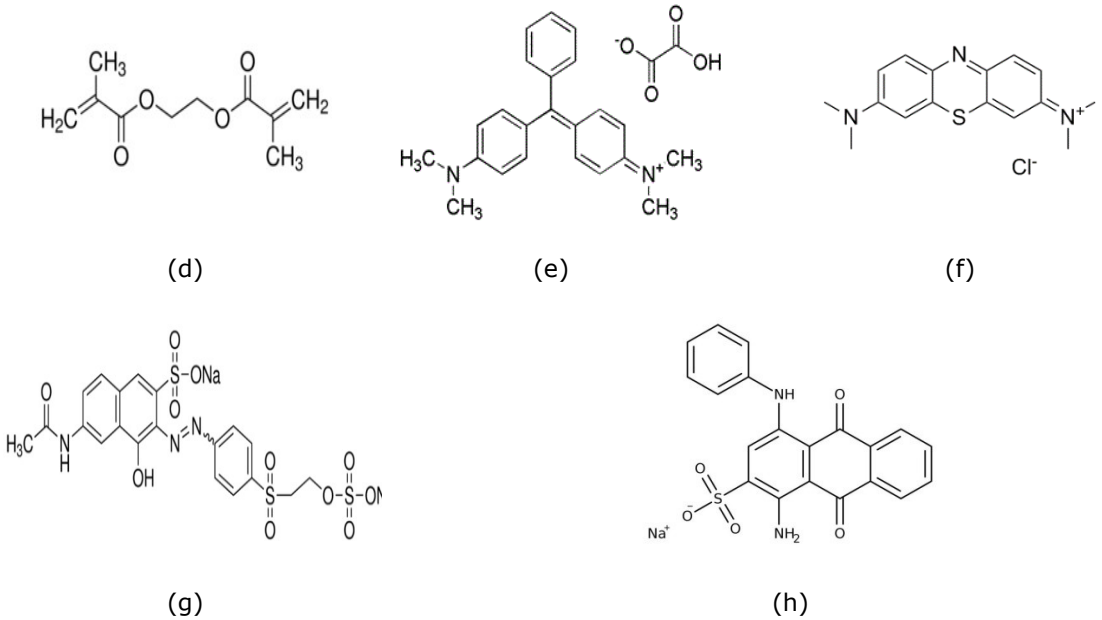

Figure 1: Chemical structures of (a) ammonium persulfate (APS), (b) methyl methacrylate (MMA), (c) chitosan, (d) ethylene glycol dimethacrylate (EGDMA), (e) malachite green (MG), (f) methylene blue (MB), (g) reactive orange 25 (RO16), (h) acid blue 25 (AB25).

RESULTS AND DISCUSSION

Characterization

FTIR analysis

FTIR spectra of PMMAC-MIC, PMMAC-NIC composites are illustrated in Figure 2a. As can be seen from Figure 2a, there are peaks at 2988, 2951, 2988, and 2952 cm^{-1} in the PMMAC-NIC and PMMAC-MIC spectrum corresponding to the stretching vibration peak of the saturated C–H stretching vibration, respectively (17-20). The peak in the PMMAC-NIC spectrum at 1724 cm^{-1} and in the PMMAC-MIC spectrum at 1722 cm^{-1} demonstrated the carbonyl group of the ester group of PMMA.

It is probable that there is no peak related to the characteristic bands of the MG dye (template) in the PMMAC-MIC spectra as the peak belongs to the aromatic ring at 1560-1580 cm^{-1} which demonstrate the purification of MIC composite from MG template dye molucules (Figure 2a) (21). The peaks observed at 1449, 1451, and 1387 cm^{-1} are bending vibrations of CH_2 and CH_3 also, the peak at 1144, 1142; 750, 752; 962, and 953 cm^{-1} correspond to the vibration of CO; CH_2; CC stretching in the spectra of PMMAC-NIC and PMMAC-MIC, respectively (22). As a result, it can be demonstrated that differences between peaks in the PMMAC-NIC and PMMAC-MIC FTIR spectra may also be based on the spaces between the functional groups caused by the removal of MG dye molecules from the structure by the imprinting method.

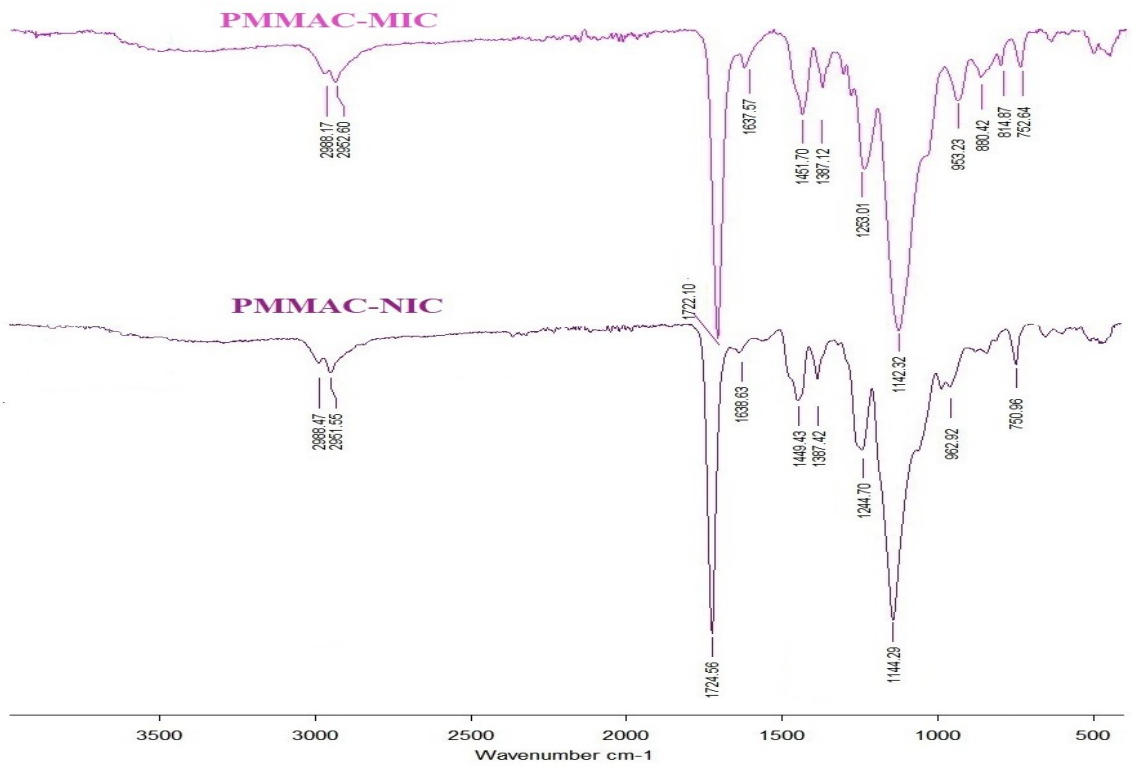
PMMAC-MIC
2988.17
2952.60
1637.57
1451.70
1387.12
1263.01
953.23
880.42
814.87
752.64
PMMAC-NIC
1722.10
2988.47
2951.55
1638.63
1449.43
1387.42
1244.70
1142.32
962.92
750.96
1724.56
1144.29
3500
3000
2500
2000
1500
1000
500
Wavenumber cm-1

(a)

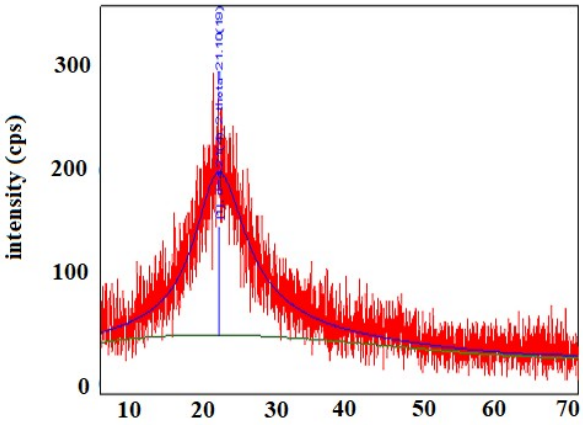
intensity (cps)
300
200
100
0
10
20
30
40
50
60
70

(b)

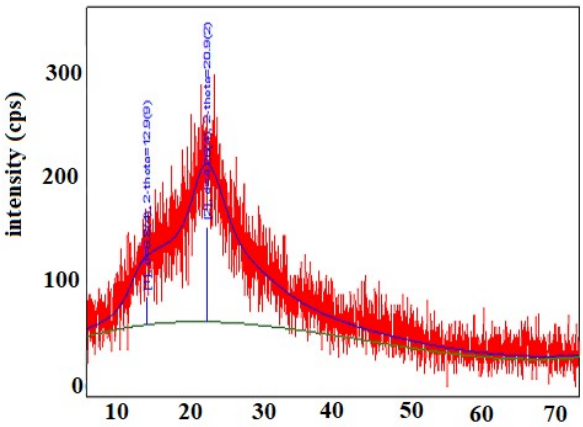
intensity (cps)
300
200
100
0
10
20
30
40
50
60
70

(c)

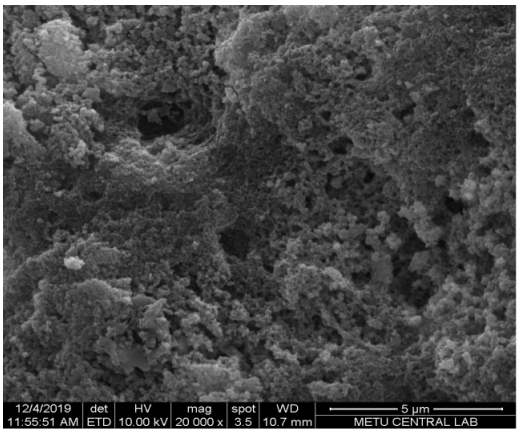

(d)

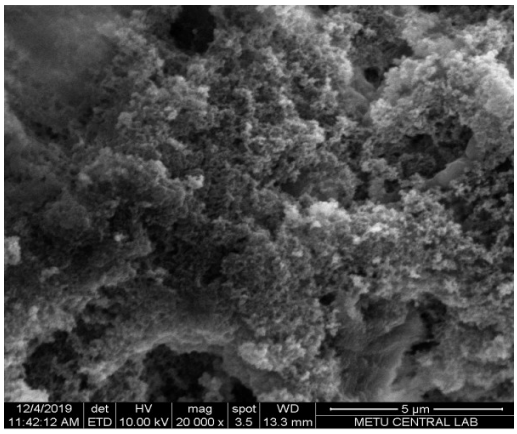

(e)

Figure 2: FTIR spectra of PMMAC-MIC and PMMAC-NIC (a), XRD patterns of PMMAC-MIC (b) PMMAC-NIC (c), SEM images of PMMAC-MIC (d), PMMAC-NIC (e).

XRD analysis

The XRD patterns that indicate the crystallinity of composites of PMMAC-NIC and PMMAC-MIC were depicted in Figure 2b and 2c (23). The characteristic peaks of chitosan 2-theta degree were recorded at 21.10°, 20.9° for PMMAC-MIC and PMMAC-NIC, respectively. The XRD patterns revealed the successful differences between PMMAC-MIC and PMMA-NIC which may be caused by the removal of dye template molecules. The crystallite sizes of the PMMAC-MIC and PMMA-NIC were found at 9.50 nm and 11.0 nm, respectively as the results obtained from XRD analysis.

SEM analysis of composites

The morphologies of PMMAC-NIC and PMMAC-MIC were studied by scanning electron microscope. The results of SEM images are depicted in Figure 2d and 2e. It can be observed in Figure 2d and 2e, the surface morphology of the PMMA-MIC composite is different from the PMMA-NIC composite. The SEM image of the MIC composite is predicted to be more rough, orderly, and stable than that of the NIC composite, which may be caused by voids created by removing imprinted MG dye molecules on its surface (24,25). Besides, it is predicted that the SEM image of the MIC composite was more porous than that of the NIC composite and that this porosity of the MIC composite may account for better adsorption capacity for MG dye.

DSC analysis

DSC profiles of PMMAC-MIC and PMMA-NIC are depicted in Figure 3a and 3b. DSC was used to determine the phase behavior and thermal transitions of PMMAC-MIC and PMMAC-NIC (Figure 3a and 3b). According to the results, the endothermic peak of PMMAC-NIC was located at 87.95 °C (Figure 3a). PMMAC-MIC composite indicated three endothermic peaks at 59.92 °C, 230.95 °C, and 293.68 °C, respectively which suggests that the surface modification was formed and the thermal stability was improved by increasing the temperature (supporting the increasing thermal resistance) after the imprinting process (Figure 3b) (26).

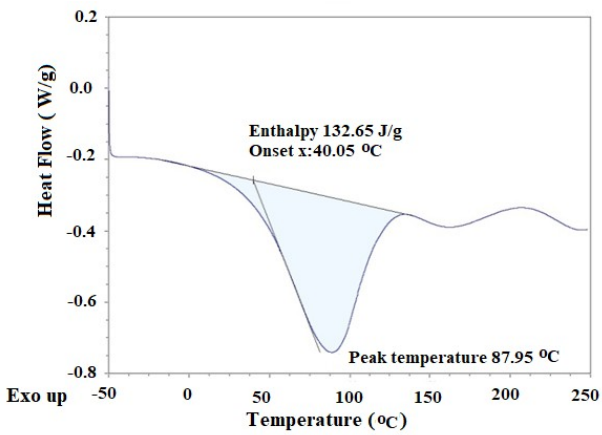

(a)

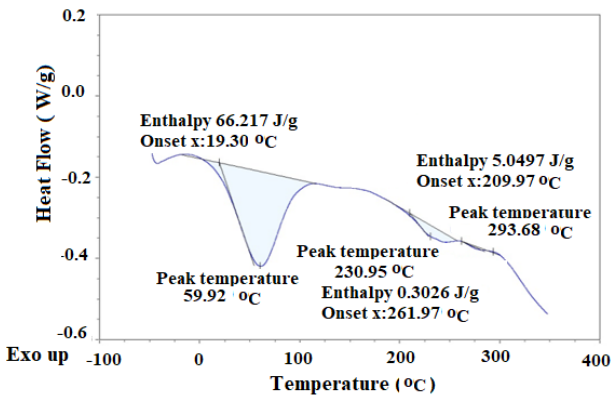

(b)

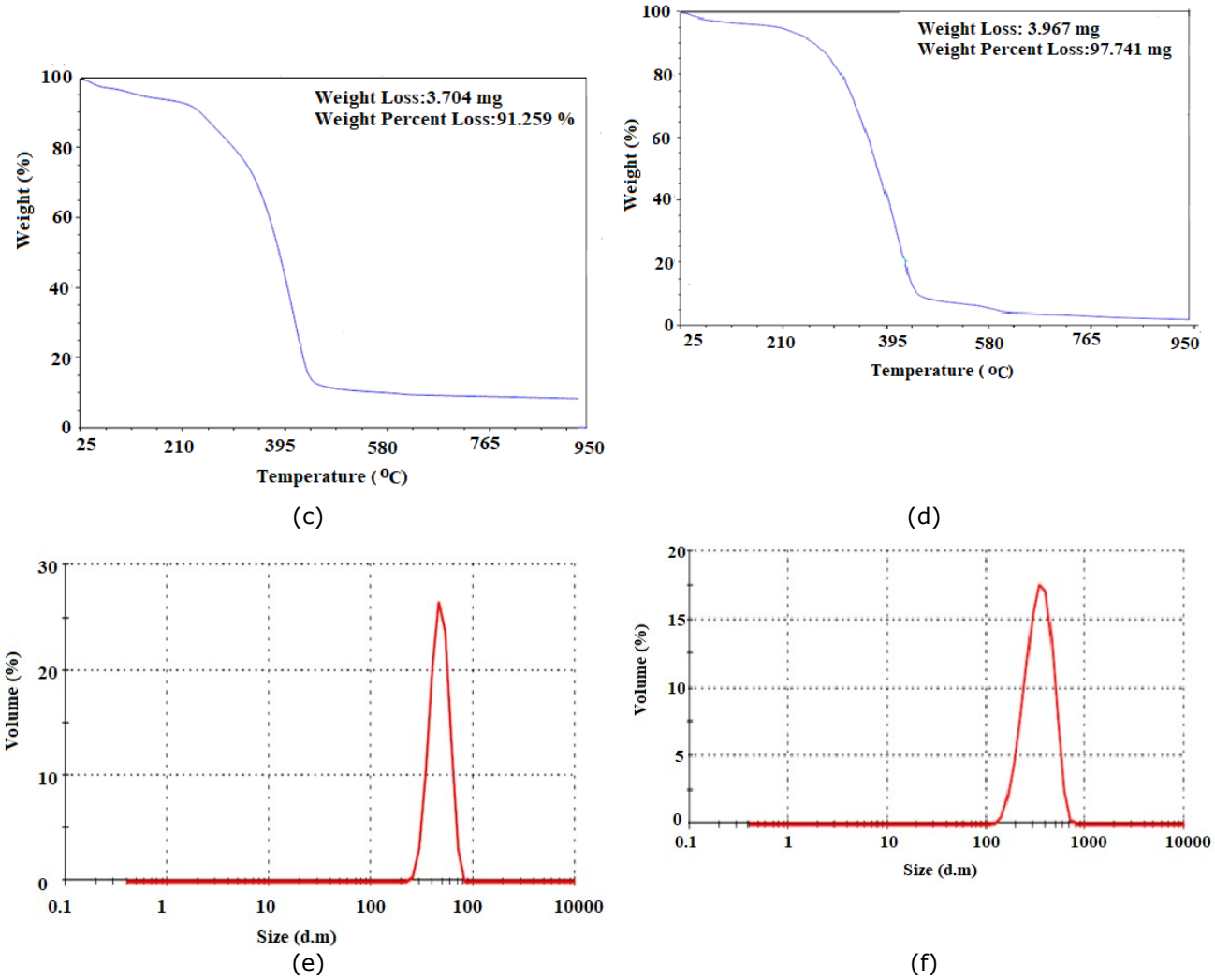

Figure 3: DSC thermogram of (a) PMMAC-NIC (b) PMMAC-MIC, TGA analysis of (c) PMMAC-NIC (d) PMMAC-MIC, size distribution of (e) PMMA-NIC, (f) PMMA-MIC.

TGA analysis of the composites

The thermal stability and degradation profile of the composites were assessed by thermogravimetric analysis (27). Figure 3c and 3d exhibited the TGA curves of the PMMAC-NIC, PMMAC-MIC that exhibited the amount of mass loss and its percent of PMMAC-NIC, PMMAC-MIC were 3.704 mg, 3.987mg, and 91.259%, 97.741%, respectively. Below 200 °C the mass losses have pertained to the polar groups or moisture in the composites (28). The mass losses between 0-100 °C indicated the evaporation of moisture in the samples (29). The results showed that the thermal stability of the MIC composite was better than NIC adsorbent slightly due to the addition of dye adsorbed, which also confirmed the successful imprinting of dye ions. A similar result has been found by Lewandowska et al., (30) in which the SBF-treated chitosan composite was investigated (Sohni et al., 2019).

Zeta potential analysis

Zeta potential measurement is used to describe the charge performance of the nanoparticle surface (31). Figure 3e and 3f show the size distribution of PMMA-NIC and PMMA-MIC, respectively. The particle size obtained of the PMMA-NIC particles is about 860.3 nm while the PMMA-MIC particle 449.0 nm. The positive Zeta potential value of both the MIC (40.3 mV) and the NIC (30.2 mV) composite indicates that the surface of both composites is predominantly loaded with a positive charge. Also, the fact that both PMMA-NIC (0.777) and PMMA-MIC (0.473) composites have PDI values greater than 0.2, explains that the composite surfaces are heterogeneous.

Effect of pH and Point of Zero Charge (P_{pzc})

pH has an absolute impression on the adsorption capacity as it changes the surface properties of the composite due to the ionization of the degree of dye molecules for the adsorption process. Figure 4a

illustrates that the percent adsorption capacity of MG dye on PMMAC-MIC adsorbent increased by raise of pH in the range of 2-8. At low pH, since the zero-point charge of the adsorbent was found to be 6.3 (pH < pHzpc, Figure 4b), the surface of the adsorbent becomes positively charged and protonation occurs on the surface of the adsorbent with the functional groups. Nonetheless, the electrostatic contradiction between cationic dye molecules and positively charged adsorbent is formed and so, the adsorption capacity of MG dye is reduced. In contrast, at the higher pH, above zero-point charge (pH > pHzpc), the adsorbent surface becomes negatively chargeable leading to electrostatic interaction between adsorbent and cationic dye, resulting from an increase in adsorption capacity.

Effect of Contact Time and Initial Dye Concentrations

The adsorption of MG dye by PMMAC-MIC and PMMAC-NIC is shown in Figure 4c. In the beginning, adsorption rapidly increases and reaches equilibrium at 180 min for both NIC and MIC composites. Initially, the adsorption was rapid due to the availability of abundant vacant adsorption sites, then the adsorption slowed down as they reached saturation. As seen in Figure 4c, the adsorption capacity of PMMAC-MIC (93.78 mg/g) was much higher than PMMAC-NIC (17.70 mg/g). This was verifying the enhancement of suitable coordinations between the MIC and MG dye.

To investigate the effect of the initial dye concentration, three initial MG dye concentrations (C_o=50, 75, 100 mg/L) were used at pH 8. Adsorption of both PMMAC-MIC and PMMAC-NIC increased when initial MG dye concentration increased. When initial dye concentration increased from 50 mg/L to 100 mg/L, the adsorption capacity was increased from 59.70 mg/g to 93.78 mg/g and from 10.26 mg/g to 17.70 mg/g for MIC and NIC composites, respectively. These results prove that the adsorption mechanism depends on the initial concentration of dyestuff and the formation of many suitable centers on the surface of the templated adsorbent (PMMAC-MIC). Thus, the molecular imprinting adsorbent (PMMAC-MIC) could be an excellent adsorbent for the removal of MG dye from aqueous solutions comparing with the non-imprinting adsorbent (PMMAC-NIC). Besides, as can be seen in Table 1, it can be interpreted that the synthesized composite is quite suitable for MG dye removal compared to previous studies.

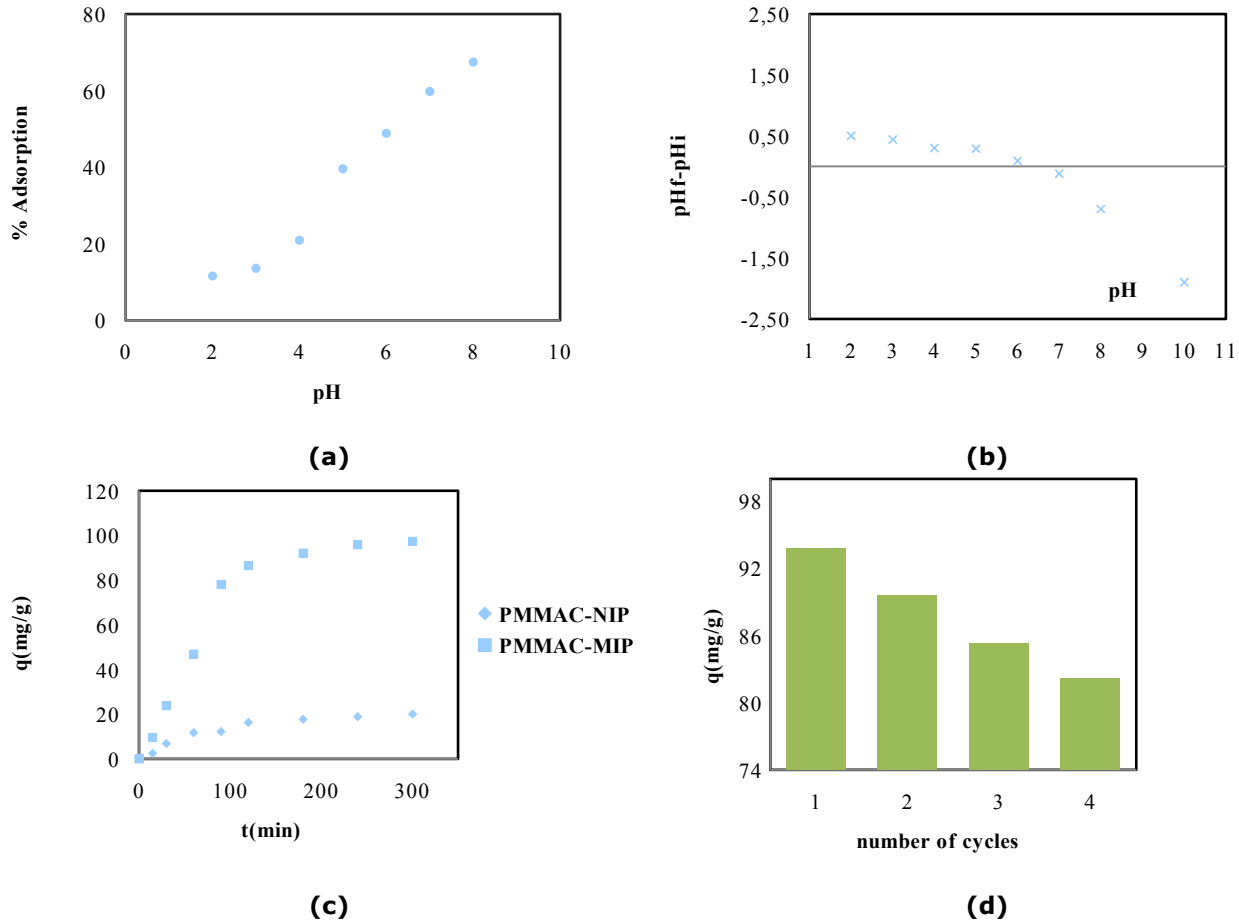

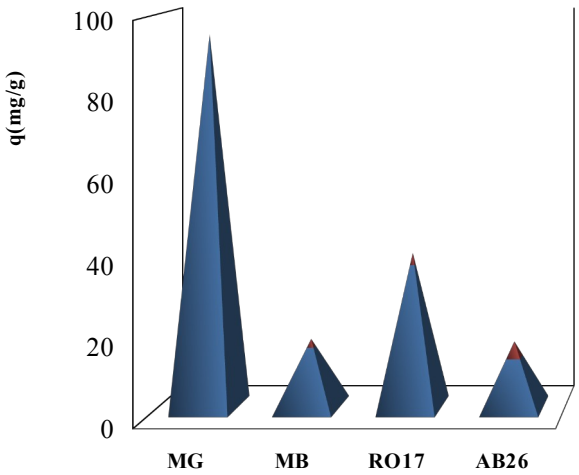

(e)

Figure 4: Effect of (a) pH (b) point of zero charge (c) contact time (d) regeneration (e) selectivity on MG dye adsorption.

Table 1: Adsorption capacities of various adsorbent in the literature about the MIM method for dye adsorption.

Adsorbent	Dye	C_o (mg/L)	q_e (mg/g)	References
Lewis acid-crosslinked chitosan	Active brilliant red	200	161.1	(8)
Crosslinked-chitosan	Remazol red	70	14.3	(9)
Epichlorohydrin and glutaraldehyde-magnetic chitosan	Chalcone dye	100	51.71 and 39.23	(10)
Chitosan-TiO_2 nanocomposite	Rose bengal	64	79.36	(11)
Cross-linked polyacrylamide grafted /chitosan hydrogels	Acid blue 113	300	286	(12)
Zeolitic imidazolate framework /chitosan/polyvinyl alcohol composite	Malachite green	29.66	62.2	(13)
Chitosan-magnetite	Alizarin red	100	40.12	(14)
Styrene-Methacrylate based	Malachite green	500	200.00	(32)
polymethacrylic acid	Malachite green	250	303.03	(33)
PMMAC-MIC	Malachite green	100	93.78	This study

Adsorption Kinetics

The kinetics of adsorption of dye onto adsorbents can be represented by the pseudo-first-order (Figure 5a) and pseudo-second-order (Figure 5b) kinetic models by the following equations, respectively (Eq.4,5) (34).

$$\log(q_e - q_t) = \frac{\log q_e - k_1}{2.303} \times t \quad \text{(Eq. 4)}$$

$$\frac{t}{q_t} = \frac{1}{k_2 q_e^2} + \frac{1}{q_e t} \quad \text{(Eq. 5)}$$

Where q_e (mg/g), q_t (mg/g) are the amount of adsorbed dye at equilibrium and time; k_1 (1/min) and k_2 (g/mg min) represent the rate constants of pseudo-first-order and pseudo-second-order, respectively, while t is time.

While the pseudo-first-order kinetic model defines the first stage in adsorption, the pseudo-second,

order kinetic model which defines the rate control mechanism is compatible with chemisorption. As is seen from Table 2, correlation coefficients (R^2) of the pseudo-first-order model were higher than the pseudo-second model (R^2>0.980), so the best fit model has been chosen based on the pseudo-first-order kinetic model for adsorption of MG dye onto PMMAC-MIC composite. Also, calculated q_e values obtained from the pseudo-first-order were closer to the experimental q_e (q_{exp}) values, which supports that the adsorption of the MG dye onto the PMMAC-MIC adsorbent is more compatible with the pseudo-first-order model. The studies of noxious textile dyes adsorption onto amorphous carbon nanotubes (35) and malachite green on graphene oxide adsorption (36) have indicated similar results. According to Table 2, based on the initial concentration, the rate constant (k_1) increase can be predicted generally by the physisorption system in MG dye adsorption onto PMMAC-MIC and PMMAC-NIC adsorbent surfaces.

Table 2: Kinetic data for the adsorption of MG dye onto PMMAC-MIC

	Pseudo first order			Pseudo second order		
q_{exp} (mg/g)	q_e (mg/g)	k_1 (1/min)	R^2	q_e (mg/g)	k_2 (g/mgmin)	R^2
59.70	65.9	0.014	0.9802	111.1	0.608	0.9381
78.84	89.8	0.017	0.9806	120.5	1.044	0.9383
93.78	97.3	0.019	0.9968	140.8	1.246	0.9693

Adsorption Isotherms and Thermodynamic Parameters

The Langmuir and Freundlich isotherm models were used to describe the distribution of adsorbed dye molecules between the adsorbents and the liquid solutions at equilibrium conditions (37). The Langmuir isotherm model is the most widely used isotherm equation related to monolayered adsorption of dye molecules on the surface of the adsorbent. Langmuir isotherm model is expressed by the following equation (Figure 5c) (Eq. 6):

$$\frac{C_e}{q_e}=\frac{1}{Q_{max}\times K_L}+\frac{1}{Q_{max}}\times C_e \qquad \text{(Eq. 6)}$$

Where q_e is the amount of MG dye adsorbed at equilibrium, C_e is the equilibrium concentration in the aqueous solution of MG dye, K_L is the Langmuir constant (L/mg) and Q_{max} is the maximum monolayer adsorption capacity.

The dimensionless separation factor, R_L indicates whether the adsorption process is favorable or not is a significant parameter of the Langmuir isotherm model. The R_L can be represented by the following equation (Eq 7).

$$R_L=\left(\frac{1}{1+K_L}\right)\times C_0 \qquad \text{(Eq. 7)}$$

The adsorption process is unfavorable while the value of R_L>1, favorable when 0<R_L<1, irreversible or linear when R_L=0 or R_L = 1, respectively (38).

Freundlich isotherm model assumes molecules form multilayers on the adsorbent surface with adsorbed dye molecules interaction and is identified by the following equation (Figure 5d) (Eq 8) (39).

$$q_e=K_F\times\left(\frac{C_e^1}{n}\right) \qquad \text{(Eq. 8)}$$

Where K_F and 1/n are constants depicting the adsorption capacity and adsorption intensity, respectively.

Adsorption isotherm studies were carried out at different temperatures T: 298, 308, 318 K, six

different initial dye concentrations C_o: 25, 50, 75, 100, 125 mg/L, equilibrium time of 180 min, pH: 5 by PMMAC-MIC adsorbent for MG dye. According to Table 3, the adsorption of MG dye by PMMAC-MIC is better described by Langmuir isotherm as correlation coefficients (R^2>0.99) were higher compared to Freundlich throughout the ranges of initial dye concentration. The value of K_L was decreased with rising temperature which showed that the intensity of adsorption was improved at lower temperatures. Besides, the maximum Langmuir adsorption capacity that was decreased with increasing temperature was 166.67 mg/g at 298 K (Table 3). Due to the R_L values of PMMAC-MIC adsorbent at different temperatures were between 0 and 1, the adsorption of MG dye on the PMMAC-MIC is favorable. The same result was reported in a previously conducted study (40).

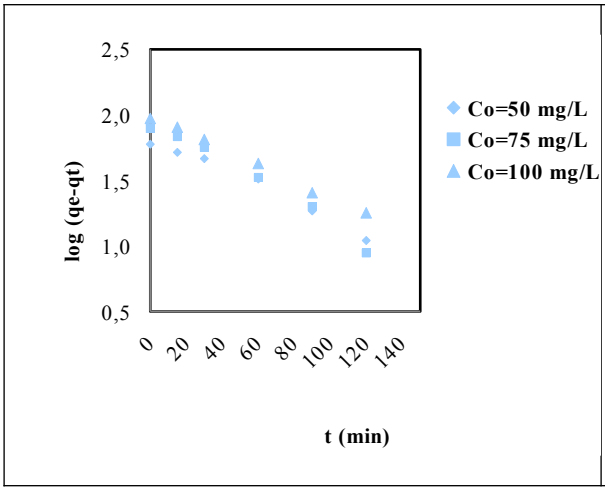
2,5
2,0
1,5
1,0
0,5
log (qe-qt)
0
20
40
60
80
100
120
140
t (min)
Co=50 mg/L
Co=75 mg/L
Co=100 mg/L

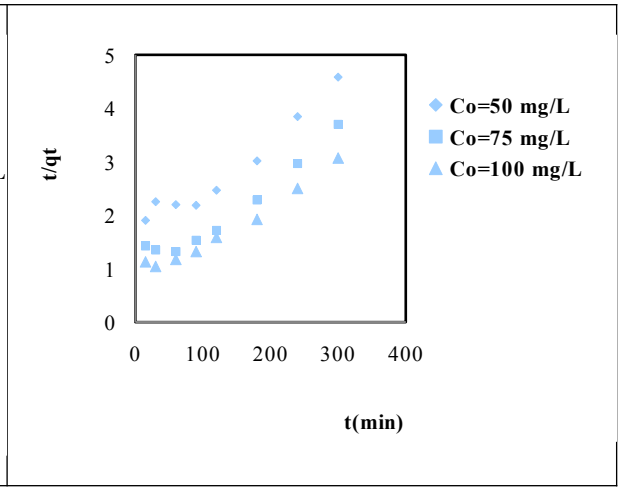
5
4
3
2
1
0
t/qt
0
100
200
300
400
t(min)
Co=50 mg/L
Co=75 mg/L
Co=100 mg/L

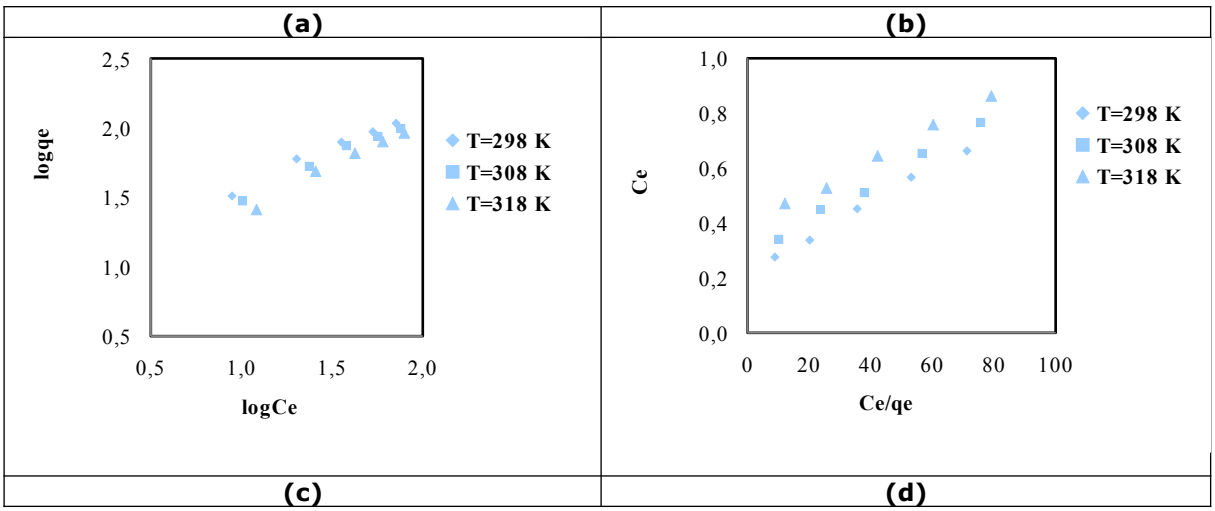

Figure 5: (a) Pseudo-first-order, (b) pseudo-second-order kinetic studies; (c) Langmuir, (d) Freundlich adsorption isotherms of MG dye on PMMAC-MIC.

Table 3: Isotherm data for the adsorption of MG dye onto PMMAC-MIC.

T (K)	Langmuir isotherm				Freundlich isotherm		
	Q_{max} (mg/g)	K_L (L/mg)	R_L	R^2	$1/n$ (mg/g)	K_F (mg/g) (L/mg)$^{1/n}$	R^2
298	166.67	0.027	0.121	0.9969	0.57	9.87	0.9832
308	156.85	0.023	0.122	0.9951	0.60	7.64	0.9880
318	155.25	0.016	0.123	0.9963	0.67	5.09	0.9875

Free energy (ΔG^o), enthalpy (ΔH^o), and entropy (ΔS^o) of adsorption which are known as thermodynamic parameters were calculated to investigate the temperature effect on the adsorption of MG dye by the PMMAC-MIC composite. The following equation is used for the calculation of thermodynamic parameters (Eq. 9,10).

$$\log K_L = -\Delta H^0 (2.303 \times R) \times T + \Delta S^0 (2.303 \times R) \quad \text{(Eq. 9)}$$

$$\Delta G^0 = R \times T \times \ln K_L \quad \text{(Eq. 10)}$$

Where K is the equilibrium constant ratio of adsorbate on the adsorbent, R (8.314 J/mol K) is the molar gas constant and T (K) is the temperature.

The adsorption experiments were conducted at three temperatures (298, 308, 318 K) and the plot of $\ln K_L$ vs. $1/T$ using the first above equation was drawn (not shown). Also, slope and intercept of the linear plot give values of $\Delta H^o/R$ and $\Delta S^o/R$, respectively. Table 4 represented the calculated results of the thermodynamic parameters. According to Table 4, negative values of ΔG^o, the positive value of ΔH^o, and the positive value of ΔS^o demonstrate the spontaneous, endothermic, and favorable adsorption reaction of MG dye on the surface of the PMMAC-MIC adsorbent, respectively.

Table 4: Thermodynamic parameters of MG dye adsorption onto PMMAC-MIC._

T(K)	ΔG (kJ/mol)	ΔH (kJ/mol)	ΔS (kJ/molK)
298	-8.02		
308	-7.81	22.36	93.94
318	-7.21		

Due to the values of ΔG are between 20 and 0 kJ/mol, the adsorption mechanism is called physisorption (while 80-400 kJ/mol is chemisorption) (41).

Regeneration of the Composite

In the case of the regeneration experiments, HCl eluent was used for desorption and reused to adsorb the MG dye with four adsorption cycles. Figure 4d shows that the adsorption capacity of MG was 93.80 mg/g in the first cycle and was 82.20 mg/g after four cycles on PMMAC-MIC adsorbent. This slight reduction indicates that the PMMAC-MIC composite is stable and can be reutilized several times with good productivity in adsorption capacity for MG dye.

Selectivity Analysis

PMMAC-MIC composite was researched for the selective binding with MG dye. Hence, the adsorption performance of MB, RO16, and AB25 dyes was performed for reusability of PMMAC-MIC adsorbent towards MG dye as utilized in Figure 4e. It was seen that MG dye showed the best binding performance and adsorption capacity, 93.78 mg/g

while the adsorption capacity was 36.11 mg/g, 15.20 mg/g, and 12.55 mg/g for RO16, MB, and AB25, respectively. As a result, the imprinting method selectively detects the MG dye, thereby effectively improving its adsorption performance through selective bonding points.

CONCLUSION

It was found that PMMAC-MIC composite obtained by the imprinting method increased MG adsorption capacity. The average particle size of PMMAC-MIC and PMMAC-NIC was obtained by Zeta potential as 449.0 nm and 860.3 nm, respectively. Also, the results from the XRD analysis revealed that the crystalline size of PMMAC-MIC and PMMA-NIC was 9.50 nm and 11.0 nm, respectively. According to the adsorption performance, reusability has been determined four times. DSC and TGA analyses showed that the thermal stability of MIC was better than NIC confirming the successful imprinting dye ions. The adsorption of MG dye was described well with pseudo-first-order kinetic model, suggesting that physical adsorption processes by quite a low surface coverage. According to calculations of thermodynamic parameters, the adsorption mechanism can be called a spontaneous reaction resulting from negative $\Delta G°$ values. Due to the small value of $\Delta G°$ (7.2-8.1 kJ/mol< 80 kJ/mol), the adsorption reaction can be described as physisorption. The positive value of $\Delta H°$ indicated endothermic adsorption; therefore, higher temperatures will facilitate the adsorption of MG dye by PMMAC-MIC adsorbent interface while the positive value of $\Delta S°$ verified the favorability. The results represented the monolayer adsorption process and the maximum monolayer adsorption capacity was found as 93.78 mg/g. Indeed, regeneration experiments indicated that the molecular imprinting method for MG adsorption is very suitable for adsorption and PMMAC-MIC can be used as an efficient and selective adsorbent for the treatment of dyes from aqueous solutions when compared to the previous studies. Due to this favorable performance for MG, it is promising that this imprinting composite may be applied to remove other dyes. Also, this study is expected to improve chromatographic adsorbents, sensors, membranes, enzyme, and receptor mimetic areas by molecular imprinting method, with the development of higher capacity adsorbents.

REFERENCES

1. Yildirim A, Acay H. Biosorption Studies of Mushrooms for Two Typical Dyes. JOTCSA. 2020; 7(1): 295-306.

2. Zhang Y, Huang Y, Zhai F, Du R, Liu Y, Lai K. Analyses of enrofloxacin, furazolidone and malachite green in fish products with surface-enhanced Raman spectroscopy. Food Chemistry. 2012; 13: 845–50.

3. Li Q, Su H, Li J, Tan T. Application of surface molecular imprinting adsorbent in expanded bedfor the adsorption of Ni^{2+} and adsorption model. Journal of Environmental Management. 2007; 85: 900–7.

4. Hui Y, Yan-Fei C, Hui-Qin G, Wen-Tian M, Jing L, Shui-Gen Z, Sen L, Liu-Shui Y, Ke-Xin L. Preparation of Molecularly Imprinted Carbon Microspheres by One-Pot Hydrothermal Method and Their Adsorption Properties to Perfluorooctane Sulfonate. Chinese Journal of Analytical Chemistry. 2019; 47: 1776–84.

5. He Q, Liang JJ, Chen LX, Chen SL, Zheng HL, Liu HX, Zhang HJ. Removal of the environmental pollutant carbamazepine using molecular imprinted adsorbents: Molecular simulation, adsorption properties, and mechanisms. Water Research. 2000; 168: 1151642, 1-13.

6. Yi Z, Huajie L, Mingchun L, Meihua X. Adsorption of aniline on aminated chitosan/graphene oxide composite material. Journal of Molecular Structure. 2020; 1209: 127973, 1-6.

7. Wang R, Zhang X, Zhu J, Bai J, Gao L, Liu S, Ji T. Facile preparation of self-assembled chitosan-based composite hydrogels with enhanced adsorption performances. Colloids and Surfaces A: Physicochemical and Engineering Aspects. 2020; 598: 124860, 1-9.

8. Deng H, Wei Z, Wang XN. Enhanced adsorption of active brilliant red X-3B dye on chitosan molecularly imprinted polymer functionalized with Ti(IV) as Lewis acid. Carbohydrate Polymers. 2017; 157: 1190-7.

9. Kyzas GZ, Lazaridis NK, Bikiaris DN. Optimization of chitosan and β-cyclodextrin molecularly imprinted polymer synthesis for dye adsorption. Carbohydrate Polymers. 2013; 91: 198-208.

10. MR Fat'hi, S.J.H. Nasab. Synthesis of calcon-imprinted magnetic chitosan nanoparticles as a novel adsorbent and its application in selective removal of calcon dye from aqueous solutions. International Journal of Biological Macromolecules. 2018; 114: 1151-60.

11. Ahmed MA, Abdelbar NM, Mohamed AA. Molecular imprinted chitosan-TiO_2 nanocomposite for the selective removal of Rose Bengal from wastewater, International Journal of Biological Macromolecules. 2018; 107: 1046-53.

12. da Silva RC, de Aguiar SB, da Cunha PLR, de Paula RCM, Feitosa JPA. Effect of microwave on the

synthesis of polyacrylamide-g-chitosan gel for azo dye removal. Reactive and Functional Polymers. 2020; 148: 104491, 1-10.

13. Khajavian M, Salehi E, Vatanpour V. Chitosan/polyvinyl alcohol thin membrane adsorbents modified with zeolitic imidazolate framework (ZIF-8) nanostructures: Batch adsorption and optimization. Separation and Purification Technology. 2020; 241: 116759, 1-16.

14. Fan L, Zhang Y, Li X, Luoa C, Lu F, Qiu H. Removal of alizarin red from water environment using magnetic chitosan with Alizarin Red as imprinted molecules. Colloids and Surfaces B: Biointerfaces. 2012; 91: 250-7.

15. Baran, MF Acay H, C Keskin. Determination of antimicrobial and toxic metal removal activities of plant-based synthesized (Capsicum annuum L. Leaves), Ecofriendly, Gold Nanomaterials. Global challenges. 2020; 1900104: 1-7.

16. Bhomick CP, Supong A, Baruah MC, Sinha D. Pine Cone biomass as an efficient precursor for the synthesis of activated biocarbon for adsorption of anionic dye from aqueous solution: Isotherm, kinetic, thermodynamic and regeneration studies. Sustainable Chemistry and Pharmacy. 2018; 10. 41-9.

17. Acay H, Baran MF. Biosynthesis and characterization of silver nanoparticles using king oyster (Pleurotus eryngii) extract: effect on some microorganisms. Applied Ecology And Environmental Research. 2019; 17: 9205-14.

18. Baran MF, Acay H. Antimicrobial Activity of Silver Nanoparticles Synthesized with Extract of Tomato plant Against Bacterial and Fungal Pathogens. Middle Black Sea Journal of Health Science. 2019; 5: 67-73.

19 Yildirim A, Acay H, Baran F. Synthesis and characterisation of mushroom-based nanocomposite and its efficiency on dye biosorption via antimicrobial activity. International Journal of Environmental Analytical Chemistry. 2020; 1739664, 1-18.

20. Baran MF, Yildirim A, Acay H, Keskin C, Aygun H. Adsorption performance of Bacillus licheniformis sp. bacteria isolated from the soil of the Tigris River on mercury in aqueous solutions. International Journal of Environmental Analytical Chemistry. 2020; 1746779, 1-16.

21. Yildirim A, Bulut Y. Adsorption behaviors of malachite green by using crosslinked chitosan/polyacrylic acid/bentonite composites with different ratios. Environmental Technology & Innovation. 2020; 7: 100560, 1-13.

22 Rajabi M, Mahanpoor K, Moradi O. Preparation of PMMA/GO and PMMA/GO-Fe_3O_4 nanocomposites for malachite green dye adsorption: Kinetic and thermodynamic studies. Composites Part B. 2019; 167: 544–55.

23 Labidi A, Salaberria AM, Labidi J, Abderrabba M. Preparation of novel carboxymethyl chitosan-graft-poly(methylmethacrylate) under microwave irradiation as a chitosan-based material for Hg^{2+} removal. Microchemical Journal. 2019; 148: 531–40.

24. Kumari S, Khan AA, Chowdhury A, Bhakta AK, Hussain ZMS. Efficient and highly selective adsorption of cationic dyes and removal of ciprofloxacin antibiotic by surface modified nickel sulfide nanomaterials: Kinetics, isotherm, and adsorption mechanism. Colloids and Surfaces A: Physicochemical and Engineering Aspects. 2020; 586: 124264, 1-15.

25. Bhatti HN, Safa Y, Yakout SM, Shair OH, Iqbalf M, Nazir A. Efficient removal of dyes using carboxymethyl cellulose/alginate/polyvinyl alcohol/rice husk composite: Adsorption/desorption, kinetics and recycling studies. International Journal of Biological Macromolecules. 2020; 150: 861-70.

26. Yang K., Dang H, Liu L, Hu X, Li X, Ma Z, Wang X, Ren T. Effect of syringic acid incorporation on the physical, mechanical, structural and antibacterial properties of chitosan film for quail eggs preservation, International Journal of Biological Macromolecules. 2019; 141: 876–84.

27. Habiba U, Siddique TA, Lee JJL, Joo TC, Afifi AM. Adsorption study of methyl orange by chitosan/polyvinyl alcohol/zeolite electrospun composite nanofibrous membrane. Carbohydrate Polymers. 2018; 191: 79–85.

28. Boggione MJ, Mahl CRA, Beppu MM, Farruggia B. Synthesis and characterization of chitosan membranes functionalized with amino acids and copper for adsorption of endoglucanase, Powder Technology. 2017; 315: 250–7.

29. Zhang H, Omer AM, Hu Z, Yang LY, Ji C, Ouyang XK. Fabrication of magnetic bentonite/carboxymethyl chitosan/sodium alginate hydrogel beads for Cu (II) adsorption. International Journal of Biological Macromolecules. 2019; 135: 490–500.

30. Lewandowska K, Furtos G. Study of apatite layer formation on SBF-treated chitosan composite thin films. Polymer Testing. 2018; 71: 173–81.

31. Yekeen N, Padmanabhan E, Idris AK, Ibad SM. Surfactant adsorption behaviors onto shale from

Malaysian formations: Influence of silicon dioxide nanoparticles, surfactant type, temperature, salinity and shale lithology. Applied Clay Science. 2016; 123: 64–75.

32. Awokoya KN, Oninla VO, Babalola JO, Mbaeyi NN, Folorunso FT. Adsorption of malachite green onto styrene-methacrylate based molecularly imprinted polymer. Ife Journal of Science. 2019; 21: 67-80.

33. Farhadia K, Matin AA, Hashemia P. Removal of malachite green from aqueous solutions using molecularly imprinted polymer. Desalination and Water Treatment. 2010; 24: 20–7.

34. Yildirim A. Kinetic, equilibrium and thermodynamic investigations for the bio-sorption of dyes onto crosslinked Pleurotus ostreatus-based bio-composite. International Journal of Environmental Analytical Chemistry. 2020; 1802441, 1-16.

35. Banerjee D, Bhowmick P, Pahari D, Santra S, Sarkar S, Chattopadhyay BDKK. Pseudo-first ordered adsorption of noxious textile dyes by low-temperature synthesized amorphous carbon nanotubes. Physica E. 2017; 87: 68–76.

36. Robati D, Rajabi M, Moradi O, Najafi F, Tyagi I, Agarwal S, Gupta VK. Kinetics and thermodynamics of malachite green dye adsorption from aqueous solutions on graphene oxide and reduced graphene oxide. Journal of Molecular Liquids. 2016; 214: 259–63.

37. Shang Y, Shi YCR, Yang P, Wang J, Wang Y. Regenerated $WO_{2.72}$ nanowires with superb fast and selective adsorption forcationic dye: Kinetics, isotherm, thermodynamics, mechanism. Journal of Hazardous Materials. 2019; 379: 120834, 1-10.

38. Bonetto LR, Ferrarini F, Marco CD, Crespo JS, Ruégan R, Giovanela M. Removal of methyl violet 2B dye from aqueous solution using a magnetic composite as an adsorbent. J. Water Process Eng. 2015; 6: 11-20.

39. De Castro MLFA, Abad MLB, Sumalinog DAG, Abarca RRM, Paoprasert P, de Luna MDG. Adsorption of Methylene Blue dye and Cu(II) ions on EDTA-modified bentonite: Isotherm, kinetic and thermodynamic studies. Sustainable Environment Research. 2018; 28: 197-205.

40. Dastgerdi ZH, Abkhiz V, Meshkat SS, Ghorbana N. Preparation of novel magnetic grafted raft agent nanocomposite: Application in carmine dye adsorptive removal from waste water. Journal of Environmental Chemical Engineering. 2019; 7: 103109, 1-9.

41. Wang L, Zhang J, Wang A. Fast removal of methylene blue from aqueous solution by adsorption onto chitosan-g-poly (acrylic acid)/attapulgite composite. Desalination. 2011; 266: 33–9.

JOTCSA Journal of the Turkish Chemical Society Section: A Chemistry

TURKISH CHEMICAL SOCIETY

Photophysical properties of a newly synthesized unsymmetrically substituted zinc phthalocyanine

Ayfer Kalkan Burat *, Hande Pekbelgin Karaoğlu*

Istanbul Technical University, Department of Chemistry, TR34469, İstanbul, Turkey.

Abstract: A novel unsymmetrically substituted zinc phthalocyanine (ZnPc) containing six hexylthio units and a morpholinoethoxy group was synthesized and characterized. Statistical condensation reaction of two different phthalonitriles was used for the preparation of unsymmetrical ZnPc. The novel compound was purified using chromatographic methods with the help of high solubility differences of phthalonitrile derivatives. Characterization of the compound was achieved by using NMR, FT-IR, UV-Vis, and mass spectroscopic methods. The photophysical measurements were made in tetrahydrofuran (THF). Fluorescent quantum yield (Φ_F) and fluorescence lifetime (τ_F) of unsymmetrical ZnPc were determined. Fluorescent quenching experiments were done by adding benzoquinone (BQ) in THF, and Stern-Volmer constant (Ksv) and quenching constant (k_q) values were calculated.

Keywords: Fluorescence, phthalocyanine, quenching, unsymmetric, zinc.

Submitted: January 28, 2021. **Accepted:** April 30, 2021.

Cite this: Kalkan Burat A, Pekbelgin Karaoğlu H. Photophysical properties of a newly synthesized unsymmetrically substituted zinc phthalocyanine. JOTCSA. 2021;8(2):623–32.

DOI: https://doi.org/10.18596/jotcsa.870010.

***Corresponding author.** E-mail: kalkanayf@itu.edu.tr, pekbelgin@itu.edu.tr

INTRODUCTION

Phthalocyanines (Pcs) can be functionalized for a variety of applications, from medicine to technology (1-5). They are also used as second-generation photosensitizers for the photodynamic therapy (PDT) of cancers and for inactivation of bacteria and viruses due to strong absorption in the red-visible region and high efficiency in producing reactive oxygen species (6, 7). The photochemical and physicochemical properties of Pcs can be altered by changing the substituents in the peripheral and non-peripheral positions or by inserting different metal ions in the central cavity (8, 9). Both peripherally and non-peripherally substituted Pcs have already been investigated as photosensitizers for PDT applications because the substituents affect the physicochemical properties of Pcs and the possibility of using them in *vivo* and in *vitro* studies (10, 11). Due to their unique photophysical and photochemical properties, Pc compounds can be applied in medical and industrial product development. For suitable applications, the design of phthalocyanines with desired properties can be accomplished by varying the central metal atoms and the substituents of Pc molecules. The most important problem encountered in the application of unsubstituted Pc is its low solubility in common organic solvents and in water. To improve the solubility of the Pc compound, long alkyne chains or bulky groups can be attached at the peripheral or non-peripheral positions of the macrocycle (8, 9, 12, 13).

Synthesis of Pcs for medical purposes is an important subject of research because it is preferred that the designed molecules do not show aggregation and have a lipophilic-hydrophilic balance. Aggregation of Pcs can be also prevented by peripheral, non-peripheral, or axial substitution of different groups (12, 13). One of these groups is morpholine (1,4-tetrahydro-oxazine), of great industrial importance and a wide range of applications. Morpholine and its derivatives are used as solvents, corrosion inhibitors, rubber additives, antioxidants, as well as in the production of drugs

and herbicides. Morpholine derivatives are also of interest as they show biological activities such as anti-inflammatory, analgesic, antidepressant, and antitumor (14-17).

It has been found that the substitution of morpholine groups into the Pc structure modulates the physicochemical properties and amphiphilic nature of Pcs, thereby facilitating their potential applications in biology and medicine (18). Recently, zinc phthalocyanines conjugated with biotinylated graphene quantum dots (GQDs) have been synthesized by Nyokong et al., and their photophysicochemical properties, and in *vitro* photodynamic activities have been studied. It was reported that cationic ZnPc conjugated with the biotin functionalized GQDs exhibited a relatively better performance (19). In another study published in 2019, tetra-substituted Pcs and their cationic derivatives with morpholine groups at the peripheral and non-peripheral positions were synthesized, and their photodynamic antimicrobial chemotherapy activities were examined, and it was determined that cationic Pcs showed better photodynamic antimicrobial activity (20). In 2017, nonperipherally octasubstituted magnesium Pc (MgPc), and its cationic derivative carrying N-methyl morpholiniumethoxy groups were synthesized, and their photocytotoxicity against bacteria, fungi, and cancer cells were investigated. This work showed that quarternized MgPc has excellent photodynamic activity against planktonic cells of both Gram-negative and Gram-positive bacteria (21). These studies show that morpholine groups positively change the biological activity of Pcs (22). In addition, axially morpholine-disubstituted silicon phthalocyanines exhibited better antifungal photodynamic activity and DNA/BSA binding (23-25).

Symmetrical and unsymmetrical morpholine substituted Pcs, synthesis, and investigation of their electrochemical and physicochemical properties were carried out by our group in previous years (26, 27). In addition, the symmetric octasubstituted Pcs derivative containing hexylthio groups was synthesized beforehand in the literature, and its photophysical and thermal properties were investigated (12). Here, we studied the synthesis and characterization of a novel unsymmetrically substituted zinc phthalocyanine (ZnPc) containing six hexylthio units and a morpholinoethoxy group at peripheral positions. The photophysical properties of this new compound were investigated by fluorescence measurements and compared with its octakis hexylthio substituted derivative in the literature (12). Hexylthio group was chosen for the electron donor property of the sulfur atom and its effect on the electronic properties of Pcs was investigated. In addition, morpholine groups also improve the biological properties of Pcs (18-22). Therefore, in the study the effect of the combination of morpholine group with hexylthio groups, which shifts the Q band absorption to the red, on the photophysical properties of phthalocyanine was also investigated.

EXPERIMENTAL SECTION

Materials and apparatus

An Agilent VNMRS 500 MHz spectrometer was used to determine the ^{1}H-NMR spectrum of the synthesized complex. The FT-IR spectrum of the complex was recorded by using a Perkin-Elmer Spectrum One FT-IR UATR spectrometer. The UV-Vis spectrum of the compound was obtained using a Scinco LabProPlus UV/Vis spectrophotometer. Fluorescence spectra were obtained on Perkin-Elmer LS55 fluorescence spectrophotometer. Bruker Microflex LT MALDI-TOF MS spectrometer was used to record the mass spectrum.

4,5-bis(hexylthio)phthalonitrile (**1**) (28) and 4-(2-morpholinoethoxy)phthalonitrile (**2**) (29) were synthesized as given in the literature. The chemicals and solvents used for the synthesis and purification of compounds **1** and **2** were also obtained from Sigma-Aldrich, Germany.

Preparation

*Synthesis of 2,3,9,10,16,17-Hexakis(hexylthio)-23-(2-morpholinoethoxy)) phthalocyaninatozinc(II) (**3**)*: 100 mg (0.28 mmol) of compound **1**, 23.8 mg (0.09 mmol) compound **2,** 17.0 mg (0.09 mmol) $Zn(CH_3COO)_2$ and a catalytic amount of 1,8-diazabicyclo[5.4.0]undec-7-ene (DBU) were refluxed in dry *n*-hexanol under nitrogen (N_2) atmosphere for 24 hours. The mixture of reaction first cooled down to room temperature then precipitated by pouring it into ice-water, and the solid product was washed with methanol (MeOH). Purification of the green compound was carried out by column chromatography on silica gel with dichloromethane (DCM): MeOH (25:1) and then with THF:n-hexane (1:1) as eluent. The compound was finally purified by thin layer chromatography using 25: 1 DCM: n-hexane mixture. Solubility: Soluble in dimethylformamide (DMF), DCM, dimethylsulfoxide (DMSO) and THF. $C_{74}H_{99}N_9O_2S_6Zn$ (1404.41g/mol) Yield: 21 mg, (16 %). FT-IR (υ_{max}/cm^{-1}): 3071 (Ar-C-H), 2953 (Aliph. -C-H), 1240 (C-N), 1100 (C-O-C). UV-Vis λ_{max} (nm) THF: 363, 699. ^{1}H-NMR (500 MHz, $CDCl_3$): δ, ppm 7.63-7.52 (6H, m, Ar-H), 6.97 (2H, s, Ar-H), 6.61 (1H, s, Ar-H), 4.74-4.69 (2H, brs, OCH_2), 3.88-3.87 (4H, t, OCH_2, morpholine), 3.19 (2H, brs, NCH_2), 2.83 (4H, t, NCH_2, morpholine), 2.05-2.02 (12H, t, SCH_2), 1.73-1.69 (12H, m, S-C-CH_2), 1.50-1.42 (36H, m, C-C-CH_2), 1.01-0.92 (18H, t, CH_3). ^{13}C-NMR (500 MHz, $CDCl_3$): δ, ppm 186.30, 151.51, 149.33, 149.11, 148.89, 144.63, 144.35, 135.88, 135.63, 135.43, 135.24, 130.84, 129.45, 128.76, 128.22, 125.47, 123.31, 123.11, 122.91, 119.53, 68.12, 67.09, 58.12, 54.37, 34.22, 31.65, 30.30, 29.39,

22.66, 14.14. Anal. Calc. for $C_{74}H_{99}N_9O_2S_6Zn$ (1404.41 g/mol) %: C, 63.29; H, 7.11; N, 8.98 Found: C, 63.65; H, 7.34; N, 8.61. MS (MALDI-TOF): m/z 1404.5 $[M]^+$.

Photophysical parameters

Fluorescence quantum yield and fluorescence lifetime:

The fluorescence quantum yield (Φ_F) was determined by using a comparative method. The equation used in the comparative method is as follows, and ZnPc in DMF solution was used as standard. (Φ_F = 0.17) (30, 31):

$$\Phi = \Phi_{F(STD)} \frac{F A_{Std} \eta^2}{F_{Std} A \eta_{Std}^2} \qquad \text{(Eq. 1)}$$

In Eq. 1, F and F_{Std} denote areas under the fluorescent emission curves of compound **3** and its standard, respectively. The absorbances of standard solution and compound **3** are expressed as A_{Std} and A, respectively. n_{Std} and n indicate the refractive indices of solvents (n_{DMF} = 1.496, n_{THF} =1.4072).

Fluorescence lifetime (τ_F) indicates the meantime of the substance in the excited state prior to fluorescence and is calculated by the PhotochemCAD program using the Strickler-Berg equation. As an expected result of Eq. 2, the fluorescence quantum yield (Φ_F) and the fluorescence lifetime (τ_F) are directly proportional. In addition, the natural radiative lifetime (τ_o) was calculated using Eq. 2. (30, 31):

$$\Phi_F = \frac{\tau_F}{\tau_0} \qquad \text{(Eq. 2)}$$

Fluorescent quenching by 1,4-benzoquinone

Fluorescent quenching experiments were done by adding the different concentrations of BQ solutions up to 0.040 M to the fixed concentration solution of compound **3**. As a result of fluorescent quenching experiments, an energy transfer took place between compound **3** and BQ. Fluorescence spectra of compound **3** were recorded after each BQ addition. The change in the fluorescence spectra of compound **3** was evaluated to be consistent with the kinetic mechanism of the Stern-Volmer (SV) equation (Eq 3) (32):

$$\frac{I_0}{I} = 1 + K_{SV}[BQ] \qquad \text{(Eq. 3)}$$

I_0 is the fluorescence intensity of the fluorophore before the quencher is added, while I is the fluorescence intensity in the presence of the quencher. The concentration of the quencher is represented by [BQ] and the Stern-Volmer constant by K_{SV} found in the graph from [BQ] to I_0/I. The bimolecular quenching constant (k_q) is calculated from Eq. (4) (33):

$$K_{SV} = k_q \times \tau_F \qquad \text{(Eq. 4)}$$

RESULT AND DISCUSSION

Synthesis and spectroscopic characterization

Basically, three different methods are used for the synthesis of unsymmetrical Pcs. These are polymeric support method (34, 35), ring-expansion of sub-phthalocyanine (SubPc) (36, 37) and statistical condensation of phthalonitriles (two different phthalonitrile derivative, A and B) (38-40), respectively. In order to use the polymeric support method, the Pc must have a group that can be attached to the polymer. In the ring-expansion method, the SubPc is first synthesized in the A_3 structure, and then the ring expansion is made. Here, the statistical condensation method was used to prepare the A_3B type unsymmetrical Pc. Pc derivatives containing mostly A_4 and A_3B were synthesized as a result of cyclotetramerization of two different phthalonitrile compounds whose reactivities were close to each other. While the solubility of the phthalonitrile derivative (**1**) containing the hexylthio group is too high, the low solubility of compound **2** facilitated the isolation of the unsymmetric Pc. Targeted A_3B Pc was isolated by sequential chromatographic purification methods.

Compound **1** and compound **2** were used as starting materials to obtain compound **3**. Compound **1** was synthesized as a result of the base-catalyzed aromatic displacement reaction of hexanethiol with 4,5-dichlorophthalonitrile. The reaction was accomplished in dry DMF, with the addition of K_2CO_3 at 60 °C for 8 h, and the product was purified by crystallization in MeOH. Compound **2** was obtained, under conditions similar to the synthesis of compound **1**, by the reaction of 4-nitro phthalonitrile with 2-morpholinoethanol. The reaction was completed at 50 °C for 72 hours using dry DMF and K_2CO_3 under nitrogen atmosphere. Column chromatography was used for the purification of the white product (silica gel, 1:1 chloroform ($CHCl_3$):acetone). Cyclotetramerization of the phthalonitrile derivatives **1** and **2** with anhydrous $Zn(CH_3COO)_2$ and DBU in *n*-hexanol at 160 °C over a 24-hour period at an appropriate ratio led to the formation of the desired compound **3** (Scheme 1). A number of chromatographic methods were used to purify the raw product. 25: 1 DCM: MeOH followed by 1: 1 THF: hexane solution mixtures were used as the mobile phase in column chromatography. Finally, pure compound (**3**) was obtained by thin-layer chromatography using a 25: 1 DCM: hexane mixture as eluent. Compound **3** dissolves in THF, DCM, DMSO, and DMF with a reaction yield of 16%.

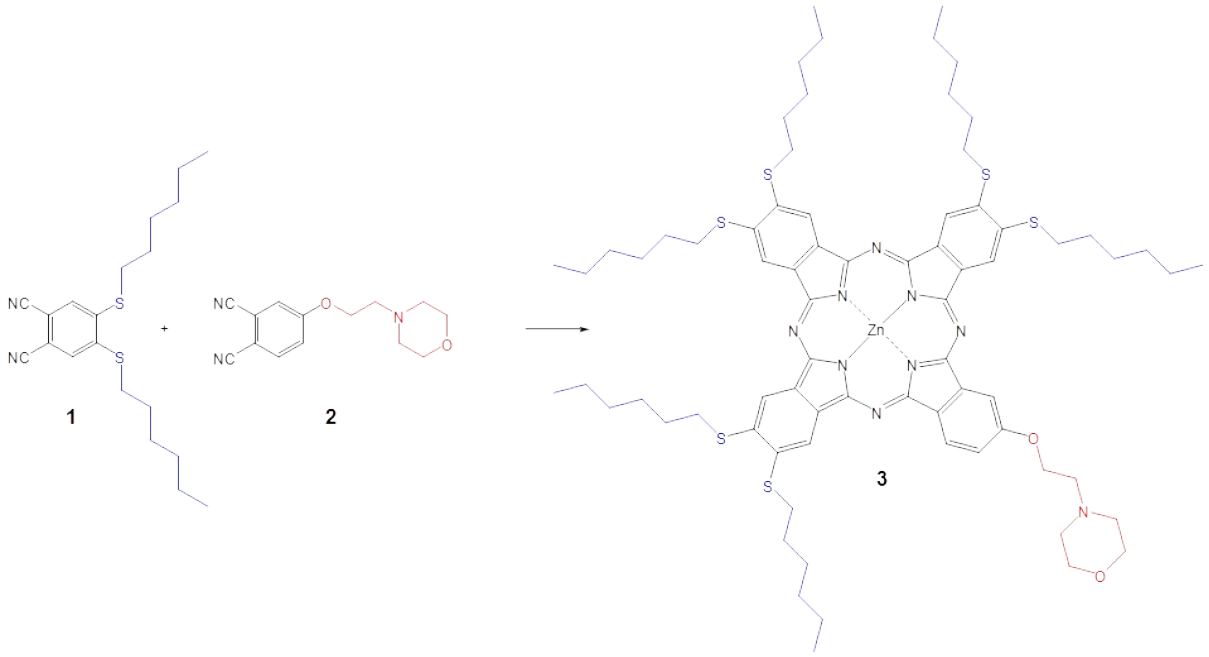

Scheme 1: Synthetic route to unsymmetric ZnPc (**3**): $ZnCl_2$, DBU, n-hexanol, 24 h, reflux.

The novel unsymmetric Pc compound (**3**) was characterized by using NMR, FT-IR, UV-Vis and mass spectroscopic methods. In the FT-IR spectrum, aromatic and aliphatic C-H vibrations were observed at 3071 cm^{-1} and 2953 cm^{-1}, C-N and C-O-C vibrations were observed at 1240 and 1100 cm^{-1}, respectively. The ^{1}H NMR spectrum of **3** in $CDCl_3$ indicated the Pc protons between 7.63-6.61 ppm, the aliphatic protons of morpholine group at 4.74 ($O–CH_2$), 3. 88 ($O–CH_2$), 3.19 ($N–CH_2$), and 2.83 ppm ($N–CH_2$), respectively. The SCH_2, $SCCH_2$, and CH_3 protons were observed at 2.05, 1.73-1.42, and 1.02 ppm, respectively. The ^{13}C NMR spectrum of **3** is compatible with the structure. While the carbons of the phthalocyanine ring were observed between 186-119 ppm, aliphatic carbons were detected between 68-14 ppm. The molecular ion peak observed at m/z = 1404.5 $[M]^+$ for compound **3** confirms the proposed structure.

The simplest Pc unit is the 18-π electron system giving electronic spectra with two absorption regions. These are the B band in the UV region at about 300–400 nm and the Q band in the visible region ranging between 600–700 nm, both correlating to π-π* transitions. UV-Vis spectrum of **3** recorded in THF exhibits an intense single Q band absorption at 699 nm and B band at 363 nm. The spectrum shows the typical pattern of metallo-phthalocyanine complexes (29, 30). When the electronic absorption spectrum of **3** is compared with its derivatives in the literature, the Q band of **3** was shifted to 5 nm blue according to octakis(hexylthio)-substituted ZnPc and 22 nm red according to tetrakis(morpholinoetoxy)-substituted ZnPc.

Upon excitation at 615 nm, fluorescence measurements and fluorescent quenching tests of compound **3** were carried out in THF. The fluorescent emission, excitation, and absorption spectra of compound **3** are as in Figure 1. The fluorescence emission of **3** was found to be at 719 nm. The Stokes shift value calculated as 20 nm for compound **3** is consistent with the Stokes shift of Pcs calculated as 20-30 nm (41). The absorption and excitation spectra of **3** were similar and also observed as a mirror image of the fluorescent spectrum (30, 31).

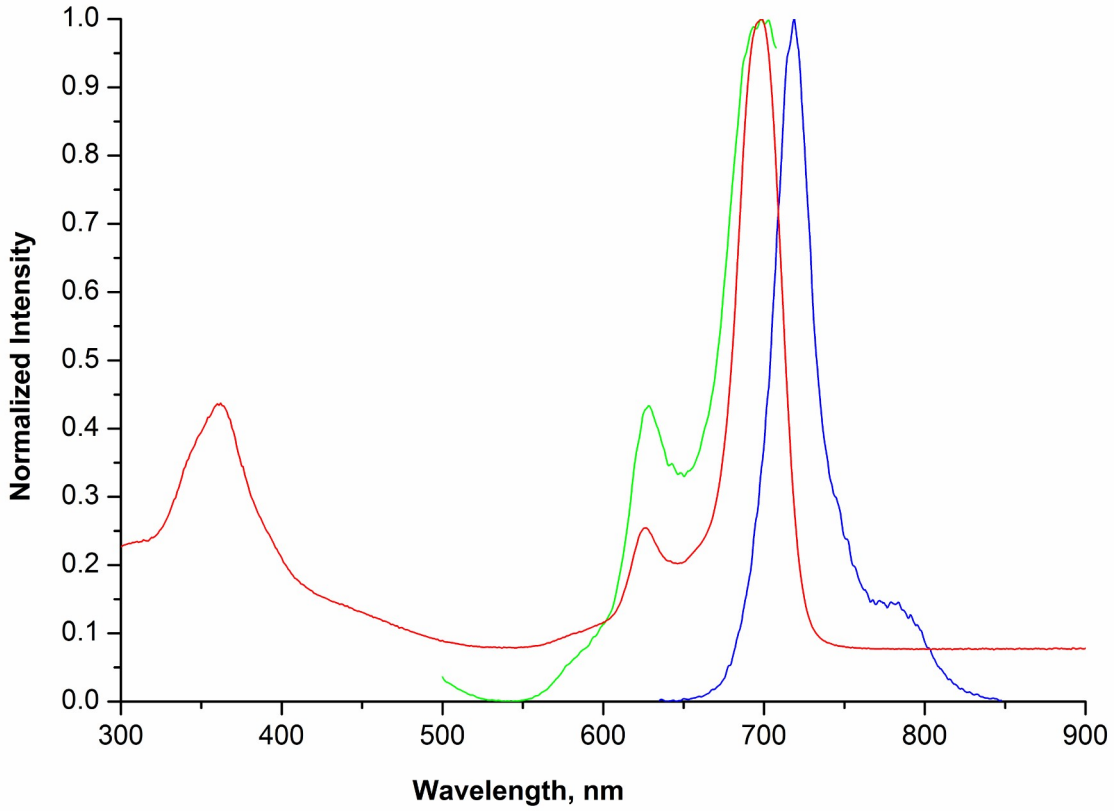

Figure 1: Absorption (red), excitation (blue) and emission (green) spectra of **3** in THF (4×10^{-6} M).

The fluorescence quantum yield (Φ_F) of unsubstituted ZnPc is 0.17 in DMF and was used as a reference in calculating the Φ_F value of compound **3**. The Φ_F value of **3** in the THF has been determined as 0.21, and this value is greater than the Φ_F value of the reference ZnPc (30, 31, 42). According to the literature, Dinçer and coworkers synthesized symmetric and unsymmetric Pcs bearing dipentoxymalonyl, chloro, and hexylthio units. They studied their photophysical properties and reported that the unsymmetric Pc (Φ_F = 0.13) exhibited a greater fluorescence quantum yield in $CHCl_3$ than the symmetric analog (Φ_F = 0.072) (12). In this study, the fluorescence quantum yield of morpholine substituted unsymmetric Pc (**3**) was found to be greater than the value of the symmetric and unsymmetric derivatives in the literature (12).

The natural radiation life (τ_o) and fluorescence life (τ_F) of compound **3** were determined as 6.34 ns and 1.33 ns, respectively. When the calculated values were compared with the values of the unsubstituted ZnPc (τ_o = 6.05, k_F = 1.03 ns), it was found that compound **3** have higher τ_o and k_F values (30, 31).

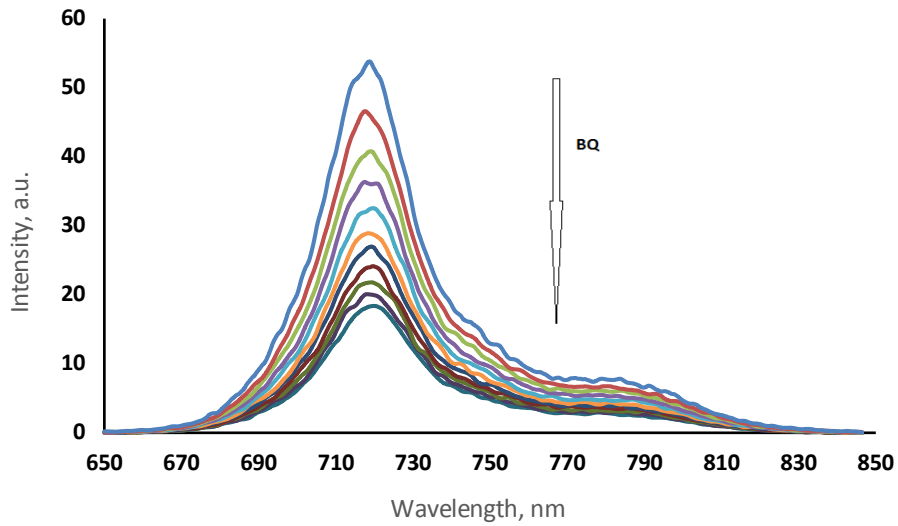

Figure 2: Fluorescent emission spectral changes of **3** (4 x 10^{-6} M) in THF in which different concentrations of hydroquinone in THF was added as quencher. [BQ] = 0.000, 0.008, 0.016, 0.024, 0.032, 0.040 M.

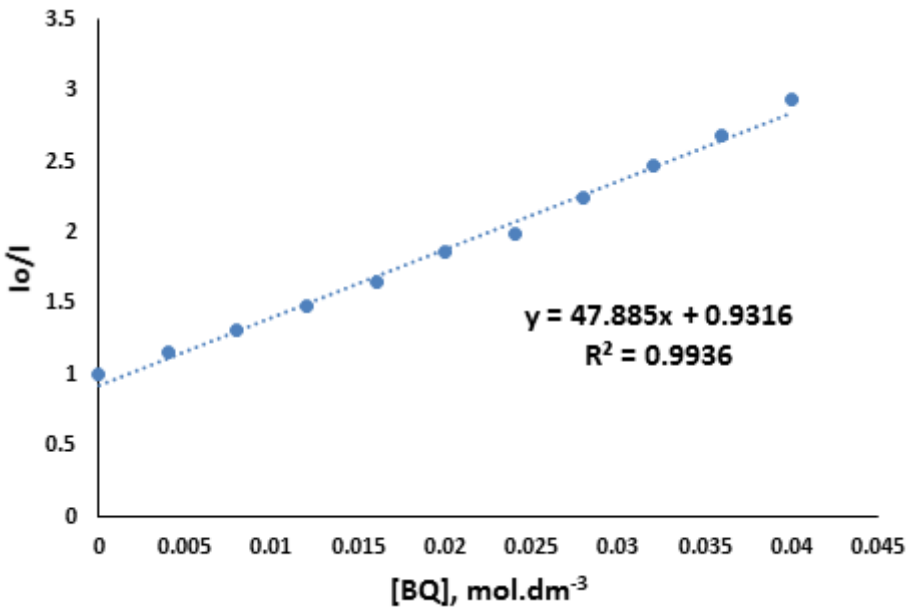

Figure 3: Stern-Volmer plot of **3** for BQ ([BQ] = 0.000, 0.008, 0.016, 0.024, 0.032, 0.040 M).

Fluorescent quenching studies of compound **3** were done by adding benzoquinone at different concentrations in THF, and it was observed that it complied with Stren-Volmer kinetics. The emission plots recorded after adding different concentrations of BQ to compound **3** are given in Figure 2. As the concentration of the BQ increases, the intensity of the emission peak appears to decrease. In addition, as seen in Figure 3, as a result of the diffusion-controlled quenching mechanism, the slope is linear, and the K_{SV} value was calculated as 47.89 M^{-1} (32, 33). kq (bimolecular quenching constant) value of compound **3** was calculated as 3.60x10^{10} s^{-1}. The K_{SV} and k_q values of compound **3** are smaller than the reference unsubstituted ZnPc (K_{sv} = 57.60 M^{-1}, k_q = 5.59x10^{10} s^{-1}).

CONCLUSION

It is reported from studies in the literature that morpholine groups positively change the biological activity of phthalocyanines. In addition, due to the electron donor feature of the sulfur atom, the hexylthio groups shift the Q band of phthalocyanines to the near IR region. Therefore, the synthesis of zinc phthalocyanine carrying hexylthio and morpholinoethoxy groups was thought to be a suitable candidate for biological applications. In this study, a novel peripherally substituted unsymmetric ZnPc (**3**) containing six hexylthio units, and a morpholine group was synthesized. The compound's characterization was successfully performed using various spectroscopic methods and

supported the accuracy of the proposed structure. Photophysical measurements of **3** were examined in THF. The fluorescence quantum yield and fluorescence lifetime for **3** were calculated and compared with the unsubstituted reference ZnPc, and octakis hexylthio substituted ZnPc and found to be greater than both unsubstituted and octa-substituted ZnPcs. Fluorescence quenching studies for compound **3** were performed in THF and with the addition of various concentrations of BQ. K_{SV} and kq values were calculated as a result of the fluorescence quenching studies. In comparison with unsubstituted zinc phthalocyanine, compound **3** showed lower Ksv and kq values. Compound **3** is a good candidate for biological applications due to its absorption in the near IR region and its higher fluorescence quantum yield than its derivatives in the literature.

ACKNOWLEDGMENTS

This work was supported by the Research Fund of the Istanbul Technical University.

REFERENCES

1. Hanack M, Schneider T, Barthel M, Shirk JS, Flom SR, Pong RGS. Indium phthalocyanines and naphthalocyanines for optical limiting. Coord Chem Rev. 2001;219:235–58.

2. Idowu M, Loewenstein T, Hastall A, Nyokong T, Schlettwein D. Photoelectrochemical properties of electrodeposited ZnO thin films sensitized by octacarboxymetallophthalocyanine derivatives. J Porphyr Phthalocyanines 2010;14:142–9.

3. Staicu A, Pascu A, Nuta A, Sorescu A, Raditoiu V, Pascu ML. Studies about phthalocyanine photosensitizers to be used in photodynamic therapy. Rom Rep Phys. 2013;65: 1032–51.

4. Jia X. Yang, FF, Li J, Liu JY, Xue JP. Synthesis and in vitro photodynamic activity of oligomeric ethylene glycol – quinoline substituted zinc(II) phthalocyanine derivatives. J Med Chem. 2013;56: 5797–805.

5. Ranyuk E, Cauchon N, Klarskov K, Gue B, van Lier JE. Phthalocyanine−peptide conjugates: receptor-targeting bifunctional agents for imaging and photodynamic therapy. J Med Chem. 2013; 56:1520–34.

6. Li X, Zheng BD, Peng XH, Li SZ, Ying JW, Zhao Y, Huang JD, Yoon J. Phthalocyanines as medicinal photosensitizers: Developments in the last five years. Coord Chem Rev. 2019; 379:147-60.

7. Zhao Y, Ying JW, Sun Q, Ke MR, Zheng BY, Huang JD. A novel silicon(IV) phthalocyanine-oligopeptide conjugate as a highly efficient photosensitizer for photodynamic antimicrobial therapy. Dye Pigment. 2020;172:107834, 1-8.

8. Korkmaz E, Ahmetali E, Atmaca GY, Karaoğlu HP, Erdoğmuş A, Koçak MB. Investigation of photophysical and photochemical properties of phthalocyanines bearing fluorinated groups. Monatshefte für Chemie. 2020;151:181–90.

9. Yenilmez HY, Sevim AM, Bayır ZA. Synthesis and photophysics of new metallo phthalocyanine complexes with thiazole groups and their fluorescence quenching studies with benzoquinone. Synthetic Metals. 2013;176:11– 7.

10. Özçeşmeci M, Baş SS, Akkurt B, Hamuryudan E, Bolkent Ş. Synthesis and Biological Uses of A3B Type Water-Soluble Phthalocyanine Alternate to Alcian Blue. ChemistrySelect. 2018;3,12805– 12.

11. Uslan C, İşleyen ND, Öztürk Y, Yıldız BT, Çakar ZP, Göksel M, Durmus M¸ Gürsel YH, Sesalan BŞ. A novel of PEG-conjugated phthalocyanine and evaluation of its photocytotoxicity and antibacterial properties for photodynamic therapy. J. Porphyrins Phthalocyanines. 2018;22:10–24.

12. Uğur AL, Dinçer HA, Erdoğmuş A. Synthesis, photophysical and thermal studies of symmetrical and unsymmetrical zinc phthalocyanines. Polyhedron. 2012;31:431–7.

13. Sakamoto K, Sakaguchi Y, Watabiki S, Igarashi Y, Komoriya T, Yoshino S. Synthesis of phthalocyanines having thio-alkyl substituents at non-peripheral positions and their photochemical and photophysical properties. J. Med. Chem. Sci. 2019;2:64-70.

14. Chen SX, Du SY, Wang YT, Zhao HC, Zhang YL, Yao L. Retinoic acid morpholine amide (RAMA) inhibits expression of Fas ligand through EP1 receptor in colon cancer cells. Tumor Biol. 2016; 37:323–9.

15. Pal'chikov VA. Morpholines. Synthesis and Biological Activity. Russian Journal of Organic Chemistry, 2013;49(6):787–814.

16. Poupin P, Mazure N, Truffaut N. Morpholine degradation by strain Mycobacterium aurum MOI : improvement of cells growth and morpholine degradation rate by cells immobilization. in R.H. Wijffels, R.M. Buitelaar, C. Bucke and J. Tramper (Eds) Immobilized Cells: Basics and Applications, Elsevier Science B.V; 1996.

17. Jachak GR, Ramesh R, Sant DG, Jorwekar SU, Jadhav MR, Tupe SG, Deshpande MV, Reddy DS. Silicon Incorporated Morpholine Antifungals: Design, Synthesis, and Biological Evaluation. ACS Med. Chem. Lett. 2015;6:1111−6.

18. Zhu YJ, Huang JD, Jiang XJ, Sun JC. Novel silicon phthalocyanines axially modified by morpholine: synthesis, complexation with serum protein and in vitro photodynamic activity. Inorg Chem Commun. 2006;9:473–7.

19. Nene LC, Managa M, Nyokong T. Photo-physicochemical properties and in vitro photodynamic therapy activity of morpholine-substituted Zinc(II)-Phthalocyanines π-π stacked on biotinylated graphene quantum dots. Dye Pigment. 2019;165:488–98.

20. Sindelo A, Kobayashi N, Kimura M, Nyokong T. Physicochemical and photodynamic antimicrobial chemotherapy activity of morpholine-substituted phthalocyanines: Effect of point of substitution and central metal. J Photochem Photobio A: Chemistry. 2019;374:58–67.

21. Dlugaszewska J, Szczolko W, Koczorowski T, Skupin-Mrugalska P, Teubert A, Konopka K, Kucinska M, Murias M, Düzgüneş N, Mielcarek J, Goslinski T. Antimicrobial and anticancer photodynamic activity of a phthalocyanine photosensitizer with N-methyl morpholiniumethoxy substituents in nonperipheral positions. J Inorg Biochem. 2017;172:67–79.

22. Kucinska M, Skupin-Mrugalska P, Szczolko W, Sobotta L, Sciepura M, Tykarska E, Wierzchowski M, Teubert A, Fedoruk-Wyszomirska A, Wyszko E, Gdaniec M, Kaczmarek M, Goslinski T, Mielcarek J, Muria M. Phthalocyanine derivatives possessing 2-(morpholin-4-yl)ethoxy groups as potential agents for photodynamic therapy. J Med Chem. 2015;58:2240−55.

23. Zheng BY, Lin T, Yang HH, Huang JD. Photodynamic inactivation of Candida albicans sensitized by a series of novel axially di-substituted silicon (IV) phthalocyanines. Dye Pigment. 2013;96:547-53.

24. Barut B, Demirbaş Ü, Şenocak A, Özel A, Kantekin H. Water soluble axially morpholine disubstituted silicon phthalocyanines: Synthesis, characterisation, DNA/BSA binding, DNA photocleavage properties. Synth Met. 2017;229:22–32.

25. Biyiklioglu Z. Electrochemical and aggregation properties of newly synthesized dendritic axially morpholine-disubstituted silicon phthalocyanine, mono-substituted subphthalocyanine and their quaternized derivatives. Inorg Chem Commun. 2015;55:60–4.

26. Burat AK, Koca A, Lewtak JP, Gryko DT. Synthesis, physicochemical properties and electrochemistry of morpholine-substituted phthalocyanines. J Porphyr Phthalocyanines. 2010;14:605-14.

27. Burat AK, Koca A, Lewtak JP, Gryko DT. Preparation, electrochemistry and optical properties of unsymmetrical phthalocyanines bearing morpholine and tert-butylphenoxy substituents. Synth Met. 2011,161:1537-45.

28. Gurek AG, Bekaroglu O. Octakis (alkylthio)-substituted phthalocyanines and their interactions with silver (I) and palladium (II) ions. J Chem Soc Dalton Trans. 1994;1419-23.

29. Koçan H, Kaya K, Özçeşmeci İ, Sesalan BŞ, Göksel M, Durmuş M, Burat AK. Photophysicochemical, calf thymus DNA binding and in vitro photocytotoxicity properties of tetra-morpholinoethoxy-substituted phthalocyanines and their water-soluble quaternized derivatives. J Biol Inorg Chem 2017;22:1251–66.

30. Karaoğlu HRP, Yenilmez HY, Koçak MB. Phthalocyanines formed from several precursors: synthesis, characterization, and comparative fluorescence and quinone quenching. Journal of Coordination Chemistry. 2018;71(15):2340-57.

31. Zorlu Y, Dumoulin F, Durmuş M, Ahsen V. Comparative studies of photophysical and photochemical properties of solketal substituted platinum (II) and zinc (II) phthalocyanine sets. Tetrahedron. 2010; 66(17):3248-58.

32. Du H, Fuh RCA, Li J, Corkan LA, Lindsey JS. PhotochemCAD: A Computer-Aided Design and Research Tool in Photochemistry. Photochem. Photobiol. 1998;68:141-2.

33. Rose J. Advanced Physico-chemical Experiments, first ed., Sir Isaac Pitman & Sons Ltd., London; 1964, p.257.

34. Leznoff CC, Hall TW. The synthesis of a soluble, unsymmetrical phthalocyanine on a polymer support. Tetrahedron Lett. 1982;23:3023-6.

35. Erdem SS, Nesterova IV, Soper SA, Hammer RP. Solid-phase synthesis of asymmetrically substituted "AB3-type" phthalocyanines. J Org Chem. 2008;73:5003-7.

36. Kobayashi N, Kondo R, Nakajima S, Osa T. New route to unsymmetrical phthalocyanine analogs by the use of structurally distorted subphthalocyanines. J Am Chem Soc. 1990;112:9640-1.

37. Kobayashi N, Ishizaki T, Ishii K, Konami H. Synthesis, spectroscopy, and molecular orbital calculations of subazaporphyrins, subphthalocyanines, subnaphthalocyanines, and

compounds derived therefrom by ring expansion. J Am Chem Soc. 1999:121;9096-110.

38. Kalkan A, Koca A, Bayır ZA. Unsymmetrical phthalocyanines with alkynyl substituents. Polyhedron. 2004;23:3155–62.

39. Haas M, Liu SX, Kahnt A, Leiggener C, Guldi DM, Hauser A, Decurtins S. Photoinduced energy transfer processes within dyads of metallophthalocyanines compactly fused to a ruthenium(II) polypyridine chromophore. J Org Chem. 2007;72:7533-43.

40. Kimura T, Kanota N, Matsui K, Tanaka I, Tsuboi T, Takaguchi Y, Yomogita A, Wakahara T, Kuwahara S, Nagatsugi F, Akasaka T. Preparation and electrochemical and optical properties of unsymmetrically substituted phthalocyanines with one or two trithiole rings and related symmetric derivatives. Inorg Chem. 2008;47:3577-83.

41. Özçeşmeci M, Nar I, Hamuryudan E. Synthesis and electrochemical and spectroelectrochemical characterization of chloromanganese(III) phthalocyanines. Turk. J. Chem. 2014;38:1064-72.

42. McKeown NB, Li H, Helliwell M, J. Porphyr. Phthalocyanines. A non-planar, hexadeca-substituted, metal-free phthalocyanine. 2005;9(12):841-5.

JOTCS A
Journal of the Turkish Chemical Society
Section: A
Chemistry
TURKISH CHEMICAL SOCIETY

Synthesis, characterization and antibacterial study of Co(II) and Cu(II) complexes of mixed ligands of piperaquine and diclofenac

Yusuf Oloruntoyin Ayipo[1,2*], Wahab Adesina Osunniran[2], Umar Muhammad Badeggi[3], Ismaila Olalekan Saheed[2], Akeem Adebayo Jimoh[2], Halimah Funmilayo Babamale[4], Emmanuel Olawuyi Olaide[2]

[1] Center for Drug Research, Universiti Sains Malaysia, 11800, Pulau Pinang, Malaysia.
[2] Department of Chemical, Geological and Physical Sciences, Kwara State University, Malete, P. M. B. 1530, Ilorin, Nigeria.
[3] Department of Chemistry, Cape Pennisula University of Technology, Cape Town, South Africa.
[4] Department of Chemistry, University of Ilorin, P. M. B. 1515, Ilorin, Nigeria.

Abstract: Pathogenic microorganisms develop incessant resistance toward antibiotics through various cellular defense mechanisms, thereby creating a search for chemotherapeutic alternatives, the potentials of which metal complexes of small-molecule drugs offer. In this study, Cu(II) and Co(II) complexes of mixed piperaquine and diclofenac were synthesized and characterized *via* magnetic moment determination, elemental analysis, FTIR, UV-Visible, 1D ^{1}H NMR, ^{13}C NMR spectroscopy and powder XRD, then evaluated for biological activities *in silico* and *in vitro*. The results provide evidence of coordination of the metal ions to ligands through N, COO and Cl groups with proposed octahedral geometry, low spin, paramagnetic, polycrystalline complexes. The physicochemical and pharmacokinetic parameters predicted *in silico* support bio-functionality and safety of the complexes. The complexes demonstrate strong inhibition against bacterial strains especially *Staphylococcus aureus in vitro*. Specifically, Cu(II) complex at 1% *w/w* inhibited a zone of 100 mm which is in multi-folds of the effects of piperaquine and diclofenac with 32 and 25 mm respectively, and better than ciprofloxacin with 92 mm. On DPPH assay, both complexes display better antioxidant potentials with respective IC_{50} of 165.09 and 382.7 µg/mL compared to ascorbic acid with 7526 µg/mL. Thus, the complexes represent therapeutic models for overcoming antibacterial resistance upon further study.

Keywords: Antibiotic resistance, bioinorganic, spectroscopy, powder XRD, biological study.

Submitted: March 18, 2021**. Accepted:** May 02, 2021**.**

Cite this: Ayipo Y, Osunniran W, Badeggi U, Saheed I, Jimoh A, Babamale H, et al. Synthesis, characterization and antibacterial study of Co(II) and Cu(II) complexes of mixed ligands of piperaquine and diclofenac. JOTCSA. 2021;8(2):633–50.

DOI: https://doi.org/10.18596/jotcsa.898523.

***Corresponding author. E-mail:** yusuf.ayipo@kwasu.edu.ng.

INTRODUCTION

Coordination chemistry between transition metal ions and various bioactive organic ligands have been employed to prepare several metal-organic chemical frameworks with enhanced pharmacological properties than the parent ligands. Upon coordination to metal ions, the systematic bioavailability, solubility, inertness for substitution, planar biocompatibility and other pharmaceutical profiles of the ligands become enhanced as well as the lipophilicity of the metal ions (1–3). The interesting medicinal profiles of these metal-based biomaterials stimulate the innovative design of various complex analogues for biological applications. A number of these hybrids are already approved or in clinical trials as anticancer/anti-pathogenic chemotherapeutics. Notably, the platinum-based anticancer drugs, Ga-68- and In-111-based complexes for radioimaging,

radiolabeling and therapy, gold-based Auranofin for treating rheumatoid arthritis, bismuth(III) ion-inclined bis(maltolato)oxovanadium(IV) with enhanced bioavailability and ability to reduce blood glucose in a clinical trial of diabetes, bismuth subcitrate and bismuth subsalicitrate (Pepto-Bismol) for treating peptic ulcers (4,5). Due to its coordination-induced action on bile acids and the disruption of charged cell walls of bacteria, the latter was proposed for further medicinal applications as an antacid and antibacterial agent. Some other new Bi(III)-containing bioactive complexes are continually under evaluation for antifungal, anticancer and antibacterial applicability (4).

Pathogenic microorganisms, especially bacteria, rapidly develop several defense mechanisms against antibiotics. These include the formation of biofilm, cell wall, encase efflux pumps, regulation of genetic and other intracellular materials (6). The intensive application of antibiotics over a long period and frequent exposure to non-lethal concentration also contribute to the incessant resistance of bacteria towards small-molecule drugs with specifically "bullet target" mode of action, which has, in turn, poses a great threat to the global healthcare (7), and thereby make a search for innovative therapeutic designs to overcome these healthcare challenge becomes imperative. Consequently, several conjugates involving antimalarial and antimicrobial ligands have been designed with improved combinatorial pharmacology (8). However, metal complex polymers inclusively exhibit a multi-target mechanism that favours several cellular processes, leading to their pleiotropic effects on the drug-resistant bacterial cells, thus become promising agents under the United Nation (UN) sustainable developmental goal 3.3 for prevention and treatment of communicable diseases (9). Some of these agents have been designed using organic small-drug molecules such as sulfadoxine, sulfisoxazole, quinazoline, pyrimethamine, quinoline, pyrazolone, phenylhydrazine etc with improved pharmacological profiles due to favourable pharmacophoric moieties of ligands (singly/mixed) in coordination to metal ions such as Co(II), Cu(II), Mn(II), and Zn(II) (10–15). However, none has been reported of mixed ligands involving piperaquine (Pip) and sodium diclofenac (NaD). In our previous studies, we have demonstrated impressive antioxidant and bactericidal activities of Cu(II), Zn(II), and Co(II) complexes consisting of piperaquine, acetaminophen and acetylsalicylic acid as mixed ligands (16).

Therefore, this study aims at the preparation of coordination compounds consisting of Co(II) and Cu(II) ions in complex with sodium NaD and Pip as mixed ligands using solvent-based inorganic synthetic approach, characterization and evaluation of antioxidant and antibacterial activity *in vitro* as well as some *in silico* biological studies, while adopting some reported protocols (10,14–18) with modifications.

MATERIALS AND METHOD

Materials

The materials were used as commercially obtained without further purification. These include copper(II) chloride hexahydrate ($CuCl_2.6H_2O$), cobalt(II) chloride hexahydrate ($CoCl_2.6H_2O$), distilled H_2O, ethanol, methanol, acetone, dimethyl sulfoxide (DMSO), lactic acid, acetic anhydride, and silica gel-coated thin layer chromatographic (TLC) plate from Sigma Aldrich, England. The ligands, Pip and NaD were obtained from Zhuhai Rundu Pharmaceuticals, China and Tuyil Pharmaceutical, Nigeria, respectively.

Synthesis of Copper(II) Complex of Mixed Piperaquine and Diclofenac

The Cu(II) complex of mixed Pip and NaD ligands was prepared by reacting a 0.002 mol of $CuCl_2.6H_2O$ previously dissolved in 20 mL of distilled H_2O with 0.002 mol Pip in 20 of mL hot distilled water and subsequently adding a solution containing 0.002 mol NaD in 20 mL of methanol. The mixture was refluxed for 2 hours and 30 minutes after which the resulting stable precipitates formed (Scheme 1) were filtered, washed with hot water, then cold water twice to remove unreacted ligands and kept in a desiccator with $CaSO_4$ for 24 hours. The progress of the reaction was monitored using TLC. Yield: 3.62 g (38%); M.P. 231 – 232 °C; UV (DMSO) λ_{max} (nm): 248, 342, 704; FTIR (KBr) ν_{max} (cm^{-1}) 3323 (H_2O), 1592 $(COO)_{asy}$, 1380 $(COO)_{sym}$, 741, 662 (CCl), 504, 562 (Cu-O/N); ^1H NMR (d_6-DMSO, 400 MHz) 6.27 (d, J = 7.2 Hz), 6.86 (d), 7.05 (d), 7.18 (d), 7.51 (d, 8.4 Hz), 7.66 (d, J= 9.6 Hz), 8.21(br, s), 3.45 (br), 3.21 (br), 3.16 (s), 2.06 (br, s), 3.91(br), 1.20 (s) ppm. ^{13}C-NMR (d_6-DMSO, ~100 MHz) 49.1, 49.4, 51.4, 53.7, 116.4, 121.3, 124.4, 126.1, 127.1, 128.1, 129.6, 130.4, 131.4, 137.5, 143.1 ppm. Anal. Calcd. Mass fractions of elements, w/%, for $C_{43}H_{53}Cl_6CuN_7O_8$ (M_r = 1073) are C 48.17, H 4.98, Cu 5.93, N 9.14; Found: C 47.21, H 5.35, Cu 6.14, N 9.80.

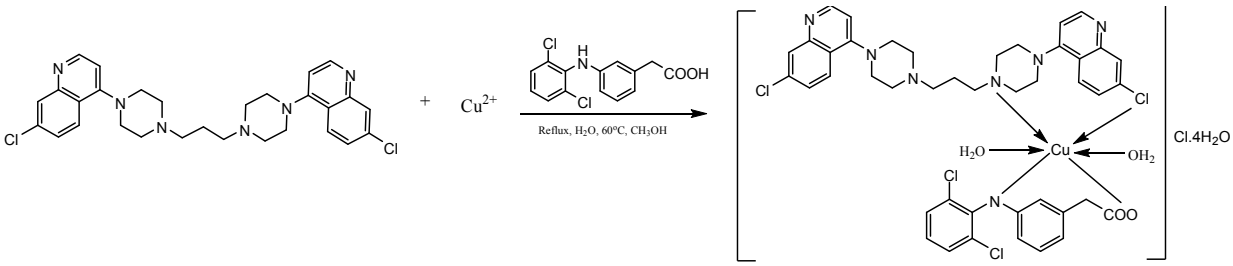

Scheme 1: Proposed reaction pattern between mixed piperaquine/diclofenac and Cu(II) ion.

Synthesis of Cobalt(II) Complex of Mixed Piperaquine and Diclofenac

The Co(II) complex of mixed Pip and NaD was synthesized by refluxing 0.002 mol of NaD previously dissolved in 20 mL methanol with 0.002 mol of Pip dissolved in 20 mL hot water and 0.002 mol of $CoCl_2.6H_2O$ under constant stirring for 5 hours and 30 minutes after which a stable pink precipitate was formed (Scheme 2). The precipitates were filtered, washed with hot water, then twice with cold water and dried in a desiccator for 24 hours. The progress of the reaction was monitored using TLC. Yield: 4.12 g (47%); M.P. 230 – 234 °C; UV (DMSO) λ_{max} (nm): 232, 450, 662; IR (KBr) ∇_{max} (cm^{-1}) 3323 (H_2O), 1590 $(COO)_{asy}$, 1380 $(COO)_{sym}$, 741, 662 (CCl), 520, 574 (Co-O/N); ^1H NMR (d_6-DMSO, 400 MHz) 2.07 (s), 3.17 (s), 3.71 (s), 6.28 (d, J= 8.4Hz), 6.86 (t), 7.06 (t), 7.16 (s), 7.19 (d, J=8.0Hz), 7.50 (d, J-=8.00Hz), 7.20 (d, J=8.8 Hz) ppm. ^{13}C-NMR (d_6-DMSO, ~100 MHz) 49.3, 116.5, 121.5, 125.9, 128.2, 129.8, 130.4, 131.5, 137.5, 143.2. Q= 125.9, 130.4, 139.5, 143.2 ppm. Anal. Calcd. Mass fractions of elements, w/%, for $C_{43}H_{51}Cl_6CoN_7O_7$ (M_r = 1050) are C 49.21, H 4.90, Co 5.62, N 9.34; Found: C 48.16, H 4.85, Co 5.81, N 9.48.

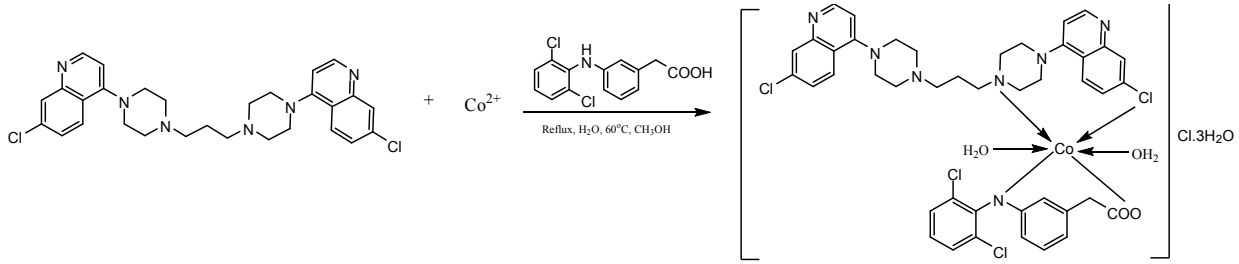

Scheme 2: Proposed reaction pattern between mixed piperaquine/diclofenac and Co(II) ion.

Characterization

The melting point of the synthesized complexes was recorded on a Gallenkamp melting point apparatus. Solubility tests of the ligands and the complexes were carried out using acetone, dilute lactic acid, distilled water, methanol and dimethyl sulfoxide while the ionic properties of the ligands and their corresponding metal complexes were measured using a conductivity meter CDM 210, MeterLab model. The functional groups in the ligands and the complexes as well as the coordination-induced shifts in spectral bands were identified by loading their disc-powder on FTIR (Shimadzu, Japan) with a scan range of 400-4000 cm^{-1} wavenumber, resolution of 4 cm^{-1} using KBr pellets as blank. The electronic (UV-Visible) spectra of the complexes in solution were run in the range 190-900 nm on a Perkin Elmer *20λ* spectrophotometer with the samples placed in quartz cuvettes of 1 cm path length and DMSO was used as a blank. The magnetic susceptibility of the metal chelates was determined on a Gouy balance at room temperature using $Hg[Co(SCN)_4]$ with the corrections of diamagnetic on Pascal's constants.

Powder X-ray Diffraction Spectroscopy

D8 Advance diffractometer, with the measurement of continuous ∂-∂ scan in a locked coupled-mode having a tube of Cu-Kα radiation ($\lambda K\alpha_1$=1.5406Å) and detector of LynxEye (Position sensitive detector) was employed for the powder X-ray diffraction analysis at iThemba Scientific Lab., South Africa. The diffractograms were studied to identify the powdered-crystal structures and morphology of the complexes while the value for 2θ for Miller indices estimation was determined using the Bragg's law (Eq. 1) (19,20):

$$\lambda = 2\, d_{hkl} \sin\theta \qquad \text{(Eq. 1)}$$

Where λ = X-ray wavelength (Cu = 1.5406 Å), d = interplanar distance and θ = diffraction angle.

The crystalline domain sizes indicated by the broadening of the peak especially when the sizes of the crystal become small were estimated theoretically using the Scherrer equation (Eq. 2) (21):

$$D = \frac{k\lambda}{\beta \cos\theta} \quad \text{(Eq. 2)}$$

Where D = crystalline domain size, k = Scherrer constant usually given as 0.9 and β = peak width at half of its height

^{1}H NMR, ^{13}C NMR and DEPT-135 NMR Spectroscopy

The Nuclear magnetic resonance (NMR) spectroscopy NMR spectra of the complexes were recorded at 25 °C on a Bruker Avance 400 MHz NMR spectrometer (Germany), with deuterated Dimethyl sulfoxide (DMSO) used as a solvent. Chemical shifts of ^{1}H (δH) and ^{13}C (δC) and DEPT (δC) were determined in ppm, relative to tetramethylsilane as reference.

Elemental Analyses

The percentage by mass of some major elements in the complexes such as C, H, N and Cu/Co (M) was determined using the Vario El Cube Elemental Analyzer at the Central Analytical Facilities, Stellenbosch University, South Africa.

Preliminary Test for Water Molecule and Chloride Ion

The presence of water of crystallization within or outside the coordination sphere of each complex was assessed using cobalt chloride paper. The color change of the paper from blue to pink indicates positive test. For the chloride ion outside the coordination sphere, aqueous $AgNO_3$ and NH_4OH were used for confirmation on the solution of each complex while a white precipitate soluble in excess NH_4OH indicate the presence of uncoordinated Cl^- ion.

Determination of Water of Crystallization

The presence of some water of crystallization in the complexes is confirmed by heating the sample to a constant weight, testing the gas evolved with cobalt(II) chloride paper, anhydrous copper (II) sulfate. The amount of water of crystallization was determined using the Eq. 3 below.

$$\frac{\text{mass of anhydrous complex}}{\text{molecular mass of anhydrous complex}} = \frac{\text{mass of hydrated complex}}{\text{molecular mass of hydrated complex}} \quad \text{(Eq. 3)}$$

Biological activity

In silico predictions of biological activity and ADMET properties

The broad spectrum of biological activities resulting from the interactions of the synthesized complexes with various enzymes/proteins responsible for bio-functions was predicted using the cheminformatics and bioinformatics interface of Molinspiration server (https://molinspiration.com/cgi-bin/properties) by the input of SMILES file in each case. The Java tools incorporated within the server supports computational analysis through the algorithm of active training sets generation from which the cumulative bioactivity of the target molecules is predicted through probable fragments. Each sample was scored for likeliness in activity through various inhibition mechanisms on G protein-coupled receptor (GPCR), kinase, nuclear receptor, and enzyme as well as ability to modulate ion channel.

The physicochemical and pharmacokinetics profiles of the complexes were predicted in terms of adsorption, distribution, metabolism, excretion and toxicity (ADMET) using the web-based Swiss ADME computational tools by inputting the SMILES file of each complex (17,22). The properties further reveal the drug-likeness of the molecules under study.

Antioxidant properties

The sample of each complex and the standard, ascorbic acid was weighed into the sample bottle, 9 mL of the solvent was added to each sample to make a solution of 100, 200, 300, 400 and 500 µg/mL. Each solution was then partitioned into three (3 mL each) for triplicate tests and transferred into the test tube. A 0.0039 g of DPPH was weighed into a reagent bottle and 100 mL of the ethanol was added and 3 mL of DPPH solution was added into each test tube containing the test sample. The setup in test tubes was kept in a dark room for thirty minutes after which absorbance was read at 517 nm wavelength. The IC_{50}, which stands for the concentration of fraction required for 50% scavenging activity, was calculated from the dose-inhibition linear regression equation (eqn. 4) for each complex.

$$\%\text{inhibition} = \frac{(\text{Abs}_{control} - \text{Abs}_{sample})}{\text{Abs}_{control}} \times 100 \quad (4)$$

Antibacterial Screening

The solutions of the ligands and the synthesized complexes were tested against strains of some gram-positive and gram-negative bacteria, *Pneumonia aeruginosa, Escherichia coli* and *Staphylococcus aureus* to determine and compare their potential bactericidal activities by measuring their inhibition zones around the inoculated organism wells, adopting agar dilution techniques as well as the standard recommendation of Clinical and Laboratory Standards Institute, 29th Edition (16,23).

RESULTS AND DISCUSSION

Some physicochemical properties such as solubility, melting point, and color of the ligands and the corresponding metal complexes are presented in Table 1. The complexes, ligands and metal salts

were mostly insoluble in organic solvents of acetone and methanol but all are soluble in DMSO, possibly due to its high polarity and donor strength (14) which enhance its ionic interaction with the samples in solution. The ionic nature of the complexes as shown by the conductivity results could be traced to the presence of electropositive metal ions in their structures compared to the parent ligands. The melting points of the complexes are lower when compared to the salts/ligands and the sharpness could imply a good purity of the complexes (24). The significant changes in the melting points, as well as colors between the ligands and their respective metal complexes, indicate a change in the atomic structures, possibly due to chemical coordination. Invariably, this could affect new electronic transitions and the ligand-metal lattice structures (12,25) as we observed in the subsequent characterization results.

The Infra-Red spectroscopy data of the ligands and the metal complexes are presented in Table 2, Figures 1 & 2. The spectra of the ligands and metal complexes were studied and compared to identify the mode and sites of metal-ligand chelation. The band at 3259 cm^{-1} which could be assigned to the N-H group of NaD ligand disappeared in the two complexes. Similarly, the stretching bands at 3286 and 3433 cm^{-1} attributable to the two asymmetric piperazinyl and imine N-groups of the Pip ligand have significantly undergone bathochromic and hypsochromic shifts respectively in the complexes, indicating the possibility of their participation in coordination. More so, the spectral bands of 1398 and 1575 cm^{-1} which are assignable to the symmetric and asymmetric COO group in the NaD ligand have shifted to a higher and lower wavenumber of 1592/1590 and 1380/1380 in the Cu(II) and Co(II) complexes respectively with a significant difference. The difference in the asymmetric and symmetric stretching vibration of the COO groups, $\Delta = \nu(COO)_{asy} - \nu(COO)_{sym}$ gave a value of 212 and 210 cm^{-1} for Cu(II) and Co(II) complex respectively, indicating the contribution of the COO of NaD to coordination as a monodentate ligand (15) with the Δ value of 177 cm^{-1} which agrees with the ionic value of NaD. These also support the possibility of bidentate-chelation between NaD to both Cu(II) and Co(II) ions through the NH and COO (25,26). In a similar pattern, Pip, a nitrogen-based ligand, shows coordination to the metal ions through the amine N and the Cl as evidenced by the disappearance of the band 3286 cm^{-1} attributable to the amine N with Δ value of 147 cm^{-1}, and also the hypsochromic shift of C-Cl band at 650 cm^{-1} in the ligand to 662 cm^{-1} in the metal complexes, indicating the possibility of coordination through the Cl group. These rationally suggest the ligand to act as a bidentate ligand (16). The complexes show weak/medium bands in the range 504 – 662 cm^{-1} which are tentatively assigned to M-N/O/Cl stretching vibrations and also contributing to the evidence of coordination. The spectra bands at 3433 and 3323 in both ligands and the complexes indicate H_2O-metal chelation (Figures 1 & 2) (27).

Table 2: Major IR bands of the ligands and their complexes.

Ligands/ Complexes	**ν (NH)asy (NH)sym cm^{1-}**	**δ (NH) cm^{1-}**	**ν (COO)asy (COO)sym cm^{1-}**	**ν (CCl) cm^{-1}**	**Δ cm^{-1}**	**ν (MO/N) cm^{-1}**
NaD	3259	1507	1575 1398	747	177	--
Pip	3433 3286	1503	-	650	147	-
[Cu(NaD)(Pip)]	3323	1506	1592 1380	741 662	212	504, 562 614
[Co(NaD)(Pip)]	3323	1506	1590 1380	741 662	210 for COO	520, 574, 611

Table 1: Some physicochemical parameters of the ligands and metal complexes.

Complexes/ Ligands/Metals	**Cond. ($\Omega^{-1}cm^{-1}$)**	**Solubility**						**M.P. (°C)**	**Color**
		D. H_20	LA	AES	DMSO	Me_2CO	MeOH		
NaD	-	NS	S	PS	S	PS	S	289-290°C	White
Pip	-	PS	S+Δ	PS	S	PS	NS	250-252°C	White
$CuCl_2.6H_2O$	ND	S	S	NS	S	NS	NS	486-490°C	Blue
$CoCl_2.6H_2O$	ND	S	S	S	S	S	NS	735-737°C	Brick Red
[Cu(NaD)(Pip)]	1.6×10^{-4}	PS+Δ	NS	PS+Δ	S	NS	S+Δ	231-232°C	Blue
[Co(Pip)(NaD)]	2.1×10^{-4}	NS	NS	NS	S	NS	PS+Δ	230-234°C	Brown

S = Soluble, NS = Not soluble, PS = Partially soluble, Δ =Heat, AES= Aqua ethanolic solution LA= Lactic acid, D.H_2O=Distilled water, DMSO= Dimethyl sulfoxide, MeOH = Methanol, Me_2CO = Acetone, ND = Not determined.

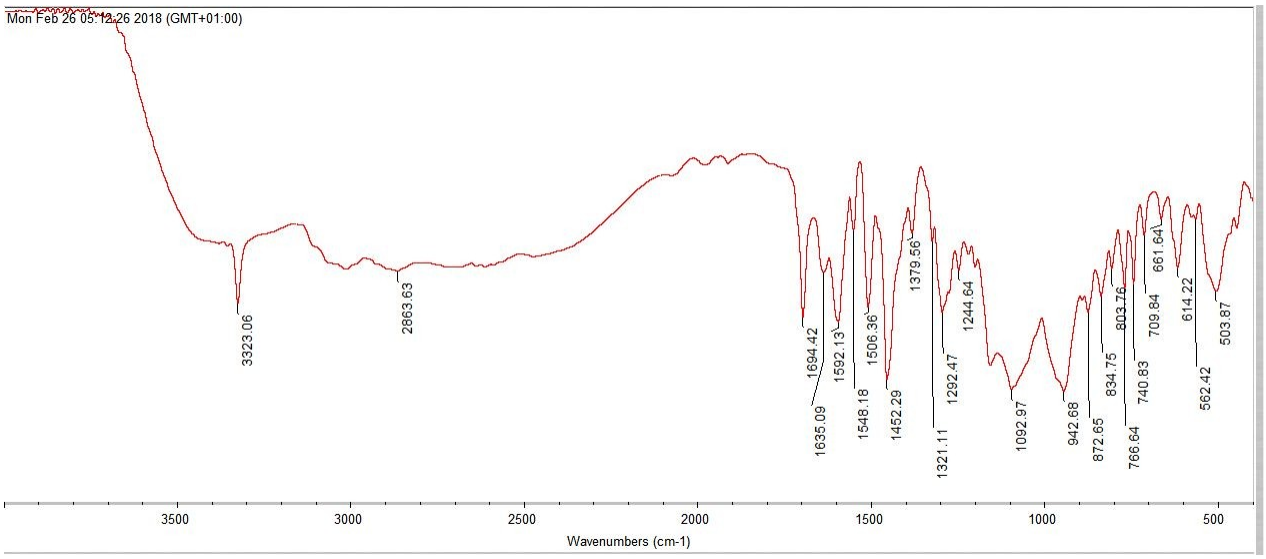

Figure 1: FTIR Image of [Cu(NaD)(Pip)].

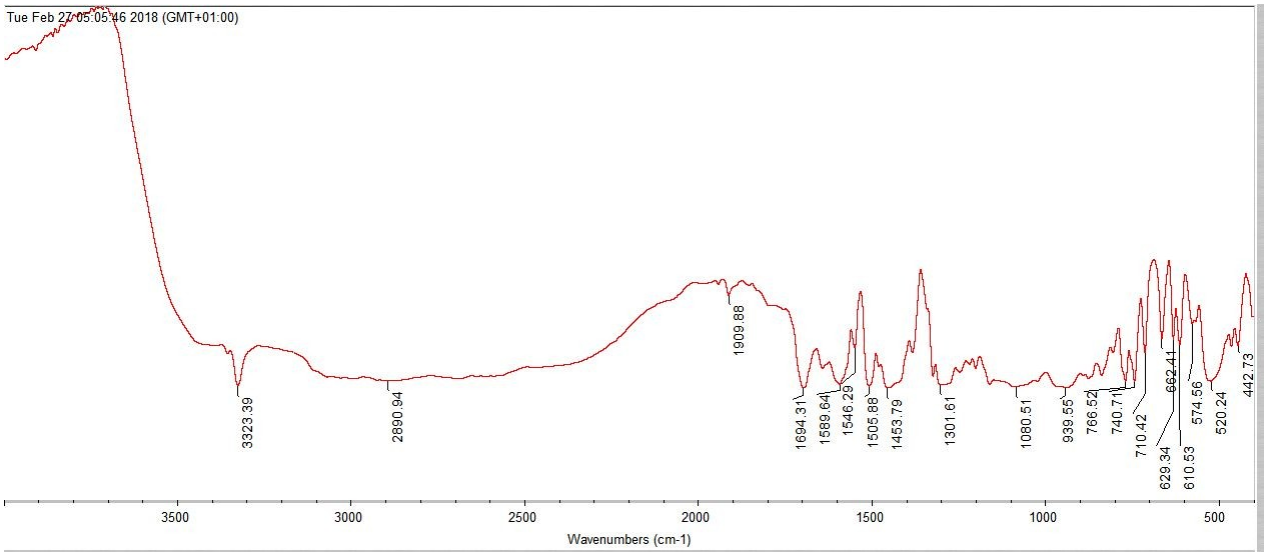

Figure 2: FTIR Image of [Co(NaD)(Pip)].

The electronic spectra, magnetic moment, and elemental analysis results of the synthesized metal complexes are reported in Table 3. The Cu(II) and Co(II) complexes have a low spin of d^9 and d^7 configurations respectively with the highest filled orbital as $^2t_{2g}$ (xy, xz, yz). Thus, the ground state is paramagnetic and labelled ^2E_g and $^4T_{1g}$ respectively. The electronic spectra of the ligands in DMSO exhibited transition at 202 nm – 379 nm which were assigned to intra-ligand transitions (n → σ*, n → π* and π → π*). The UV-Visible spectra of the [Cu(Pip)(NaD)] show a single broad absorption band at 704 nm assignable to $^2E_g \rightarrow {}^2T_{2g}$ transition, while [Co(Pip)(NaD)] had three bands within the visible region, 450, 539, and 662 nm assignable to $^4T_{1g}(F) \rightarrow {}^4T_{2g}(F)$, $^4T_{1g}(F) \rightarrow {}^4A_{2g}(F)$ and $^4T_{1g}(F) \rightarrow {}^4T_{1g}(P)$ transitions respectively, thus, suggesting the formation of octahedral geometry with hybridizations of sp^3d^2 and dsp^3d for [Cu(Pip)(NaD)] and [Co(Pip)(NaD)] respectively (17,28,29). The magnetic susceptibility measurement revealed that the Cu(II)- and Co(II)-containing complexes have effective magnetic moments of 1.53 and 1.47 B.M. respectively, further strengthening the octahedral geometry suggested for the complexes arising from their unpaired electrons (17,30,31). The presence of the ligands in the complexes as proposed (Schemes 1 & 2) was supported with good consistency between the CHNS elemental analysis results (Supplementary file) and the suggested molecular formulas.

The preliminary assay by heating indicates the presence of water of crystallization in the complexes when each sample was gently heated to a constant weight of 3.38 and 3.91 g for Cu(II) and Co(II) complex, respectively. This was further confirmed by testing the evolved gases with cobalt chloride paper which changed from blue to pink color. The estimates using Eq. 3 support the proposal of 4 and 3 molecules water of crystallization in one molecule of their respective complexes. Although, a more accurate analysis

such as the thermogravimetric analysis (TGA) is required for further confirmation. In a similar preliminary test, a white precipitate was observed upon the addition of aqueous $AgNO_3$ to the solution of each complex. The precipitates became dissolved when excess NH_4OH was added, tentatively indicating the presence of Cl^- outside the coordination sphere.

^{1}H NMR, ^{13}C NMR and DEPT-135 NMR Spectroscopy

The ^{1}HNMR spectrum (Figure 3A) of [Cu(Pip)(NaD)] whose formation was reported at the synthesis section (Scheme 1), was run in deuterated DMSO. From the NaD moiety, the signals at 8.21 and 3.45 ppm are both singlets and can be assigned to nitrogen proton between the aromatic rings and methylene proton situated between carbonyl carbon and aromatic ring which might have shifted them further upfield. In the aromatic region, the signals at 7.18 (s) and the doublet 7.66 ppm (d, J= 9.6 Hz) can be assigned to other unsubstituted benzene rings of the NaD ligand. The chemical shifts were rather downfield compared to neighboring benzene which is doubly substituted with chlorine atoms. On the Pip moiety, the chemical shifts at 6.27 ppm (d, J = 7.2 Hz) and 7.51 ppm (d, J = 8.4 Hz) could be rationally assigned to the unsubstituted benzene rings while the downfield signals at 1.20, 2.06, 3.16 and 3.21 ppm are assignable to the shielded CH_2 groups of the piperazinyl moieties. The ^{13}C-NMR (Figure 3B) in the same vein shows 21 carbon atoms as expected of both Pip and NaD in the aromatic carbons (116.1 - 143.1) ppm. However, the reduced intensities of signals at 49.1, 49.4, 51.5 and 53.7 ppm can be ascribed to the methylene of the two ligands contained in the aliphatic region. Thus, the two ligands are represented in the complex accordingly.

From the nuclear magnetic resonance spectroscopy values obtained for [Co(Pip)(NaD)] using DMSO, both ligands were adequately represented. More study of the NaD moiety (Scheme 2) reveals two conspicuous singlets at 3.17 and 3.71 ppm (Figure 3C), corresponding to the protons adjacent to the carbonyl carbon and the amino proton in between the benzene rings respectively. Downfield the aromatic region, the only singlet at 7.16 ppm is due to an aromatic proton adjacent to the chloro-substituted carbon in the Pip ring. Since there are four doublets overall, the more deshielded protons would be those close to the chlorine atom in the diclofenac moiety. This is because of the electron-withdrawing ability of chlorine atoms, thereby shifting the protons further downfield at 7.50 ppm. Similarly, the doublet on the chloro substituted ring on the Pip would also feel this effect and their neighborhood with chlorine. This has also caused the protons deshielded although not as the previous one. Therefore, the signal at 7.20 ppm can be reasonably assigned to them. Other signals at 7.19 and 6.25 ppm are assignable to the doublet of the remaining rings in Pip and NaD moiety respectively. Also, the triplets at 6.86 ppm and 7.06 ppm from the spectra can be unambiguously assigned to signals of the two rings of the NaD ligand. The difference in values is due to the proximity of protons to an electron-withdrawing entity (7.06 ppm) and others for electron donor substituents attach to the resonating rings.

The ^{13}C-NMR (Figure 3D) supports the above assignment and further corroborated by DEPT-135 values. When intensities of the signals are carefully observed, the total number of carbon atoms from the spectra matches the two ligands which further explain their involvement in the coordination. The DEPT-135 (Figures 3E & 3F) also revealed quaternary carbons between 130.4 – 143.2 ppm (15,25).

Some copper(II) complexes reported exhibit paramagnetism in relevance to their electronic configurations which allow a $d_{x^2-y^2} \rightarrow d_{xy}$ transition and this supports various biomedical applications including imaging, on-site delivery and antimicrobial effects (32). Suggestively, the broad, almost unreadable signals between 3.45 – 3.91 ppm and 3.17 – 3.89 ppm in Cu(II) and Co(II) complex, respectively (Figure 3A & 3C) could have rationally resulted from the effects of the unpaired electron spin exerted on the nuclear spin relaxation, depending strongly on the spatial distance of the paramagnetic centre to the nucleus and the nature of the paramagnetic center itself. The pseudo-contact shifts possibly induced by the interaction between nucleus spin and the magnetic dipole produced by the spinning of unpaired electrons. It could be suggested that the nucleus of atoms bond directly to the paramagnetic center (33,34) and further supports the argument for paramagnetic complex formation in both cases as previously proposed from the electronic configuration, possible hybridization, electronic transition and magnetic moments. The essential application mostly relevant to this study is their DNA cleaving ability peculiar to Cu(II) and Co(II) ions (35), which further supports the bactericidal activity of their complexes. Nonetheless, electron paramagnetic resonance (EPR) is necessarily required for further validation of this biologically important hypothesis.

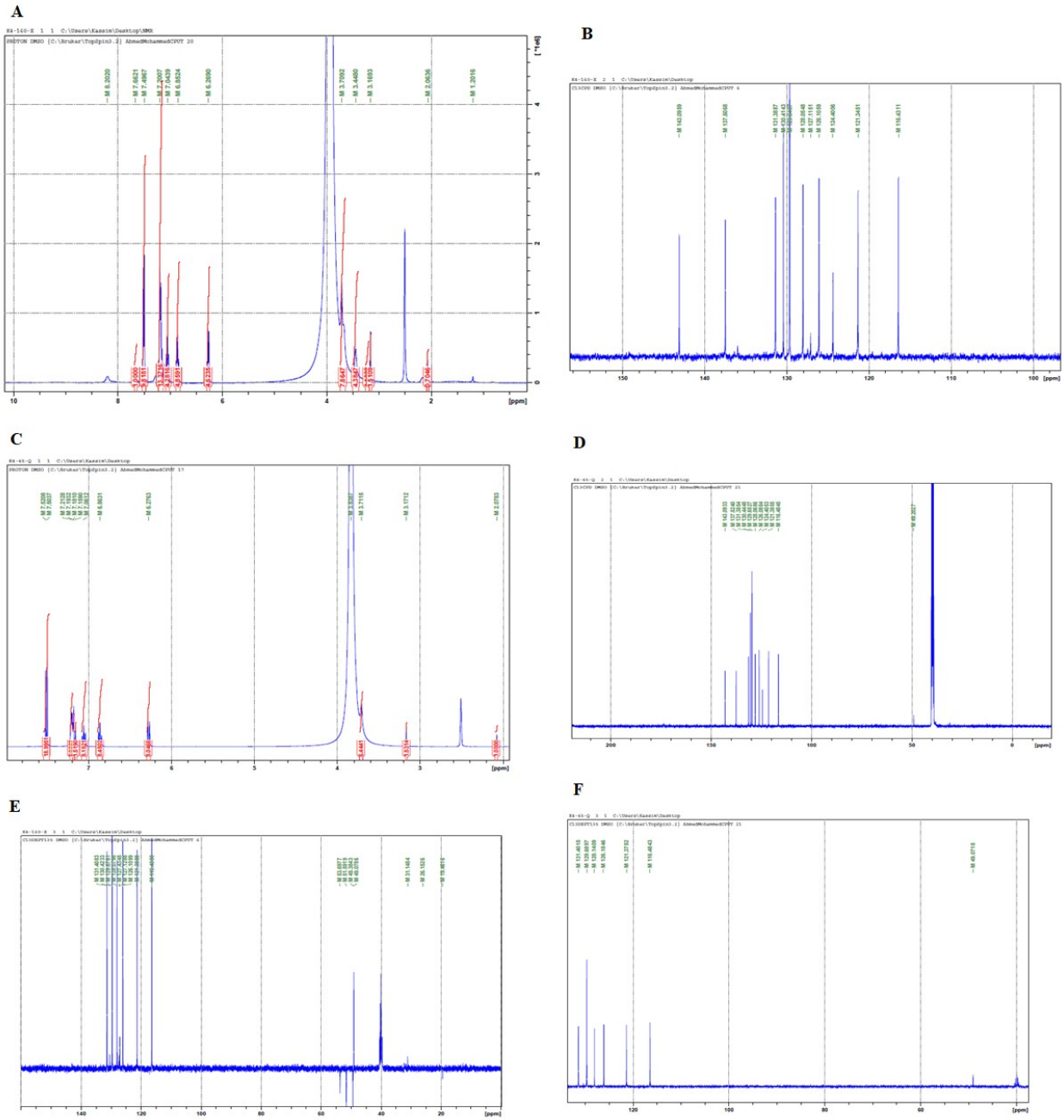

Figure 3: Nuclear magnetic spectra of the complexes (A) ^{1}H NMR of [Cu(Pip)(NaD)] (B) ^{13}C NMR of [Cu(Pip)(NaD)] (C) ^{1}H NMR of [Co(Pip)(NaD)] (D) ^{13}C NMR of [Co(Pip)(NaD)] (E) DEPT-135 NMR of [Cu(Pip)(NaD)] (F) DEPT-135 NMR of [Co(Pip)(NaD)]

Table 3: Results of Electronic Transition and Elemental Analysis.

Compounds	λ_{max} (nm)	$\bar{\upsilon}$ (cm^{-1})	Transition	$\mu_{eff\ (B.M)}$	Elemental % Calculated (Found)			
					C	H	N	M
NaD	270	42553	$\pi \rightarrow \pi^*$	-				
	364	25381	$n \rightarrow \pi^*$					
Pip	202	49505	$n \rightarrow \sigma^*$	-				
	379	26385	$n \rightarrow \pi^*$					
[Cu(Pip)(NaD)]	704	14205	$^2E_g \rightarrow {}^2T_{2g}$	1.53				5.93 (6.14)
	342	29240	$n \rightarrow \pi^*$					
	248	40323	$\pi \rightarrow \pi^*$		48.17 (47.21)	4.98 (5.35)	9.14 (9.80)	
[Co(Pip)(NaD)]	662	15106	$^4T_{1g}(F) \rightarrow {}^4T_{2g}(F)$	1.47				
	539	18553	$^4T_{1g}(F) \rightarrow {}^4A_{2g}(F)$					5.62 (5.81)
	450	22222	$^4T_{1g}(F) \rightarrow {}^4T_{1g}(P)$					
	232	43103	$n \rightarrow \pi^*$		49.21 (48.16)	4.90 (4.85)	9.34 (9.48)	

Powder X-ray Diffraction

The XRD data presented in Tables 4 & 5 revealed the diffraction patterns of the complexes, the estimated Miller indexing (hkl) and the crystal structures by mathematical method (36). The interplanar distances, "d" was determined using Bragg's equation (Eq. 1). The diffractograms indicate that the two complexes are polycrystallites in structure due to their peak profiles. The result data in Table 4 & 5 confirm some of the crystals as simple, body-centered, face-centered cubic and overall orthorhombic having conformed to the eqn. 5 & 6 (36–38):

$$\frac{1}{d^2}=\frac{h^2+k^2+l^2}{a^2} \qquad \text{(Eq. 5)}$$

for reflections cubic crystal and

$$\frac{1}{d^2}=\frac{h^2}{a^2}+\frac{k^2}{b^2}+\frac{l^2}{c^2} \qquad \text{(Eq. 6)}$$

for overall orthorhombic conformations (28,36).

The data also confirmed the novelty of the complexes, i.e. different from those of the existing organic and inorganic compounds on the JCPDS files, as supporting evidence of new compounds. Also, the atomic lattice structure of the ligands and that of the metal salts (found in the existing JCPDS data files) have changed in the complexes possibly due to coordination. The sharp distinctive peaks in the diffractograms (Figures 4 & 5) further indicate good purity of the complexes, although, purer single crystals could not be obtained from the recrystallization process after several attempts.

Table 4: Miller indexing, interplanar distances and crystalline system of [Cu(Pip)(NaD)].

Peak No.	$h^2+k^2+l^2$	hkl	2θ obs.	2θ Cal.	d-sp obs.	d-sp cal.	Rel. I	Lattice
1	3	111	15.22	15.21	5.82	5.82	69	10.0856
2	4	200	18.82	18.55	4.78	4.71	78	9.4283
3	5	210	20.4	20.49	4.33	4.35	89	9.7203
4	8	220	24.41	25.06	3.55	3.64	97	10.3051
5	10	310	28.49	27.34	3.26	3.13	100	9.8952
6	12	222	30.04	28.68	3.11	2.97	78	10.2936
7	13	320	32.06	32.9	2.72	2.79	78	10.0547

Lattice Parameters: a = 10.09 Å, b = 9.43 Å, c = 9.72 Å, Average Lattice = 9.97 (Å); Cubic Crystals with Reflections in Simple, Face-centered and Body-centered.
Overall Orthorhombic, $a_1 \neq a_2 \neq a_3$; $\alpha = \beta = \gamma = 90^\circ$

Table 5: Miller indexing, interplanar distances and crystal system of [Co(Pip)(NaD)].

Peak No.	$h^2+k^2+l^2$	hkl	2θ obsd.	2θ Calcd.	d-sp obsd.	d-sp calcd.	Rel. I	Lattice
1	3	111	10.73	10.73	8.24	8.24	92	14.3041
2	6	211	15.26	15.21	5.82	5.8	95	14.2226
3	9	300, 221	18.93	18.83	4.71	4.68	80	14.0637
4	11	311	20.54	20.4	4.35	4.32	90	14.3266
5	16	400	24.44	24.71	3.6	3.64	98	14.5573
6	21	421	28.53	27.77	3.21	3.13	100	14.3277

Lattice Parameters: a = 14.30 Å, b = 14.22 Å, c = 14.06 Å, Average Lattice = 14.30 (Å); Cubic Crystals with Reflections in Simple, Face-centered and Body-centered.
Overall Orthorhombic, $a_1 \neq a_2 \neq a_3$; $\alpha = \beta = \gamma = 90^\circ$

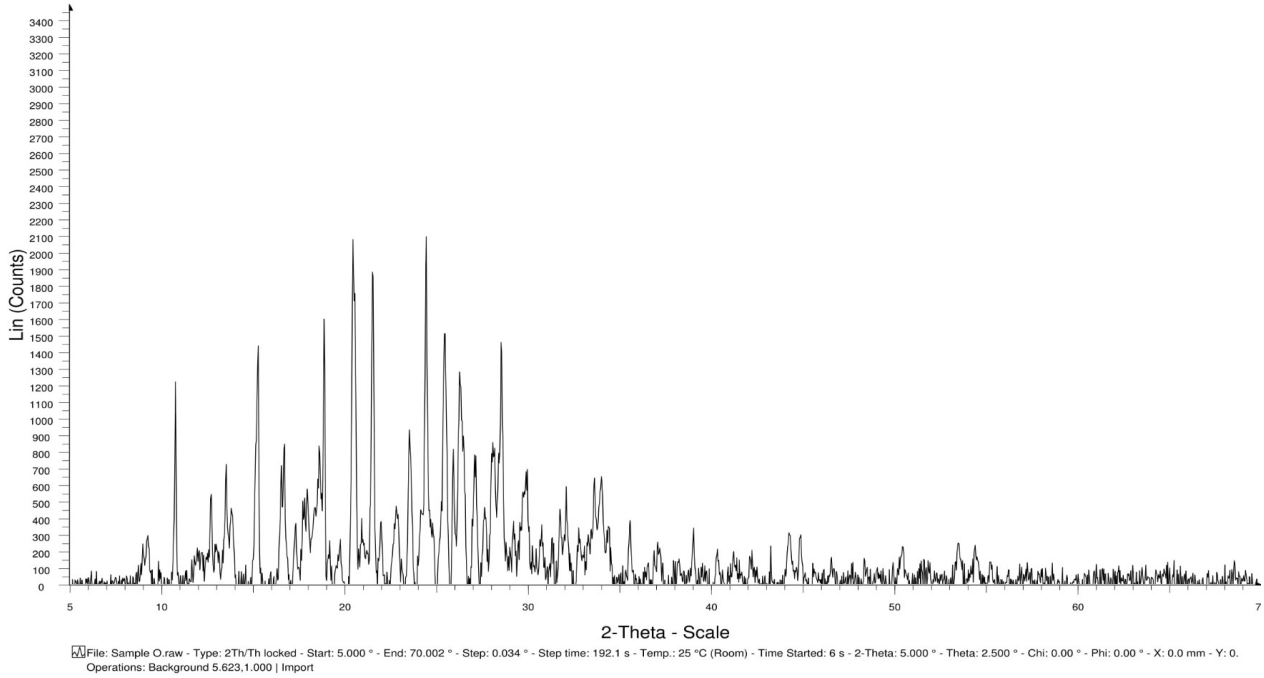

Figure 4: X-ray Diffraction Pattern of [Cu(Pip)(NaD)].

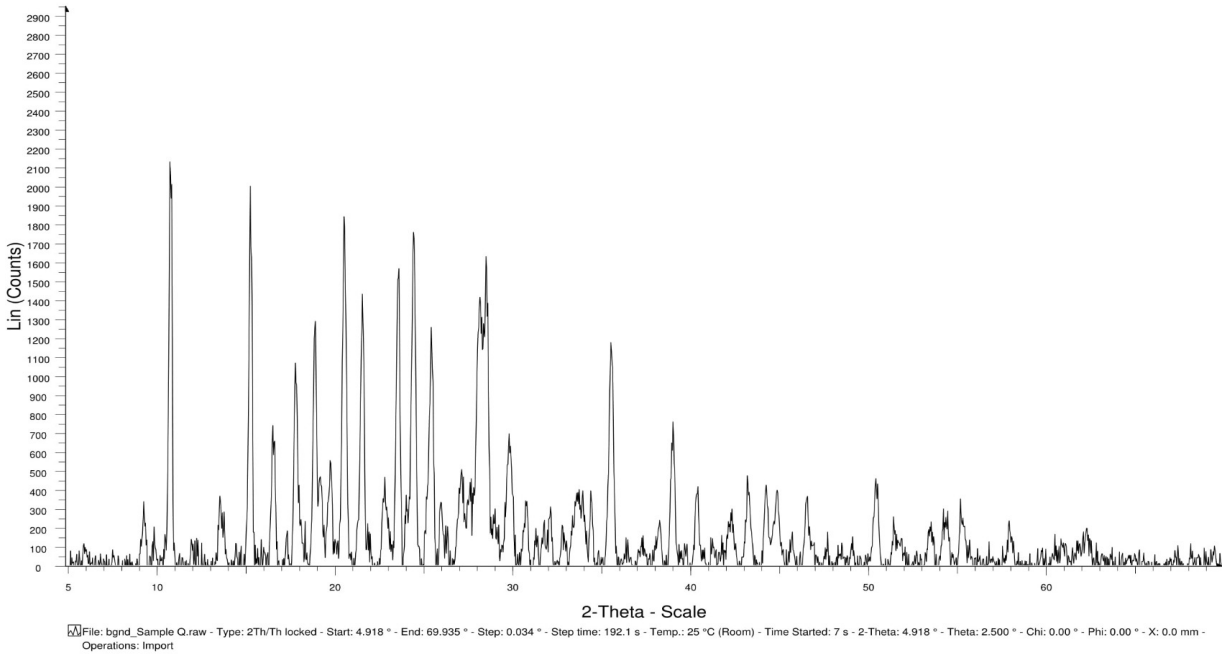

Figure 5: X-ray Diffraction Pattern of [Co(Pip)(NaD)]

Water of Crystallization

In addition to the positive result obtained for the presence of molecules of water of crystallization in the complexes using preliminary chloride paper test, the amount of the water molecules in each complex was determined using thermal analysis (Eq. 3). When 1.00 g of each for Cu(II) and Co(II) complexes with respective estimated molecular weights of 1073 and 1050 were subjected to heating gently. The weight continuously reduced until it

became constant at 0.93 and 0.95 g, respectively. Using Eq. 3, the water of crystallization was deduced as 4.19 (≈4) and 2.91 (≈3) for Cu(II) and Co(II) complex, respectively. These values together with other characterization data were used to propose the structure of the complexes in the absence of single crystals.

Biological Study

In silico predictions of biological activity and ADMET properties

The bioactivity profiles of the complexes are predicted *in silico* in comparison with the parent ligands, Pip and NaD to observe the possibility of enhanced interaction with biological targets and pharmacology due to coordination (Table 6). These interactions with major targets for essential biofunctionalities such as the GPCR, ion channel, kinases, nuclear receptor, protease and enzymes are evaluated in terms of binding affinity. All the complexes virtually demonstrate higher binding affinity against the receptors than the parent Pip and NaD as indicated by lower binding scores (especially the more negative ones). Although the geometric structures of the complexes are larger than the respective ligands, however, the enhanced binding affinity to the receptor as deduced for the complexes could be due to additive interactions of the metal ions and stabilization to the protein structures which sometimes naturally contain Cu(II) and Co(II) as cofactors (39). The theoretical interactions with these targets further predict their applicability as bioactive agents and promising bioactivity (17).

Table 6: Predicted bioactivity profile of the ligands and their complexes.

Compound	GPCR Ligand	Ion Channel Modulator	Kinase Inhibitor	Nuclear Receptor Ligand	Protease Inhibitor	Enzyme Inhibitor
Pip	0.22	0.12	0.25	-0.09	0.01	0.09
NaD	0.16	0.20	0.19	0.11	-0.06	0.25
[Cu(Pip)(NaD)]	-1.58	-2.69	-2.35	-2.64	-1.26	-2.14
[Co(Pip)(NaD)]	-2.00	-3.00	-2.78	-3.04	-1.59	-2.58

The physicochemical parameters predicted for both the ligands, Pip and NaD and their metal complexes are presented (Table 7). Only the ligand, NaD possesses a molecular weight <500, others are higher especially the complexes due to the coordination with the metal ions and other ligands. They are poorly soluble in water with fair molar refractivity except for NaD which is moderately soluble. This could be traced to the lipophilicity induced by the aromatic rings in the ligand moieties. They have hydrogen bond donor (HBD) groups <5 and hydrogen bond acceptors (HBA) <10 except the ligands. These are favorable pharmacophores for interaction with residues within various biological targets. They display topological polar surface area (TPSA) >60Å standard compared to the parent ligands possibly due to their new structural morphology brought about by coordination.

Table 7: Physicochemical properties of Pip, NaD and their complexes.

Compound	Mol.wt	Fraction Csp3[a]	HBA[b]	HBD[c]	Molar Refractivity	Water Solubility	TPSA[d] (Å^2)
Pip	535.51	0.38	4	0	168.72	Poorly soluble	38.74
NaD	296.15	0.07	2	2	77.55	Moderately soluble	49.33
[Cu(Pip)(NaD)]	893.19	0.28	6	0	246.70	Poorly soluble	68.28
[Co(Pip)(NaD)]	924.61	0.28	8	2	252.79	Poorly soluble	86.74

a: The ratio of sp^3 hybridized carbon over the total number of carbon atoms in a molecule; b: The number of hydrogen bond acceptors; c: The number of hydrogen bond donors; d: Topological polar surface area.

The predicted pharmacokinetic profiles of the ligands and their complexes (Table 8) indicate that the complexes have low ability for gastrointestinal absorption compared to the ligand and none of them can predictably penetrate the blood-brain barrier (BBB), inhibit the cytochrome P450, indicating their insignificance for drug-drug interaction to induce adverse effects. We observed that the NaD as a ligand on its own virtually displays expression for CYP1A2 as a sign of possible side effects, and this has been mitigated upon coordination to metal ions, further suggesting less side effect of the metal complexes. They all possess low skin permeation indicated by Log Kp value of -4.47 to -5.56 cm/s and are P-G substrates except the ligand Pip and Cu(II) complex. Although some of them show slight violations to Lipinski's Rule of 5 for drugability (40) due to higher molecular weights than 500 g/mol, commonly to coordination compounds (17,18), however, they demonstrate good pharmacokinetics

and bioavailability amenable for further bioactivity probes.

Table 8: Pharmacokinetics and toxicological properties of Pip, NaD, and their complexes.

Compound	GI Abs.	BBB Permeation	P-G Substrate	CYP1A2 Inhibitor	Log Kp (cm/s)
Pip	High	Yes	Yes	No	-5.56
NaD	High	Yes	No	Yes	-5.14
[Cu(Pip)(NaD)]	Low	No	Yes	No	-4.47
[Co(Pip)(NaD)]	Low	No	No	No	-5.34

Antioxidant Assay

The generation of free radicals in the body often results in inflammation and some other ailments including heart diseases and cancer (15). Therefore, a bioactive agent with the ability to scavenge the generated free radicals in a biological system is advantageously preferred for therapeutic applications. The result of antioxidant studies of the synthesized metal complexes in comparison with ascorbic acid as a standard is contained in Table 9. From the IC_{50} values of 165.09 and 382.7 µg/mL, the synthesized metal complexes demonstrate stronger potentials to scavenge free radicals than ascorbic acid whose IC_{50} value stands at 7526 µg/mL and thus, could be good as antioxidants.

Table 9: Results for the DPPH screening for ascorbic acid and the metal complexes.

Concentration (µg/mL)	[Cu(Pip)(NaD)]		[Co(Pip)(NaD)]		Ascorbic Acid	
	Absorbance	% Inhibition	Absorbance	% Inhibition	Absorbance	% Inhibition
100	0.209±0.167	3308	0.137±0.001	2736.7	0.0074±0.003	87.17
200	0.225±0.218	4348.9	0.159±0.007	3144.8	0.079±0.001	86.31
300	0.270±0.242	4838.8	0.355±0.004	7144.89	0.081±0.003	85.96
400	0.375±0.233	4955	0.345±0.003	6940.81	0.075±0.002	87.00
500	0.336±0.179	5553.1	0.319±0.024	6410.2	0.079±0.001	86.31
IC_{50}	382.7		165.09		7526	

Antibacterial activity

The average zones of inhibitions shown in Figure 6 indicate that the metal complexes exhibit stronger inhibition effects on the test organisms than the parent ligands and in good competition with a renowned antibiotic, ciprofloxacin at all concentrations *in vitro*. It could also be observed that antibacterial potency in each case appears to be concentration-dependent as the degree of inhibition increases with an increase in concentration (41). The complexes inhibit the bacterial growth at similar minimal bactericidal concentration and in strong competition with a renowned antibiotic for treating bacterial resistance, ciprofloxacin. The improved activity of the metal-drug chelates can be justified based on the chelation effect (42) and this indicates the worthiness of the complexes for therapeutic transformational probes against drug-resistant bacterial infections upon further studies.

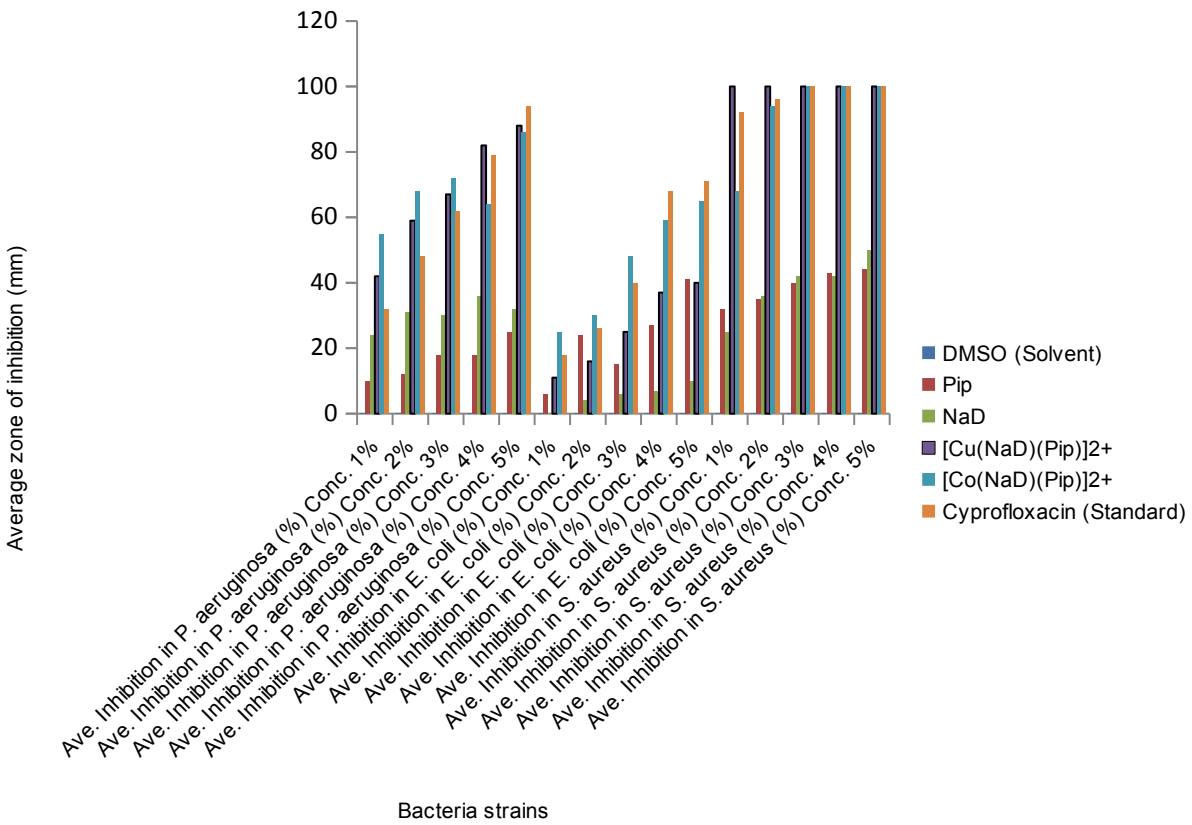

Figure 6: Antibacterial Activities of the ligands, the complexes and the controls.

CONCLUSIONS

Synthesis of coordination compounds consisting of Cu(II), Co(II), piperaquine, and diclofenac have been carried through a reflux mechanism. The characterization results provide succinct evidence of coordination involving the two ligands, piperaquine and diclofenac each as bidentate, through NH, COO and Cl groups, suggesting octahedral geometry, low spin, paramagnetism in both Cu(II) and Co(II) complexes. Powder XRD data reveals the basic morphology of the complexes as polycrystallites consisting of simple, face-centered and body-centered cubes with the overall orthorhombic arrangement but not as single crystals possibly due to the presence of some impurity even after recrystallization. The *in silico* biological studies show that the synthesized complexes possess strong potentials for interaction with various biological targets as therapeutic agents and demonstrate lesser expression for toxicity. The *in vitro* antioxidant and antibacterial assays portray the complexes with higher antioxidant and bactericidal efficacy than the parent ligands and some renowned standards. Although, the limitations in this study include the inability to obtain single crystals of the complexes through which the exact atomic arrangements could be depicted by X-ray crystallography. Further analyses such as the TGA and EPR could provide more accurate information on the coordinated water molecules as well as the suggested paramagnetism, and more robust biological experiments are required for future study. However, the research represents a promising model for novel antioxidant and antibacterial therapeutic designs.

CONFLICT OF INTEREST

The authors declare no conflict of interest in the study.

ACKNOWLEDGEMENT

The authors wish to acknowledge the Tetfund Nigeria for PhD scholarship awarded to YOA.

REFERENCES

1. Naglah AM, Al-Omar MA, Almehizia AA, AlKahtani HM, Bhat MA, Al-Shakliah NS, et al. Synthesis, thermogravimetric, and spectroscopic characterizations of three palladium metal(II) ofloxacin drug and amino acids mixed ligand complexes as advanced antimicrobial materials. Journal of Molecular Structure. 2021 Feb;1225:129102. DOI: https://doi.org/10.1016/j.molstruc.2020.129102.

2. Mohamed GG, El-Sherif AA, Saad MA, El-Sawy SEA, Morgan ShM. Mixed-ligand complex formation of tenoxicam drug with some transition metal ions in

presence of valine: Synthesis, characterization, molecular docking, potentiometric and evaluation of the humeral immune response of calves. Journal of Molecular Liquids. 2016 Nov;223:1311–32. DOI: https://doi.org/10.1016/j.molliq.2016.09.065.

3. Bergamo A, Dyson PJ, Sava G. The mechanism of tumour cell death by metal-based anticancer drugs is not only a matter of DNA interactions. Coordination Chemistry Reviews. 2018 Apr;360:17–33. DOI: https://doi.org/10.1016/j.ccr.2018.01.009.

4. Boros E, Dyson PJ, Gasser G. Classification of Metal-Based Drugs according to Their Mechanisms of Action. Chem. 2020 Jan;6(1):41–60. DOI: https://doi.org/10.1016/j.chempr.2019.10.013.

5. Schmidt C, Karge B, Misgeld R, Prokop A, Franke R, Brönstrup M, et al. Gold(I) NHC Complexes: Antiproliferative Activity, Cellular Uptake, Inhibition of Mammalian and Bacterial Thioredoxin Reductases, and Gram-Positive Directed Antibacterial Effects. Chem Eur J. 2017 Feb 3;23(8):1869–80. DOI: https://doi.org/10.1002/chem.201604512.

6. Zhou G, Shi Q-S, Huang X-M, Xie X-B. The Three Bacterial Lines of Defense against Antimicrobial Agents. IJMS. 2015 Sep 9;16(9):21711–33. DOI: https://doi.org/10.3390/ijms160921711.

7. Paladini F, Pollini M, Sannino A, Ambrosio L. Metal-Based Antibacterial Substrates for Biomedical Applications. Biomacromolecules. 2015 Jul 13;16(7):1873–85. DOI: https://doi.org/10.1021/acs.biomac.5b00773.

8. Alven S, Aderibigbe BA, Balogun MO, Matshe WMR, Ray SS. Polymer-drug conjugates containing antimalarial drugs and antibiotics. Journal of Drug Delivery Science and Technology. 2019 Oct;53:101171. DOI: https://doi.org/10.1016/j.jddst.2019.101171.

9. Turner RJ. Metal-based antimicrobial strategies. Microb Biotechnol. 2017 Sep;10(5):1062–5. DOI: https://doi.org/10.1111/1751-7915.12785.

10. Fiori ATM, Nakahata DH, Cuin A, Lustri WR, Corbi PP. Synthesis, crystallographic studies, high resolution mass spectrometric analyses and antibacterial assays of silver(I) complexes with sulfisoxazole and sulfadimethoxine. Polyhedron. 2017 Jan;121:172–9. DOI: https://doi.org/10.1016/j.poly.2016.09.046.

11. Divya K, Narayana B, Samshuddin S. New spectrophotometric methods for the determination of sulfadoxine by the formation of Co(II) complexes. Journal of Saudi Chemical Society. 2016 Sep;20:S536–40. DOI: https://doi.org/10.1016/j.jscs.2013.03.011.

12. K. O. Ogunniran. Cu(II) and Fe(III) complexes of sulphadoxine mixed with pyramethamine: Synthesis, characterization, antimicrobial and toxicology study. Int J Phys Sci [Internet]. 2012 Mar 23 [cited 2021 May 3];7(13). Available from: http://www.academicjournals.org/IJPS/abstracts/abstracts/abstract2012/23Mar/Ogunniran%20et%20al.htm

13. Hu Y-Q, Gao C, Zhang S, Xu L, Xu Z, Feng L-S, et al. Quinoline hybrids and their antiplasmodial and antimalarial activities. European Journal of Medicinal Chemistry. 2017 Oct;139:22–47. DOI: https://doi.org/10.1016/j.ejmech.2017.07.061.

14. Idemudia O, Sadimenko A, Hosten E. Metal Complexes of New Bioactive Pyrazolone Phenylhydrazones; Crystal Structure of 4-Acetyl-3-methyl-1-phenyl-2-pyrazoline-5-one phenylhydrazone Ampp-Ph. IJMS. 2016 May 18;17(5):687. DOI: https://doi.org/10.3390/ijms17050687.

15. Kakoulidou C, Gritzapis PS, Hatzidimitriou AG, Fylaktakidou KC, Psomas G. Zn(II) complexes of (E)-4-(2-(pyridin-2-ylmethylene)hydrazinyl)quinazoline in combination with non-steroidal anti-inflammatory drug sodium diclofenac: Structure, DNA binding and photo-cleavage studies, antioxidant activity and interaction with albumin. Journal of Inorganic Biochemistry. 2020 Oct;211:111194. DOI: https://doi.org/10.1016/j.jinorgbio.2020.111194.

16. Ayipo YO, Obaleye JA, Badeggi UM. Novel metal complexes of mixed piperaquine-acetaminophen and piperaquine-acetylsalicylic acid: Synthesis, characterization and antimicrobial activities. Journal of the Turkish Chemical Society, Section A: Chemistry. 2016 Nov 11;4(1):313–313. DOI: https://doi.org/10.18596/jotcsa.287331.

17. Okasha RM, AL-Shaikh NE, Aljohani FS, Naqvi A, Ismail EH. Design of Novel Oligomeric Mixed Ligand Complexes: Preparation, Biological Applications and the First Example of Their Nanosized Scale. IJMS. 2019 Feb 10;20(3):743. DOI: https://doi.org/10.3390/ijms20030743.

18. Syed Ali Fathima S, Paulpandiyan R, Nagarajan ER. Expatiating biological excellence of aminoantipyrine derived novel metal complexes: Combined DNA interaction, antimicrobial, free radical scavenging studies and molecular docking simulations. Journal of Molecular Structure. 2019 Feb;1178:179–91. DOI: https://doi.org/10.1016/j.molstruc.2018.10.021.

19. Bunaciu AA, Udriştioiu E gabriela, Aboul-Enein HY. X-Ray Diffraction: Instrumentation and Applications. Critical Reviews in Analytical Chemistry. 2015 Oct 2;45(4):289–99. DOI: https://doi.org/10.1080/10408347.2014.949616.

20. Dorset DL. Crystal Structure Analysis. In: Structural Electron Crystallography [Internet]. Boston, MA: Springer US; 1995 [cited 2021 May 3]. p. 95–133. Available from: http://link.springer.com/10.1007/978-1-4757-6621-9_4.

21. Holder CF, Schaak RE. Tutorial on Powder X-ray Diffraction for Characterizing Nanoscale Materials. ACS Nano. 2019 Jul 23;13(7):7359–65. DOI: https://doi.org/10.1021/acsnano.9b05157.

22. Daina A, Michielin O, Zoete V. SwissADME: a free web tool to evaluate pharmacokinetics, drug-likeness and medicinal chemistry friendliness of small molecules. Sci Rep. 2017 May;7(1):42717. DOI: https://doi.org/10.1038/srep42717.

23. Limbago B. M100-S11, Performance standards for antimicrobial susceptibility testing. Clinical Microbiology Newsletter. 2001 Mar;23(6):49. DOI: https://doi.org/10.1016/S0196-4399(01)88009-0.

24. Nichols L. 6.1C: Melting Point Theory [Internet]. Chemistry LibreTexts; 2020. Available from: https://chem.libretexts.org/Bookshelves/Organic_Chemistry/Book%3A_Organic_Chemistry_Lab_Techniques_(Nichols)/06%3A_Miscellaneous_Techniques/6.01%3A_Melting_Point/6.1C%3A__Melting_Point_Theory

25. Refat MS, Mohamed GG, Ibrahim MYS, Killa HMA, Fetooh H. Synthesis and Characterization of Coordination Behavior of Diclofenac Sodium Drug Toward Hg(II), Pb(II), and Sn(II) Metal Ions: Chelation Effect on Their Thermal Stability and Biological Activity. Synthesis and Reactivity in Inorganic, Metal-Organic, and Nano-Metal Chemistry. 2014 Feb 7;44(2):161–70. https://doi.org/10.1080/15533174.2012.752009.

26. Perontsis S, Dimitriou A, Fotiadou P, Hatzidimitriou AG, Papadopoulos AN, Psomas G. Cobalt(II) complexes with the non-steroidal anti-inflammatory drug diclofenac and nitrogen-donor ligands. Journal of Inorganic Biochemistry. 2019 Jul;196:110688. DOI: https://doi.org/10.1016/j.jinorgbio.2019.04.002.

27. Osunniran W, Obaleye J, Ayipo Y, Rajee A, Enemose E. Six Coordinate Transition Metal (II) Complexes of Mixed Ligands of Eflornithine Hydrochloride Hydrate and 2,2-Bipyridine: Synthesis, Characterization and Antibacterial Study. Jordan J Chem. 2018;13(3):149–57. URL: http://jjc.yu.edu.jo/index.php/jjc/article/view/39.

28. Al-Adilee K, Dakheel H. Synthesis, Spectral and Biological Studies of Ni(II), Pd(II), and Pt(IV) Complexes with New Heterocyclic ligand Derived from Azo-Schiff Bases Dye. Eurasian J Anal Chem [Internet]. 2018 Oct 2 [cited 2021 May 3];13(6). Available from: http://www.journalssystem.com/ejac/,97267,0,2.html

29. Lakshmi S, Endo T, Siva G. Electronic (Absorption) Spectra of 3d Transition Metal Complexes. In: Akhyar Farrukh M, editor. Advanced Aspects of Spectroscopy [Internet]. InTech; 2012 [cited 2021 May 3]. Available from: http://www.intechopen.com/books/advanced-aspects-of-spectroscopy/electronic-absorption-spectra-of-3d-transition-metal-complexes

30. Radoń M, Rejmak P, Fitta M, Bałanda M, Szklarzewicz J. How can [Mo IV (CN) 6] 2− , an apparently octahedral (d) 2 complex, be diamagnetic? Insights from quantum chemical calculations and magnetic susceptibility measurements. Phys Chem Chem Phys. 2015;17(22):14890–902. DOI: https://doi.org/10.1039/C4CP04863F.

31. Salazar-Medina AJ, Gámez-Corrales R, Ramírez JZ, González-Aguilar GA, Velázquez-Contreras EF. Characterization of metal-bound water in bioactive Fe(III)-cyclophane complexes. Journal of Molecular Structure. 2018 Feb;1154:225–31. DOI: https://doi.org/10.1016/j.molstruc.2017.10.018.

32. Xu X-H, Kuang M-Q. Interpretation of the Electron Paramagnetic Resonance Spectra of Copper(II)–Tyrosine Complex. Zeitschrift für Naturforschung A. 2017 Dec 20;73(1):75–8. DOI: https://doi.org/10.1515/zna-2017-0239.

33. Ott JC, Wadepohl H, Enders M, Gade LH. Taking Solution Proton NMR to Its Extreme: Prediction and Detection of a Hydride Resonance in an Intermediate-Spin Iron Complex. J Am Chem Soc. 2018 Dec 19;140(50):17413–7. DOI: https://doi.org/10.1021/jacs.8b11330.

34. Müntener T, Böhm R, Atz K, Häussinger D, Hiller S. NMR pseudocontact shifts in a symmetric protein homotrimer. J Biomol NMR. 2020 Sep;74(8–9):413–9. DOI: https://doi.org/10.1007/s10858-020-00329-7.

35. Ramotowska S, Wysocka M, Brzeski J, Chylewska A, Makowski M. A comprehensive approach to the analysis of antibiotic-metal complexes. TrAC Trends in Analytical Chemistry. 2020 Feb;123:115771. DOI: https://doi.org/10.1016/j.trac.2019.115771.

36. Speakman S. Basics of X-Ray Powder Diffraction [Internet]. MIT; 2018. Available from: http://prism.mit.edu/xray.

37. Wang Q, Huang YM, Ma XL, Li SS, Li H. X-ray powder diffraction data for piperaquine, C 29 H 32 Cl 2 N 6. Powder Diffr. 2015 Sep;30(3):289–92. DOI: https://doi.org/10.1017/S0885715615000524.

38. Ibragimov A, Ashurov J, Dusmatov A, Ibragimov A. Crystal structure and Hirshfeld surface analysis of the orthorhombic polymorph of a Zn II complex with 3,5-dinitrobenzoic acid and ethylenediamine. Acta Crystallogr E Cryst Commun. 2020 Jul 1;76(7):1113–6. DOI: https://doi.org/10.1107/S2056989020007938.

39. Marino SF, Regan L. Secondary ligands enhance affinity at a designed metal-binding site. Chemistry & Biology. 1999 Sep;6(9):649–55. DOI: https://doi.org/10.1016/S1074-5521(99)80116-1.

40. Lipinski CA. Lead- and drug-like compounds: the rule-of-five revolution. Drug Discovery Today: Technologies. 2004 Dec;1(4):337–41. DOI: https://doi.org/10.1016/j.ddtec.2004.11.007.

41. Kuti JL. OPTIMIZING ANTIMICROBIAL PHARMACODYNAMICS: A GUIDE FOR YOUR STEWARDSHIP PROGRAM. Revista Médica Clínica Las Condes. 2016 Sep;27(5):615–24. DOI: https://doi.org/10.1016/j.rmclc.2016.08.001.

42. Coraça-Huber DC, Dichtl S, Steixner S, Nogler M, Weiss G. Iron chelation destabilizes bacterial biofilms and potentiates the antimicrobial activity of antibiotics against coagulase-negative Staphylococci. Pathogens and Disease [Internet]. 2018 Jul 1 [cited 2021 May 3];76(5). Available from: https://academic.oup.com/femspd/article/doi/10.1093/femspd/fty052/5026171.

JOTCS A
Journal of the Turkish Chemical Society
Section: A
Chemistry
TURKISH CHEMICAL SOCIETY

Investigation of Chemical Modification and Enzymatic Degradation of Poly(vinyl alcohol)/Hemoprotein Particle Composites

Sameer Awad

Department of Chemistry, College of Education for Pure Science, University of Anbar-Iraq.

Abstract: Polyvinyl alcohol (PVA) composite films with different hemp protein particles (HPP) as additives were successfully synthesized by a solution casting method. The properties of HPP-based PVA composites films were investigated. The characterizations of pure PVA and PVA composite films were performed regarding Fourier transform infrared spectroscopy (FTIR), ultra-violet (UV-Vis) to investigate the chemical properties. The formation of hydrogen bond in the PVA-HPP films, which could improve the compatibility of the two components was investigated by FTIR spectroscopy and UV-Vis analysis. The overall results showed that a higher loading of HPP into the PVA matrix improved the chemical interactions significantly. The swelling degree decreased while the water contact angle values increased as the HPP content increased.

Keywords: Polyvinyl alcohol, hemp protein, composites, chemical modification, enzymatic degradation

Submitted: February 11, 2021. **Accepted:** May 07, 2021.

Cite this: Awad S. Investigation of chemical modification and enzymatic degradation of poly (vinyl alcohol)/hemoprotein particle composites. JOTCSA. 2021;8(2):651–8.

DOI: https://doi.org/10.18596/jotcsa.878495.

***Corresponding author. E-mail:** Sameer.msc1981@gmail.com.

INTRODUCTION

Production of biodegradable material from natural materials resources instead of non-biodegradable synthetic polymers increases great attention due to the developing consciousness of the green environment (1-4). Several researchers have synthesized biodegradation composites, applying many forms of natural polymers as fillers such as cellulose, lignin, starch, chitin, chitosan, soy protein, and wheat protein. These fillers were used as bioabsorbable composites due to their low cost, excellent processability, biodegradability, and simplicity of physical and chemical improvements (5,6).

Generally, the natural materials as additives, which revealed are difficult to melt or dissolve in a normal solvent procedure as a result of their strong intermolecular bonding between cellulose and lignin even though the abundance of these natural materials (6). Hence, the addition of the synthetic polymer is regularly studied to convert these into an expected form. While these materials are significant mainly due to their environmentally friendly nature, to prepare a completely green material, the biodegradable synthetic polymer's utilities are more advantageous rather than the non-biodegradable (7-9).

PVA is considered a great low-cost option because it is recognized for its chemical, thermal stability, and biodegradability. Renewable fillers (carbohydrates and fibers) are cheap and biodegradable naturally in the environment (10). Many plant materials are derived from renewable crops or their wastes processed, adding a good source of fibers for many industrial applications (11-14). The hydrophilic composition, which consists of hydroxyl groups in the PVA structure, is well-linked with carbohydrates, creating significant agreement in composites (15-18).

Fiber-reinforced polymer matrix became substantial attention in many applications as a result of the good properties and superior advantages of natural fiber in term of its relatively low weight, low cost,

less damage to processing equipment, and good relative mechanical properties (19).

This study was investigated based on the chemical and HPP biodegradation treatment, defibrillated and distributed in an aqueous suspension. The films of PVA/HPP composite were prepared by the casting method. PVA-HPP films containing different HPP loadings of 3, 7, and 12% (w/w), were formed as composites. The chemical, biological, and physical characterizations were assessed. The purpose of this work was to assess the impact of incorporating HPP addition in PVA films, evaluating their compositions, chemical and biodegradation characterizations of PVA composites.

EXPERIMENTAL

Materials

Polyvinyl alcohol material was provided from Sigma-Aldrich, UK, MW= 124,000-186,000; the hydrolysis degree is in the range 87-89 mol%; hydrolysis rate: 90%; density: 1.3 g/cm^3. The α-amylase and β-amylase were provided from Merck KGaA Co. Germany. Hemp protein particles were purchased locally, containing 1.7% moisture, 0.23% protein and 0.075% fat, and used without further chemical treatments.

PVA Composite Preparations

A 7% (w/v) PVA solution was prepared by inserting 10 g of PVA into 90 mL of distilled water. Then, the solution was heated and stirred at ~80 °C for 6 hours to achieve complete homogeneity, after that the solution was kept at room temperature. The 10% (w/v) PVA solution was mixed with 3, 7, and 12% of HPP powder (HPP particle size 300 μm), creating the casting solution. The composite mixture was poured into a glass dish and positioned on a levelled smooth surface with the right thickness (40 μm). The composite mixture was kept for three days at room temperature and then by drying in a vacuum oven at 60 °C for three days. After drying, the composite films were later removed from their dishes and put up in a desiccator for future use. Figure 1 shows the chemical covalent interaction between HPP and PVA to form PVA composites.

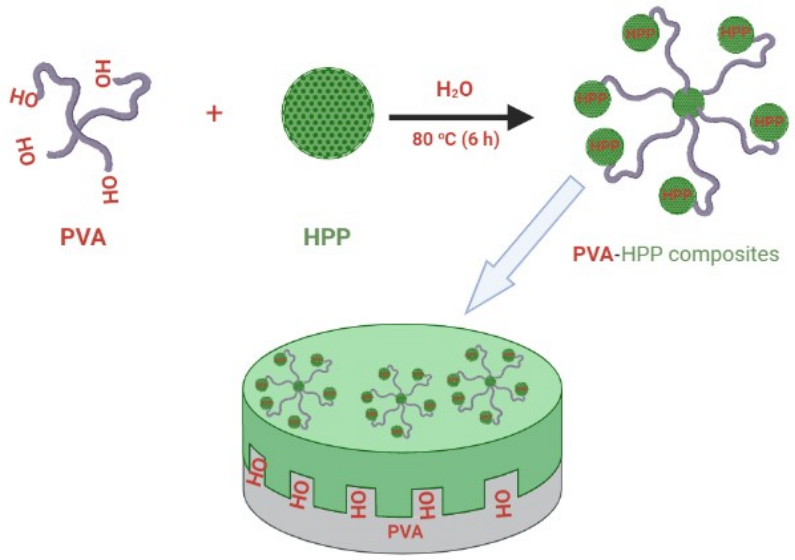

Figure 1: Chemical covalent interaction between HPP and PVA to form PVA composites.

CHARACTERIZATION

Fourier Transform Infrared Spectroscopic analysis

FT-IR analysis of composite films was carried out utilizing an FTIR Spectrum 400 (Perkin Elmer, USA). The investigation was performed within the range between 4000 to 500 cm^{-1} with a 4 cm^{-1} resolution and a total of 20 scans. The spectra of FTIR were recorded in the absorbance mode.

UV-VIS Analysis

A UV–Visible-NIR spectrometer was utilized a double beam Lambda-25 UV-VIS spectrophotometer (Bandwidth: 1 nm and minimum spectral resolution: 0.5 nm) to determine the maximum absorbance spectra within the wavelength range (200 to 700 nm).

X-Ray Diffraction

The XRD test for all samples was carried out utilizing an X-ray spectrometer model a (PANalytical, USA) at a scan rate (0. 02°. s^{-1}) and the 2θ range were between 0 and 80. The wavelength of the X-ray was 1.5 Å with a radiation source (CuKa). All samples were conducted at 40 kV and 15 mA.

Swelling Degree (SD) and Contact Angle Analysis

PVA and PVA composite samples were cut off into pieces of 3 × 3 cm, weighed, and immersed in deionized water at 25 ºC for 60 days with different crosslinking times. The swollen sample was taken out and wiped with tissue paper to eliminate the residual water on the surface of the film and then weighed. The swelling degree is calculated by utilizing the following equation.

$$SD(\%)=\frac{W_S-W_D}{W_D}\times 100 \quad \text{(Eq. 1)}$$

Where W_s = the weight of swollen samples,
W_D = the weight of dried specimens.

The water contact angle values were tested of PVA composites, using an optical contact angle meter type (SL200KB, USA) to support the surface hydrophilicity of samples.

Enzymatic Testing

Specific quantities of α-amylase, β-amylase, and distilled water form an enzymatic mixture placed in a plastic test tube. The films were cut to species with dimensions (2×2 cm^2), and then, they were weighed by utilizing a digital sensitive balance. The samples were immersed in plastic test tubes and subjected to a shaking incubator at a rate of speed 100 rpm at 27 °C and kept for 120 h. Any residual enzyme mixture was removed, washed, utilizing distilled water. The samples were dried in a desiccator under vacuum for 48 h, and then they were weighted. The degree of enzymatic degradation [DED %] was accounted based on the following equation.

$$DED(\%)=\frac{W_D-W_I}{W_D}\times 100 \quad \text{(Eq. 2)}$$

Where W_D= the dry weight of the samples after the enzymatic treatment, W_I = the initial dry weight of the samples,

RESULTS AND DISCUSSION

FT-IR Analysis: Chemical Linkage

The FT-IR spectra of the PVA and PVA/HPP composites are shown in Figure 2. PVA showed a wide-ranging peak at 3500–3600 cm^{-1} that is attributable to O-H stretching. The specific peaks at 2850 cm^{-1}, 1400 cm^{-1} and 1100 cm^{-1} were attributed to C-H stretching, C-H bending and C-O stretching, respectively. In the FT-IR absorbance spectra of PVA and PVA/HPP, the band at 2854 cm^{-1} involves the stretching of the C-H bond in the crosslinked PVA and PVA/HP composites be attributed to the alkyl chain of aldehydes. The bands observed at 1100–1145 cm^{-1}. Similar groups seem in 2935/2905 cm^{-1}, instead of CH_2 asymmetric and symmetric stretching; 1605 cm^{-1} is the C-O vibration and 1435 cm^{-1} due to CH_2 bending. The broad groups between 3000–3500 cm^{-1}, which are related to the stretching vibration of the hydroxyl group, display the presence of intermolecular, intramolecular hydrogen bands, and the reduced band intensity after the increase of HPP loading in PVA and gave higher crosslinking that indicated the formation of the hydroxyl group.

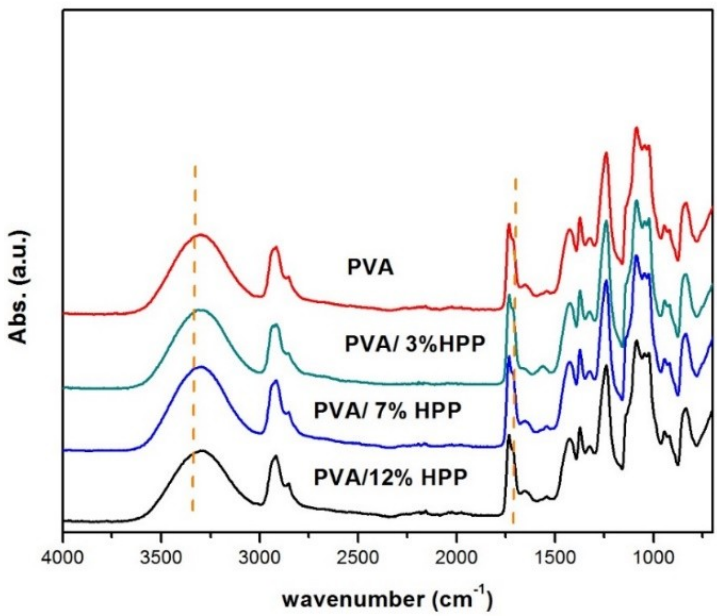

Figure 2:FTIR Spectra of PVA and PVA composites.

UV Absorption

Figure 3 shows the UV–vis absorption of the PVA with different HPP loading. The UV absorption of PVA-HPP composites showed an absorption peak at 260 nm corresponding to n —> π* transition of HPP filler. Pure HPP represented an absorption at about 260 nm related to its chromophoric groups. In addition, pure PVA did not show any absorption peak in the range of 200–600 nm. As it is shown in Figure 3, pure PVA-HPP shows an absorption peak related to HPP absorption peak. After incorporation of HPP in the PVA matrix, the peak shifted to higher absorption which indicates the interaction between HPP and PVA matrix. The minimal absorption of PVA showed that the PVA has a clarity characteristic. In the UV region (200-400 nm), the pure PVA displayed weak UV blocking as a result of the low light absorption. The intensity of UV absorption of PVA raised greatly as the amount of HPP rose from 3 to 12 wt.% in the PVA matrix (Figure 3).

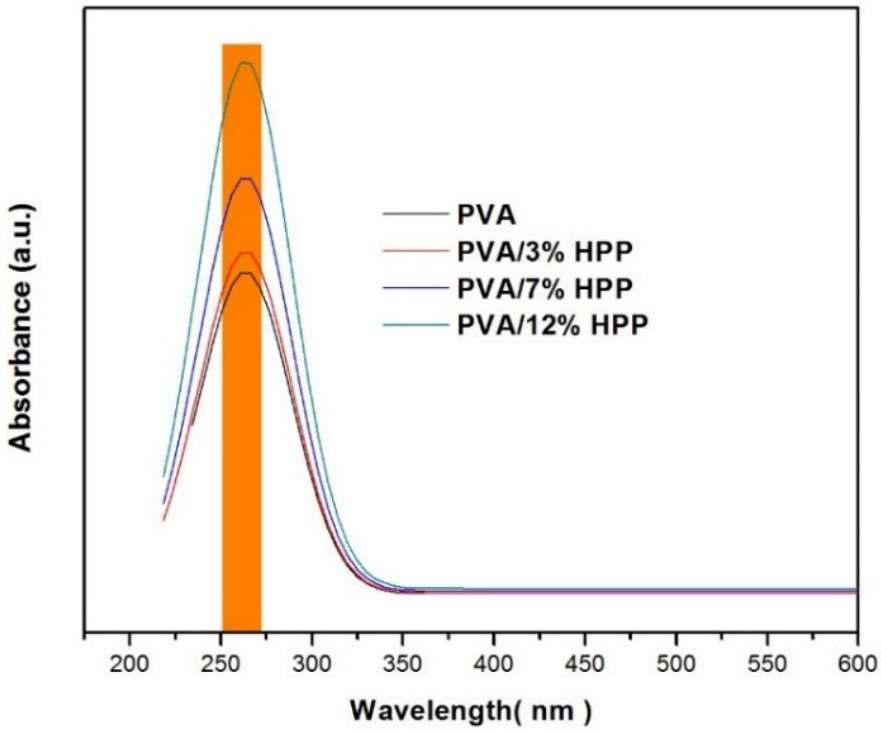

Figure 3: UV-Vis absorption spectra of PVA and PVA/HPP composite samples with different loadings of HPP.

X-ray Diffraction

X-ray diffraction was carried out to test the PVA nature and PVA composites' crystallinity. Figure 4 illustrates the diffraction pattern for the PVA and PVA/HPP composites, as shown clearly in Figure 8, a broad peak at 17.5º (peak 1) for the pure PVA film. However, it was also obviously noticed that the PVA composite intensity exhibited higher values and significantly shifted toward the higher value of the angles as the HPP additives were increased. Thus, it indicates that incorporating HPP additives into the PVA matrix significantly increased the amorphous region domain. When the PVA composite becomes much amorphous, it can be enhanced by reducing the PVA composite relative crystallization. As shown in the XRD spectra of PVA, there were two peaks around 2θ= 11.0º and 2θ = 19.5º (16). From Figure 4, it is shown that as the content of HPP was increased from 3 wt. % to 12 wt. % in PVA, the peak at 2θ = 18.2º slightly increased to 2θ =20.6º. Therefore, these diffractograms proposed that HPP in PVA has included a combination of crystalline and amorphous peaks (20). These results also indicate that the addition of HPP does not affect the uniformity in the blended PVA matrix structure. However, rather enhance molecular ordering in the amorphous phase of the PVA matrix (21).

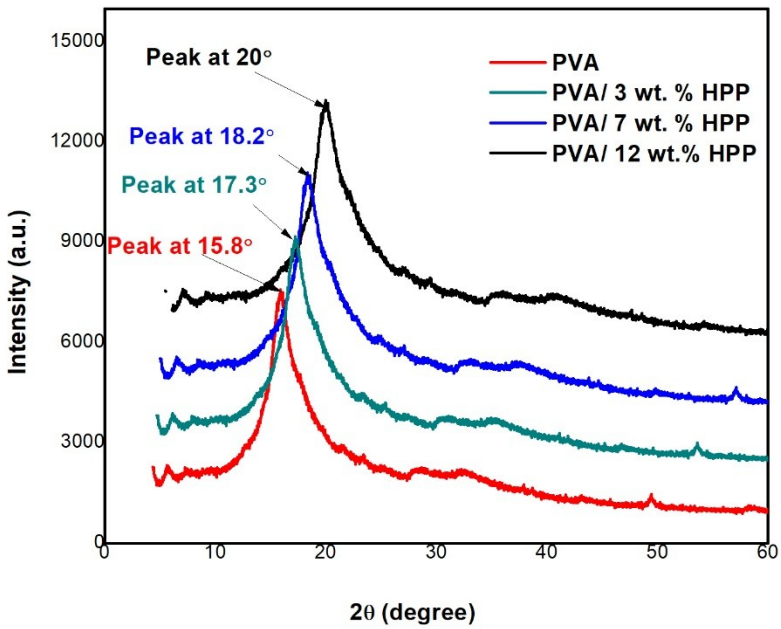

Figure 4. XRD spectra for PVA and PVA/HPP composites with different loadings of HPP.

Effect of the Water Uptake on the Properties of PVA/HPP Composites

The wetting behavior of PVA composites was investigated by the static angle with a contact angle meter by drop method. It was analyzed that neat PVA is hydrophilic with a contact angle of 48.8º as shown in Figure 5 A. However, the water contact angle of PVA composites was reduced as the concentration of HNT nanoparticles was increased. The 12 wt.% of HNT in the PVA matrix have the highest hydrophobicity with a contact angle of 83º while the water contact angle 3 and 7 wt.% HNT in PVA increased slightly in comparison to that of pure PVA (48.8º) as shown in Figure 5(A).

The value of water absorption in terms of swelling percentage crosslinked PVA and PVA composite samples are shown in Figure 5.B.

PVA has a higher value of swelling percentage of 82% due to the presence of a large number of hydroxy groups. These hydroxyl groups allow incoming water to occur in the interspaces between mobile polymer chains in the amorphous region of polymer and hence cause large swelling. In crosslink films, a smaller number of hydroxyl groups and restricted chain movement results in significantly are lower water absorption compared to PVA (21-24).

In composite films, crosslinking of PVA-12% HPP also demonstrates a significant lowering in the water absorption of PVA (52.8%) while 3 and 7 wt% of HNT loading showed slightly decreased by 72.5% and 67.5%, respectively, which is slightly better than the swelling percentage of PVA (82.5%). This is because the crosslinked PVA with HPP is less hydrophilic and absorbs less water.

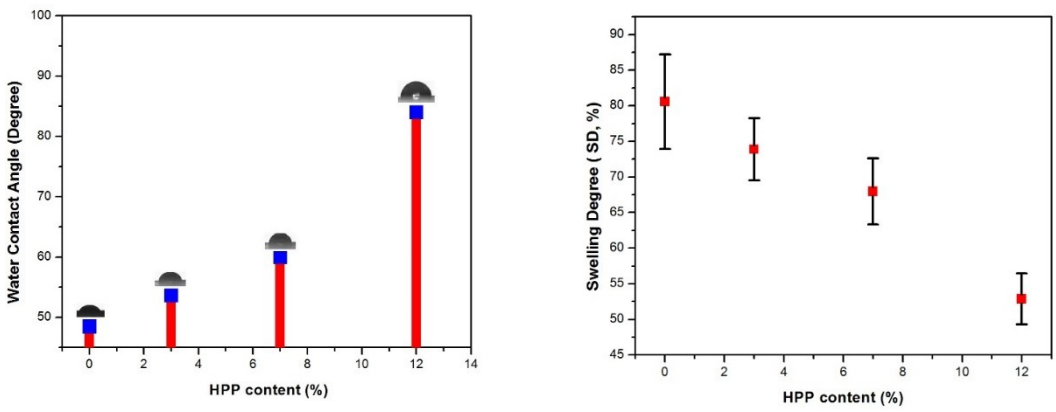

Figure 5: The water contact angle (left) and swelling degree (right) of PVA and PVA/HPP composites.

Enzymatic Testing

The weight loss of pure PVA and PVA composites is displayed in Figure 6. The percentage of DED was accounted for later the PVA composites had been immersed in enzymatic solution up to 100 h. The degree of enzymatic degradation (DED, %) was

increased with increasing the enzymatic treatment times, as shown in Figure 6. With the addition of the biodegradable HPP, the PVA blends became much easier to degrade, as shown in Figure 6. After 20 h immersion time, the degree of enzymatic degradation of PVA composites increased slightly in comparison to the PVA matrix. The DED, % of PVA increased up to 64.2% while (DED, %) values of 3, 7, and 12 wt.% HP in PVA was 26, 30, and 37.4%, respectively. Pure PVA exhibited a slower rate of degradation than PVA composites. After 100 h immersion treatment time, 12 wt. % of HPP in PVA exhibited a higher enzymatic degradation rate (95.5%) while the pure PVA was 67.5%. This higher observation of the amylase solution in PVA/12 wt.% HPP the film was due to the hydroxyl group that enhanced the diffusion of α amylase and β-amylase into the PVA/HPP composite films and then improved the attack of amylase on the HPP.

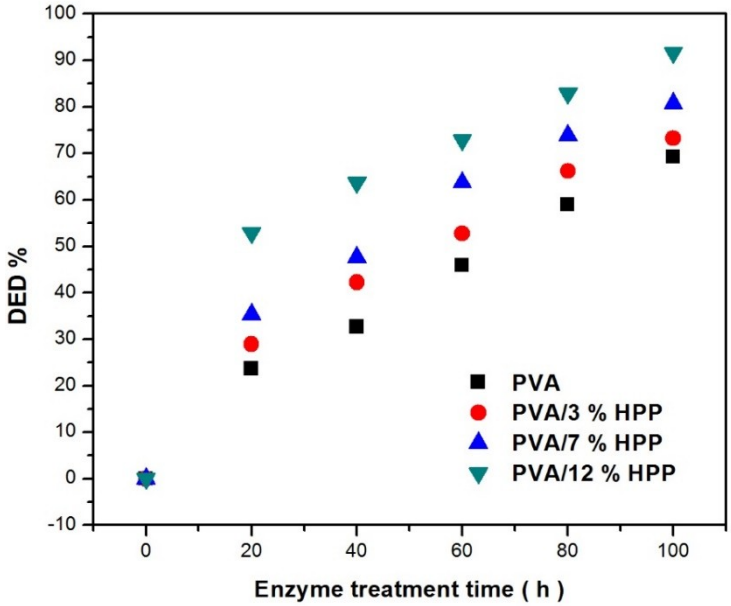

Figure 6: Enzymatic biodegradation of PVA and PVA/HPP composite films using α-amylase and β-amylase.

CONCLUSIONS

HPP has been used as reinforcement in the PVA matrix and prepared with sample solution casting. There is a remarkable improvement in chemical interaction that noticed in FT-IR and UV-VIS spectral analyses. The chemical stability was enhanced with increasing HPP loading. The overall results showed that a higher loading of HPP into the PVA matrix improved the chemical interactions significantly. The swelling coefficient decreased while the water contact angle values increased as the HPP content increased. From the XRD results, crystallinity was decreased by incorporating HPP in the PVA matrix. The degree of enzymatic degradation (DED, %) was increased with increasing the enzymatic treatment times of PVA composites and swelling degree decreased with increasing HPP loading in the PVA matrix. Overall, an environmentally friendly technique was investigated to HPP in wide applications such as biodegradable packaging.

REFERENCES

1. Silva EL da, Reis CA, Vieira HC, Santos JX dos, Nisgoski S, Saul CK, et al. Evaluation Of Poly(Vinyl Alcohol) Addition Effect On Nanofibrillated Cellulose Films Characteristics. CERNE. 2020 Mar;26(1):1–8. Doi: https://doi.org/10.1590/01047760202026012654.

2. Mendes JF, Paschoalin RT, Carmona VB, Sena Neto AR, Marques ACP, Marconcini JM, et al. Biodegradable polymer blends based on corn starch and thermoplastic chitosan processed by extrusion. Carbohydrate Polymers. 2016 Feb;137:452–8. Doi: https://doi.org/10.1016/j.carbpol.2015.10.093.

3. Haque ANMA, Remadevi R, Wang X, Naebe M. Biodegradable cotton gin trash/poly(vinyl alcohol) composite plastic: Effect of particle size on physicochemical properties. Powder Technology. 2020 Sep;375:1–10. Doi: https://doi.org/10.1016/j.powtec.2020.07.096.

4. Tan B, Ching Y, Poh S, Abdullah L, Gan S. A Review of Natural Fiber Reinforced Poly(Vinyl Alcohol) Based Composites: Application and Opportunity. Polymers. 2015 Nov 2;7(11):2205–22. Doi: https://doi.org/10.3390/polym7111509.

5. Guirguis OW, Moselhey MTH. Thermal and structural studies of poly (vinyl alcohol) and hydroxypropyl cellulose blends. NS.

2012;04(01):57–67. Doi: https://doi.org/10.4236/ns.2012.41009.

6. Eaysmine S, Haque P, Ferdous T, Gafur MA, Rahman MM. Potato starch-reinforced poly(vinyl alcohol) and poly(lactic acid) composites for biomedical applications. Journal of Thermoplastic Composite Materials. 2016 Nov;29(11):1536–53. Doi: https://doi.org/10.1177/0892705715569824.

7. Julinová M, Kupec J, Alexy P, Hoffmann J, Sedlařík V, Vojtek T, et al. Lignin and starch as potential inductors for biodegradation of films based on poly(vinyl alcohol) and protein hydrolysate. Polymer Degradation and Stability. 2010 Feb;95(2):225–33. Doi: https://doi.org/10.1016/j.polymdegradstab.2009.10.008.

8. Gadhave RV, S. K. V, Mahanwar PA, Gadekar PT. Effect of addition of boric acid on thermo-mechanical properties of microcrystalline cellulose/polyvinyl alcohol blend and applicability as wood adhesive. Journal of Adhesion Science and Technology. 2020 Oct 20;1–15. Doi: https://doi.org/10.1080/01694243.2020.1832775.

9. Awad SA, Khalaf EM. Evaluation of the photostabilizing efficiency of polyvinyl alcohol–zinc chloride composites. Journal of Thermoplastic Composite Materials. 2020 Jan;33(1):69–84. Doi: https://doi.org/10.1177/0892705718804585.

10. Mok CF, Ching YC, Muhamad F, Abu Osman NA, Singh R. Poly(vinyl alcohol)-α-chitin composites reinforced by oil palm empty fruit bunch fiber-derived nanocellulose. International Journal of Polymer Analysis and Characterization. 2017 May 19;22(4):294–304. Doi: https://doi.org/10.1080/1023666X.2017.1288345.

11. Jensen B, Kepley W, Guarner J, Anderson K, Anderson D, Clairmont J, et al. Comparison of Polyvinyl Alcohol Fixative with Three Less Hazardous Fixatives for Detection and Identification of Intestinal Parasites. Journal of Clinical Microbiology. 2000;38(4):1592–8. Doi: https://doi.org/10.1128/JCM.38.4.1592-1598.2000.

12. Oviedo IR, Méndez NAN, Gómez MPG, Rodríguez HC, Martínez AR. Design of a Physical and Nontoxic Crosslinked Poly(Vinyl Alcohol) Hydrogel. International Journal of Polymeric Materials. 2008 Oct 13;57(12):1095–103. Doi: https://doi.org/10.1080/00914030802341661.

13. Kobayashi M, Hyu HS. Development and Evaluation of Polyvinyl Alcohol-Hydrogels as an Artificial Atrticular Cartilage for Orthopedic Implants. Materials. 2010 Apr 14;3(4):2753–71. Doi: https://doi.org/10.3390/ma3042753.

14. Pervez Md, Stylios G. Investigating the Synthesis and Characterization of a Novel "Green" H2O2-Assisted, Water-Soluble Chitosan/Polyvinyl Alcohol Nanofiber for Environmental End Uses. Nanomaterials. 2018 Jun 1;8(6):395. https://doi.org/10.3390/nano8060395.

15. Salleh MSN, Nor NNM, Mohd N, Draman SFS. Water resistance and thermal properties of polyvinyl alcohol-starch fiber blend film. In İstanbul, Turkey; 2017 [cited 2021 May 7]. p. 020045. Available from: http://aip.scitation.org/doi/abs/10.1063/1.4975460

16. Wan W, Bannerman AD, Yang L, Mak H. Poly(Vinyl Alcohol) Cryogels for Biomedical Applications. In: Okay O, editor. Polymeric Cryogels [Internet]. Cham: Springer International Publishing; 2014 [cited 2021 May 7]. p. 283–321. (Advances in Polymer Science; vol. 263). Available from: http://link.springer.com/10.1007/978-3-319-05846-7_8

17. Awad SA, Khalaf EM. Investigation of Photodegradation Preventing of Polyvinyl Alcohol/Nanoclay Composites. J Polym Environ. 2019 Sep;27(9):1908–17. Doi: https://doi.org/10.1007/s10924-019-01470-7.

18. Imam SH, Cinelli P, Gordon SH, Chiellini E. Characterization of Biodegradable Composite Films Prepared from Blends of Poly(Vinyl Alcohol), Cornstarch, and Lignocellulosic Fiber. J Polym Environ. 2005 Jan;13(1):47–55. Doi: https://doi.org/10.1007/s10924-004-1215-6.

19. Awad SA, Khalaf EM. Investigation of improvement of properties of polypropylene modified by nano silica composites. 2019; 12: 59-63. Doi: https://doi.org/10.1016/j.coco.2018.12.008.

20. Lawton JW, Fanta GF. Glycerol-plasticized films prepared from starch—poly(vinyl alcohol) mixtures: effect of poly(ethylene-co-acrylic acid). Carbohydrate Polymers. 1994 Jan;23(4):275–80. Doi: https://doi.org/10.1016/0144-8617(94)90190-2.

21. Bodin A, Ahrenstedt L, Fink H, Brumer H, Risberg B, Gatenholm P. Modification of Nanocellulose with a Xyloglucan–RGD Conjugate Enhances Adhesion and Proliferation of Endothelial Cells: Implications for Tissue Engineering. Biomacromolecules. 2007 Dec 1;8(12):3697–704. Doi: https://doi.org/10.1021/bm070343q.

22. Awad SA. Mechanical and thermal characterisations of low-density polyethylene/nanoclay composites. Polymers and Polymer Composites 2020: 0967391120968441. Doi: https://doi.org/10.1177/0967391120968441.

23. Awad SA, Khalaf EM. Characterization and modifications of low-density polyethylene-nano cellulose composites. Suranaree Journal of Science&Technology. 2020; 27(1): 1-6.

24. Awad SA, Khalaf EM. Improvement of the chemical, thermal, mechanical and morphological properties of polyethylene terephthalate-graphene particle composites. Bulletin of Materials Science. 2018; 41: 1-6. Doi: https://doi.org/10.1007/s12034-018-1587-1.

JOTCS A
Journal of the Turkish Chemical Society
Section: A
Chemistry
TURKISH CHEMICAL SOCIETY

Novel Mixed Ligand Complexes of Alkaline Earth Metals with Coumarilic Acid and Nicotinamide

Emrah Karaer , Dursun Ali Köse*

Department of Chemistry, Faculty of Arts and Sciences, Hitit University, 19030, Çorum, TURKEY

Abstract: Coordination compounds with mixed ligands were synthesized with 2A group (Mg^{2+}, Ca^{2+}, Ba^{2+}, Sr^{2+}) alkaline earth metal cations of coumarilic acid and nicotinamide ligands. Afterward, the structural properties of these new molecules were investigated by melting point, elemental analysis, infrared spectroscopy, thermal analysis (TGA / DTA) curves, powder X-ray diffraction (P-XRD) spectroscopy. It has been suggested that the complex structure with the Mg^{2+} metal center is different from the other three structures. In this structure, it was determined that four aqua and two nicotinamide ligands were located in the coordination sphere, and the coordination number was six, as expected. With two monoanionic coumarilic acids located outside the coordination sphere, complex charge equivalence was achieved. The other three molecules, Sr^{2+} and Ba^{2+}, have iso-structural properties, and it is suggested that both structures contain a dinuclear metal center, and two aqua ligands are located in the bridging position between metal centers. Besides, the two coumarilate ligands involved in coordination are thought to coordinate with the primary metal cation through carbonyl and acidic oxygens while coordinating with the secondary metal cation through furan oxygen, providing the third bridge connection between metal centers. Metal cations with nine coordination numbers complete the coordination sphere with two terminal aqua and one nicotinamide ligands, each included in the structure. In the molecule with Ca^{2+} cation, which differs little from these metal cation structures, the difference according to these structures can be interpreted as the coordination of furan oxygen with the secondary metal center due to the octet coordination of the Ca^{2+} cation. From the thermal analysis curves, it was determined that only the Mg^{2+} cation complex contained hydrate. As a result of thermal decomposition, it was determined that relevant metal oxide residues remained in all structures, and this situation was defined by powder XRD.

Keywords: Coumarilic acid, alkaline earth metals, coumarin-2-carboxylic acid, spectroscopy, thermal analysis.

Submitted: April 10, 2021. **Accepted:** May 10, 2021.

Cite this: Karaer E, Köse DA. Novel Mixed Ligand Complexes of Alkaline Earth Metals with Coumarilic Acid and Nicotinamide. JOTCSA. 2021;8(2):659–76.

DOI: https://doi.org/10.18596/jotcsa.912967.

***Corresponding author. E-mail:** dalikose@hitit.edu.tr Tel.:+90(364)2277000-1635.

INTRODUCTION

Furan, benzofuran, and thiophene are aromatic heterocyclic molecules that have been widely studied by chemists and biologists (1). A wide range of biological activity such as benzofuran derivatives, anticancer, antimicrobial, anti-inflammatory, antiviral, anti-oxidant, cytotoxic, pesticidal, HIV and enzyme inhibitory (2-6), cardiovascular and antibacterial properties (7,8) is presented. Coumarilic acid with benzofuran ring group (coumarin-2-carboxylic acid, benzo[b]furan carboxylic acid, HCCA) is one example of many derivatives of the coumarin molecule. It is a functional ligand that shows binding properties to monoanionic monodentate or monoanionic

bidentate through its carboxylate group. It has pharmacophore properties over the benzo[b]furan ring in the structure and can be easily isolated from natural sources (9). Benzo[b]furan functional ring and derivatives are found in different herbal natural food sources such as fruits, herbs, and vegetables (10). It is also one of the main component molecules of drugs (such as amiodarone and bergapten) that have been synthesized recently and were used in many applications (11,12). It is well known that many heterocyclic compounds containing oxygen atoms in the ring chain exhibit important biological properties such as antiarrhythmic, spasmolytic, antiviral, anticancer, antifungal, and anti-inflammatory activities (13-19). In particular, benzofuran carboxylic derivatives are applied in different fields such as biological, electronic, pharmaceutical, and agricultural chemicals (20,21).

Although the coordination compounds in which coumarilic acid uses metal cations as central atoms exist in the literature (22-27), the number of studies on structural characterizations is limited (25,26,28). Whether the coumarilate ligand binds as a monodentate bridge or terminal ligand or participates in coordination as a bidentate chelating ligand depends on the reaction conditions and the type of metal cation (22-24, 28-31). The synthesis of these complexes has gained importance due to the therapeutic properties of the element copper against common diseases of our time such as cancer, Parkinson's, Alzheimer's, diabetes, and cardiovascular diseases (32-35). By using the electrochemical synthesis method, pure ligand complexes of coumarilic acid with Cu(II) and Zn(II) metal cations were synthesized and structurally investigated. In addition, mixed ligand complex structures of Co(II), Ni(II), Cu(II), and Zn(II) metal cations secondary to nicotinamide, *N,N*-diethylnicotinamide, and 1,10-phenanthroline were synthesized, and their structural properties were investigated. (36-41).

Coordination compounds of alkali and alkaline earth metal cations are preferred over transition or lanthanide metal cations due to their cheap, water-soluble, and non-toxic properties (42). Magnesium, one of the alkaline earth metals, is known to play an important role in various biological systems due to its binding to proteins, complexing with anions, and free availability (43). Magnesium deficiency may be an essential factor in the pathogenesis of ischemic heart disease, cardiomyopathy, and some arrhythmias (43–47). Coordination compounds containing alkaline earth metal cations have begun to see considerable favor, especially in bioinorganic chemistry (48). The coordination behavior of Mg^{2+} and Ca^{2+} metal cations has attracted the attention of many studies because of the important role of these ions in biological processes (49-51). Coordination occurs mainly through ion-dipole and ion-induced dipole interactions that contribute to binding. However, covalent interaction is possible through the transfer of electron density from bound ligand orbitals to empty or p-orbitals (52,53).

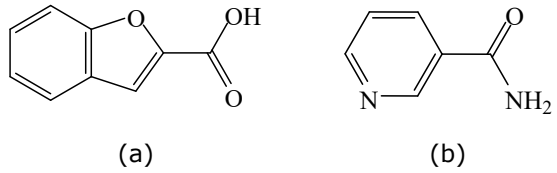

Figure 1: Molecular formulas of ligands (a) coumarilic acid, (b) nicotinamide.

In the report presented, coordination compounds containing 2A group metal cations [Mg^{2+}, Ca^{2+}, Sr^{2+}, and Ba^{2+}] coumarilic acid (Figure 1a) and nicotinamide (Figure 1b) ligands of the periodic table were synthesized. The structural properties of the molecules obtained were characterized using powder X-ray diffraction (P-XRD), UV-Vis spectroscopy, and infrared analysis methods. TG/DTG/DTA curves were recorded to determine the thermal behavior of molecules.

EXPERIMENTAL

Material and synthesis

$(CH_3COO)_2Mg.4H_2O$ (magnesium acetate), $(CH_3COO)_2Ca.xH_2O$ (calcium acetate), $(CH_3COO)_2Sr.½H_2O$ (strontium acetate), $Ba(CH_3COO)_2$ (barium acetate), coumarilic acid, and nicotinamide used in the synthesis of the complexes were obtained from Sigma-Aldrich.

0.001 moles of magnesium acetate, calcium acetate, strontium acetate, and barium acetate were taken and dissolved in 30 milliliters of distilled water and transferred to flat-bottomed flasks. The solutions of 0.002 mol of coumarilic acid prepared in 30 mL of ethyl alcohol and 0.002 mol of nicotinamide prepared in 30 mL of water were added separately on them. These solutions were placed in the distillation apparatus and heated with stirring at a temperature between 70 - 80 °C for 5 hours. After the items were removed from the setup, they were left on hold for a day. Then each substance was taken into separate beakers and placed in the heater, and the mixture of 50 mL of water and 50 mL of ethyl alcohol was added over time to evaporate the acetate. During this process, the temperature was tried to be kept between 70 – 75 °C. The beakers were then sealed with a perforated paraffin film and allowed to stand until the crystal formed. The reaction schemes

showing the synthesis mechanisms of the coordination compounds are shown in Scheme 1.

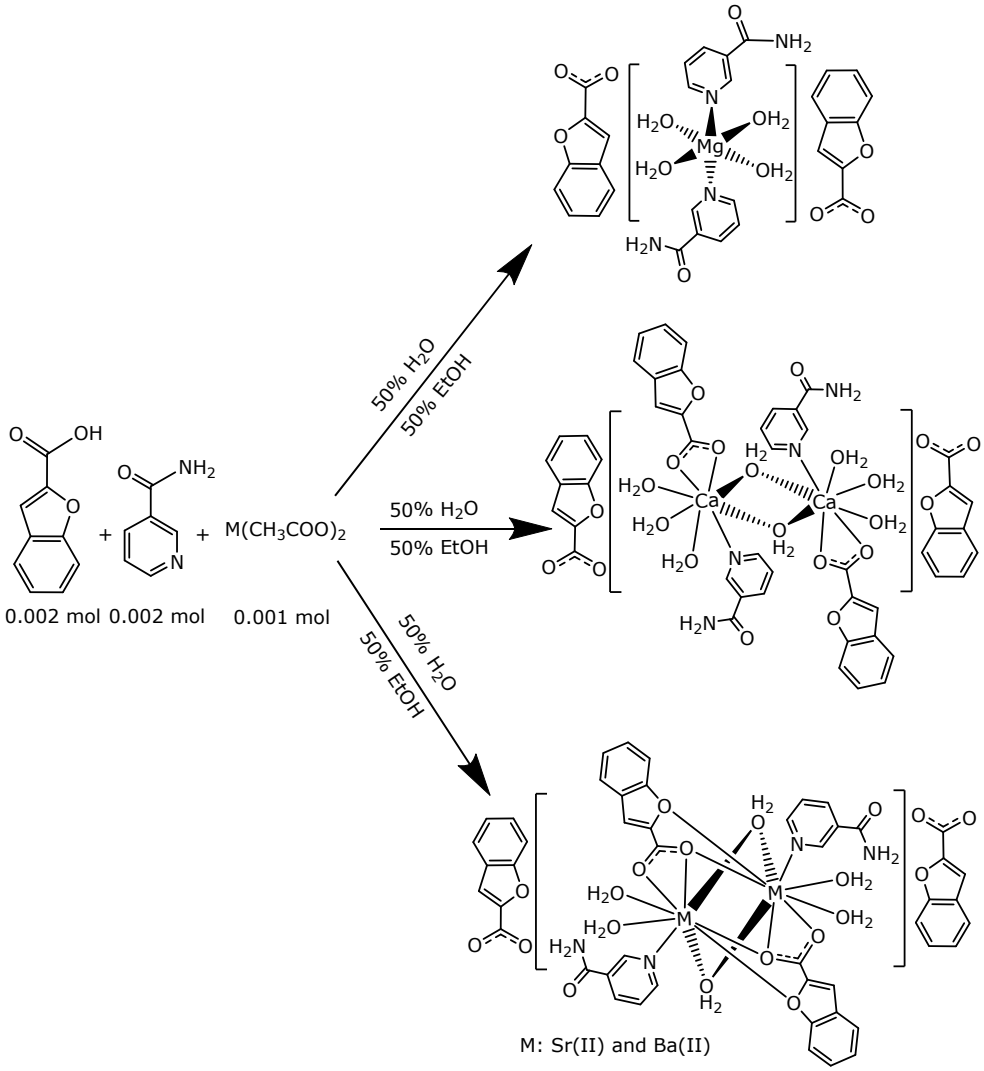

Scheme 1: The synthesis reaction schemes of metal-coumarilate / nicotinamide mixed ligand complexes.

Elemental analysis

The elemental analysis results of coordination compounds with coumarilate – nicotinamide mixed ligands of alkaline earth metal cations are given in Table 1.

Thermal Analysis

Thermal analysis curves (TG, DTG, and DTA) showing the thermal behavior of the synthesized alkaline earth metal cations of mixed ligand coordination compounds containing coumarilate / nicotinamide (Figure 2). In addition, the data showing the thermal behavior of the complexes are summarized in Table 2.

The DTG curve of the complex compound of the Mg(II) cation, which is one of the coumarilate / nicotinamide-containing mixed-ligand complexes of the alkaline earth metal cations, was found to be degraded in four steps corresponding to the maximum temperatures of 125, 263, 428 °C and 575; 647; 758; 825 °C.

As the first degradation step, removing uncoordinated hydrate in the structure occurred in the temperature range of 85-147 °C (exp. 2.65%; calc. 2.65%). Decomposition corresponding to the maximum temperature step at 125 °C is endothermic.

$$[Mg(C_6H_6N_2O)_2(H_2O)_4].2(C_9H_5O_3).H_2O \xrightarrow{85\text{-}147^{O}C} [Mg(C_6H_6N_2O)_2(H_2O)_4].2(C_9H_5O_3) + H_2O \uparrow$$

The second degradation step is still the dehydrated degradation step and takes place in the temperature range of 158-304 °C. At the 263 °C DTA peak, the four moles of coordination water remaining in the coordination sphere in the endothermic degradation step decay away (exp. 11.07%; calc. 10.58%).

$$[Mg(C_6H_6N_2O)_2(H_2O)_4].2(C_9H_5O_3) \xrightarrow{158\text{-}304^oC} [Mg(C_6H_6N_2O)_2].2(C_9H_5O_3) + 4\ H_2O\uparrow$$

From the coordination compound, which has become entirely dehydrated, in the third degradation step, two moles of nicotinamide (na) ligand in the structure burns and degrades in the temperature range of 351-482 °C. It is thought that NO/NO_2, CO/CO_2, and H_2O combustion gases and vapors are formed as decomposition products in the reaction that takes place at 428 °C maximum decomposition step endothermically (exp. 34.97%; calc. 35.84%).

$$[Mg(C_6H_6N_2O)_2].2(C_9H_5O_3) \xrightarrow{351\text{-}482^oC} [Mg].2(C_9H_5O_3) + NO/NO_2\uparrow + CO/CO_2\uparrow + 4\ H_2O\uparrow$$

The last step of decay can be attributed to the separation of the two moles of coumarilate ligands located outside the coordination sphere as the stabilizing ion in the structure in the 485-908 °C temperature region. Endothermic degradation has DTA peaks at 575; 647; 758; 825 °C. Experimental and theoretical mass losses also support this claim (exp. 44.11%; calc. 44.94%). After this decomposition step, it was determined that the oxide compound of the corresponding metal cation remained in the reaction vessel. The fact that the color of the oxide is black instead of white can be said to be caused by the carbonized carbon remaining in the environment (exp. 7.20%; calc. 5.92%).

$$[Mg].2(C_9H_5O_3) \xrightarrow{351\text{-}482^oC} MgO + CO/CO_2\uparrow + 4\ H_2O\uparrow$$

DTA curve of the coordination compound with mixed ligands of Ca metal cation shows that decays occur in four steps, at 118, 254, -414 and 481;-688;708 °C maximum temperatures. The first degradation step is involved in the removal of all aqua ligands in the structure (three moles of aqua at the two-molar bridge position and six moles of aqua ligands in total, three moles attached to each Ca cation) in the temperature range 65-186 °C. These decays are endothermic and occur at 118 °C maximum degradation step (exp. 11.98%; calc. 12.94%).

$$\mu\text{-}(H_2O)_2[Ca(C_9H_5O_3)(C_6H_6N_2O)(H_2O)_3]_2.2(C_9H_5O_3) \xrightarrow{65\text{-}186^oC} [Ca(C_9H_5O_3)(C_6H_6N_2O)]_2.2(C_9H_5O_3) + 8\ H_2O\uparrow$$

In the temperature range of 188-290 °C, two moles of neutral nicotinamide ligands are located in the coordination sphere at a maximum degradation step of 254 °C burn away from the structure (exp. 21.93%; calc. 21.92%). It is thought that NO/NO_2, CO/CO_2, and H_2O gas and vapors are formed as combustion products.

$$[Ca(C_9H_5O_3)(C_6H_6N_2O)]_2.2(C_9H_5O_3) \xrightarrow{188\text{-}290^oC} [Ca(C_9H_5O_3)]_2.2(C_9H_5O_3) + NO/NO_2\uparrow + CO/CO_2\uparrow + H_2O\uparrow$$

The degradation of the two moles of coumarilate ligand, which is located outside the coordination sphere and provides the charge balance of the structure as the counter-ion, occurs in the temperature region of 343-424 °C, exothermic at a maximum decomposition temperature of -414 °C (exp. 28.72%; calc. 28.93%).

$$[Ca(C_9H_5O_3)]_2.2(C_9H_5O_3) \xrightarrow{343\text{-}424^oC} [Ca(C_9H_5O_3)]_2 + CO/CO_2\uparrow + H_2O\uparrow$$

The fourth and last degradation step can be attributed to the decomposition of two-mole coumarilate ligands coordinated to the metal cation inside the coordination sphere. Decomposition occurs in the temperature range of 427-905 °C and at maximum decomposition temperatures of 481; -688; 708 °C provided that one is exothermic. The coherence of the experimental and calculated mass losses attributed to the decay supports the claimed degradation (exp. 25.82%; calc. 26.06%).

$$[Ca(C_9H_5O_3)]_2 \xrightarrow{427\text{-}905^{O}C} 2CaO + CO/CO_2\uparrow + H_2O\uparrow$$

After all the degradation, the remaining decomposition product is two moles of CaO. The black color of the expected decomposition product in white color can be attributed to the carbonized carbon remaining in the environment due to the inability of complete combustion. This is supported by the fact that the percentage of the experimental residual product is higher than the calculated percentage (exp. 11.55%; calc. 10.06%). The thermal analysis curves of the Sr-centered coumarilate/nicotinamide compound determined that six degradation steps correspond to the maximum decomposition temperatures of 85, 148 226, -229, -410; 470 and -742; 848 °C. The first of these is the coordinated four molecule aqua ligand, coordinated at the terminal position to the Sr cations in the compound in the temperature range 59-106 °C, separated from the structure (exp. 5.83%; calc. 6.14%).

$$\mu\text{-}(H_2O)_2[Sr(C_9H_5O_3)(C_6H_6N_2O)(H_2O)_2]_2.2(C_9H_5O_3) \xrightarrow{59\text{-}106^{o}C} \mu\text{-}(H_2O)_2[Sr(C_9H_5O_3)(C_6H_6N_2O)]_2.2(C_9H_5O_3) + 4\ H_2O\uparrow$$

In the next step of decay, it was determined that the two molecule aqua ligands, which are bridging between the two Sr atoms, which act as central cations in the structure, were decomposed in the 108-192 °C temperature range in the 148 °C DTA max. (exp. 2.72%; calc. 3.07%).

$$\mu\text{-}(H_2O)_2[Sr(C_9H_5O_3)(C_6H_6N_2O)]_2.2(C_9H_5O_3) \xrightarrow{108\text{-}192^{o}C} [Sr(C_9H_5O_3)(C_6H_6N_2O)]_2.2(C_9H_5O_3) + 2\ H_2O\uparrow$$

In the next degradation step, it was determined that the two molecule aqua ligands, which are bridging between the two Sr atoms, were decomposed in the 108-192 °C temperature range, in the 148 °C DTA maximum temperature (exp. 2.72%; calc. 3.07%). In the subsequent decomposition stage of the dehydrated complex starts to burn organic residues. Comparing the experimental and calculated mass losses (exp. 7.31%; calc. 7.51%) estimates that partial combustion of the nicotinamide ligand in the neutral position occurs primarily. The carbonyl and amide functional groups of the nicotinamide ligand form NO/NO_2, CO/CO_2, and H_2O combustion products and move away from the structure in the 195-282 °C temperature region, at the maximum decomposition temperature of 226 °C.

$$[Sr(C_9H_5O_3)(C_6H_6N_2O)]_2.2(C_9H_5O_3) \xrightarrow{195\text{-}282^{o}C} [Sr(C_9H_5O_3)(C_5H_4N)]_2.2(C_9H_5O_3) + NO/NO_2\uparrow + CO/CO_2\uparrow + H_2O\uparrow$$

Table 1: Elemental analysis data of molecules.

Complex	M.A. (g/mol)	Yield (%)	C% exp-(calc)	H% exp-(calc)	N% exp-(calc)
$[Mg(C_{10}H_{14}N_2O)_2(H_2O)_4].2(C_9H_5O_3).H_2O$ (I)	662.89	91	53.92-(54.36)	4.77-(4.56)	8.32-(8.45)
μ-$(H_2O)_2[Ca(C_9H_5O_3)(C_6H_6N_2O)(H_2O)_3]_2.2(C_9H_5O_3)$ (II)	1113.07	90	51.33-(51.80)	4.71-(4.35)	4.97-(5.03)
μ-$(H_2O)_2[Sr(C_9H_5O_3)(C_6H_6N_2O)(H_2O)_2]_2.2(C_9H_5O_3)$ (III)	1172.13	87	48.77-(49.19)	3.92-(3.78)	4.84-(4.78)
μ-$(H_2O)_2[Ba(C_9H_5O_3)(C_6H_6N_2O)(H_2O)_2]_2.2(C_9H_5O_3)$ (IV)	1271.54	86	45.73-(45.34)	3.79-(3.49)	4.35-(4.41)

Subsequent degradation has been attributed to the burning of the more stable pyridine rings of nicotinamide ligands. In the temperature range of 372-403 °C, in the exothermic -299 °C decomposition step, the pyridine rings remove from the structure by giving the combustion gases and vapors of NO/NO_2, CO/CO_2, and H_2O (exp. 13.51%; calc. 13.31%).

$$[Sr(C_9H_5O_3)(C_6H_6N_2O)]_2.2(C_9H_5O_3) \xrightarrow{372\text{-}403^oC} [Sr(C_9H_5O_3)]_2.2(C_9H_5O_3) + NO/NO_2\uparrow + CO/CO_2\uparrow + H_2O\uparrow$$

The combustion reactions taking place in the degradation steps in the temperature range of 404-685 °C, one exothermic -410 °C, and the other endothermic 470 °C, can be attributed to two mole stabilizing coumarilate anions located outside the coordination sphere. The compatibility of experimental and theoretical results with each other also supports this situation (exp. 26.92%; calc. 27.47%).

$$[Sr(C_9H_5O_3)]_2.2(C_9H_5O_3) \xrightarrow{404\text{-}685^oC} [Sr(C_9H_5O_3)]_2 + CO/CO_2\uparrow + H_2O\uparrow$$

The sixth and final degradation step is the step in which all combustion events occur, and the degradation ends, and the last black-colored molecule of SrO remains. The coherence of experimental and theoretical mass losses in the combustion reaction occurring at the maximum decomposition temperatures of 742 °C and endothermic 848 °C in the 687-891 °C temperature region also supports this result (exp. 24.91%; calc. 24.74%). It is suggested that CO/CO_2 and H_2O combustion gas and vapors are formed as combustion products. The fact that the experimental mass amount of the final residual product is slightly higher than the theoretical amount indicates that the black color of the residual product is due to carbonized carbon remaining from combustion due to an inert nitrogen environment (exp. 18.80%; calc. 17.68%).

$$[Sr(C_9H_5O_3)]_2 \xrightarrow{687\text{-}891^oC} 2SrO + CO/CO_2\uparrow + H_2O\uparrow$$

Thermal analysis curves of the coumarilate / nicotinamide complex of the Ba metal cation are given in Figure 4. Six degradation steps were observed in the DTA curve at maximum decomposition temperatures of 86, 205, 333, -401, -417; 454; 617 and -707; -774; 842 °C. The degradation pattern of the Ba complex is very similar to that of the Sr complex. The first decay step can be attributed to the removal of the coordinated four molecules of aqua ligand at the terminal position to the Ba cations in the temperature range 59-94 °C (exp. 6.02%; calc. 5.66%).

$$\mu\text{-}(H_2O)_2[Ba(C_9H_5O_3)(C_6H_6N_2O)(H_2O)_2]_2.2(C_9H_5O_3) \xrightarrow{59\text{-}94^oC} \mu\text{-}(H_2O)_2[Ba(C_9H_5O_3)(C_6H_6N_2O)]_2.2(C_9H_5O_3) + 4\ H_2O\uparrow$$

The second degradation step is still the dehydrated degradation step and belongs to the degradation of the aqua ligands, which are the bridges connecting the two Ba cations, which takes place in the temperature range 95-215 °C with a maximum decomposition temperature of 86 °C (exp. 3.04%; calc. 2.83%).

$$\mu\text{-}(H_2O)_2[Ba(C_9H_5O_3)(C_6H_6N_2O)]_2.2(C_9H_5O_3) \xrightarrow{95\text{-}215^oC} [Ba(C_9H_5O_3)(C_6H_6N_2O)]_2.2(C_9H_5O_3) + 2\ H_2O\uparrow$$

It is thought that the neutral ligand, nicotinamide - NH_2 group, leaves the structure in the form of ammonia gas in the next decaying step of the dehydrated coordination compound, with the water

removed from its structure. The decomposition's experimental and theoretical mass losses in the temperature range of 217-384 °C are consistent with this fragmentation (exp. 2.42.04%; calc. 2.52%).

$$[Ba(C_9H_5O_3)(C_6H_6N_2O)]_2.2(C_9H_5O_3) \xrightarrow{217\text{-}384^oC} [Ba(C_9H_5O_3)(C_6H_3NO)]_2.2(C_9H_5O_3) + 2\ NH_3\uparrow + CO/CO_2\uparrow + H_2O\uparrow$$

The subsequent degradation belongs to the combustion reaction of the remaining parts of nicotinamide ligands, leaving the structure by forming NO/NO_2, CO / CO_2, and H_2O combustion products. In the temperature range of 385-407 °C, in the exothermic -401 °C degradation step, the nicotinamide residue burns completely (exp. 16.52%; calc. 16.67%).

$$[Ba(C_9H_5O_3)(C_6H_3NO)]_2.2(C_9H_5O_3) \xrightarrow{385\text{-}407^oC} [Ba(C_9H_5O_3)]_2.2(C_9H_5O_3) + NO/NO_2\uparrow + CO/CO_2\uparrow + H_2O\uparrow$$

The degradation continues with the combustion of the coumarilate anions in the counter-ion position outside the coordination sphere, among the four molecule coumarilate ligands, which are organic residues in the structure. In the temperature range of 408-580 °C, one exothermic -410 °C, others endothermic 454; 617 °C decomposition products are formed as a result of the combustion reactions that take place in the decomposition steps (exp.25.22%; calc. 25.33%).

$$[Ba(C_9H_5O_3)]_2.2(C_9H_5O_3) \xrightarrow{408\text{-}580^oC} [Ba(C_9H_5O_3)]_2 + CO/CO_2\uparrow + H_2O\uparrow$$

The final degradation step of the thermal analysis of the complex occurs in the temperature region of 585-880 °C, while it takes place in three steps, two exothermic -707; -774 °C and the other endothermic 842 °C. After all the combustion and disintegration processes, it was determined that 25.21% BaO residue remained in the reaction vessel as the final product. The fact that this value is slightly higher than the theoretically calculated residual value (24.12%) is that complete combustion cannot occur by conditioning the reaction medium with inert nitrogen gas to determine the disintegration steps more clearly since complete combustion could not take place, some carbon residue accumulated on the surface of the metal oxide as carbonized coal, which can be interpreted as the reason for the expected black color of the residual metal oxide.

$$[Ba(C_9H_5O_3)]_2 \xrightarrow{585\text{-}880^oC} 2BaO + CO/CO_2\uparrow + H_2O\uparrow$$

Infrared spectroscopy

FTIR stretching modes of the coumarilic acid/nicotinamide complexes of alkaline earth metal cations are given in Figure 3, and the important band stretching modes of the FT-IR spectra of the compounds are summarized in Table 4.

When FTIR spectra of alkaline earth metal cation complexes with mixed ligands containing coumarilate / nicotinamide ligands are examined, the resulting strong and broadband 3680-2850 cm^{-1} indicates the presence of -OH group in the structures of the coordination compounds. The Mg metal cation complex is salt type, and the coumarilate ligands are located outside the coordination sphere. In other structures, coumarilate ligands entered the coordination sphere. Accordingly, different FTIR peaks were observed in the Mg cation mixed ligand complex from other structures. While the peak of the C=O stress vibration of the carboxylic acid group in the Mg complex is observed at 1663 cm^{-1}, it is also understood from the difference between asymmetric and symmetrical stress vibrations that the same group is monodentately coordinated ($v(C=O)_{asym.}$-$v(C=O)_{sym.}$: 1562 cm^{-1} - 1441 cm^{-1} = $\Delta v_{asym-sym}$: 121 cm^{-1}). In other complexes, the bonding is of bidentate fashion, and the differences between asymmetric and symmetrical stress vibrations are found to be greater than the difference (130 cm^{-1}) between the coumarilic acid's own asymmetric and symmetrical stress vibrations (170 cm^{-1} for complex **II**, 142 cm^{-1} for complex **III**, 160 cm^{-1} for complex **IV** respectively). The appearance of both the N-H peaks of the nicotinamide ligand and the fact that the peaks of the carbonyl group of the amide group do not show any shift compared to the pure nicotinamide ligand can be considered as evidence that this ligand participates in the coordination via the characteristic pyridine nitrogen. The peaks belonging to the coordination of the ligands are generally the peaks indicating the attachment to the metal center. In contrast, three different coordination is observed in the Mg complex, which is different from the other compounds (649 cm^{-1} for v(M–N), 559 cm^{-1} $v(M–O–)_{carboxyl,}$ and 425 cm^{-1} for $v(M–O)_{aqua}$), while in the other three cation complexes, four different coordination with the metal was observed due to the carboxylate group oxygens that show bidentate bonding. The stresses belonging to these coordinations have been found for the Ca complex v(M–N) is 646 cm^{-1}, $v(M–O–)_{carboxyl}$ is 581 cm^{-1}, $v(M–O=)_{carbonyl}$ 535 cm^{-1} and $v(M–O)_{aqua}$ 427 cm^{-1}; for the Sr complex v(M–N) is 617 cm^{-1}, $v(M–O–)_{carboxyl}$ is 578 cm^{-1}, $v(M–O=)_{carbonyl}$ 526 cm^{-1} and $v(M–O)_{aqua}$ 445 cm^{-1}; for the Ba complex v(M–N) is 669 cm^{-1}, $v(M–O–)_{carboxyl}$ is 581 cm^{-1}, $v(M–O=)_{carbonyl}$ 526 cm^{-1} and $v(M–O)_{aqua}$ 426 cm^{-1}.

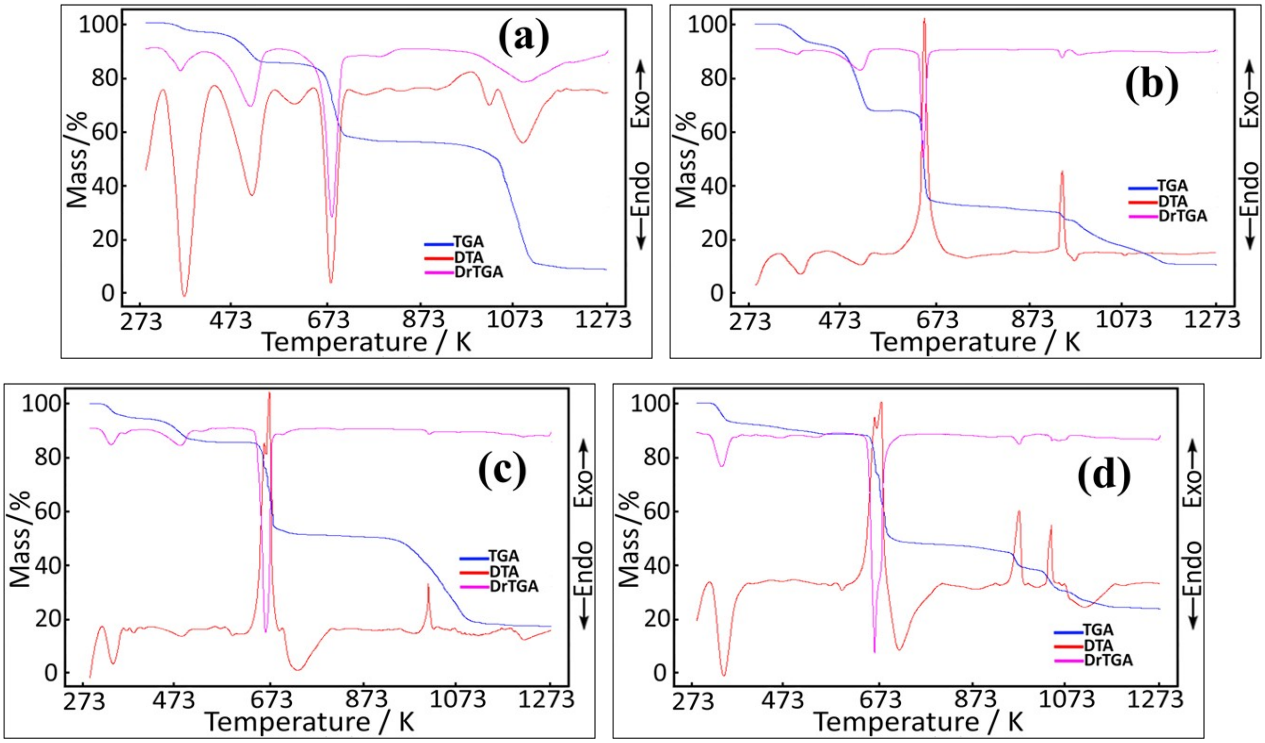

Figure 2: Thermal analysis curves of metal-coumarilate / nicotinamide mixed ligand complexes. (**a**) Mg^{2+} complex, (**b**) Ca^{2+} complex, (**c**) Sr^{2+} complex and (**d**) Ba^{2+} complex.

Powder x-ray diffraction analysis

It has been determined that all of the molecules whose powder X-ray diffraction patterns are formed have good crystallinities (Figure 4). However, single-crystal structure analysis could not be made due to the small size of the crystals selected for single-crystal structure analysis. The apparent difference in the powder x-ray diffraction pattern of the Mg^{2+} cation-centered complex from that of the other three complexes supports this molecule's proposed salt structure claim. The general similarity of powder X-ray diffraction patterns in Ca^{2+}, $Sr^{2+,}$ and Ba^{2+}-centered structures strengthens the suggestion that these three structures are iso-structural with each other.

Table 2: Thermal analysis data of metal-coumarilate / nicotinamide mixed ligand complexes.

Complexes		Temp. Range (˚C)	DTA_{max} (˚C)	Removed Groups	Mass Loss (%)		Remaining Product (%)		Decomp. Product	Color
					Exp.	Calc.	Exp.	Calc.		
$[Mg(C_6H_6N_2O)_2(H_2O)_4].2(C_9H_5O_3).H_2O$										Pink
$C_{30}H_{30}MgN_4O_{12}$	1	85-147	125	H_2O	2.65	2.65				
662.89 g/mol	2	158-304	263	4 H_2O	11.07	10.58				
	3	351-482	428	2 $C_6H_6N_2O$	34.97	35.84				
	4	485-908	575, 647, 758, 825	$C_9H_5O_2$; $C_9H_5O_3$	44.11	44.94	7.20	5.92	MgO	Black
μ-$(H_2O)_2[Ca(C_9H_5O_3)(C_6H_6N_2O)(H_2O)_3]_2.2(C_9H_5O_3)$										White
$C_{48}H_{48}Ca_2N_4O_{22}$	1	65-186	118	8 H_2O	11.98	12.94				
1113.07 g/mol	2	188-290	254	2 $C_6H_6N_2O$	21.93	21.92				
	3	343-424	-414	2 $C_9H_5O_3$	28.72	28.93				
	4	427-905	481, -688, 708	2 $C_9H_5O_2$	25.82	26.06	11.55	10.06	2 CaO	Black
μ-$(H_2O)_2[Sr(C_9H_5O_3)(C_6H_6N_2O)(H_2O)_2]_2.2(C_9H_5O_3)$										Blue
$C_{48}H_{44}N_4O_{20}Sr_2$	1	59-106	85	4 $H_2O_{(terminal)}$	5.83	6.14				
1172.13 g/mol	2	108-192	148	2 $H_2O_{(bridge)}$	2.72	3.07				
	3	195-282	226	2 C_2H_2NO	7.31	7.51				
	4	372-403	-299	2 C_5H_4N	13.51	13.31				
	5	404-685	-410, 470	2 $C_9H_5O_3$	26.92	27.47				
	6	687-891	-742, 848	2 $C_9H_5O_2$	24.91	24.74	18.80	17.68	2 SrO	Black
μ-$(H_2O)_2[Ba(C_9H_5O_3)(C_6H_6N_2O)(H_2O)_2]_2.2(C_9H_5O_3)$										White
$C_{48}H_{44}Ba_2N_4O_{20}$	1	59-94	86	4 $H_2O_{(terminal)}$	6.02	5.66				
1271.54 g/mol	2	95-215	205	2 $H_2O_{(bridge)}$	3.04	2.83				
	3	217-384	333	2 NH_3	2.42	2.52				
	4	385-407	-401	2 C_6H_4NO	16.52	16.67				
	5	408-580	-417, 454, 617	2 $C_9H_5O_3$	25.22	25.33				
	6	585-880	-707, -774, 842	2 $C_9H_5O_2$	21.57	22.81	25.21	24.12	2 BaO	Grey

CONCLUSIONS

This study was presented as a master's thesis, complex compounds with coumarilic acid / nicotinamide mixed ligands of magnesium, calcium, strontium, and barium cations are alkaline earth metal cations, were synthesized. Elemental analysis, Fourier transform infrared spectroscopy (FTIR), thermogravimetric analysis (TGA/DTA), powder x-ray diffraction diffractometer (P-XRD), and melting point determination methods were used to examine the structural characterization of the complexes. It was determined that compounds with mixed ligands were 1:2:1 except for the Mg complex. In the Mg complex, the ratio was determined as 1:2:2. Molecular formulas of the compounds determined to contain water in their structures according to thermal analysis curves and infrared spectra are proposed as follows by chemical composition analysis.

(I)	$[Mg(C_6H_6N_2O)_2(H_2O)_4].2(C_9H_5O_3).H_2O$	$C_{30}H_{30}MgN_4O_{12}$
(II)	μ-$(H_2O)_2[Ca(C_9H_5O_3)(C_6H_6N_2O)(H_2O)_3]_2.2(C_9H_5O_3)$	$C_{48}H_{48}Ca_2N_4O_{22}$
(III)	μ-$(H_2O)_2[Sr(C_9H_5O_3)(C_6H_6N_2O)(H_2O)_2]_2.2(C_9H_5O_3)$	$C_{48}H_{44}N_4O_{20}Sr_2$
(IV)	μ-$(H_2O)_2[Ba(C_9H_5O_3)(C_6H_6N_2O)(H_2O)_2]_2.2(C_9H_5O_3)$	$C_{48}H_{44}Ba_2N_4O_{20}$

Table 3: FT-IR spectral data of metal-coumarilate / nicotinamide mixed ligand complexes.

Groups	**Mg^{2+}**	**Ca^{2+}**	**Sr^{2+}**	**Ba^{2+}**
$v(OH)_{H2O}$	3500-3100	3550-2850	3670-3000	3680-3000
$v(N-H)_{amide}$	3358, 3198	3354, 2850	3498, 3180	3423, 3175
$v(=C-H)_{ar}$	3252	3257	3280	3280
$v(C=C)_{ar}$	3061	3061, 3081	3058, 3001	3061, 3011
$v(CH_2)$	2910, 2825	2850, 2885	2924, 2872	2928, 2866
$v(C=O)_{carbonyl}$	1663	1657	1643	1649
$v(C=O)_{amide}$	1705	1709	1699	1697
$v(COO-)_{asym.}$	1562	1566	1552	1572
$v(COO-)_{sym.}$	1441	1396	1410	1412
Δv_{as-s}	121	170	142	160
$\delta(OH)_{H2O}$	1474	1467	1474	1474
$v(C-N-C)_{pyridine}$	1328	1334	1337	1337
$v(C_9-O_1-C_1)$	1259/1184	1262/1178	1259/1178	1262/1181
$v(C-O)_{carboxyl}$	1298	1295	1305	1308
v(Ring)	1106-816	1125-812	1109-835	1109-835
$v(C-N)_{amide}$	943-741	943-744	943-741	943-741
v(M-N)	649	646	617	669
$v(M-O-)_{carboxyl}$	559	581	578	581
v(M-O=)	-	535	526	526
$v(M-O-)_{aqua}$	425	427	445	426

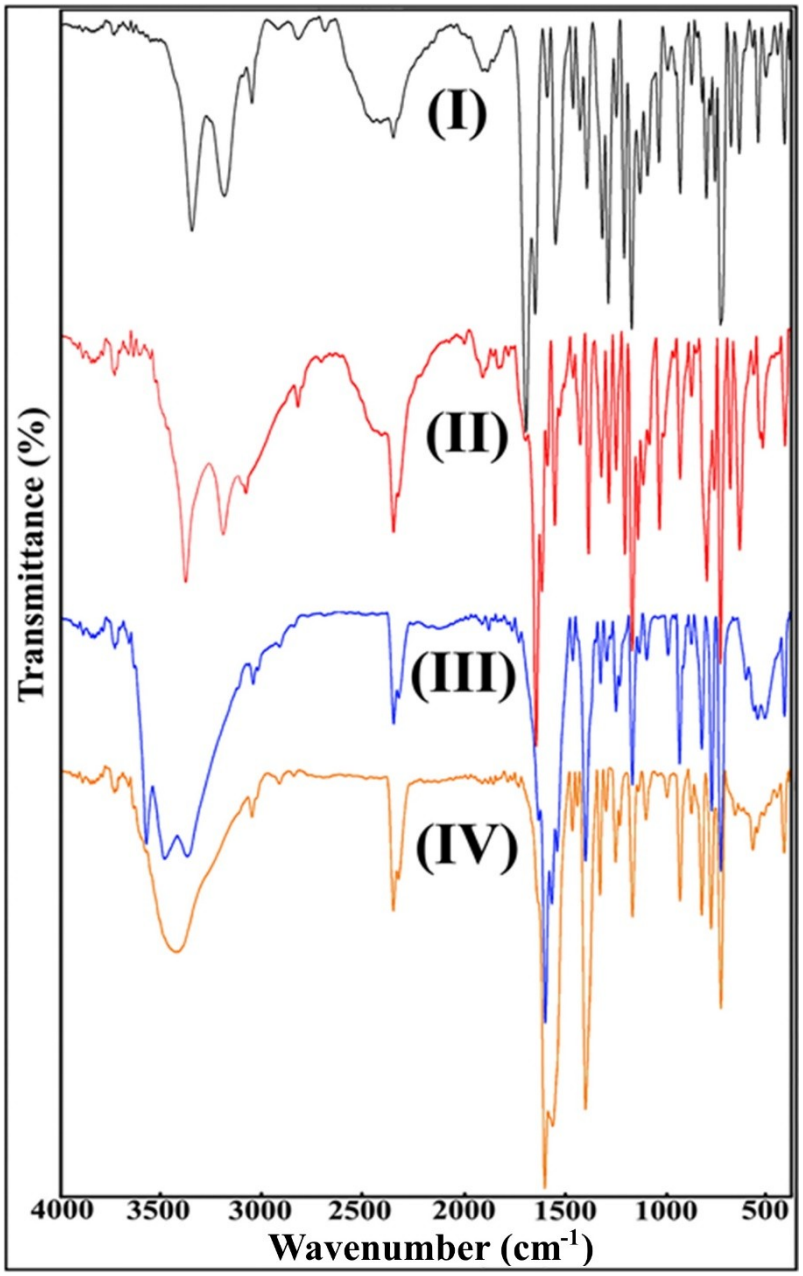

Figure 3. FT-IR spectra of the complex structures **I**, **II**, **III** and **IV**.

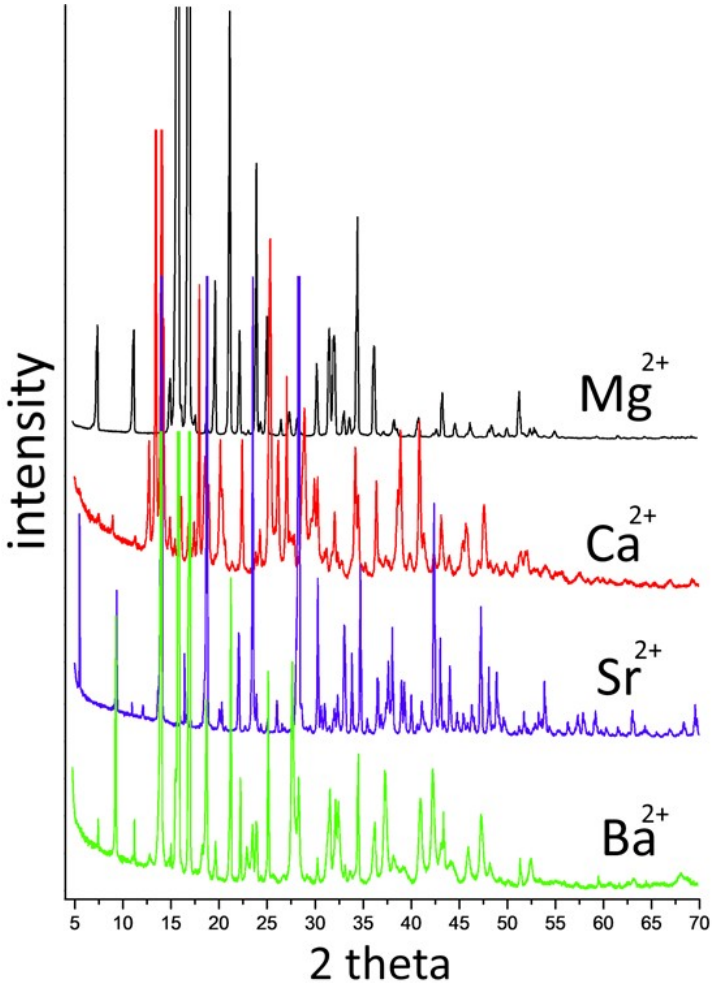

Figure 4: P-XRD patterns of the complex structures Mg^{2+}, Ca^{2+}, $Sr^{2+,}$ and Ba^{2+}.

The images of the synthesized complexes taken with light microscopy were given in Figure 5. The Mg^{2+} complex is salt-type, and the coumarilate ligands are located outside the coordination sphere. In other structures, coumarin ligands entered the coordination sphere. Accordingly, different infrared peaks were observed in the Mg^{2+} cation mixed ligand complex from other structures. The appearance of both the N-H peaks of the nicotinamide ligand and the fact that the peaks of the carbonyl group of the amide group do not show any shift compared to the pure nicotinamide ligand can be considered as evidence that this ligand participates in the coordination via the characteristic pyridine nitrogen. The coordination of the ligands is generally supported by infrared peaks that signal their bonding to the metal center. While three different coordination is observed in the Mg^{2+} complex, which is different from other compounds in its structure, in the other three cation complexes (Ca^{2+}, $Sr^{2+,}$ and Ba^{2+}), the infrared peak of four different coordination with the metal has been determined due to the carboxylate group oxygens showing bidentate bonding. Thermal degradation analysis of the coordination compounds of the synthesized alkaline earth metal cations has been interpreted in detail in the thermal analysis section. The degradation steps started with removing hydrate waters located outside the coordination sphere and continued with the decay of the terminal waters located within the coordination sphere. The complete dehydration of the complexes ended with the departure of the aqua ligands, which were bridging between the two metal cation centers, from the structures. The degradation of organic ligands started with the decomposition of the neutral ligand, nicotinamide, and then continued with the burning of the coumarilic acid ligands. The cleavage sequence of coumarilic acid ligands showing two different types of binding in the complexes was also noticed. First of all, the coumarilate ligands acting as the stabilizing anion of the complexes located outside the coordination sphere have been removed. Afterward, the degradation of the coumarilate ligands that provide bidentate coordination to the metal in the coordination sphere was observed. It was determined that oxide compounds of the respective metals remained in the reaction vessel as the final products of all thermal degradation.

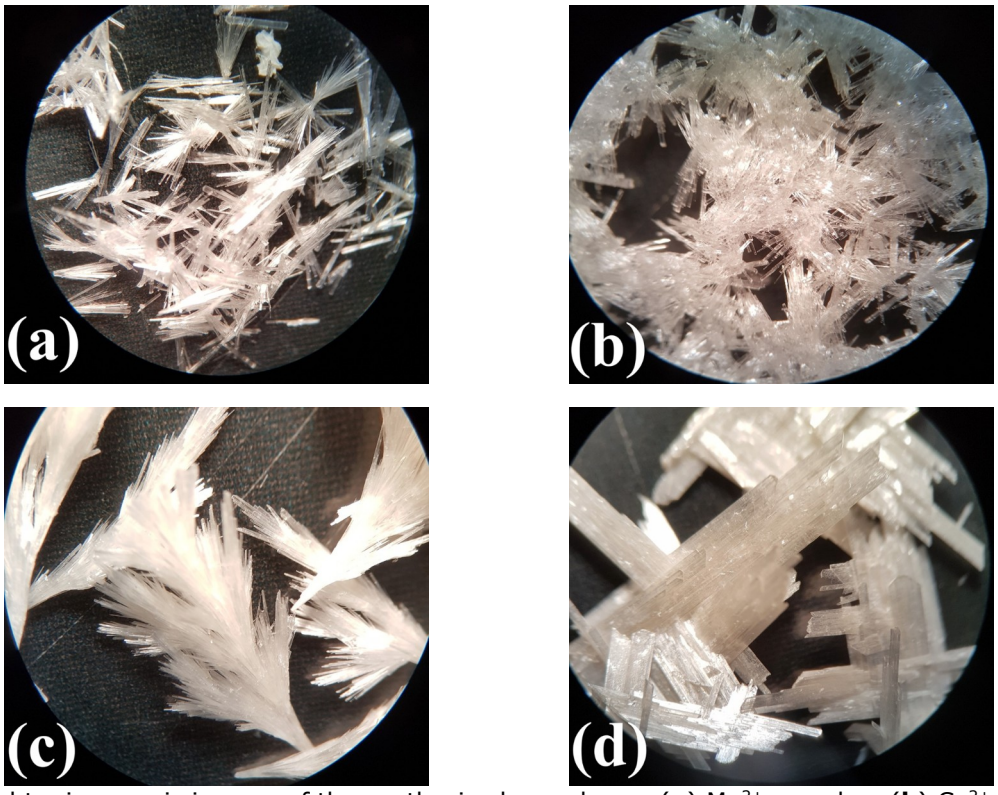

Figure 5: Light microscopic images of the synthesized complexes. (**a**) Mg^{2+} complex, (**b**) Ca^{2+} complex, (**c**) Sr^{2+} complex and (**d**) Ba^{2+} complex.

ACKNOWLEDGMENTS

This study was financially supported by Hitit University in Turkey (Project No. FEF19004.18.001).

REFERENCES

1. Bosshard P, Eugster CH. The development of the chemistry of furans, 1952-1963. In: Advances in Heterocyclic Chemistry [Internet]. Elsevier; 1967 [cited 2021 May 10]. p. 377–490. Available from: https://linkinghub.elsevier.com/retrieve/pii/S0065272508605942

2. Khanam H, Shamsuzzaman. Bioactive Benzofuran derivatives: A review. European Journal of Medicinal Chemistry. 2015 Jun;97:483–504. Doi: https://doi.org/10.1016/j.ejmech.2014.11.039.

3. Hiremath SM, Suvitha A, Patil NR, Hiremath CS, Khemalapure SS, Pattanayak SK, et al. Molecular structure, vibrational spectra, NMR, UV, NBO, NLO, HOMO-LUMO and molecular docking of 2-(4, 6-dimethyl-1-benzofuran-3-yl) acetic acid (2DBAA): Experimental and theoretical approach. Journal of Molecular Structure. 2018 Nov;1171:362–74. Doi: https://doi.org/10.1016/j.molstruc.2018.05.109.

4. Radadiya A, Shah A. Bioactive benzofuran derivatives: An insight on lead developments, radioligands and advances of the last decade. European Journal of Medicinal Chemistry. 2015 Jun;97:356–76. Doi: https://doi.org/10.1016/j.ejmech.2015.01.021.

5. Dawood KM. Benzofuran derivatives: a patent review. Expert Opinion on Therapeutic Patents. 2013 Sep;23(9):1133–56. Doi: https://doi.org/10.1517/13543776.2013.801455.

6. Naik R, Harmalkar DS, Xu X, Jang K, Lee K. Bioactive benzofuran derivatives: Moracins A–Z in medicinal chemistry. European Journal of Medicinal Chemistry. 2015 Jan;90:379–93. Doi: https://doi.org/10.1016/j.ejmech.2014.11.047.

7. Oka T. Enantioselective synthesis and absolute configuration of (−)-1-(benzofuran-2-yl)-2-propylaminopentane, ((−)-BPAP), a highly potent and selective catecholaminergic activity enhancer. Bioorganic & Medicinal Chemistry. 2001 May;9(5):1213–9. Doi: https://doi.org/10.1016/S0968-0896(00)00341-2.

8. Fukai T, Oku Y, Hano Y, Terada S. Antimicrobial Activities of Hydrophobic 2-Arylbenzofurans and an Isoflavone against Vancomycin-Resistant Enterococci and Methicillin-Resistant Staphylococcus aureus. Planta med. 2004 Jul;70(7):685–7. Doi: https://doi.org/10.1055/s-2004-827196.

9. Gilchrist T. Aromatic heterocycles. In: Heterocyclic chemistry. Harlow, UK: Longman Scientific & Technical; 1985. p. 5–19.

10. Hattori M, Hada S, Watahiki A, Ihara H, Shu Y-Z, Kakiuchi N, et al. Studies on dental caries prevention by traditional medicines. X Antibacterial action of phenolic components from mace against Streptococcus mutans. Chem Pharm Bull. 1986;34(9):3885–93. Doi: https://doi.org/10.1248/cpb.34.3885.

11. Erber S, Ringshandl R, von Angerer E. 2-Phenylbenzo[b]furans: relationship between structure, estrogen receptor affinity and cytostatic activity against mammary tumor cells. Anticancer Drug Des. 1991 Nov;6(5):417–26. Url: https://pubmed.ncbi.nlm.nih.gov/1764164/.

12. Cui B, Chai H, Santisuk T, Reutrakul V, Farnsworth NR, Cordell GA, et al. Novel cytotoxic 1H-cyclopenta[b]benzofuran lignans from Aglaia elliptica. Tetrahedron. 1997 Dec;53(52):17625–32. Doi: https://doi.org/10.1016/S0040-4020(97)10231-9.

13. Lee SK, Cui B, Mehta RR, Kinghorn AD, Pezzuto JM. Cytostatic mechanism and antitumor potential of novel 1H-cyclopenta[b]benzofuran lignans isolated from Aglaiaelliptica. Chemico-Biological Interactions. 1998 Oct;115(3):215–28. Doi: https://doi.org/10.1016/S0009-2797(98)00073-8.

14. Kodama I, Kamiya K, Toyama J. Amiodarone: ionic and cellular mechanisms of action of the most promising class III agent. The American Journal of Cardiology. 1999 Nov;84(9):20–8. Doi: https://doi.org/10.1016/S0002-9149(99)00698-0.

15. Hayakawa I, Shioya R, Agatsuma T, Furukawa H, Naruto S, Sugano Y. 4-Hydroxy-3-methyl-6-phenylbenzofuran-2-carboxylic acid ethyl ester derivatives as potent anti-tumor agents. Bioorganic & Medicinal Chemistry Letters. 2004 Jan;14(2):455–8. Doi: https://doi.org/10.1016/j.bmcl.2003.10.039.

16. Hwang BY, Su B-N, Chai H, Mi Q, Kardono LBS, Afriastini JJ, et al. Silvestrol and Episilvestrol, Potential Anticancer Rocaglate Derivatives from Aglaia silvestris. J Org Chem. 2004 Sep;69(18):6156–6156. Doi: https://doi.org/10.1021/jo040008h.

17. Masche UP, Rentsch KM, von Felten A, Meier PJ, Fattinger KE. No clinically relevant effect of Iornoxicam intake on acenocoumarol pharmacokinetics and pharmacodynamics. European Journal of Clinical Pharmacology. 1999 Jan 20;54(11):865–8. Doi: https://doi.org/10.1007/s002280050568.

18. Karaliota A, Kretsi O, Tzougraki C. Synthesis and characterization of a binuclear coumarin-3-carboxylate copper(II) complex. Journal of Inorganic Biochemistry. 2001 Mar;84(1–2):33–7. Doi: https://doi.org/10.1016/S0162-0134(00)00214-2.

19. Kossakowski J, Krawiecka M, Kuran B, Stefańska J, Wolska I. Synthesis and Preliminary Evaluation of the Antimicrobial Activity of Selected 3-Benzofurancarboxylic Acid Derivatives. Molecules. 2010 Jul 6;15(7):4737–49. Doi: https://doi.org/10.3390/molecules15074737.

20. Tsuji H, Mitsui C, Ilies L, Sato Y, Nakamura E. Synthesis and Properties of 2,3,6,7-Tetraarylbenzo[1,2- b:4,5- b ‘]difurans as Hole-Transporting Material. J Am Chem Soc. 2007 Oct 1;129(39):11902–3. Doi: https://doi.org/10.1021/ja074365w.

21. Anderson S, Taylor PN, Verschoor GLB. Benzofuran Trimers for Organic Electroluminescence. Chem Eur J. 2004 Jan 23;10(2):518–27. Doi: https://doi.org/10.1002/chem.200305284.

22. Creaven BS, Devereux M, Georgieva I, Karcz D, McCann M, Trendafilova N, et al. Molecular structure and spectroscopic studies on novel complexes of coumarin-3-carboxylic acid with Ni(II), Co(II), Zn(II) and Mn(II) ions based on density functional theory. Spectrochimica Acta Part A: Molecular and Biomolecular Spectroscopy. 2011 Dec;84(1):275–85. Doi: https://doi.org/10.1016/j.saa.2011.09.041.

23. Castellani CB, Carugo O. Studies on fluorescent lanthanide complexes. New complexes of lanthanides(III) with coumarinic-3-carboxylic acid. Inorganica Chimica Acta. 1989 May;159(2):157–61. Doi: https://doi.org/10.1016/S0020-1693(00)80560-5.

24. Georgieva I, Trendafilova N, Aquino AJA, Lischka H. Theoretical Study of Metal−Ligand Interaction in Sm(III), Eu(III), and Tb(III) Complexes of Coumarin-3-Carboxylic Acid in the Gas Phase and Solution. Inorg Chem. 2007 Dec 1;46(25):10926–36. Doi: https://doi.org/10.1021/ic7016616.

25. Georgieva I, Trendafilova N, Creaven BS, Walsh M, Noble A, McCann M. Is the CO frequency shift a reliable indicator of coumarin binding to metal ions through the carbonyl oxygen? Chemical Physics. 2009 Nov;365(1–2):69–79. Doi: https://doi.org/10.1016/j.chemphys.2009.10.004.

26. Mihaylov Tz, Trendafilova N, Kostova I, Georgieva I, Bauer G. DFT modeling and spectroscopic study of metal–ligand bonding in La(III) complex of coumarin-3-carboxylic acid.

Chemical Physics. 2006 Sep;327(2–3):209–19. Doi: https://doi.org/10.1016/j.chemphys.2006.04.009.

27. Roh, Soo-Gyun, Baek, Nam Seob, Hong, Kyong-Soo, 김환규. Synthesis and Photophysical Properties of Luminescent Lanthanide Complexes Based on Coumarin-3-carboxylic Acid for Advanced Photonic Applications. Bulletin of the Korean Chemical Society. 2004 Mar 20;25(3):343–4. Doi: https://doi.org/10.5012/BKCS.2004.25.3.343.

28. Köse DA, Öztürk B, Şahin O, Büyükgüngör O. Mixed ligand complexes of coumarilic acid/nicotinamide with transition metal complexes: Synthesis and structural investigation. J Therm Anal Calorim. 2014 Feb;115(2):1515–24. Doi: https://doi.org/10.1007/s10973-013-3415-6.

29. Ng SW. Coordination complexes of triphenyltin coumarin-3-carboxylate with O -donor ligands: (coumarin-3-carboxylato)triphenyltin– L (L = ethanol, diphenylcyclopropenone and quinoline N -oxide) and bis[(coumarin-3-carboxylato)triphenyltin]– L (L = triphenylphosphine oxide and triphenylarsine oxide). Acta Crystallogr C Cryst Struct Commun. 1999 Apr 15;55(4):523–31. Doi: https://doi.org/10.1107/S0108270198014991.

30. Ng SW, Kumar Das VG. Tetramethylammonium Bis(coumarin-3-carboxylato)triphenylstannate Ethanol Solvate. Acta Crystallogr C Cryst Struct Commun. 1997 Aug 15;53(8):1034–6. Doi: https://doi.org/10.1107/S0108270197004307.

31. Mosa AI, Emara AAA, Yousef JM, Saddiq AA. Novel transition metal complexes of 4-hydroxy-coumarin-3-thiocarbohydrazone: Pharmacodynamic of Co(III) on rats and antimicrobial activity. Spectrochimica Acta Part A: Molecular and Biomolecular Spectroscopy. 2011 Oct;81(1):35–43. Doi: https://doi.org/10.1016/j.saa.2011.05.035.

32. Weder JE, Dillon CT, Hambley TW, Kennedy BJ, Lay PA, Biffin JR, et al. Copper complexes of non-steroidal anti-inflammatory drugs: an opportunity yet to be realized. Coordination Chemistry Reviews. 2002 Oct;232(1–2):95–126. Doi: https://doi.org/10.1016/S0010-8545(02)00086-3.

33. Tisato F, Marzano C, Porchia M, Pellei M, Santini C. Copper in diseases and treatments, and copper-based anticancer strategies. Med Res Rev. 2009;30(4): 708-49. Doi: https://doi.org/10.1002/med.20174.

34. Bareggi SR, Cornelli U. Clioquinol: Review of its Mechanisms of Action and Clinical Uses in Neurodegenerative Disorders: Clioquinol. CNS Neuroscience & Therapeutics. 2012 Jan;18(1):41–6. Doi: https://doi.org/10.1111/j.1755-5949.2010.00231.x.

35. Duncan C, White AR. Copper complexes as therapeutic agents. Metallomics. 2012;4(2):127–38. Doi: https://doi.org/10.1039/C2MT00174H.

36. a) Drzewiecka A, Koziol AE, Klepka MT, Wolska A, Jimenez-Pulido SB, Lis T, et al. Two coordination modes around the Cu(II) cations in complexes with benzo[b]furancarboxylic acids. Chemical Physics Letters. 2013 Feb;559:41–5. Doi: https://doi.org/10.1016/j.cplett.2013.01.011. .b) Drzewiecka A, Koziol AE, Klepka MT, Wolska A, Jimenez-Pulido SB, Struga M. Electrochemical synthesis and structural studies of zinc(II) complexes with derivatives of benzo[b]furancarboxylic acids. Chemical Physics Letters. 2013 Jun;575:40–5. Doi: https://doi.org/10.1016/j.cplett.2013.04.078.

37. Dağlı Ö, Köse DA, Şahin O, Şahin ZS. The synthesis and structural characterization of transition metal coordination complexes of coumarilic acid. J Therm Anal Calorim. 2017 Jun;128(3):1373–83. Doi. https://doi.org/10.1007/s10973-016-6053-y.

38. Dağlı Ö, Köse DA, İçten O, Avcı GA, Şahin O. The mixed ligand complexes of Co(II), Ni(II), Cu(II) and Zn(II) with coumarilic acid/1,10-phenanthroline: Synthesis, crystal characterization and biological applications. J Therm Anal Calorim. 2019 May;136(4):1467–80. Doi: https://doi.org/10.1007/s10973-018-7773-y.

39. Koç S, Köse DA, Avcı E. Synthesis, Structural Characterization and Biological Application of Mixed Ligands Complexes of Coumaric Acid/Coumarine with Some Transition Metal Cation. European Chemical Bulletin. 2016;5(4):132–7.

40. Koc S, Kose DA, Avci E. Synthesis and Thermal Characterization of p-Coumaric Acid Complexes of CoII, NiII, CuII and ZnII Metal Cations and Biological Applications. Hittite J Sci Eng. 2016;3(1):15–22. Doi: https://doi.org/10.17350/HJSE19030000027.

41. Dağlı Ö, Köse DA, Avcı GA, Şahin O. Novel mixed-ligand complexes of coumarilate/N,N'-diethylnicotinamide with some transition metals: Synthesis and structural characterization. J Therm Anal Calorim. 2017 Sep;129(3):1389–402. Doi: https://doi.org/10.1007/s10973-017-6373-6.

42. Srinivasan BR, Shetgaonkar SY, Näther C, Bensch W. Solid state synthesis and characterization of a triple chain calcium(II) coordination polymer showing two different bridging 4-nitrobenzoate coordination modes. Polyhedron. 2009 Feb;28(3):534–40. Doi: https://doi.org/10.1016/j.poly.2008.11.022.

43. Elin RJ. Assessment of magnesium status. Clinical Chemistry. 1987 Nov 1;33(11):1965–70. Doi: https://doi.org/10.1093/clinchem/33.11.1965.

44. Purvis JR, Movahed A. Magnesium disorders and cardiovascular diseases. Clin Cardiol. 1992 Aug;15(8):556–68. Doi: https://doi.org/10.1002/clc.4960150804.

45. Rabbani LE, Antman EM. The role of magnesium therapy in acute myocardial infarction. Clin Cardiol. 1996 Nov;19(11):841–4. Doi: https://doi.org/10.1002/clc.4960191103.

46. Ralston MA, Murnane MR, Kelley RE, Altschuld RA, Unverferth DV, Leier CV. Magnesium content of serum, circulating mononuclear cells, skeletal muscle, and myocardium in congestive heart failure. Circulation. 1989 Sep;80(3):573–80. Doi: https://doi.org/10.1161/01.CIR.80.3.573.

47. Lim P, Jacob E. Magnesium Deficiency in Patients on Long-Term Diuretic Therapy for Heart Failure. BMJ. 1972 Sep 9;3(5827):620–2. Doi: https://doi.org/10.1136/bmj.3.5827.620.

48. Radecka-Paryzek W, Patroniak V. The template synthesis and characterization of alkaline earth metal ion nitrate macroacyclic Schiff base complexes. Polyhedron. 1994 Jul;13(14):2125–8. Doi: https://doi.org/10.1016/S0277-5387(00)81492-8.

49. Bock CW, Katz AK, Glusker JP. Hydration of Zinc Ions: A Comparison with Magnesium and Beryllium Ions. J Am Chem Soc. 1995 Apr;117(13):3754–65. Doi. https://doi.org/10.1021/ja00118a012.

50. Katz AK, Glusker JP, Beebe SA, Bock CW. Calcium Ion Coordination: A Comparison with That of Beryllium, Magnesium, and Zinc. J Am Chem Soc. 1996 Jan;118(24):5752–63. Doi: https://doi.org/10.1021/ja953943i.

51. Carugo O, Djinovi? K, Rizzi M. Comparison of the co-ordinative behaviour of calcium(II) and magnesium(II) from crystallographic data. J Chem Soc, Dalton Trans. 1993;(14):2127. Doi: https://doi.org/10.1039/dt9930002127.

52. Peschke M, Blades AT, Kebarle P. Hydration Energies and Entropies for Mg 2+ , Ca 2+ , Sr 2+ , and Ba 2+ from Gas-Phase Ion−Water Molecule Equilibria Determinations. J Phys Chem A. 1998 Nov 1;102(48):9978–85. Doi: https://doi.org/10.1021/jp9821127.

53. Refat MS, Alghool S, El-Halim HFA. Alkaline earth metal (II) complexes of vitamin B13 with bidentate orotate ligands: Synthesis, structural and thermal studies. Comptes Rendus Chimie. 2011 May;14(5):496–502. Doi: https://doi.org/10.1016/j.crci.2010.04.024.

JOTCS A
Journal of the Turkish Chemical Society
Section: A
Chemistry
TURKISH CHEMICAL SOCIETY

Kinetic and Thermodynamic Study on Adsorption of Cadmium from Aqueous Solutions Using Natural Clay

Brahim Abbou[1*], Imane Lebkiri[1], Hanae Ouaddari[2], Omar Elkhattabi[1], Amar Habsaoui[1], Ahmed Lebkiri[1] and El Housseine Rifi[1]

[1]Laboratory of Advanced Materials and Process Engineering, Chemistry Department, Ibn Tofail University, B.P. 133, Kenitra, Morocco.
[2]Laboratory of Materials, Membranes and Environment, Faculty of Sciences and Technologies of Mohammedia, Hassan II University, Casablanca, Morocco.

Abstract: Heavy metal pollution poses a great risk for the environment and the human health. Cadmium is among the most common pollutants found in wastewater, known for its great toxicity even in small doses. This work aims to study the removal of cadmium using natural Moroccan clay (MC). The clay was characterized using X-ray diffraction, X-ray fluorescence, Fourier transform infrared spectroscopy, BET, and SEM. The effects of several experimental parameters on the clay adsorption capacity towards cadmium ions, such as MC dose, initial concentration and contact time, initial pH, and temperature were studied. The kinetic models Pseudo-first order, Pseudo-second order, and Elovich are evaluated to identify the adsorption process. The adsorption mechanism was determined by the use of the adsorption isotherms: Langmuir, Freundlich, and Temkin model. The results show that the heavy metal retention obeys the Pseudo-second order ($R^2 \geq 0.99$). The Langmuir isotherm model provided the best fit ($R^2 \geq 0.99$) to the experimental data for the adsorption of Cd(II) by MC as compared to the Freundlich and Temkin model. The maximum monolayer adsorption capacity of Cd(II), using the Langmuir model equation, is equal to 5.25 mg/g. The adsorption is a spontaneous and an endothermic process characterized by a disorder of the medium.

Keywords: Clay, heavy metal, cadmium, adsorption, isotherm.

Submitted: February 17, 2021. **Accepted:** May 11, 2021.

Cite this: Abbou B, Lebkiri I, Ouaddari H, Elkhattabi O, Habsaoui A, Lebkiri A, et al. Kinetic and Thermodynamic Study on Adsorption of Cadmium from Aqueous Solutions Using Natural Clay. JOTCSA. 2021;8(2):677–92.

DOI: https://doi.org/10.18596/jotcsa.882016.

***Corresponding author. E-mail:** abbou.brahim@gmail.com.

INTRODUCTION

Increased urbanization and industrialization activities have led to global economic development, which has significantly contributed to human well-being, but this had a negative effect on the environment. Indeed, the uncontrollable control of waste and wastewater discharges creates a series of environmental problems, making it difficult to access adequate quality water for human consumption (1). Heavy metals pollution, in particular, is an environmental problem of global interest (2). They are considered one of the most dangerous inorganic contaminants among many others released into the environment. The reason behind this is their persistence in nature and their toxicity even at a very low concentration (3).

The protection of Aquatic Resources and the environment and the elimination of heavy metals are always a great challenge. The accumulation of this toxic waste comes mainly from human activities

such as agriculture, mining, and industry. Currently, they are of great concern because of their toxicity to ecosystems and their harmful effects on human health. Cadmium is considered to be dangerous micropollutants (4), the toxicity caused by this metal is considered to be high even to the state of traces (5).

Numerous studies have made it possible to develop various industrial effluent treatment processes to reduce these contaminants quantity in aquatic environments. These studies include chemical precipitation processes, coagulation/flocculation, ion exchange, membrane processes, and adsorption (6–14).

The adsorption process has proven to be highly efficient and cost-effective for removing organic substances (pesticides, dyes, phenolic compounds, etc.) and heavy metals (cadmium, lead, mercury, etc.). (7–11).

Moreover, the research and development of new low-cost, cost-effective, and efficient adsorbents for ecosystem treatment remains a great challenge. Natural adsorbents such as agricultural solid waste, algae, soils, and clays modified or not have shown promising profitability for trapping pollutants (4,6,15,16). Recently clay minerals have received considerable attention as alternative adsorbent materials that are less expensive, abundant and have multifunctional properties depending on the type of clay (17). The main advantages of using these materials are due to their different characteristics, abundant availability, and low cost (18).

This work aims to enhance Moroccan natural clay's value in the retention of cadmium ions from synthetic aqueous solutions. The influence of adsorption conditions such as MC dose, initial concentration and contact time, initial pH, and temperature were investigated. To better understand the nature of the reaction mechanisms involved in the adsorption phenomenon, the linear shapes of different kinetic and isothermal models were calculated and evaluated.

EXPERIMENTAL SECTION

Characterization techniques

The X-ray diffraction analyses were carried out using a PANalytical X'Pert PRO Plus diffractometer, using Cu-Kα radiation (λ=1.5406 Å). The value of 2θ angle was scanned between 3 and 90° range at a goniometer rate of 2θ = 4°/min. The chemical composition of MC was determined with X-ray fluorescence using an Axios-Panalytical device. The analysis of the MC by Fourier Transform Infrared Spectroscopy was carried out by using a Vertex 70 spectrometer, the analysis was performed by scanning from 4000 cm^{-1} to 400 cm^{-1} with a resolution of 4 cm^{-1}. BET Nitrogen adsorption measurements were obtained using a Micromeritics Flex 3 to obtain the specific surface area of MC. The morphology of MC was observed by Scanning electron microscopy (SEM) and Energy Dispersive X-ray (EDAX) (FEI Company, Quanta 200).

Adsorbent and Adsorbate

The adsorbent used in this work is an unmodified clay collected from Marrakech region in southern Morocco. Before any use, the material was crushed and sieved; only the granulometry below 120 µm is retained. The particles were then dried at 100 °C overnight and before any use.

The used stock solution of metal ions (Cd(II)) was prepared by dissolving a known amount of metal salt $Cd(NO_3)_2$ $4H_2O$ (98%), purchased from Solvachim (Casablanca, Morocco), in distilled water. The desired working concentrations solution is prepared by diluting the stock solution.

Adsorption Experiments

The adsorption tests were conducted in the batch method under different experimental parameters, such as the adsorbent dose, initial concentration and contact time, pH of the solution, and temperature. After the adsorption process, MC was separated from the liquid phase using a 0.45 µm membrane filter; the recovered filtrate was analyzed by Inductively Coupled Plasma Optical Emission Spectroscopy (ICP-OES). The data obtained from the adsorption experiments are used to calculate the adsorption efficiency and capacity by the following equations:

$$R\% = \frac{(C_0 - C_r)}{C_0} \times 100 \qquad \text{(Eq. 1)}$$

$$q_{(mg/g)} = \frac{(C_0 - C_r)}{m} V \qquad \text{(Eq. 2)}$$

Where C_0(mg/L) and C_r(mg/L) are respectively the initial and the residual concentration of adsorbate, V(L) is the solution volume, and m(g) is the adsorbent mass.

RESULTS AND DISCUSSION

Characterization of the adsorbent

X-ray diffraction

X-ray diffraction was done to determine the mineralogical composition of MC. The obtained XRD patterns for MC are shown in Figure 1. According to the XRD pattern, our compound is not pure and contains a high quantity of quartz (JCPDS file No:

01-085-0797; peaks around 4.26 Å (20.81° 2θ), 2,46 Å (36.43° 2θ), 2.28 Å (39.45° 2θ), 2.23 Å (40.38° 2θ), 2.12 Å (42.62° 2θ), 1.98 Å (45.90° 2θ), 1.82 Å (50.11° 2θ), 1.67 Å (54.72° 2θ), and 1,66 Å (55.24° 2θ). X-ray diffraction analysis indicated that the clay's mineralogical composition is mainly composed of illite (JCPDS file No: 00-001-1098), with the presence of a small amount of kaolinite (JCPDS file No: 01-083-0971) 7.24 Å (12.5° 2θ), albite (JCPDS file No: 01-084-0752) 1.45 Å (64.06° 2θ), and vermiculite (JCPDS file No: 01-076-0847) 4.46 Å (19.81° 2θ).

Illite was characterized by interreticular distances (Å) and 2θ position of the diffractometric reflects at 10.11, 8.76°; 5.01, 17.71° ; 3.68, 24.18° ; 3.50, 25.42° ; 3.24, 27.45° and 3.20, 27.86°.

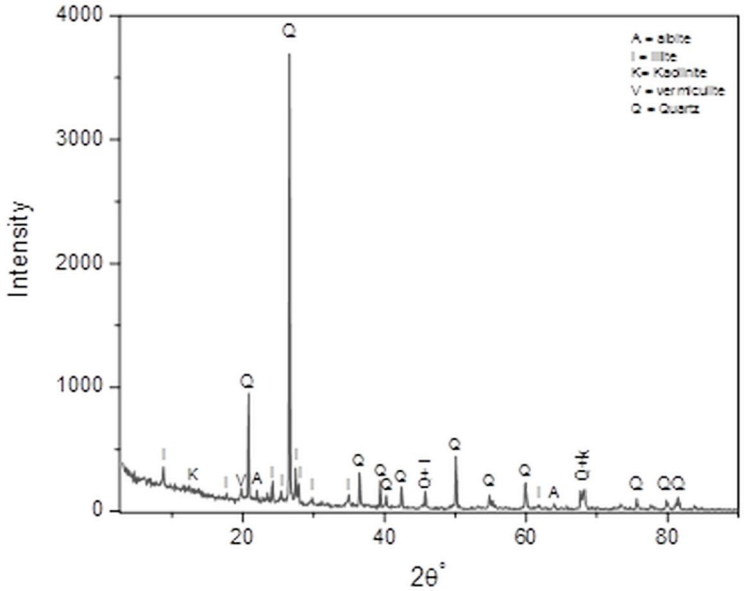

Figure 1: X-ray diffraction patterns of MC.

X-ray fluorescence

Elemental chemical analysis of the raw clay shown in Table 1 shows that silica and alumina are the predominant constituents. They are found in a SiO_2/Al_2O_3 ratio equal to 3.64, which is an indication of large proportion of quartz (19,20). The low CaO content indicates a low amount of calcium carbonate (21). The loss on ignition (LoI) equal to 5.77% by mass. It is due to the decomposition of carbonates and dehydroxylation of clay minerals (18,22).

Fourier Transform Infrared Spectroscopy

The FT-IR spectra (Figure 2) show a band that ranges between 3100-3700 cm^{-1} located at 3436 cm^{-1} due to the presence of the stretching vibrations of the internal OH groups of H_2O molecule (23,24), the two bands at 1637 cm^{-1} and 1381 cm^{-1} are attributed to the deformation of H_2O (25,26). The bands located at 693, 776, 1005 cm^{-1}, and 1031 cm^{-1} correspond to Si—O stretching vibrations (16,23,26–29). Intense peaks at 472 cm^{-1} and 533 cm^{-1} are attributable respectively to the deformation of Si—O—Mg and Si—O—Al (30). The band located at 912 cm^{-1} is attributed to the bending vibrations of the groups Al–Al–OH and Al—Mg–OH (31,32).

Table 1: Chemical composition of MC.

Elemental Composition	Weight %
SiO_2	65.80
Al_2O_3	18.10
Fe_2O_3	3.56
K_2O	2.12
MgO	1.41
Na_2O	1.07
CaO	0.78
TiO_2	0.76
LoI (Loss on ignition)	5.77

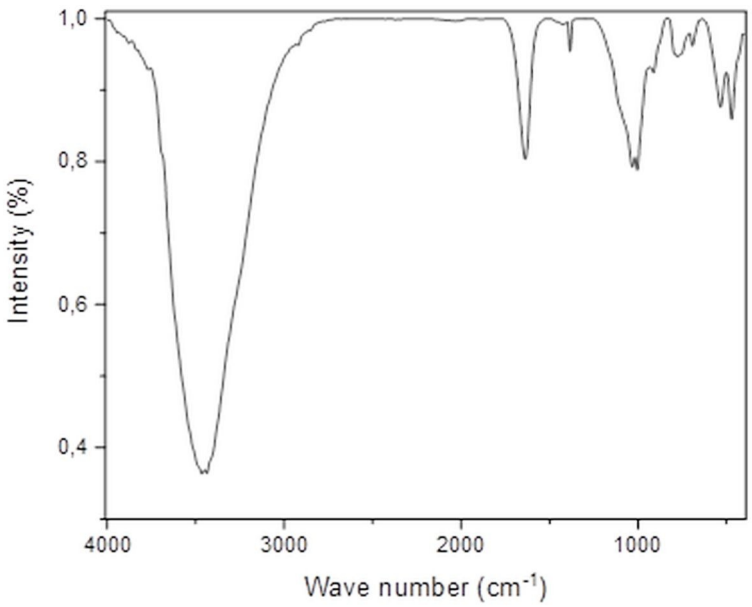

Figure 2: FT-IR spectrum of MC.

Specific surface areas - BET

Figure 3 presents the nitrogen adsorption–desorption isotherm at 77 K of MC. The obtained isotherm is the type IV, with a hysteresis loop of type H4 and those according to the IUPAC classification (33). The specific surface area of MC obtained by the BET method is 23.07 m^2/g.

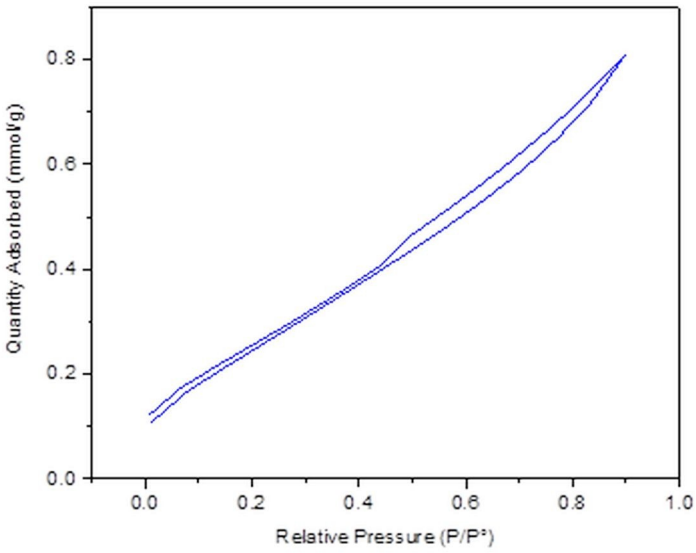

Figure 3: Adsorption–desorption isotherms of N_2 at 77 K of MC.

Scanning electron microscopy (SEM) and Energy Dispersive X-ray (EDAX)

The Scanning electron microscopy (SEM) for MC before and after adsorption are shown in Figure 4. The shape of the MC adsorbent particles have irregular structures (Figure 4a). The loaded MC showed some white particles on the surface of the mineral (Figure 4b), indicating the adsorption of cadmium on the surface of MC.

The elemental compositions of MC before and after adsorption were obtained with EDAX analysis, and the spectra were shown in Figure 5. The results showed that O, Si, Al, Fe, and K were the major elements of MC clay, with the presence of small quantities of C, Ti, Na, Mg, and Ca (Figure 5a). However, the additional peak corresponding to Cd element was observed in Figure 5b, which confirm the adsorption of Cd(II) onto MC.

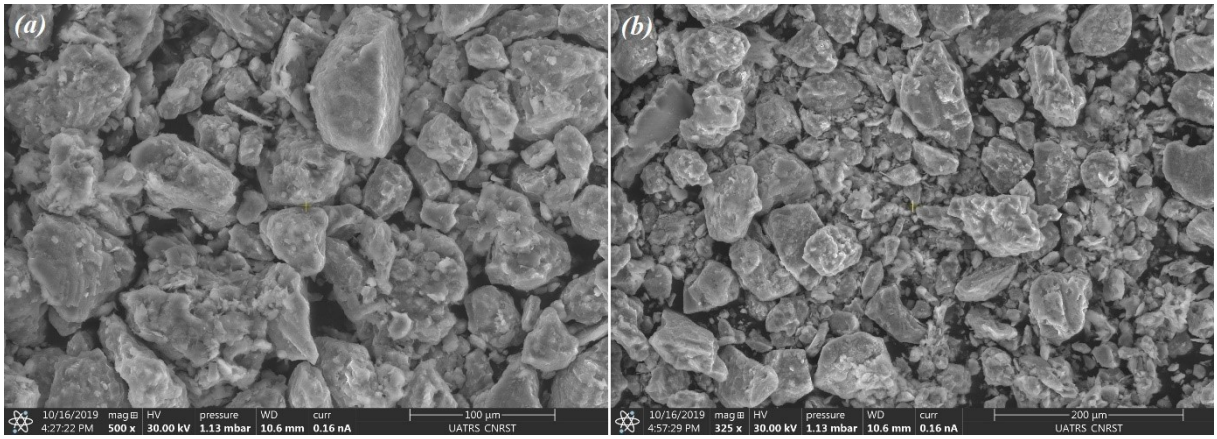

Figure 4*:* SEM of MC before (a) and after (b) adsorption.

Adsorption experiments

Adsorbent mass effect

The mass effect on the adsorption of cadmium ions onto MC was conducted by contacting different masses of MC (0.1 g to 1.2 g) with 0.1 L of Cd(II) 10 mg/L solution for 180 minutes. The results are illustrated in Figure 6. The efficiency of adsorption increases when MC mass increases in the solution. This is due to the increase in specific surface area and the adsorption active sites attributed to the increase in the adsorbent mass (34). From this result, a MC mass of 0.8 g will be used in all the following experiments.

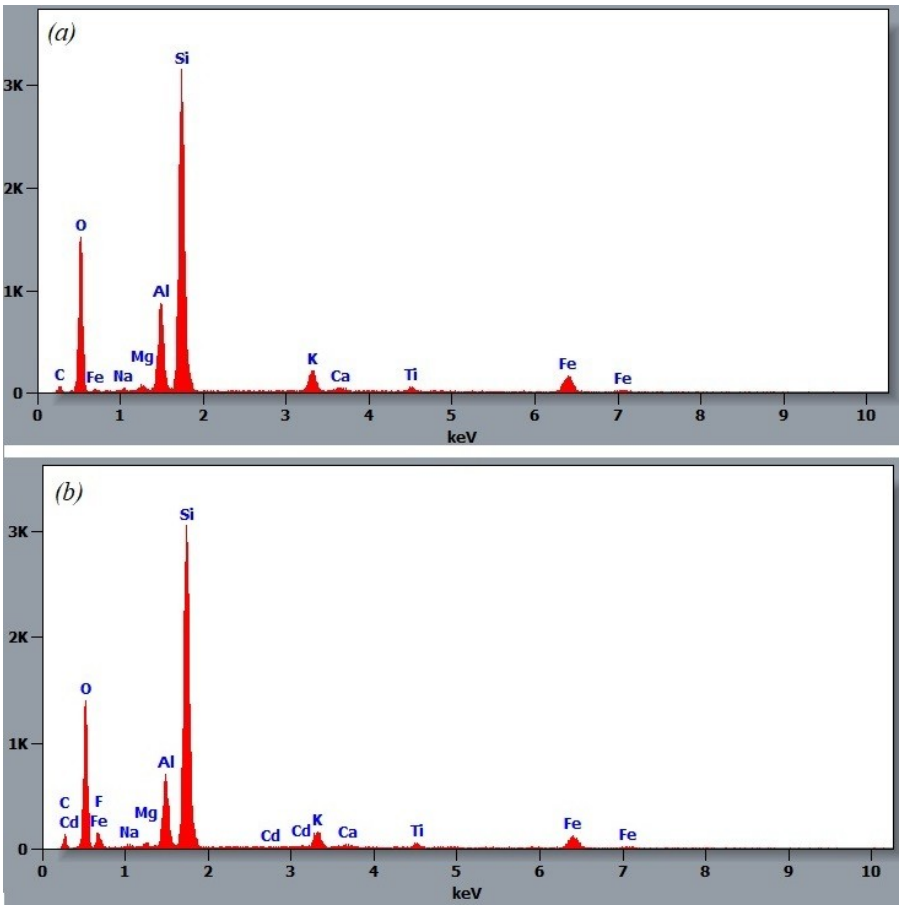

Figure 5*:* EDAX of MC before (a) and after (b) adsorption.

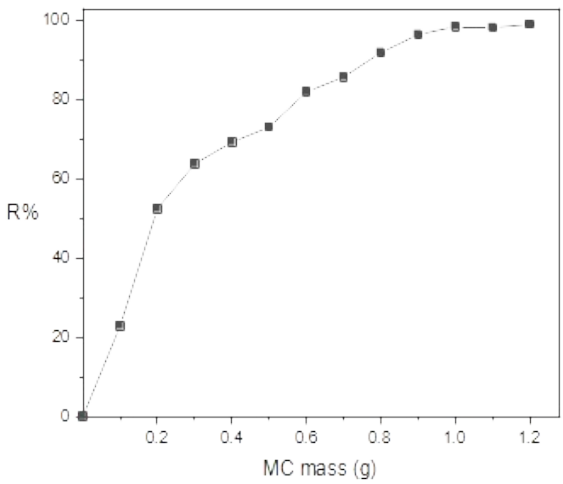

Figure 6*:* Evolution of heavy metal removal efficiency versus MC mass.

Initial concentration and contact time effect
Contact time is a major parameter that controls the effectiveness of the adsorption phenomenon. Figure 7 shows the evolution of the adsorption capacity q_t versus contact time for different cadmium concentrations (10—200 mg/L). It is found that the adsorption capacity (q_t) increases with time in proportion as the concentration of the metal ion increases.

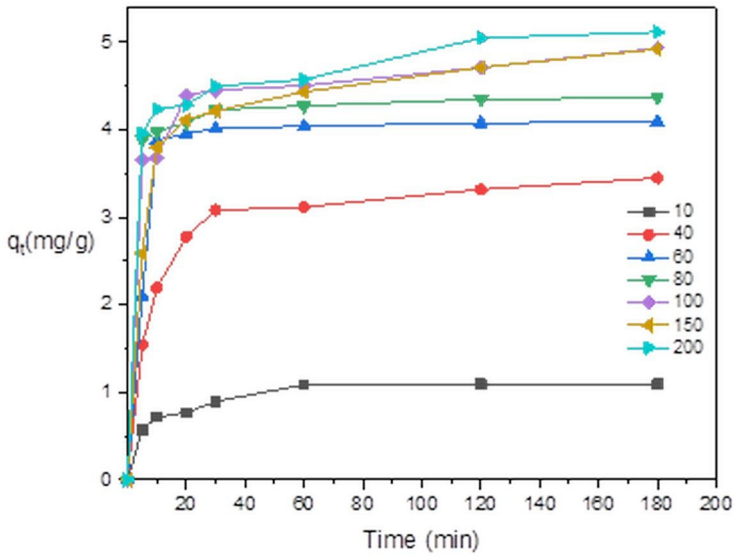

Figure 7: Time effect on the adsorption capacity of MC clay versus various initial concentrations of Cd(II).

Monitoring the initial concentration effect (Figure 8) shows that q_e(mg/g) increases with the accrues of the initial metal concentration, this increase is over when MC reaches its maximum adsorption capacity and becomes saturated with the adsorbed metal. In fact, at weak concentrations, the adsorption sites of MC are unoccupied and tend to fix more cadmium ions. In general, the amount of metal adsorbed increases from 1.09 mg/g to 5.12 mg/g with increasing initial concentration from 10 mg/L to 200 mg/L of the metal solution and then reach a plateau corresponding to the adsorption sites saturation (35). The maximum adsorption capacity value obtained is 5.12 $mg.g^{-1}$.

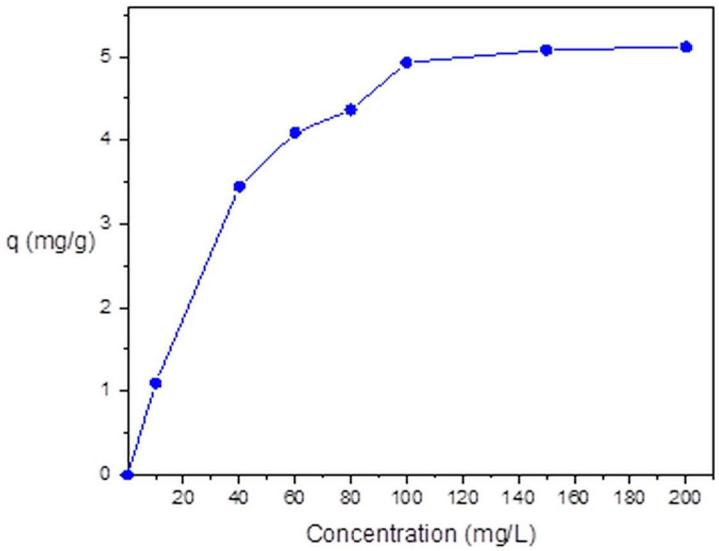

Figure 8: Adsorption capacity of MC.

Initial solution pH effect

To understand the influence of pH on Cd(II) adsorption onto MC, adsorption tests were conducted in a different value of pH (2–6); the results are shown in Figure 9. At acidic pH the adsorption efficiency is too low, which can be explained by the competition between metal ions and hydronium H_3O^+ ions present in the acid solution; hydronium ions are more adsorbed than metal ions due to their high mobility. At a slightly acidic pH (from 4 to 6), adsorption is more pronounced, and the adsorption efficiency increases with increasing pH. The mechanism involved at this pH range is an ion exchange that occurs between Cd(II) and the cations localized in the MC exchange sites (36). The almost total elimination of Cd(II) is obtained beyond pH = 5.

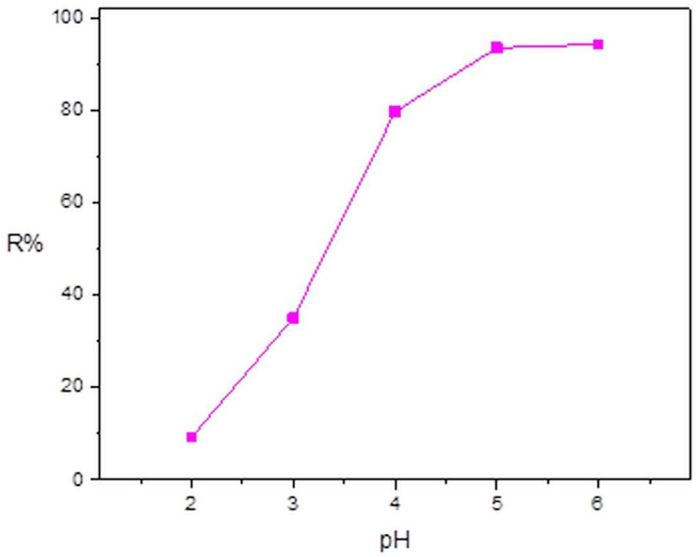

Figure 9*:* pH effect on Cd(II) adsorption onto MC.

Temperature Effect

The temperature effect on MC adsorption capacity was studied. The experiments were conducted at various temperatures varied from 25 °C to 55 °C. The amount of adsorbed cadmium ions increased with temperature (Figure 10), indicating an endothermic nature of adsorption. The rise in temperature leads to an increase in the adsorption capacity of MC clay. This increase may be due either to an increase in the MC available active sites or to an increase of the cadmium ions mobility in the solution (37).

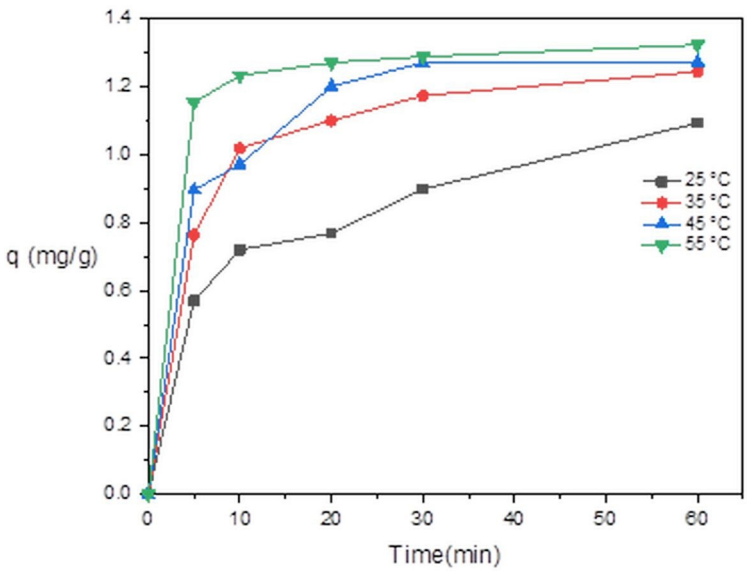

Figure 10: Temperature effect on the absorption capacity of MC.

Adsorption Kinetics

For the kinetic study of the adsorption process, the obtained experimental data were fitted by three kinetic models, pseudo-first-order, pseudo-second-order, and Elovich, to describe the adsorption process.

The pseudo-first-order kinetic model expressed by Eq. (3) (38) :

$$\log\left(q_e - q_t\right) = \log q_e - \frac{k_1}{2.303} t \qquad \text{(Eq. 3)}$$

The pseudo-second-order equation is given by Eq. (4) (39) :

$$\frac{t}{q_t} = \frac{1}{k_2 q_e^2} + \frac{1}{q_e} t \qquad \text{(Eq. 4)}$$

Where q_e and q_t are respectively the amounts of Cd(II) adsorbed on MC clay at equilibrium and at time t expressed in (mg/g). k_1(min^{-1}) and k_2(g/mg min) are the pseudo-first-order and pseudo-second-order rate constants, respectively.

The Elovich kinetic model, describe chemisorption adsorption. Expressed by the equation (5) (40):

$$q_t = \frac{1}{\beta} \ln\left(\alpha \beta\right) + \frac{1}{\beta} \ln t \qquad \text{(Eq. 5)}$$

Where α (mg.g^{-1}.min^{-1}) and β (g.mg^{-1}) are respectively the initial adsorption rate and the desorption constant.

Table 2 summarizes the kinetic data.; the curves are shown in Figure 11. The pseudo-second-order model's obtained correlation coefficients are superior to those of pseudo-first-order and Elovich models. Also, the calculated values of the adsorption capacities at equilibrium q_e, from the pseudo-second-order are closer to the experimental values. From these results, it can be concluded that the adsorption of Cd(II) on MC is based on a chemical reaction, involving an exchange of electrons between the MC and the metallic solution (41,42).

Table 2: Kinetic parameters for Cd(II).

Concentration (mg/L)	q_e (exp)	pseudo-first-order			pseudo-second-order			Elovich		
		q_e (cal)	K_1	R_1^2	q_e (cal)	K_2	R_2^2	α	β	R_E^2
10	1.10	0.75	0.0539	0.9444	1.14	0.1371	0.9989	1.3862	6.3572	0.9352
40	3.45	1.63	0.0239	0.7992	3.54	0.0456	0.9995	4.1336	2.0121	0.8878
60	4.09	0.78	0.0387	0.6750	4.14	0.1301	0.9995	157.4839	2.5336	0.4992
80	4.37	0.85	0.0366	0.7933	4.39	0.1981	0.9999	2.83E+10	7.0824	0.9576
100	4.93	1.53	0.0190	0.6284	4.96	0.0578	0.9991	2017.6545	2.7966	0.9016
150	4.92	2.01	0.0211	0.7619	5.00	0.0394	0.9992	30.1701	1.8206	0.8643
200	5.12	1.88	0.0275	0.8306	5.19	0.0501	0.9989	1.43E+04	3.1313	0.9530

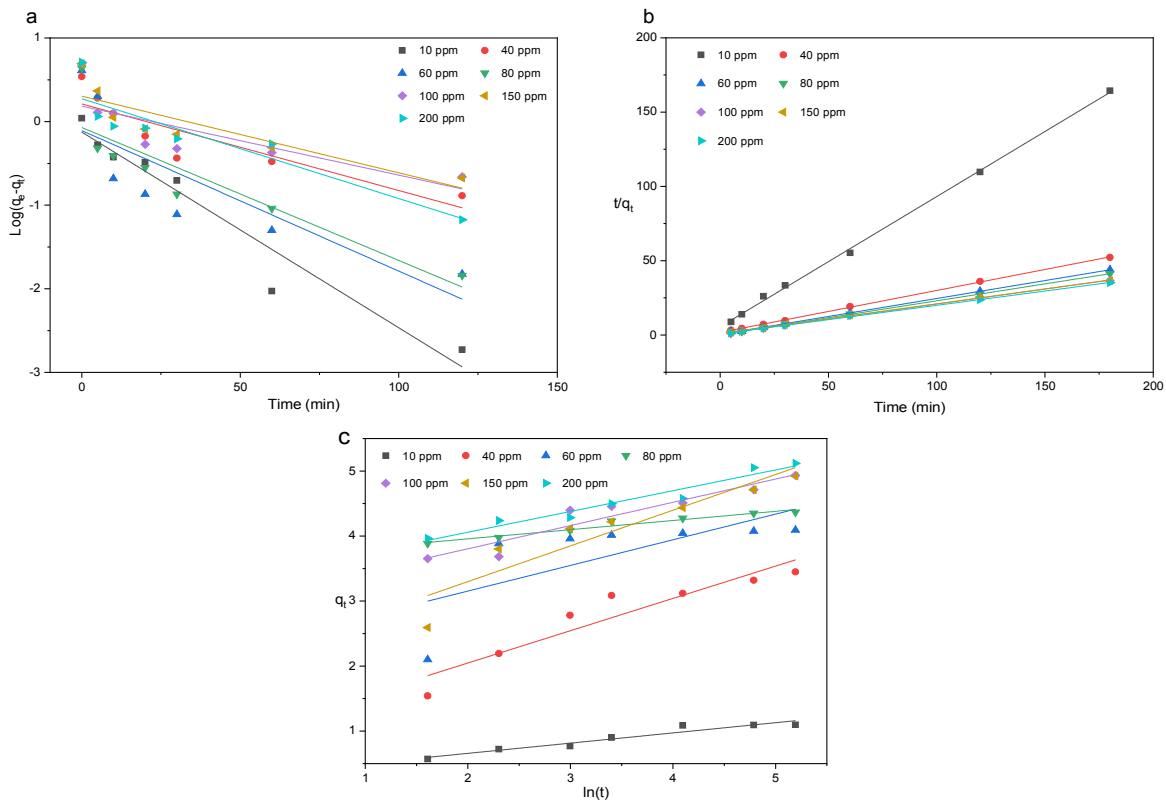

Figure 11: Kinetic models: Pseudo-first order (a), Pseudo-second order (b) and Elovich (c).

Adsorption isotherms

To understand the mechanisms that take place during the adsorption of Cd(II) onto MC and estimating MC adsorption capacity, three isotherm models are used, the Langmuir, Freundlich, and Temkin models.

The Langmuir isotherm model assumes monolayer coverage of a defined adsorption site without any interactions between the adsorbed ions (43).

The following equation gives Langmuir linear form:

$$\frac{C_e}{q_e} = \frac{1}{K_L q_m} + \frac{C_e}{q_m} \qquad \text{(Eq. 6)}$$

Where: q_m: maximum adsorbed capacity (mg/g), K_L(L/mg): equilibrium constant characteristic of the adsorbent, C_e(mg/L): adsorbate concentration at equilibrium.

The separation factor constant R_L is an essential characteristic used to ascertain the Langmuir isotherm model, which is defined by (44):

$$R_L = \frac{1}{(1+K_L C_0)} \quad \text{(Eq. 7)}$$

Where C_0(mg/L) is the initial concentration and K_L(L/mg) is the Langmuir constant.

Depending on the separation factor constant values, the adsorption is favorable if $0 < R_L < 1$, unfavorable if $R_L > 1$, irreversible if $R_L = 0$ or linear if $R_L = 1$.

The Freundlich isotherm model assumes that the adsorption processes occur on heterogeneous surfaces with a non-uniform energy distribution of adsorption sites on the surface. The Freundlich model admits the existence of interactions between the adsorbed molecules (45).

The following equation gives Freundlich linear equation:

$$\log q_e = \log K_F + \frac{1}{n} \log C_e \quad \text{(Eq. 8)}$$

Where K_F adsorption capacity, n : the adsorption intensity, q_e: adsorption capacity at equilibrium (mg/g), and Ce: the solute concentration at equilibrium (mg/L).

The Temkin isotherm assumes that sorption's free energy is a function of the surface coverage. The linear form is written as follows (46) :

$$q_e = \frac{RT}{b_T} \ln K_T + \frac{\mathrm{RT}}{b_T} \ln C_e \quad \text{(Eq. 9)}$$

Where T: temperature (K), R : universal gas constant (8.314 $J.mol^{-1}.K^{-1}$), b_T (J/mol) : heat of adsorption constant, and K_T(L/min) : equilibrium binding constant.

The calculated parameters of the adsorption isotherms with their correlation coefficients are reported in Table 3, and the curves are shown in Figure 12. According to the correlation coefficients, the Langmuir model is the most representative of the adsorption mechanism with correlation coefficients close to unity (R^2=0.9981). Overall, it seems that the adsorption of metal cations is done by monolayer on identical sites of energy. This result showed that the heavy metal cations are homogeneously adsorbed through ionic adsorption assured by the negatively charged surface of MC.

Table 3: Isothermal parameters for Cd(II).

Langmuir				Freundlich			Temkin			
$q_{e(exp)}$	$q_{m,cal}$	K_L	R^2	K_F	1/n	R^2	K_T	b_T(J/mol)	B	R^2
5.12	5.25	0.1741	0.9981	1.4797	0.2758	0.9501	0.2006	1817.1277	1.3635	0.9850

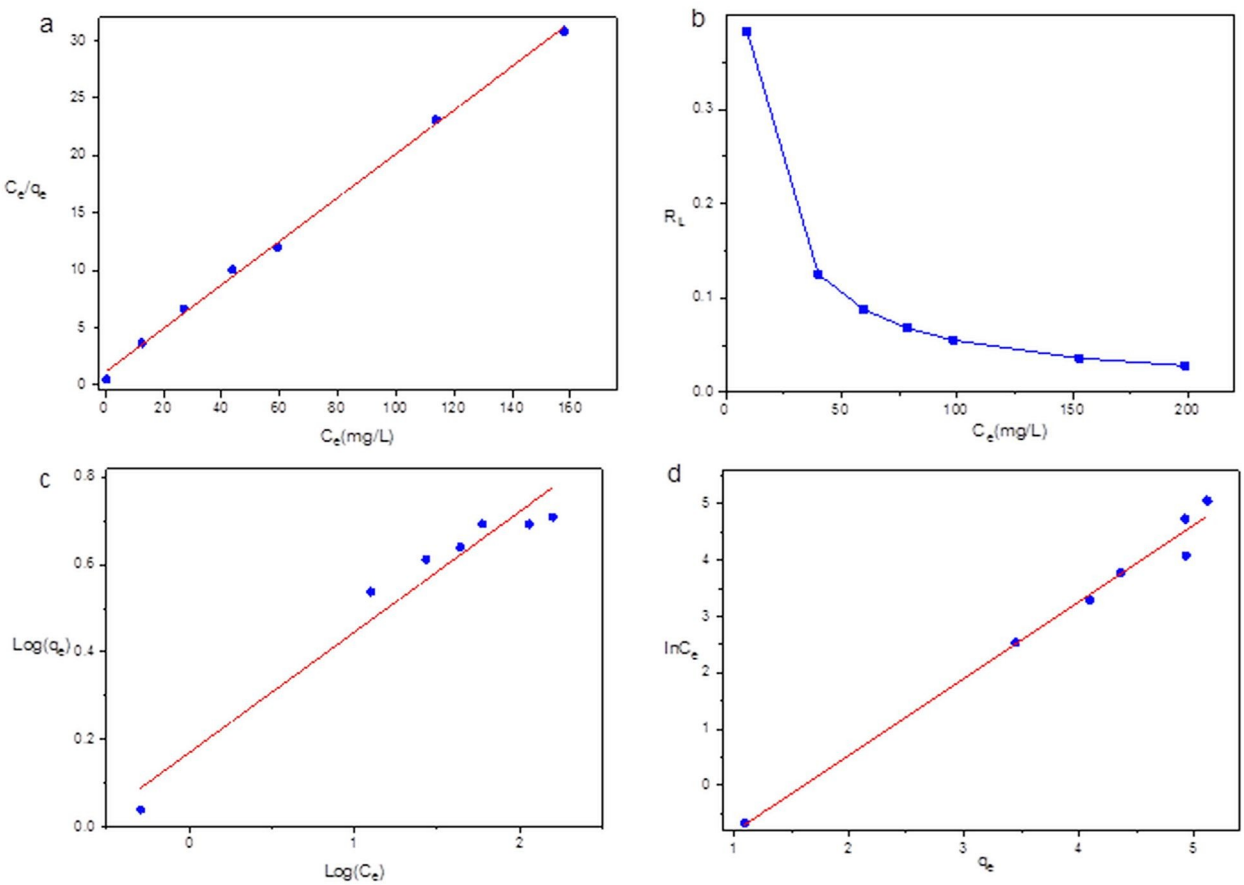

Figure 12 *:* Adsorption isotherms: Langmuir (a), Separation factor R_L (b), Freundlich (c) and Temkin (d).

The R_L values of different concentrations are tabulated in Table 4. All values are less than unity, implying that the Langmuir isotherm best describes heavy metal cations adsorption on MC (47). Freundlich and Temkin's models are not suitable for modeling the metal cations' adsorption on the studied adsorbent.

Table 4: Separation factor R_L of the Langmuir isotherm.

Concentration (mg/L)	**10**	**40**	**60**	**80**	**100**	**150**	**200**
R_L	0.3825	0.1252	0.0876	0.0680	0.0550	0.0361	0.0281

Thermodynamic parameters

To completely understand the adsorption nature and to describe thermodynamic behavior of the adsorption of Cd(II) onto MC clay, the free energy (ΔG), enthalpy (ΔH), and entropy (ΔS) were evaluated.

The equilibrium constant of adsorption K_d is related to the free energy of the reaction ΔG(J.mol^{-1}) and thus to the enthalpy ΔH(J.mol^{-1}) and the entropy ΔS(J.mol^{-1}.K^{-1}) of adsorption by the relation:

$$\Delta G = \Delta H - T\,\Delta S = -RT \ln K_d \qquad \text{(Eq. 10)}$$

It is therefore:

$$\ln k_d = \frac{\Delta S}{R} - \frac{\Delta H}{RT} \qquad \text{(Eq. 11)}$$

Where K_d: equilibrium constant, T: temperature (K), and R: universal gas constant (8.314 J.mol^{-1}.K^{-1}).

Figure 13 represents the plots of ln(K_d) as a function of 1/T. The slope and the intercept allow calculating respectively the standard variations of ΔH, ΔS and ΔG. The obtained results are illustrated in Table 5.

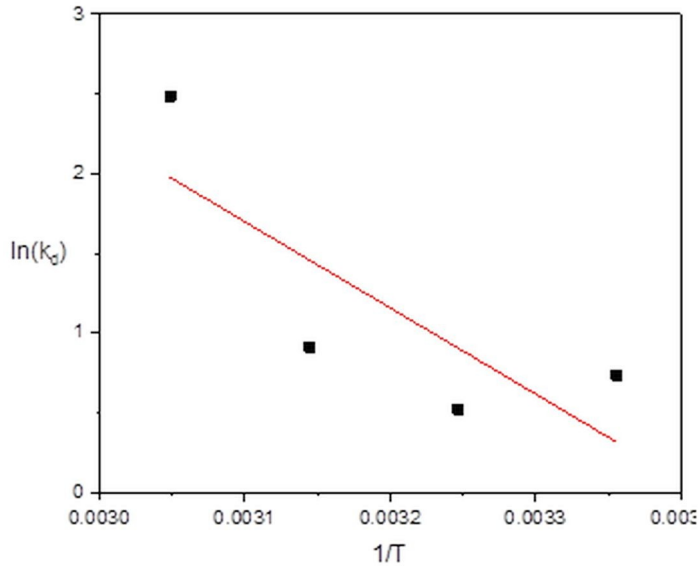

Figure 13*:* Representation of ln(K_d) as a function of (1/T).

The endothermic character of the adsorption process is confirmed by the positive values of ΔH, and as they are higher than 40 kJ/mol, it is, therefore, chemisorption (48). The spontaneous nature of the adsorption process is confirmed by the negative values of ΔG. Positive values of ΔS evokes the increase of disorder at the solid/liquid interface during adsorption (49).

Table 5: Thermodynamic parameters.

T(k)	K_d(g/L)	ΔG° (KJ.mol^{-1})	ΔH°(KJ.mol^{-1})	ΔS° (KJ.mol^{-1}.K^{-1})
298	2.08	-1.82	44.97	0.15
308	1.68	-1.33		
318	2.49	-2.41		
328	12.03	-6.78		

Mechanism of adsorption

To understand the nature of interactions between the MC clay and the metal cations and to identify the different functional groups involved in this interaction, FTIR spectrophotometric analyses of the unloaded and the Cd-loaded clay were carried out. The FTIR spectrum is illustrated in Figure 14. The reduction in peak size at 3436 cm^{-1} and 1637 cm^{-1} indicates the hydroxyl group's involvement in the adsorbent-adsorbate interaction. Thus, the reduction of peaks attributed to the Si—O and Al—Al—OH group indicates the involvement of the silanol and aluminol groups in the adsorption mechanism (50).

Possible mechanism (51):

$$2SO^- + Cd^{2+} \text{-->} (SO)_2Cd$$

With S = Si or Al.

Comparison with other adsorbents

Table 6 shows a comparison of the maximum adsorption capacity (q_{max}) of MC with different adsorbents reported in literature. As can be seen, the q_{max} of MC for cadmium is higher compared with other adsorbent clay materials. Nevertheless, MC is promising adsorbent in the removal of cadmium ions from aqueous solutions considering of its low cost and its availability.

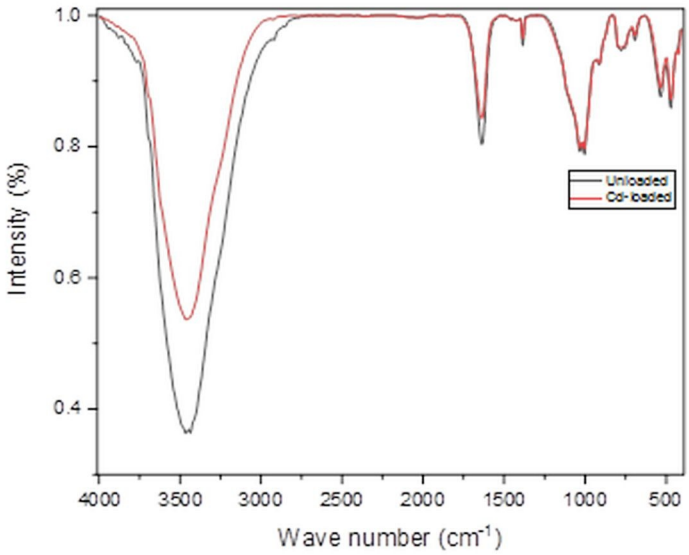

Figure 14: FTIR spectrum of MC before and after adsorption.

Table 6: Comparison of adsorption capacity of Cd(II) on different adsorbents.

Adsorbent	q_{max}(mg.g^{-1})	Reference
Ball clay	2.75	(52)
Kaolinite	4.38	(53)
Palygorskite	4.54	(54)
Kaolin	3.04	(55)
Diatomite	3.24	(55)
Kaolinite	0.88	(56)
Moroccan Clay	5.12	This study

CONCLUSION

The results of this study indicate that MC, a low-cost adsorbent, can be very effective for cadmium removal from aqueous solution. The effect of different factors on adsorption was studied. The amount of Cd(II) adsorbed by MC increased with increasing MC dose, solution initial pH, and contact time. The obtained kinetic values were well fitted by the pseudo-second-order thus proving that the process takes place as chemisorption.

Equilibrium data were also fitted by Langmuir isotherm, so the cadmium ions adsorb in monolayers and without any interactions between them. The maximum monolayer adsorption capacity for metal ions, using the Langmuir isotherm model equation, is equal to 5.25 mg/g. The negative values of ΔG reveal the spontaneous nature during the adsorption process of metal ions onto MC. ΔH and ΔS positive values have proved the endothermic and randomness of the adsorption process. On the basis of these results, it can be concluded that natural clay (MC) can be used as an inexpensive and efficient adsorbent in the elimination of cadmium ions from wastewater.

ACKNOWLEDGMENTS

The authors are pleased to acknowledge Centre National de la Recherche Scientifique et Technique (CNRST) Morocco.

REFERENCES

1. Jiménez-Castañeda M, Medina D. Use of Surfactant-Modified Zeolites and Clays for the Removal of Heavy Metals from Water. Water. 2017 Mar 24;9(4):235. Doi: https://doi.org/10.3390/w9040235.

2. Bouazza D, Miloudi H, Adjdir M, Tayeb A, Boos A. Competitive adsorption of Cu (II) and Zn (II) on impregnate raw Algerian bentonite and efficiency of extraction. Applied Clay Science. 2018 Jan;151:118–23. Doi: https://doi.org/10.1016/j.clay.2017.10.026.

3. Ezzeddine Z, Batonneau-Gener I, Pouilloux Y, Hamad H, Saad Z. Synthetic Nax Zeolite as a Very Efficient Heavy Metals Sorbent in Batch and Dynamic Conditions. Colloids and Interfaces. 2018 May 24;2(2):22. Doi: https://doi.org/10.3390/colloids2020022.

4. Essaadaoui Y, Lebkiri A, Rifi E, Kadiri L, Ouass A. Adsorption of lead by modified Eucalyptus camaldulensis barks: equilibrium, kinetic and thermodynamic studies. Dwt. 2018;111:267–77. Doi: https://doi.org/10.5004/dwt.2018.22191.

5. Zhang R, Zhou L, Zhang F, Ding Y, Gao J, Chen J, et al. Heavy metal pollution and assessment in the tidal flat sediments of Haizhou Bay, China. Marine Pollution Bulletin. 2013 Sep;74(1):403–12. Doi: https://doi.org/10.1016/j.marpolbul.2013.06.019.

6. Bensalah J, Habsaoui A, Abbou B, Kadiri L, Lebkiri I, Lebkiri A, et al. Adsorption of the anionic dye methyl orange on used artificial zeolites: kinetic study and modeling of experimental data. MediterrJChem,. 2019 Nov 18;9(4):311–6. Doi: https://doi.org/10.13171/mjc941911181112jb.

7. Fu F, Wang Q. Removal of heavy metal ions from wastewaters: A review. Journal of Environmental Management. 2011 Mar;92(3):407–18. Doi: https://doi.org/10.1016/j.jenvman.2010.11.011.

8. Gupta VK, Mittal A, Gajbe V, Mittal J. Removal and Recovery of the Hazardous Azo Dye Acid Orange 7 through Adsorption over Waste Materials: Bottom Ash and De-Oiled Soya. Ind Eng Chem Res. 2006 Feb;45(4):1446–53. Doi: https://doi.org/10.1021/ie051111f.

9. Gupta VK, Carrott PJM, Ribeiro Carrott MML, Suhas. Low-Cost Adsorbents: Growing Approach to Wastewater Treatment—a Review. Critical Reviews in Environmental Science and Technology. 2009 Oct 9;39(10):783–842. Doi: https://doi.org/10.1080/10643380801977610.

10. Kabdaşlı I, Arslan T, Ölmez-Hancı T, Arslan-Alaton I, Tünay O. Complexing agent and heavy metal removals from metal plating effluent by electrocoagulation with stainless steel electrodes. Journal of Hazardous Materials. 2009 Jun 15;165(1–3):838–45. Doi: https://doi.org/10.1016/j.jhazmat.2008.10.065.

11. Ouallal H, Dehmani Y, Moussout H, Messaoudi L, Azrour M. Kinetic, isotherm and mechanism investigations of the removal of phenols from water by raw and calcined clays. Heliyon. 2019 May;5(5):e01616. Doi: https://doi.org/10.1016/j.heliyon.2019.e01616.

12. Huisman JL, Schouten G, Schultz C. Biologically produced sulphide for purification of process streams, effluent treatment and recovery of metals in the metal and mining industry. Hydrometallurgy. 2006 Sep;83(1–4):106–13. Doi: https://doi.org/10.1016/j.hydromet.2006.03.017.

13. Wang L, Hung Y-T, Shammas N. Volume 3: Physicochemical Treatment Processes. In: Handbook of Environmental Engineering [Internet]. Totowa, NJ: Humana Press; 2005. p. 1–703. ISBN: 978-1-59259-820-5. Available from: https://www.springer.com/gp/book/9781588291653

14. Keng P-S, Lee S-L, Ha S-T, Hung Y-T, Ong S-T. Removal of hazardous heavy metals from aqueous environment by low-cost adsorption materials. Environ Chem Lett. 2014 Mar;12(1):15–25. Doi: https://doi.org/10.1007/s10311-013-0427-1.

15. Kadiri L, Lebkiri A, Rifi EH, Ouass A, Essaadaoui Y, Lebkiri I. Mathematical modeling and thermodynamic study of copper (II) removal from aqueous solution by Coriandrum Sativum seeds. MediterrJChem,. 2019 Jan 20;7(6):478–90. Doi: https://doi.org/10.13171/mjc7619012111lk.

16. Essebaai H, Ismi I, Lebkiri A, Marzak S, Rifi EH. Kinetic and Thermodynamic Study of Adsorption of Copper (II) Ion on Moroccan Clay. Mediterr J Chem. 2019 Sep 13;9(2):102–15. Doi: https://doi.org/10.13171/mjc92190909510he.

17. Uddin MK. A review on the adsorption of heavy metals by clay minerals, with special focus on the past decade. Chemical Engineering Journal. 2017 Jan;308:438–62. Doi: https://doi.org/10.1016/j.cej.2016.09.029.

18. Abbou B, Lebkiri I, Ouaddari H, Kadiri L, Ouass A, Habsaoui A, et al. Removal of Cd(II), Cu(II), and Pb(II) by adsorption onto natural clay: a kinetic and thermodynamic study. Turk J Chem. 2021;45:362–76. Doi: https://doi.org/10.3906/kim-2004-82.

19. Arbaoui F, Boucherit MN. Comparison of two Algerian bentonites: Physico-chemical and retention capacity study. Applied Clay Science. 2014 Apr;91–92:6–11. Doi: https://doi.org/10.1016/j.clay.2014.02.001.

20. Besq A, Malfoy C, Pantet A, Monnet P, Righi D. Physicochemical characterisation and flow properties of some bentonite muds. Applied Clay Science. 2003 Oct;23(5–6):275–86. Doi: https://doi.org/10.1016/S0169-1317(03)00127-3.

21. Sadki H, Ziat K, Saidi M. Adsorption of dyes on activated local clay in aqueous solution. J Mater Environ Sci. 2014;5(1):2060-5.

22. Ouaddari H, Karim A, Achiou B, Saja S, Aaddane A, Bennazha J, et al. New low-cost ultrafiltration membrane made from purified natural clays for direct Red 80 dye removal. Journal of Environmental

Chemical Engineering. 2019 Aug;7(4):103268. Doi: https://doi.org/10.1016/j.jece.2019.103268.

23. Essaadaoui Y, Lebkiri A, Rifi EH, Kadiri L, Ouass A. Adsorption of cobalt from aqueous solutions onto Bark of Eucalyptus. Mediterr J Chem. 2018 Sep 15;7(2):145–55. Doi: https://doi.org/10.13171/mjc72/01808150945-essaadaoui.

24. Ouaddari H, Beqqour D, Bennazha J, El Amrani I-E, Albizane A, Solhy A, et al. Natural Moroccan clays: Comparative study of their application as recyclable catalysts in Knoevenagel condensation. Sustainable Chemistry and Pharmacy. 2018 Dec;10:1–8. Doi: https://doi.org/10.1016/j.scp.2018.07.003.

25. Bedelean H, Măicăneanu A, Burcă S, Stanca M. Removal of heavy metal ions from wastewaters using natural clays. Clay miner. 2009 Dec;44(4):487–95. Doi: https://doi.org/10.1180/claymin.2009.044.4.487.

26. Mobarak M, Selim AQ, Mohamed EA, Seliem MK. A superior adsorbent of CTAB/H_2O_2 solution−modified organic carbon rich-clay for hexavalent chromium and methyl orange uptake from solutions. Journal of Molecular Liquids. 2018 Jun;259:384–97. Doi: https://doi.org/10.1016/j.molliq.2018.02.014.

27. Adebowale KO, Olu-Owolabi BI, Chigbundu EC. Removal of Safranin-O from Aqueous Solution by Adsorption onto Kaolinite Clay. JEAS. 2014;04(03):89–104. Doi: https://doi.org/10.4236/jeas.2014.43010.

28. Bentahar Y, Hurel C, Draoui K, Khairoun S, Marmier N. Adsorptive properties of Moroccan clays for the removal of arsenic(V) from aqueous solution. Applied Clay Science. 2016 Jan;119:385–92. Doi: https://doi.org/10.1016/j.clay.2015.11.008.

29. Chinoune K, Bentaleb K, Bouberka Z, Nadim A, Maschke U. Adsorption of reactive dyes from aqueous solution by dirty bentonite. Applied Clay Science. 2016 Apr;123:64–75. Doi: https://doi.org/10.1016/j.clay.2016.01.006.

30. Eloussaief M, Kallel N, Yaacoubi A, Benzina M. Mineralogical identification, spectroscopic characterization, and potential environmental use of natural clay materials on chromate removal from aqueous solutions. Chemical Engineering Journal. 2011 Apr;168(3):1024–31. Doi: https://doi.org/10.1016/j.cej.2011.01.077.

31. Gourouza M, Zanguina A, Natatou I, Boos A. Characterization of a mixed clay Niger. Revue CAMES—Sciences et Structure de la Matière. 2013;1:29–39.

32. Madejová J, Pálková H. NIR Contribution to The Study of Modified Clay Minerals. In: Developments in Clay Science [Internet]. Elsevier; 2017 [cited 2021 May 12]. p. 447–81. Available from: https://linkinghub.elsevier.com/retrieve/pii/B9780081003558000138

33. Sing KSW, Everett DH, Haul RAW, Moscou L, Pierotti RA, Rouquerol J, et al. Reporting physisorption data for gas/solid systems with special reference to the determination of surface area and porosity (Recommendations 1984). Pure Appl Chem. 1985 Jan 1;57(4):603–19. Doi: https://doi.org/10.1351/pac198557040603.

34. Gopal Reddi MR, Gomathi T, Saranya M, Sudha PN. Adsorption and kinetic studies on the removal of chromium and copper onto Chitosan-g-maliec anhydride-g-ethylene dimethacrylate. International Journal of Biological Macromolecules. 2017 Nov;104:1578–85. Doi: https://doi.org/10.1016/j.ijbiomac.2017.01.142.

35. Dincer A, Gunes Y, Karakaya N, Gunes E. Comparison of activated carbon and bottom ash for removal of reactive dye from aqueous solution. Bioresource Technology. 2007 Mar;98(4):834–9. Doi: https://doi.org/10.1016/j.biortech.2006.03.009.

36. Kaya A, Ören AH. Adsorption of zinc from aqueous solutions to bentonite. Journal of Hazardous Materials. 2005 Oct;125(1–3):183–9. Doi: https://doi.org/10.1016/j.jhazmat.2005.05.027.

37. Ozdes D, Duran C, Senturk HB. Adsorptive removal of Cd(II) and Pb(II) ions from aqueous solutions by using Turkish illitic clay. Journal of Environmental Management. 2011 Dec;92(12):3082–90. Doi: https://doi.org/10.1016/j.jenvman.2011.07.022.

38. Lagrergen S. Zur theorie der sogenannten adsorption gelöster stoffe kungliga svenska vetenskapsakademiens. Handlingar. 1898;24(4):1–39.

39. Gurses A, Dogar C, Yalcin M, Acikyildiz M, Bayrak R, Karaca S. The adsorption kinetics of the cationic dye, methylene blue, onto clay. Journal of Hazardous Materials. 2006 Apr 17;131(1–3):217–28. Doi: https://doi.org/10.1016/j.jhazmat.2005.09.036.

40. Gupta S, Babu BV. Removal of toxic metal Cr(VI) from aqueous solutions using sawdust as

adsorbent: Equilibrium, kinetics and regeneration studies. Chemical Engineering Journal. 2009 Aug 1;150(2–3):352–65. Doi: https://doi.org/10.1016/j.cej.2009.01.013.

41. Abbas M, Kaddour S, Trari M. Kinetic and equilibrium studies of cobalt adsorption on apricot stone activated carbon. Journal of Industrial and Engineering Chemistry. 2014 May;20(3):745–51. Doi: https://doi.org/10.1016/j.jiec.2013.06.030.

42. Saeed A, Sharif M, Iqbal M. Application potential of grapefruit peel as dye sorbent: Kinetics, equilibrium and mechanism of crystal violet adsorption. Journal of Hazardous Materials. 2010 Jul;179(1–3):564–72. Doi: https://doi.org/10.1016/j.jhazmat.2010.03.041.

43. Langmuir I. The Adsorption of Gases on Plane Surfaces of Glass, Mica And Platinum. J Am Chem Soc. 1918 Sep;40(9):1361–403. Doi: https://doi.org/10.1021/ja02242a004.

44. Obayomi KS, Auta M. Development of microporous activated Aloji clay for adsorption of lead (II) ions from aqueous solution. Heliyon. 2019 Nov;5(11):e02799. Doi: https://doi.org/10.1016/j.heliyon.2019.e02799.

45. Freundlich H. Über die Adsorption in Lösungen. Zeitschrift für Physikalische Chemie [Internet]. 1907 Jan 1 [cited 2021 May 12];57U(1). Available from: https://www.degruyter.com/document/doi/10.1515/zpch-1907-5723/html.

46. Tempkin M, Pyzhev V. Kinetics of ammonia synthesis on promoted iron catalyst. Acta Phys Chim USSR. 1940;12(1):327.

47. Ouass A, Ismi I, Elaidi H, Lebkiri A, Cherkaoui M, Rifi EH. Mathematical Modeling Of The Adsorption Of Trivalent Chromium By The Sodium Polyacrylate Beads. J Mater Environ Sci. 2017;8(10):3448–56. URL: https://www.jmaterenvironsci.com/Document/vol8/vol8_N10/363-JMES-2585-Ouass.pdf.

48. Benguella B, Yacouta-Nour A. Elimination des colorants acides en solution aqueuse par la bentonite et le kaolin. Comptes Rendus Chimie. 2009 Jun;12(6–7):762–71. Doi: https://doi.org/10.1016/j.crci.2008.11.008.

49. Lebkiri I, Abbou B, Kadiri L, Ouass A, Essaadaoui Y, Habssaoui A, et al. Removal of methylene blue dye from aqueous solution using a superabsorbant hydrogel the polyacrylamide: isotherms and kinetic studies. Mediterr J Chem. 2019 Nov 25;9(5):337–46. Doi: https://doi.org/10.13171/mjc941911251089il.

50. Qiu W, Zheng Y. Removal of lead, copper, nickel, cobalt, and zinc from water by a cancrinite-type zeolite synthesized from fly ash. Chemical Engineering Journal. 2009 Jan;145(3):483–8. Doi: https://doi.org/10.1016/j.cej.2008.05.001.

51. Yavuz Ö, Altunkaynak Y, Güzel F. Removal of copper, nickel, cobalt and manganese from aqueous solution by kaolinite. Water Research. 2003 Feb;37(4):948–52. Doi: https://doi.org/10.1016/S0043-1354(02)00409-8.

52. Rao RAK, Kashifuddin M. Adsorption studies of Cd(II) on ball clay: Comparison with other natural clays. Arabian Journal of Chemistry. 2016 Nov;9:S1233–41. Doi: https://doi.org/10.1016/j.arabjc.2012.01.010.

53. Unuabonah EI, Adebowale KO, Olu-Owolabi BI, Yang LZ. Comparison of sorption of Pb^{2+} and Cd^{2+} on Kaolinite clay and polyvinyl alcohol-modified Kaolinite clay. Adsorption. 2008 Dec;14(6):791–803. Doi: https://doi.org/10.1007/s10450-008-9142-9.

54. Alvarez-Ayuso E, Garcia-Sanchez A. Removal of cadmium from aqueous solutions by palygorskite. Journal of Hazardous Materials. 2007 Aug 17;147(1–2):594–600. Doi: https://doi.org/10.1016/j.jhazmat.2007.01.055.

55. Ulmanu M, Marañón E, Fernández Y, Castrillón L, Anger I, Dumitriu D. Removal of Copper and Cadmium Ions from Diluted Aqueous Solutions by Low Cost and Waste Material Adsorbents. Water, Air, and Soil Pollution. 2003;142(1/4):357–73. Doi: https://doi.org/10.1023/A:1022084721990.

56. Jiang M, Jin X, Lu X-Q, Chen Z. Adsorption of Pb(II), Cd(II), Ni(II) and Cu(II) onto natural kaolinite clay. Desalination. 2010 Mar;252(1–3):33–9. Doi: https://doi.org/10.1016/j.desal.2009.11.005.

JOTCSA Journal of the Turkish Chemical Society Section: A Chemistry

TURKISH CHEMICAL SOCIETY

Residual Determination of Multiple Pesticides in Vegetable Samples by LC-MS/MS Coupled with Modified QuEChERS-dSPE Ionic Liquid-Based DLLME Method

Abubakar Lawal [1,2*] and Kah Hin Low [1]

[1] Department of Chemistry, University of Malaya, Kuala Lumpur, Malaysia.
[2] Department of Pure and Industrial Chemistry, Umaru Musa Yar'adua University Katsina, Nigeria.

Abstract: As a matter of fact, the Dietary Guidelines of the United States of America recommended the consumption of more fruits and vegetables to support the healthy condition of the body. Unfortunately, these food materials are being accumulated with pesticidal residues due to the continuous miss-management and excessive application of the chemicals during pre and post-agricultural practices, which compels multiple analysis of pesticidal residues to know their concentration levels for the betterment of food security and safety. For that matter, multi-residues of Thiamethoxam, Propamocarb, Carbaryl, Metalaxyl, Baycarb, Thiobencarb, Diazinon, and Dursban pesticides were determined in the samples of lettuce, garlic, ginger, and bell-pepper using modified QuEChERS-dSPE Ionic Liquid-based dispersive liquid-liquid microextraction (DLLME) method coupled with LC-MS/MS instrument and validated (European Union Guideline). Resultantly, the accuracy (87-127%) and precision (0–22%) were mostly within the acceptable range for the former (70-120%) and latter (≤20%). Meanwhile, the limit of detections (0.01-0.28 µg/kg) and limit of quantitations (0.03-0.93 µg/kg) were satisfactory. The concentration range (5–400 µg/kg) of calibration curves for the evaluated linearity were linear with coefficient of regressions greater than 0.99. The matrix effects for all the analyzed samples were very weak and less effective (≤ -86%). The range (1–25%) for the estimated measurement uncertainties were certifiable and acceptable (≤ 50%). Therefore, the sample preparation method prove effective as validated and useful for the multiple determination of pesticides residues in the analyzed vegetable samples, which are presumably safe for consumption against health issues.

Keywords: Pesticide residues; fruits and vegetables; QuEChERS-dSPE and DLLME cleanups; ionic liquid-based; liquid chromatography tandem mass spectrometry.

Submitted: December 24, 2020. **Accepted:** May 20, 2021.

Cite this: Lawal A, Low KH. Residual Determination of Multiple Pesticides in Vegetable Samples by LC-MS/MS Coupled with Modified QuEChERS-dSPE Ionic Liquid-Based DLLME Method. JOTCSA. 2021;8(2):693–704.

DOI: https://doi.org/10.18596/jotcsa.845578.

***Corresponding Author. E-mail:** abubakarlawal360@yahoo.com.

INTRODUCTION

Fruit and vegetable foods are one of the bases that constitute healthy diets worldwide, playing vital roles nutritionally for the attainment of a healthy life (1). Moreover, fresh fruits and vegetables provide dietary fibers, carbohydrate, vitamins (particularly vitamin C), minerals (particularly electrolytes), and bioactive compounds (2-4). The bioactive compounds include phytochemicals, which possesses antioxidant, phytoestrogen activities and anti-inflammatory agents (5,6). Moreover, the dietary fibers supplied by these foods prevent gastrointestinal cancers and contribute to lowering the cholesterol level in the blood (cholesterolemia) (7). Consequently, reducing the high peril of cardiovascular diseases and the reduction of high risks of obesity (8,9).

Meanwhile, the derived nutrients and biological compounds in fruits and vegetables depend on nature, size, geographical locations they were cultivated (10). In the year 2010, it was recommended by the Dietary Guidelines of the United States of America suggested that one-half of a person's plate of food should contain fruits and vegetables (11). Unfortunately, the percentage of nutrients in fruits and vegetables has been decreasing over the years due to soil depletion of essential materials caused by intensive modern agricultural techniques (12,13), which results in consumption of more fruits and vegetables to support the healthy condition of the body (11).

Notwithstanding, the fresh vegetables and fruits of today have been accumulated with pesticide residues because of the continuous miss-management and excessive application of pesticides during pre and post-agricultural practices (14-17). For example, the triazole fungicides, carbamates, pyrethroids, and organochlorine pesticides (OCPs) are most well-known for controlling pests in vegetables and fruits (18-20). This could lead to disastrous health-related issues such as different forms of cancer and congenital disabilities (1). Based on these facts, the food quality controllers and the analytical scientists have periodically analyzed the concentration levels of pesticides residue in vegetable and fruit samples using conventional methods and instruments such as gas and liquid chromatography.

Illustratively, the conventional methods include liquid-liquid extraction (LLE), solid phase extraction (SPE) and liquid phase microextraction (LPME) (20). Unfortunately, most of the methods possess poor selectivity. Meanwhile, many detectors such as diode array, photodiode array and mass spectrometry instrumentally possesses poor sensitivity towards targeted analytes because most of the instruments were operated at default settings lacking optimization (21). Fortunately, the recent reports suggested the use of a modified quick, easy, cheap, effective, rugged, and safe (QuEChERS)-dispersive SPE (dSPE) coupled with LPME as dispersive liquid-liquid microextraction (DLLME) technique instrumented with an optimized liquid chromatography tandem mass spectrometry (LC-MS/MS) for analysis of multiple pesticidal residues in fruits and vegetables (15, 21). Also, the optional used of 1-hexyl-3-methylimidazolium hexafluorophosphate ([C_6MIM][PF_6]) ionic liquid-based in the DLLME technique increases the extraction efficiency and chromatographic properties of the analysis (22, 23).

Therefore, this study was aimed to determine the multi-pesticide residues of Thiamethoxam, Propamocarb, Carbaryl, Metalaxyl, Baycarb, Thiobencarb, Diazinon, and Dursban (Figure 1) in some selected sample of vegetables. The analyses were carried out using the modified QuEChERS-dSPE Ionic Liquid-based DLLME coupled with optimized LC-MS/MS method revealed by Lawal et al. (15) and Lawal, et al. (21). It is hoped that this study will serve as a reference guide for the future studies of pesticide residues in other vegetable samples to provide betterment of food security and safety.

MATERIALS AND METHODS

Chemicals and Reagents

The pesticidal standards (100 mg/kg) for Thiamethoxam, Propamocarb, Carbaryl, Metalaxyl, Baycarb, Thiobencarb, Diazinon, and Dursban were obtained from AccuStandard® (New Haven, USA) and were later diluted to 0.1 mg/kg (100 µg/kg) with estimated volume of methanol, respectively. Meanwhile, the LC-MS grade organic solvents were used for this research work. The solvents include methanol and ACN (Merck, Germany), acetic acid (HOAc), and formic acid were obtained from Fisher Scientific. The Millipore-filtered (deionized) water was obtained using Merck Millipore water purification system (Billerica, USA). The ProElut™ AOAC 2007.01 QuEChERS-dSPE kits for general vegetables and fruits were obtained from Dikma Technologies Inc. (Lake Forest, USA), as well as the molten salt (HPLC grade) of [C_6MIM][PF_6] ionic liquid-based (P ≥ 97.0%) was purchased from Sigma-Aldrich, (Germany).

Apparatus and Equipments

The 2, 15, and 50 mL polypropylene centrifuge tubes by LabServ Fisher-Scientific (Kuala Lumpur, Malaysia), and 100 and 500 µL microsyringes were obtained from Agilent (Australia). The HPLC autosampler vials were purchased from Agilent Technologies (USA) and other equipments such as Dynamica refrigerated centrifuge by CNG instruments (Selangor, Malaysia), vortexer VTX-3000L by Copens Scientific (Tokyo, Japan) and glass jug blender MX-GX1581WSK (Panasonic, Malaysia) and Supelco HPLC column [Ascentis® Express C_{18} (5 cm x 2.1 mm, 2.7 µm)] (Sigma-Aldrich, USA). The others include weighing balance (Sartorius Technology Park, Germany), pH meter PB (Sartorius group, Germany) and Agilent triple quadrupole LC/MS G6490A [built in Electrosprays ESI (±) MS/MS Sensitivity and Jet stream Technology] instrument (Singapore).

Conditioning the LC-MS/MS Instrument

The setup for contributory factors of the LC-MS/MS instrument were optimized. These include; analyte injection volume (5 µL), column temperature (30 ºC), flow rate (0.1 mL/min), gas temperature (200 ºC), gas flow (14 L/min), nebulizer gas (45 psi), sheath gas temperature (400 ºC), sheath gas flow

(11 L/min), capillary voltage (3000 V) and delta$^{(+)}$ EMV (200 V). The factors were used for the determination of optimum fragmentary voltage and the four-fragmentary product ions with their respective retention time (RT) and collision energy (CE) by the Auto-tuning and Mass-Hunter instrumental optimization using 1 mg/kg multi-pesticides mixture of standard solutions (Table 1) and the total ion chromatography (TIC) were highlighted (Figure 2). Moreover, the setup was also used for the estimated gradient (elution) time for the mobile phase-B at 15% (0 - 1.6 min), 15 – 100% (1.6 – 10.4 min), and 100 – 15% (10.4 – 12 min) at the pressure of 600 bar. Moreover, the mobile phase-B (acetonitrile + 0.1% formic acids) and "A" (deionized water + 0.1% formic acid) instrumentally started from 15 and 85%, respectively, and transported through the column by a stream of nitrogen gas after the column was injected with 5 µL analyte solution.

Sample Treatment and QuEChERS-dSPE Ionic Liquid-based DLLME Method

The 250 g for each of the purchased vegetable (Petaling Jaya, Malaysia) samples of lettuce, garlic, ginger and bell-pepper were homogenized, and refrigerated (reserved) at 4 °C. The methodological procedure occurred by transferring 20 g for each of the homogenized vegetable sample into 50 mL centrifuge tube and the content was spiked with 200 µL of 100 µg/kg multi-pesticides mixture of standard solutions. 1% HOAc in 15 mL ACN was added before covering and vortexing the tube for 1 min. A sachet of QuEChERS extraction salt was added to the tube's content, covered, shaken vigorously (1 min) and centrifuged (4000 rpm) for 2 min. 1 mL supernatant was transferred into 2 mL centrifuge tube that was occupied with a sachet of the cleanup agent. The tube was centrifuged (4000 rpm) for 5 min after vortexing it for 30 sec. Subsequently, the resulted supernatant from the d-SPE cleanup was transferred into 15 mL centrifuge tube containing 10% NaCl in 9 mL of Milli-Q-water. The tube was covered, shaken vigorously (1 min) and centrifuged (7000 rpm) for 5 min after addition of 130 µL ionic liquid-based. Then, the 100 µL [C_6MIM][PF_6] ionic liquid-based extract was diluted with 400 µL of methanol (1:5) in 2 mL HPLC auto-sampler vial and vortexed for 1 min and the solution was analyzed with LC-MS/MS instrument. Consequently, the sum of the resulted total chromatographic peak areas (TCPAs) of the multiple reaction monitoring (MRM) scans for each of the analyte was used as an index that correspond to the concentration levels of analytes quantified in the analyzed samples (24).

Similarly, results were obtained for the construction of calibration curves and validation studies for each analyte respectively using parts of the refrigerated samples, weighed equally and spiked serially with estimated volumes of analyte mixture of standard solutions to provide equivalent known concentrations.

Validation Studies of Sample Treatment Method

The sample treatment method for the analysis of multiple pesticides residues was validated to express its effectivity, desirability and certification (25). The method was validated using the European Union Guideline (26) that include; accuracy (relative recovery) and precision (relative standard deviation) were estimated using triple concentration levels (5, 100 and 300 µg/kg) and the samples were analyzed in triplicates (n=3), the limit of detections (LODs) and limit of quantitations (LOQs) were correspondingly estimated to 3 and 10 factors of signal-to-noise ratio respectively (27), the calibration curve for each analyte was used for the estimation of linearity based on the regression coefficient (R^2) at five spiked concentration levels ranging 5 – 400 µg/kg, the matrix effect (ME) was also estimated mathematically using the calibration curves (Equation 1) and ultimately, the empirical model and coverage factor (k=2) were used for the estimation of measurement uncertainties (MU) at 95% confidence level (28).

$$ME(\%)=\left[\left(\frac{\text{Slope of calibration curve for analyte in matrix}}{\text{Slope of calibration curve for analyte in ACN}}\right)-1\right]\times 100 \quad \text{(Eq. 1)}$$

RESULTS AND DISCUSSION

The modified QuEChERS-dSPE Ionic Liquid-based DLLME method was successfully validated based on the parameters that include relative recoveries (RRs), relative standard deviations (RSDs), LODs, LOQs, R^2, ME and MU. However, 98 and 99% of the RR (87 - 127%) and RSDs (3 - 22%) tabulated in Table 2 were within the recommended guideline (70 – 120%) value (26) and conforms to the report of Nantia et al. (29). The range results of 0.01-0.28 and 0.03-0.93 µg/kg for LODs and LOQs (Table 3) respectively were excellent and lower that than the least concentration of the calibration curve (5 µg/kg) and European Union maximum residue limits (EU-MRLs) recommendation (30). The R^2 obtained were linear and greater than 0.99 value as indicated in Table 4. The results were similar to the documentation of Camino-Sánchez et al. (31) and Lawal et al. (32). Table 4 also shows that the method's performance capability (matrix effect) against matrix inferences towards recovery

of analytes is very strong i.e. the matrix effects for all the analyzed samples were very weak, less effective (≤ -86) as referenced by the guideline; suppression (-20%) or enhancement (20%) of analytes' recovery, which could be attributed to the excessive cleanup of matrix interferences by the modified sample preparation method. Moreover, the matrix effect results were in line with the recent reports on the analysis of fruits and vegetables (1, 15, 21). The recommended range (50%) for the measurement uncertainties (MU) supported the obtained results (Table 4) range estimated (1 – 25%). Eventually, the modified QuEChERS-dSPE Ionic Liquid-based DLLME sample treatment method coupled with the LC-MS/MS instrumentation were reliably and credibly used for quantitative analysis of the unspiked (reserved) vegetable samples and most of the analytes detected (Table 5) were lower than the LOQ and the EU-MRLs.

CONCLUSION

The determination of the multi-pesticide residues were successfully carried out in the samples of lettuce, garlic, ginger, and bell-pepper using modified QuEChERS-dSPE Ionic Liquid-based DLLME method. The extraction method efficiently cleanup the matrix interferences toward improving the detectability, selectivity and recovery of the targeted analytes using the sensitive instrument for better determination and recovery of the targeted analytes. Consequently, the sample preparation and instrumentation techniques proved reliable and successfully used for multi-residue determination of pesticides in lettuce, garlic, ginger, and bell-pepper samples. What is more, the obtained results for their concentration levels were less than the EU-MRLs, which presumed the safe consumption of the vegetables from the sampled area.

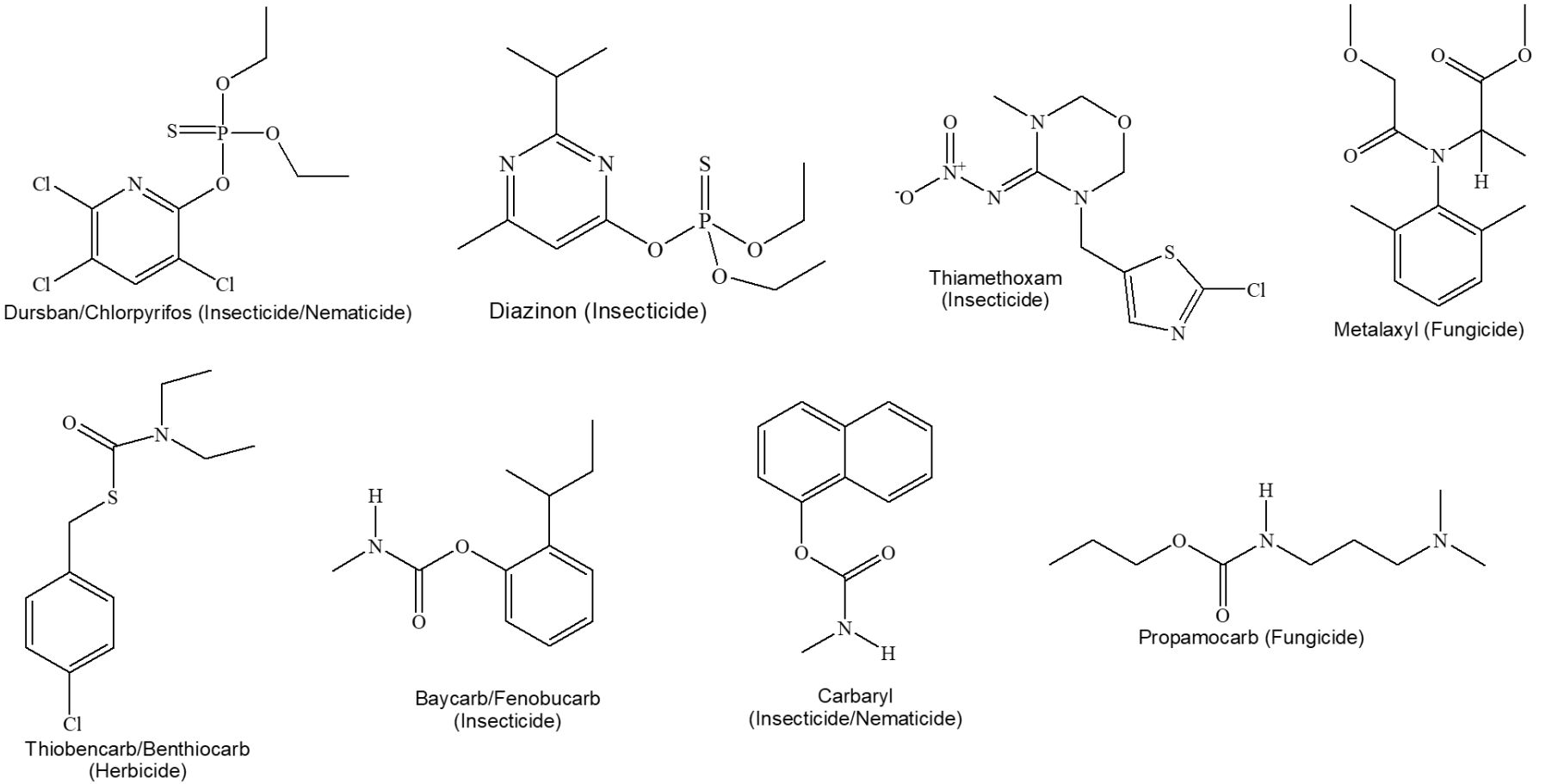

Figure 1: The Structures of the analyzed residue of pesticides

Table 1: The Mass-Hunter and auto-tuned optimization for setup of the LC-MS/MS instrument

No.	Pesticides	Molecular Formula	Pesticide Type	Ionization Mode	Precursor Ion, m/z	Product Ions (m/z)	Collision Energies (eV)	RT_1;RT_2 (min)
8	Dursban	$C_9H_{11}Cl_3NO_3PS$	Insecticide/Nematicide	$[M+H]^+$	350	97;198	34;22	11.36;11.36
7	Diazinon	$C_{12}H_{21}N_2O_3PS$	Insecticide	$[M+H]^+$	305	97;169	42;22	10.22;10.22
6	Thiamethoxam	$C_8H_{10}ClN_5O_3S$	Insecticide	$[M+H]^+$	292	132;211	26;10	2.68;2.68
5	Metalaxyl	$C_{15}H_{21}NO_4$	Fungicide	$[M+H]^+$	280	160;220	26;10	7.33;7.33
4	Thiobencarb	$C_{12}H_{16}ClNOS$	Herbicide	$[M+H]^+$	258	89;125	54;26	10.34;10.34
3	Baycarb	$C_{12}H_{17}NO_2$	Insecticide	$[M+H]^+$	208	77;95	42;10	8.34;8.34
2	Carbaryl	$C_{12}H_{11}NO_2$	Insecticide/Nematicide	$[M+H]^+$	202	127;145	30;6	7.16;7.16
1	Propamocarb	$C_9H_{20}N_2O_2$	Fungicide	$[M+H]^+$	189	74;102	26;14	1.36;1.36

No., identified pesticide analyte on the TIC chart

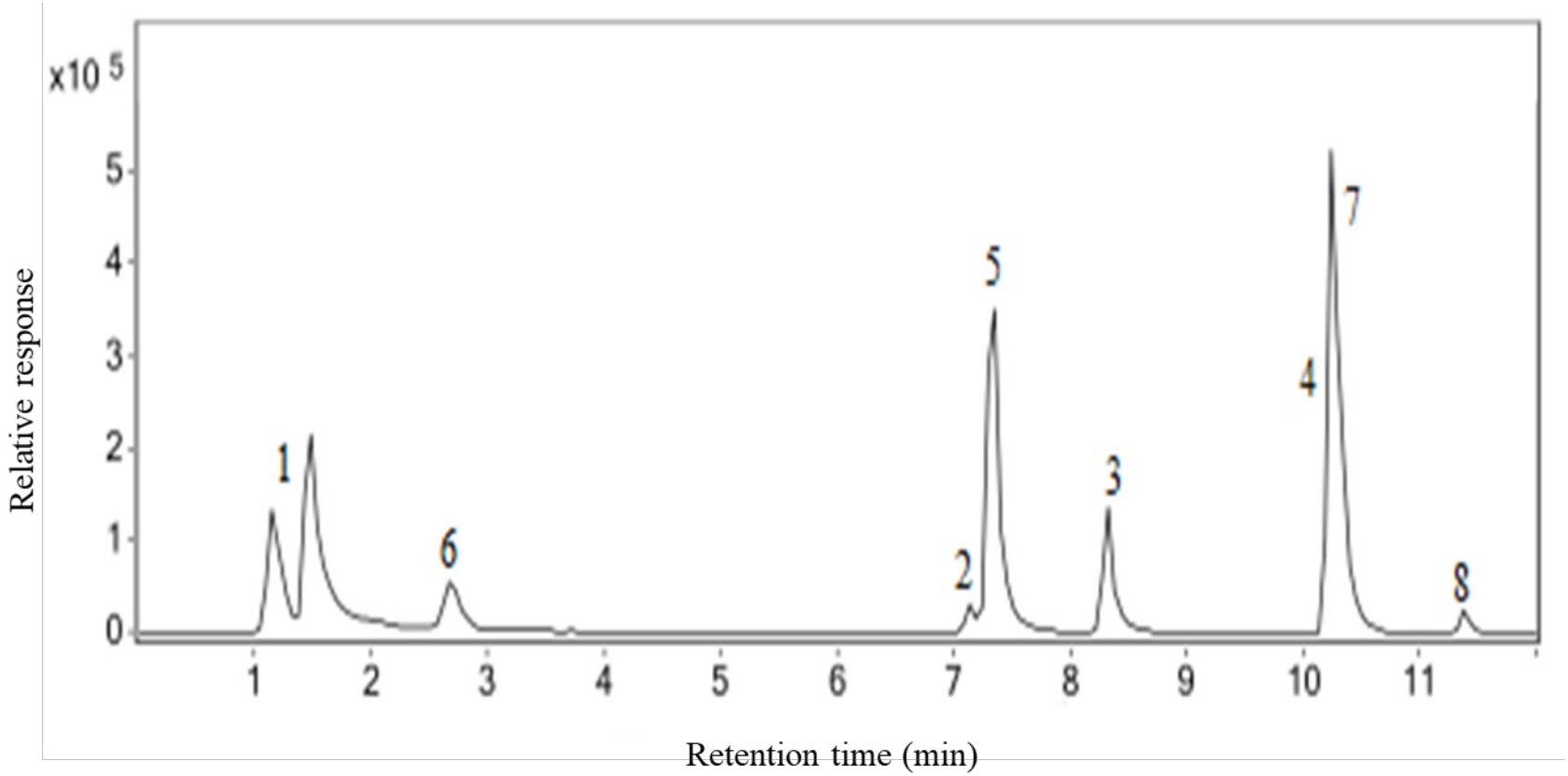

Figure 2: The TIC chart of the multi-pesticide analytes.

Table 2: The accuracies, precisions at three concentration levels for the analyzed samples.

Pesticides		**Lettuce**		**Garlic**		**Ginger**		**Bell-pepper**	
	Spike (μg/kg)	RR (%)	RSD (%)	RR (%)	RSD (%)	RR (%)	RSD (%)	RR (%)	RSD (%)
Durban	5	99	6	111	6	106	2	108	6
	100	99	6	100	5	100	0	96	5
	300	99	4	99	10	100	13	101	7
Diazinon	5	100	4	103	5	99	2	105	4
	100	101	4	97	7	101	4	99	3
	300	100	6	97	4	101	4	99	4
Thiamethoxam	5	111	7	103	7	100	2	91	4
	100	102	4	99	2	104	1	99	3
	300	99	5	99	8	96	1	100	5
Metalaxyl	5	91	6	102	3	87	0	101	10
	100	99	7	98	12	100	11	99	12
	300	100	22	100	11	101	8	100	16
Thiobencarb	5	88	11	100	7	102	5	91	3
	100	100	4	102	8	101	3	101	4
	300	101	5	98	1	101	3	98	3
Baycarb	5	112	4	106	2	124	0	102	2
	100	99	5	101	3	99	0	100	3
	300	100	5	97	2	99	1	100	4
Carbaryl	5	95	6	101	6	94	1	98	3
	100	101	6	99	4	99	4	100	2
	300	100	4	99	8	99	15	101	11
Propamocarb	5	106	6	106	5	127	3	92	5
	100	101	3	99	4	101	1	103	5
	300	100	4	100	2	99	17	100	3
Ranges	5-300	88-112	3-22	97-111	1-12	87-127	0-17	91-108	2-16

Table 3: The pesticides detection and quantitation limits for the analyzed samples.

	Lettuce		**Garlic**		**Ginger**		**Bell-pepper**	
	LOD (μg/kg)	LOQ (μg/kg)	LOD (μg/kg)	LOQ (μg/kg)	LOD (μg/kg)	LOQ (μg/kg)	LOD (μg/kg)	LOQ (μg/kg)
Dursban	0.05	0.17	0.08	0.28	0.01	0.03	0.11	0.37
Diazinon	0.03	0.12	0.20	0.66	0.10	0.33	0.08	0.27
Thiamethoxam	0.09	0.29	0.05	0.18	0.28	0.93	0.05	0.18
Metalaxyl	0.05	0.17	0.08	0.26	0.08	0.27	0.04	0.13
Thiobencarb	0.05	0.17	0.11	0.36	0.07	0.23	0.10	0.33
Baycarb	0.02	0.07	0.16	0.53	0.06	0.21	0.03	0.09
Carbaryl	0.05	0.15	0.07	0.22	0.10	0.32	0.04	0.12
Propamocarb	0.06	0.19	0.02	0.07	0.10	0.33	0.07	0.23
Ranges	0.02-0.09	0.07-0.29	0.02-0.20	0.07-0.66	0.01-0.28	0.03-0.93	0.03-0.11	0.09-0.37

Table 4: The linearity of regression coefficient, matrix effects and measurement uncertainties for the analyzed samples.

Pesticides	**Lettuce**			**Garlic**			**Ginger**			**Bell-pepper**		
	R^2	ME (%)	MU (%)	R^2	ME (%)	MU (%)	R^2	ME (%)	MU (%)	R^2	ME (%)	MU (%)
Dursban	0.9998	-91	11	0.9996	-98	14	0.9999	-91	10	0.9994	-86	12
Diazinon	0.9999	-97	9	0.9986	-98	11	0.9996	-100	7	0.9996	-96	7
Thiamethoxam	0.9996	-100	11	0.9998	-100	11	0.9973	-100	3	0.9999	-100	8
Metalaxyl	0.9999	-99	23	0.9997	-99	17	0.9998	-100	13	0.9998	-100	25
Thiobencarb	0.9999	-96	13	0.9995	-98	11	0.9997	-98	7	0.9996	-93	7
Baycarb	0.9998	-98	9	0.9990	-96	5	0.9996	-97	1	0.9999	-88	6
Carbaryl	0.9999	-100	11	0.9997	-100	12	0.9996	-100	13	0.9999	-100	11
Propamocarb	0.9998	-100	9	0.9999	-100	7	0.9994	-100	14	0.9998	-100	9
Ranges	> 0.999	≤ -91	≤ 23	> 0.99	≤ -96	≤ 17	> 0.99	≤ -91	≤ 14	> 0.999	≤ -86	≤ 25

Table 5: The pesticides residues in the analyzed samples.

	Lettuce		**Garlic**		**Ginger**		**Bell-pepper**	
	RC (μg/kg)	EU-MRL (μg/kg)	RC (μg/kg)	EU-MRL (μg/kg)	RC (μg/kg)	EU-MRL (μg/kg)	RC (μg/kg)	EU-MRL (μg/kg)
Dursban	< LOQ	10	< LOQ	200	95.99±3.1	3000	< LOQ	10
Diazinon	< LOQ	50	< LOQ	20	7.34±2.4	10	< LOQ	50
Thiamethoxam	9.03±1.2	20	< LOQ	10	178.30±7	300	393±4.1	700
Metalaxyl	< LOQ	1000	< LOQ	500	13.41±1.0	100	< LOQ	50
Thiobencarb	< LOQ	100	8.50±2.5	10	9.41±1.0	10	< LOQ	10
Baycarb	< LOQ	10	< LOQ	10	< LOQ	10	< LOQ	10
Carbaryl	7.23±1.2	10	12.06±1.1	20	6.83±2.1	10	8.29±2.5	10
Propamocarb	4.15±0.5	700	< LOQ	2000	45.06±0.5	50	< LOQ	3000

ACKNOWLEDGMENT

The Postgraduate Research Project (IPPP), University of Malaya Kuala Lumpur, Malaysia (PG 174-2014B) is acknowledged for the support rendered.

CONFLICT OF INTEREST

The authors of this research agreed with no conflicts of interest.

REFERENCES

1. Lawal A, Koki IB. Determination of multi - pesticide residues in coconut water by QuEChERS - dSPE ionic liquid - based DLLME couple with high performance Liquid Chromatography - Tandem Mass Spectrometry (LCMS/MS). ChemSearch J. 2019;10(1):87–93. Url: https://www.ajol.info/index.php/csj/article/view/187964.

2. Koki IB, Lawal A, Taqui SN. Source identification and evaluation of surface water quality using factor and discriminant analysis. Bayero J Pure App Sci. 2019 May 9;11(2):169. Doi: https://doi.org/10.4314/bajopas.v11i2.21.

3. Baba A, Garba ST, Bello HS. Bioremediation Potential of Immobilized corynebacterium kutsceri in the Treatment of Tannery Industrial Effluent from Challawa Industrial Estate, Kano State, Nigeria. Journal of the Turkish Chemical Society Section A: Chemistry. 2020 Mar 30;335–50. Doi: https://doi.org/10.18596/jotcsa.643771.

4. Lawal A. Comparative analysis on selected bulb species. Sokoto, Nigeria: Usmanu Danfodiyo University. 2011;

5. Slavin JL, Lloyd B. Health Benefits of Fruits and Vegetables. Advances in Nutrition. 2012 Jul 1;3(4):506–16. Doi: https://doi.org/10.3945/an.112.002154.

6. Özer Z. Chemical Composition and Antioxidant Activities of Leaf and Flower Essential Oils of Origanum onites L. Growing in Mount Ida-Turkey. JOTCSA. 2020 Oct 30;7(3):813–20. Doi: https://doi.org/10.18596/jotcsa.780334.

7. Lattimer JM, Haub MD. Effects of Dietary Fiber and Its Components on Metabolic Health. Nutrients. 2010 Dec 15;2(12):1266–89. Doi: https://doi.org/10.3390/nu2121266.

8. Lawal A, Matazu S. Comparative Studies of White and Red Allium cepa Cultivated in Sokoto, Nigeria. ChemSearch J. 2015;6(2):14–20. Url: https://www.ajol.info/index.php/csj/article/view/130149.

9. Lawal A, Tan G, Alsharif A. Edibility and Medicinal Studies of Crinum ornatum inComparison with Allium sativum. Pakistan J Nutr. 2015;14(11):773–81.

10. Roth RA. Nutrition & diet therapy. Eleventh edition. Clifton Park, NY: Delmar Cengage Learning; 2014. 604 p. Isbn: 978-1-133-96050-8.

11. Kaiser KA, Brown AW, Bohan Brown MM, Shikany JM, Mattes RD, Allison DB. Increased fruit and vegetable intake has no discernible effect on weight loss: a systematic review and meta-analysis. The American Journal of Clinical Nutrition. 2014 Aug 1;100(2):567–76. Doi: https://doi.org/10.3945/ajcn.114.090548.

12. Esther G, Newark N. Dirt Poor: Have Fruits and Vegetables become Less Nutritious [Internet]. Scientific American; 2015. Available from: http://www.scientificamerican.com/article/soil-depletion-and-nutrition-loss/

13. Landsman J. The untold fruit and vegetable scandal [Internet]. Naturalhealth365.com; 2016. Available from: http://www.naturalhealth365.com/produce_scandal.html/

14. Kaur P, Bedi J, Sharma A, Gill J. Occurrence of Pesticide Residues in Water Collected from Different Water Sources in Punjab (India). Journal of Veterinary Public Health. 2016;12(2):75–9.

15. Lawal A, Wong RCS, Tan GH, Abdulra'uf LB, Alsharif AMA. Multi-pesticide Residues Determination in Samples of Fruits and Vegetables Using Chemometrics Approach to QuEChERS-dSPE Coupled with Ionic Liquid-Based DLLME and LC–MS/MS. Chromatographia. 2018 May;81(5):759–68. Doi: https://doi.org/10.1007/s10337-018-3511-7.

16. Lawal A, Abdulra'uf LB. Chemometrics Approach to QuEChERS-dSPE for Multi-Standard Determination of Pesticides in Blank Samples of Milli-Q-Water Using High-Performance Liquid Chromatography-Tandem Mass Spectrometry (LC-MS/MS). ChemSearch J. 2020;11(1):66–73. Url: https://www.ajol.info/index.php/csj/article/view/197383.

17. Erdoğan G, Yilmaz İ. Determination of Some Pesticides Harmful To Environment and Human Health in Bogazköy(Turkey) Dam Water by LC-MS/MS. JOTCSA. 2020 Oct 18;801–12. Doi: https://doi.org/10.18596/jotcsa.749021.

18. Zhang Y, Zhang Y, Nie J, Jiao B, Zhao Q. Determination of Triazole Fungicide Residues in Fruits by QuEChERS Combined with Ionic Liquid-Based Dispersive Liquid-Liquid Microextraction: Optimization Using Response Surface Methodology. Food Anal Methods. 2016 Dec;9(12):3509–19. Doi: https://doi.org/10.1007/s12161-016-0548-9.

19. Lawal A, Wong RCS, Tan GH, Abdulra'uf LB, Alsharif AMA. Recent Modifications and Validation of QuEChERS-dSPE Coupled to LC–MS and GC–MS Instruments for Determination of Pesticide/Agrochemical Residues in Fruits and Vegetables: Review. Journal of Chromatographic Science. 2018 Aug 1;56(7):656–69. Doi: https://doi.org/10.1093/chromsci/bmy032.

20. Lawal A, Tan GH, Alsharif AMA. Recent Advances in Analysis of Pesticides in Food and Drink Samples Using

LPME Techniques Coupled to GC-MS and LC-MS: a Review. Journal of AOAC INTERNATIONAL. 2016 Nov 1;99(6):1383–94. Doi: https://doi.org/10.5740/jaoacint.16-0272.

21. Lawal A, Wong RCS, Tan GH, Abdulra'uf LB. Determination of Pesticide Residues in Fruit and Vegetables by High-Performance Liquid Chromatography–Tandem Mass Spectrometry with Multivariate Response Surface Methodology. Analytical Letters. 2019 Jan 22;52(2):231–48. Doi: https://doi.org/10.1080/00032719.2018.1459655.

22. Xie Q, Liu S, Fan Y, Sun J, Zhang X. Determination of phthalate esters in edible oils by use of QuEChERS coupled with ionic-liquid-based dispersive liquid–liquid microextraction before high-performance liquid chromatography. Anal Bioanal Chem. 2014 Jul;406(18):4563–9. Doi: https://doi.org/10.1007/s00216-014-7814-8.

23. Gunatilake SR, Kwon J-W, Mlsna TE, Xia K. A novel approach to determine estrogenic hormones in swine lagoon wastewater using the QuEChERS method combined with solid phase extraction and LC/MS/MS analysis. Anal Methods. 2014 Sep 23;6(23):9267–75. Doi: https://doi.org/10.1039/C4AY01804D.

24. Abdulra'uf LB, Tan GH. Chemometric approach to the optimization of HS-SPME/GC–MS for the determination of multiclass pesticide residues in fruits and vegetables. Food Chemistry. 2015 Jun;177:267–73. Doi: https://doi.org/10.1016/j.foodchem.2015.01.031.

25. Li M, Dai C, Wang F, Kong Z, He Y, Huang YT, et al. Chemometric-assisted QuEChERS extraction method for post-harvest pesticide determination in fruits and vegetables. Sci Rep. 2017 Mar;7(1):42489. Doi: https://doi.org/10.1038/srep42489.

26. SANTE-11813. Guidance document on analytical quality control and method validation procedures for pesticide residues and analysis in food and feed. European Commission; 2017.

27. Xiu-ping Z, Lin M, Lan-qi H, Jian-Bo C, Li Z. The optimization and establishment of QuEChERS-UPLC–MS/MS method for simultaneously detecting various kinds of pesticides residues in fruits and vegetables. Journal of Chromatography B. 2017 Aug;1060:281–90. Doi: https://doi.org/10.1016/j.jchromb.2017.06.008.

28. Kaczyński P. Large-scale multi-class herbicides analysis in oilseeds by rapid one-step QuEChERS-based extraction and cleanup method using liquid chromatography–tandem mass spectrometry. Food Chemistry. 2017 Sep;230:411–22. Doi: https://doi.org/10.1016/j.foodchem.2017.03.076.

29. Nantia EA, Moreno-González D, García-Campaña AM, Gámiz-Gracia L. High-Throughput Methodology for the Determination of Carbamates in Food Supplements by UHPLC–MS/MS. Chromatographia. 2017 Jan;80(1):63–70. Doi: https://doi.org/10.1007/s10337-016-3211-0.

30. Anonymous. Commission regulation. European Union; 2016.

31. Camino-Sánchez FJ, Zafra-Gómez A, Oliver-Rodríguez B, Ballesteros O, Navalón A, Crovetto G, et al. UNE-EN ISO/IEC 17025:2005-accredited method for the determination of pesticide residues in fruit and vegetable samples by LC-MS/MS. Food Additives & Contaminants: Part A. 2010 Nov;27(11):1532–44. Doi: https://doi.org/10.1080/19440049.2010.506602.

32. Lawal A. Experimental Designs of QuEChERS-Hexyl-Methylimidazolium Hexafluorophosphate Method Coupled With Liquid Chromatography-Mass Spectrometry for the Determination of Multiple Pesticides in Fruits and Vegetables [PhD THesis]. [Kuala Lumpur, Malaysia]: University of Malaya; 2018.